



THE UNIVERSITY OF QUEENSLAND
A U S T R A L I A

MODELLING OF RADIATING SHOCK LAYERS FOR
ATMOSPHERIC ENTRY AT EARTH AND MARS

By

Daniel F. Potter

A THESIS SUBMITTED TO THE UNIVERSITY OF QUEENSLAND
FOR THE DEGREE OF DOCTOR OF PHILOSOPHY
SCHOOL OF MECHANICAL AND MINING ENGINEERING
MAY 2011

Declaration by Author

This thesis is composed of my original work, and contains no material previously published or written by another person except where due reference has been made in the text. I have clearly stated the contribution by others to jointly-authored works that I have included in my thesis.

I have clearly stated the contribution of others to my thesis as a whole, including statistical assistance, survey design, data analysis, significant technical procedures, professional editorial advice, and any other original research work used or reported in my thesis. The content of my thesis is the result of work I have carried out since the commencement of my research higher degree candidature and does not include a substantial part of work that has been submitted to qualify for the award of any other degree or diploma in any university or other tertiary institution. I have clearly stated which parts of my thesis, if any, have been submitted to qualify for another award.

I acknowledge that an electronic copy of my thesis must be lodged with the University Library and, subject to the General Award Rules of The University of Queensland, immediately made available for research and study in accordance with the Copyright Act 1968.

I acknowledge that copyright of all material contained in my thesis resides with the copyright holder(s) of that material.

© Daniel F. Potter, 2010.

Typeset in L^AT_EX 2_&.

Statement of Contributions to Jointly Authored Works Contained in the Thesis

No jointly authored works.

Statement of Contributions by Others to this Thesis as a Whole

Contributions by others are made to this thesis in two areas: (1) development of computational tools, and (2) acquisition of experimental data.

The implementation of the post-shock relaxation equations in the `Poshax3` code described in § 5 makes use of a `c++` ODE integration library developed by Rowan Gollan. The formulation of the Navier–Stokes equations as described in § 7 is the result of modifications made to the `Eilmer3` code developed collectively by the Compressible Flow CFD group at the University of Queensland and collaborators at other institutions. The core time-stepping and flux routines were developed by Peter Jacobs and a number of past CFD students. The chemical kinetic module was developed by Rowan Gollan as described in § 4 of Reference [1].

Experimental data from the NASA Ames EAST facility is analysed in § 6.2 and were performed by David Bogdanoff and colleagues as described in References [2] and [3]. The University of Queensland X2 shock tube experiments considered in § 6.3 are the work of Matt McGilvray. In § 8 experimental data obtained from the X2 facility operated as an expansion tunnel is considered. The subscale Hayabusa experiments were performed by Mary D’Souza as described in Reference [4] and the 25 mm cylinder experiments were performed by Troy Eichmann.

In addition, Figure 8.6 is the work of Mary D’Souza and Figures 8.7 and 8.40 are the work of Troy Eichmann.

Statement of Parts of the Thesis Submitted to Qualify for the Award of Another Degree

None.

Published Works by the Author Incorporated into the Thesis

§ 6.2.4 of this thesis is based on the following publication, however the presented results differ as improved physical modelling has since been implemented.

D. POTTER, R. GOLLAN, P. JACOBS, AND P. LEYLAND. *Numerical simulations and analysis of the 8.5 km/s CO₂-N₂ EAST shock tube condition*. In H. Lacoste and L. Ouwehand, eds., *Proceedings of the 3rd International Workshop on Radiation of High Temperature Gases in Atmospheric Entry*, ESA SP-667 (European Space Agency, Heraklion, Greece, 2008).

§ 8.3 of this thesis is based on the following publication.

D. POTTER, M. D'SOUZA, R. MORGAN AND P. JACOBS. *Modelling Of An Expansion Tunnel Experiment Simulating Re-Entry Of The Hayabusa Probe*. In H. Lacoste, ed., *Proceedings of the 4th International Workshop on Radiation of High Temperature Gases in Atmospheric Entry*, ESA SP-689 (European Space Agency, Lausanne, Switzerland, 2010).

§ 8.4 of this thesis is based on the following publication, however the presented results differ as an improved simulation strategy has since been implemented and the experiment conditions have been modified.

D. POTTER, T. EICHMANN, A. BRANDIS, R. MORGAN, P. JACOBS, AND T. MCINTYRE. *Simulation of radiating CO₂-N₂ shock layer experiments at hyperbolic entry conditions*. AIAA Paper 2008-3933, Seattle, Washington (2008).

Additional Published Works by the Author Relevant to the Thesis but not Forming Part of it

D'SOUZA, M., EICHMANN, T., POTTER, D., MORGAN, R., MCINTYRE, T., JACOBS, P. AND MUDFORD, N. *Observation of an ablating surface expansion tunnel flow.* AIAA Journal **48**(7), 1557 (2010).

BUTTSWORTH, D., D'SOUZA, M., POTTER, D., EICHMANN, T., MUDFORD, N., MCGILVRAY, M., MCINTYRE, T., JACOBS, P. AND MORGAN, R. *Expansion tunnel radiation experiments to support Hayabusa re-entry observations.* AIAA Paper 2010-634, Orlando, Florida (2010).

POTTER, D., GOLLAN, R., EICHMANN, T., MCINTYRE, T., MORGAN, R., AND JACOBS, P. *Simulation of CO₂-N₂ expansion tunnel flows for the study of radiating shock layers.* AIAA Paper 2008-1280, Reno, Nevada (2008).

EICHMANN, T., BRANDIS, A., POTTER, D., MCINTYRE, T., AND RUBINSZTEIN-DUNLOP, H. *Radiating hypersonic flow studies using a super-orbital exapnsion tube.* AIAA Paper 2008-4135, Seattle, Washington (2008).

GOLLAN, R., JACOBS, C., JACOBS, P., MORGAN, R., MCINTYRE, T., MACROSSAN, M., BUTTSWORTH, D., EICHMANN, T., AND POTTER, D. *A simulation technique for radiating shock tube flows.* 26th International Symposium on Shock Waves (2007).

POTTER, D., GOLLAN, R., EICHMANN, T., JACOBS, P., MORGAN, R., AND MCINTYRE, T. *Simulation of CO₂-N₂ expansion tunnel flows for the study of radiating shock layers.* In P. Jacobs *et al.*, eds., *16th Australasian Fluid Mechanics Conference*, pp. 373-380 (School of Engineering, The University of Queensland, 2007).

Acknowledgements

I am in indebted to many people for their help and support throughout my PhD studies.

First and foremost, I would like to acknowledge my advisors, Peter Jacobs and Richard Morgan. It was your passion for hypersonics that inspired me to undertake a PhD in this field. I greatly appreciate the freedom you both gave me in my studies, and equally appreciate the computational and experimental knowledge you had to offer. I would also like to acknowledge Pénélope Leyland for the year spent at École Polytechnique Fédérale de Lausanne in Switzerland. My studies and contributions to the AMOD project during that time greatly improved the scope and quality of this thesis.

I am very grateful to the guidance and support offered by Rowan Gollan during the development of the computational models. The excellent coding framework you created enabled this thesis to reach much deeper into the study of radiation that would have been otherwise possible. Many thanks to Sebastian Karl for answering my endless questions about radiation transport methods. Without your assistance I would have given up on building the ray-tracing model long ago. Also, *merci beaucoup* to Romain Savajano for your help in developing the collision integral based transport models.

A big thank-you to Matt McGilvray, Troy Eichmann, Mary D'Souza and the X-lab operators for obtaining and sharing the X2 data used in this thesis. From the first year of my PhD I had just a taste of how demanding and sometimes frustrating experimental work can be. Your efforts are much appreciated, as the comparisons made with your measurements form the cornerstone of this thesis.

Many thanks to Carolyn Jacobs for all your help with computer administration and all things Linux related over the past 4 years. I am glad at least one of us was organised enough to keep the cluster running!

Finally, I would like to thank my family and friends for all their love and support when times were tough – without you, this thesis would not have been possible.

Abstract

This thesis investigates the modelling of radiating shock layers encountered during atmospheric entry from space. Specifically, the conditions relevant to entry at Earth and Mars from hyperbolic trajectories are considered. Such trajectories are characteristic of the interplanetary transits that would be required for the human exploration of Mars, for example. A set of computational tools for the simulation of radiating shock layers is presented, and then applied to simulate shock tube and expansion tunnel experiments performed in both the EAST facility at NASA Ames and the X2 facility at the University of Queensland.

Appropriate thermodynamic, transport and spectral radiation models for the species of interest in the Ar–C–N–O elemental system have been developed. Expressions for multitemperature thermodynamic coefficients for 11 species air and 22 species Mars gas are derived from statistical mechanics. Viscosity, conductivity and diffusivity coefficients are calculated by applying the Gupta-Yos mixture rules. A complete set of binary collision integrals are compiled from critically selected sources in the literature, where preference is given to data based on computational chemistry and experimental measurements. A spectral radiation model describing atomic and diatomic bound-bound transitions via a line-by-line approach is presented, while continuum transitions are approximated by hydrogenic and step models. Collisional-radiative models for Ar, C, N, O, C₂, CN, CO, N₂ and N₂⁺ are implemented for calculating the non-Boltzmann electronic level populations of these species in a temporally decoupled manner.

For the simulation of shock tube experiments, two- and three-temperature formulations of the one-dimensional post-shock relaxation equations are implemented. The chemical kinetic and thermal energy exchange processes are fully coupled with the gas dynamics, and the radiation source term is modelled in the optically thin and thick limits that bound the solution space. Prior to the comparison with experimental data, the one-dimensional post-shock relaxation equations are applied to simulate flow conditions representative of hyperbolic entry at Earth and Mars; specifically, the Fire II $t = 1634\text{ s}$ and $t = 1636\text{ s}$ trajectory points and hypothetical 8.5 and 9.7 km/s Mars aerocapture conditions are considered. For these conditions comparisons are made with published solutions to verify the code implementation, and various physical models are applied to assess the sensitivity of the solutions to the underlying physics.

The one-dimensional post-shock relaxation equations are then applied to simulate shock tube experiments performed in the EAST and X2 facilities. For the EAST facility, nominally 10 km/s

air conditions and a 8.5 km/s Mars condition are considered. For the X2 facility, an 11 km/s air condition is considered. Comparisons with both ultraviolet and infrared spatially resolved spectra are made for all experiments. For the air conditions, good agreement (within the limits of experimental uncertainty) is observed for the higher pressure conditions considered (40 Pa), while some discrepancies emerge for the lower pressure conditions considered (13.3 and 16 Pa). For the 8.5 km/s Mars condition, certain spectral features such as the the important CO Fourth Positive band system, CN Violet band system and atomic C lines in the infrared are well described, while others such as and atomic C lines in the ultraviolet and atomic O lines are overestimated. Overall, shock tube comparisons show the *total* measured radiation is able to be estimated within 30% for N₂-O₂ mixtures and within 50% for CO₂-N₂ mixtures.

In contrast to shock tube experiments where the flow is well described by a one-dimensional variation of properties, expansion tunnel experiments are inherently multidimensional. For simulating these experiments, modifications to an existing time-accurate Navier-Stokes code have been made to allow the calculation of radiating, partially ionised plasmas. The governing equations for a two-temperature multi-species gas are implemented. The tangent-slab model and a ray-tracing based model are implemented for computing the radiation source term. Radiation-flowfield coupling is treated in a loosely coupled manner. The chemical kinetic and thermal energy exchange source terms are applied in an ‘operator split’ fashion; this approach is validated by comparisons with solutions from the fully coupled post-shock relaxation equations.

Two expansion tunnel experiments are then considered: (1) a 47 MJ/kg N₂-O₂ condition with a 1:10 scale Hayabusa model, and (2) a 37 MJ/kg CO₂-N₂ condition with a 25 mm diameter cylinder model. For both experiments, the freestream conditions generated by the X2 facility are firstly estimated by a novel, simplified strategy based on one-dimensional simulations of the secondary diaphragm rupture and Navier-Stokes simulation of the test gas expansion through the hypersonic nozzle. The freestream conditions so determined are then applied to simulate the radiating shock layer formed by the test gas recompression over the models. From these radiatively-coupled simulations, spatially resolved spectral intensity fields are post-processed and compared with the experimental measurements. For the 47 MJ/kg N₂-O₂ condition, comparisons with both ultraviolet and infrared spectra are made, while for the 37 MJ/kg CO₂-N₂ ultraviolet spectra are compared. While good *qualitative* agreement is found for the CO₂-N₂ condition, the intensity profiles for the N₂-O₂ condition show substantial discrepancy. Reasons for the difference between calculation and experiment are discussed. Finally, the binary scaling hypothesis is numerically assessed by comparing simulations of the subscale Hayabusa model with an effective flight equivalent. While similitude in the surface radiative flux is demonstrated for radiatively uncoupled simulations, the consideration of radiation-flowfield coupling is found to reduce the flight radiative flux disproportionately to the subscale radiative flux. The flight radiative flux at the stagnation point is calculated to be reduced by 80% when radiation coupling is considered, while the reduction is only 23% for the subscale radiative flux.

Keywords

atmospheric entry, shock layers, radiation, shock tubes, expansion tunnels

Australian and New Zealand Standard Research Classifications (ANZSRC)

090107 Hypersonic Propulsion and Hypersonic Aerodynamics, 50%

020201 Atomic and Molecular Physics, 50%

List of Symbols

Roman characters:

A_{ul}, B_{ul}, B_{lu}	Radiative transition probabilities (1/s)
a	speed of sound (m/s)
$b(\nu)$	spectral distribution function
C, n, T_a	generalised Arrhenius parameters (moles/m ³ -s, ND and K)
c	speed of light (2.99792458×10^8 m/s)
c_v	specific heat at constant volume (J/kg-K)
c_p	specific heat at constant pressure (J/kg-K)
D_e	dissociation energy (J/particle)
\tilde{D}_i	mixture average diffusion coefficients (m ² /s)
e	internal energy (J/kg)
E	total energy (J/kg), or radiative power (W)
F_J	rotational energy for level J (J/particle)
f	mass-fraction
f_{lu}	oscillator strength
G_v	vibrational energy for level v (J/particle)
G_i	gaunt factor for electronic level i , or Gibbs free energy for species i (J/kg)
g	degeneracy
h	enthalpy (J/kg), or Planck constant (6.626076×10^{-34} J-s)

I	radiative intensity ($\text{W}/\text{cm}^2\text{-sr}$) or ionisation potential ($\text{J}/\text{particle}$)
I_H	Ionisation potential of the hydrogen atom ($2.1787113 \times 10^{-18} \text{ J}/\text{particle}$)
I_ν	spectral intensity ($\text{W}/\text{cm}^2\text{-}\mu\text{m}\text{-sr}$)
J	diffusion flux ($\text{kg}/\text{m}^2\text{-s}$), radiative emissive power density (W/cm^3) or rotational quantum number
j	radiative emission coefficient ($\text{W}/\text{m}^3\text{-sr}$)
j_ν	spectral emission coefficient ($\text{W}/\text{m}^3\text{-sr-Hz}$)
K	conductivity ($\text{W}/\text{m}^2\text{-K}$) or collisional-radiative rate coefficient ($\text{particles}/\text{m}^3\text{-s}$)
K_c	Chemical kinetic equilibrium constant based on concentrations
K_p	Chemical kinetic equilibrium constant based on partial pressures
k_f, k_b	Forward and backwards chemical kinetic rate coefficient (moles/ $\text{m}^3\text{-s}$)
$L_{e,J}$	Line alternation factor
M	molecular weight (kg/mol)
m	particle mass (kg)
m_e	electron mass ($9.109390 \times 10^{-28} \text{ kg}$)
N	number density (m^{-3}) or general integer quantity
p_{atm}	atmospheric pressure (101,325 Pa)
p	pressure (Pa)
q	heat-flux (W/m^2)
Q	partition function (m^{-3})
R	specific gas constant ($\text{J}/\text{kg}\text{-K}$)
R_e	electronic transition moment
S	Spin angular momentum quantum number
$S_{J_l}^{J_u}$	Hönl-London factor for rotational transition $J_u \rightleftharpoons J_l$
s	entropy ($\text{J}/\text{kg}\text{-K}$)

t time (s)
T_i Electronic term energy for level i (J/particle)
T temperature (K)
U Treanor-Marrone pseudo-temeprature (K)
u, v velocities in the x and y directions (m/s)
\vec{u} velocity vector (m/s)
V volume (m^3)
v vibrational quantum number
X mole-fraction
x, y, z x, y, z cartesian coordinates (m)
Z Particle charge or nonequilibrium rate coefficient correction factor

Greek characters:

$\alpha_e, B_e, B_v, D_e, D_v$	Rotational coupling constants (J)
α_i, β_i stoichiometric coefficients
ϵ quantum state energy (J/particle)
δ_0 Kronecker Delta function
γ Ratio of specific heats, or Gaussian half-width at half-maximum (Hz)
κ_ν spectral absorption coefficient (1/m)
Λ Total angular momentum quantum number, or radiative escape factor
λ wavelength (nm)
μ viscosity coefficient
ν frequency (Hz)
$\Omega_{i,j}^{(l,m)}$ collision integral (m^3/s)
$\Omega_{i,j}^{(l,m)*}$ reduced collision integral
Ω_{VT} vibration-translation energy exchange source term (W/m^3)

Ω_{VE}	vibration-electron energy exchange source term (W/m ³)
Ω_{VC}	vibration-chemistry energy exchange source term (W/m ³)
Ω_{EC}	electron-chemistry energy exchange source term (W/m ³)
ω	solid angle (steradians)
$\dot{\omega}$	mass production source term (kg/m ³ -s)
$\omega_e, \omega_ex_e, \omega_ey_e, \omega_ez_e$	Klein-Dunham coefficients
ρ	density (kg/m ³)
σ	rigid sphere collision diameter (m), or homonuclear symmetry factor
$\sigma^2\Omega_{i,j}^{(l,m)*}$	collision cross section (m ²)
τ	characteristic time scale (s) or relaxation time constant (s ⁻¹)
τ	viscous stress tensor (kg/m-s)
Θ	characteristic temperature (K)

Subscripts and acronyms:

CFD	computational fluid dynamics
D	dissociation
e	free electrons
el	(bound) electronic thermal energy mode
eq	equilibrium thermochemistry
ESA	European Space Agency
froz	Frozen thermochemistry
HO	harmonic oscillator
hp	heavy particles
HWHM	half-width at half-maximum
int	internal energy modes
ion	ionised particles

- IR infrared
- LTE local thermodynamic equilibrium
- NASA National Aeronautics and Space Administration
- ND non-dimensional
- m* thermal mode
- rad radiation
- reac reactive thermochemistry
- rot rotation thermal energy mode
- s* chemical species
- TPS thermal protection system
- tr translation-rotation thermal energy mode
- trans translation thermal energy mode
- UV ultraviolet
- v (grouped) vibration thermal energy mode
- vib (individual) vibration thermal energy mode
- ve vibration-electron-electronic thermal energy mode

Contents

List of Symbols	x
1 Introduction	1
1.1 The exploration of space	1
1.2 Atmospheric entry	2
1.3 Phenomenology of radiating shock layers	6
1.4 The investigation of radiating shock layers	9
1.4.1 Experiments	9
1.4.2 Computational modelling	12
1.5 Scope and overview of the dissertation	16
I Physical Modelling	19
2 Governing equations for radiating shock layers	21
2.1 Compressible Navier–Stokes equations	21
2.1.1 Continuity equation	21
2.1.2 Selection of the conserved quantities	22
2.1.3 One-temperature formulation	23
2.1.4 Two-temperature formulation	24
2.1.5 Three-temperature formulation	25
2.2 Post-shock relaxation equations	26
2.3 Summary	27
3 Properties of high temperature gases	29
3.1 Thermodynamic properties and coefficients	29
3.1.1 Thermodynamic relations from statistical mechanics	30
3.1.2 Modal contributions to thermodynamic properties	30
3.1.3 Thermodynamic properties for a single species	35
3.1.4 Bulk thermodynamic properties	44
3.2 Transport properties	47

3.2.1	Gupta–Yos mixture rules	48
3.2.2	Binary collision parameters for partially ionised shock layers	52
3.2.3	Comparison with CEA2 [5]	55
3.2.4	Comparison with tabulated results of Bruno <i>et al.</i> [6]	56
3.3	Spectral radiation coefficients	59
3.3.1	Monatomic bound-bound transitions	60
3.3.2	Diatomc bound-bound transitions	73
3.3.3	Continuum transitions	88
3.3.4	Uncertainty of the radiation calculation	91
3.4	A comment on the consistency of data sources	91
3.5	Summary	92
4	Nonequilibrium rate processes	93
4.1	Chemical kinetics	93
4.1.1	Forwards and backwards rate coefficients	94
4.1.2	Nonequilibrium rate coefficients	95
4.2	Thermal energy exchange	99
4.2.1	Vibration-translation exchange	100
4.2.2	Translation-electron exchange	101
4.2.3	Vibration-electron exchange	102
4.2.4	Chemistry-energy coupling	104
4.3	Collisional-radiative modelling	108
4.3.1	Collisional-radiative mechanisms	109
4.3.2	Master equation formulation and solution	116
4.3.3	Collisional-radiative model for N ₂ –O ₂ mixtures	118
4.3.4	Collisional-radiative model for CO ₂ –N ₂ –Ar mixtures	131
4.3.5	A note on the selection of data sources	138
4.4	Summary	139
II	Post-shock relaxation	141
5	Implementation of the one-dimensional post-shock relaxation equations: Poschax3	143
5.1	Numerical formulation	143
5.1.1	Shock jump conditions	144
5.1.2	Spatial integration	145
5.1.3	Radiative source term	145
5.2	Application to Earth atmospheric entry	146
5.2.1	Comparison with published solutions	146

5.2.2	Thermodynamic model variation	151
5.2.3	Dissociation rate coefficient model variation	152
5.2.4	Dissociation-vibration coupling model variation	153
5.2.5	Chemistry-electron coupling model variation	154
5.2.6	Radiation model variation	155
5.2.7	Three temperature model	158
5.3	Application to Mars atmospheric entry	159
5.3.1	Comparison with published solutions	159
5.3.2	Thermodynamic model variation	160
5.3.3	Reaction model variation	161
5.3.4	Dissociation rate coefficient model variation	162
5.3.5	Dissociation-vibration coupling model variation	164
5.3.6	Chemistry-electron coupling model variation	165
5.3.7	Vibration-translation exchange model variation	165
5.3.8	Radiation model variation	166
5.3.9	Three temperature model	167
5.4	Summary	169
6	Analysis of non-reflected shock tube experiments	171
6.1	Modelling strategy	172
6.1.1	Assessment of the one-dimensional and inviscid assumptions	172
6.1.2	Radiation-flowfield coupling	175
6.1.3	Calculation of spectral intensity for comparison with experiment	176
6.1.4	Physical modelling	177
6.2	NASA Ames EAST Facility	177
6.2.1	Facility description	177
6.2.2	Spectroscopic apparatus	177
6.2.3	Air conditions	178
6.2.4	Mars conditions	197
6.3	University of Queensland X2 Facility	207
6.3.1	Facility description	208
6.3.2	Spectroscopic apparatus	208
6.3.3	Air conditions	208
6.4	Summary	217
III	Two-dimensional flowfields	219
7	Implementation of the Navier–Stokes equations: Eilmer3	221

7.1	Overview of the code	222
7.2	Governing Equations for the Gas Dynamics	222
7.2.1	Discretised Equations and Time-Stepping Procedure	225
7.2.2	Inviscid flux	227
7.2.3	Viscous flux	228
7.2.4	Boundary conditions	228
7.3	Chemical kinetics	231
7.4	Thermal energy exchange	232
7.5	Radiation transport	233
7.5.1	Flowfield coupling	234
7.5.2	Optically-thin model	234
7.5.3	Tangent-slab model	235
7.5.4	Ray-Tracing Model	236
7.6	Mass diffusion	250
7.7	Comparison with the post-shock relaxation equations	251
7.7.1	Simulation description	251
7.7.2	Results	251
7.8	Summary	253
8	Simulation of expansion tunnel experiments	255
8.1	Facility description	255
8.2	Modelling strategies	257
8.2.1	Hybrid simulation of the whole facility	257
8.2.2	Simplified modelling strategy	259
8.3	47 MJ/kg N ₂ –O ₂ condition: subscale Hayabusa model	262
8.3.1	Experiment description	262
8.3.2	Estimation of freestream conditions	264
8.3.3	Radiating shock layer simulations: subscale model	269
8.3.4	Radiating shock layer simulations: effective flight condition	283
8.4	37 MJ/kg CO ₂ –N ₂ condition	297
8.4.1	Experiment description	298
8.4.2	Estimation of freestream conditions	299
8.4.3	Radiating shock layer simulations: subscale model	301
8.5	Summary	319
9	Conclusion	321
9.1	Accomplishments and unique contributions	325
9.2	Recommendations for future work	326
9.2.1	Computational modelling	326

9.2.2 Experimental measurements	327
References	329
A Transport collision integrals	349
B Atomic electronic levels	353
B.1 Atomic Carbon, C	354
B.2 Atomic nitrogen, N	355
B.3 Atomic nitrogen, O	356
C Chemical kinetic models	359
C.1 N ₂ -O ₂ mixtures	359
C.2 CO ₂ -N ₂ -Ar mixtures	361
D Diatomic collisional-radiative models	365
D.1 Collisional-radiative model for C ₂	366
D.2 Collisional-radiative model for CN	367
D.3 Collisional-radiative model for CO	368
D.4 Collisional-radiative model for N ₂	369
D.5 Collisional-radiative model for N ₂ ⁺	370
E Multicomponent Diffusion models	371
E.1 Fick's first law	371
E.2 Stefan-Maxwell equations	372
E.3 Self-Consistent Effective Binary Diffusion (SCEBD) model	372
F Parametric study of freestream conditions for the subscale Hayabusa model	374

1

Introduction

1.1 The exploration of space

It may be that the old astrologers had the truth exactly reversed, when they believed that the stars controlled the destinies of men. The time may come when men control the destinies of stars.

Arthur C. Clarke, *First on the Moon* (1979)

Throughout history the night sky has both inspired and challenged the human mind. From the astrological interpretations of ancient civilisations to Giordano Bruno's comprehension of an infinite universe at the beginning of the modern era, our understanding of reality has been shaped by pondering the heavens. Then in the mid 20th century, the technology was finally developed to enable humankind to actually explore this final frontier that previously could only be imagined.

The Soviet and American space programs of the 1950's and 60's initiated a new era of exploration beyond the confines of Earth, beginning with the launch of the Sputnik 1 satellite in 1957 and reaching a pinnacle with the landing of Apollo 11 on the moon in 1969. Although human space flight has since continued, most notably by the 30 year long NASA Space Shuttle program that is scheduled to finish in 2011, the majority of launches have been unmanned or robotic missions. The Soviet Union pioneered robotic planetary exploration with the crash landing of the Soviet Venera 3 probe on the surface of Venus in 1965. In 1975 NASA's Viking

Program sent two space probes, Viking 1 and 2, to orbit and then land on Mars. Imagery of the Martian surface from orbit and experiments on the soil and atmosphere by the landers enabled a clearer picture to emerge of the Martian environment. Following on from the success of the Viking program, NASA has been engaged in an extensive Mars exploration program with the Pathfinder, Mars Exploration Rovers, Phoenix and forthcoming Mars Science Laboratory missions. A highlight of these missions has been the confirmation of ice water in the Martian soil by the Phoenix lander in 2008. Perhaps the most spectacular robotic missions to date were the Voyager 1 and 2 spacecraft launched by NASA in 1977. Taking advantage of a once in 175 year planetary alignment, the Voyager spacecraft took the first detailed photographs of Jupiter, Saturn, Uranus and Neptune, and their respective moons. The Voyager 1 spacecraft is currently the most distant functioning space probe to receive commands and transmit information to Earth. The European Space Agency has also made great contributions to planetary exploration with the Cassini-Huygens mission to Saturn and its moon Titan. Radar images from the Cassini orbiter made the important discovery of liquid hydrocarbon oceans on the surface of Titan.

In addition to planetary exploration, attempts have been made to intercept and even land on asteroids and comets. In 1999 NASA launched the Stardust mission that collected dust samples from the tail of the comet *Wild 2*, and returned them to Earth via a re-entry capsule. In 2004, analysis of the data recorded by 'Cometary and Interstellar Dust Analyzer' mass spectrometer on the Stardust probe confirmed the presence of organic matter [7]. Similarly, in 2003 the Japanese Aerospace Exploration Agency launched the Hayabusa mission to land on the near-earth asteroid 25143 *Itokawa* and collect samples.

These missions serve to demonstrate the immediate scientific benefits of space exploration. By enabling scientific instruments to orbit, enter the atmosphere and land on the surface of planets, moons, asteroids and comets, the formation of the solar system can be studied in great detail. Perhaps of even greater significance, however, is the potential of space exploration to allow life to expand beyond the confines of Earth. Through the development of critical technologies and gaining of experience in the intricacies of space flight, robotic missions are paving the way for the human exploration of the solar system.

1.2 Atmospheric entry

A common feature of all planetary exploration and Earth return missions is the penetration of an atmosphere, whether it be that of Earth or another planetary body, at very high velocities. Generally speaking, interplanetary atmospheric entry trajectories can be classified into three types: (1) direct entry, (2) aerobraking and (3) aerocapture. Illustrations of these three trajectories are presented in Figure 1.1. Direct entry involves entering the planetary atmosphere via a ballistic trajectory, using the friction generated by gas interaction to slow sufficiently for a controlled surface landing. Figure 1.2 illustrates the various stages of the direct entry trajectory proposed

for the Mars Science Laboratory which is scheduled to launch in late 2011 [8]. The focus of the present work is on a single element of such an atmospheric entry trajectory, namely the characterisation of the shock layer that forms around the vehicle between the entry interface and peak deceleration phases.

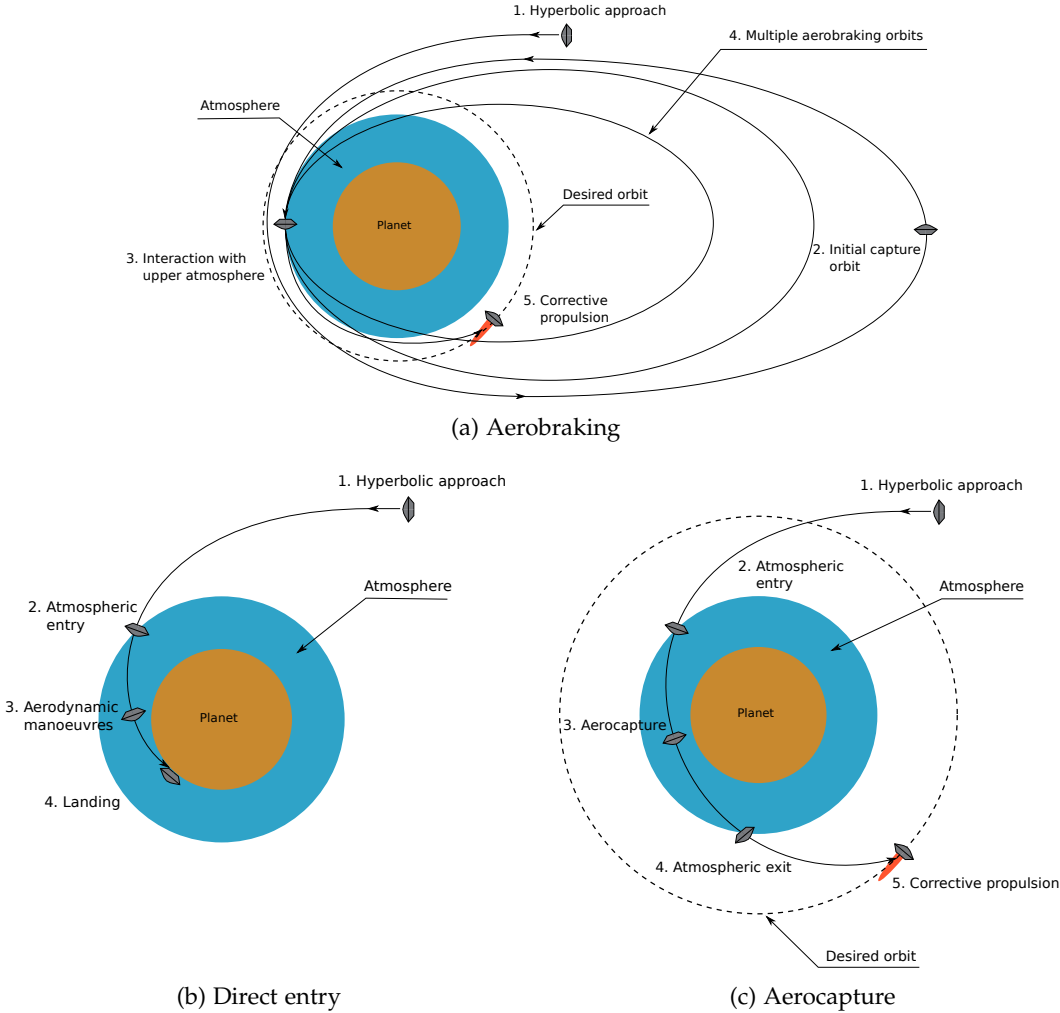


Figure 1.1: Illustrations of various atmospheric entry strategies from a hyperbolic interplanetary orbit.

For vehicles such as Galileo, Stardust, Hayabusa and Mars Science Laboratory, the direct entry is initiated from the hyperbolic trajectory the vehicle is on during its voyage through space. Such entries are characterised by very high entry velocities, in excess of 11 km/s for re-entry at Earth. For other vehicles such as the Huygens probe and the Space Shuttle, direct entry is initiated from a circularised orbit about the planet and is therefore characterised by more moderate entry velocities (*e.g.* approximately 8 km/s for the Space Shuttle). The circularised orbit is typically attained by chemical propulsion. In contrast, aerobraking reduces the need for chemical propulsion by skimming the upper rarefied atmosphere many times to achieve a

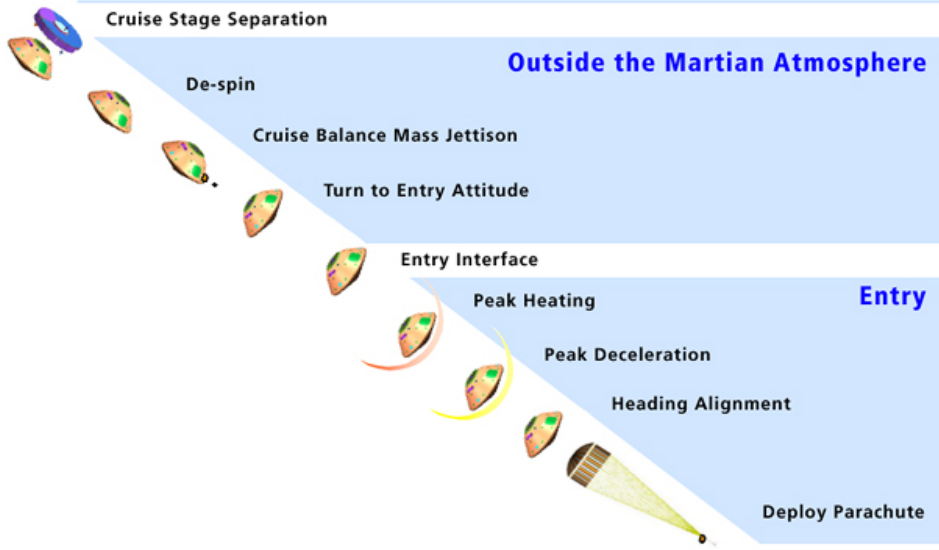


Figure 1.2: Illustration of the direct entry trajectory proposed for the Mars Science Laboratory to be launched in late 2011 (source: Reference [9]).

desired change in orbit. The Mars Reconnaissance Orbiter, for example, successfully completed an aerobraking manoeuvre reducing an initial elongated 38 hour orbit to a circular 2 hour orbit over a period of 7 months [10]. Aerocapture is a more severe form of aerobraking where the orbit change is achieved by a single pass through the atmosphere. Although aerocapture is currently an unproven technology, the ESA's *Aurora Space Exploration Programme* included a proposal for an aerocapture demonstrator [11], and the NASA *In-Space Propulsion Program* performed a number of in-depth studies into the feasibility of aerocapture at Titan [12–15].

In the present work we are primarily concerned with conditions characteristic of direct entry and aerocapture from hyperbolic trajectories. Such trajectories would be required for the human exploration of Mars in order to minimise the transit time. For a 1 to 2 year Venus swing-by mission between Earth and Mars, Braun [16] estimated the entry velocity at Mars to be between 6 and 10 km/s and between 11.5 and 12.5 km/s for re-entry at Earth.

In contrast to hypersonic vehicles performing sustained flight within the atmosphere, the vehicle design that is most suited to such high velocity atmospheric entry trajectories is a simple blunt-body. The Apollo-era blunt-body design consisted of simple spherical section forebody with a conical afterbody, Figure 1.3a, while more recent vehicles such as Huygens and the Mars Science Laboratory capsules consist of a blunted-cone forebody and a tapered afterbody, Figure 1.3b. Although more complex shapes such as raked elliptic cones have been proposed to allow for greater manoeuvrability in the atmosphere, such vehicles are yet to be proven in flight (*e.g.* the cancelled Aeroassist Flight Experiment vehicle [17]).

These vehicle designs serve to provide a large frontal area to dissipate the kinetic energy via

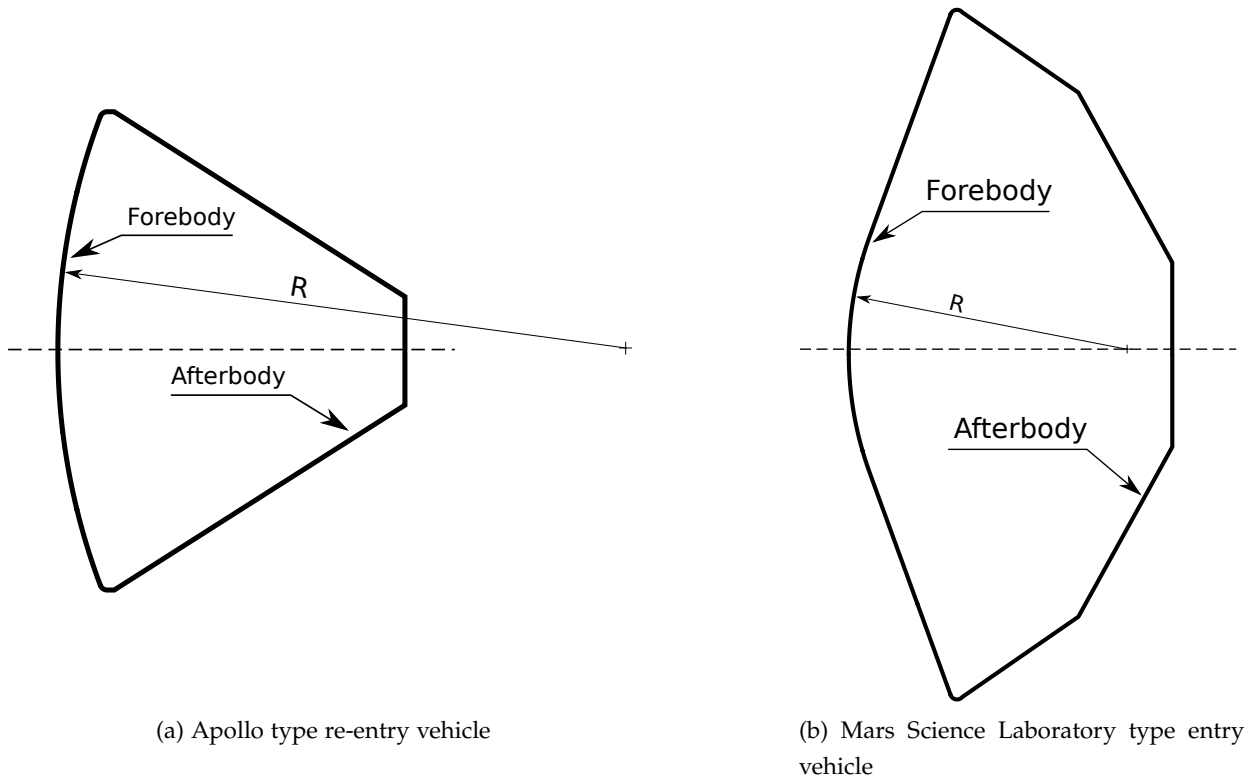


Figure 1.3: Typical designs for direct atmospheric entry vehicles.

interaction with the gaseous atmosphere. As a consequence, however, the gas in front of the spacecraft is excited to very high temperatures and the vehicle is exposed to a severe heating environment. A thermal protection system (TPS) is therefore required to be installed on the forebody¹ to protect the spacecraft. Energy is transferred to the vehicle surface via two mechanisms [18]; (1) interactions of particles with the surface (convective heating), and (2) absorption of electromagnetic radiation emitted by the shock layer. The convective heating component at the surface is comprised of a conduction component driven by temperature gradients, and a diffusion component driven by concentration gradients. For the hyperbolic entry conditions of present interest, radiation is a significant heating mechanism. For the Fire II flight experiment re-entry at Earth, for example, the convective and radiative heating rates at the $t = 1643$ s trajectory point² have been calculated as 733 and 567 W/cm^2 [19]. Although Mars missions to date have been dominated by convective heating, future crewed missions will encounter additional heating from shock layer radiation due a combination of larger size and faster entry velocity [20]. For a 20 m nose radius vehicle performing an aerocapture manoeuvre at Mars with an entry velocity of 9.79 km/s, Braun [16] estimates the radiative and convective rates at peak heating to be 187

¹The afterbody also requires a TPS, however the forebody TPS must be designed to withstand much higher heating rates and loads.

²This trajectory point is just prior to peak heating which is estimated to occur at approximately $t = 1644$ s.

and 131 W/cm^2 respectively. For such high energy trajectories ablative TPS materials such as phenolic impregnated carbon must be used to withstand the intense heating environment. The amount of ablative material required is directly dependent on the peak heating rate and total heating load; the more severe the heating environment, the more ablative material is required to dissipate the heat incident on the vehicle surface. Due to the stringent mass limitations of spaceflight, however, it is important that the TPS be as light as possible and not oversized. The accurate description of radiating shock layers and calculation of the resultant radiative heat flux is therefore crucial for future interplanetary missions.

1.3 Phenomenology of radiating shock layers

A dramatic increase in thermodynamic energy is experienced by a packet of atmospheric gas as it is processed by the bow-shock of an atmospheric entry vehicle. Although this energy first manifests as an increase in translational motion of the atmospheric molecules, collisional interactions between particles quickly give rise to a cascade of chemical kinetic processes. A diagrammatic representation of these processes occurring in the shock layer and near the surface of a Stardust-type re-entry capsule at peak heating conditions is shown in Figure 1.4. Two distinct regions of the flowfield are indicated: (1) the shock layer, and (2) the ablation layer. Due to the strong heating environment experienced by the vehicle surface, the TPS material pyrolyses and the products form an ablation layer over the surface. This ablation layer consists of strong radiators such as CO and CN, which form due to the presence of carbon in the TPS material. Although the modelling of the ablation process is a critical aspect of aerothermodynamics in itself, the present work is focused on the processes occurring in the shock layer where the influence of the ablating surface is negligible.

Figure 1.5 illustrates the key chemical kinetic processes occurring along the stagnation streamline of a vehicle with a non-ablating TPS re-entering the Earth's atmosphere. Across the strong shock formed over the vehicle, most of the kinetic energy of the freestream particles (in the vehicle's frame of reference) is rapidly³ converted into translational energy as they collide with the more dense shock layer gas. Inter-particle collisions then excite the rotational, vibrational and electronic modes of the molecules, and translational energy begins to relax. Rotational and translational energy modes quickly equalize due to efficient energy transfer (in the order of tens of collisions), while vibrational excitation is considerably slower (thousands of collisions). The molecules quickly build up large amounts of vibrational energy, to the point where the inter-nuclear bonds are overcome and dissociation occurs. Molecules in higher vibrational states have a higher probability of dissociating come the next collision due to the lowering of the dissociation potential – this behavior is called preferential dissociation. At 10 km/s Earth re-entry, over 90%

³The time for translational excitation can be appreciable in the free molecular and transitional regimes, but is typically very fast for the higher-density conditions close to peak heating.

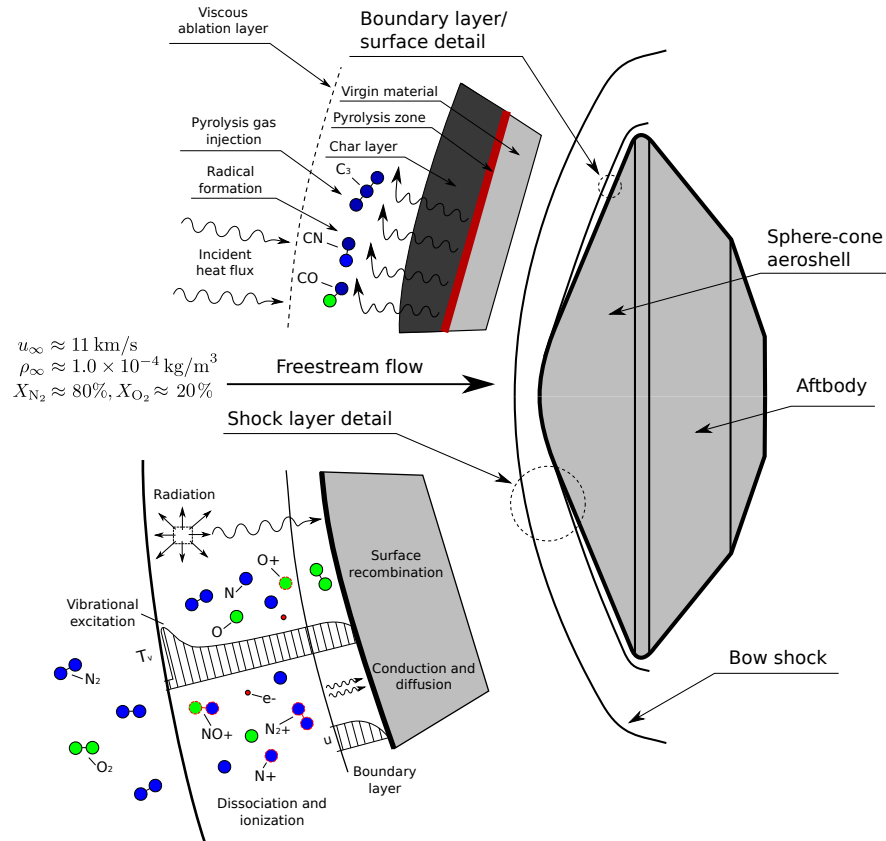
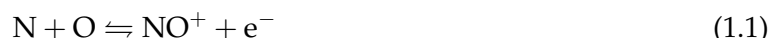


Figure 1.4: Illustration of aerothermodynamic processes occurring in the shock layer and on the surface of a Stardust-type re-entry capsule at peak heating conditions.

of the N_2 and O_2 molecules are dissociated before the peak in vibrational energy is reached. Further collisional excitation amongst the pool of molecules and atoms excites the bound electrons to elevated states, and the gas radiates electromagnetic energy as the electrons spontaneously decay to less energetic states. The coupling between these excitation and de-excitation processes occurring at different rates can lead to nonequilibrium electronic population distributions. Capturing this nonequilibrium effect is critical for the optimal design of aeroshells experiencing a significant level of radiative heating, as the assumption of equilibrium radiation can lead to the radiative flux being substantially overpredicted. For the Huygen's probe, for example, the peak radiative heating rate from an equilibrium analysis was found to be reduced by half when a nonequilibrium population model was applied to the CN molecule [21].

Given sufficiently energetic collisions, bound electrons can eventually be stripped from their parent nuclei. In air, electrons are first produced by the associative ionisation of the NO molecule⁴:



⁴For $\text{CO}_2\text{-N}_2$ mixtures, the formative electrons are produced by the associative ionisation of both NO and CO.

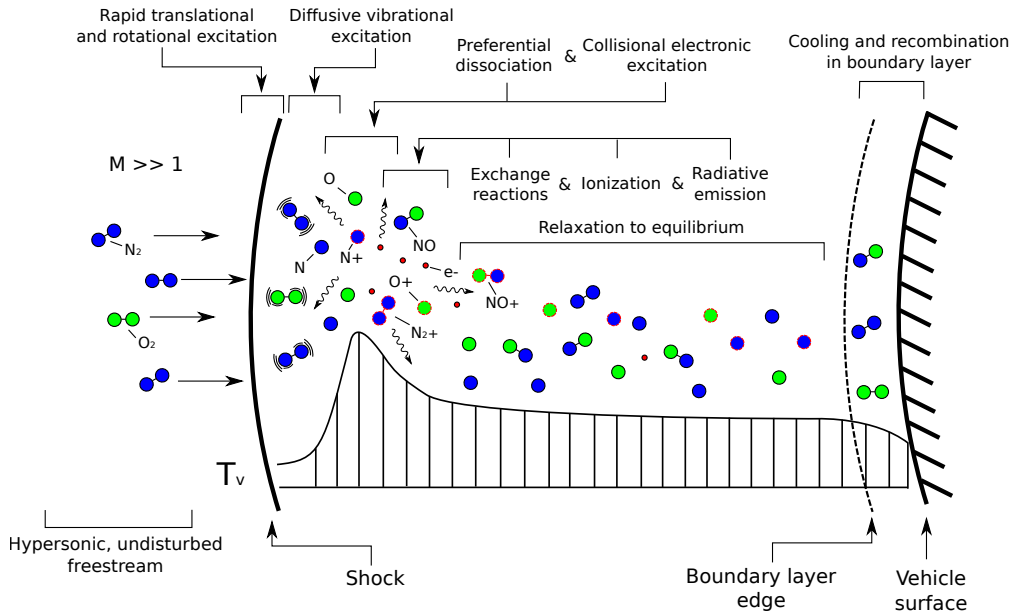


Figure 1.5: Illustration of chemical kinetic processes along the stagnation streamline for Earth re-entry.

The NO^+ ion so produced then transfers its charge to other neutral species through several charge-exchange reactions. When the resulting density of the electrons reaches a certain threshold value, a cascade of electron production can occur through the highly efficient electron induced ionisation of N and O atoms. Sufficiently far behind the shock, after many collisions have occurred, the plasma reaches a state of local thermodynamic equilibrium (LTE). For the Stardust peak heating trajectory point, for example, LTE is reached approximately 5 mm behind the shock with a temperature of 11,000 K. If the ‘equilibrium’ gas is emitting more radiation than it is absorbing, however, LTE is never truly reached and the decay of electronic states will continuously bleed off energy from the shock layer. As the plasma is swept into the boundary layer, heat convects through to the vehicle surface and the gas temperature drops, allowing some degree of recombination to occur. The catalytic effect of the vehicle surface aids this process, and the injection of ablation products further alters the chemistry of the boundary layer. The lowered temperature and increased density of the boundary layer also serves to absorb incident radiation from the shock layer.

Knowledge of the precise thermodynamic state of the plasma throughout this entire excitation and relaxation process is required for accurate radiative heat-flux calculations. In the upper atmosphere during hyperbolic entry at Earth and Mars, the characteristic time-scales for collisional, radiative and advection processes are all of a similar magnitude:

$$\tau_{\text{col.}} \approx \tau_{\text{rad.}} \approx \tau_{\text{adv.}} . \quad (1.2)$$

This situation is termed thermochemical nonequilibrium. Put simply, the distance taken to

achieve equilibrium along the stagnation streamline is a significant fraction of the shock standoff. Thus the thermodynamic state of the plasma must be solved through transient accounting of the chemical kinetic and radiative processes. Due to the complexity of these processes, the physical models which describe them have a large degree of uncertainty – as a consequence, the radiative heat-flux incident on the vehicle surface is also highly uncertain. Reducing the uncertainty associated with nonequilibrium radiation has been identified as one the highest research priorities in planetary-entry gas dynamics [18]. A combination of experiments and computational modelling is therefore required to improve our understanding of nonequilibrium radiation, and improve the accuracy of the radiative heat-flux which the TPS is designed to withstand.

1.4 The investigation of radiating shock layers

Traditionally, the heating environments experienced by atmospheric entry vehicles have been estimated via the use of analytical formulas derived from a combination of theory and empirical correlations. Such techniques must necessarily make simplifying assumptions, and consequently large safety factors must be applied when their results are used for TPS design. Furthermore, this approach does not allow insight into the physical processes driving the heating environment. With the advent of powerful computing facilities in recent decades, computational fluid dynamics (CFD) has emerged as an important tool for describing radiating shock layers. However, CFD solutions are only as accurate as the underlying physical models; experimental measurements are therefore required to develop and validate these physical models. In this section a brief review of radiating shock layer experiments and modelling relevant to hyperbolic entry at Earth and Mars is presented.

1.4.1 Experiments

Radiating shock layer experiments can be divided into two classes; (1) flight experiments, and (2) ground-based experiments. Flight experiments involve making measurements of the shock layer and vehicle surface during an actual atmospheric entry manoeuvre, while ground-based experiments involve making measurements of shock layers, high-temperature gases or subscale models in a laboratory environment. Both of these approaches have benefits and disadvantages. Flight experiments allow the conditions encountered in flight to be almost exactly replicated, however detailed measurements of the shock layer plasma are difficult to perform. In contrast, ground-based experiments allow detailed measurements to be made by virtue of the laboratory environment, although the conditions encountered in flight cannot be replicated in full.

Flight experiments

Due to the expense of launching payloads into space only a handful of flight experiments have been performed. The Fire II flight experiment performed in 1965 remains one of the best data sets available for Earth re-entry. The experiment consisted of a scaled down Apollo-type aeroshell with three separate heat-shields that were designed to be exposed to the flow at specific stages of the reentry [22, 23]. The total incident heat flux was recorded with calorimeters embedded at the stagnation point in beryllium layers covering the phenolic-asbestos heat-shields. Three total radiometers (spectral range of $200 \leq \lambda \leq 4000$ nm) were also included in the experiment to deduce the integrated broadband radiance at the stagnation point, afterbody and lee-side edge of the vehicle. A spectral radiometer was installed at the stagnation point of the vehicle to record radiative intensity in the range $200 \leq \lambda \leq 600$ nm with a resolution of 4 nm. Vacuum ultraviolet radiation, which occurs at wavelengths less than 200 nm, was inferred from the difference between the heating rates measured by the calorimeters and total radiometers. The vehicle re-entered the Earth atmosphere with a velocity of 11.4 km/s, and a peak heating rate of 1140 W/cm^2 was recorded at an altitude of 49 km and a flight velocity of 9.92 km/s, a regime dominated by equilibrium radiation. Important findings from the Fire II measurements were the velocity and altitude dependence of nonequilibrium radiation and the necessity of including vacuum ultraviolet radiation in theoretical predictions.

A full scale flight experiment was performed in 1967 with the Apollo 4 Command Module [24]. Spectral measurements were made by a single radiometer embedded at the stagnation point. In contrast to the Fire II flight experiment, the Apollo 4 heat-shield was ablative. The vehicle re-entered the Earth's atmosphere with a velocity of 11.16 km/s and a peak radiation intensity of $25 \text{ W/cm}^2\text{-sr}$ was reached at an altitude of 120 km. Due to the difficulty of modelling ablative surfaces and the lack of calorimeter measurements, however, the Apollo 4 data has not been as widely analysed as the Fire II data. Important findings have nevertheless been made in recent years from analyses of the Apollo 4 data; namely, the absorption of atomic line radiation in the boundary layer by N₂ and O₂, and the partial conversion of this absorbed radiative energy into convective heating [25].

Ground-based experiments

Although there are numerous types of ground-based experiments that attempt to simulate hypersonic flows, only a select few are capable of producing flows relevant to the hyperbolic entry regime of present interest. Conventional wind tunnels are limited to low enthalpies due to difficulties in maintaining a reservoir at sufficient pressure and temperature to generate higher enthalpies. Arc-heated and inductively coupled plasma wind tunnels are capable of producing relatively high enthalpy flows [26–28], although they are more suited to materials testing and

plasma diagnostics as high Mach number test flow cannot be produced [29]. The only facilities that are capable of reproducing the enthalpies encountered in the hyperbolic entry regime ($H_{\text{total}} \gtrsim 45 \text{ MJ/kg}$ for Earth entry) at high Mach numbers are shock tubes, expansion tubes and tunnels, and ballistic ranges. Such facilities generate the high enthalpy flow in an impulsive manner and therefore circumvent the temperature and pressure limits of continuous facilities. At the present time, shock tubes are the primary facilities implemented for the study of high enthalpy radiating shock layers.

Shock tubes drive a shock directly through the test gas at the pressures and velocities encountered in flight. Spectral measurements can then be made of the radiation emitted in the shock layer; from the shock frame-of-reference, the post-shock relaxation phenomena encountered in flight along the stagnation streamline is exactly replicated⁵. In the 1960's shock tube experiments were conducted at AVCO Everett Research Laboratories with an air test gas at velocities up to 12 km/s [30]. Similar shock tube experiments with a CO₂-N₂ test gas were also performed to simulate atmospheric entry at Venus and Mars [31, 32]. Several important findings of these experiments were the identification of the nonequilibrium radiation overshoot phenomena, and the observation that chemical kinetic processes scale with the density and length product (binary or ' ρL ' scaling). As only monochromatic spectral measurements were made, the air experiments were repeated in the NASA Ames EAST facility in the early 1990's [33]. Time-resolved broadband radiation intensity between 250 and 650 nm was recorded, as was a single spectrally resolved measurement. In the past 10 years, a wealth of both spectrally and spatially resolved shock tube data has emerged. This data is considerably more valuable than the monochromatic, spatially resolved and monospatial, spectrally resolved data previously available. Fujita *et al.* [34] measured spectrally and spatially resolved radiation for an 11.9 km/s shock tube condition with both a simulated air and pure N₂ test gas at 0.3 Torr. Lee *et al.* [35] conducted emission spectroscopy in the reflected shock region of a shock tube with 78% CO₂ – 22% N₂ test gas at equivalent shock speeds of up to 5.2 km/s. Rond *et al.* [36] made measurements of time-resolved CN violet emission in the TCM2 free-piston shock tube with a 70% CO₂ – 30% N₂ test gas at shock speeds of 6.2 km/s and 6.3 km/s. In the EAST facility, 10 km/s air and 8.5 km/s Mars conditions have been performed with both ultraviolet (UV) and infrared (IR) spectral measurements [2, 3]. Yamada *et al.* [37] have recently made spectral measurements in the vacuum ultraviolet (VUV) and UV regions for a 10.4 km/s shock tube condition with an air test gas. The VUV spectral region is of particular interest as it contains much of the radiant energy encountered during hyperbolic entry conditions. Due to its tendency to be readily absorbed, however, VUV radiation has seldom been measured; the measurements presented in Reference [37] were made possible by an evacuated optical path. VUV spectroscopy measurements have also been recently made in the EAST facility with an air test gas at 10 km/s [38].

⁵The formation of a boundary layer due to the presence of the vehicle surface is not replicated, however.

Similarly to shock tubes, expansion tubes also shock-heat the test gas; however, the total enthalpy and pressure of the test gas is then increased further by an unsteady expansion [39]. A short period (tens of microseconds to milliseconds) of steady flow is subsequently produced that can be used to study the re-compression shock formed over a subscale model. The use of a shock to add energy to the flow thermochemically excites the test gas, and the freestream gas state encountered in flight is therefore not precisely replicated. A variation of the expansion tube is the expansion tunnel, where the test gas is further expanded via a hypersonic nozzle to achieve larger core-flows and low densities. McIntyre *et al.* [40] performed two-wavelength holographic interferometry of the bow shock formed over cylindrical model in the X2 facility configured as an expansion tube. A 50 MJ/kg condition with an air test gas was investigated, and electron density contours were extracted from the measurements. Reasonable agreement was found with a CFD solution obtained with the LAURA code. Capra [41] conducted measurements of total and radiative heat transfer for subscale aeroshell models in the X1 expansion tube and X3 expansion tunnel facilities simulating both the Fire II and Titan Explorer peak heating points. Thermo-couples on the model surface recorded the total heat transfer rate, while thin-film gauges with nickel sensing element shielded behind borosilicate windows enabled the transmitted radiative component to be determined. Similarity with flight conditions was attempted using binary scaling, however the radiative heat transfer levels recorded were up to an order of magnitude less than those inferred from the flight experiment measurements. The discrepancy was attributed to radiative cooling and non-binary thermochemical phenomena.

In contrast to expansion tubes and tunnels, ballistic range facilities accelerate the subscale model, rather than the test gas, to the desired velocity. This has the advantage of producing a disturbance-free, quiescent testing environment. On their own, however, ballistic range facilities cannot reach the hyperbolic entry regime. The two-stage light gas gun in use at the NASA Ames Hypervelocity Free Flight Aerodynamic Facility, for example, has a maximum muzzle velocity of approximately 8.5 km/s [42]. Efforts were made in the 1960's at NASA Ames to combine a reflected shock tunnel with a ballistic range to produce very high enthalpy conditions [42]. The prototype facility was capable of producing effective flight velocities of up to 12.5 km/s, allowing radiation [43–46] and heat-transfer [47] experiments to be performed at conditions relevant to hyperbolic entry. Although similar facilities at NASA Ames made contributions to the Apollo command module design, the radiation facility was decommissioned in 1972.

1.4.2 Computational modelling

The computational modelling of radiating shock layers involves the numerical solution of an appropriate set of governing equations. Hypersonic flowfields in the continuum regime are well described by the compressible Navier-Stokes equations [18]. When the mean-free path of

particles becomes comparable to the characteristic length scale of the flow, however, the Navier–Stokes equations break down. In such rarefied flow regimes, the gas can no longer be considered as a continuum and statistical methods such as Discrete Simulation Monte Carlo must be applied [48]. For the design of aeroshell thermal protection systems, we are primarily interested in the state of the shock layer when surface heating becomes significant, which typically occurs after the vehicle has penetrated the rarefied upper atmosphere. Here the continuum assumption holds and the Navier–Stokes equations are applicable. While the Navier–Stokes equations will be described in detail in § 2, here an overview of the physical modelling critical to the accurate calculation of shock layer radiation is presented. Specifically, the modelling of thermochemical nonequilibrium and radiation is discussed. Although other areas such as transport coefficients and surface boundary conditions also require physical models, these are of greater importance to the modelling of convective heating than radiation.

Modelling of thermochemical nonequilibrium

The high temperature gas⁶ encountered in the shock layer formed over an atmospheric entry vehicle is comprised of a collection of molecules, atoms, and electrons. For the hyperbolic Earth and Mars entry conditions of present interest, the volume fraction of electrons can reach as high as 10%; such a gas is referred to as a partially ionised plasma.

Each of these particles can possess thermal energy in a variety of forms: molecules, atoms and electrons can all possess translational energy, molecules and atoms can possess electronic energy due to presence of bound electrons, and molecules can possess vibrational and rotational energy due to the extra degrees of freedom. The amount of energy contained in each of these *thermal modes* is dependent on the particle's quantum state. From a theoretical perspective, the most complete way to determine the energy of the plasma would be to solve for the wavefunction of all particles via the Schrödinger equation. Due to the enormous number of particles present, however, this approach is not feasible and a statistical approach must be considered.

At the moderate pressures characterising atmospheric entry plasmas, a statistical treatment of translational energy is valid due to the low numbers of collisions required to achieve an equilibrium Maxwell distribution. Furthermore, collisional interactions between particles quickly result in the translational energy of all *heavy* particles being described by Maxwell distributions at a common temperature. Owing to their much smaller relative mass, the translational energy of free electrons is less readily describable by this common temperature. Equilibrium of the internal energy modes is described by the Boltzmann distribution. While rotational equilibrium also occurs quickly due to the efficiency of rotational excitation via heavy particle collisions (rotation–translation energy exchange), the time required for vibrational and electronic equilibration is

⁶For 12 km/s entry at Earth, the temperature behind the shock can reach as high as 60,000 K, dropping to as a low as a few hundred Kelvin at the vehicle surface.

typically much longer. Given sufficient collisions between particles, the plasma tends towards a situation where all energy modes are describable by equilibrium distributions at a single temperature.

In addition to the attainment of *thermal* equilibrium just described, the chemical species also tend towards an equilibrium composition given sufficient reactive interactions. Typically more collisions are required for chemical equilibrium than thermal equilibrium in shock layer flows. The equilibrium chemical composition for a given pressure and temperature can be found via minimising the Gibbs free energy. Thus there is a temptation to assume thermochemical equilibrium within the shock layer, as the complete thermodynamic state can be described as a function of p , T and the elemental composition.

The previously described shock tube experiments performed in the 1960s, however, found that significant portions of the shock layer emitted radiation that was not consistent with a plasma in *thermal* equilibrium, let alone *thermochemical* equilibrium. Experiments performed with an N_2 test gas at the relatively low velocity of 6.4 km/s [49] revealed that each of the internal energy modes appeared to be governed by separate equilibrium temperatures, Figure 1.6. Importantly,

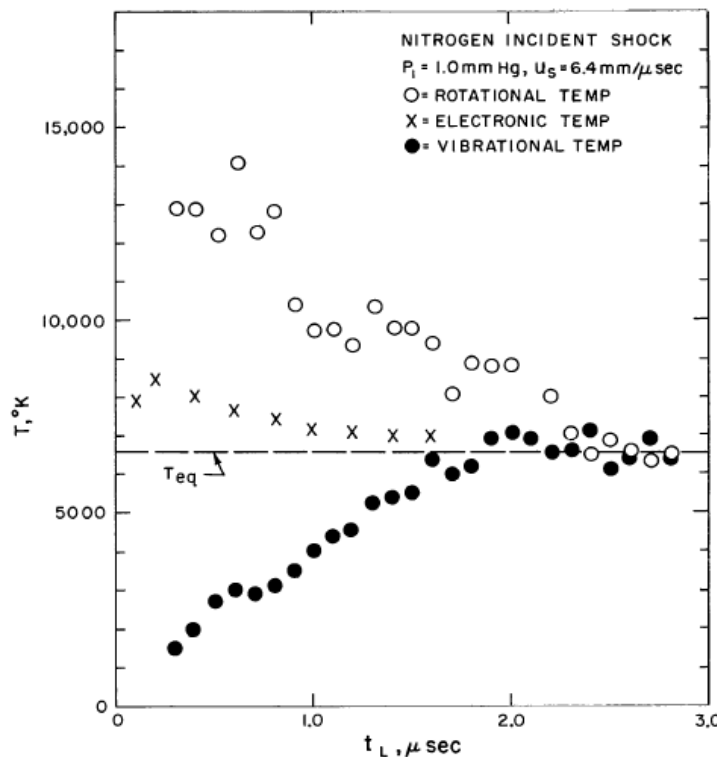


Figure 1.6: Measured rotational, vibrational and electron temperature histories for an incident nitrogen shock. The rotational and vibrational temperatures are those of the excited $N_2^+(B)$ molecule and electronic temperature is based on the relative populations of the $N_2(X)$ and $N_2(B)$ states (source: Allen [49]).

the electronic and vibrational temperatures were found to exhibit diffusive excitation, rising to a peak then decaying to the equilibrium temperature, while the rotational temperature was found to be rapidly excited to the level expected for the translational temperature. Later, results such as these motivated Park [50] to formulate the two-temperature model, where heavy particle translation and rotation are described by one temperature, and vibration, electron translation and electronic excitation by another. Modelling the electronic levels of atoms as populated by Boltzmann distributions at the vibration-electron-electronic temperature, however, did not give good agreement with experimental results at high velocities and low pressures (*e.g.* the shock tube experiments of Allen [30] with an air test gas at 0.1 Torr targeting a shock velocity of 10 km/s). It was therefore proposed that at high velocities and low pressures the population of electronic states is *collision limited* in that insufficient collisions (relative to radiative decay) occur for Boltzmann distributions to form. More recently, experiments [51, 52] and computational chemistry calculations [53, 54] have suggested that the collision limiting of vibrational and even rotational states may also be important phenomena for planetary entry.

Accordingly, the present state-of-the-art in modelling thermochemical nonequilibrium involves a combination of Boltzmann distributions and kinetic modelling. Four classes of kinetic modelling with increasing complexity can be defined; (1) species specific, (2) electronically specific, (3) vibrationally specific and (4) rotationally specific. Species specific models consider all internal energy modes to be populated by Boltzmann distributions, but reactions of *bulk* chemical species are kinetically modelled. Electronically specific models allow for nonequilibrium electronic states by the kinetic modelling of their population and depopulation mechanisms, while the other internal energy modes are populated by Boltzmann distributions. Similarly, vibrationally and rotationally specific models consider the kinetic processes of individual vibrational and rotational states. While electronically [55–58] and vibrationally [59–61] specific models have been successfully applied to planetary entry shock layers, rotationally specific models are presently limited to simple systems such as hydrogen plasmas [62]. Furthermore, only electronically specific models have been implemented for detailed aeroshell calculations (*e.g.* the calculations of Fire II with the COOLFluidD code performed by Panesi [58]).

Modelling of radiation

The modelling of radiation encompasses three domains; (1) the internal state populations of chemical species, (2) the spectral distribution of the electromagnetic energy and (3) the transport of the electromagnetic energy through the plasma. While ideally the internal state populations of chemical species would be calculated by the thermochemical nonequilibrium model as has just been discussed, such an approach is not always computationally viable. Park [29] proposed a temporally decoupled method for modelling electronic nonequilibrium by considering the balance of collisional and radiative processes in the quasi-steady-state (QSS) limit. Such a model is

attractive as it allows efficient multitemperature models to be applied to the flowfield calculation while acknowledging the non-Boltzmann population of electronic levels in the radiation calculation. Although this approach is not physically consistent, it has been applied with considerable success to both shock tube [63] and flight experiments [19].

Bound radiative transitions are characterised by discrete energy due to the quantisation of internal energy states. Furthermore, the multitude of quantum states found in molecules gives rise to many thousands of such transitions. The resulting electromagnetic spectrum therefore consists of a large number of ‘lines’ superimposed over a continuum background due to charged particle interactions. For the accurate description of such a spectrum, a very fine spectral resolution is required. The smeared rotational band model was therefore developed to approximate molecular band radiation as a continuum [64]. The Langley Optimised Radiative Nonequilibrium (LORAN) [65] and High-temperature Air Radiation (HARA) [19] codes both implement similar models. The smeared band model is unable to correctly capture absorption in plasmas close to the optically-thick limit, however, and line-by-line models must be used in these cases. The line-by-line approach is implemented in the SPRADIAN07 [66], SPECAIR [67] and PARADE [68] spectral codes, amongst others.

Radiation is inherently a non-local phenomena in that electromagnetic energy emitted at one location in a plasma may be absorbed at any location within a line-of-sight of the origin⁷. A first order approximation of radiation transport is to assume an optically thin or thick medium, representing the cases where 100% and 0% local reabsorption occur. For atmospheric entry shock layers, however, the actual local reabsorption is generally somewhere between these two limiting cases (or possibly net absorption). The tangent-slab model and moment methods (*e.g.* the modified differential approximation of Modest [69]) make various simplifications to the integro-differential equations governing radiative transport such that they can be more easily solved. However, the tangent-slab model has been shown to overpredict radiative heat-flux due to shock layer curvature [70], and moment methods have been shown to be inefficient and inaccurate for aeroshell applications [71]. The accurate solution of the radiation transport equations requires the discretisation of the computational domain via ray-tracing. Such an approach has been implemented by considering the radiation field as a continuum in the Discrete Transfer Model [72–74] and as a discrete quantity in Monte-Carlo models [75].

1.5 Scope and overview of the dissertation

The primary aim of the present thesis is to develop and implement computational models for simulating radiating shock layers in the atmospheres of Earth and Mars. Specifically, models appropriate to atmospheric entry conditions anticipated for interplanetary transit between at Earth and Mars are to be developed. We define this regime as entry velocities between 10 and 12 km/s

⁷Scattering is negligible for the gas densities of present interest.

at Earth and between 8 and 10 km/s at Mars. The immediate application of these models is the simulation of shock tube and expansion tunnel experiments performed in the University of Queensland's series of impulse facilities⁸. By performing comparisons with the experimental data, conclusions can then be drawn as to the appropriateness of the underlying physical models. Theoretical calculations can also aid in the design of new experiment techniques, such as by identifying contaminant species in shock tube experiments. Furthermore, in the case of expansion tunnel experiments, the similarity of the experiment with effective flight conditions can be investigated. A long term application of these models is the detailed simulation of flight conditions to obtain estimates of convective and radiative heat flux on the vehicle surface. Such calculations require models for gas-surface interaction and a flow-field solver with steady-state solution capabilities, which is beyond the scope of this thesis.

This thesis builds on the chemical and thermal nonequilibrium modelling foundations developed by Gollan [1]. Specifically, Gollan developed a chemical kinetic model for bulk chemical species and a thermal nonequilibrium framework for multitemperature gases consisting of neutral atoms and diatomic molecules. These models were then implemented in the time accurate Navier-Stokes solver `mbcns` [76] and the one-dimensional post-shock relaxation equations in an operator-split fashion. The specific aims of this thesis are therefore to:

1. develop thermodynamic, transport and spectral radiation models for multitemperature, multicomponent and partially ionised gases in the C-N-O-Ar elemental system,
2. develop appropriate models for the nonequilibrium rate processes occurring in such a gas,
3. validate these models via comparison with shock tube experiments,
4. implement the models in a Navier-Stokes flowfield solver with radiation-flowfield coupling, and
5. apply the Naver-Stokes solver to simulate expansion tunnel experiments.

It should also be noted that the flowfield solvers developed in this work consider bulk chemical species, rather than specific electronic or vibrational states. Also the governing equations are to be limited to those for two- and three-temperature gases. A nonequilibrium treatment of electronic level populations is to be considered for the spectral radiation calculation via a collisional-radiative model applied in a quasi-steady-state context. While it is acknowledged that a state-of-the-art flowfield solver should consider electronically and vibrationally specific kinetics and multitemperature governing equations, the work proposed above is a first step towards such a capability. The modular framework of the computer code constructed in this thesis is such that these more advanced models could be implemented in future work.

⁸Although the University of Queensland has three impulse facilities (X1,X2 and X3), only experiments from the X2 facility are considered in this work.

This thesis is divided into three parts:

Part I is concerned with the mathematical formulation of the proposed physical models for describing radiating shock layers. § 2 describes the governing equations for radiating shock layers considered in this work, namely the compressible Navier–Stokes and inviscid post-shock relaxation equations. § 3 presents the property models for high temperature gases implemented in the flowfield solvers. Specifically, models for thermodynamic, transport and spectral radiation coefficients are elaborated. § 4 describes the nonequilibrium rate processes relevant to atmospheric entry shock layers. The chemical kinetic and thermal energy exchange models implemented by the flowfield solvers are presented, as is the collisional-radiative framework for the spectral radiation module.

Part II is then focused on the implementation and application of these physical models in the one-dimensional post-shock relaxation equations. § 5 describes the implementation of the one-dimensional post-shock relaxation equations in the Poshax3 code. § 6 presents an analysis of shock tube experiments performed in the NASA Ames EAST and University of Queensland X2 facilities. For this purpose, the Poshax3 code is applied with detailed thermodynamic, chemical kinetic and collisional-radiative modelling. Conclusions are drawn as to appropriate chemical kinetic and collisional radiative models based on the experimental comparison.

Part III shifts attention from the one-dimensional post-shock relaxation equations to two-dimensional flowfields. § 7 describes the Navier–Stokes flowfield solver Eilmer3 implemented in this work. The extension of the governing equations to enable two-temperature, partially ionised and radiating flows is described. A novel ray-tracing based radiation transport model is presented. § 8 applies the Eilmer3 code to simulate two radiating shock layer experiments performed in the University of Queensland X2 facility configured as an expansion tunnel. Firstly, a 36 MJ/kg N₂–O₂ condition with a subscale Hayabusa model is considered. Secondly, a 48 MJ/kg CO₂–N₂ condition with a 25 mm diameter cylinder model is considered. For both experiments a new, simplified technique for estimating the freestream conditions is applied, and the radiating shock layers formed over the models are then simulated. Comparisons with spectral measurements are made and an investigation of the binary-scaling hypothesis is conducted for the subscale Hayabusa model experiment.

Finally, the conclusions drawn from this work and recommendations for future work are summarised in § 9.

Part I

Physical Modelling

2

Governing equations for radiating shock layers

In this chapter the governing equations for radiating shock layers are presented. As discussed in § 1.4.2, the appropriate set of governing equations for the planetary entry regime of present interest is the Navier–Stokes equations. Two- and three-temperature formulations of the compressible Navier–Stokes equations are presented in § 2.1. For the analysis of shock tube experiments and investigation of different chemical kinetic models, it is convenient to consider a reduced set of equations describing the flowfield behind a strong shock wave. Therefore the post-shock relaxation equations describing steady one-dimensional Eulerian flow are also presented in § 2.2.

2.1 Compressible Navier–Stokes equations

2.1.1 Continuity equation

The compressible Navier–Stokes equations are derived by applying the continuity equation to the conserved quantities of mass, momentum and energy¹. The differential form of the continuity equation can be expressed with vector notation as:

$$\frac{\partial \varphi}{\partial t} + \nabla \cdot \vec{F} = \Omega \quad (2.1)$$

¹Note that there may be more than one conserved mass and/or energy quantity depending on the thermodynamic model implemented

where φ is the conserved quantity, \vec{F} is a vector describing the flux of φ and Ω is a source term describing the creation and destruction of φ .

2.1.2 Selection of the conserved quantities

The conserved quantities to be applied to Equation 2.1 when deriving the compressible Navier–Stokes equations are dependent on the degree of thermochemical nonequilibrium to be considered. For a gas in thermochemical equilibrium, the conserved quantities are simply the total mass ρ , momentum $\rho\vec{u}$ and energy E of the mixture. For the planetary entry conditions of present interest, however, an accurate description of the flowfield requires the inclusion of both thermal and chemical nonequilibrium. For chemical nonequilibrium, the continuity equation of each species mass ρ_s must also be considered. The total mass continuity equation is no longer required², as the total density of the mixture can be retrieved from the sum of the species densities:

$$\rho = \sum_s^{N_{\text{species}}} \rho_s \quad (2.2)$$

For thermal nonequilibrium, the continuity of each independent thermal mode energy e_m must also be enforced. For N_{modes} thermal modes, however, only $N_{\text{modes}} - 1$ additional equations are required as the total *internal* energy e can be found from the definition of the total energy:

$$E = e + \frac{1}{2} \vec{u} \cdot \vec{u} = \sum_m^{N_{\text{modes}}} e_m + \frac{1}{2} \vec{u} \cdot \vec{u} \quad (2.3)$$

Thus the continuity equation for one of the thermal modes can be omitted given that the total energy continuity equation must be retained.

It must be noted that here we are assuming thermal nonequilibrium is modelled by a collection of independent thermal energy modes where all quantum states within a mode are populated by Boltzmann distributions at a common temperature. This approach to modelling thermal nonequilibrium is commonly referred to as the multitemperature model. A more rigorous approach to modelling thermal nonequilibrium is by the consideration of quantum states as pseudo-species³ in the mixture. Electronic [55, 56, 58], vibrational [59, 61] and even rotational [62, 77] levels of chemical species have been modelled as pseudo-species in CFD calculations in recent years. For such models the population distribution amongst the nonequilibrium quantum states are obtained by solving the continuity equation for each pseudo-species. As it is impractical to consider the detailed kinetics for every quantum state, the psuedo-species approach is typically used in conjunction with a multitemperature model.

²Although the total mass continuity equation is redundant from a mathematical standpoint, its inclusion can aid the numerical implementation as will be discussed in § 7.2

³The pseudo-species approach must be clearly distinguished from the quasi-steady-state (QSS) method proposed by Park [29] where the state resolved kinetics are decoupled from the flowfield evolution.

Here the Navier–Stokes equations for three thermal models are presented:

1. A one-temperature model considering a single translation-rotation-vibration-electron-electronic energy mode,
2. A two-temperature model considering translation-rotation and vibration-electron-electronic energy modes, and
3. A three-temperature model considering translation-rotation, vibration and electron-electronic energy modes.

For the thermal nonequilibrium models the redundant energy continuity equation is chosen to be that for the translation-rotation mode. In this thesis Navier–Stokes simulations with the two-temperature model and post-shock relaxation simulations with the two- and three-temperature models are presented. Although the three-temperature model is only implemented in the post-shock relaxation equations, it is pertinent to present the three-temperature Navier–Stokes equations from which the one-dimensional Euler equations are derived.

2.1.3 One-temperature formulation

In chemical nonequilibrium and thermal equilibrium the conserved quantities for the compressible Navier–Stokes equations are species density, total momentum and total energy. A single temperature T defines the population distributions amongst all thermal modes.

Species mass continuity equation

The species mass continuity equation is obtained by considering the species density ρ_s as the conserved quantity in Equation 2.1:

$$\frac{\partial \rho_s}{\partial t} + \nabla \cdot (\rho_s \vec{u} + \vec{J}_s) = \dot{\omega}_s \quad (2.4)$$

where \vec{u} is the velocity vector, \vec{J}_s is the diffusion vector, $\dot{\omega}_s$ is the mass production source term due to chemical reactions.

Momentum continuity equation

The continuity equation for momentum $\rho \vec{u}$ can be expressed as:

$$\frac{\partial \rho \vec{u}}{\partial t} + \nabla \cdot (\rho \vec{u} \vec{u}) = -\nabla p + \nabla \cdot \tau \quad (2.5)$$

where p is the gas pressure and τ is the viscous stress tensor. The stress tensor is derived from the Chapman Enskog approximation:

$$\tau = \mu \left(\nabla \vec{u} + \nabla \vec{u}^T \right) (\kappa + \lambda) (\nabla \cdot \vec{u}) \hat{I} \quad (2.6)$$

where μ is the viscosity coefficient, λ is the secondary viscosity coefficient and κ is the contribution due to bulk viscosity which is often omitted.

Total energy continuity equation

The total energy of a gas E is comprised of both thermal and kinetic energy components:

$$E = e + \frac{1}{2} \vec{u} \cdot \vec{u} \quad (2.7)$$

where e is the thermal energy per unit mass. The total energy continuity equation is:

$$\frac{\partial \rho E}{\partial t} + \nabla \cdot (\vec{u} (\rho E + p)) = \nabla \cdot (\tau \cdot \vec{u}) - \nabla \cdot \vec{q} \quad (2.8)$$

where the heat flux vector \vec{q} is comprised of contributions from convection, diffusion and radiation:

$$\vec{q} = \vec{q}_{\text{cond.}} + \vec{q}_{\text{diff.}} + \vec{q}_{\text{rad.}} = -K \nabla T + \sum_s h_s \vec{J}_s + \int_{\nu} \vec{I}_{\nu} d\nu \quad (2.9)$$

where K is the total conductivity coefficient, h_s is the species enthalpy and \vec{I}_{ν} is the spectral radiation intensity vector.

2.1.4 Two-temperature formulation

The two-temperature model considers a translation-rotation temperature T_{tr} and a vibration-electron-electronic temperature T_{ve} . The species mass, total momentum and total energy equations presented for the one-temperature model, Equations 2.4, 2.5 and 2.8 respectively, also hold for the two-temperature model with minor alterations. As there are now two thermal modes, the expression for total energy E becomes:

$$E = e_{\text{tr}} + e_{\text{ve}} + \frac{1}{2} \vec{u} \cdot \vec{u} \quad (2.10)$$

and the expression for the conductive heat flux vector $\vec{q}_{\text{cond.}}$ as used in Equation 2.17 is separated into translation-rotation and vibration-electron-electronic contributions:

$$\vec{q}_{\text{cond.}} = \vec{q}_{\text{cond.-tr}} + \vec{q}_{\text{cond.-ve}} = -K_{\text{tr}} \nabla T_{\text{tr}} - K_{\text{ve}} \nabla T_{\text{ve}} \quad (2.11)$$

Vibration-electron-electronic energy continuity equation

The vibration-electron-electronic energy continuity equation is:

$$\frac{\partial \rho e_{ve}}{\partial t} + \nabla \cdot (\vec{u} (\rho e_{ve} + p_e)) = -\nabla \cdot \vec{q}_{ve} + \dot{\Omega}_{VT} + \dot{\Omega}_{ET} + \dot{\Omega}_{VC} + \dot{\Omega}_{EC} \quad (2.12)$$

where \vec{q}_{ve} is the modal heat flux vector and $\dot{\Omega}_{TV}$, $\dot{\Omega}_{TE}$, $\dot{\Omega}_{CV}$ and $\dot{\Omega}_{CE}$ are the thermal energy source terms for vibration-translation exchange, electron-translation exchange, vibration-chemistry coupling and electron-chemistry coupling respectively. Note that the electron pressure p_e must be included in the advection flux term to account for pressure work of the electron translational mode. The vibration-electron-electronic heat flux vector \vec{q}_{ve} is:

$$\vec{q}_{ve} = \vec{q}_{ve-cond.} + \vec{q}_{ve-diff.} + \vec{q}_{rad.} = -K_{ve} \nabla T_{ve} + \sum_s h_{ve-s} \vec{J}_s + \int_v \vec{I}_v d\nu \quad (2.13)$$

where all radiative heating is assumed to occur via a change in electronic energy.

2.1.5 Three-temperature formulation

The three-temperature model splits the vibration-electron-electronic energy mode of the two-temperature model into two parts, a vibrational mode and an electron-electronic mode; therefore a translation-rotation temperature T_{tr} , a vibrational temperature T_v and an electron-electronic temperature T_e are considered.

Vibration energy continuity equation

The vibration energy continuity equation is:

$$\frac{\partial \rho e_v}{\partial t} + \nabla \cdot (\rho \vec{u} e_v) = -\nabla \cdot \vec{q}_v + \dot{\Omega}_{VT} + \dot{\Omega}_{VE} + \dot{\Omega}_{VC} \quad (2.14)$$

where \vec{q}_v is the modal heat flux vector and $\dot{\Omega}_{VT}$, $\dot{\Omega}_{VE}$ and $\dot{\Omega}_{VC}$ are the thermal energy source terms for vibration-translation exchange, vibration-electron exchange and vibration-chemistry coupling respectively. The vibration heat flux vector \vec{q}_v is:

$$\vec{q}_v = \vec{q}_{v-cond.} + \vec{q}_{v-diff.} = -K_v \nabla T_v + \sum_s h_{v-s} \vec{J}_s \quad (2.15)$$

where any purely vibrational component of radiation has been neglected.

Electron-electronic energy continuity equation

The electron-electronic energy continuity equation is:

$$\frac{\partial \rho e_e}{\partial t} + \nabla \cdot (\vec{u} (\rho e_e + p_e)) = -\nabla \cdot \vec{q}_e + \dot{\Omega}_{ET} + \dot{\Omega}_{EV} + \dot{\Omega}_{EC} \quad (2.16)$$

where \vec{q}_e is the modal heat flux vector and $\dot{\Omega}_{ET}$, $\dot{\Omega}_{EV}$ and $\dot{\Omega}_{EC}$ are the thermal energy source terms for electron-translation exchange, electron-vibration exchange and electron-chemistry coupling respectively. Similarly as for the vibration-electron-electronic energy continuity equation, the electron pressure must be included in the advection flux term to account for pressure work of the electron translational mode. The electron-electronic heat flux vector \vec{q}_e is:

$$\vec{q}_e = \vec{q}_{e\text{-cond.}} + \vec{q}_{e\text{-diff.}} = -K_e \nabla T_e + \sum_s h_{e-s} \vec{J}_s + \int_v \vec{I}_v d\nu \quad (2.17)$$

where all radiative heating is assumed to occur via a change in electronic energy.

2.2 Post-shock relaxation equations

The post-shock relaxation equations can be derived from the full Navier–Stokes equations presented in Section 2.1. Considering only variation of properties in the x direction and inviscid flow, the Navier–Stokes equations reduce to the one-dimensional Euler equations. For a two temperature gas we have:

$$\frac{\partial \rho_s}{\partial t} + \frac{\partial}{\partial x} (\rho_s u) = \omega_s \quad (2.18)$$

$$\frac{\partial \rho u}{\partial t} + \frac{\partial}{\partial x} (\rho u^2 + p) = 0 \quad (2.19)$$

$$\frac{\partial \rho E}{\partial t} + \frac{\partial}{\partial x} (u (\rho E + p)) = -\frac{\partial q_{rad}}{\partial x} \quad (2.20)$$

$$\frac{\partial \rho e_{ve}}{\partial t} + \frac{\partial}{\partial x} (u (\rho e_{ve} + p_e)) = -\frac{\partial q_{rad}}{\partial x} + \dot{\Omega}_{VT} + \dot{\Omega}_{ET} + \dot{\Omega}_{VC} + \dot{\Omega}_{EC} \quad (2.21)$$

where E is the total energy as defined in Equation 2.10. As we are interested in the steady flow or time invariant solution, the derivatives with respect to t are set to zero:

$$\frac{\partial}{\partial x} (\rho_s u) = \omega_s \quad (2.22)$$

$$\frac{\partial}{\partial x} (\rho u^2 + p) = 0 \quad (2.23)$$

$$\frac{\partial}{\partial x} (u (\rho E + p)) = -\frac{\partial q_{rad}}{\partial x} \quad (2.24)$$

$$\frac{\partial}{\partial x} (u (\rho e_{ve} + p_e)) = -\frac{\partial q_{rad}}{\partial x} + \dot{\Omega}_{VT} + \dot{\Omega}_{ET} + \dot{\Omega}_{VC} + \dot{\Omega}_{EC} \quad (2.25)$$

Similarly, for a three temperature gas the post-shock relaxation equations are:

$$\frac{\partial}{\partial x} (\rho_s u) = \dot{\omega}_s \quad (2.26)$$

$$\frac{\partial}{\partial x} (\rho u^2 + p) = 0 \quad (2.27)$$

$$\frac{\partial}{\partial x} (u (\rho E + p)) = -\frac{\partial q_{\text{rad}}}{\partial x} \quad (2.28)$$

$$\frac{\partial}{\partial x} (ue_v) = \dot{\Omega}_{\text{VT}} + \dot{\Omega}_{\text{VE}} + \dot{\Omega}_{\text{VC}} \quad (2.29)$$

$$\frac{\partial}{\partial x} (u (e_e + p_e)) = -\frac{\partial q_{\text{rad}}}{\partial x} + \dot{\Omega}_{\text{ET}} + \dot{\Omega}_{\text{EV}} + \dot{\Omega}_{\text{EC}} \quad (2.30)$$

2.3 Summary

The governing equations for radiating shock layers have been described. In particular, the two- and three-temperature formulations of the compressible Navier–Stokes and inviscid post-shock relaxation equations have been presented. These equations demonstrate the need for appropriate thermodynamic, transport and spectral radiation models in order to describe the gas-state, and nonequilibrium rate parameters to describe its temporal evolution. The derivation and implementation of these models are the focus of the following two chapters.

3

Properties of high temperature gases

This chapter is concerned with presenting appropriate models for calculating the properties of high temperature gases relevant to radiating shock layers. The necessary properties were identified by the formulation of the governing equations in § 2. The models for calculating the thermodynamic and transport properties are presented in § 3.1 and 3.2, respectively, while the modelling of spectral radiation properties is presented in § 3.3.

3.1 Thermodynamic properties and coefficients

As discussed in § 1, both chemical and thermal nonequilibrium are important phenomena for atmospheric entry at Earth and Mars. Although thermal nonequilibrium is only fully accounted for by modelling the rate equations of all discrete thermal states, the resulting system of equations is prohibitively large. A multitemperature model avoids the need for such a detailed calculation by assuming the thermal modes are populated by Boltzmann distributions governed by separate temperatures. Such a model therefore allows intermodal nonequilibrium to be captured, whilst neglecting intramodal nonequilibrium. Furthermore, intermolecular forces can be neglected for the planetary entry aerothermal regime of present interest as the pressures encountered are generally less than a few atmospheres. Thus, in general, we are interested in the thermodynamic properties for a mixture of thermally perfect atoms, molecules and electrons with separate temperatures governing each thermal mode. The thermodynamic properties of such a gas can be derived from a combination of chemical thermodynamics and statistical mechanics.

3.1.1 Thermodynamic relations from statistical mechanics

For a collection of quantum microstates in thermal equilibrium, the thermodynamic properties can be derived from statistical mechanics in terms of the governing temperature T , the partition function Q and the total population N [78]:

$$F = -Nk_B T \left(\ln \frac{Q}{N} + 1 \right) \quad (3.1)$$

$$S = \begin{cases} Nk_B \left[\ln \frac{Q}{N} + 1 + T \frac{\partial(\ln Q)}{\partial T} \right] & \text{for translational states} \\ Nk_B \left[\ln Q + T \frac{\partial(\ln Q)}{\partial T} \right] & \text{for internal states} \end{cases} \quad (3.2)$$

$$E = Nk_B T^2 \frac{\partial(\ln Q)}{\partial T} \quad (3.3)$$

$$p = Nk_B T \frac{\partial(\ln Q)}{\partial V} \quad (3.4)$$

$$\tilde{\mu} = -k_B T \ln \frac{Q}{N} \quad (3.5)$$

where F is the Helmholtz free energy, S is entropy, E is energy, p is pressure and $\tilde{\mu}$ is the chemical potential per molecule. For the multitemperature formulation of present interest, each thermal mode has its own equilibrium temperature and Equations 3.1 to 3.5 must be applied separately to each. As will be discussed in Section 3.1.3, the assumption of decoupled thermal modes allows the thermodynamic properties for the entire species to be calculated as the sum of modal contributions. Thus the partition functions for each thermal mode need to be defined in order to derive analytical expressions for the thermodynamic variables. The partition function for a collection of individual quantum states j is defined as [78]:

$$Q = \sum_j e^{-\epsilon_j / k_B T} \quad (3.6)$$

A set of N individual quantum states with common energy is called a level and has a degeneracy g equal to N . The partition function can therefore also be expressed by summing over all levels l rather than states, which is a more appropriate form for thermodynamics calculations:

$$Q = \sum_l g_l e^{-\epsilon_l / k_B T} \quad (3.7)$$

3.1.2 Modal contributions to thermodynamic properties

Translation

The energy of a single translational state confined in a volume V with dimensions a_1 , a_2 and a_3 and defined by quantum numbers n_1 , n_2 and n_3 is [78]:

$$\epsilon_{n_1,n_2,n_3} = \frac{h^2}{8m} \left(\frac{n_1^2}{a_1^2} + \frac{n_2^2}{a_2^2} + \frac{n_3^2}{a_3^2} \right) \quad \text{where} \quad \begin{cases} n_1 \\ n_2 \\ n_3 \end{cases} = 1, 2, 3, \dots \quad (3.8)$$

The partition function is then found by substituting Equation 3.8 into Equation 3.6, yielding:

$$Q_{\text{trans}} = \sum_{n_1=1}^{\infty} \sum_{n_2=1}^{\infty} \sum_{n_3=1}^{\infty} \exp \left[- \left(\frac{n_1^2}{a_1^2} + \frac{n_2^2}{a_2^2} + \frac{n_3^2}{a_3^2} \right) \frac{h^2}{8mkT_{\text{trans}}} \right] \quad (3.9)$$

To good accuracy a closed form expression can be derived by approximating the sum over states by an integral [78], giving:

$$Q_{\text{trans}} = \left(\frac{2\pi mk_B T_{\text{trans}}}{h^2} \right)^{3/2} V \quad (3.10)$$

By substituting Equation 3.10 into the statistical mechanics expressions for entropy, energy and pressure, Equations 3.2, 3.3 and 3.4, we obtain:

$$S_{\text{trans}} = Nk_B \left\{ \frac{5}{2} \ln T_{\text{trans}} - \ln p + \ln \left[\left(\frac{2\pi mk^{3/2}}{h^2} \right)^{3/2} k_B \right] + \frac{5}{2} \right\} \quad (3.11)$$

$$E_{\text{trans}} = \frac{3}{2} Nk_B T_{\text{trans}} \quad (3.12)$$

$$p = \frac{Nk_B T_{\text{trans}}}{V} \quad (3.13)$$

where the ‘trans’ subscript for p is omitted as only the translational mode makes a contribution to pressure. Equation 3.11 is the famous *Sackur-Tetrode equation* for the absolute translational entropy. Expressing the entropy and energy per unit mass and using the definition of the species gas constant $R = k_B/m$ gives:

$$s_{\text{trans}} = \frac{5}{2} R \ln T_{\text{trans}} - R \ln p + R \left\{ \ln \left[\left(\frac{2\pi m^2 R}{h^2} \right)^{3/2} Rm \right] + \frac{5}{2} \right\} \quad (3.14)$$

$$e_{\text{trans}} = \frac{3}{2} RT_{\text{trans}} \quad (3.15)$$

$$p = \rho RT \quad (3.16)$$

The specific heat at constant volume follows from the derivative of energy e_{trans} with respect to temperature T :

$$c_{v,\text{trans}} = \left(\frac{\partial e_{\text{trans}}}{\partial T_{\text{trans}}} \right)_v = \frac{3}{2} R \quad (3.17)$$

The specific heat at constant pressure assuming an ideal gas is found from Mayer’s relation:

$$c_{p,\text{trans}} = c_{v,\text{trans}} + R = \frac{5}{2}R \quad (3.18)$$

Note that translation is the only thermal mode with c_p being different from c_v , as it alone determines the gas pressure.

Electronic

The degeneracies and energies of electronic levels for most commonly encountered atoms and molecules have been experimentally determined and are tabulated in the literature (eg Reference [79, 80]). For $l_{\max} + 1$ electronic levels the electronic partition function is:

$$Q_{\text{el}} = \sum_{l=0}^{l_{\max}} g_l e^{-\epsilon_l/kT_{\text{el}}} = \sum_{l=0}^{l_{\max}} g_l e^{-\Theta_l/T_{\text{el}}} \quad (3.19)$$

where $\Theta_l = \epsilon_l/k$ is the characteristic temperature for electronic excitation of level i . At low temperatures ($T_{\text{el}} \lesssim 8000$ K) only the ground and first excited levels are significantly populated for some species [26, 78], and an analytical form of the partition function can be derived:

$$Q_{\text{el-2L}} = g_0 + g_1 e^{-\Theta_1/T_{\text{el}}} \quad (3.20)$$

where the characteristic temperature of the excited state Θ_1 is taken relative to the ground state. At the high electronic temperatures encountered during atmospheric re-entry ($T_{\text{el}} \lesssim 20000$ K), however, many species require more than two electronic levels to retain a high level of accuracy. Therefore thermodynamic expressions are required for both the multi- and two-level cases:

$$s_{\text{el}} = R \left[\ln \left(\sum_{l=0}^{l_{\max}} g_l e^{-\Theta_l/T_{\text{el}}} \right) + \frac{1}{T_{\text{el}}} \frac{\sum_{l=0}^{l_{\max}} g_l \Theta_l e^{-\Theta_l/T_{\text{el}}}}{\sum_{l=0}^{l_{\max}} g_l e^{-\Theta_l/T_{\text{el}}}} \right] \quad (3.21)$$

$$s_{\text{el-2L}} = R \left[\ln g_0 + \ln \left(1 + \frac{g_1}{g_0} e^{-\Theta_1/T_{\text{el}}} \right) + \frac{(g_1/g_0) e^{-\Theta_1/T_{\text{el}}}}{1 + (g_1/g_0) e^{-\Theta_1/T_{\text{el}}}} \right] \quad (3.22)$$

$$e_{\text{el}} = R \frac{\sum_{l=0}^{l_{\max}} g_l \Theta_l e^{-\Theta_l/T_{\text{el}}}}{\sum_{l=0}^{l_{\max}} g_l e^{-\Theta_l/T_{\text{el}}}} \quad (3.23)$$

$$e_{\text{el-2L}} = R \Theta_1 \frac{(g_1/g_0) e^{-\Theta_1/T_{\text{el}}}}{1 + (g_1/g_0) e^{-\Theta_1/T_{\text{el}}}} \quad (3.24)$$

$$c_{v,\text{el}} = \frac{R}{T_{\text{el}}^2} \left[\frac{\sum_{l=0}^{l_{\max}} g_l \Theta_l^2 e^{-\Theta_l/T_{\text{el}}} - \sum_{l=0}^{l_{\max}} g_l \Theta_l e^{-\Theta_l/T_{\text{el}}}}{\sum_{l=0}^{l_{\max}} g_l e^{-\Theta_l/T_{\text{el}}}} \right] \quad (3.25)$$

$$c_{v,\text{el-2L}} = R \left(\frac{\Theta_1}{T_{\text{el}}} \right)^2 \frac{(g_1/g_0) e^{-\Theta_1/T_{\text{el}}}}{\left[1 + (g_1/g_0) e^{-\Theta_1/T_{\text{el}}} \right]^2} \quad (3.26)$$

Vibration

The energy of vibrational level v is given by the Dunham expansion which accounts for small anharmonicity¹ of the oscillating system:

$$\epsilon_v = \omega_e(v + \frac{1}{2}) - \omega_e x_e(v + \frac{1}{2})^2 + \omega_e y_e(v + \frac{1}{2})^3 + \omega_e z_e(v + \frac{1}{2})^4 \quad (3.27)$$

The $\omega_e(v + \frac{1}{2})$ term represents the contribution from purely harmonic vibration, whilst the higher order terms represent anharmonic corrections. Although the anharmonic corrections have been shown to be significant for air species at temperatures as low as 2000 K [26], it is common practice to retain only the harmonic terms for computational efficiency. Furthermore, the vibrational energy exchange models to be implemented in Eilmer3 all assume harmonic oscillations. Thus for computational efficiency and to achieve consistency between the thermodynamics and energy exchange models, the harmonic oscillator model will be used.

Assuming a harmonic oscillator, the energy of vibrational level v referenced from the ground state energy is:

$$\epsilon_v = \omega_e v = k_B \Theta_{\text{vib}} v \quad (3.28)$$

where $\Theta_{\text{vib}} = \omega_e/k$ is the characteristic temperature of the vibrational mode. Noting that the degeneracy of vibrational levels is 1, the vibrational partition function for the harmonic oscillator is:

$$Q_{\text{vib-HO}} = \sum_{v=0}^{\infty} e^{-v\Theta_{\text{vib}}/T_{\text{vib}}} = \frac{1}{1 - e^{-\Theta_{\text{vib}}/T_{\text{vib}}}} \quad (3.29)$$

where the analytical expression for the infinite geometric series has been applied. The summation over an infinity of vibrational levels, however, is erroneous as high lying vibrational levels will have energy above the dissociation energy $D_e = k_B \Theta_D$. The truncated harmonic oscillator model accounts for a finite number of vibrational levels by terminating the summation when $\omega_e(v + 1/2) > D_e$:

$$Q_{\text{vib-THO}} = \sum_{v=0}^{v_{\max}} e^{-v\Theta_{\text{vib}}/T_{\text{vib}}} = \frac{1 - e^{-\Theta_D/T_{\text{vib}}}}{1 - e^{-\Theta_{\text{vib}}/T_{\text{vib}}}} \quad (3.30)$$

where:

$$v_{\max} = \frac{D_e}{k_B \Theta_{\text{vib}}} - \frac{1}{2}$$

The entropy, energy and specific heat expressions for each of the harmonic and truncated harmonic oscillator vibration models can now be derived:

¹This is defined in Reference [79] as when $g \ll f$ where the potential function is approximated by $U \approx f(r - r_e)^2 - g(r - r_e)^3$ where $r - r_e$ is the distance from the equilibrium internuclear separation.

$$s_{\text{vib-HO}} = R \left[-\ln \left(1 - e^{-\Theta_{\text{vib}}/T_{\text{vib}}} \right) + \frac{\Theta_{\text{vib}}/T_{\text{vib}}}{e^{\Theta_{\text{vib}}/T_{\text{vib}}} - 1} \right] \quad (3.31)$$

$$\begin{aligned} s_{\text{vib-THO}} &= R \left[-\ln \left(\frac{1 - e^{-\Theta_{\text{vib}}/T_{\text{vib}}}}{1 - e^{-\Theta_D/T_{\text{vib}}}} \right) + \dots \right. \\ &\quad \left. \dots + \frac{1}{T_{\text{vib}}} \left(\frac{\Theta_{\text{vib}} e^{-\Theta_{\text{vib}}/T_{\text{vib}}}}{1 - e^{-\Theta_{\text{vib}}/T_{\text{vib}}}} - \frac{\Theta_D e^{-\Theta_D/T_{\text{vib}}}}{1 - e^{-\Theta_D/T_{\text{vib}}}} \right) \right] \end{aligned} \quad (3.32)$$

$$e_{\text{vib-HO}} = \frac{R\Theta_{\text{vib}}}{e^{\Theta_{\text{vib}}/T_{\text{vib}}} - 1} \quad (3.33)$$

$$e_{\text{vib-THO}} = R \left[\frac{\Theta_{\text{vib}}}{e^{\Theta_{\text{vib}}/T_{\text{vib}}} - 1} - \frac{\Theta_D}{e^{\Theta_D/T_{\text{vib}}} - 1} \right] \quad (3.34)$$

$$c_{v,\text{vib-HO}} = R \left(\frac{\Theta_{\text{vib}}}{T_{\text{vib}}} \right)^2 \frac{e^{\Theta_{\text{vib}}/T_{\text{vib}}}}{(e^{\Theta_{\text{vib}}/T_{\text{vib}}} - 1)^2} = R \left[\frac{\Theta_{\text{vib}}/2T_{\text{vib}}}{\sinh(\Theta_{\text{vib}}/2T_{\text{vib}})} \right]^2 \quad (3.35)$$

$$\begin{aligned} c_{v,\text{vib-THO}} &= R \left\{ \left[\left(\frac{\Theta_{\text{vib}}}{T_{\text{vib}}} \right)^2 \frac{e^{\Theta_{\text{vib}}/T_{\text{vib}}}}{(e^{\Theta_{\text{vib}}/T_{\text{vib}}} - 1)^2} \right] - \left[\left(\frac{\Theta_D}{T_{\text{vib}}} \right)^2 \frac{e^{\Theta_D/T_{\text{vib}}}}{(e^{\Theta_D/T_{\text{vib}}} - 1)^2} \right] \right\} \\ &= R \left\{ \left[\frac{\Theta_{\text{vib}}/2T_{\text{vib}}}{\sinh(\Theta_{\text{vib}}/2T_{\text{vib}})} \right]^2 - \left[\frac{\Theta_D/2T_{\text{vib}}}{\sinh(\Theta_D/2T_{\text{vib}})} \right]^2 \right\} \end{aligned} \quad (3.36)$$

Rotation

The degeneracy and energy for rotational level J of a rigid rotator are:

$$g_J = 2J + 1 \quad (3.37)$$

$$\epsilon_J = \Theta_{\text{rot}} J(J + 1) \quad (3.38)$$

where Θ_{rot} is the characteristic temperature for rotation (approximately 2 or 3 K for most molecules of interest). The partition function then follows from its definition:

$$Q_{\text{rot}} = \frac{1}{\sigma} \sum_{J=0}^{\infty} (2J + 1) e^{-\Theta_{\text{rot}}/T_{\text{rot}}} \quad (3.39)$$

where the homonuclear factor σ (equal to 2 for homonuclear and 1 for heteronuclear molecules) is required to be introduced due to symmetry considerations. By replacing the summation over states by an integral, and acknowledging that $\Theta_{\text{rot}} \ll T_{\text{rot}}$ for the regime of present interest, a closed form expression for Q_{rot} is obtained [78]:

$$Q_{\text{rot}} = \frac{1}{\sigma} \left(\frac{T_{\text{rot}}}{\Theta_{\text{rot}}} \right) \quad (3.40)$$

Expressions for rotational entropy and energy can now be found from Equations 3.2 and 3.3 respectively:

$$s_{\text{rot}} = R \left[\ln \frac{T_{\text{rot}}}{\sigma \Theta_{\text{rot}}} + 1 \right] \quad (3.41)$$

$$e_{\text{rot}} = RT_{\text{rot}} \quad (3.42)$$

The rotational specific heat at constant volume is therefore simply:

$$c_{v,\text{rot}} = R \quad (3.43)$$

Equations 3.38 - 3.43 are only strictly correct for linear polyatomic and spherical top diatomic molecules. For nonlinear polyatomic molecules such as NO₂, the partition function is [81]:

$$Q_{\text{rot}} = \sqrt{\frac{\pi}{\Theta_{A_0} \Theta_{B_0} \Theta_{C_0}}} T^3 \quad (3.44)$$

where Θ_{A_0} , Θ_{B_0} and Θ_{C_0} are the characteristic rotational temperatures of the molecular principal moments of inertia. The expressions for the entropy, energy and specific heat of non-linear polyatomic molecules are therefore:

$$s_{\text{rot}} = R \left[\ln \left(\sqrt{\frac{\pi}{\Theta_{A_0} \Theta_{B_0} \Theta_{C_0}}} T^3 \right) + \frac{3}{2} \right] \quad (3.45)$$

$$e_{\text{rot}} = \frac{3}{2} RT_{\text{rot}} \quad (3.46)$$

$$c_{v,\text{rot}} = \frac{3}{2} R \quad (3.47)$$

3.1.3 Thermodynamic properties for a single species

The Born-Oppenheimer approximation states that, for internuclear distances close to equilibrium, the electronic and nuclear dynamics of molecules can be treated independently [82]. Therefore when solving the time independent Schrödiner equation describing the quantum state of a molecule, the total wavefunction can be separated into two independent contributions:

$$\Psi_{\text{total}} = \psi_{\text{electronic}} \cdot \psi_{\text{nuclear}} \quad (3.48)$$

Although the Born-Oppenheimer approximation does not make a case for further separation of the individual nuclear components (vibration and rotation), it has been widely interpreted by the aerospace community as justifying the separation of all thermal modes [83]. While the separation of the translational dynamics from the internal components is entirely appropriate where intermolecular forces can be neglected, the omission of rovibrational coupling can lead to significant error in highly excited gases [78]. Jaffe [84] accordingly proposed a method for calculating the two-temperature partition functions where the interaction energy between modes is accounted for. This model, however, was found by Panesi [58] to not give a great improvement

over assuming complete mode separation, and to be computationally inefficient. Assuming the separation of all thermal modes, the degeneracy and energy of a rovibronic molecular quantum level can be calculated as the sum of the modal contributions:

$$g_{n,l,v,J} = g_n + g_l + g_v + g_J \quad (3.49)$$

$$\epsilon_{n,l,v,J} = \epsilon_n + \epsilon_l + \epsilon_v + \epsilon_J \quad (3.50)$$

Upon substituting Equation 3.50 into the definition of the equilibrium partition function, Equation 3.7, a simplified expression for the molecular partition function emerges:

$$\begin{aligned} Q_{\text{total}} &= \sum_n \sum_l \sum_v \sum_J (g_n + g_l + g_v + g_J) e^{-(\epsilon_n + \epsilon_l + \epsilon_v + \epsilon_J)/k_B T} \\ &= \sum_n g_n e^{-\epsilon_n/k_B T} \sum_l g_l e^{-\epsilon_l/k_B T} \sum_v g_v e^{-\epsilon_v/k_B T} \sum_J g_J e^{-\epsilon_J/k_B T} \\ \therefore Q_{\text{total}} &= Q_{\text{trans}} Q_{\text{el}} Q_{\text{vib}} Q_{\text{rot}} \end{aligned} \quad (3.51)$$

Thus the separation of modes allows the total partition function to be factorised into the modal partition function contributions. This important property enables the use of separate temperatures for each thermal mode, as will be considered in this thesis.

Decoupled thermal modes

Referring to the modal thermodynamic expressions elaborated in Sections 3.1.2 to 3.1.2, the specific entropy, specific energy, specific heats and partial pressure expressions for atoms in thermal nonequilibrium are:

$$e_{\text{atom}} = e_{\text{trans}} + e_{\text{el}} \quad (3.52)$$

$$s_{\text{atom}} = s_{\text{trans}} + s_{\text{el}} \quad (3.53)$$

$$c_{v,\text{atom}} = c_{v,\text{trans}} + c_{v,\text{el}} \quad (3.54)$$

$$c_{p,\text{atom}} = c_{v,\text{atom}} + R \quad (3.55)$$

$$p_{\text{atom}} = p_{\text{trans}} \quad (3.56)$$

The thermodynamic expressions for molecules are:

$$e_{\text{mol.}} = e_{\text{trans}} + e_{\text{el}} + \sum_{m=1}^{N_{\text{vib.}}} e_{\text{vib},m} + e_{\text{rot}} \quad (3.57)$$

$$s_{\text{mol.}} = s_{\text{trans}} + s_{\text{el}} + \sum_{m=1}^{N_{\text{vib.}}} s_{\text{vib},m} + s_{\text{rot}} \quad (3.58)$$

$$c_{v,\text{mol.}} = c_{v,\text{trans}} + c_{v,\text{el}} + \sum_{m=1}^{N_{\text{vib.}}} c_{v,\text{vib},m} + c_{v,\text{rot}} \quad (3.59)$$

$$c_{p,\text{mol.}} = c_{v,\text{mol.}} + R \quad (3.60)$$

$$p_{\text{mol.}} = p_{\text{trans}} \quad (3.61)$$

where multiple vibrational modes have been included to allow for polyatomic species. Finally, the thermodynamic expressions for free electrons are:

$$e_e = e_{\text{trans}} \quad (3.62)$$

$$s_e = s_{\text{trans}} + s_{\text{el}} \quad (3.63)$$

$$c_{v,e} = c_{v,\text{trans}} \quad (3.64)$$

$$c_{p,e} = c_{v,e} + R \quad (3.65)$$

$$p_e = p_{\text{trans}} \quad (3.66)$$

where the electronic contribution only affects entropy as the internal electronic energy of free electrons is obviously zero, but the degeneracy is two owing to the possible spin states.

Fully coupled internal modes

For the validation of the thermodynamic properties derived under the assumption of decoupled thermal modes, it is useful to consider a model where all internal modes remain fully coupled. The present formulation neglects intermolecular forces, therefore it is superfluous to consider the coupling between translational and the internal modes. As atoms and free electrons only have one internal thermal mode (electronic), the concept of fully coupled internal modes only pertains to molecules. The total internal partition function for a fully coupled (FC) diatomic molecule evaluated at the equilibrium temperature T is:

$$Q_{\text{int,FC}} = \sum_l \sum_v \sum_J g_{l,v,J} e^{-(\epsilon_{l,v,J})/k_B T} \quad (3.67)$$

where $g_{l,v,J}$ and $\epsilon_{l,v,J}$ are the degeneracy and energy of the rovibronic level with electronic, vibrational and rotational quantum numbers l , v and J respectively. As intermolecular forces can be neglected, the total partition function is then:

$$Q_{\text{total,FC}} = Q_{\text{trans}} Q_{\text{int,FC}} \quad (3.68)$$

The thermodynamic properties for a diatomic molecule with fully coupled internal modes can then be derived from their definitions.

Thermodynamic properties of atomic species

From both a mathematical and practical standpoint, the summation over electronic levels must be truncated. The number of electronic levels considered can significantly affect the resulting thermodynamic properties. Although various cutoff formulae exist, it is useful to examine the sensitivity of certain atomic species to the number of electronic levels included. The level data implemented here is derived from the NIST Atomic Spectra Database [80], where the individual levels have been grouped into multiplet levels.

Figure 3.1 compares the ratio of specific heats calculated with varying number of electronic levels for the important atomic species of interest to high speed Mars entry, namely Ar, Ar⁺, C, C⁺, He, He⁺, N, N⁺, O and O⁺. Although He and He⁺ are not constituents of the Martian atmosphere, there thermochemical properties are required in the present work for simulating impulse facility conditions where helium is used as a driver gas. Anions and multiply charged cations are not considered as they are trace species for the conditions of present interest. The spectroscopic parameters for all atomic species are obtained from the NIST Atomic Species Database [80]. The ratio of specific heats derived from the tabulated data of Capitelli *et al.* [81] is included for reference, however no data is available for He and He⁺.

Table 3.1 summarises the number of electronic levels retained for atomic species considered in the present work.

Table 3.1: Number of electronic levels retained for atomic species considered in the present work

Atomic Species	Ar	Ar ⁺	C	C ⁺	He	He ⁺	N	N ⁺	O	O ⁺
Electronic levels	5	3	5	3	2	2	5	4	5	3

Thermodynamic properties of diatomic species

The accuracy of molecular thermodynamic properties calculated via the present multitemperature formulation is affected by:

1. the decoupling of thermal modes,
2. approximate rotational partition function,
3. the maximum vibrational quantum number, and

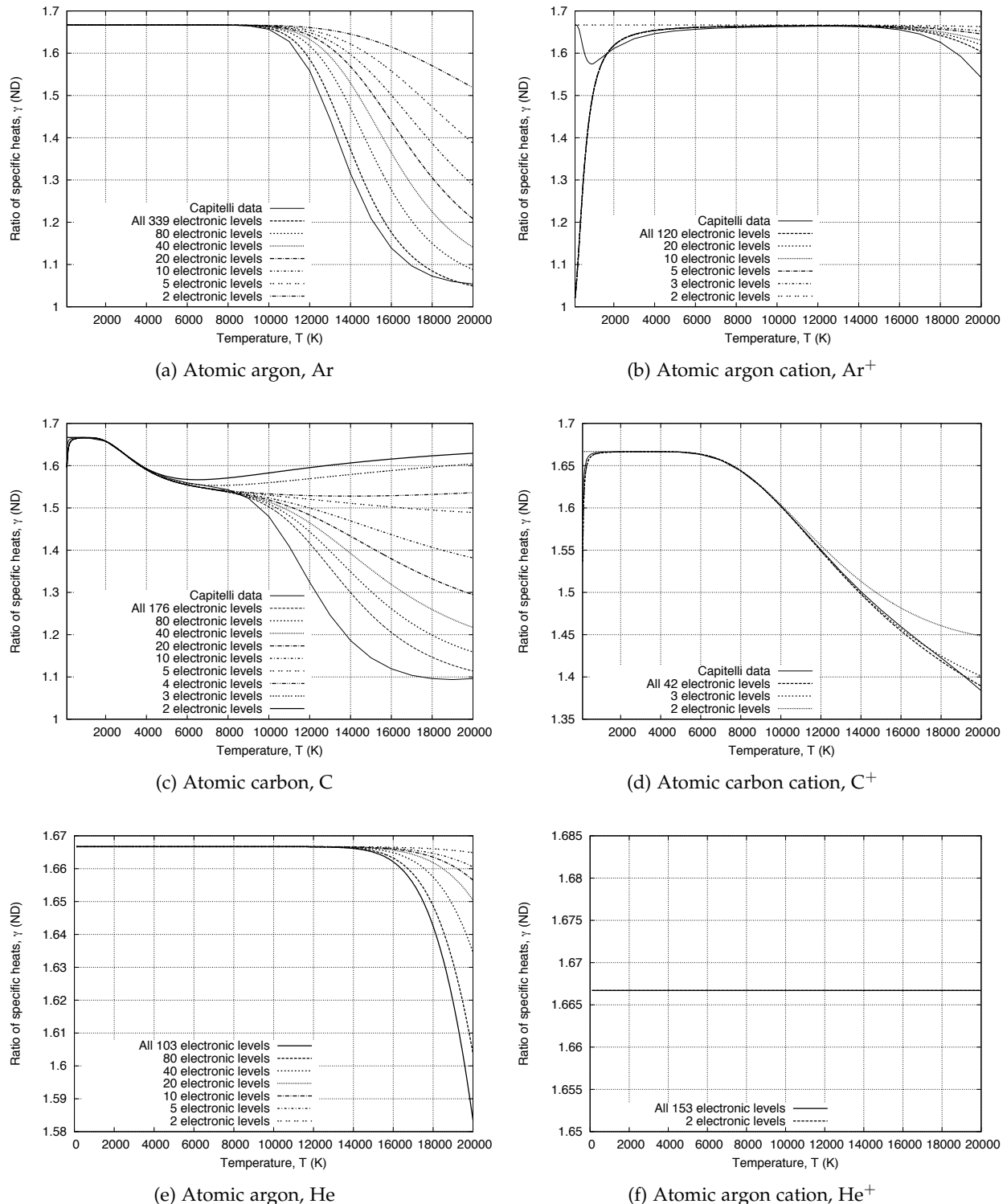


Figure 3.1: Comparison of specific heat ratio γ for key atomic species relevant to high velocity Mars aerothermodynamics and impulse facility experiments

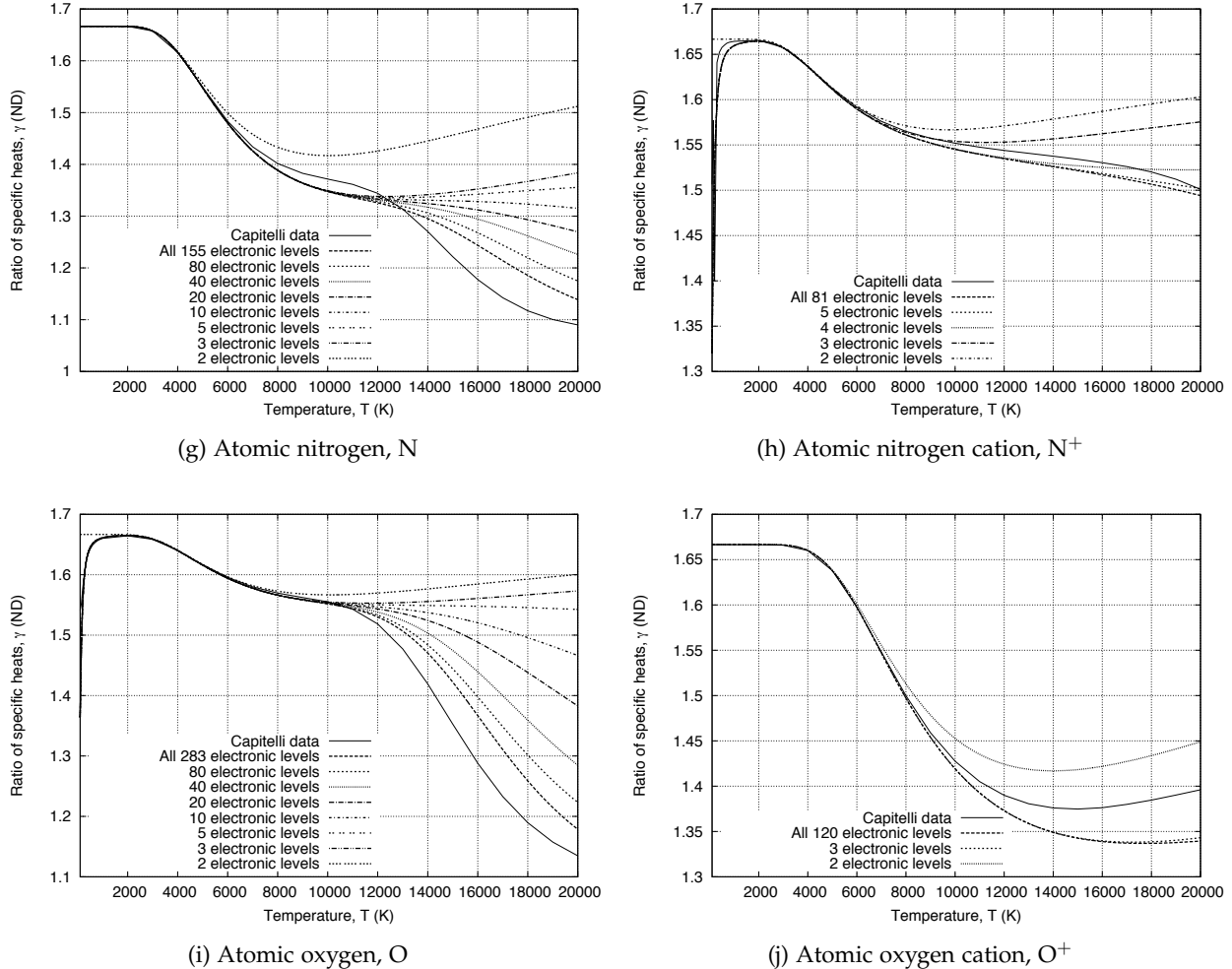


Figure 3.1: (Continued) Comparison of specific heat ratio γ for atomic species relevant to high velocity Mars aerothermodynamics and impulse facility experiments

4. the maximum electronic quantum number.

Figure 3.2 compares the ratio of specific heats calculated with varying number of electronic levels for the important diatomic species of interest to high speed Mars entry, namely C₂, C₂⁺, CO, CO⁺, CN, CN⁺, N₂, N₂⁺, NO, NO⁺, O₂ and O₂⁺. The spectroscopic parameters for all diatomic molecules are taken from the *Constants of Diatomic Molecules* chapter of the NIST Chemistry WebBook [85]. This database is a compilation of the spectroscopic parameters presented in the text of Huber and Herzberg [79].

Table 3.2 summarises the number of electronic levels retained for diatomic species considered in the present work.

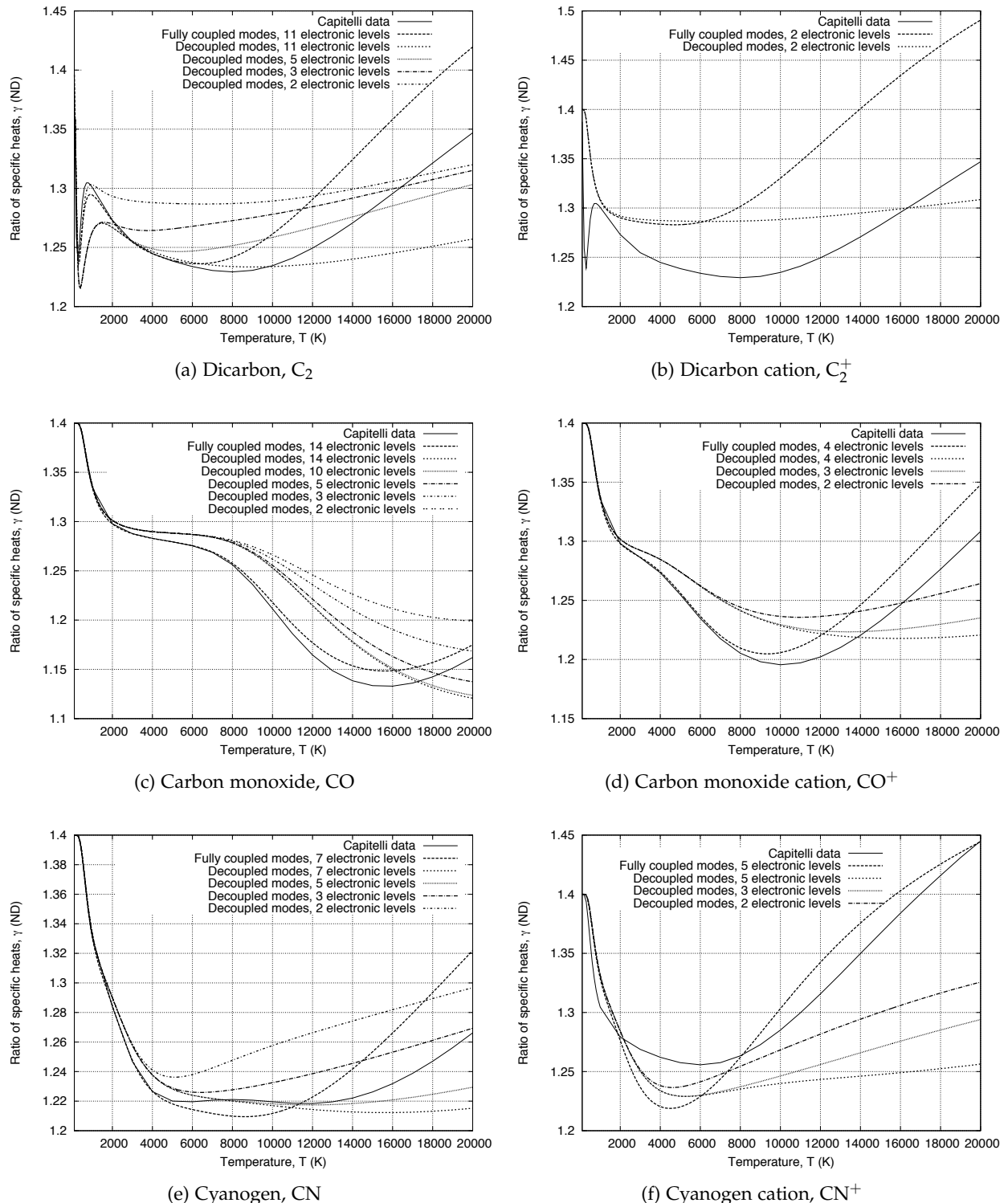


Figure 3.2: Comparison of specific heat ratio γ for diatomic species relevant to high velocity Mars aerothermodynamics and impulse facility experiments

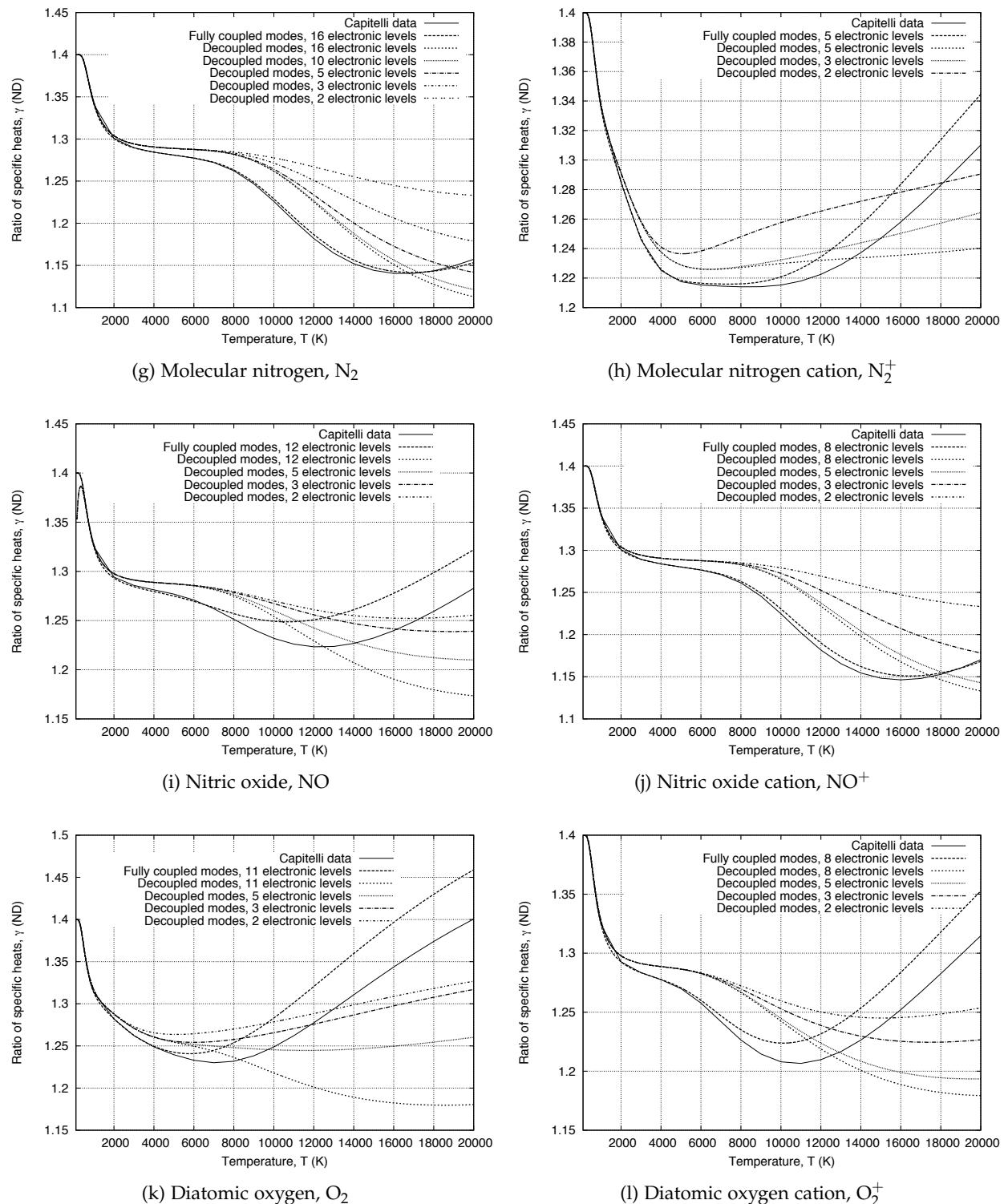


Figure 3.2: Comparison of specific heat ratio γ for key diatomic species relevant to high velocity Mars aerothermodynamics and impulse facility experiments

Table 3.2: Number of electronic levels retained for diatomic species considered in the present work

Atomic Species	C_2	C_2^+	CO	CO^+	CN	CN^+	N_2	N_2^+	NO	NO^+	O_2	O_2^+
Electronic levels	5	2	5	4	5	5	5	5	5	5	5	5

Thermodynamic properties of polyatomic species

Figure 3.3 compares the ratio of specific heats calculated with varying number of electronic levels for the important polyatomic species of interest to high speed Mars entry, namely NCO and CO_2 . The spectroscopic parameters for all polyatomic molecules are taken from Capitelli *et al.* [81]. In addition to NCO and CO_2 , Reference [6, 81] consider the polyatomic species CO_2^+ , N_3 , NO_2 , N_2O , N_2O^+ , O_3 , O_3^- , C_2N , C_2O and CO_2^- when calculating high temperature Mars thermodynamic and transport properties. In the present work these species are omitted on the grounds that they are trace species in the high enthalpy regime of interest and do not contribute significantly to the bulk thermodynamic or transport properties.

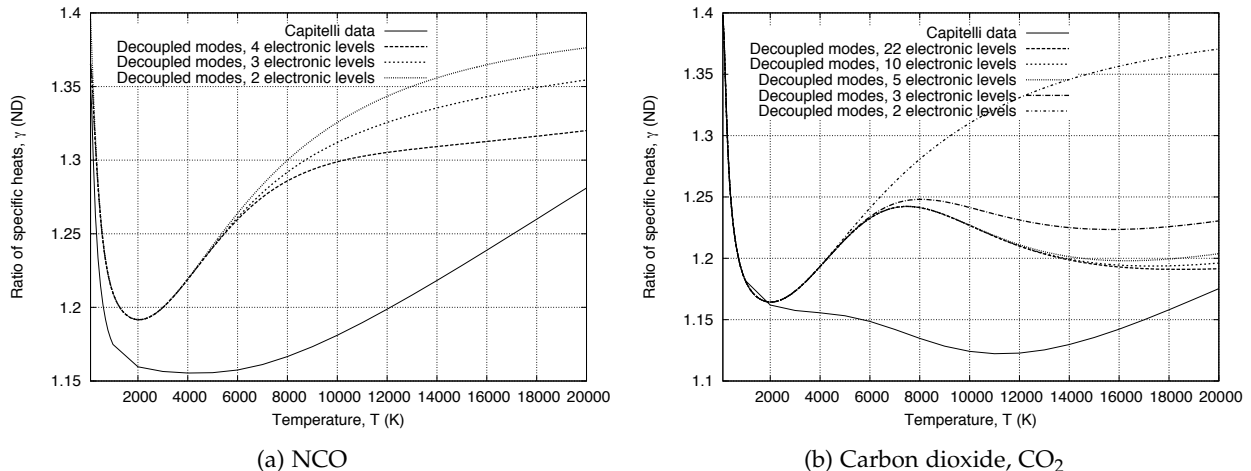


Figure 3.3: Comparison of specific heat ratio γ for polyatomic species relevant to high velocity Mars aerothermodynamics and impulse facility experiments

Table 3.3 summarises the number of electronic levels retained for polyatomic species considered in the present work.

Table 3.3: Number of electronic levels retained for polyatomic species considered in the present work

Atomic Species	NCO	CO_2
Electronic levels	4	5

3.1.4 Bulk thermodynamic properties

Bulk thermodynamic properties for the gas as a whole are required as inputs for the governing equations presented in § 2. In this section the bulk thermodynamic properties for both two- and three-temperature gases are derived.

Modal energies

The energies for each bulk thermal mode are calculated as the mass-fraction weighted sum of the contributions from each relevant species mode. For the two-temperature model, the translation-rotation and vibration-electron-electronic energies are:

$$e_{\text{tr}} = \sum_s^{N_{\text{species}}} f_s e_{\text{trans},s} + \sum_m^{N_{\text{mol}}} f_m e_{\text{rot},m}, \quad (3.69)$$

$$e_{\text{ve}} = \sum_m^{N_{\text{mol}}} f_m e_{\text{vib},m} + \sum_s^{N_{\text{species}}} f_s e_{\text{el},s} + f_e e_{\text{trans},e} \quad (3.70)$$

For the three temperature model, the definition of e_{tr} in Equation 3.69 is retained and the vibration and electron-electronic energies are calculated as separate quantities:

$$e_{\text{ve}} = \sum_m^{N_{\text{mol}}} f_m e_{\text{vib},m} \quad (3.71)$$

$$e_e = \sum_s^{N_{\text{species}}} f_s e_{\text{el},s} + f_e e_{\text{trans},e} \quad (3.72)$$

Modal specific heats

The modal specific heats at constant volume are also calculated as the mass-fraction weighted sum of the contributions from each relevant species mode. For the two-temperature model, the translation-rotation and vibration-electron-electronic specific heats are:

$$c_{v,\text{tr}} = \sum_s^{N_{\text{species}}} f_s c_{v,\text{trans},s} + \sum_m^{N_{\text{mol}}} f_m c_{v,\text{rot},m}, \quad (3.73)$$

$$c_{v,\text{ve}} = \sum_m^{N_{\text{mol}}} f_m c_{v,\text{vib},m} + \sum_s^{N_{\text{species}}} f_s c_{v,\text{el},s} + f_e c_{v,\text{trans},e} \quad (3.74)$$

For the three-temperature model, the separated vibration and electron-electronic specific heats are:

$$c_{v,v} = \sum_m^{N_{\text{mol}}} f_m c_{v,\text{vib},m} \quad (3.75)$$

$$c_{v,e} = \sum_s^{N_{\text{species}}} f_s c_{v,\text{el},s} + f_e c_{v,\text{trans},e} \quad (3.76)$$

The modal specific heats at constant pressure are similarly calculated as:

$$c_{p,tr} = \sum_s^{N_{\text{species}}} f_s c_{p,\text{trans},s} + \sum_m^{N_{\text{mol}}} f_m c_{p,\text{rot},m} \quad (3.77)$$

$$c_{p,ve} = \sum_m^{N_{\text{mol}}} f_m c_{p,\text{vib},m} + \sum_s^{N_{\text{species}}} f_s c_{p,\text{el},s} + f_e c_{p,\text{trans},e} \quad (3.78)$$

$$c_{p,v} = \sum_m^{N_{\text{mol}}} f_m c_{p,\text{vib},m} \quad (3.79)$$

$$c_{p,e} = \sum_s^{N_{\text{species}}} f_s c_{p,\text{el},s} + f_e c_{p,\text{trans},e} \quad (3.80)$$

(3.81)

The frozen ratio of specific heats γ is required for the flux solvers and is calculated as:

$$\gamma = \frac{c_p}{c_v} = \frac{c_{p,tr} + c_{p,ve}}{c_{v,tr} + c_{v,ve}} = \frac{c_{p,tr} + c_{p,v} + c_{p,e}}{c_{v,tr} + c_{v,v} + c_{v,e}} \quad (3.82)$$

Modal temperatures

As the translational and rotational modes are modelled as fully excited, $c_{v,tr}$ is a constant value and the temperature is simply calculated as:

$$T_{\text{tr}} = \frac{e_{\text{tr}}}{c_{v,tr}} \quad (3.83)$$

The vibrational, electron and electronic specific heats on the other hand are functions of temperature, and therefore an iterative method must be employed to solve for the temperatures(s) governing these modes. In the present work the Newton-Raphson method is implemented for calculating T_{ve} or T_{v} and T_{e} from their respective energies. The procedure as applied to the vibration-electron-electronic mode is:

$$T_{\text{ve}}^{(n+1)} = T_{\text{ve}}^{(n)} - \frac{f_{\text{ve}}(T_{\text{ve}}^{(n)})}{f'_{\text{ve}}(T_{\text{ve}}^{(n)})} \quad (3.84)$$

where f_{ve} is the modal zero function:

$$f_{ve}(T_{ve}) = e_{ve}(T_{ve}) - e_{ve}^* \quad (3.85)$$

and e_{ve}^* is the given modal energy. The derivative of the zero function is simply the modal specific heat:

$$f'_{ve}(T_{ve}) = c_{v,ve}(T_{ve}) \quad (3.86)$$

The solution is deemed to be converged when the normalised zero function is less than one part in one million:

$$\frac{e_{ve}(T_{ve}) - e_{ve}^*}{e_{ve}^*} < 10^{-6} \quad (3.87)$$

Equation of state

When expressing the equation of state, it is important to note that with both the two- and three-temperature models free electron and heavy particle translation are governed by different temperatures. The gas pressure p is therefore divided into the contributions from heavy particles and free electrons. For the two-temperature model the equations of state is therefore:

$$p = \sum_{s \neq e^-}^{N_{\text{species}}} p_s + p_e = \sum_{s \neq e^-}^{N_{\text{species}}} \rho_s R_s T_{tr} + \rho_e R_e T_{ve} \quad (3.88)$$

while for the three-temperature model T_{ve} in Equation 3.88 is replaced by T_e .

Speed of sound

The distinction of separate heavy particle and free electron temperatures invalidates the traditional equilibrium sound speed expression:

$$a^2 = \gamma RT = \gamma \frac{p}{\rho} \quad (3.89)$$

The sound speed expression corrected for the presence of a separate electron-temperature proposed by Cinnella and Grossman [86] has been implemented. For the two-temperature mode we have:

$$a^2 = \gamma \left(\frac{p}{\rho} \right) + (\gamma - 1) \left(\frac{T_{tr}}{T_{ve}} - 1 \right) \frac{p_e}{\rho} \quad (3.90)$$

while for the three-temperature model T_{ve} in Equation 3.90 is replaced by T_e . Note that when $T_{tr} = T_{ve}$ Equation 3.90 reduces to Equation 3.89.

3.2 Transport properties

The Navier–Stokes equations described in § 2 consider the flux of mass, momentum and energy due to concentration, temperature and velocity gradients. In light of the multicomponent, multitemperature thermodynamic model outlined in the previous section, expressions for the modal thermal conductivities K_{tr} , K_{ve} , K_v and K_e , species diffusion mass flux \vec{J}_s and viscosity coefficients μ and λ in the presence of a partially ionised flowfield are therefore required. Under translational equilibrium conditions, these ‘bulk’ transport properties can be obtained by solving the Boltzmann distribution equation via an appropriate method. The Chapman–Enskog theory of dilute gases approximates the Boltzmann equation by a Sonine polynomial expansion [87]. Due to the rapid convergence of the resulting series, only the first order terms are typically retained, and the transport properties become functions of only three binary interaction parameters: the diffusion collision integral $\Omega^{(1,1)}$, the viscosity collision integral $\Omega^{(2,2)}$ and the ratio $B^* = (5\Omega^{(1,2)} - 4\Omega^{(1,3)})/\Omega^{(1,1)}$ [88]. The resulting equations remain computationally intensive, however, and various approximations have been proposed that attempt to find a compromise between accuracy and efficiency.

Palmer and Wright [89] compared three of the commonly used methods for computing the viscosity of an ionised gas-mixture with the full multicomponent equations; namely, the mixture rules of Wilke [90], Armaly and Sutton [91] and Gupta, Yos, Thompson and Lee [92]. Figure 3.4 compares the viscosity coefficient calculated using these methods over the temperature range 200 to 20,000 K for 11 species air in chemical equilibrium at pressures of 100 and 10 kPa.

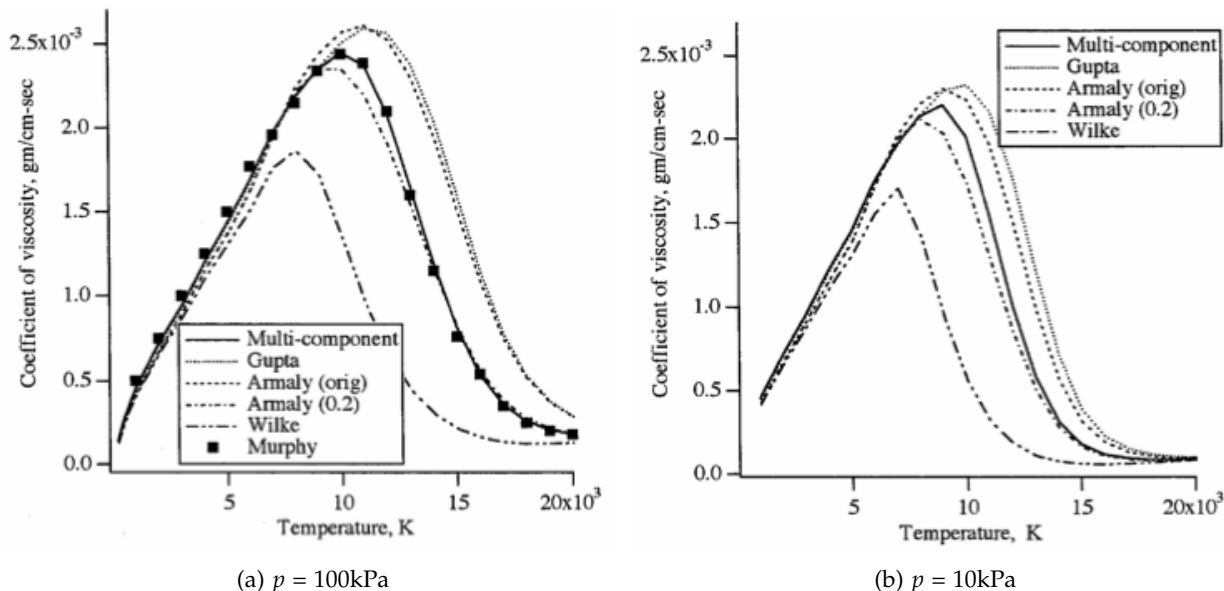


Figure 3.4: Comparison of the viscosity coefficient calculated using various methods over the temperature range 200 to 20,000 K for 11 species air (source: Reference [89]).

Solving the full multicomponent equations gave the most accurate results when compared to the well regarded calculations of Murphy and Arundell [93] as expected, but required approximately twice the computational time as the other methods. The Armaly–Sutton mixture rule was the second most accurate method, yielding good agreement with the multicomponent equations over a wide temperature range extending into the strongly ionised regime, yet requiring approximately half the computation time. The Gupta–Yos mixture rule was the next most accurate and the most computationally efficient method, closely matching the multicomponent results at temperatures up to 10,000 K but losing accuracy when charged species begin to dominate the mixture at higher temperatures. The Wilke mixture rule is the most commonly implemented method and was determined to be the least accurate, and yet required more computational effort than the Gupta–Yos mixture rule. The Armaly–Sutton and Gupta–Yos mixture rules therefore appear the best candidates for accurate and efficient calculation of transport properties. Although the the Armaly–Sutton equations perform better at high temperatures and only requires the pure species collision integrals, accurate or appropriately tuned collision integral ratios A^* , B and F are required. These parameters were determined for air and hydrogen-helium mixtures in Reference [91]. In contrast, the Gupta–Yos equations require 15% less computational time but require a complete and accurate set of the diffusion and viscosity collision integrals. As the gas temperature in the equilibrium region of the shock layers of present interest is approximately 10,000 K, the additional accuracy provided by the Armaly–Sutton mixture rule for the higher temperatures is not required. Furthermore, accurate and largely complete sets of collision cross sections are available for the Martian atmosphere components [6, 94], making the Gupta–Yos equations the most appropriate choice for the present work.

3.2.1 Gupta–Yos mixture rules

Gupta *et al.* [92] implement the approximate mixture rules originally proposed by Yos [95]. The transport coefficients are presented as functions of $\Delta_{i,j}^{(1,1)}$ and $\Delta_{i,j}^{(2)}$, which are in turn functions of the binary collision cross sections $\sigma^2\Omega_{i,j}^{(1,1)*}$ and $\sigma^2\Omega_{i,j}^{(2,2)*}$:

$$\Delta_{i,j}^{(1)}(T) = \frac{8}{3} \left[\frac{2m_i m_j}{\pi k_B T (m_i + m_j)} \right]^{\frac{1}{2}} \pi \sigma^2 \Omega_{i,j}^{(1,1)*}(T) \quad (3.91)$$

$$\Delta_{i,j}^{(2)}(T) = \frac{16}{5} \left[\frac{2m_i m_j}{\pi k_B T (m_i + m_j)} \right]^{\frac{1}{2}} \pi \sigma^2 \Omega_{i,j}^{(2,2)*}(T) \quad (3.92)$$

where m_i is the mass per particle of species i , and $\sigma^2\Omega_{i,j}^{(l,m)*}$ are the binary collision cross sections between species i and j . It is necessary to make a brief comment here regarding the terminology and nomenclature used for collision integrals, as there are many approaches in the literature. In the present work we adopt that of Palmer *et al.* [89] and Bruno *et al.* [6]:

$\Omega_{i,j}^{(l,m)}$ is the [dimensional] collision integral with SI units m^3/s ,

$\Omega_{i,j}^{(l,m)*}$ is the reduced collision integral with non-dimensional units, and

$\sigma^2 \Omega_{i,j}^{(l,m)*}$ is the collision cross section with SI units m^2 where σ is the rigid sphere collision diameter.

What is commonly referred to as the ‘collision integral’ $\Omega_{i,j}^{(l,m)}$ (e.g. as in Reference [88, 94]) is more formally referred to as the collision cross section $\sigma^2 \Omega_{i,j}^{(l,m)*}$. The ‘average collision cross section’ $\bar{\Omega}_{i,j}^{(l,m)}$ used by Gupta *et al.* [92] is therefore replaced by $\sigma^2 \Omega_{i,j}^{(l,m)*}$ in the present formulation of the Gupta–Yos equations. Furthermore, the present formulation assumes SI units for all parameters, whereas those presented in Reference [92] are in empirical units.

Species viscosity

The viscosity contribution of species i is calculated as:

$$\mu_i = \frac{X_i m_i}{\sum_j^{N_{\text{species}}} X_j \Delta_{ij}^{(2)}(T_{\text{trans},i})} \quad (3.93)$$

where $T_{\text{trans},i}$, X_i and m_i are the translational temperature, mole-fraction and particle mass of species i .

Species modal conductivities

The translational conductivity contribution of species i is calculated as:

$$K_{\text{trans},i} = \frac{15}{4} k_B \left[\frac{X_i}{\sum_j^{N_{\text{species}}} \alpha_{ij} X_j \Delta_{ij}^{(2)}(T_{\text{trans},i})} \right] \quad (3.94)$$

where α_{ij} is a function of the colliding species mass:

$$\alpha_{ij} = 1 + \frac{\left[1 - \frac{m_i}{m_j} \right] \left[0.45 - 2.54 \frac{m_i}{m_j} \right]}{\left[1 + \frac{m_i}{m_j} \right]^2} \quad (3.95)$$

The rotational conductivity contribution of molecule i is calculated as:

$$K_{\text{rot},i} = k_B \left[\frac{\frac{(c_{v-\text{rot}})_i}{R_i} X_i}{\sum_j^{N_{\text{species}}} X_j \Delta_{ij}^{(1)}(T_{\text{trans},i})} \right] \quad (3.96)$$

As outlined in Section 3.1.2, in the present work we are assuming fully excited rotation; that is, $(c_{v-\text{rot}})_i = R_i$. Therefore, the $(c_{v-\text{rot}})_i/R_i$ term in Equation 3.96 can be omitted.

The vibrational conductivity contribution of molecule i is calculated as:

$$K_{\text{vib},i} = k_B \left[\frac{\frac{(c_{v,\text{vib}})_i}{R_i} X_i}{\sum_j^{N_{\text{species}}} X_j \Delta_{ij}^{(1)}(T_{\text{trans},i})} \right] \quad (3.97)$$

Gupta *et al.* [92] suggest that the ratio $(c_{v-\text{vib}})_i/R_i$ can be omitted for temperatures greater than the characteristic temperature for vibration θ_v , as it is approximately one. Figure 3.5 plots the ratio $(c_{v-\text{vib}})_i/R_i$ for N₂ and CO modelled as both truncated and infinite harmonic oscillators over the temperature range 200 to 20,000 K. While $(c_{v-\text{vib}})_i/R_i$ asymptotically approaches unity at $T \gg \theta_v$ for the harmonic oscillator model, significant deviation occurs at high temperatures for the truncated harmonic oscillator model. Furthermore, tests have found the additional computational effort required to compute the $(c_{v-\text{vib}})_i/R_i$ term negligible when compared to the transport calculation as a whole. Therefore Equation 3.97 will be used for all temperature in the present work.

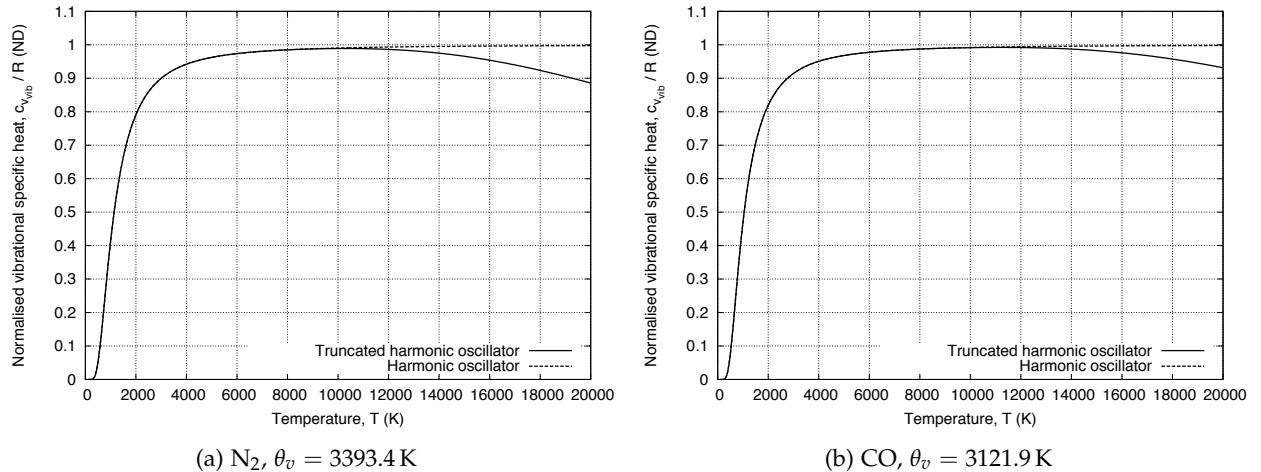


Figure 3.5: Normalised vibrational specific heats for key molecules modeled as truncated and infinite harmonic oscillators as a function of temperature.

Finally, the electronic conductivity contribution of species i is similarly calculated as:

$$K_{\text{el},i} = k_B \left[\frac{\frac{(c_{v,\text{el}})_i}{R_i} X_i}{\sum_j^{N_{\text{species}}} X_j \Delta_{ij}^{(1)}(T_{\text{trans},i})} \right] \quad (3.98)$$

Binary diffusion coefficients

Gupta *et al.* [92] obtain the binary diffusion coefficient D_{ij} from the complete first Chapman-Enskog approximation:

$$D_{ij} = \frac{kT}{p \Delta_{ij}^{(1)}} \quad (3.99)$$

The binary diffusion coefficients are then used by the diffusion model of the flowfield solver to calculate diffusion flux J_s for all species s . The diffusion model implemented in the present work is discussed in Section 7.6.

Mixture transport coefficients

The mixture transport coefficients are simply the sum of the individual species contributions. The mixture viscosity is therefore:

$$\mu = \sum_i^{N_{\text{species}}} \mu_i \quad (3.100)$$

For the two-temperature thermal model, the translation-rotational thermal conductivity is:

$$K_{\text{tr}} = \sum_{s \neq e^-}^{N_{\text{species}}} K_{\text{trans},s} + \sum_m^{N_{\text{mol}}} K_{\text{rot},m} \quad (3.101)$$

and the vibration-electronic-electron thermal conductivity is:

$$K_{\text{ve}} = \sum_m^{N_{\text{mol}}} K_{\text{vib},m} + \sum_s^{N_{\text{species}}} K_{\text{el},s} + K_{\text{trans},e} \quad (3.102)$$

Separating out the vibration and electron-electronic contributions for the three-temperature model yields:

$$K_{\text{v}} = \sum_m^{N_{\text{mol}}} K_{\text{vib},m} + \sum_s^{N_{\text{species}}} K_{\text{el},s} + K_{\text{trans},e} \quad (3.103)$$

$$K_e = \sum_m^{N_{\text{mol}}} K_{\text{vib},m} + \sum_s^{N_{\text{species}}} K_{\text{el},s} + K_{\text{trans},e} \quad (3.104)$$

3.2.2 Binary collision parameters for partially ionised shock layers

The binary collision parameters for partially ionised shock layers are compiled from a number of sources. Bruno *et al.* [6] proposed a complete set of binary collision parameters for Mars atmosphere components in the temperature range 50 to 50,000 K. For heavy particle interactions, a phenomenological interaction potential is implemented that is an improvement on the Lennard Jones model [96, 97]. For electron-neutral interactions, diffusion and velocity cross sections are calculated by integration of the momentum and energy transfer cross sections as functions of electron energy. For charged particle interactions a shielded Coulomb potential is implemented. By implementing phenomenological potentials, the collision integrals of Bruno *et al.* [6] represents a complete and consistent database covering all possible binary interactions.

Wright *et al.* [88, 94, 98, 99] proposed a set of binary collision parameters for the dominant interactions of Mars atmosphere components in the temperature range 300 to 15,000 K. Notably, recent *ab initio* calculations [100–103] from quantum-mechanically derived potential energy surfaces are employed for some of the most important heavy particle interactions, namely C–C, C–N, N–N, O–O, N–O, N₂–N₂, N₂–N and O₂–O. These calculations are of a high fidelity and have a stated accuracy of less than 5%. The remaining heavy particle collision integrals are compiled from a variety of the best available *ab initio* calculations, experimentally determined measurements and phenomenological potentials [88, 94]. Ion neutral interactions for air species are calculated assuming a modified Tang–Toennies potential [104], whilst a Langevin potential [105] is employed for the ion neutral interactions involving carbonaceous species. Charged particle collision integrals are calculated via the shielded Column potential curve fits proposed by Stallcop *et al.* [106].

Figure 3.6 compares the Bruno *et al.* [6] and Wright *et al.* [88, 94] diffusion and viscosity collision cross sections for C–C and O–O interactions. It is clear that significant discrepancy exists between the two datasets, especially at high temperatures. Although the large temperature range, completeness and consistency of the Bruno *et al.* [6] collision integral data is initially appealing, the reliance on phenomenological potentials limits the accuracy to between approximately 25% and 40% [94]. Furthermore, for the high speed Mars entry conditions of present interest the accuracy of the transport coefficients is most important in the viscous boundary layer where the translational temperature drops from approximately 8,000 K to 1,000 K – well within the range of validity for the Wright *et al.* [88, 94, 98, 99] collision integrals. Therefore the collision integral data of Wright *et al.* [88, 94, 98, 99] is preferred in the present work, with the remaining heavy particle interactions implementing the collision integral data of Bruno *et al.* [6]. The collision integrals for e[–]–C₂ and e[–]–NCO are not available in any of the above references and are omitted on the grounds of the negligible influence of these traces species. The collision integrals for the C–N–O–Ar elemental system implemented in the present work are summarised in Table A.1. For shock tube simulations where helium is present as a driver gas, the collision integral curve fits

of Neufeld [107] based on the Lennard Jones potential are implemented for neutral interactions involving He. It should be noted that all collision cross sections are firstly calculated in units of \AA^2 and then converted to S.I. units (m^2) for use in the mixture rules.

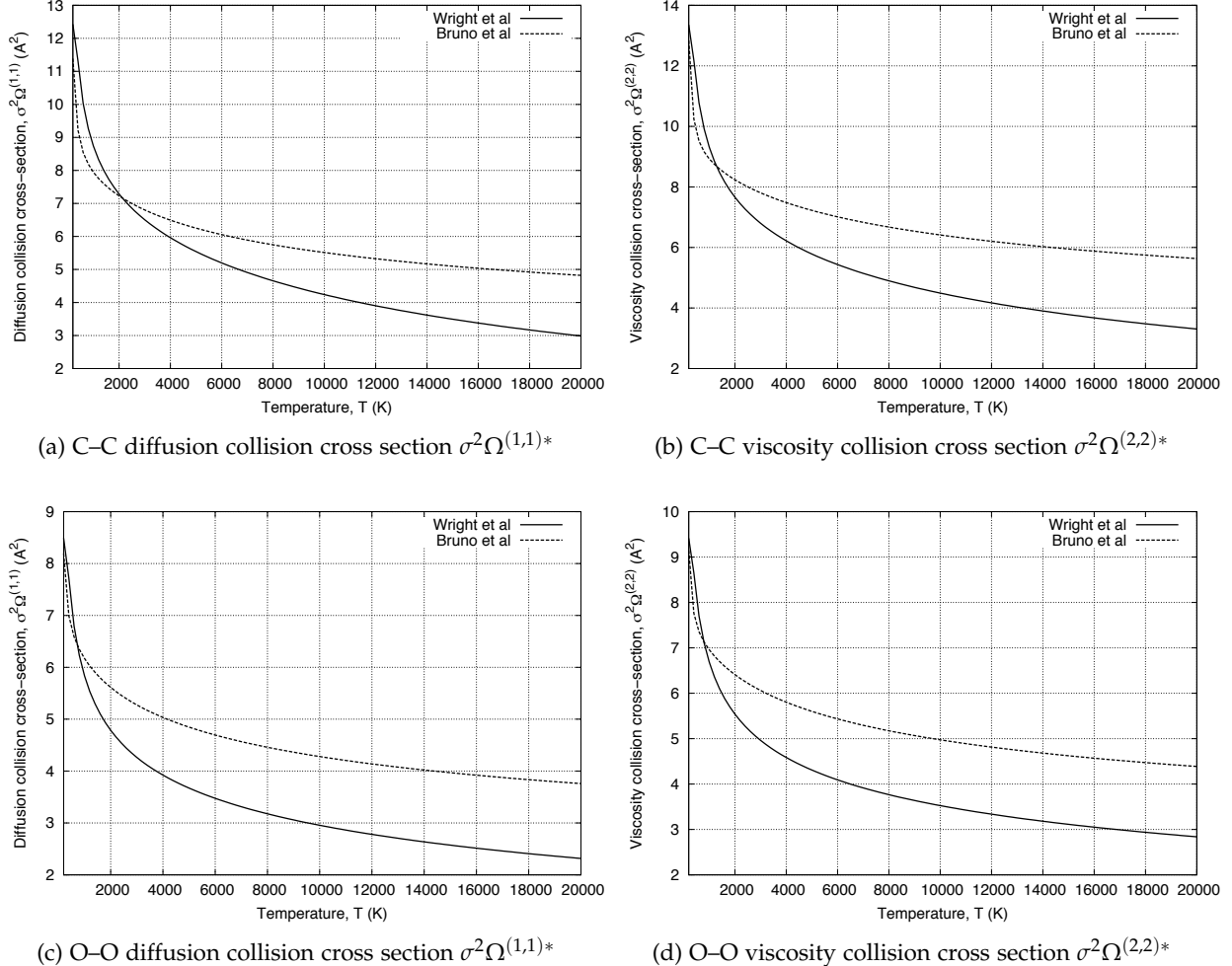


Figure 3.6: Comparison of the Bruno *et al.* [6] and Wright *et al.* [88, 94] diffusion and viscosity collision cross sections for C–C and O–O interactions.

Implementation of Wright *et al.* [88, 94, 98, 99] collision cross sections

Wright *et al.* [88, 94, 98, 99] present data points for the diffusion and viscosity collision cross sections, $\sigma^2\Omega_{ij}^{(1,1)*}$ and $\sigma^2\Omega_{ij}^{(2,2)*}$ respectively, corresponding to neutral-neutral, neutral-ion and neutral-electron interactions in the temperature range 300 to 15,000 K. For implementation in the flowfield solver these data points are curve fitted to the expression proposed by Gupta *et al.* [92]:

$$\pi\sigma^2\Omega_{i,j}^{(1,1)*} = \left[\exp\left(D_{\sigma^2\Omega_{i,j}^{(1,1)*}}\right) \right] T_{\text{trans}}^{\left[A_{\sigma^2\Omega_{i,j}^{(1,1)*}}(\ln T_{\text{trans}})^2 + B_{\sigma^2\Omega_{i,j}^{(1,1)*}}\ln T_{\text{trans}} + C_{\sigma^2\Omega_{i,j}^{(1,1)*}}\right]} \quad (3.105)$$

$$\pi\sigma^2\Omega_{i,j}^{(2,2)*} = \left[\exp\left(D_{\sigma^2\Omega_{i,j}^{(2,2)*}}\right) \right] T_{\text{trans}}^{\left[A_{\sigma^2\Omega_{i,j}^{(2,2)*}}(\ln T_{\text{trans}})^2 + B_{\sigma^2\Omega_{i,j}^{(2,2)*}}\ln T_{\text{trans}} + C_{\sigma^2\Omega_{i,j}^{(2,2)*}}\right]} \quad (3.106)$$

Implementation of Stallcop *et al.* [106] charged particle collision cross sections

Stallcop *et al.* [106] presented an expression to compute the shielded Coulomb collision cross section that can be curve fit by:

$$\sigma^2\Omega_{i,j}^{(N,N)*} = 5 \times 10^{15} (\lambda/T^*)^2 \ln \{D_N T^* [1 - C_N \exp(-c_N T^*)] + 1\} \quad (3.107)$$

where the reduced temperature T^* is calculated as:

$$T^* = 4132.5 \left(T_{\text{trans}}^{\frac{3}{2}} / \sqrt{N_e} \right) \quad (3.108)$$

where N_e is the electron number density in cm^{-3} . The values of the constants D_N , C_N and c_N are presented in Reference [106] for $N = 1$ and $N = 2$ and for both attractive and repulsive interactions.

Implementation of Bruno *et al.* [6] heavy particle collision cross sections

In the report of Bruno *et al.* [6], heavy particle interactions refer to neutral-neutral and ion-neutral (or neutral-ion) interactions. The collision integrals for heavy particle interactions are calculated by integrating the classical equations of motion with the phenomenological interaction potential of Pirani *et al.* [96, 97]. This interaction potential is a function of the binding energy ϵ_0 , equilibrium position r_e and a parameter β that is a function of the species polarizability [108]. The collision cross section for species pair $i-j$ is calculated via the following curve fit:

$$\sigma^2\Omega_{ij}^{(l,s)*} = \sigma_{ij}^2 \exp \left\{ [a_1(\beta_{ij}) + a_2(\beta_{ij})x] \frac{\exp [(x - a_3(\beta_{ij}))/a_4(\beta_{ij})]}{\exp [(x - a_3(\beta_{ij}))/a_4(\beta_{ij})] + \exp [(a_3(\beta_{ij}) - x)/a_4(\beta_{ij})]} \right. \\ \left. + a_5(\beta_{ij}) \frac{\exp [(x - a_6(\beta_{ij}))/a_7(\beta_{ij})]}{\exp [(x - a_6(\beta_{ij}))/a_7(\beta_{ij})] + \exp [(a_6(\beta_{ij}) - x)/a_7(\beta_{ij})]} \right\} \quad (3.109)$$

where $x = \ln(k_B T / \epsilon_{0,ij})$ and the parameters a_i are polynomial functions of β of the form:

$$a_i(\beta_{ij}) = c_0 + c_1\beta_{ij} + c_2\beta_{ij}^2$$

The σ_{ij}^2 parameter in Equation 3.109 is the rigid sphere collision cross section and is calculated as:

$$\sigma_{ij}^2 = (x_{0,ij} r_{e,ij})^2 = (\xi_1 \beta_{ij}^{\xi_2} r_{e,ij})^2 \quad (3.110)$$

where the characteristic range of intermolecular forces x_0 has been approximated by a power function of β . Sets of constants c_i and ξ_i are given in Reference [6] for both neutral-neutral and neutral-ion interactions.

3.2.3 Comparison with CEA2 [5]

The NASA Chemical Equilibrium with Analysis program version 2 (CEA2) [5] enables the thermodynamic and transport properties of a gas in chemical equilibrium to be calculated. The thermal viscosity and conductivities in the CEA2 program are calculated from collision integrals obtained by a wide variety of sources including empirical potentials, computational chemistry calculations and experimental measurements as documented by Svehla [109]. As not all the binary interactions for 11 species air were considered, however, Svehla resorts to pure species binary interactions to derive the transport coefficients for some species. Although the transport coefficient model developed in the present work is therefore likely to be of a higher fidelity than that of the CEA2 program, the comparison is still useful as a verification of the model implementation.

The thermal conductivity given by the CEA2 program is the so called ‘equilibrium’ value, K_{eq} , that consists of frozen and reactive components:

$$K_{\text{eq}} = K_{\text{froz}} + K_{\text{reac}} \quad (3.111)$$

The frozen thermal conductivity is the contribution from the thermal modes:

$$K_{\text{froz}} = K_{\text{trans}} + K_{\text{rot}} + K_{\text{vib}} + K_{\text{el}} + K_e \quad (3.112)$$

and the reactive thermal conductivity is the contribution due to the existence of local chemical equilibrium. The reactive thermal conductivity can be calculated by considering a set of reactions that give rise to chemical equilibrium as done by Gordon and McBride [5], or by the following diffusion dependent expression as presented by Gupta *et al.* [92]:

$$K_{\text{reac}} = \rho \sum_{i=1}^{N_{\text{species}}} \tilde{D}_i h_i \frac{\partial f_i}{\partial T} \quad (3.113)$$

Here we implement Equation 3.113 for computational simplicity, and to include the diffusion coefficients in the calculation. The mixture average diffusion coefficients \tilde{D}_i are calculated via the ambipolar corrected Wilke mixing rule as described in Appendix E.

Figures 3.7 and 3.8 compare the viscosity and conductivity respectively for 11 species air in chemical equilibrium calculated by the model proposed in the present work and by the CEA2 program. The temperature range considered is 200 to 20,000 K, although it must be noted that

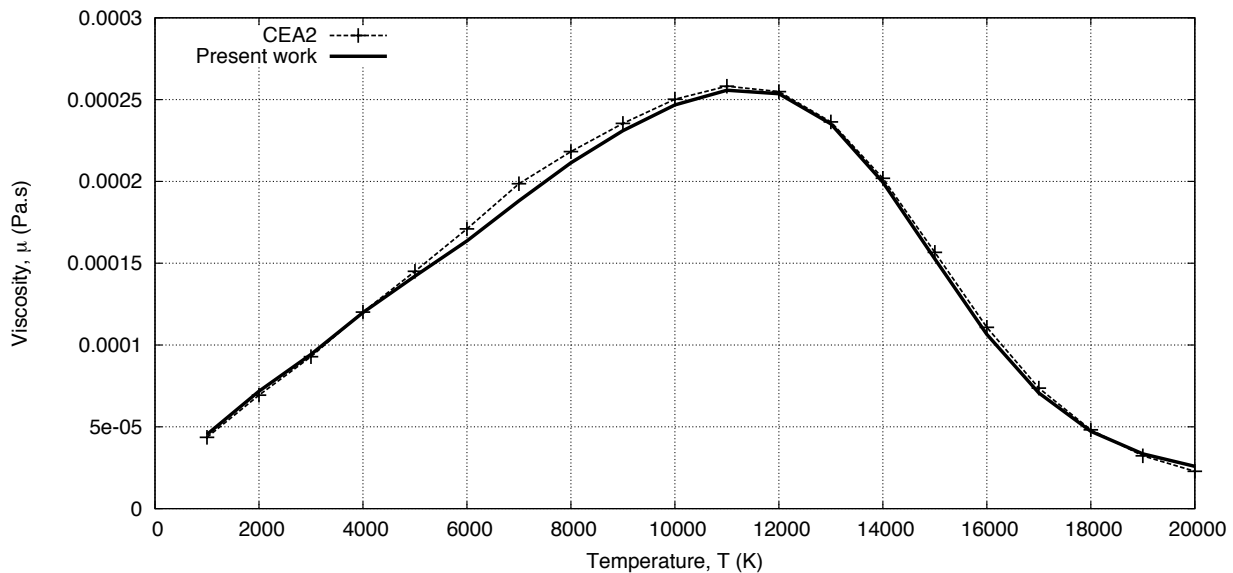


Figure 3.7: Comparison of viscosity for 11 species air in chemical equilibrium with the NASA CEA2 program [5]

the majority of the CEA2 transport data from Svehla [109] is quoted as only being accurate in the 200 to 15,000 K range. The quantitative agreement for viscosity over the full temperature range is good, with a maximum discrepancy of 5% at 7000 K. Given the difference between the two calculation methodologies, a maximum discrepancy of 5% is quite acceptable. The total conductivity is in close agreement for temperatures up to 9000 K, while for higher temperatures where charged particles are significant CEA2 gives substantially larger total conductivity compared to the present work. This discrepancy can be attributed to the assumption of ambipolar diffusion, which drives the reactive conductivity to zero as ionisation increases.

3.2.4 Comparison with tabulated results of Bruno *et al.* [6]

Bruno *et al.* [6] presented tabulated Mars atmosphere transport coefficients in the temperature range 50 to 50,000 K for the various equilibrium compositions. A high-order Chapman Enskog approximation was applied for the calculation of the transport coefficients from the set of binary collision cross sections presented in the same reference. Although both the mixture rule and binary collision cross sections implemented in the present work differ from that implemented by Bruno *et al.* [6], the resulting transport coefficients should not be drastically different especially at lower temperatures. Thus comparing with the tabulated results of Bruno *et al.* [6] allows the present implementation to be verified.

The diffusion, thermal diffusion, partial thermal conductivity and viscosity coefficients for five sets of equilibrium compositions are presented by Bruno *et al.* [6]. The five equilibrium compositions are those corresponding to 1 atmosphere of pressure and temperatures of 50 K, 3,000 K,

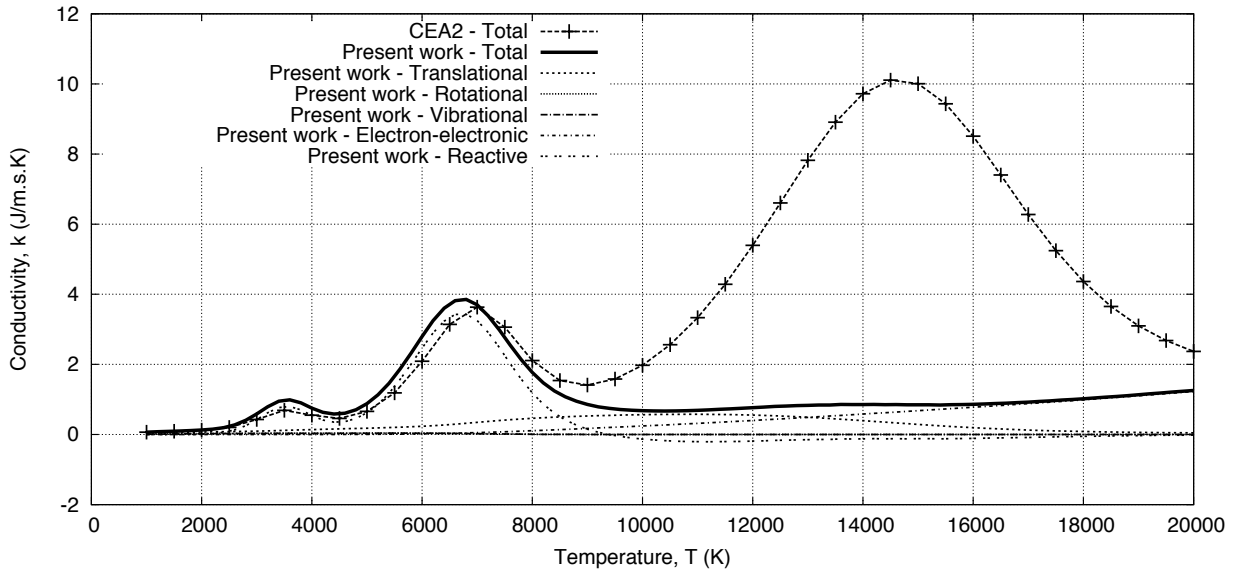


Figure 3.8: Comparison of conductivity for 11 species air in chemical equilibrium with the NASA CEA2 program [5]

8,000 K, 20,000 K and 50,000 K. A total of 53 species are considered by Bruno *et al.* [6], whilst the present calculations consider the 23 species described in Section 3.1. The additional species considered by Bruno are C^{2+} , C^{3+} , C^{4+} , C^- , N^{2+} , N^{3+} , N^{4+} , N^- , O^{2+} , O^{3+} , O^{4+} , O^- , C_2^- , N_2^- , O_2^- , CN^- , C_3 , N_3 , O_3 , O_3^- , C_2N , CO_2^+ , CO_2^- , C_2O , NO_2 , N_2O , N_2O^+ , Ar^{2+} , Ar^{3+} and Ar^{4+} . Figure 3.9 compares the bulk viscosity coefficients obtained from the present transport model implementation with that tabulated by Bruno *et al.* [6]. Reasonable agreement is observed for the first 3 equilibrium compositions. For the equilibrium compositions corresponding to 20,000 K and 50,000 K, however, there are substantial differences with the present transport model implementation giving a much higher bulk viscosity. The differences can be attributed to the consideration of multiply charged ions by Bruno *et al.* [6] that occur in significant proportions for the 20,000 K and 50,000 K equilibrium compositions. These species were not considered in the present analysis.

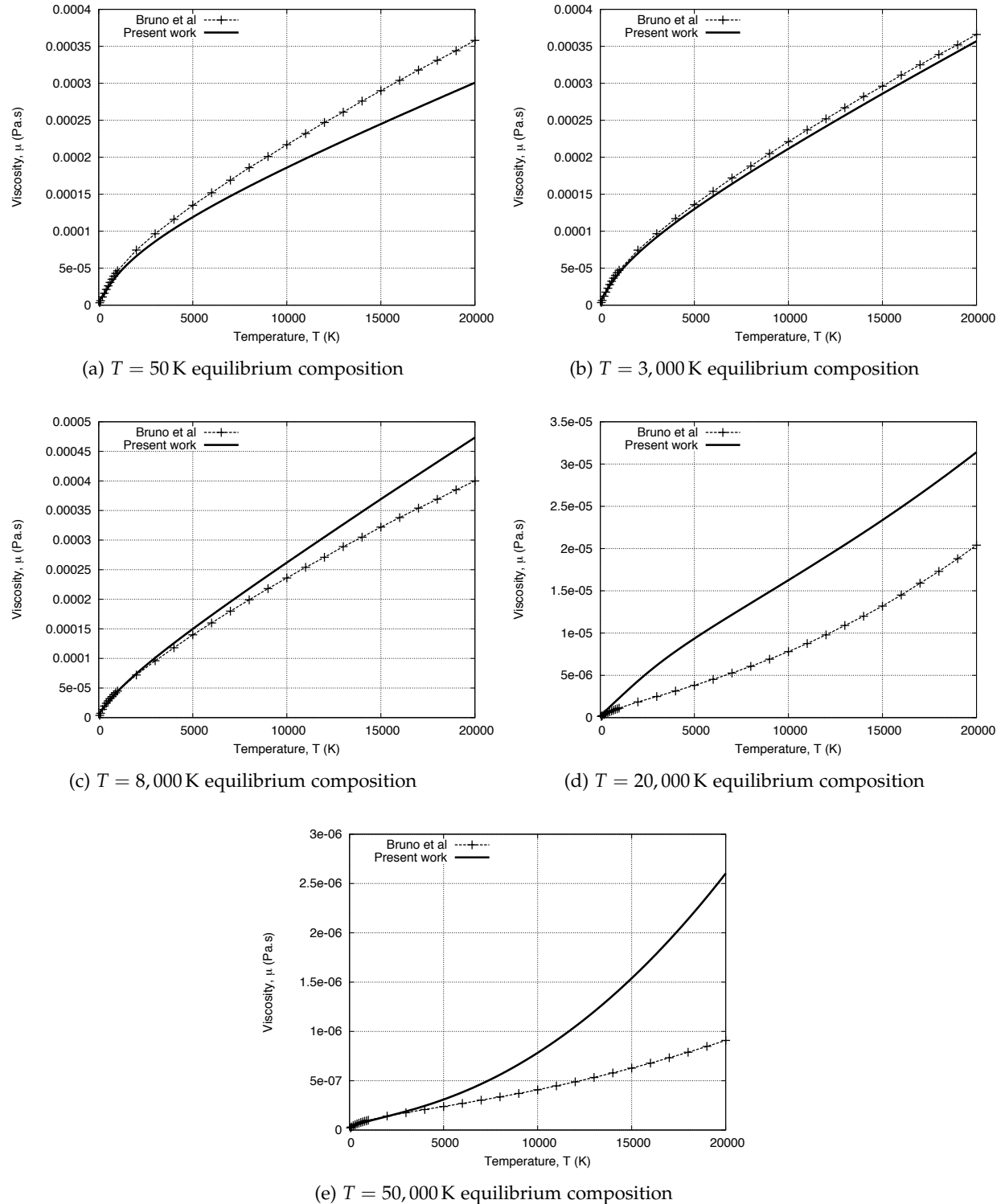


Figure 3.9: Comparison of the bulk viscosity coefficients obtained from the present transport model implementation with that tabulated by Bruno *et al.* [6].

3.3 Spectral radiation coefficients

The calculation of the spectral radiation coefficients, namely the emission j_ν and absorption κ_ν coefficients, are required when solving the radiation transport equations to be described in Section 7.5. For an ionised gas, there are three types of radiative mechanisms that make contributions to the bulk spectral coefficients:

1. Bound-bound transitions,
2. Bound-free transitions, and
3. Free-free transitions.

Bound-bound radiative transitions occur between two bound electronic states, whilst bound-free and free-free radiative transitions involve a free electron state. Figure 3.10 presents a sample vacuum ultraviolet absorption coefficient spectra with the contributions from bound-bound, bound-free and free-free transitions identified. As bound electronic states are quantised, the spectrum of a bound-bound transition is distributed about a discrete wavelength characterised by the energy gap between the upper and lower states. In contrast, the energy spectrum of bound-free and free-free radiative transitions are distributed into a continuum due to the arbitrary free electron energy. The spectrum of bound-free transitions are further characterised by a limiting wavelength corresponding to the ionisation threshold.

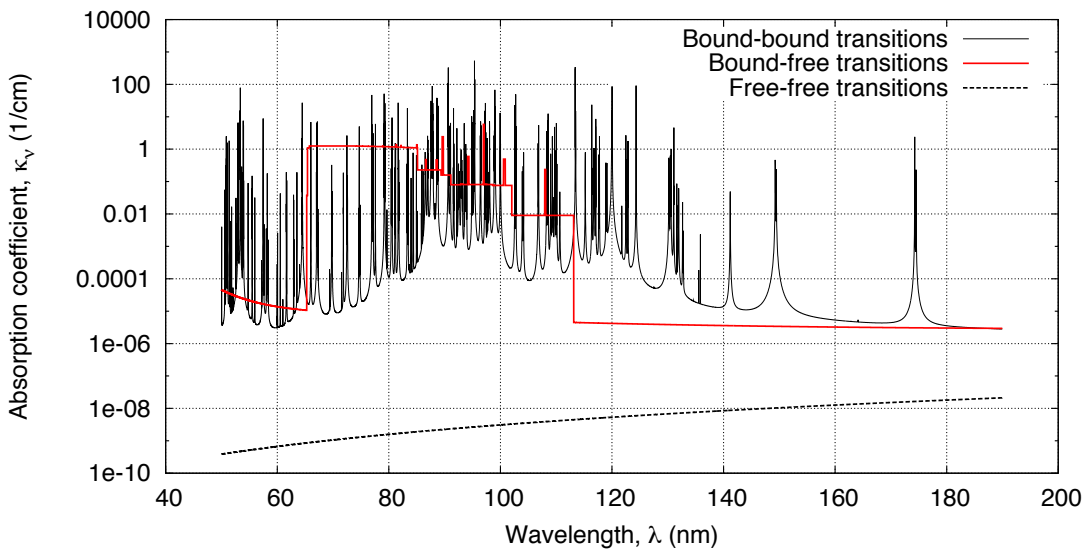


Figure 3.10: Components of the equilibrium vacuum ultraviolet absorption coefficient spectra for a 10 km/s shock through 0.1 Torr air.

At the most fundamental level, bound-bound transitions in both atoms and molecules occur between two Zeeman states of a hyperfine line due to the change in nuclear spin. In the present

work bound-bound transitions are described by a line-by-line model that considers the hyperfine structure where necessary. Continuum transitions are described by step models presented in the literature or hydrogenic approximations when unavailable. For an indepth discussion of the theory behind the models implemented here, see the texts of Zel'dovich and Razier [110], Huber and Herzberg [79] and Kovács [111].

3.3.1 Monatomic bound-bound transitions

The spectral emission and absorption coefficients for an atomic or molecular bound-bound transition with energy $h\nu_{ul}$ are:

$$j_{\nu,ul} = \frac{n_u h\nu_{ul} A_{ul}}{4\pi} b_{ul}(\nu) , \quad (3.114)$$

and,

$$\kappa_{\nu,lu} = (N_l B_{lu} - N_u B_{ul}) h\nu_{ul} b_{ul}(\nu) , \quad (3.115)$$

where l and u denote the lower and upper energy levels, N is the level number density, A_{ul} , B_{lu} and B_{ul} are the Einstein coefficients for spontaneous emission, absorption and induced emission, and $b_{ul}(\nu)$ is the spectral distribution function. The absorption and induced emission B_{ul} Einstein coefficients B_{lu} and B_{ul} can be related to the spontaneous emission Einstein coefficient A_{ul} via the principal of detailed balancing [110]. Equation 3.115 is then expressed as:

$$\kappa_{lu} = \left(N_l \frac{g_u}{g_l} - N_u \right) \frac{c^2}{8\pi\nu_{ul}^2} A_{ul} b_{ul}(\nu) \quad (3.116)$$

Level populations

For monatomic species, the electronic level populations are bound by two limiting distributions:

1. Boltzmann thermal equilibrium distribution, and
2. Saha-Boltzmann ionisation equilibrium distribution.

At thermal equilibrium conditions the electronic levels are populated according to the Boltzmann distribution, where the number density of level i is expressed as:

$$N_i = N_{\text{atom}} \frac{Q_{\text{el-}i}}{Q_{\text{int-atom}}} = N_{\text{atom}} \frac{g_i \exp\left(\frac{-E_i}{kT_{\text{el}}}\right)}{\sum_j^{j_{\max}} g_j \exp\left(\frac{-E_j}{kT_{\text{el}}}\right)} , \quad (3.117)$$

where N_{atom} is the total number density of the atom, E_i is the electronic energy of level i , T_{el} is the electronic temperature and $Q_{\text{int-atom}}$ is the total internal (electronic) partition function². Another constraint is imposed by considering chemical equilibrium between the electronic level, ions and free electrons. The Saha equation relates the number densities of an atom, its ion and free electrons via the principle of detailed balancing:

$$\frac{N_{\text{atom}}}{N_{\text{ion}} N_e} = \frac{Q_{\text{atom}}}{Q_{\text{ion}} Q_e} \exp\left(\frac{I_{\text{atom}}}{k_B T_e}\right), \quad (3.118)$$

where T_e is the free electron translation temperature, Q and N are respectively the *total* partition function and total number density of the denoted species and I_{atom} is the ionisation potential of the atom. By substituting the Boltzmann equation for an electronic level, Equation 3.117, into the Saha equation for an atomic species, Equation 3.119, the Saha-Boltzmann equation is obtained:

$$N_i = N_{\text{ion}} N_e \frac{Q_{\text{atom}}}{Q_{\text{ion}} Q_e} \exp\left(\frac{I_{\text{atom}}}{k_B T_e}\right) \frac{g_i \exp\left(\frac{-E_i}{kT_{\text{el}}}\right)}{Q_{\text{int-atom}}} \quad (3.119)$$

In compression flows, the Saha-Boltzmann distribution forms the lower bound and the Boltzmann distribution the upper bound, whilst in expanding flows they are reversed. As thermochemical equilibration occurs, the atom number density approaches that predicted by the Saha equation and the Saha-Boltzmann and Boltzmann distributions converge to the same result.

To model the level populations in nonequilibrium, the rate of all transitions affecting the level must be considered. As all transitions can be grouped into those occurring due to particle collisions and those due to radiative transitions, the nonequilibrium modelling of quantum levels is often referred to as ‘collisional-radiative modelling’. In the present work we consider the electronic levels of neutral atoms to possess nonequilibrium populations, whilst the electronic levels of atomic ions are assumed to be in Boltzmann equilibrium. The collisional-radiative framework is described in Section 4.3.

Electronic level energies and degeneracies

The critical data for calculating monatomic partition functions are the energies and degeneracies of the electronic levels. In the present work these parameters are obtained from the NIST Atomic Spectra Database [80], with data for high lying states of neutral atoms taken from Park [29]. Table 3.4 summarises the total, individual and grouped electronic levels and lines considered for monatomic species in the present work. Following the recommendations of Johnston [19], the majority of levels are included as individual multiplets for maximum precision in the collisional-radiative modelling. For the neutral monatomic species C, N and O levels up to energies of

²Whereas only the first few electronic levels were retained when calculating the partition function for determining thermodynamic properties, all the electronic levels up to the ionisation limit are included for the spectral coefficient calculations. This is necessary as transitions originating from near the ionisation limit are often very strong, and their populations need to be determined to a high degree of accuracy.

$84,000\text{ cm}^{-1}$, $108,000\text{ cm}^{-1}$ and $106,000\text{ cm}^{-1}$ respectively are treated individually, with the remaining levels included via the groupings proposed by Park [29]. For neutral Ar levels with energy $120,000\text{ cm}^{-1}$ and less are treated individually, with the remaining grouped according to energy proximity. For the ionic monatomic species significantly less levels are required as only the first few excited states can be excited at the conditions of present interest; the levels for Ar^+ , C^+ , N^+ and O^+ are truncated at energies of $150,000\text{ cm}^{-1}$, $160,000\text{ cm}^{-1}$, $160,000\text{ cm}^{-1}$ and $200,000\text{ cm}^{-1}$ respectively. Figure 3.11 compares the electronic partition function for the monatomic radiators using the electronic levels from NIST [80], Park [29] and the present work. For the neutral monatomic species good agreement between all three level sets is achieved at temperatures less than $14,000\text{ K}$, with the Park and present work level sets rising above the NIST results at higher temperatures. This is due to the Park level sets including super-ionised levels, whereas the NIST level sets have been truncated at the ionisation limit. For the ionic monatomic species the NIST and present work level sets agree for the whole temperature range, indicating the chosen truncated energies are adequate. While the C^+ Park and NIST level sets show good agreement, those for N^+ and O^+ do not. These discrepancies have been found to be due to anomalies in the tabulated level data presented by Park [29] for N^+ and O^+ .

Table 3.4: Summary of monatomic electronic levels from the NIST Atomic Spectra Database [80] implemented in the present work.

Species	Total number of levels	Individual levels	Grouped levels
Ar	29	1 - 17	17 - 29
Ar^+	10	1 - 10	-
C	43	1 - 34	35 - 43
C^+	11	1 - 11	-
N	37	1 - 27	28 - 37
N^+	17	1 - 10	-
O	32	1 - 27	28 - 32
O^+	8	1 - 8	-

Electronic transitions

Table 3.5 summarises the lines considered for monatomic species in the present work. Following the recommendations of Johnston [19], when performing radiatively coupled Navier–Stokes simulations transitions with energy less than 6 eV are modelled as multiplet lines whilst higher energy transitions are modelled as individual lines. This line selection strategy was shown in Reference [19] to enable the radiant energy to be accurately captured whilst optimising the efficiency of the calculation. It should be noted that the multiplet treatment of spectral lines inevitably leads to some error in the transport calculation, and future work should seek to treat

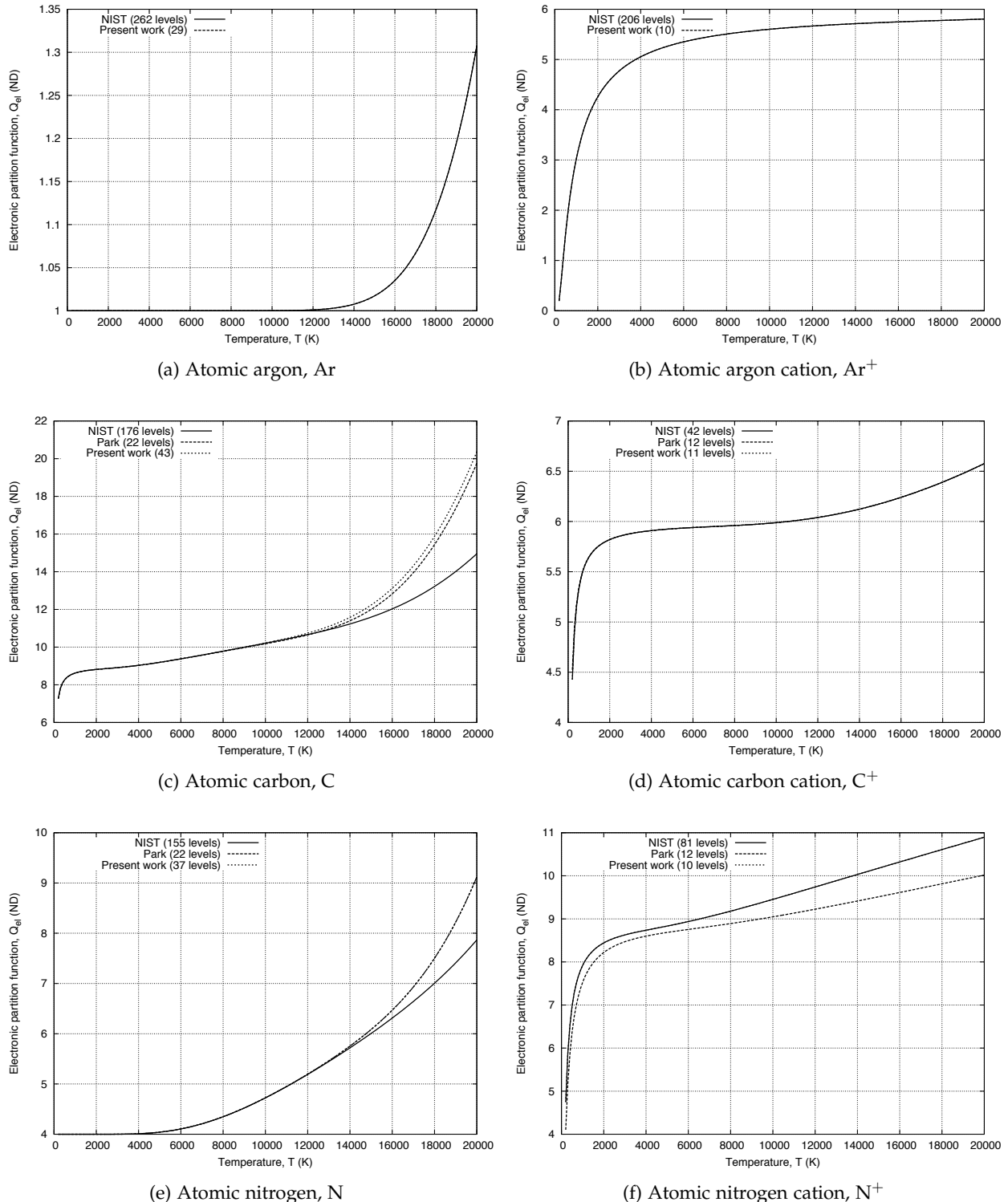


Figure 3.11: Comparison of electronic partition function Q_{el} for the monatomic radiators using various levels sets.

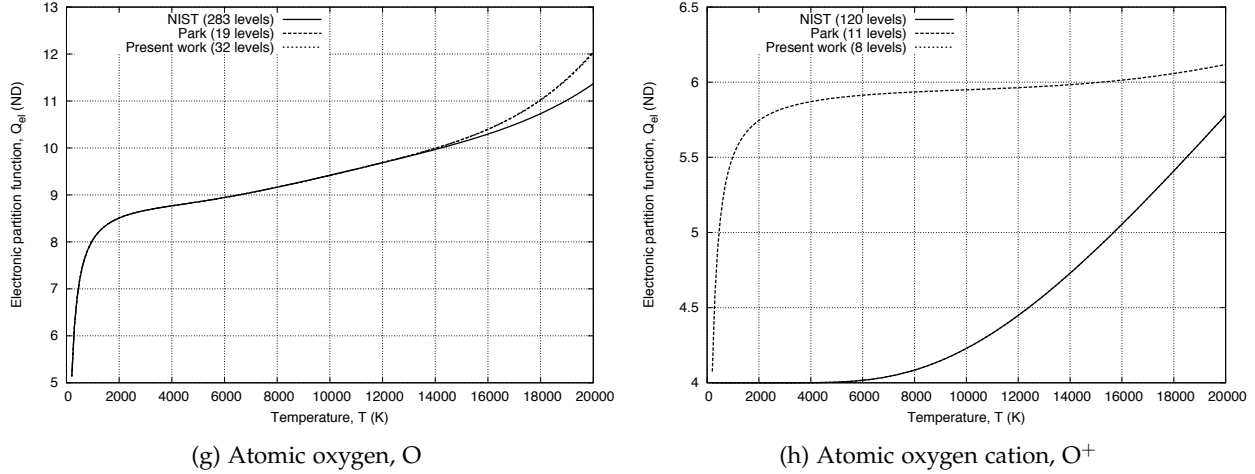


Figure 3.11: (Continued) Comparison of electronic partition function Q_{el} for the monatomic radiators using various levels sets.

all lines individually if sufficient computational resources are available to make the calculations possible. Also, when performing comparisons with experimental spectra in the present work, all lines are treated individually to best represent the observed spectra. This is possible as the single line-of-sight calculations required for spectra comparisons are not computationally intensive.

Table 3.5: Summary of atomic electronic levels and lines from the NIST Atomic Spectra Database [80] implemented in the present work.

Species	Number of individual lines		Number of multiplet lines	
	$\Delta E \leq 6 \text{ eV}$	$\Delta E > 6 \text{ eV}$	$\Delta E \leq 6 \text{ eV}$	$\Delta E > 6 \text{ eV}$
Ar	422	6	204	6
Ar^+	297	10	98	3
C	1141	157	390	56
C^+	358	278	89	69
N	970	129	223	44
N^+	481	241	71	89
O	691	163	125	55
O^+	617	259	175	77

As the electronic level data for each atomic species used for partition function calculations consists of multiplet and grouped levels, a mapping strategy is required for calculating the upper and lower line state populations. This is achieved by assuming Boltzmann equilibrium with the associated multiplet or grouped electronic level. For an upper state of a line denoted by * with associated grouped electronic level i , for example, the upper state population is calculated as:

$$N^* = N_i \frac{g^*}{g_i} \exp \left[\frac{-(E^* - E_i)}{kT_{\text{el}}} \right] \quad (3.120)$$

where the associated grouped electronic levels for each line are determined from the NIST tabulations upon initialisation.

Spectral distribution function

The spectral distribution function $b(\nu)$ in Equations 3.114 and 3.115 describes the spectral distribution of the emission and absorption coefficients of a line transition. Although the energy gap characterising a transition is discrete, the energy spectrum of the resulting photon is smeared over a finite range due to various broadening mechanisms. These broadening mechanisms can be classified into two types: those described by a Lorentzian distribution, and those described by a Gaussian distribution. The Lorentzian broadening mechanisms considered in the present work for monatomic radiators are:

- Resonant pressure broadening
- Van der Waals broadening
- Stark broadening
- Natural broadening

The only Gaussian broadening mechanism considered is Doppler broadening. The resultant spectral distribution function is therefore modelled as a Voigt profile which is a convolution of a Lorentzian and a Gaussian distribution. A Gaussian and Lorentzian profile with equal half-widths and the convolved Voigt profile are shown in Figure 3.12. The Gaussian profile exhibits a rapid rise to the central peak, whilst the Lorentzian profile is characterised by slowly decaying ‘wings’.

In the present work the Voigt profile approximation proposed by Whiting [112] is implemented:

$$b(\nu) = \frac{(1 - R_D) \exp(-2.772R_L^2) + \frac{R_D}{1+4R_L^2} + 0.016(1 - R_D)R_D \exp\left(\frac{-0.4R_L^{2.25}-10}{10+R_L^{2.25}}\right)}{2\gamma_V (1.065 + 0.447R_D + 0.058R_D^2)} \quad (3.121)$$

where R_D and R_L are defined as:

$$R_D = \frac{\gamma_L}{\gamma_V}, \text{ and } R_L = \frac{\nu_{ul}}{2\gamma_V}, \quad (3.122)$$

and γ_L , γ_D and γ_V are respectively the Lorentzian, Doppler and Voigt half-widths at half-maximum (HWHM) in frequency units. The Voigt half-width is a function of the Lorentzian

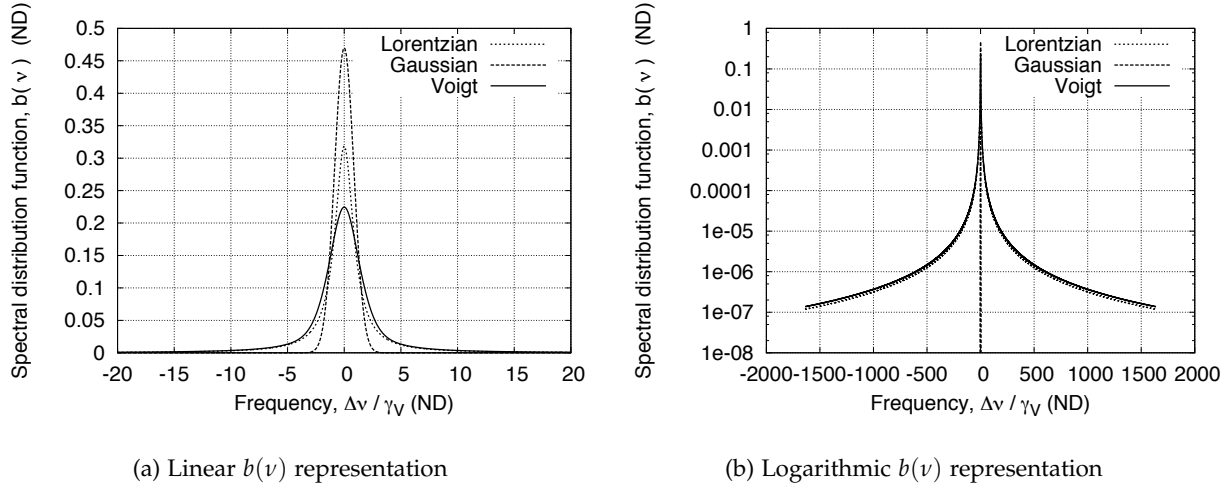


Figure 3.12: Gaussian, Lorentzian and Voigt profiles as a function of the normalised frequency. The Gaussian and Lorentzian profiles have the same half-widths.

and Doppler (Gaussian) half-widths, and is calculated by the following approximation of Olivero and Longbothum [113]:

$$\gamma_V = (1 - 0.18121(1 - d^2) - [0.023665 \exp(0.6d) + 0.0418 \exp(-1.9d) \sin(\pi d)]) (\gamma_L + \gamma_D) \quad (3.123)$$

where d is defined as:

$$d = \frac{\gamma_L - \gamma_D}{\gamma_L + \gamma_D} . \quad (3.124)$$

The Lorentzian half-width γ_L is the sum of the contributions from the Lorentzian broadening mechanisms:

$$\gamma_L = \gamma_R + \gamma_{VW} + \gamma_S + \gamma_N \quad (3.125)$$

where γ_R , $\gamma_V W$, γ_S and γ_N are the resonance, Van der Waals, Stark and natural broadening half-widths respectively. Resonant pressure broadening is modelled via the expression of Nicolet [114]:

$$\gamma_R = 3\pi \sqrt{\frac{g_l}{g_u}} \left[\frac{e^2 f_{lu}}{2\pi m v_{ul}} \right] N_a \quad (3.126)$$

where f_{lu} is the transition oscillator strength and N_a is the number density of perturbing atoms. In the present work N_a is set to the number density of the lower state. Van der Waals broadening accounts for pressure broadening due to non-resonant interactions, and is modelled by the expression given by Traving [115]:

$$\gamma_{VW} = 1.95 \times 10^{-28} \sqrt{\frac{2T}{M_{av}}} N_{hp} \nu_{ul}^2 \quad (3.127)$$

where M_{av} is the average molecular weight of the mixture and N_{hp} is the heavy particle number density. Although accurate Stark widths for some atomic species are tabulated in the literature (*e.g.* Reference [116]), in the present work Stark broadening is modelled via the following approximate expression observed by Page [117]:

$$\gamma_S = \gamma_S^0 \left(\frac{T_e}{T_e^0} \right)^{\alpha_S} \left(\frac{N_e}{N_e^0} \right) \quad (3.128)$$

where α_S is a fitting constant and γ_S^0 is a reference Stark half-width per electron at electron temperature T_e^0 and electron number density N_e^0 . The reference half-widths are approximated by the following curve-fit proposed by Johnston [19]³:

$$\gamma_S^0 = \frac{8.45 \times 10^9}{(I - E_u)^{2.623}} \quad (3.129)$$

where the reference electron temperature T_e^0 and number density N_e^0 are 10,000 K and $1 \times 10^{16} \text{ cm}^{-1}$ respectively, and the fitting constant α_S is set to 0.33. This curve-fit is shown in Reference [19] to be a good approximation of the accurate N and O Stark widths presented by Griem [116] and others. Natural line broadening is modelled using the following classical expression [118]:

$$\gamma_N = \frac{2\pi e^2 \nu_{ul}^2}{3\epsilon_0 m c^3} \quad (3.130)$$

and Doppler broadening is modelled by the half-width expression given by Nicolet [114]:

$$\gamma_D = \frac{\nu_{ul}}{c} \sqrt{\frac{2k_B T_{tr} \ln(2)}{m_s}} \quad (3.131)$$

where m_s is the species mass per particle.

Figures 3.13a and 3.13b compare the monatomic half-widths calculated at conditions characteristic of typical lunar return peak heating gas states in the boundary and shock layers respectively (Fire II $t = 1642.66$ s). The line widths in the boundary layer are dominated by Doppler broadening with Van der Waals broadening becoming significant at the higher wavelengths, whilst those in the shock layer are largely dominated by Stark broadening. Furthermore the Stark widths in the shock layer are on average approximately 10^3 times greater than in the boundary layer. This is explained by the much higher free electron temperature and density in the shock layer, and that the Stark width is proportional to $T_e^{1/3} N_e$. In both the boundary and

³Note that the original expression presented by Johnston [19] is for the full-width in wavelength units, whereas that presented here is for the half-width in frequency units.

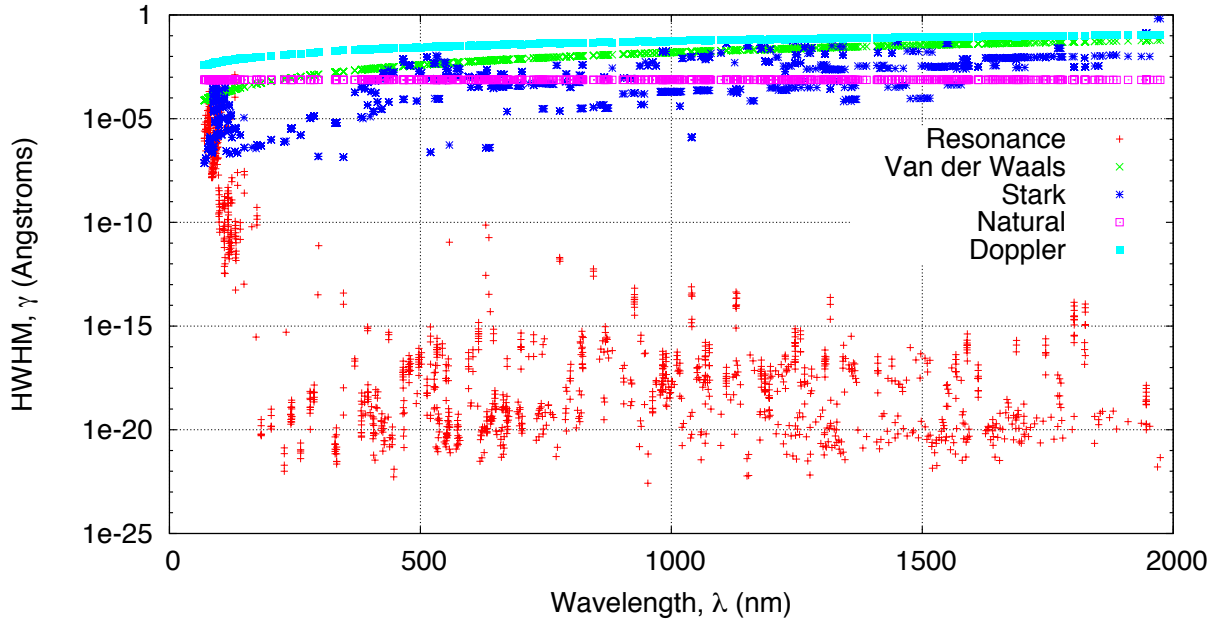
shock layers the natural and resonance broadening contributions are negligible for the spectral range considered.

Figures 3.14a and 3.14b compare the monatomic half-widths calculated at conditions characteristic of a hypothetical high-speed Mars entry trajectory point with a freestream pressure and velocity of 18 Pa and 8 km/s respectively. Here the line widths in the boundary layer are also dominated by Doppler broadening, with both Stark and Van der Waals broadening making minor contributions especially at the higher wavelengths. In contrast to the lunar return case, both Stark and Doppler broadening make approximately equal contributions to the line widths for the Mars entry shock layer. This is due to the significantly lower free electron number density and temperature for the Mars entry case. From these results it is evident that both natural and resonance broadening can be omitted without significant loss of line width accuracy for the thermodynamic regimes of present interest.

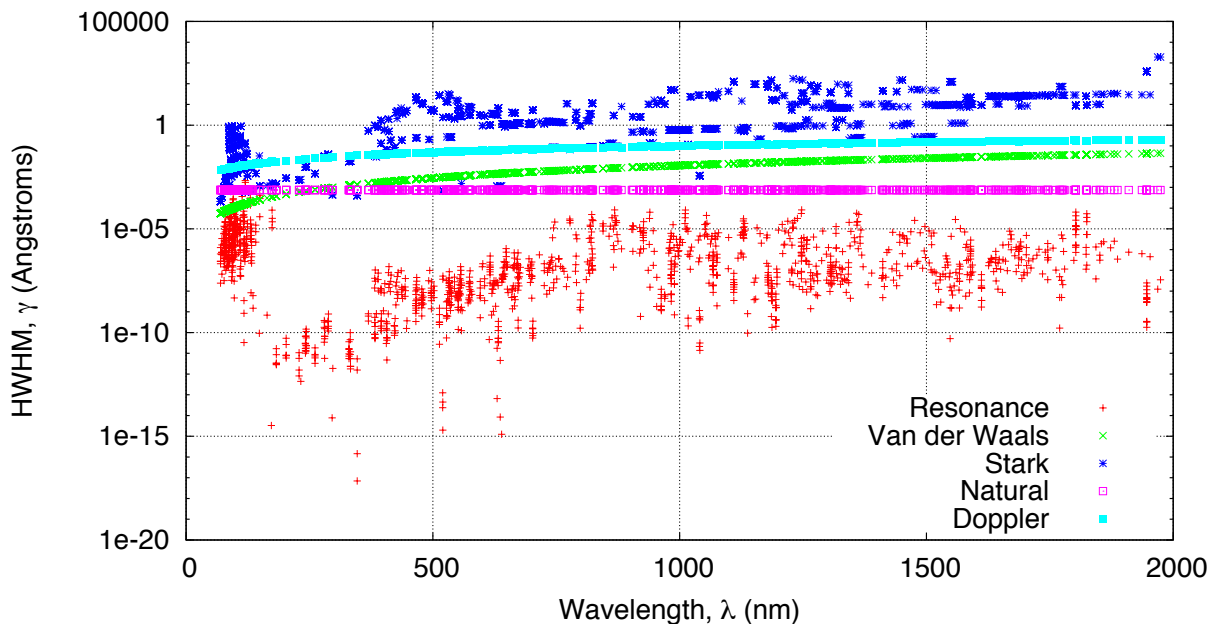
Finally, an appropriate cut-off limit for each line must be determined. Although the wings of the Voigt profile are many orders of magnitude weaker than the central peak (see Figure 3.12), the wings extend far beyond the line-centre and the rate of decay is low. Figures 3.15a and 3.15b compare the sensitivity of atomic bound-bound emissive power density and intensity for a 10 cm slab of atmospheric pressure equilibrium air to the atomic line cut-off limit. The line cut-off limit $\Delta\nu_{\text{limit}}$ has been normalised by the voigt HWHM γ_V , and the emissive power density and intensity are normalised by the respective values at $\Delta\nu_{\text{limit}} = 10,000\gamma_V$. While the emissive power density is reasonably well described with $\Delta\nu_{\text{limit}}/\gamma_V \geq 10$, the intensity is much more sensitive, requiring $\Delta\nu_{\text{limit}}/\gamma_V \geq 1000$. To optimise the efficiency of the calculation, it is desirable to use the minimum cut-off limit; therefore in the present work the atomic line cut-off limit is set to $\Delta\nu_{\text{limit}} = 1000\gamma_V$.

Comparison with SPRADIAN07

The Structured Package for Radiation Analysis 2007 (SPRADIAN07) program has been recently developed by the Japanese Aerospace Exploration Agency (JAXA) and Korea Advanced Institute of Science and Technology (KAIST). The theory and implementation of SPRADIAN07 is described in the PhD thesis of Hyun [66]. Both SPRADIAN07 and the model developed in the present work implement the spectroscopic data from the NIST Atomic Spectra Database [80]. Comparisons with the SPRADIAN07 code [66] have therefore been made in order to verify the calculation of atomic bound-bound spectral coefficients. The test case consists of a 10 cm slab of gas with temperature $T = 10,000$ K and pressure $p = 1$ atm. The number density of each radiator is $1 \times 10^{16} \text{ cm}^{-3}$, the electron number density is also $1 \times 10^{16} \text{ cm}^{-3}$ and total number density is $2.2 \times 10^{17} \text{ cm}^{-3}$. The bound-bound transitions of Ar, Ar⁺, C⁺, N⁺, O⁺ are not included in the comparison as the SPRADIAN07 code does not consider them. For each radiator, the emissive power density J (W/cm³) and intensity I (W/cm²) is calculated in the spectral range



(a) Boundary layer conditions ($T_{tr} = 3,510\text{ K}$, $T_{ve} = 3,870\text{ K}$, $p = 77,900\text{ Pa}$ and $N_e = 1.8 \times 10^{13}\text{ cm}^{-3}$)



(b) Shock layer conditions ($T_{tr} = 11,220\text{ K}$, $T_{ve} = 11,200\text{ K}$, $p = 79,000\text{ Pa}$ and $N_e = 3.6 \times 10^{16}\text{ cm}^{-3}$)

Figure 3.13: Monatomic line half-widths at half-maximum for typical Lunar return peak heating conditions (Fire II $t = 1642.66\text{ s}$).

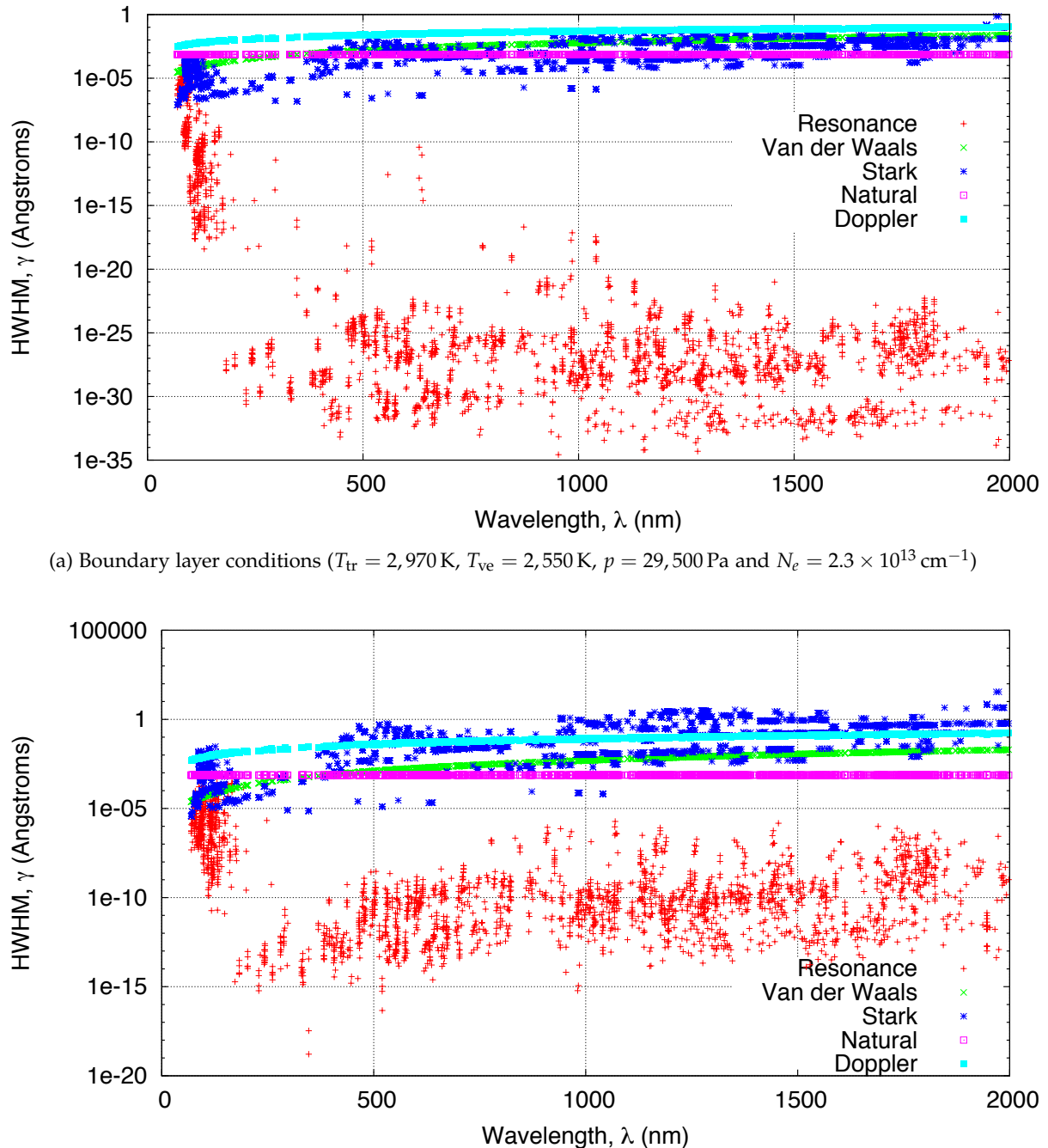


Figure 3.14: Monatomic line half-widths at half-maximum for a hypothetical high-speed Mars entry trajectory point with a freestream pressure and velocity of 18 Pa and 8 km/s respectively.

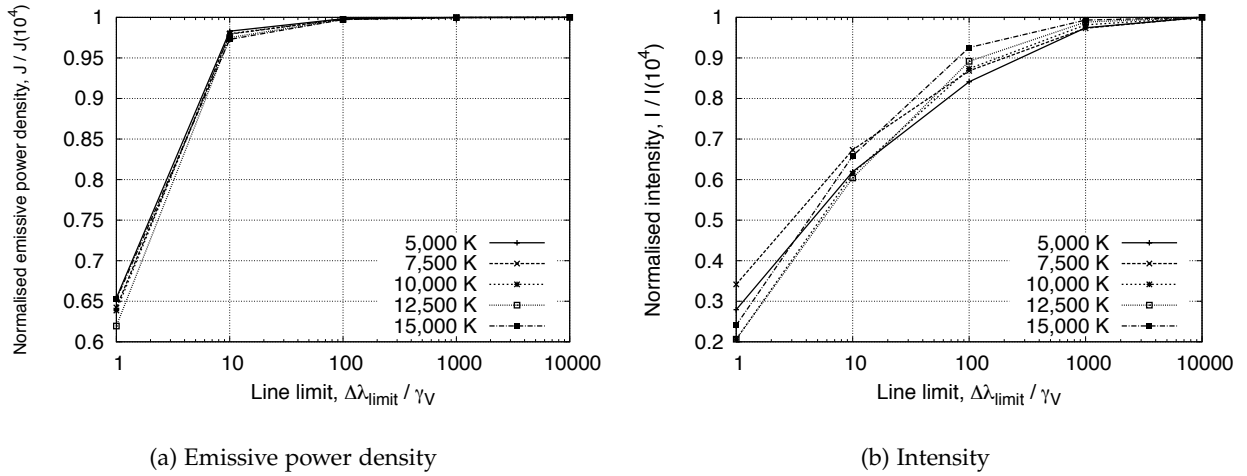


Figure 3.15: Sensitivity of atomic bound-bound emissive power density and intensity for a 10 cm slab of equilibrium air to the atomic line cut-off limit ($p = 1 \text{ atm}$).

$50 \leq \lambda \leq 2,000 \text{ nm}$ with 1,950,000 equidistant frequency intervals.

Table 3.6 summarises the comparison between the SPRADIAN07 code [66] and the present work for atomic bound-bound transitions. While the agreement for emissive power density is within 1% for all the key atomic radiators, the SPRADIAN07 predicts between 16 and 28% lower intensity through the 10 cm slab. The difference in intensity can be attributed to slight discrepancies in the line half-widths. Figures 3.16a, 3.16b and 3.16c presents the intensity, absorption coefficient and emission coefficient spectra for the atomic oxygen lines in the spectral range $128 \leq \lambda \leq 133 \text{ nm}$. The SPRADIAN07 emission and absorption spectra peaks higher and drops lower than that from the present work, indicating the SPRADIAN07 line-widths for these transitions are slightly lower. The resultant cumulative intensity is almost 25% lower, however, indicating the high sensitivity of intensity to the line half-widths. While the SPRADIAN07 code uses experimentally determined Stark broadening parameters, the present model uses an approximate curve-fit. Unfortunately the approximate method for calculating the Stark width is a limitation of the spectral model developed for the present work.

Table 3.6: Comparison of atomic bound-bound model from the present work with the SPRADIAN07 code [66].

Species	Emissive power density, J (W/cm ³)			Intensity, I (W/cm ²)		
	SPRADIAN07	Present work	Difference (%)	SPRADIAN07	Present work	Difference (%)
C	1265	1269	0.34	20.58	25.76	20.12
N	179.8	181.0	0.65	3.77	4.54	16.92
O	59.85	60.28	0.72	1.55	2.13	27.35

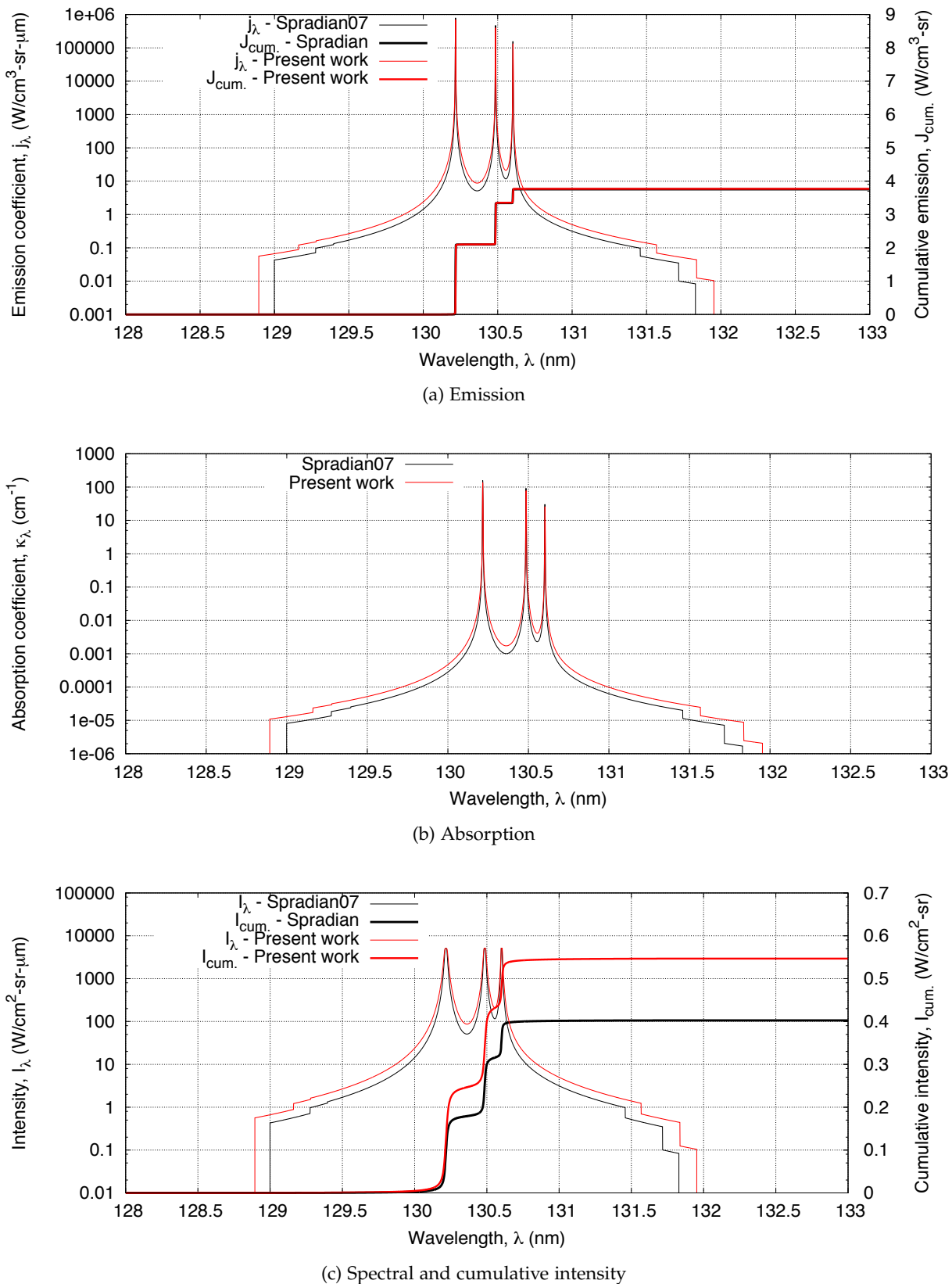


Figure 3.16: Comparison between SPRADIAN07 and the present work for the spectra of atomic oxygen lines in the range $128 \leq \lambda \leq 133$ nm.

3.3.2 Diatomic bound-bound transitions

Diatomic bound-bound transitions occur between individual rovibronic⁴ states of the molecule. The resulting rotational lines are clustered into bands and systems corresponding to individual vibrational and electronic transition groups. The spectral emission and absorption coefficients for an individual diatomic bound-bound transition are the same as for monatomic transitions:

$$j_{\nu,ul} = \frac{n_u h \nu_{ul} A_{ul}}{4\pi} b_{ul}(\nu) \quad (3.132)$$

$$\kappa_{\nu,lu} = \left(n_l \frac{g_u}{g_l} - n_u \right) \frac{c^2}{8\pi \nu_{ul}^2} A_{ul} b_{ul}(\nu) \quad (3.133)$$

where l and u denote the lower and upper energy levels, n is the level number density, A_{ul} is the Einstein coefficient for spontaneous emission and $b_{ul}(\nu)$ is the spectral distribution function.

Rovibronic transitions

The determination of allowed transitions, their energies and probabilities is dependent on the coupling between electronic orbital \vec{L} , electron spin \vec{S} and nuclear rotation \vec{N} angular momentum vectors for the upper and lower rovibronic states. The Hund's coupling cases⁵ (a), (b), (c) and (d) illustrated in Figure 3.17 define idealised limiting cases of angular momentum couplings [79]. In Hund's case (a) nuclear rotation is completely decoupled from electronic motion, whilst electronic motion is strongly coupled to the internuclear axis. In Hund's case (b) electron spin decouples from the internuclear axis due to strong coupling with the rotational motion. When the interaction between the electronic orbital and electron spin angular-momentum is very strong we have Hund's case (c), and when the electronic orbital is strongly coupled to the axis of rotation we have Hund's case (d).

In the present work we consider cases (a) and (b) and an intermediate (a)-(b) case. This selection is a good compromise between speed and accuracy, as spin splitting is captured when important whilst Λ -type doubling which involves much finer perturbations is neglected. Here we will present a brief overview of the selection rules for these three transitions; for a complete discussion the reader is directed to the texts of Huber and Herzberg [79] and Kovács [111]. The energy and transition probability expressions for each case will be presented in the following sections.

For all coupling cases the selection rule for the total angular momentum quantum number J is:

⁴A rovibronic state is a molecular configuration with a complete set of rotational, vibrational and electronic quantum numbers.

⁵A fifth coupling case (e) theoretically exists where \vec{L} and \vec{S} are strongly coupled, however such behaviour has not been observed for any species [79].

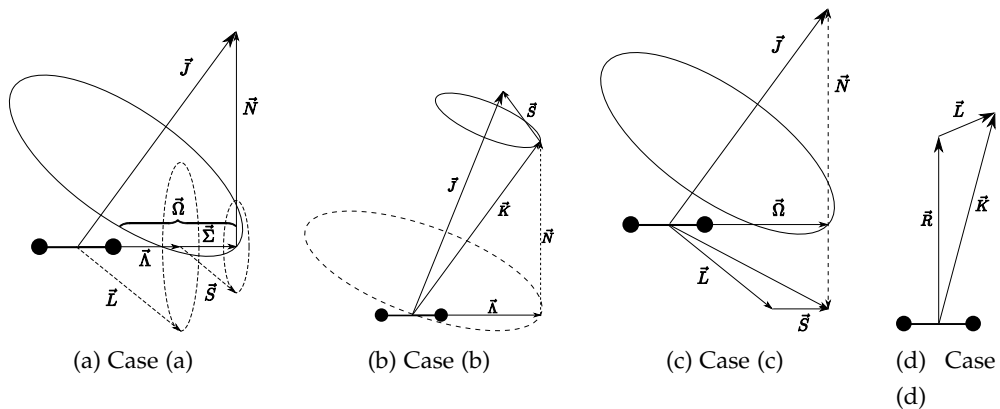


Figure 3.17: Diagrammatic representations of the (a), (b), (c) and (d) Hund's coupling cases describing the limiting angular momentum interactions for rovibronic transitions.

$$J_u - J_l = \Delta J = 0, \pm 1, \text{ and } J_u = J_l \neq 0 \quad (3.134)$$

For Hund's case (a) the electronic angular momentum $\vec{\Omega}$ and rotational angular momentum \vec{N} couple to form the resultant angular momentum vector \vec{j} . Therefore the total angular momentum quantum number J cannot be smaller than the electronic component $\Omega = |\Lambda + \Sigma|$:

$$J = \Omega, \Omega + 1, \Omega + 2, \dots \quad (3.135)$$

An additional restriction for $\Sigma --\Sigma$ transitions belonging to Hund's case (a) is that $\Delta J = 0$ transitions are universally prohibited. Therefore Hund's case (a) transitions have three branches P , Q and R corresponding to $\Delta J = +1, 0$ and -1 respectively, where only P and R branches exist for $\Sigma --\Sigma$ transitions. In the present work all singlet ($X^1 - X^1$ where $X = \Sigma, \Pi, \Delta, \dots$) and multiplet parallel ($X^n - Y^n$ where $n > 1$ and $|L_m - L_n| = 1$) transitions except from the CN Violet system are assumed to belong to Hund's case (a).

For Hund's case (b) a total angular momentum quantum number *apart from spin K* is defined with one-to-one correspondence with J as defined for Hund's case (a). Therefore the selection rules pertaining to J outlined above are now applied to K . As $\vec{\Omega}$ and \vec{N} are coupled in Hund's case (b), the permitted range for K is:

$$K = \Lambda, \Lambda + 1, \Lambda + 2, \dots \quad (3.136)$$

As total angular momentum \vec{j} is the resultant of \vec{K} and the spin angular momentum \vec{S} , the possible values of J are:

$$J = (K + S), (K + S - 1), (K + S - 2), \dots, |K - S|. \quad (3.137)$$

Therefore Hund's case (b) considers three ΔJ branches that each consist of $2S + 1$ spin split components. In the present work only the CN Violet $\Sigma^2 - \Sigma^2$ transition is described by Hund's case (b) coupling; for this transition, we have a total of 6 branches with designations R_1 , R_2 , ${}^RQ_{21}$, ${}^PQ_{12}$, P_2 and P_1 . Figure 3.18 compares the absorption coefficient for the CN Violet 0-0 band modelled via Hund's case (a) and Hund's case (b). Although the two coupling cases produce similar results for branches close to the band head at 388.45 nm, the effect of spin splitting becomes more pronounced with increasing J .

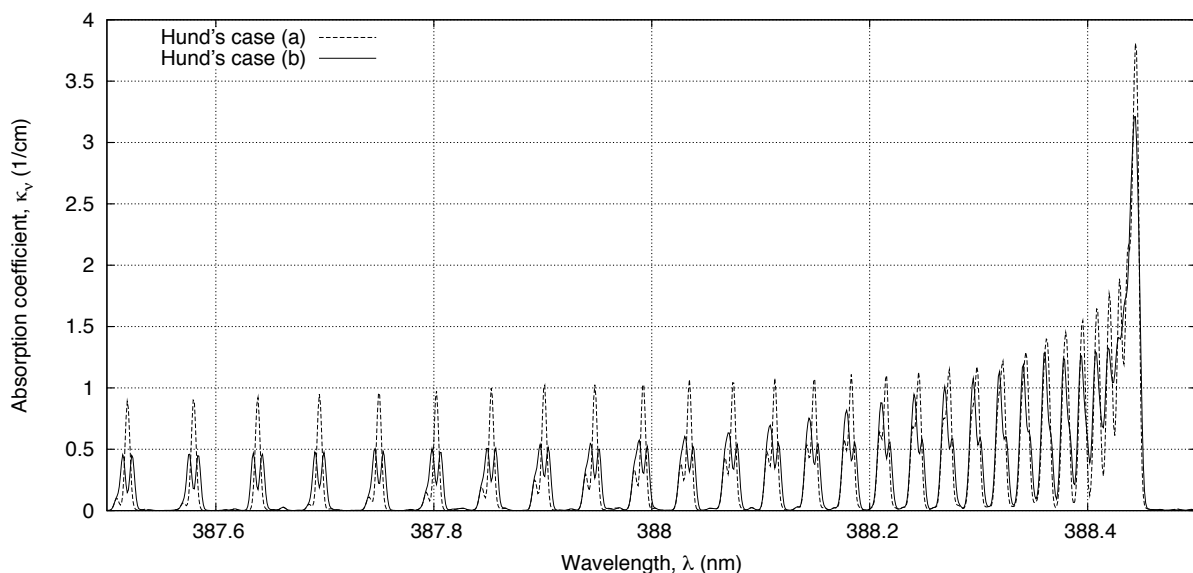


Figure 3.18: Absorption coefficient for the CN Violet 0-0 band modelled via Hund's case (a) and Hund's case (b).

The remaining transitions, which are the parallel doublets, are described by an intermediate (a)-(b) coupling case, where \vec{S} is strongly coupled to the internuclear axis for low J and becomes coupled with rotation with increasing J – hence this case is referred to as *spin uncoupling*. The quantum numbers K , S and J and their previous defined selection rules are all applicable to the intermediate (a)-(b) case. Intermediate (a)-(b) coupling transitions have three ΔJ branches each with $(2S + 1)^2$ spin split components. A common transition that is modelled via the intermediate (a)-(b) coupling case is a perpendicular doublet such as ${}^2\Pi - {}^2\Sigma$. These transitions have 12 branches with designations P_1 , P_2 , P_{12} , P_{21} , Q_1 , Q_2 , Q_{12} , Q_{21} , R_1 , R_2 , R_{12} and R_{21} .

Level populations

The electronic level populations of molecular species are bounded by two limiting distributions:

1. Boltzmann thermal equilibrium distribution, and
2. Dissociation equilibrium distribution.

Whereas the chemical equilibrium constraint for atomic species is via ionisation, the chemical equilibrium constraint for molecular species is via dissociation. This is due to the fact that the dissociation energy for a molecule is lower than the ionisation energy; thus a molecule will more readily dissociate before it ionises.

Where sufficient collisions have occurred to achieve thermal equilibrium conditions, the internal quantum states are populated according to the Boltzmann distribution. The number density of *electronic* level i is then:

$$N_i = N_{\text{diatom}} \frac{Q_{\text{el-}i}}{Q_{\text{int-diatom}}} = N_{\text{diatom}} \frac{Q_{\text{el-}i}}{\sum_e^{\text{e}_{\max}} Q_{\text{el-}e}}, \quad (3.138)$$

where N_{diatom} is the total species population, $Q_{\text{el-}i}$ is the electronic partition function of level i and $Q_{\text{int-diatom}}$ is the total internal partition function. The electronic partition function for diatomic level i is:

$$Q_{\text{el-}i} = g_i \exp \left(-\frac{T_i}{k_B T_{\text{el}}} \right) \sum_v^{v_{\max}} \exp \left(-\frac{G_v}{k_B T_{\text{vib}}} \right) \frac{1}{\sigma} \sum_J^{J_{\max}} (2J+1) \exp \left(-\frac{F_J}{k_B T_{\text{rot}}} \right), \quad (3.139)$$

where g_i and T_i are the electronic degeneracy and energy, G_v is the energy of vibrational state with quantum number v , F_J is the energy of rotational state with quantum number J and $2J+1$ is the rotational state degeneracy⁶. The electronic degeneracy g_i is the product of the orbital and spin multiplicity of the state:

$$g_i = (2 - \delta_{0,\Lambda_i}) (2S_i + 1) \quad (3.140)$$

where $\delta_{0,\Lambda}$ is the Kronecker Delta function which is unity when $\Lambda = 0$ and zero otherwise and $2S + 1$ is the spin multiplicity. The homonuclear factor σ in Equation 3.139 accounts for the symmetry of molecules with alike nuclei, and is equal to 2 for homonuclear molecules and 1 for heteronuclear molecules. To good accuracy the summation over the rotational states can be approximated by the following expression derived by Golden [119]:

$$Q_{i,v-\text{rot}} = \frac{1}{\sigma} \sum_J^{J_{\max}} (2J+1) \exp \left(-\frac{F_J}{k_B T_{\text{rot}}} \right) \approx \frac{1}{\sigma} \left(\frac{k_B T_{\text{rot}}}{B_e - (v + 1/2)\alpha_e} \right), \quad (3.141)$$

where α_e and B_e are spectroscopic constants of the electronic level.

As the characteristic time for chemical reactions is typically much shorter than that for thermal energy exchange, dissociation equilibrium provides another constraint on the population distribution. For a diatomic species comprised of atoms X and Y the dissociation equilibrium relation is found from the principal of detailed balancing:

⁶The degeneracy of vibrational levels does not appear as it is always unity.

$$\frac{N_{\text{diatom}}}{N_X N_Y} = \frac{Q_{\text{diatom}}}{Q_X Q_Y} \exp\left(\frac{D_{\text{diatom}}}{k_B T_{\text{tr}}}\right), \quad (3.142)$$

where N and Q denote the total population and total partition function of the indicated species and D_{diatom} is the average dissociation potential of the molecule⁷. The dissociation equilibrium population of electronic level i is found by substituting the Boltzmann relation in Equation 3.138 into Equation 3.142:

$$N_i = N_X N_Y \frac{Q_{\text{diatom}}}{Q_X Q_Y} \exp\left(\frac{D_i}{k_B T_{\text{tr}}}\right) \frac{Q_{\text{el-}i}}{Q_{\text{int-diatom}}} \quad (3.143)$$

where D_i is the dissociation potential taken from electronic level i .

To model the level populations in nonequilibrium, the rate of all transitions affecting the level must be considered. In the present work only *electronic* nonequilibrium is considered, where the electronic levels populations are solved via the collisional-radiative framework to be described in Section 4.3.

Irrespective of the electronic level population distribution, the rotational and vibrational populations are modelled via Boltzmann distributions governed by the respective modal temperatures, T_{rot} and T_{vib} . For a rovibronic level with quantum numbers e , v and J , the Boltzmann population in terms of an arbitrary electronic level population $N_{\text{el-}e}$ is:

$$N_{e,v,J} = N_{\text{el-}e} \frac{Q_{e,v,J}}{Q_{\text{el-}e}} \frac{L_{e,J}}{\sigma} \quad (3.144)$$

where $L_{e,J}$ is the line alternation factor due to nuclear spin and $Q_{e,v,J}$ is the rovibronic partition function. $L_{e,J}$ is set to unity for heteronuclear molecules and is a function of the wave function symmetry for homonuclear molecules. Laux [67] gives the line alternation factor for integer nuclear spin (I) as:

$$L_{e,J} = \begin{cases} \frac{I+1}{2I+1} & \text{for } P_{ef} \times P_{gu} \times (-1)^{J^*} = 1 \\ \frac{I}{2I+1} & \text{for } P_{ef} \times P_{gu} \times (-1)^{J^*} = -1 \end{cases} \quad (3.145)$$

and for half integer nuclear spin as:

$$L_{e,J} = \begin{cases} \frac{I}{2I+1} & \text{for } P_{ef} \times P_{gu} \times (-1)^{J^*} = 1 \\ \frac{I+1}{2I+1} & \text{for } P_{ef} \times P_{gu} \times (-1)^{J^*} = -1 \end{cases} \quad (3.146)$$

where P_{ef} is 1 for e parity and -1 for f parity, P_{gu} is 1 for gerade and -1 for ungerade and $J^* = J$ for integer J and $J^* = J - \frac{1}{2}$ for half integer J . The rovibronic state is of e parity if $(-1)^{J^*} \times$ rotational level parity > 0 and -1 otherwise. The rotational level parity for Σ states is inferred from Figure 114 in the text of Huber and Herzberg [79]. As Λ type doubling is not considered in the present work, the line alternation factors for non- Σ states do not need to be

⁷It is assumed dissociation is governed by the translational temperature T_{tr} , thus the term $\exp(D_{\text{diatom}}/k_B T_{\text{tr}})$.

considered. Figure 3.19 compares the intensity spectra of the N_2^+ First Negative 0-0 band head calculated with and without $L_{e,J}$. The spectra calculated via the Specair code of Laux [67, 120] is also shown for reference. Apart from slight discrepancies in the calculated line-widths, good agreement with Specair is observed. The alternation of $L_{e,J}$ between 2/3 1/3 for adjacent lines is successfully achieved by the present model.

The rovibronic partition function is:

$$Q_{e,v,J} = g_e \exp\left(-\frac{T_e}{k_B T_{\text{el}}}\right) \exp\left(-\frac{G_v}{k_B T_{\text{vib}}}\right) \frac{1}{\sigma} (2J+1) \exp\left(-\frac{F_J}{k_B T_{\text{rot}}}\right) \quad (3.147)$$

Substituting Equations 3.147, 3.139 and 3.141 into Equation 3.144 yields a simplified expression for $N_{e,v,J}$ that is amenable to numerical implementation:

$$N_{e,v,J} = N_{\text{el}-e} \sum_{v=1}^{v_{\max}} \frac{\exp\left(-\frac{G_v}{k_B T_{\text{vib}}}\right) (2J+1) \exp\left(-\frac{F_J}{k_B T_{\text{rot}}}\right)}{\exp\left(-\frac{G_v}{k_B T_{\text{vib}}}\right) \frac{k_B T_{\text{rot}}}{B_e - (v + 1/2)\alpha_e}} \frac{L_{e,J}}{\sigma} \quad (3.148)$$

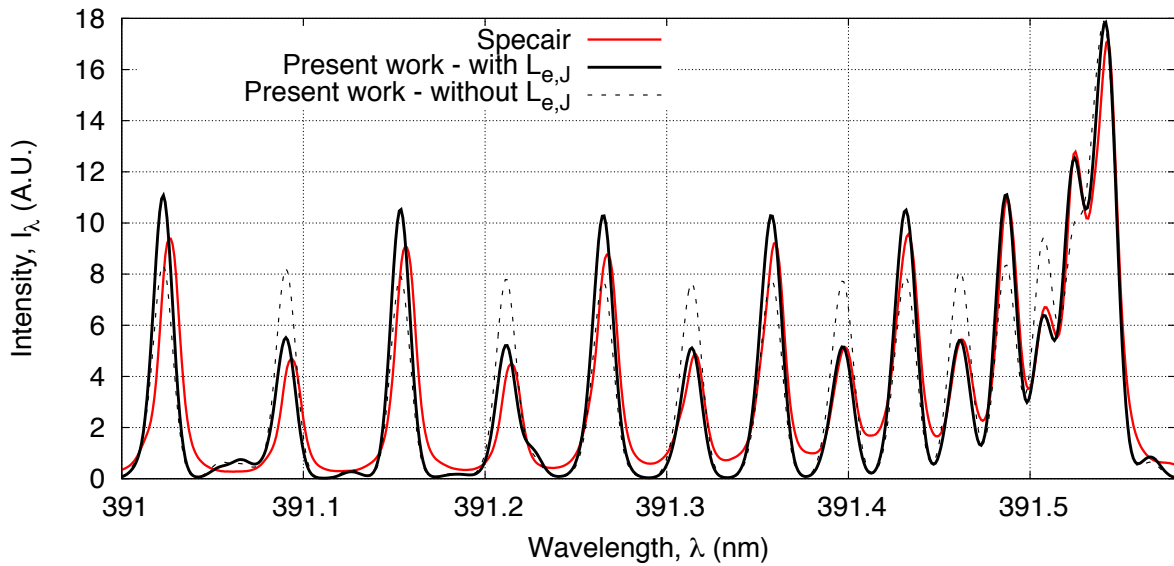


Figure 3.19: Comparison of intensity spectra for the N_2^+ First Negative 0-0 band head calculated with and without $L_{e,J}$.

Maximum vibrational and rotational quantum numbers

When calculating the electronic partition functions in Equation 3.139, the summation over the vibrational and rotational levels must be truncated at v_{\max} and J_{\max} respectively. The strategy for determining these parameters described by Babou *et al.* [121] is adopted. The maximum vibrational quantum number v_{\max} is the last that has energy within the dissociation limit referenced from the minimum of the levels potential curve:

$$G_{v_{\max}} \leq D \quad \text{and} \quad G_{v_{\max}+1} > D \quad (3.149)$$

For some electronic states the vibrational energy begins to drop before the dissociation limit is reached⁸; the maximum vibrational quantum number in these cases are taken as the last level within the turning point:

$$\frac{\partial G_{v_{\max}}}{\partial v} \geq 0 \quad \text{and} \quad \frac{\partial G_{v_{\max}+1}}{\partial v} \leq 0 \quad (3.150)$$

For each permitted vibrational level $v \leq v_{\max}$ a maximum rotational quantum number J_{\max} must be determined. This is achieved by considering the last rotational level that remains within the potential energy curve:

$$G_v + F_{J_{\max}} \leq V_{J_{\max}}(r_{\max}) \quad \text{and} \quad G_v + F_{J_{\max}+1} > V_{J_{\max}+1}(r_{\max}) \quad (3.151)$$

The potential energy curve is the sum of the Morse and centrifugal potentials:

$$V_J(r) = D \left[1 - \exp \left(-2\beta \frac{r - r_e}{r_e} \right) \right]^2 + B_e \left(\frac{r_e}{r} \right)^2 J(J+1) \quad (3.152)$$

where r_e is the location of potential minimum and β is:

$$\beta = \frac{\omega_e}{4\sqrt{B_e D}} . \quad (3.153)$$

r_{\max} is the location of the potential maximum after the potential minimum, and is therefore found when:

$$\frac{\partial V_J(r_{\max})}{\partial r} = 0 \quad \text{and} \quad \frac{\partial^2 V_J(r_{\max})}{\partial r^2} < 0 \quad (3.154)$$

Rovibronic energies

The energy of a rovibronic level is comprised of electronic T_e , vibrational G_v and rotational F_J contributions. The unperturbed electronic term energies of diatomic species are available directly from the literature (*e.g.* Reference [85]). In contrast, the vibrational G_v and rotational F_J energies are calculated from expressions derived via quantum mechanics. The energy of vibrational level v is calculated by the Dunham expansion which accounts for rigid rotation and anharmonic oscillations:

$$G_v = \omega_e(v + \frac{1}{2}) - \omega_e x_e(v + \frac{1}{2})^2 + \omega_e y_e(v + \frac{1}{2})^3 + \omega_e z_e(v + \frac{1}{2})^4 + \dots \quad (3.155)$$

⁸It should be noted this is not a physical phenomena, but rather an error due to extrapolation of spectroscopic data by the Dunham expansion

where ω_e , ω_{ex_e} , ω_{ey_e} and ω_{ez_e} are the Dunham coefficients⁹. The $\omega_e(v + \frac{1}{2})$ term represents the contribution from purely harmonic vibration, whilst the higher order terms represent anharmonic corrections. Whilst the anharmonic corrections are neglected for the thermodynamic model, they must be retained for the spectral radiation model in order to produce a high fidelity spectra.

The appropriate expression for the rotational energy is dependent on the coupling case the transition is being modelled by. For Hund's case (a) the fine molecular structure is not considered, and the rotational energy is only a function of the rotational quantum number $J = N$ only:

$$F_J = B_v J(J+1) - D_v J^2(J+1)^2 , \quad (3.156)$$

where,

$$B_v = B_e(v + \frac{1}{2}) - \alpha_e(v + \frac{1}{2})^2 + \dots , \quad (3.157)$$

$$D_v = D_e(v + \frac{1}{2}) + \beta_e(v + \frac{1}{2})^2 + \dots , \quad (3.158)$$

and B_e and D_e are coupling constants for the electronic state which are also tabulated in the literature.

For a doublet state belonging to Hund's case (b) ($\Sigma^2 - \Sigma^2$ transition) separate expressions are required for the two spin split states:

$$F_{K=J-1/2} = B_v K(K+1) - D_v K^2(K+1)^2 + \frac{1}{2}\gamma K , \quad (3.159)$$

$$F_{K=J+1/2} = B_v K(K+1) - D_v K^2(K+1)^2 - \frac{1}{2}\gamma(K+1) , \quad (3.160)$$

where γ is the spin splitting constant for the vibrational band. In the present work the γ values for the CN Violet transition are those presented by Prasad and Bernath [122]. The energies of the two spin split components for doublet states belonging to the intermediate (a)-(b) are:

$$F_{K=J-1/2} = B_v \left[K(K+1) - \Lambda^2 + \frac{Y(4-Y)}{8(K+1)}\Lambda^2 \right] - D_v(K + \frac{1}{2})^4 , \quad (3.161)$$

$$F_{K=J+1/2} = B_v \left[K(K+1) - \Lambda^2 + \frac{Y(4-Y)}{8K}\Lambda^2 \right] - D_v(K + \frac{1}{2})^4 , \quad (3.162)$$

where $Y = A/B_v$. For triplet states belonging to the intermediate (a)-(b) case, the energies of the three spin split components are:

⁹Although the Dunham expansion is an infinite series, typically only the first 3 or 4 coefficients are available in the literature [79].

$$F_{J=K+1} = B_v \left[J(J+1) - \sqrt{Z_1} - 2Z_2 \right] - D_v \left(J - \frac{1}{2} \right)^4 \quad (3.163)$$

$$F_{J=K} = B_v \left[J(J+1) + 4Z_2 \right] - D_v \left(J + \frac{1}{2} \right)^4 \quad (3.164)$$

$$F_{J=K-1} = B_v \left[J(J+1) + \sqrt{Z_1} - 4Z_2 \right] - D_v \left(J + \frac{3}{2} \right)^4 \quad (3.165)$$

where Z_1 and Z_2 are calculated as:

$$Z_1 = \Lambda^2 Y (Y - 4) + \frac{4}{3} + 4J(J+1) \quad (3.166)$$

$$Z_2 = \frac{1}{3Z_1} \left[\Lambda^2 Y (Y - 1) - \frac{4}{9} - 2J(J+1) \right] \quad (3.167)$$

Radiative transition probabilities

The radiative transition probability A_{ul} given in Equations 3.132 and 3.133 is calculated as:

$$A_{ul} = \frac{64\pi^4 \nu_{ul}^3}{3hc^3} \frac{(a_0e)^2 (R_e^{v_u v_l})^2}{(2 - \delta_{0,\Delta_u}) (2S + 1)} \frac{S_{J_l}^{J_u}}{2J_u + 1} \quad (3.168)$$

where ν_{ul} is the transition frequency in Hz, $(a_0e)^2 (R_e^{v_u v_l})^2$ is the square of the electronic-vibrational transition moment expressed in statcoulombs and $S_{J_l}^{J_u}$ is the Hönl–London factor for the rotational transition. The electronic-vibrational transition moments proposed by Chauveau *et al.* [123] and Babou *et al.* [124] have been implemented in the present work. These two datasets were selected as they represent the most recent set of transition moments calculated with up-to-date electronic transition moment functions and a consistent treatment of the potential energy function (an RKR potential was used for all species). These diatomic systems and the respective references are summarised in Table 3.7. Note that the additional systems considered by Hyun [66] that are not covered in References [123, 124] have also been included.

Table 3.7: Diatomic systems considered in the present work.

Diatom Species	System name	Transition designation	Included bands (0 : $v_{u,\max}$; 0 : $v_{l,\max}$)	$R_e^{v_u v_l}$	Reference
CO	Infrared	$X^1\Sigma^+ - X^1\Sigma^+$	(0:50; 0:50)	[124]	
	Fourth–Positive	$A^1\Pi - X^1\Sigma^+$	(0:23; 0:50)	[124]	

table continued on next page...

table continued from previous page...

Diatomeric Species	System name	Transition designation	Included bands (0 : $v_{u,\max}$; 0 : $v_{l,\max}$)	$R_e^{v_u v_l}$	Reference
BX (Hopfield–Birge)	BX (Hopfield–Birge)	$B^1\Sigma^+ - X^1\Sigma^+$	(0:2; 0:50)	[124]	
	CX	$C^1\Sigma^+ - X^1\Sigma^+$	(0:9; 0:9)	[66]	
	EX	$E^1\Pi - X^1\Sigma^+$	(0:5; 0:5)	[66]	
	FX	$F^1\Sigma^+ - X^1\Sigma^+$	(0:1; 0:0)	[66]	
	GX	$G^1\Pi - X^1\Sigma^+$	(0:2; 0:0)	[66]	
	Third–Positive	$b^3\Sigma^+ - a^3\Pi$	(0:2; 0:18)	[124]	
CO ⁺	Comet-tail	$A^2\Pi_i - X^2\Sigma^+$	(0:33; 0:31)	[124]	
	Baldet–Johnson	$B^2\Sigma^+ - A^2\Pi_i$	(0:33; 0:50)	[124]	
	First Negative	$B^2\Sigma^+ - X^2\Sigma^+$	(0:22; 0:35)	[124]	
CN	Red	$A^2\Pi_i - X^2\Sigma^+$	(0:38; 0:34)	[124]	
	Violet	$B^2\Sigma^+ - X^2\Sigma^+$	(0:25; 0:36)	[124]	
	LeBlanc	$B^2\Sigma^+ - A^2\Pi_i$	(0:25; 0:38)	[124]	
C ₂	Phillips	$A^1\Pi_u - X^1\Sigma_g^+$	(0:35; 0:21)	[124]	
	Mulliken	$D^1\Sigma_u^+ - X^1\Sigma_g^+$	(0:22; 0:21)	[124]	
	Delandres–D’Azambuja	$C^1\Pi_g - A^1\Pi_u$	(0:9; 0:32)	[124]	
	Ballik–Ramsay	$b^3\Sigma_g^- - a^3\Pi_u$	(0:41; 0:39)	[124]	
	Swan	$d^3\Pi_g - a^3\Pi_u$	(0:18; 0:33)	[124]	
	Fox–Herzberg	$e^3\Pi_g - a^3\Pi_u$	(0:15; 0:35)	[124]	
	Freymark	$E_1\Sigma_g^+ - A^1\Pi_u$	(0:6; 0:4)	[66]	
N ₂	First–Positive	$B^3\Pi_g - A^3\Sigma_u^+$	(0:21; 0:16)	[123]	
	Second–Positive	$C^3\Pi_u - B^3\Pi_g$	(0:4; 0:21)	[123]	
	Birge–Hopfield 1	$b^1\Pi_u - X^1\Sigma_g^+$	(0:19; 0:15)	[123]	
	Birge–Hopfield 2	$b'^1\Sigma_u^+ - X^1\Sigma_g^+$	(0:28; 0:15)	[123]	
	Carroll–Yoshino	$c'^1\Sigma_u^+ - X^1\Sigma_g^+$	(0:8; 0:15)	[123]	
	Worley–Jenkins	$c^1_3\Pi_u - X^1\Sigma_g^+$	(0:4; 0:15)	[123]	
	Worley	$o^1_3\Pi_u - X^1\Sigma_g^+$	(0:4; 0:15)	[123]	
N ₂ ⁺	Meinel	$A^2\Pi_u - X^2\Sigma_g^+$	(0:27; 0:21)	[123]	
	First–Negative	$B^2\Sigma_u^+ - X^2\Sigma_g^+$	(0:8; 0:21)	[123]	
	Second–Negative	$C^2\Sigma_u^+ - X^2\Sigma_g^+$	(0:6; 0:21)	[123]	
NO	γ	$A^2\Sigma^+ - X^2\Pi_r$	(0:8; 0:22)	[123]	
	β	$B^2\Pi_r - X^2\Pi_r$	(0:37; 0:22)	[123]	
	δ	$C^2\Pi_r - X^2\Pi_r$	(0:9; 0:22)	[123]	
	ϵ	$D^2\Sigma^+ - X^2\Pi_r$	(0:5; 0:22)	[123]	

table continued on next page...

table continued from previous page...

Diatomc Species	System name	Transition designation	Included bands (0 : $v_{u,\max}$; 0 : $v_{l,\max}$)	$R_e^{v_u v_l}$ Reference
γ'		$E^2\Sigma^+ - X^2\Pi_r$	(0:4; 0:22)	[123]
β'		$B'^2\Delta - X^2\Pi_r$	(0:6; 0:22)	[123]
11,000 Å		$D^2\Sigma^+ - A^2\Sigma^+$	(0:5; 0:8)	[123]
Infrared		$X^2\Pi_r - X^2\Pi_r$	(0:22; 0:22)	[123]
O_2	Schumann–Runge	$B^3\Sigma_u^- - X^3\Sigma_g^-$	(0:19; 0:21)	[123]

The Hönl–London factor describes the strength of the rotational lines. The sum of all Hönl–London factors ending in a given lower rotational state must equate to the total degeneracy of the level:

$$\sum_{J_u} S_{J_l}^{J_u} = (2 - \delta_{0, \Lambda_u + \Lambda_l}) (2S_l + 1) (2J_l + 1) \quad (3.169)$$

The selection of the Hönl–London factors therefore depends on the transition type under consideration. The Hönl–London factors for all transitions belonging to Hund’s case (a) are shown in Table 3.8.

Table 3.8: Hönl–London factors for Hund’s case (a).

Branch	$S_{J_l}^{J_u}$ for $\Lambda_u = \Lambda_l = 0$	$S_{J_l}^{J_u}$ for $\Delta\Lambda = 0$	$S_{J_l}^{J_u}$ for $\Delta\Lambda = \pm 1$
P ($\Delta J = +1$)	$J_u + 1$	$\frac{(J_u + 1 + \Lambda_u)(J_u + 1 - \Lambda_u)}{J_u + 1}$	$\frac{(J_u + 1 \mp \Lambda_u)(J_u + 2 \mp \Lambda_u)}{2(J_u + 1)}$
Q ($\Delta J = 0$)	0	$\frac{(2J_u + 1)\Lambda_u^2}{J_u(J_u + 1)}$	$\frac{(J_u \pm \Lambda_u)(J_u + 1 \mp \Lambda_u)(2J_u + 1)}{2J_u(J_u + 1)}$
R ($\Delta J = -1$)	J_u	$\frac{(J_u + \Lambda_u)(J_u - \Lambda_u)}{J_u}$	$\frac{(J_u \pm \Lambda_u)(J_u - 1 \pm \Lambda_u)}{2J_u}$

For ${}^2\Sigma - {}^2\Sigma$ transitions belonging to Hund’s case (b), the Hönl–London factors presented by Mulliken [125] are implemented, Table 3.9.

Table 3.9: Hönl–London factors for ${}^2\Sigma - {}^2\Sigma$ transitions belonging to Hund’s case (b).

Branch	$S_{J_l}^{J_u}$
R ($\Delta J = +1$)	$\frac{(J_l + 1)^2 - \frac{1}{4}}{J_l + 1}$
Q ($\Delta J = 0$)	$\frac{(2J_l + 1)}{4J_l(J_l + 1)}$
P ($\Delta J = -1$)	$\frac{J_l^2 - \frac{1}{4}}{J_l}$

For the parallel doublet transitions modelled by the intermediate (a)-(b) case, the Hönl–London factors used by Arnold *et al.* [126] in the RAD/EQUIL code are implemented, Table 3.10. In this table the upper sign corresponds with upper listed branch and U is defined as:

$$U = [Y^2 - 4Y + (2J + 1)] , \quad (3.170)$$

where $Y = A/B_v$.

Table 3.10: Hönl–London factors for $^2\Pi - ^2\Sigma$ transitions belonging to Hund’s intermediate (a)-(b) case.

$^2\Pi \Rightarrow ^2\Sigma$	$^2\Sigma \Rightarrow ^2\Pi$	$S_{J_l}^{J_u}$
P_2	R_2	$\frac{(2J_u+1)^2 \pm (2J_u+1)U_u(4J_u^2+4J_u+1-2Y_u)}{16(J_u+1)}$
${}^O P_{12}$	${}^S R_{21}$	
${}^Q P_{21}$	${}^Q R_{12}$	$\frac{(2J_u+1)^2 \mp (2J_u+1)U_u(4J_u^2+4J_u-7+2Y_u)}{16(J_u+1)}$
P_1	R_1	
Q_2	Q_2	$\frac{(2J_u+1)[(4J_u^2+4J_u-1)\pm U_u(8J_u^3+12J_u^2-2J_u+1-2Y_u)]}{16J_u(J_u+1)}$
${}^P Q_{12}$	${}^R Q_{21}$	
${}^R Q_{21}$	${}^P Q_{12}$	$\frac{(2J_u+1)[(4J_u^2+4J_u-1)\mp U_u(8J_u^3+12J_u^2-2J_u-7+2Y_u)]}{16J_u(J_u+1)}$
Q_1	Q_1	
R_2	P_2	$\frac{(2J_u+1)^2 \pm (2J_u+1)U_u(4J_u^2+4J_u-7+2Y_u)}{16J_u}$
${}^Q R_{12}$	${}^Q P_{21}$	
${}^S R_{21}$	${}^O P_{12}$	$\frac{(2J_u+1)^2 \mp (2J_u+1)U_u(4J_u^2+4J_u+1-2Y_u)}{16J_u}$
R_1	P_1	

Spectral distribution function

The spectral distribution function for diatomic lines is the same as that described for monatomic lines in Section 3.3.1, however resonance broadening is not considered. The trends observed for the monatomic linewidths in Figures 3.13 and 3.14 are therefore also applicable to the diatomic linewidths.

Figures 3.15a and 3.15b compare the sensitivity of diatomic bound-bound emissive power density and intensity for a 10 cm slab of atmospheric pressure equilibrium air to the diatomic line cut-off limit. The line cut-off limit $\Delta\nu_{\text{limit}}$ has been normalised by the voigt HWHM γ_V , and the emissive power density and intensity are normalised by the respective values at $\Delta\nu_{\text{limit}} = 1,000\gamma_V$. Both the emissive power density and intensity are reasonably well described with $\Delta\nu_{\text{limit}}/\gamma_V \geq 10$, although significant improvement is achieved with $\Delta\nu_{\text{limit}}/\gamma_V \geq 100$. In the present work the diatomic line cut-off limit is set to $\Delta\nu_{\text{limit}} = 10\gamma_V$ as a compromise between accuracy and efficiency.

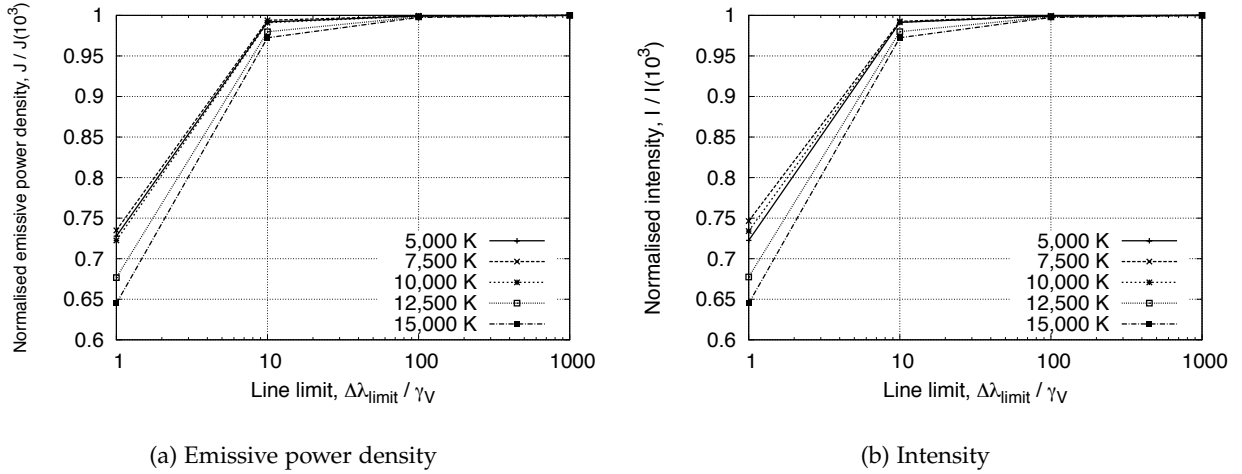


Figure 3.20: Sensitivity of diatomic bound-bound emissive power density and intensity for a 10 cm slab of equilibrium air to the diatomic line cut-off limit ($p = 1 \text{ atm}$).

Comparison with SPRADIAN07

As was done for monatomic bound-bound transitions, comparisons with the SPRADIAN07 code [66] have been made in order to verify the calculation of diatomic bound-bound spectral coefficients. For this purpose, the electronic-vibrational transition moments presented by Hyun [66] are used so that both codes are using the same fundamental data. Also, the line-alternation factor $L_{e,j}$ for homonuclear molecules is omitted and the CN Violet system is modelled via Hund's case (a) for consistency with SPRADIAN07. The test case consists of a 10 cm slab of gas with temperature $T = 10,000 \text{ K}$ and pressure $p = 1 \text{ atm}$. The number density of each radiator is $1 \times 10^{16} \text{ cm}^{-3}$, the electron number density is also $1 \times 10^{16} \text{ cm}^{-3}$ and total number density is $2.2 \times 10^{17} \text{ cm}^{-3}$. For each radiator, the emissive power density $J (\text{W/cm}^3)$ and intensity $I (\text{W/cm}^2)$ is calculated in the spectral range $50 \leq \lambda \leq 2,000 \text{ nm}$ with 1,950,000 equidistant frequency intervals.

Table 3.11 summarises the comparison between the SPRADIAN07 code [66] and the present work for diatomic bound-bound transitions. The agreement for both emissive power density and intensity is within 5% for all the diatomic radiators considered, with key species such as C₂, CN and N₂⁺ agreeing within 2%. Figures 3.21a, 3.21b and 3.21c presents the emission coefficient, absorption coefficient and intensity spectra for the CN Violet 0-0 band-head in the spectral range $387 \leq \lambda \leq 388.5 \text{ nm}$. Calculations using the vibration-electronic transition moments of both Hyun [66] and Babou *et al.* [124] are presented. The SPRADIAN07 data exhibits lower troughs between lines, indicating the line-widths are slightly smaller. While the cumulative emission for the Hyun R_e case shows only a 0.4% difference with SPRADIAN07, the differences in line shape between the two coefficient spectrums result in a slightly higher difference in cumulative intensity of 0.6%. Using the transition moments of Babou results in 10% higher intensity, and

additional lines appear as a consequence of Babou considering more bands than Hyun. Overall, the agreement with SPRADIAN07 is very good and verifies the implementation of the equations describing bound-bound transitions in the present work.

Table 3.11: Comparison of diatomic bound-bound model from the present work with the SPRADIAN07 code [66].

Species	Emissive power density, J (W/cm ³)			Intensity, I (W/cm ²)		
	SPRADIAN07	Present work	Difference (%)	SPRADIAN07	Present work	Difference (%)
C ₂	1342	1328	-1.06	772.1	768.5	-0.46
CN	1079	1075	-0.42	470.6	473.6	0.62
CO	584.3	560.8	-4.03	181.2	177.1	-2.32
N ₂	8.85	8.48	-4.08	5.61	5.42	-3.60
N ₂ ⁺	1235	1244	0.71	646.8	655.7	1.36
NO	112.0	109.0	-2.67	84.44	82.75	-2.04
O ₂	78.79	82.31	4.47	61.12	62.51	2.22

Comparison of transition moment data sets

As the transition moments of Chauveau *et al.* [123] and Babou *et al.* [124] and are being used in preference to the Hyun [66] data set, it is appropriate to compare the two. Table 3.12 presents a comparison of the diatomic species integrated emission and intensities using the Babou¹⁰ and Hyun transition moments. While C₂, CN, CO, N₂⁺ and O₂ show only minor deviations of 20% or less, NO and N₂ emission are increased by 74% and 787% when using the Babou transition moments.

Table 3.12: Comparison of integrated emission and intensity using the transition moments of Hyun [66] and of Babou *et al.* [124].

Species	Emissive power density, J (W/cm ³)			Intensity, I (W/cm ²)		
	Hyun R_e	Babou R_e	Difference (%)	Hyun R_e	Babou R_e	Difference (%)
C ₂	1328	1479	11.37	768.5	698.6	-10.0
CN	1075	1181	9.91	473.6	569.7	16.9
CO	560.8	473.6	-15.54	177.1	198.8	10.93
N ₂	8.48	75.25	787	5.42	27.3	80.2
N ₂ ⁺	1244	1204	-3.21	655.7	501.6	-30.7
NO	109.0	189.9	74.21	82.75	140.86	41.3
O ₂	82.31	99.66	21.08	62.51	76.12	17.9

¹⁰Here ‘Babou’ denotes the set of transition moments described in Table 3.7, which are mainly from Babou *et al.* [124].

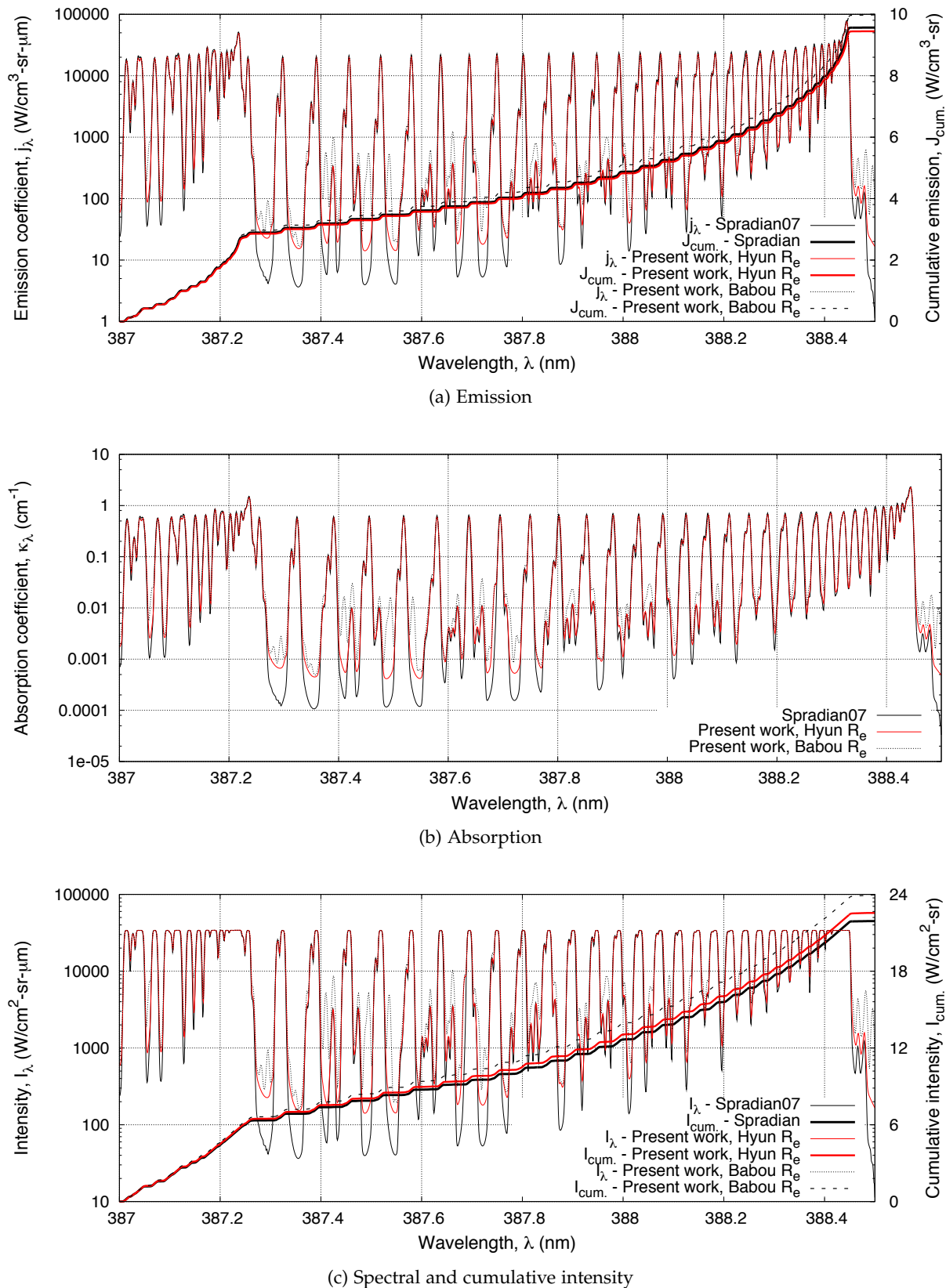


Figure 3.21: Comparison between SPRADIAN07 and the present work for the spectra of the CN Violet 0-0 band-head in the range $387 \leq \lambda \leq 388.5$ nm.

The large difference for the N₂ molecule warrants further investigation, especially considering Hyun uses the well regarded data of Laux [127, 128] for the N₂ transitions¹¹. Table 3.13 presents a comparison of the integrated emission and intensities using the Chauveau *et al.* [123] and Hyun [66] transition moments for each system of the N₂ molecule. The well known First-Positive and Second-Positive systems, which radiate in the ultraviolet spectral region, are in good agreement, whilst the remaining systems exhibit significant differences. These systems with large differences — Birge–Hopfield 1, Birge–Hopfield 2, Carroll–Yoshino, Worley–Jenkins and Worley — are all vacuum ultraviolet systems. Due to the difficulty of performing emission spectroscopy in the VUV spectral region, there has been little experimental corroboration for theoretical calculation of the transition moments for these systems. Consequently there is a significant degree of uncertainty associated with the intensity of the N₂ VUV systems, and it is not uncommon for different sets of theoretical calculations to show substantial discrepancies. For example, Liebhart *et al.* calculated the electronic transition moments for N₂ VUV systems via an RKR reconstruction of the potential energy surface. Calculations of equilibrium air absorption spectra at 7,000 K deviated by up to an order of magnitude from the results obtained by Chauveau *et al.* [123], most notably for the strong band peaks at 95 nm. As the transition moments for the N₂ VUV systems used by Hyun [66] are from a yet to be published source, the Chauveau *et al.* [123] data is felt to be more appropriate for the present work.

Table 3.13: Comparison of integrated emission and intensity using the transition moments from Hyun [66] and Chauveau *et al.* [123].

N ₂ systems	Emissive power density, J (W/cm ³)			Intensity, I (W/cm ²)		
	Hyun R_e	Chauveau R_e	Difference (%)	Hyun R_e	Chauveau R_e	Difference (%)
First–Positive	0.75	0.83	-9.33	0.60	0.66	-9.30
Second–Positive	1.18	1.18	-0.02	0.94	0.94	-0.02
Birge–Hopfield 1	57.09	3.88	1372	29.09	2.77	950
Birge–Hopfield 2	6.68	0.40	1566	4.47	0.32	1319
Carroll–Yoshino	5.91	1.65	257	1.86	0.52	259
Worley–Jenkins	2.07	0.17	1094	0.71	0.11	554
Worley	1.58	0.37	329	0.74	0.23	217

3.3.3 Continuum transitions

In the present work the continuum transitions for atomic species and their ions are considered, whilst continuum transitions for molecular species are neglected. Furthermore, the models for atomic continuum transitions are based on approximate curve-fits and hydrogenic assumptions. Such a simplified treatment of continuum transitions is justified based on the:

¹¹The calculations for the VUV system transition moments, however, are stated by Hyun [66] to be from Laux but are from a yet to be published source.

1. Low concentration of molecules and their ions for high-speed Earth and Mars entry,
2. Small contribution of continuum mechanisms to optically thin emission in CO₂-N₂ plasmas at temperature less than 15,000 K [124], and
3. Demonstrated efficacy of photoionisation curve-fits for N and O in high temperature air plasmas [129].

This rationale, however, is not valid for the cool boundary layer surrounding an aeroshell, as at low temperatures ($T \lesssim 6000$ K) the photoionisation and photodissociation continua of diatomic species can be significant [124, 130]. As a consequence, the omission of these mechanisms may lead to an underprediction of the radiative energy absorbed or emitted by the boundary layer. In addition, photodetachment processes for negative ions are estimated to be significant at temperatures up to temperatures of 12,000 K [130]. Nevertheless, the present approximate models capture the majority of the continuum transitions to a reasonable degree of accuracy.

Bound-free mechanisms

For atomic species, bound-free mechanisms refers to photoionisation and the inverse recombination process:



The spectral absorption coefficient due to photoionisation (PI) of electronic level i is:

$$\kappa_{\nu,i} = \sigma_{\nu,i} N_i \quad (3.172)$$

where $\sigma_{\nu,i}$ and N_i are the spectral photoionisation cross section and number density for level i . The spectral emission coefficient can then be derived by applying the microscopic reversibility principle [110]:

$$j_{\nu,i}^{PI} = N_{\text{ion}} N_e \frac{2h\nu^3}{c^2} \frac{g_i}{2Q_{\text{ion}}} \left(\frac{h^2}{2\pi m k_B T_e} \right)^{3/2} \sigma_{\nu,i} \exp \left[\frac{I - E_i - h\nu}{k_B T_e} \right] \quad (3.173)$$

Although accurate tabulations of spectral photoionisation cross sections are available via astrophysics databases such as TOPbase [131], the spectral resolution required to correctly implement them is excessive. Two approximate models for calculating the spectral photoionisation cross section are therefore implemented in the present work:

1. A Gaunt-factor corrected hydrogenic model, and
2. A step-model representation of the TOPbase tabulations [19]

Zeldovich and Raizer present the following expression for the hydrogenic spectral photoionisation cross section:

$$\sigma_{\nu,i} = \frac{64}{3\sqrt{3}} \frac{\pi^4 m Z^4 e^{10}}{\nu^3 c h^6} n_{\text{eff},i} G_i \quad (3.174)$$

where G_i is the corrective Gaunt factor and $n_{\text{eff},i}$ is the effective shell number for level i :

$$n_{\text{eff},i} = \sqrt{\frac{I_H}{I - E_i}} \quad (3.175)$$

In the present work the following Gaunt factor proposed by Zeldovich and Raizer is implemented:

$$G_i = 1 - 0.173 \left(\frac{h\nu}{IZ^2} \right)^{1/3} \left[\frac{2}{n_{\text{eff},i}} \frac{IZ^2}{h\nu} - 1 \right] \quad (3.176)$$

As discussed by Johnston [19], although Equation 3.174 includes the hydrogenic approximations for the level degeneracy and ion partition function, replacing these parameters with their exact values (*e.g.* Reference [71]) does not improve the accuracy of the expression. Johnston postulates that this is because the Gaunt factor expressions may have been calculated for use with the original hydrogenic approximation.

For the first three levels of atomic nitrogen and oxygen, step model representations of the accurate TOPbase tabulations were constructed by Johnston [19]. The cross sections for the remaining levels are approximated by simple power function. For details of the step model the reader is referred to Reference [19] and [129]. In the present work the step model is preferred over the hydrogenic model for N and O.

Free-free mechanisms

Free-free or bremsstrahlung (literally meaning ‘braking radiation’ in German) radiation results from the acceleration of electrons due to the presence of an electric field. The bremsstrahlung absorption coefficient is presented by Zel’dovich and Raizer [110] as:

$$\kappa_\nu = \frac{4}{3} \sqrt{\frac{2\pi}{3m_e k_B T_e}} \left(\frac{Z^2 e^6}{h c m_e \nu^3} \right) N_{\text{ion}} N_e , \quad (3.177)$$

The spectral emission coefficient can then be derived via the principle of detailed balancing:

$$j_\nu = \frac{8}{3} \sqrt{\frac{2\pi}{3k_B T_e m_e}} \left(\frac{Z^2 e^6}{m_e c^3} \right) n_{\text{ion}} N_e \exp \left[-\frac{h\nu}{k_B T_e} \right] . \quad (3.178)$$

Generally speaking, bremsstrahlung radiation is most significant in the far-IR spectral region due to the negative exponential dependence on frequency.

3.3.4 Uncertainty of the radiation calculation

Many of the parameters required for the calculation of plasma radiation are highly uncertain. For example the transition probabilities proposed by Wiese [132], which the NIST data implemented in the present work is based on, have uncertainties ranging from $\pm 3\%$ to $\pm 75\%$. Kleb and Johnston [133] performed an uncertainty analysis of air radiation for lunar return shock layers. Epistemic uncertainty was considered for atomic line oscillator strengths, atomic line Stark broadening widths, atomic photoionisation cross sections, negative ion photodetachment cross sections, molecular bands oscillator strengths and electron impact excitation rates. When direct numerical differentiation and Monte Carlo based methods were applied to a hypothetical lunar return peak heating condition at 10.3 km/s, the uncertainty in radiative heat-flux was found to be $\pm 30\%$. The largest contributors to this total uncertainty level were the atomic nitrogen oscillator strengths and Stark widths and the negative ion continuum. In the present work similar oscillator strengths¹² were considered, however a Stark widths are modelled via a less accurate method and the negative ion continuum. Therefore the $\pm 30\%$ uncertainty found in Reference [133] can be considered as a lower bound for the radiation modelling presented in this thesis.

3.4 A comment on the consistency of data sources

It should be noted that, where possible, an effort has been made to use consistent data sources both within and between the thermodynamic, transport and spectral radiation models. For example, the spectroscopic constants used by both the thermodynamic and spectral radiation models are from the same sources (namely References [80] and [85] for atoms and diatoms, respectively), and are used consistently for all species. In the spectral radiation model the transition probabilities for atoms are taken from same source as the spectroscopic constants (Reference [80]), while the diatomic transition moments are required to be taken from a different source (Reference [124]), as Huber and Herzberg [85] do not list them. As the spectroscopic constants for radiating levels of diatomic molecules are fairly well known, however, this should not produce significant errors, as has been shown by the comparison of the spectral radiation model with the SPRADIAN07 code [66]. The consistency of the transport model is a little less clear, as the collision-integrals are compiled from a variety sources (namely References [6, 88, 98–103, 106]), although the majority of these sources are from the collaboration of Wright and Levin and are therefore based on consistent datasets. Also, these sources use fully coupled thermodynamic models in their calculations which is at variance with the decoupled assumption used in the present work. Despite these inconsistencies, the good agreement with the CEA2 code [5] and the tabulations of Bruno *et al.* [6] show that the implemented model nonetheless produces sufficiently accurate results.

¹²Implemented as transition probabilities in the present work.

3.5 Summary

Models for calculating the properties of high temperature gases required for simulating radiating shock layers have been presented. Specifically, thermodynamic, transport and spectral radiation properties for a multicomponent, partially ionised gas with multiple temperatures have been provided. The thermodynamic coefficients for such a gas have been derived based on the assumption of completely decoupled thermal modes. In addition, appropriate cutoff limits for the electronic level summation have been selected to minimise the associated error. Comparisons with the fully coupled thermodynamic properties tabulated by Capitelli *et al.* [81] show good agreement for most atomic species at temperatures less than 10,000 K, while diatomic species show discrepancies at temperatures as low as 4,000 K. Due to the strongly dissociated shock layers of present interest, however, such discrepancies are tolerable. Viscosity, thermal conductivity and binary diffusion coefficients have been calculated with the Gupta–Yos [92] equations. A near complete set of binary collision cross sections for the Ar–C–N–O elemental system have been compiled by searching the literature for best available data [6, 88, 98–103, 106]. Comparisons with the viscosity of air as calculated with the CEA2 code [5] show good agreement for temperatures up to 20,000 K. Comparisons with the Mars viscosity tabulations of Bruno *et al.* [6] calculated with a high-order Chapman–Enskog method show good agreement for partially ionised mixtures, but poor agreement for strongly ionised mixtures. This is acceptable given the range of ionisation of present interest¹³. Finally, a line-by-line spectral radiation model for atomic and diatomic species has been built. Electronic level and atomic line data was obtained from NIST [80, 85], and the diatomic electronic transition moments presented by Chauveau *et al.* [123] and Babou *et al.* [124] are implemented. Continuum transitions were modelled by the step model of Johnston [19] for N and O photoionisation and with hydrogenic approximations otherwise. The model implementation was verified by comparisons with the SPRADIAN07 code [66].

¹³A maximum of approximately 10% ionisation for 12 km/s entry at Earth.

4

Nonequilibrium rate processes

In the preceding chapter (§ 3) the properties of a high temperature gas at a temporally ‘frozen’ thermodynamic state were described. In this chapter the models for *nonequilibrium* rate processes that occur due to collisional and radiative interactions of the chemical species are presented. In the Navier–Stokes and post-shock relaxation equations these processes are treated in a temporally coupled manner, where bulk species mass-production ω_i , modal thermal energy exchange Ω_{lm} and radiative exchange $\nabla \cdot \vec{q}_{\text{rad}}$ appear as source terms (see Equations 2.4, 2.8 and 2.12). In the present work nonequilibrium rate processes are also considered when determining electronic level populations for the spectral radiation calculations, however they are applied in a temporally decoupled fashion via a quasi-steady-state collisional-radiative model. The models for the chemical kinetic and thermal energy exchange source terms are presented in § 4.1 and 4.2, and the collisional-radiative modelling is presented in § 4.3.

4.1 Chemical kinetics

A simple reversible chemical reaction can be represented as:

$$\sum_i^{N_{\text{species}}} \alpha_i [X_i] \xrightleftharpoons[k_b]{k_f} \sum_i^{N_{\text{species}}} \beta_i [X_i] \quad (4.1)$$

where X_i is the concentration of species i , α_i and β_i are the reactant and product stoichiometric

coefficients and k_f and k_b are the reaction rate coefficients in the forward and backwards directions. Through the Law of Mass action [134, 135] the species molar production rate $\dot{\omega}_i$ for species i due to a single reaction of the form in Equation 4.1 can be calculated as:

$$\dot{\omega}_i = \frac{(\beta_i - \alpha_i)}{M_i} \left\{ k_f \prod_i [X_i]^{\alpha_i} - k_b \prod_i [X_i]^{\beta_i} \right\} \quad (4.2)$$

This section is concerned with the selection of appropriate models for the forward and backwards rate coefficients; models for energy exchange due to chemical reactions are presented in § 4.2.

4.1.1 Forwards and backwards rate coefficients

The chemical reaction models of Park *et al.* [136, 137] and others [36, 138–140] considered in the present work provide forward rate coefficients in the generalised Arrhenius form:

$$k_f(T_f) = CT_f^n \exp(-T_a/T_f) \quad (4.3)$$

where T_a is the activation temperature, T_f is the forward rate controlling temperature and C and n are model parameters. The backwards rate coefficient is then able to be calculated from the forward rate coefficient k_f and the equilibrium constant for concentrations K_c evaluated at the backward rate controlling temperature T_b :

$$k_b(T_b) = \frac{k_f(T_b)}{K_c(T_b)} \quad (4.4)$$

In the present work the Gibb's free energy approach is implemented for calculating the equilibrium constant for concentrations:

$$K_c = K_p \left(\frac{p_{\text{atm}}}{RT_b} \right)^v \quad (4.5)$$

where p_{atm} is the atmospheric pressure, $v = \sum_i^{N_{\text{species}}} (\beta_i - \alpha_i)$ and K_p is the equilibrium constant evaluated at atmospheric pressure:

$$K_p(T_b) = \exp \left(\frac{-\Delta G(T_b, p_{\text{atm}})}{RT_b} \right) \quad (4.6)$$

The change in Gibb's free energy ΔG is calculated as:

$$\Delta G(T_b, p_{\text{atm}}) = \sum_i^{N_{\text{species}}} \nu_i G_i(T_b, p_{\text{atm}}) \quad (4.7)$$

where,

$$G_i(T_b, p_{\text{atm}}) = h_i(T_b) - T_b \times s_i(T_b, p_{\text{atm}}) \quad (4.8)$$

As demonstrated in § 3.1.3, the decoupling of thermal modes leads to errors in the thermodynamic properties of some species, especially at high temperatures. As slight deviations in the equilibrium constant can substantially affect the predicted equilibrium composition, in the present work the fully coupled thermodynamic curve fits from Gordon and McBride [141] are used to calculate h_i and s_i in Equation 4.8. Although this is not ideal as thermodynamic data is not being used in a consistent manner, it is necessary to affect a more physically correct solution.

4.1.2 Nonequilibrium rate coefficients

In the presence of thermal nonequilibrium, the chemical reaction rate coefficients must take into consideration what thermal modes are contributing to the reaction energy. Ideally this would be achieved by considering reactions of individual rovibronic states, however such an approach is computationally prohibitive and outside the scope of this thesis. In the present work we limit ourselves to ‘engineering’ models that obtain nonequilibrium rate coefficients k_{neq} that can be expressed as the generalised Arrhenius rate coefficient k_{eq} modified by a corrective factor Z :

$$k_{\text{neq}}(T_{\text{trans}}, T_{\text{vib}}, T_{\text{rot}}, T_{\text{el}}, T_e) = Z(T_{\text{trans}}, T_{\text{vib}}, T_{\text{rot}}, T_{\text{el}}, T_e)k_{\text{eq}}(T_{\text{trans}}) \quad (4.9)$$

where Z is in general a function of all the nonequilibrium temperatures and the Arrhenius rate is evaluated at the gas temperature T_{trans} . The nonequilibrium corrective factor Z can be either be explicitly calculated or implied via the use of rate controlling temperatures.

Rate controlling temperature approach

A simple method for computing the nonequilibrium rate coefficients is via appropriately selected forwards and backwards rate controlling temperatures, T_f and T_b in Equations 4.3 and 4.4. Although this approach can be expressed via a corrective factor as defined in Equation 4.9, from a practical standpoint it is simpler to implement Equations 4.3 and 4.4 as given. The rate controlling temperatures applied in the present work are summarised in Table 4.1. The forward rate controlling temperature for heavy particle impact dissociation $T_{\text{trans}}^s T_{\text{vib}}^{s-1}$ is a generalisation of the geometric average temperature approach proposed by Park [29]:

$$T_f = \sqrt{T_{\text{trans}} T_{\text{vib}}} \quad (4.10)$$

The rationale for such a model is that dissociation energy is obtained from the vibrational mode of the dissociating molecule and translational energy of the colliding molecule in approximately equal proportions. In a similar manner, the forward rate controlling temperature for electron impact dissociation is $T_{\text{vib}}^s T_e^{s-1}$ as T_e governs the translational mode of the free electrons. Exchange and molecular recombination (the backwards dissociation process) reactions are assumed to be driven by heavy particle collisions, and are therefore governed by T_{trans} . Electron-impact ionisation and the corresponding recombination process are assumed to be governed

by the free electron temperature T_e due to the high efficiency of free electron colliders. For this reason, Knab *et al.* [142] recommend using the free electron temperature T_e for associative ionisation-recombination reactions. Due to numerical difficulties in implementing this, however, in the present work T_{trans} is used instead. The effect of using T_{trans} instead of T_e for associative ionisation-recombination reactions is to reduce the initial rate of electron production behind the shock. This in turn delays the onset of rapid electron production due to electron impact ionisation.

Table 4.1: Forward and backward rate controlling temperatures for bulk chemical kinetics (Note: for compression flows, $s = 0.7$ for N₂-O₂ mixtures and 0.5 for CO₂-N₂-Ar mixtures).

Reaction type	Forward rate controlling temperature, T_f	Backwards rate controlling temperature, T_b
Heavy particle impact dissociation	$T_{\text{vib}}^s T_{\text{trans}}^{s-1}$	T_{trans}
Electron impact dissociation	$T_{\text{vib}}^s T_e^{s-1}$	T_e
Exchange	T_{trans}	T_{trans}
Associative ionisation	T_{trans}	T_{trans}
Electron-impact ionisation	T_e	T_e

Nonequilibrium models for dissociation

The reaction energy for dissociation is mostly obtained from vibration of the dissociating molecule and translation of the colliding species. The corrective factor for dissociation is therefore typically expressed as a function of T_{trans} and T_{vib} only:

$$k_{f,\text{neq}}(T_{\text{trans}}, T_{\text{vib}}) = Z(T_{\text{trans}}, T_{\text{vib}}) k_f(T_{\text{trans}}) \quad (4.11)$$

(a) Park model The original model of Park [29] evaluates the dissociation rate coefficient with the so called ‘geometric average temperature’, $\sqrt{T_{\text{trans}} T_{\text{vib}}}$. The geometric average temperature approach, however, has been shown by Lino da Silva *et al.* [143] through comparison with vibrationally specific N₂ dissociation rates to be inaccurate where strong translation-vibration nonequilibrium exists. Moderately improved results were obtained when s was set to 0.7 for $T_{\text{vib}} < T_{\text{trans}}$, and this recommendation is implemented in the present work for nitrogen dominated mixtures (*i.e.* air). By substituting $T_f = T_{\text{trans}}^s T_{\text{vib}}^{s-1}$ into Equation 4.3 and equating with Equation 4.11, the corrective factor for the modified Park dissociation model is found to be:

$$Z(T_{\text{trans}}, T_{\text{vib}}) = \left(T_{\text{trans}}^{s-1} T_{\text{vib}}^{s-1} \right) \exp \left(-\frac{T_a}{T_{\text{trans}}^s T_{\text{vib}}^{s-1}} + \frac{\Theta_D}{T_{\text{trans}}} \right) \quad (4.12)$$

where Θ_D is the characteristic dissociation temperature.

(b) Marrone–Treanor model Marrone and Treanor [144] proposed a semi-empirical correction factor for nonequilibrium dissociation that considers preferential dissociation from elevated vibrational levels. The corrective factor for the Marrone–Treanor model is valid where $T_{\text{trans}} > T_{\text{vib}}$ and is calculated as:

$$Z(T_{\text{trans}}, T_{\text{vib}}) = \frac{Q_{\text{vib-THO}}^{\Theta_D}(T_{\text{trans}}) Q_{\text{vib-THO}}^{\Theta_D}(\Gamma)}{Q_{\text{vib-THO}}(T_{\text{vib}}) Q_{\text{vib-THO}}(U)} \quad (4.13)$$

where the pseudo-temperature Γ is defined as:

$$\frac{1}{\Gamma} = \frac{1}{T_{\text{vib}}} - \frac{1}{T_{\text{trans}}} - \frac{1}{U} \quad (4.14)$$

and $Q_{\text{vib-THO}}^{\Theta_D}$ is the vibrational partition function for a harmonic oscillator truncated at the dissociation energy $k\Theta_D$ (see Equation 3.30). U is a model parameter that controls the degree of preferential dissociation taking place, and is typically given values between $\Theta_D/3$ and $\Theta_D/6$ where Θ_D is the characteristic temperature for dissociation. Setting $U = \infty$ yields the non-preferential dissociation rate coefficient. For $U = \Theta_D/6$ and assuming truncated harmonic oscillators, Lino da Silva [143] observed that the Marrone–Treanor model accurately reproduces state-to-state rates for N–N₂ collisions, while the rates for N₂–N₂ collisions are accurately reproduced at temperatures above 2,000 K. Slight variations in U and the vibrational partition functions, however, were found to give less favourable results.

(c) Knab model Knab *et al.* [142, 145] proposed a physically consistent coupled vibration-chemistry-vibration model that is an extension of the assumptions applied by Marrone and Treanor [144] to include exchange and associative ionisation reactions. The non-equilibrium factor for both dissociation and exchange reactions is calculated as:

$$Z(T_{\text{trans}}, T_{\text{vib}}) = \frac{Q_{\text{vib-THO}}^{\Theta_D}(T_{\text{trans}})}{Q_{\text{vib-THO}}^{\Theta_D}(T_{\text{vib}})} \times \frac{\exp\left(\frac{-\alpha A}{k_B T}\right) Q_{\text{vib-THO}}^{\alpha A}(\Gamma) + Q_{\text{vib}}^{\Theta_D}(T^0) - Q_{\text{vib}}^{\alpha A}(T^0)}{\exp\left(\frac{-\alpha A}{k_B T}\right) Q_{\text{vib-THO}}^{\alpha A}(-U) + Q_{\text{vib}}^{\Theta_D}(T^*) - Q_{\text{vib}}^{\alpha A}(T^*)} \quad (4.15)$$

where $Q_{\text{vib-THO}}^{\Theta_x}(T_x)$ is the vibrational partition function for a harmonic oscillator truncated at energy $k\Theta_x$ and evaluated at temperature T_x . In addition to Γ which retains the definition given by Marrone and Treanor [144] as defined in Equation 4.14, the following additional pseudo-temperatures are defined:

$$\frac{1}{T^0} = \frac{1}{T_{\text{vib}}} - \frac{1}{U} \quad (4.16)$$

$$\frac{1}{T^*} = \frac{1}{T_{\text{trans}}} - \frac{1}{U} \quad (4.17)$$

For dissociation $A = k\Theta_D$ and for dissociation-recombination $A = 0$. In addition to the variable parameter U introduced by Marrone and Treanor [144] for describing the degree of preferential dissociation, the Knab model considers the variable parameter α . Based on calibration studies against shock tube experiments with an air test gas, values of $U = \Theta_d/5$ and $\alpha = 0.8$ are recommended in Reference [142].

(d) Macheret–Fridman model For dissociation reactions in N₂ mixtures, Lino da Silva *et al.* [143] demonstrated that the forced harmonic oscillator model of Macheret and Fridman [146] provides the best agreement with state-to-state rates. The Macheret–Fridman model is based on vibrationally specific rates coefficients for dissociation of homonuclear molecules by atomic or diatomic species, and acknowledges collision dominated dissociation from low lying vibrational levels at high temperatures and vibration dominated dissociation from high lying vibrational levels at low temperatures. Furthermore, the Macheret–Fridman model is free of any variable parameters, which is in contrast to both the Park and Marrone–Treanor models. The corrective factor for the Macheret–Fridman model is calculated as:

$$Z(T_{\text{trans}}, T_{\text{vib}}) = \frac{1 - \exp(-\Theta_v/T_{\text{vib}})}{1 - \exp(-\Theta_v/T_{\text{trans}})} (1 - L) \times \exp \left[-\Theta_D \left(\frac{1}{T_{\text{vib}}} - \frac{1}{T_{\text{trans}}} \right) \right] + L \times \exp \left[-\Theta_D \left(\frac{1}{T_a} - \frac{1}{T_{\text{trans}}} \right) \right] \quad (4.18)$$

where,

$$\begin{aligned} T_a &= \alpha T_{\text{vib}} + (1 - \alpha) T_{\text{trans}} \\ \alpha &= \left(\frac{m_A}{m_A + m_B} \right)^2, \text{ and} \\ L &= \begin{cases} \frac{9\sqrt{\pi(1-\alpha)}}{64} \left(\frac{T_{\text{trans}}}{\Theta_D} \right)^{1-n} \left[1 + \frac{5(1-\alpha)T}{2\Theta_D} \right] \\ \text{for atomic third-bodies} \\ \frac{2(1-\alpha)}{\pi^2 \alpha^{3/4}} \left(\frac{T_{\text{trans}}}{\Theta_D} \right)^{3/2-n} \left[1 + \frac{7(1-\alpha)(1+\sqrt{\alpha})T_{\text{trans}}}{2\Theta_D} \right] \\ \text{for molecular third-bodies} \end{cases}. \end{aligned}$$

Here m_A and m_B are the constituent atom masses and Θ_v and Θ_D are the characteristic temperatures for vibration and dissociation respectively.

Comparison of dissociation models A comparison of the nonequilibrium N₂ dissociation rate coefficients at $T_{\text{vib}} = 3,000$ K via collisions with N and N₂ are presented in Figures 4.1a and 4.1b respectively. The equilibrium rate is from the reaction model of Park [136] which is presented in Table C.1. Computational chemistry rate coefficients from the NASA Ames database presented

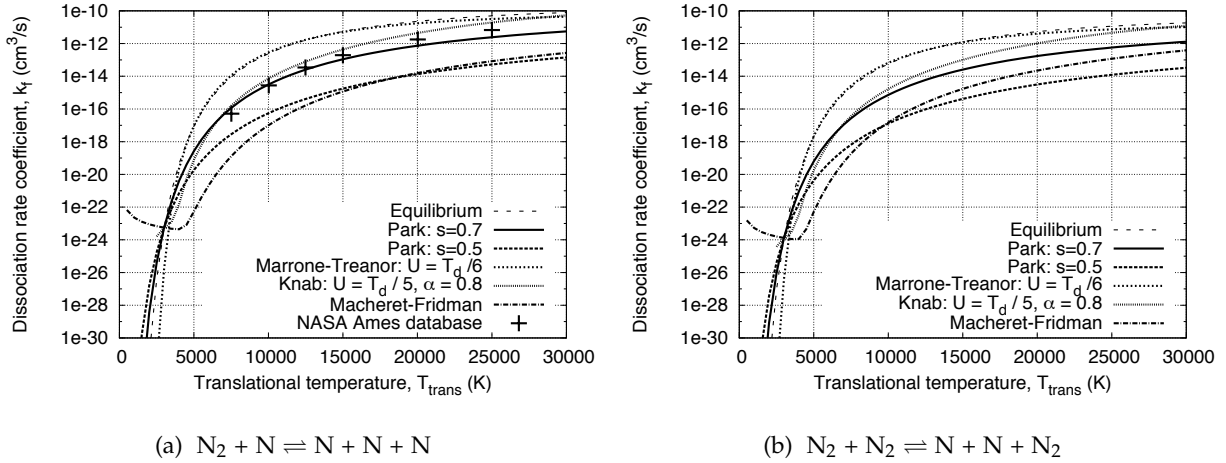


Figure 4.1: Comparison of rate coefficients for nonequilibrium N_2 dissociation via collisions with N and N_2 at a vibrational temperature of $T_{\text{vib}} = 3,000$ K.

in Reference [147] are overlayed for reference in Figure 4.1a. Surprisingly, the Park model with $s = 0.7$ is observed to give best agreement with the NASA Ames data for the N collider case, with the $s = 0.5$ case underestimating the NASA Ames data by an order of magnitude. The Knab model performs almost as well as the $s = 0.7$ Park model, overestimating the NASA Ames data by a factor of approximately 2 for the temperature range considered. The Macheret–Fridman model underestimates the NASA Ames data significantly, giving quantitatively similar results to the Park $s = 0.5$ case for $T \geq 15,000$ K. It is important to note that the Macheret–Fridman model exhibits qualitatively different behaviour at low translational temperatures compared to the other models. This is due to Macheret–Fridman model considering dissociation from high lying vibrational states at low translational temperatures. For the post-shock compression flows of present interest, however, accuracy in the dissociation rate coefficients is most critical immediately behind the shock where $T_{\text{trans}} \gg T_{\text{vib}}$. For the N_2 collider case in Figure 4.1b, similar trends are observed however the Macheret–Fridman model is closer to the Park $s = 0.7$ model at high temperatures. The Marrone–Treanor model gives results very close to the equilibrium rate for both cases. Due to its simplicity and demonstrated efficacy for reproducing both experimental and theoretical rate coefficients, the Park model is retained as the default nonequilibrium dissociation model.

4.2 Thermal energy exchange

Interaction between the thermal modes of colliding species and chemical reactions can lead to thermal energy exchange between modes. For a hypothetical chemical kinetic model considering individual quantum states as species, the thermal energy exchanges would be implicitly

accounted for. As bulk chemical species with Boltzmann distributions of internal states are assumed in the present work, the thermal energy exchanges must instead be explicitly modelled.

4.2.1 Vibration-translation exchange

The rate of vibrational energy change for molecular species p due to translational exchange with colliding species c is modelled via the Landau-Teller formula:

$$\left(\frac{de_{\text{vib},p}}{dt} \right)_{VT} = \sum_{c=1}^{N_c} x_c \frac{e_{\text{vib},p}^* - e_{\text{vib},p}}{\left(\tau_{\text{vib}}^{p-c} \right)_{VT}} \quad (4.19)$$

where τ_{vib}^{p-c} is the relaxation time. The following modification to Equation 4.19 was proposed by Park [29] to account for the diffusive vibrational excitation observed in experiment:

$$\left(\frac{de_{\text{vib},p}}{dt} \right)_{VT_{\text{bridging}}} = \sum_{c=1}^{N_c} x_c \frac{e_{\text{vib},p}^* - e_{\text{vib},p}}{\left(\tau_{\text{vib}}^{p-c} \right)_{VT}} \left| \frac{T_{\text{trans}}^* - T_{\text{vib}}}{T_{\text{trans}}^* - T_{\text{vib}}^*} \right|^{3.5e^{-5000/T_{\text{tr}}^*}-1} \quad (4.20)$$

where T_{trans}^* and T_{vib}^* denote the post-shock translational and vibrational temperatures respectively. This so called ‘bridging’ model, however, is difficult to implement in the Navier–Stokes equations as the shock is captured and T_{trans}^* and T_{vib}^* are not explicitly defined. In the present work Equation 4.19 is therefore retained.

Following the formulation presented by Thivet *et al.* [148] a net relaxation time τ_v^p can be defined:

$$\left(\frac{de_{\text{vib},p}}{dt} \right)_{VT} = \frac{e_{\text{vib},p}^* - e_{\text{vib},p}}{\left(\tau_{\text{vib}}^p \right)_{VT}} \quad (4.21)$$

where,

$$\left(\tau_{\text{vib}}^p \right)_{VT} = \sum_{c=1}^{N_c} \frac{x_c}{\left(\tau_{\text{vib}}^{p-c} \right)_{VT}}. \quad (4.22)$$

In the present formulation the vibrational energy of all molecular species is governed by a common temperature T_{vib} and the total vibration-translation energy exchange is required. Multiplying Equation 4.21 by the species density and summing over all molecules and gives the vibration-translation energy exchange source term:

$$\Omega_{VT} = \sum_{p=1}^{n_m} \rho_p \frac{e_{\text{vib},p}^* - e_{\text{vib},p}}{\left(\tau_{\text{vib}}^p \right)_{VT}} \quad (4.23)$$

The translation-vibration relaxation times $\left(\tau_{\text{vib}}^{p-c} \right)_{VT}$ are calculated using the empirical Millikan and White [149] correlation with a high temperature correction as implemented by Park *et*

al. [137]:

$$\left(\tau_{\text{vib}}^{p-c} \right)_{VT} = \tau_{MW} + \left[N_{\text{total}} \sigma_v \sqrt{8k_B T_{\text{trans}} / \pi m_{\text{av}}} \right]^{-1} \quad (4.24)$$

$$p \tau_{MW} = \exp \left[a \left(T^{-1/3} - b \right) - 18.42 \right] \quad (4.25)$$

where,

$$a = 0.00116 \mu^{0.5} \Theta_{\text{vib}}^{1.333}, \quad b = 0.015 \mu^{0.25}. \quad (4.26)$$

Here N_{total} and m_{av} are the total number of particles and average particle mass of the mixture, respectively, σ_v the collision-limiting cross section, μ and p the reduced molecular weight and pressure of the colliding particles and Θ_{vib} the characteristic temperature of the vibrational mode under consideration. For CO₂–N₂–Ar mixtures the experimentally fitted a and b values presented by Park [137] are preferred to those in Equation 4.26. The model proposed by Park [136, 137] for the limiting cross section is a function of the inverse square of translational temperature:

$$\sigma_v = \sigma'_v (50000 / T_{\text{trans}})^2 \quad (4.27)$$

For N₂–O₂ mixtures the reference cross sections σ'_v were selected as 3.0×10^{-17} for N₂, O₂ and NO [136], while for CO₂–N₂–Ar mixtures σ'_v were selected as 3.0×10^{-17} for N₂, 3.0×10^{-18} for CO and 1.0×10^{-16} for CO₂ based on experimental measurements [137]. It should be noted that the reference cross section for air mixtures recommended in Park's earlier work [50] is 1.0×10^{-17} , three times lower than in Reference [136]. This value was implemented by Johnston [19], who also limited the temperature in Equation 4.27 to 20,000 K to achieve adequate results with the viscous shock layer equations. In the present work the recommended reference cross sections for air in Reference [136] are preferred and no limit is placed on Equation 4.27. The resultant effect on post-shock relaxation of this selection is to make the equilibration process more diffusive.

The coupled rotation-vibration-dissociation analysis of CO by state-resolved DSMC of Fujita [77], however, demonstrates that the Park model may exhibit excessive temperature dependence at high temperatures. The following expression was recommended based on DSMC-QCT modelling at high temperatures and experimental data at low temperatures:

$$\sigma_v = \frac{1.8 \times 10^{-18}}{\sqrt{T}} + \frac{1.0 \times 10^{-8}}{T^3} \quad (4.28)$$

The Fujita expression results in faster vibrational excitation immediately behind the shock compared to the standard Park cross sections, and are preferred for the CO molecule in the present work.

4.2.2 Translation-electron exchange

The heating of electrons through elastic collisions with heavy particles is modelled by the rate equation derived by Appleton and Bray [150]:

$$\Omega_{TE} = 3\rho_e \bar{R} (T - T_e) \sum_{i \neq e^-} \frac{\nu_{e,i}}{M_i}, \quad (4.29)$$

where M_i is the molecular weight for species i and ρ_e is the electron density. For Coulomb collisions between electrons and ions the expression for effective collision frequency $\nu_{e,i}$ is:

$$\nu_{e,i} = \frac{8}{3} \left(\frac{\pi}{m_e} \right)^{1/2} n_i e^4 \frac{1}{(2k_B T_e)^{3/2}} \ln \left(\frac{k_B^3 T_e^3}{\pi n_e e^6} \right) \quad (4.30)$$

where n_e is the electron number density and n_i is the ionic species i number density. For electron-neutral interactions the effective collision frequency is:

$$\nu_{es} = n_s \sigma_{es} \left(\frac{8k_B T_e}{\pi m_e} \right)^{1/2} \quad (4.31)$$

where σ_{es} is the energy exchange cross section. This parameter is available in the paper of Gnoffo [151] for N, O, N₂, O₂ and NO as quadratic curve fits in the form of:

$$\sigma_{es} = a_s + b_s T_e + c_s T_e^2. \quad (4.32)$$

As no data for the energy exchange cross section of C or CO is available in the literature, they are equated to that for O and O₂ respectively. Coulomb collisions between electrons and ions are significantly more efficient than elastic collisions between electrons and neutrals, therefore this approximation should be sufficient at the high velocity conditions of interest in the present work.

4.2.3 Vibration-electron exchange

Free electrons can also efficiently produce excited vibrational states through inelastic collisions with molecules. Electron-impact vibrational excitation must be included when considering nonequilibrium between T_e and T_{vib} in the three-temperature model. A Landau-Teller form of the rate equation is implemented:

$$\Omega_{VE} = \sum_p^{N_{\text{mol}}} \rho_p \frac{e_{\text{vib},p}^* - e_{\text{vib},p}}{(\tau_{\text{vib}}^p)_{VE}} \quad (4.33)$$

where $e_{\text{vib},p}^*$ is the vibrational energy of molecule p evaluated at the electron temperature T_e .

Most vibration-electron relaxation time models have focused on the resonant N₂-e⁻ interaction as it is the dominant mechanism for air plasmas. Lee [152] initially obtained an empirical expression for the N₂-e⁻ relaxation time based on vibrational state master equation calculations with multi-quantum transitions from the vibrational ground state. The results were curve fit to the following form by Candler and Park [153]:

$$\log[p_e \tau] = A[\log(T_e)]^2 + B[\log(T_e)] + C \quad (4.34)$$

In Reference [154], Lee revised the initial calculations by considering multi-quantum transitions from all vibrational levels. Similarly, a later study by Bourdon and Vervisch [155] also obtained an empirical curve fit for the N₂-e⁻ relaxation time based on vibrational state master

equation calculations with multi-quantum transitions. Whilst the models of Lee [152, 154] implemented excitation cross sections obtained from quantum chemistry calculations, the model of Bourdon and Vervisch [155] is based on excitation cross sections derived from experiment. Figure 4.2 compares the e-V relaxation time for N₂ obtained from the above three models, where the values for the coefficients in Equation 4.34 are listed in Table 4.2. The original relaxation times of Lee [152] are approximately 3 times longer than the revised relaxation times of Lee [154] and those of Bourdon and Vervisch [155]. The curve fits of Bourdon and Vervisch [155] and Lee [154] give reasonably similar relaxation times, however that of Lee [154] exhibits a discontinuity at the 7000 K temperature switch. Thus in the present work the curve fit of Bourdon and Vervisch is implemented for the N₂ relaxation time.

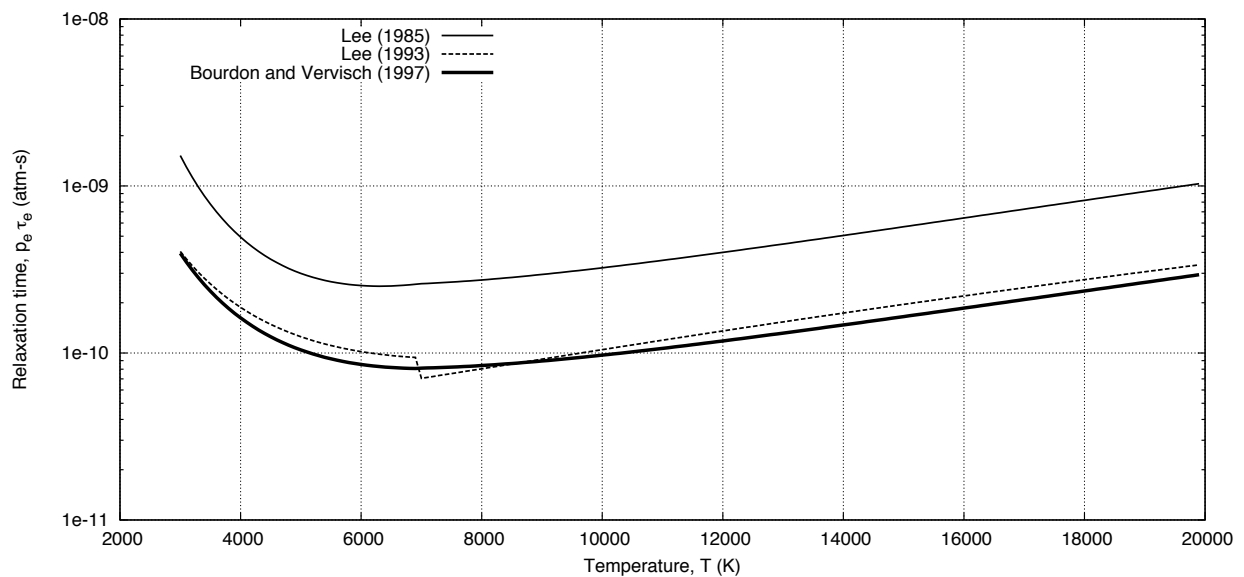


Figure 4.2: Comparison of vibration-electron energy relaxation times computed via various models in the temperature range $3000 \text{ K} \leq T_e \leq 20000 \text{ K}$

For the CO₂-based atmosphere of Mars, CO is the dominant molecule behind the shock. The experiments of Schultz [156] performed with a double electrostatic analyzer demonstrate that the electron impact vibrational excitation cross sections for N₂ and CO in the ground electronic state are similar — therefore as a first approximation in the present work, the Lee N₂ relaxation times are also used for CO.

Table 4.2: Coefficients for the vibration-electron relaxation time curve fit, Equation 4.34, from various models

Temperature range	A	B	C
<i>Lee [152]</i>			
$T_e \leq 7000 \text{ K}$	7.5	-57.0	98.70
$T_e \geq 7000 \text{ K}$	2.36	-17.9	24.35
<i>Lee [154]</i>			
$1000 \text{ K} \leq T_e \leq 7000 \text{ K}$	3.91	-30.36	48.90
$7000 \text{ K} \leq T_e \leq 20000 \text{ K}$	1.30	-9.09	5.58
<i>Bourdon and Vervisch [155]</i>			
$3000 \text{ K} \leq T_e \leq 7000 \text{ K}$	5.019	-38.625	64.219
$7000 \text{ K} \leq T_e \leq 20000 \text{ K}$	2.448	-18.704	25.635

4.2.4 Chemistry-energy coupling

As chemical species are created and destroyed, the thermal energy they contain must be appropriately book-kept in the governing equations. Additionally, certain reactions such as electron impact ionisation may deplete thermal energy from modes other than heavy particle translation¹. Both these phenomena are modelled by the chemistry-energy coupling source terms, Ω_{CV} and Ω_{CE} . In general, the thermal energy source term for arbitrary mode X due to chemical reactions can be written as the summation of contributions from all species and reactions:

$$\Omega_{CX} = \sum_i^{N_{\text{species}}} \sum_{j=1}^{N_r} \left[-G_{va,ij} (\dot{\omega}_i)_{va,j} + G_{app,ij} (\dot{\omega}_i)_{app,j} \right] \quad (4.35)$$

where $G_{va,ij}$ is the modal energy change per unit mass associated with the consumption of species i due to reaction j occurring at rate $(\dot{\omega}_i)_{va,j}$, and $G_{app,ij}$ is the change associated with the production of species i due to reaction j occurring at rate $(\dot{\omega}_i)_{app,j}$. This expression is sufficiently general to be applicable to both chemistry-vibration Ω_{CV} and chemistry-electron-electronic Ω_{CE} coupling source terms in the governing equations (see § 2).

Chemistry-vibration coupling

Chemistry-vibration coupling represents the loss or gain of vibrational energy due to molecules being created or destroyed. The most basic model that can be applied is to assume all molecules are created or destroyed at the current average vibrational energy. Therefore the vanishing and

¹By forming the governing equations without an explicitly written conservation equation for the translation-rotation energy as presented in § 2, the translation-rotation mode provides (or receives) the reaction energy if chemistry-energy coupling is not considered.

appearing components may both be calculated as the species i vibrational energy evaluated at the current vibrational temperature T_{vib} :

$$G_{app,ij} = G_{va,ij} = e_{\text{vib},i}(T_{\text{vib}}) \quad (4.36)$$

When applied to dissociation reactions, this model is often referred to as ‘non-preferential dissociation’ — that is, dissociation from all vibrational levels is assumed equally probable. For the high energy atmospheric entry trajectories of present interest, the post-shock translational temperature is very high (up to 60,000 K) and it may be argued there is sufficient collisional energy for molecular reactions to readily occur from all vibrational levels. In the present work Equation 4.36 is therefore the default chemistry-vibration coupling model for all reactions involving molecules.

Due to vibrational excitation reducing the energy required for molecular reactions to take place, however, the vibrational energy associated with molecular consumption and production may be greater than the average vibrational energy. In the present work we refer to this phenomena as preferential chemistry-vibration coupling. For each of the nonequilibrium dissociation models presented in § 4.1.2, corresponding chemistry-vibration coupling models with consistent physical assumptions have been proposed in the literature. Unless otherwise state, in the present work these models are always used in conjunction with each other to maintain physical consistency. The appearing component for all preferential chemistry-vibration coupling models is the vanishing component evaluated at the backwards rate controlling temperature:

$$G_{app,ij} = G_{va,ij}(T_{\text{vib}} = T_b) \quad (4.37)$$

For all molecular reactions except electron impact dissociation, the backwards rate controlling temperature is T_{trans} . For electron impact dissociation, $T_b = T_e$ (see Table 4.1).

(a) Park model For dissociation reactions with rate coefficients obtained from the model of Park [29], Knab *et al.* [145] proposed a dissociation-vibration coupling model that is consistent with its assumptions. The dissociation component is calculated as:

$$G_{va,ij-\text{Park}} = (1 - s) \left[nR_i T_{\text{vib}} + D_i \left(\frac{T_{\text{vib}}}{T_{\text{trans}}} \right)^s \right] + e_{\text{vib},i}(T_{\text{vib}}) \quad (4.38)$$

$$(4.39)$$

where s is the rate controlling temperature exponent, n is the Arrhenius rate exponent and D_i is the dissociation energy. It should be noted, however, that Park’s two-temperature model was developed without the consideration of preferential dissociation-vibration coupling [157], and Equation 4.38 simply represents the amount of vibrational energy removal that is mathematically implied.

(b) Treanor–Marrone model Treanor and Marrone [158] proposed a dissociation-vibration coupling model to be used alongside the preferential dissociation model of Marrone and Treanor [144]. The Treanor–Marrone dissociation component is calculated as:

$$G_{va,i-\text{TM}} = e_{vib,i}(\Gamma) \quad (4.40)$$

where the pseudo-temperature Γ has been defined in Equation 4.14.

(c) Knab model For the coupled vibration-chemistry-vibration model of Knab *et al.* [142, 145], the vibrational energy lost by the consumption of a molecule is calculated as:

$$G_{va,i-\text{Knab}} = \frac{\exp\left(\frac{-\alpha A}{kT_{\text{trans}}}\right) Q_{\text{vib}}^{\alpha A}(\Gamma) e_{\text{vib-THO}}^{\alpha A}(\Gamma) + Q_{\text{vib}}^{\Theta_d}(T^0) e_{\text{vib-THO}}^{\Theta_d}(T^0) - Q_{\text{vib}}^{\alpha A}(T^0) e_{\text{vib-THO}}^{\alpha A}(T^0)}{\exp\left(\frac{-\alpha A}{kT_{\text{trans}}}\right) Q_{\text{vib}}^{\alpha A}(\Gamma) + Q_{\text{vib}}^{\Theta_d}(T^0) - Q_{\text{vib}}^{\alpha A}(T^0)} \quad (4.41)$$

where $e_{\text{vib-THO}}^{\Theta_x}(T_x)$ is the vibrational energy of a harmonic oscillator truncated at energy $k\Theta_x$ and evaluated at temperature T_x (see Equation 3.34). The pseudo temperatures Γ , T^0 and T^* have been previously defined in Equations 4.14, 4.16 and 4.17 respectively, and the variable parameters α and A should assume the same values as applied to the reaction rate nonequilibrium factor (see § 4.1.2).

(d) Macheret–Fridman model For dissociation reactions with rate coefficients obtained from the Macheret–Fridman model [146], the dissociation component is calculated as:

$$G_{va,i-\text{MF}} = R_i \left[\frac{\alpha \Theta_D \left(\frac{T}{T_a} \right)^2 k_{f,l}(T_{\text{trans}}, T_{\text{vib}}) + \Theta_D k_{f,h}(T_{\text{trans}}, T_{\text{vib}})}{k_{f,neq}(T_{\text{trans}}, T_{\text{vib}})} \right] \quad (4.42)$$

where $k_{f,neq}(T_{\text{trans}}, T_{\text{vib}})$ is Macheret–Fridman dissociation rate defined by Equations 4.9 and 4.18, and the dissociation rates at low $k_{f,l}(T_{\text{trans}}, T_{\text{vib}})$ and $k_{f,h}(T_{\text{trans}}, T_{\text{vib}})$ high temperatures are calculated as:

$$\begin{aligned} k_{f,l}(T_{\text{trans}}, T_{\text{vib}}) &= (1 - L) A T_{\text{trans}}^n \exp\left(-\frac{\Theta_D}{\sqrt{T_{\text{trans}} T_{\text{vib}}}}\right) \\ k_{f,h}(T_{\text{trans}}, T_{\text{vib}}) &= \frac{1 - \exp(-\Theta_{\text{vib}}/T_{\text{vib}})}{1 - \exp(-\Theta_{\text{vib}}/T_{\text{trans}})} L A T_{\text{trans}}^n \exp\left(-\frac{\Theta_D}{T_{\text{vib}}}\right) \end{aligned}$$

where A and n are the generalised Arrhenius rate parameters for the dissociation reaction.

Chemistry-electron-electronic coupling

Chemistry-electron-electronic coupling accounts for the change in free electron and bound electronic energy due to chemical reactions. Similarly as for chemistry-vibration coupling, the most basic model to consider is where the free electron and electronic energy of the species being produced or consumed is the average value:

$$G_{app,ij} = G_{va,ij} = \begin{cases} e_{el,i}(T_{el}) & \text{for } i = \text{heavy particle} \\ e_{trans,i}(T_e) & \text{for } i = \text{free electron} \end{cases} \quad (4.43)$$

In the present work Equation 4.43 is the default chemistry-electron-electronic coupling model for all reactions where free electrons are not created or destroyed. For associative ionisation and electron impact ionisation, however, more advanced models are required to correctly account for the change in free electron energy.

(a) Electron impact ionisation When a free electron collides with an atom and causes it to ionise, the free electron translational energy is depleted by some fraction of the ionisation energy of the bound electron. In addition, the freed electron is assumed to be formed at the average energy. The change of free electron energy due to electron impact ionisation (the appearing component) can therefore approximated by :

$$G_{app,i-EII} = e_e(T_e) - \alpha_{EII} I_i^* \quad (4.44)$$

where I_i^* is the ionisation energy of the bound electron and α_{EII} is an energy transformation coefficient. As impacting free electrons are very efficient colliders, they can be assumed to provide the bulk of the reaction energy for ionisation reactions. α_{EII} is therefore set to 1 in the present work to represent all of the ionisation energy coming from the impacting electron. Lee [159], Gnoffo [151] and Park [29], amongst others, set I_i as the ground state ionisation energy, whereas Hartung *et al.* [160] and Johnston [19] recommend the following reduced values to represent ionisation from excited electronic states:

$$\frac{I_N^*}{M_N} = 4.05 \times 10^5 \text{ J/mol} \approx 0.3 \frac{I_N}{M_N} \quad (4.45)$$

$$\frac{I_O^*}{M_O} = 4.30 \times 10^5 \text{ J/mol} \approx 0.3 \frac{I_O}{M_O} \quad (4.46)$$

Without considering the rate equation for each electronic level, it is difficult to justify either method. In the present work the classical model of the ground state energy is preferred as the default model. This represents the maximum possible energy removal and will reduce the rate of electron equilibration accordingly. The recombination component must be equal to the ionisation component at thermal equilibrium to ensure convergence of the temperatures. Therefore the energy gained due to electron impact ionisation-recombination is:

$$G_{va,i-\text{EII}} = G_{app,i-\text{EII}} \quad (4.47)$$

(b) Associative ionisation It can be argued that free electrons produced via associative ionisation are formed at an energy greater than the average free electron energy [161]. Considering that the gas temperature T_{trans} would provide a theoretical upper limit via collisions, the gain in free electron energy due to associative ionisation can be approximated as:

$$G_{app,i-\text{AI}} = e_e(T_e) + \alpha_{\text{AI}} [e_e(T_{\text{trans}}) - e_e(T_e)] \quad (4.48)$$

where α_{AI} is an energy transformation coefficient. Setting $\alpha_{\text{AI}} = 0$ represents free electron formation at the (bound) electronic temperature and $\alpha_{\text{AI}} = 1$ represents free electron formation at the heavy particle temperature. In the present work α_{AI} is conservatively varied between 0 and 0.1. The recombination component must be equal to the ionisation component at thermal equilibrium to ensure convergence of the temperatures. Therefore the energy gained due to associative ionisation-recombination is:

$$G_{va,i-\text{AI}} = G_{app,i-\text{AI}} \quad (4.49)$$

4.3 Collisional-radiative modelling

Fundamental to the calculation of the spectral radiation coefficients is the determination of the electronic level populations. Under thermal equilibrium conditions, the level populations assume a Boltzmann distribution. When insufficient collisions have occurred for thermal equilibrium to be achieved, the rate equation for each level must be considered. The net population rate of level i (also referred to in the literature as the ‘master-equation’ [29]) is the difference between the rate of transitions moving electrons in and out of the level:

$$\frac{dN_i}{dt} = \left(\frac{dN_i}{dt} \right)_{\text{in}} - \left(\frac{dN_i}{dt} \right)_{\text{out}} \quad (4.50)$$

Although multidimensional simulations with the collisional-radiative equations fully coupled with the flowfield have recently been performed (*e.g.* Reference [58]), this is computationally prohibitive for the time accurate Navier–Stokes calculations performed in the present work. Rather, the quasi-steady-state (QSS) approximation proposed by Park [29] is applied to decouple the solution from the temporal evolution of the flowfield. The QSS approximation assumes the net population rate of level i to be much smaller than the individual incoming and outgoing rates:

$$\frac{dN_i}{dt} \ll \left(\frac{dN_i}{dt} \right)_{\text{in}}, \quad \text{and} \quad \frac{dN_i}{dt} \ll \left(\frac{dN_i}{dt} \right)_{\text{out}}.$$

The net population rate-of-change in Equation 4.50 can therefore be approximated as zero, and the QSS solution is found when the incoming and outgoing rates are balanced:

$$0 = \left(\frac{dN_i}{dt} \right)_{\text{in}} - \left(\frac{dN_i}{dt} \right)_{\text{out}} \quad (4.51)$$

As the population rates are functions of the immediate flow state only, the QSS solution is decoupled from the temporal evolution of the flowfield. However the QSS approximation is known not to be valid for the ground state [29]. The QSS approximation is therefore only applied to the excited levels, and the ground state population is solved by considering the number density balance for the species:

$$N_{i=1} = N_{\text{total}} - \sum_{i=2}^{N_{\text{levels}}} N_i \quad (4.52)$$

4.3.1 Collisional-radiative mechanisms

The collisional-radiative mechanisms considered in the present work are:

1. Heavy particle impact excitation,
2. Electron impact excitation,
3. Heavy particle impact dissociation,
4. Electron impact dissociation,
5. Electron impact ionisation, and
6. Bound-bound radiative transitions.

Free-bound radiative transitions are omitted as the depopulation rates due to bound-bound radiative transitions are considerably more significant for the conditions of interest [19].

Heavy particle impact excitation

Heavy particle impact excitation reactions have the following form:



where M denotes an arbitrary heavy particle species, X denotes an arbitrary atomic species and i and j denote the lower (initial) and upper (final) electronic levels respectively. The net population rate of level i due to heavy particle impact excitation (HPIE) reactions is:

$$\left(\frac{dN_i}{dt} \right)_{\text{HPIE}} = \sum_{j \neq i} K_M(j, i) N_j N_M - \sum_{j \neq i} K_M(i, j) N_i N_M \quad (4.54)$$

In the present work, heavy particle impact excitation processes are only considered for diatomic species as the electron impact mechanisms dominate in the flow regime where atomic nonequilibrium is significant [19, 29]. The forward rate coefficients for heavy particle impact excitation are obtained from the literature in generalised Arrhenius form:

$$K_M(i,j) = CT_x^n \exp\left(-\frac{E_a}{kT_x}\right) \quad (4.55)$$

where the rate controlling temperature for the excitation process is the geometric average of the translational and vibrational temperatures:

$$T_x = \sqrt{T_{\text{trans}} T_{\text{vib}}} \quad (4.56)$$

The backward reaction rate coefficients are calculated via the principle of detailed balancing:

$$K_M(j,i) = \left[K_M(i,j) \frac{Q_i}{Q_j} \right]_{T_{\text{trans}}} \quad (4.57)$$

where Q_i and Q_j are the partition functions of the lower and upper electronic levels respectively. The rate controlling temperature for the de-excitation process is the translational temperature, and therefore $K_M(i,j)$, Q_i and Q_j in Equation 4.57 are evaluated at T_{trans} .

Electron impact excitation

Electron impact excitation reactions have the following form:



The net population rate of level i due to electron impact excitation (EIE) reactions is:

$$\left(\frac{dN_i}{dt} \right)_{\text{EIE}} = \sum_{j \neq i} K_e(j,i) N_j N_e - \sum_{j \neq i} K_e(i,j) N_i N_e \quad (4.59)$$

The forward rate coefficients are assumed to be governed by the free electron temperature T_e , and the backward reaction rate coefficient is calculated via the principle of detailed balancing:

$$K_e(j,i) = \left[K_e(i,j) \frac{Q_i}{Q_j} \right]_{T_e} \quad (4.60)$$

where the de-excitation process is assumed to be governed by the free electron temperature T_e .

Electron impact excitation processes for both diatomic and atomic species are considered in the present work. The forward rate coefficients for diatomic electron impact excitation are either obtained directly from the literature in generalised Arrhenius form, or calculated by integrating cross sections. In the present work, the following method proposed by Park [29] for calculating the diatomic electron impact excitation rate coefficient from the respective cross section is implemented:

$$K_e(i,j) = \frac{S \sum_{v_i} \sum_{v_j} q(v_i, v_j) \exp\left[-\frac{G_{v_i}}{kT_{\text{vib.}}}\right]}{\frac{kT_r}{B_{e,i}} Q_{\text{vib.},i}} \quad (4.61)$$

where $q(v_i, v_j)$ is the Frank-Condon factor for the vibronic transition between v_i and v_j , G_{v_i} is the vibrational energy of vibrational state v_i and $Q_{\text{vib.},i}$ is the vibrational partition function for electronic level i . The parameter S is defined as:

$$S = 5.47 \times 10^{-11} \sqrt{T_e} \exp\left(-\frac{T_j + G_{v,j} - T_i - G_{v,i}}{k_B T_e}\right) \quad (4.62)$$

where I is:

$$I = \left(\frac{B_{e,j} - B_{e,i}}{k_B T_e} + \frac{B_{e,i}}{k_B T_{\text{rot.}}} \right)^{-3/2} [C\Gamma(1.5)BD\Gamma(2.5)] \quad (4.63)$$

with:

$$C = \frac{T_j + G_{v,j} - T_i - G_{v,i}}{k_B T_e} B + A, \quad (4.64)$$

$$D = \frac{B_{e,j} - B_{e,i}}{k_B T_e} \left(\frac{B_{e,j} - B_{e,i}}{k_B T_e} + \frac{B_{e,i}}{k_B T_e} \right)^{-1}. \quad (4.65)$$

The parameters A and B are defined as:

$$A = \int_0^\infty \left[\frac{\sigma(\xi)}{\pi a_0^2} \right] \exp(-\xi) \xi d\xi \quad (4.66)$$

$$B = \int_0^\infty \left[\frac{\sigma(\xi)}{\pi a_0^2} \right] \exp(-\xi) d\xi \quad (4.67)$$

where a_0 is the first Bohr radius and σ is the electron impact excitation cross section with $\xi = x - 1$ and $x = E/E^*$ where E is the electron energy and E^* is the threshold energy (ΔT_e).

Although experimental and theoretical electron impact excitation cross sections for atomic species are available for some transitions from low lying states, for the majority of transitions we must rely on semi-empirical models. Here we will briefly describe the approximate electron impact excitation models considered for atoms, whilst a detailed description of the rate coefficient models selected for each species will be presented later.

Numerous empirical electron impact excitation models for atomic species were investigated in the comprehensive studies of Johnston [19] and Panesi [58]. As a baseline model, Panesi [58] implemented electron impact excitation reaction rate coefficients obtained by analytical integration of the Drawin [162] cross sections over a Maxwell-Boltzmann velocity distribution:

$$K_e(i,j) = \begin{cases} \sqrt{\frac{8k_B T_e}{\pi m_e}} 4\pi a_0^2 \alpha \left(\frac{I_H}{k_B T_e}\right)^2 I_1(a) & \text{for an optically allowed transition} \\ \sqrt{\frac{8k_B T_e}{\pi m_e}} 4\pi a_0^2 \alpha \left(\frac{E_j - E_i}{k_B T_e}\right)^2 I_2(a) & \text{for an optically forbidden transition} \end{cases} \quad (4.68)$$

where m_e is the mass of an electron, a_0 is the first Bohr radius, $\alpha = 0.05$, I_H is the ionisation energy of the hydrogen atom from the ground state and $I_1(a)$ and $I_2(a)$ are calculated as:

$$I_1(a) = 0.63255 a^{-1.6454} e^{-a}, \quad \text{where} \quad a = \frac{E_j - E_i}{k_B T} \quad (4.69)$$

$$I_2(a) = 0.23933 a^{-1.4933} e^{-a}, \quad \text{where} \quad a = \frac{E_{\text{ionise},i} - E_i}{k_B T} \quad (4.70)$$

The hydrogenic model of Gryzinski [163] was implemented by both Johnston [19] and Panesi [58]. Similarly as for the Drawin model, the Gryzinski model is semi-empirical and universally applicable to all transition types. The electron impact excitation reaction rate coefficients are calculated by integrating the Gryzinski cross section σ_{ij} over a Maxwellian velocity distribution:

$$K_e(i,j) = \frac{8\pi}{\sqrt{m}} \left(\frac{1}{2\pi m k_B T_e} \right)^{1.5} \left[\int_{\Delta E_{i,j}}^{\infty} \sigma_{i,j}(E) \exp\left(-\frac{E}{k_B T_e}\right) E dE + \int_{\Delta E_{i,j+1}}^{\infty} \sigma_{i,j+1}(E) \exp\left(-\frac{E}{k_B T_e}\right) E dE \right] \quad (4.71)$$

where $\sigma_{ij}(E)$ is given by Eq. 4.72 for $\Delta E_{ij} + E_{\text{ionise}} - E_i \leq E$ and by Eq. 4.73 for $\Delta E_{ij} + E_{\text{ionise}} - E_i \geq E$:

$$\begin{aligned} \sigma_{i,j}(E) &= \frac{4.2484 \times 10^{-6}}{\Delta E_{ij}^2} \left(\frac{E}{E_{\text{ionise}} - E_i + E} \right)^{1.5} \\ &\times \left\{ \frac{2}{3} \left[\frac{E_{\text{ionise}} - E_i}{E} + \frac{\Delta E_{ij}}{E} \left(1 - \frac{E_{\text{ionise}} - E_i}{E} \right) - \left(\frac{\Delta E_{ij}}{E} \right)^2 \right] \right\} \end{aligned} \quad (4.72)$$

$$\begin{aligned} \sigma_{i,j}(E) &= \frac{4.2484 \times 10^{-6}}{\Delta E_{ij}^2} \left(\frac{E}{E_{\text{ionise}} - E_i + E} \right)^{1.5} \\ &\times \left\{ \frac{2}{3} \left[\frac{E_{\text{ionise}} - E_i}{E} + \frac{\Delta E_{ij}}{E} \left(1 - \frac{E_{\text{ionise}} - E_i}{E} \right) - \left(\frac{\Delta E_{ij}}{E} \right)^2 \right] \right. \\ &\times \left. \left[\left(1 + \frac{\Delta E_{ij}}{E_{\text{ionise}} - E_i} \right) \left(1 - \frac{\Delta E_{ij}}{E} \right) \right]^{0.5} \right\} \end{aligned} \quad (4.73)$$

In the present implementation the cross section integration is performed by a change of variables to shift the limits to [-1,1] and applying 10 point Gaussian quadrature.

Johnston [19] and Panesi [58] also considered the empirical models proposed by Allen [164], Van Regmoter [165] and Park [29, 166]. Both authors found the Park [29, 166] models to give substantially larger rates than other more accurate models for electron impact excitation of N and O, and were therefore not implemented. Although Johnston [19] preferred the models of Allen [164] and Van Regmoter [165] over that of Gryzinski [163], Panesi [58] found the Drawin model described in Equation 4.68 to be in good agreement with these models. Therefore in the present work only the Gryzinski [163] and Drawin [162] empirical models will be considered.

Heavy particle impact dissociation

Heavy particle impact dissociation reactions have the following form:



where A and B are the constituent atoms of the diatomic molecule AB. The net population rate of level i due to heavy particle impact dissociation (HPID) reactions is:

$$\left(\frac{dN_i}{dt} \right)_{\text{HPID}} = K_M(d, i) N_A N_B N_M - K_M(i, d) N_i N_M \quad (4.75)$$

where d denotes the dissociated state. The forward rate coefficients for diatomic heavy particle impact dissociation are obtained from the literature in generalised Arrhenius form, where the rate controlling temperature for the excitation process is the geometric average of the translational and vibrational temperatures:

$$T_x = \sqrt{T_{\text{trans}} T_{\text{vib}}} \quad (4.76)$$

The heavy particle impact recombination rate coefficient is related to the heavy particle impact dissociation rate coefficient via the principle of detailed balancing:

$$K_M(d, i) = \left[K_M(i, d) \frac{Q_i}{Q_A Q_B} \right]_{T_{\text{trans}}} \quad (4.77)$$

where the total partition functions Q must include the formation energy contribution $\exp(-h_f/k_B T_{\text{trans}})$ to account for the dissociation potential of the lower state, and the rate controlling temperature for the de-excitation process is the translational temperature T_{trans} .

Electron impact dissociation

Similarly as for heavy particle impact dissociation, electron impact dissociation reactions have the following form:



where A and B are the constituent atoms of the molecule AB. The net population rate of level i due to electron impact dissociation (EID) reactions is:

$$\left(\frac{dN_i}{dt} \right)_{\text{EID}} = K_e(d, i) N_A N_B N_e - K_e(i, d) N_i N_e \quad (4.79)$$

where c denotes the ionised state. The forward rate coefficients for diatomic electron impact dissociation are obtained from the literature in generalised Arrhenius form, where the rate controlling temperature for the dissociation process is the free electron temperature:

$$T_x = T_e \quad (4.80)$$

The electron impact recombination rate coefficient is calculated via the principle of detailed balancing:

$$K_e(d, i) = \left[K_e(i, d) \frac{Q_i}{Q_A Q_B} \right]_{T_e} \quad (4.81)$$

where the total partition functions Q must include the formation energy contribution $\exp(-h_f/k_B T_{\text{trans}})$ to account for the dissociation potential of the lower state, and the rate controlling temperature for the recombination process is assumed to be the free electron temperature T_e .

Electron impact ionisation

Electron impact ionisation reactions have the following form:



where X^+ is the ionised species. The net population rate of level i due to electron impact excitation (EII) reactions is:

$$\left(\frac{dN_i}{dt} \right)_{\text{EII}} = K_e(c, i) N_{\text{ion}} N_e N_e - K_e(i, c) N_i N_e \quad (4.83)$$

where c denotes the ionised states. The ionisation process is assumed to be governed by the free electron temperature T_e , and the electron impact recombination rate coefficient is related to the electron impact ionisation rate coefficient via the principle of detailed balancing:

$$K_e(c, i) = \left[K_e(i, c) \frac{Q_i}{Q_{\text{ion}} Q_e} \right]_{T_e} \quad (4.84)$$

where the total partition functions Q must include the formation energy contribution $\exp(-h_f/k_B T_{\text{trans}})$ to account for the ionisation potential of the lower state, and the rate controlling temperature for the recombination process is assumed to be the free electron temperature T_e .

Electron impact ionisation processes are only considered for atomic species in the present work, as the dissociation and excitation processes are much more significant for diatomic species. Similarly as for electron impact excitation, electron impact ionisation rate coefficients based on experimental measurements or theoretical calculations are preferred in the present work. The ionisation cross sections, however, are typically only provided for low lying states and we must rely on empirical models for the remainder. Two empirical models for electron impact ionisation are considered, both based on the hydrogenic cross sections of Drawin [162]. The model implemented by Johnston [19] gives the electron impact ionisation reaction rate coefficients as:

$$K_e(i, c) = 1.46 \times 10^{-10} \sqrt{T_e} \left(\frac{I_H}{I - E_i} \right)^2 \zeta y \psi_1(y) \quad (4.85)$$

where the number of equivalent electrons ζ is 3 for ground electronic states and 1 for excited states and y is the reduced energy of the incoming electrons:

$$y = \frac{I - E_i}{k_B T_e}, \quad (4.86)$$

and the function ψ_1 is:

$$\psi_1(y) = \frac{\exp(-y)}{1 + y} \left\{ \frac{1}{20 + y} + \ln \left[1.25 \left(1 + \frac{1}{y} \right) \right] \right\} \quad (4.87)$$

Panesi [58, 167] implemented another model for electron impact ionisation that is also based on the Drawin cross sections. For this model the ionisation rate coefficients are calculated by the optically allowed expression presented in Equation 4.68 with $\alpha = 1$ and $a = (I - E_i)/(k_B T_e)$.

Bound-bound radiative transitions

Bound-bound radiative transitions have the following form:

$$X_j \rightleftharpoons X_i + h\nu \quad (4.88)$$

where the emitted photon energy is equivalent to the energy difference between the two levels:

$$h\nu = E_j - E_i \quad (4.89)$$

The net population rate of level i due to bound-bound radiative transitions (BBRT) is:

$$\left(\frac{dN_i}{dt} \right)_{\text{BBRT}} = \sum_{j>i} \Lambda_{j,i} A(j, i) N_j - \sum_{j< i} \Lambda_{i,j} A(i, j) N_i \quad (4.90)$$

where $A(i, j)$ is the spontaneous transition probability from level i to level j and $\Lambda_{i,j}$ is the associated escape factor. For atomic radiators, the total transition probability between two nonequilibrium electronic levels is calculated by averaging the degeneracy weighted transition probabilities for all transitions between the two levels:

$$A(i,j) = \frac{\sum_{i'} \sum_{j'} g'_i A(i', j')}{\sum_{i'} \sum_{j'} g'_i} \quad (4.91)$$

where i' and j' denote sub-levels belonging to grouped-levels i and j respectively. For diatomic radiators, the total transition probability between two nonequilibrium electronic levels can be calculated either from radiative lifetimes $\gamma_{i,j}$ where available:

$$A(i,j) = \frac{1}{\gamma_{i,j}} , \quad (4.92)$$

or by averaging over the weighted vibrational transition probabilities [66]:

$$A(i,j) = \frac{\sum_{v_i} Q_{\text{vib},v_i} \sum_{v_j} A_{\text{vib.}}(v_i, v_j)}{\sum_{v_i} Q_{\text{vib},v_i}} \quad (4.93)$$

where Q_{vib,v_i} is the vibrational partition function for vibrational level v_i and $A_{\text{vib.}}(v_i, v_j)$ is the vibrational transition probability corresponding to the v_i, v_j band. The inverse process of radiative absorption is accounted for by the escape factor Λ that is the ratio of re-absorbed to emitted radiative energy²:

$$\Lambda = \frac{E_{\text{abs.}}}{E_{\text{em.}}} \quad (4.94)$$

As radiative re-absorption is determined by solving the radiation transport equations, the introduction of an escape factor here implies that the collisional-radiative and radiative transport equations should be solved in a coupled manner. Unfortunately such a procedure is computationally prohibitive, and therefore the escape factor is approximated in the present work — specifically, solutions with optically thick and optically thin transitions are presented, providing approximate lower and upper bounds for the solution space.

4.3.2 Master equation formulation and solution

The implemented master equation for an electronic level i is:

²An escape factor of one represents an optically thin transition where no re-absorption occurs, while an escape factor of zero represents an optically thick transition where complete re-absorption occurs.

$$\begin{aligned}
\frac{\partial N_i}{\partial t} = & \underbrace{\sum_{j \neq i} K_e(j, i) N_j N_e - \sum_{j \neq i} K_e(i, j) N_i N_e}_{\text{electron impact excitation}} \\
& + \underbrace{\sum_{j \neq i} K_M(j, i) N_j N_M - \sum_{j \neq i} K_M(i, j) N_i N_M}_{\text{heavy particle impact excitation}} \\
& + \underbrace{K_e(c, i) N_c N_e^2 - K_e(i, c) N_i N_e}_{\text{electron impact ionisation}} + \underbrace{K_e(d, i) N_d N_e - K_e(i, d) N_i N_e}_{\text{electron impact dissociation}} \\
& + \underbrace{\sum_{j > i} \Lambda_{j,i} A(j, i) N_j - \sum_{j < i} \Lambda_{i,j} A(i, j) N_i}_{\text{radiative excitation}}
\end{aligned} \tag{4.95}$$

As quenching or exchange reactions amongst different species are not considered in the present work, a linear QSS system can be formulated independently for each nonequilibrium radiator. For a radiator with N_{levels}^* nonequilibrium electronic levels³, the QSS system is formed by considering the master equations (see Equation 4.95) for non-ground states in the QSS limit (see Equation 4.51) with closure provided by the total population of the radiator (see Equation 4.52). The resulting system can be expressed in matrix form as:

$$\mathbf{M}\vec{x} = \vec{b} \tag{4.96}$$

where \mathbf{M} is a square matrix of dimension N_{levels}^* and \vec{x} and \vec{b} are vectors of dimension N_{levels}^* . The elements of \mathbf{M} are:

$$\begin{aligned}
\mathbf{M}(i=1, j) &= 1 + \sum_{j^*}^{N_{\text{eqs}}} f_{\text{eq}, j^*} \\
\mathbf{M}(i \neq 1, j=i) &= - \left[\sum_{k \neq i} (K_M(i, k) N_M + K_e(i, k) N_e) + K_e(i, c) N_c \right. \\
&\quad \left. + K_M(i, d) N_M + K_e(i, d) N_e + \sum_{k < i} (\Lambda_{i,k} A(i, k)) \right] \\
\mathbf{M}(i \neq 1, j \neq i) &= \begin{cases} K_e(j, i) N_e + K_M(j, i) N_M & \text{for } j < i \\ K_e(j, i) N_e + K_M(j, i) N_M + \Lambda_{j,i} A(j, i) & \text{for } j > i \end{cases}
\end{aligned} \tag{4.97}$$

and the elements of \vec{b} are:

³As will be discussed, the number of nonequilibrium electronic levels N_{levels}^* is not necessarily the total number of electronic levels N_{levels}

$$\begin{aligned}\vec{b}(i=1) &= N_s \\ \vec{b}(i \neq 1) &= -K_e(i, c)N_e - K_M(i, d)N_M - K_e(i, d)N_e - \Lambda_{c,i}A(c, i)N_+N_e\end{aligned}\quad (4.98)$$

where N_s is the total species number density from the CFD solver. The elements of \vec{x} are the nonequilibrium level number densities:

$$\vec{x}(i) = N_i \quad (4.99)$$

The matrix line corresponding to the ground state ($i = 1$) is the population summation from Equation 4.52, while the remaining matrix lines are each of the master equations from Equation 4.95. As mentioned previously, the nonequilibrium levels may be a sub-set of the electronic levels for the species. A level not considered by the collisional-radiative model with index j^* can be equilibrated with a nonequilibrium level j by the Boltzmann equation:

$$N_{j^*} = N_j \frac{Q_{\text{int},j^*}}{Q_{\text{int},j}} = N_j f_{\text{eq.},j^*} \quad (4.100)$$

where Q_{int,j^*} and $Q_{\text{int},j}$ are the internal partition functions of the equilibrated and nonequilibrium levels respectively, and the ratio of these two partition functions is defined as the Boltzmann equilibrium factor $f_{\text{eq.},j^*}$. To correctly account for the level equilibration in the collisional-radiative model, the $M(i = 1, j)$ matrix elements must include the sum of all Boltzmann equilibrium factors for nonequilibrium level j :

$$\sum_{j^*}^{N_{\text{eqs}}} f_{\text{eq.},j^*} \quad (4.101)$$

Equation 4.96 can then be easily solved via direct matrix inversion:

$$\vec{x} = M^{-1} \vec{b} \quad (4.102)$$

where M^{-1} is calculated via Gaussian elimination in the current implementation of the model. At low temperatures, however, there are insufficient collisions for the QSS condition (Equation 4.51) to remain valid, and the results of Equation 4.102 cannot be used. Therefore in the present work the electronic levels of nonequilibrium radiators are assumed to be in Boltzmann distributions for free electron temperatures of 2,000 K and under.

4.3.3 Collisional-radiative model for N₂–O₂ mixtures

Before deciding upon an appropriate collisional-radiative model for N₂–O₂ mixtures, it is instructive to consider a typical Earth re-entry shock layer. Figures 4.3a and 4.3b present post-shock species number density and radiative emission profiles respectively for the Fire II $t = 1634$ s

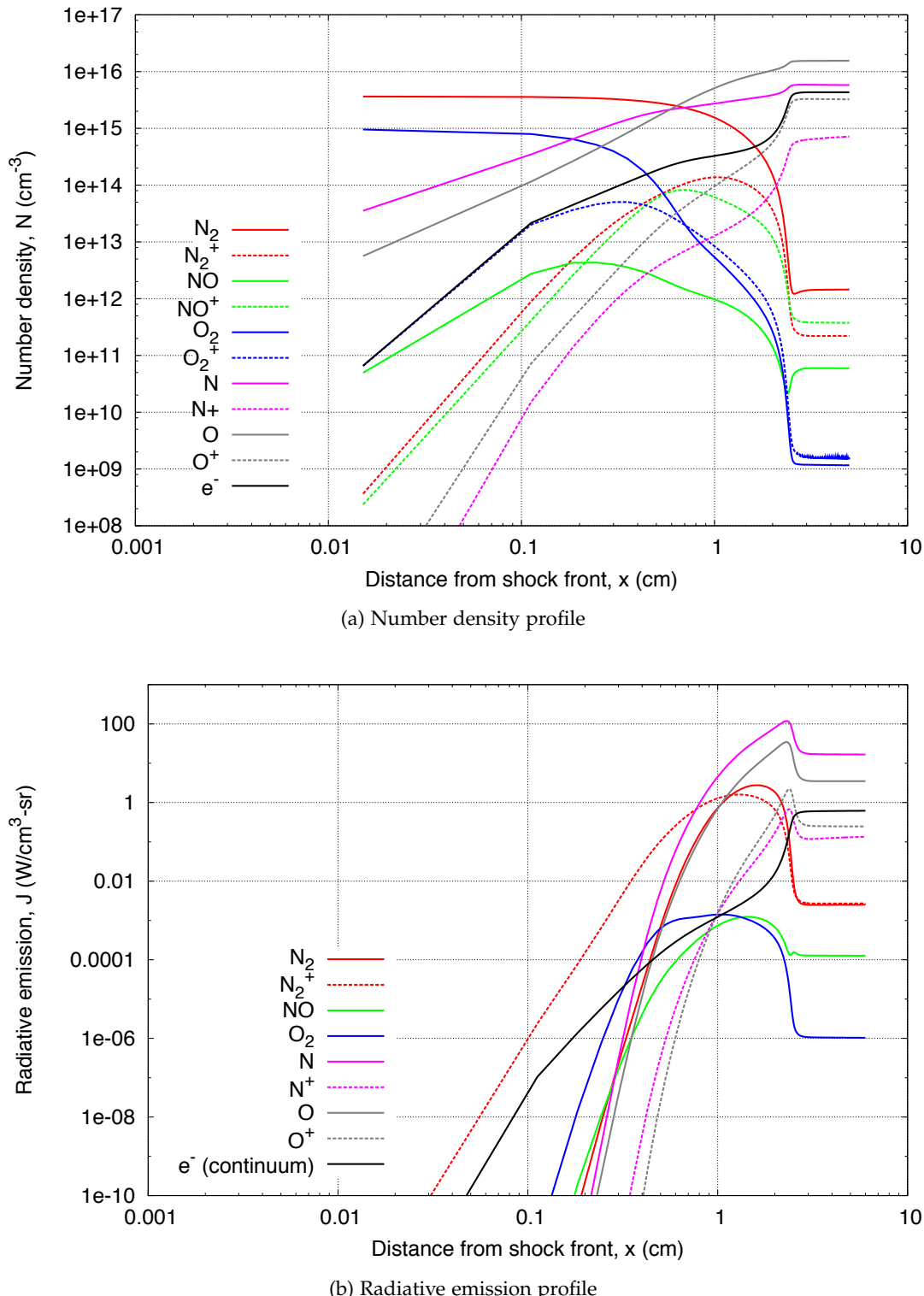


Figure 4.3: Post-shock species number density and radiative emission profiles along the stagnation streamline of the Fire II $t = 1634$ s condition ($p_\infty = 2 \text{ Pa}$, $T_\infty = 195 \text{ K}$, $u_\infty = 11,360 \text{ m/s}$).

condition. For this analysis, the electronic states of the radiators are assumed to be populated by Boltzmann distributions. Immediately behind the shock, O_2 rapidly dissociates and quickly forms a large population of O atoms, while N_2 dissociation proceeds at a slightly slower rate, leading to significant N_2 and N_2^+ radiation up to 2 cm behind the shock. The radiative emission of N_2 and N_2^+ , however, is quickly exceeded by the lines of N and O as the heavily dissociated and partially ionised equilibrium state is approached. As bound-bound transitions of NO, O_2 , N^+ and O^+ only make minor contributions to the radiative emission, it is sufficient to consider the electronic levels of these species as being populated by Boltzmann distributions. Conversely the radiative emission from N_2 , N_2^+ , N and O bound-bound transitions are significant, and the electronic levels of these species should be calculated via collision-radiative modelling. Furthermore, as the free electron number density is almost the same order of magnitude as that of the heavy particles, reactions due to heavy particle impact can be omitted.

(a) Atomic species: N and O

The collisional processes considered for the atomic species N and O are electron impact excitation and ionisation, and the radiative processes considered are bound-bound optically allowed transitions. Table 4.3 summarises the implemented rate coefficients for each of these mechanisms. Where more than one model are presented for a mechanism, they are listed in order of preference (*e.g.* for the electron impact excitation of N, the rates of Frost *et al.* [168] are preferred with the remaining transitions described by the semi-empirical model of Gryzinski [163]). In the present work all the levels presented in Tables B.2 and B.3 for N and O respectively are considered as nonequilibrium levels.

For the radiative transitions, the transition probabilities $A(i,j)$ for the nonequilibrium levels are calculated using Equation 4.91 where the individual line transition probabilities are obtained from the NIST Atomic Species Database [80] (see Table 3.5). For the electron impact transitions, the rate coefficients $K_e(i,j)$ and $K_e(i,c)$ are either calculated using semi-empirical models or obtained directly from the literature in the form of curve-fits.

Although all electron impact excitation and ionisation rates for N and O are able to be calculated by the previously-described semi-empirical models, the hydrogenic assumptions of these models are not appropriate for transition originating from the inner core of electronic levels [29]. Rates derived from experimental measurements or theoretical calculations are therefore preferred for transitions originating from the ground and low lying metastable states. Fortunately, experimental measurements and quantum mechanical calculations of these transitions are much simpler and more readily available than for the high lying levels.

Table 4.3: Summary of the collisional-radiative mechanisms implemented for N and O.

Species	Electronic levels	CR mechanisms	Models
N	All	Electron impact excitation	(a) Frost <i>et al.</i> [168] (b) Gryzinski [163]
		Electron impact ionisation	(a) Soon and Kunc [169] (b) Drawin (Reference [58])
		Radiative decay	NIST Atomic Spectra Database [80]
O	All	Electron impact excitation	(a) Zatsarinny and Tayal [170] (b) Gryzinski [163]
		Electron impact ionisation	(a) Soon and Kunc [169] (b) Drawin (Reference [58])
		Radiative decay	NIST Atomic Spectra Database [80]

(a) Electron impact excitation of N

Frost *et al.* [168] performed R-matrix calculations for N and N⁺ electron impact excitation transitions from the first 3 energy levels to all levels with principle quantum number n less than 3. Panesi [171] demonstrated improved agreement with the EAST shock tube data when implementing this model for N. The rate coefficient is given as a function of the effective collision strength $\gamma_{i,j}$:

$$K_e(i,j) = 2\sqrt{\pi}\alpha c a_0^2 \sqrt{\frac{E_H}{kT_e}} \frac{\gamma_{i,j}(T_e)}{g_i} \exp\left(-\frac{\Delta E_{i,j}}{kT_e}\right), \quad (4.103)$$

where α is the fine structure constant and the effective collision strength $\gamma_{i,j}$ has been curve fitted against the tabulated values provided by Frost in the range $0.5 \leq T_e \leq 12.0$ eV.

Bultel *et al.* [55] presented electron impact excitation and ionisation rates for the ground and metastable states of N and O. These rates were presented as generalised Arrhenius curve-fits in the temperature range $2,000 \leq T \leq 10,000$ K and were implemented in the collisional-radiative model of Panesi [58]. The excitation rates from the ground state of nitrogen are based on the R-matrix calculations of Berrington [172].

Figure 4.4 compares the electron impact excitation rate coefficient for a selection of optically allowed and optically forbidden transitions of atomic nitrogen for which Frost *et al.* [168] present rate coefficients. The indices of the initial i and final j electronic levels are given in the y-axis label in the form $K_e(i,j)$. For the ground to first and second excited level transitions, Figures 4.4a and 4.4b respectively, the Bultel rates (obtained from Berrington [172]) are more than two orders of magnitude less than the rates of Frost. This is surprising as both sets of rates are based on theoretical R-matrix calculations, although the Berrington calculations precede those of Frost by 23 years. The semi-empirical Gryzinski and Drawin models differ by approximately two orders

of magnitude and bound the Frost results. For these transitions the theoretical calculations of Frost *et al.* [168] are preferred as they are more recent than those of Berrington [172]

The Frost, Drawin and Gryzinski models exhibit qualitative agreement for the remaining transitions shown, Figures 4.4c to 4.4h. Quantitatively, it is encouraging to observe that the data of Frost is bounded by the Gryzinski and Drawin models for almost all transitions, although there is no trend as to which forms the upper or lower bound. For the 1-5 and 3-15 transitions in Figures 4.4c and 4.4f, for example, the Gryzinski data shows exceptional agreement with the calculations of Frost. In contrast, for the 1-20 and 3-20 transitions in Figures 4.4c and 4.4h, the Gryzinski model substantially underestimates the data of Frost while the Drawin model shows good agreement. Furthermore the semi-empirical models differ by up to two orders of magnitude for some transitions. In the present work the accurate calculations of Frost *et al.* [168] are preferred where available, with the remaining transitions described by the Gryzinski [163] model. The decision to implement the Gryzinski model in preference to the Drawin model is based on the findings of Panesi [58, 171], where the Gryzinski model gave improved agreement with the air shock tube spectroscopy experiments performed in the EAST facility.

(b) Electron impact ionisation of N

Johnston [19] implemented the ionisation rate coefficients proposed by Kunc and Soon [173] for the ground and first two excited levels of atomic nitrogen. The rate coefficients are calculated as:

$$K_e(i, c) = 1.0 \times 10^{-8} \left[\frac{I_H}{I - E_i} \right] \frac{Q_i}{2l_i + 1} \exp(-\beta) G_i(\beta) \quad (4.104)$$

where,

$$G_i(\beta) = \sqrt{\frac{\beta}{\beta + 1}} \frac{A}{\beta + \chi}, \quad (4.105)$$

and,

$$\beta = \frac{I - E_i}{kT_e}. \quad (4.106)$$

The parameter I_H is the ionisation energy of the hydrogen energy (Rydberg energy), l_i is the angular momentum quantum number of the level i , A and χ are fitting constants for the species and G_i is level dependent angular factor. For atomic nitrogen A is equal to 27.71, χ is equal to 5.58 and Q_i is equal to 3 for the ground state and 3/2 for the first and second excited states. This expression is a curve-fit based on the rate coefficient derived from experimentally measured electron impact ionisation cross sections for the ground state of N.

Panesi [58] implemented the ionisation rate coefficients presented by Bultel *et al.* [55], which were obtained from the compilation of Tawara and Kato [174] and the combined binary-encounter Bethe (BEB) and scaled plane-wave Born (PWB) calculations of Kim and Desclaux [175]. The rates

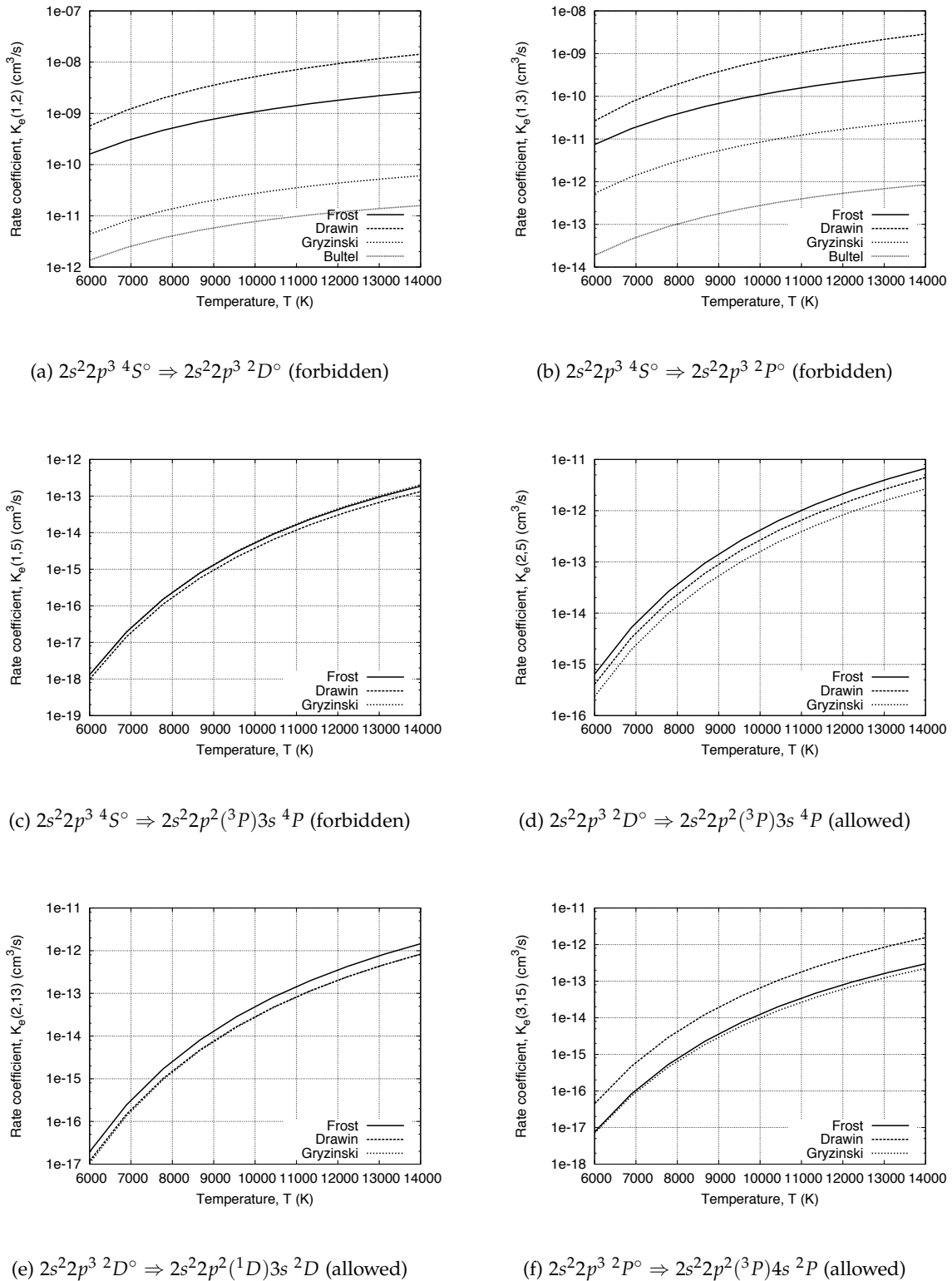


Figure 4.4: Comparison of electron impact excitation rate coefficients for atomic nitrogen.

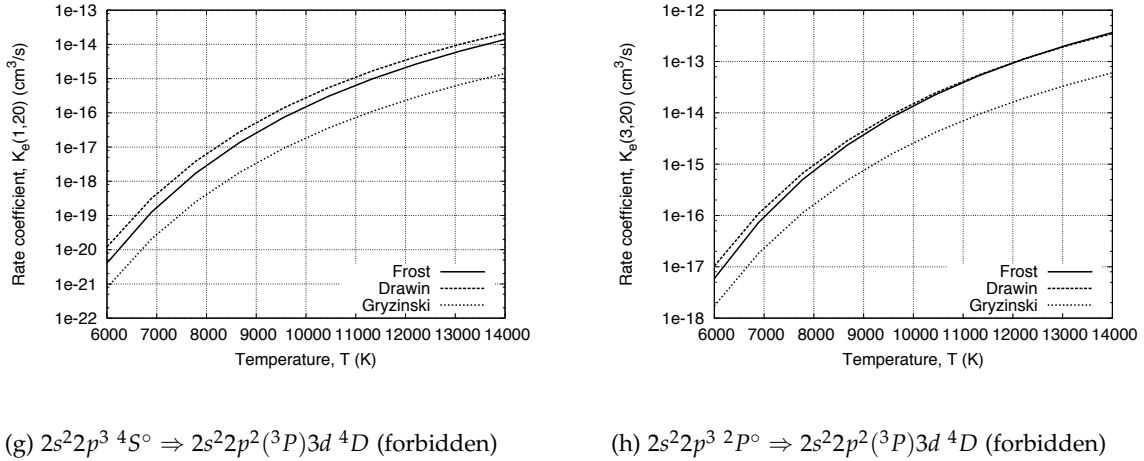


Figure 4.4: (Continued) Comparison of electron impact excitation rate coefficients for various transitions of N.

for the ground and first two excited states of N were presented as generalised Arrhenius curve-fits in the temperature range $2,000 \leq T_e \leq 10,000$ K.

Figure 4.5 compares the electron impact ionisation rate coefficient for various transitions of N. As was observed for the electron impact excitation rates, the Bultel generalised Arrhenius expressions substantially underestimate the rates of all other models — by as much as six orders of magnitude for ionisation of the metastable states, Figures 4.5b and 4.5c. It is unclear how the Bultel rates are able to be valid in the quoted $2,000 \leq T_e \leq 10,000$ K temperature range when the minimum electron temperature considered in the calculations of Kim and Desclaux [175] is 12 eV ($\approx 140,000$ K). The Drawin models implemented by Johnston [19] and Panesi [58] bound the experimentally fitted model of Soon and Kunc [169], with Panesi's implementation being in closer agreement. Although the difference between the two Drawin models decreases as ionisation from higher levels and low electron temperatures is considered (see Figure 4.5d), Johnston's implementation is between approximately 2 and 100 times smaller for all levels. Therefore in the present work the electron impact ionisation coefficients of Soon and Kunc [169] are preferred for the first three levels, while the Drawin model implemented by Panesi [19] is used for the remaining levels.

(a) Electron impact excitation of O

Zatsarinny and Tayal [170] calculated electron impact excitation rates for the ground and first two excited states of atomic oxygen using a *B*-spline *R*-matrix approach. The forward rate coefficients for the Zatsarinny and Tayal model are calculated as:

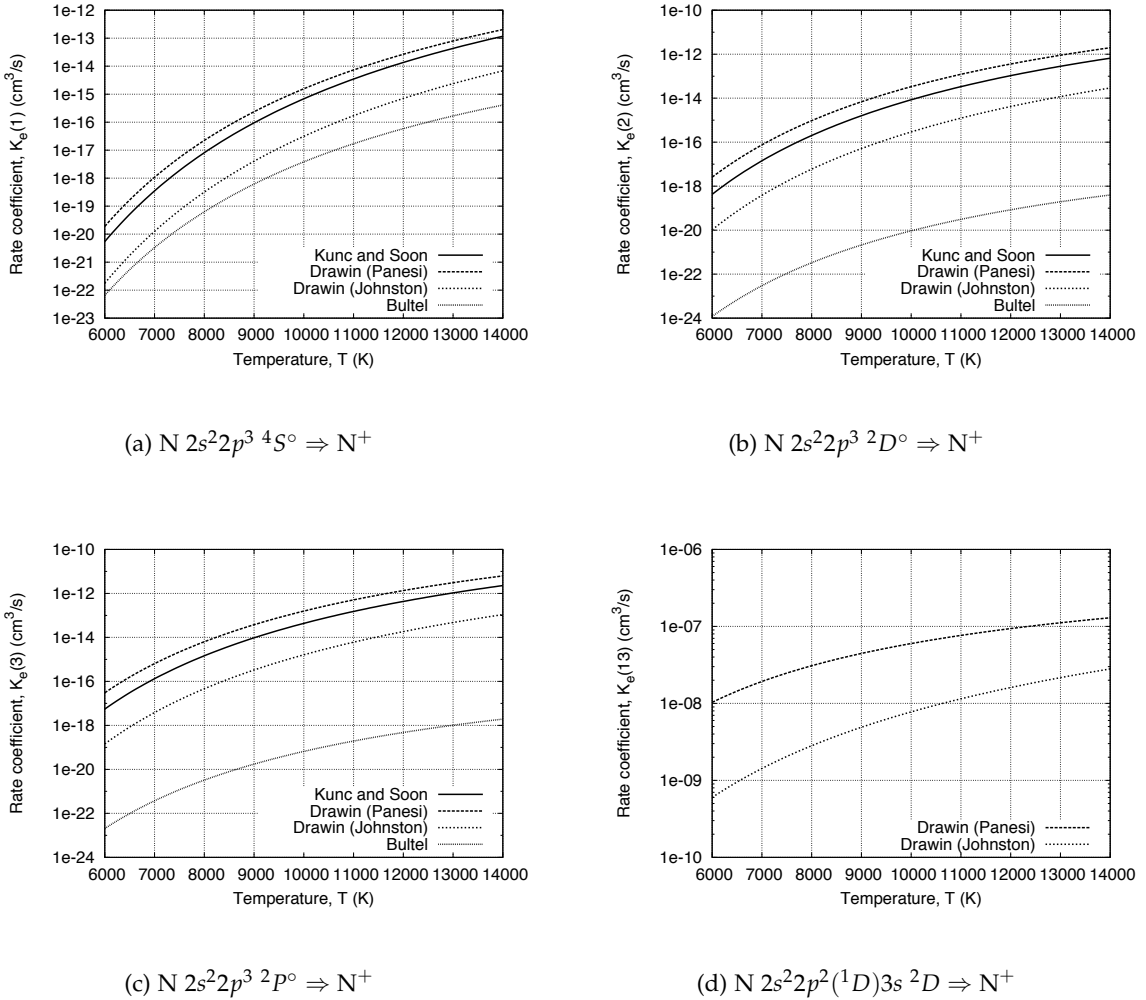


Figure 4.5: Comparison of electron impact ionisation rate coefficients for atomic nitrogen.

$$K_e(i,j) = \frac{8.629 \times 10^{-6}}{g_i \sqrt{T_e}} \gamma_{ij}(T_e) \exp\left(\frac{-\Delta E_{ij}}{kT_e}\right) \quad (4.107)$$

where the dimensionless effective collision strength γ_{ij} is tabulated as a function of the free electron temperature in Reference [170]. The Zatsarinny and Tayal [170] data was the preferred source of accurate atomic oxygen electron impact excitation rates in the collisional-radiative model proposed by Johnston [19].

Panesi [58] implemented the electron impact excitation rate coefficients presented by Bultel *et al.* [55] which are based on the literature survey of Itikawa and Ichimura [176]. Electron impact excitation rate coefficients for transitions from the ground state to the two metastable states of atomic oxygen were presented as generalised Arrhenius curve-fits in the temperature range $2,000 \leq T_e \leq 10,000$ K.

Figure 4.11 compares the electron impact excitation rate coefficient for various transitions of atomic oxygen for which Zatsarinny and Tayal [170] present data. For the transitions to the metastable states, Figures 4.6a and 4.6b, the Drawin and Gryzinski models substantially overestimated the theoretical calculations of Zatsarinny and Tayal. Such a discrepancy is to be expected for these inner core transitions due to the hydrogenic assumptions of the Drawin and Gryzinski models. The accuracy of the Bultel rates is questionable as they more closely follow the approximate models rather than the theoretical calculations of Zatsarinny and Tayal. Although the *B*-spline *R*-matrix calculations of Zatsarinny and Tayal are bounded by the semi-empirical models for most transitions, for some forbidden transitions such as 2 – 5 and 3 – 7, Figures 4.6d and 4.6f, the semi-empirical models underestimate the theoretical rates by at least an order of magnitude for the temperature range considered. Some some transitions such as 1-16 and 1-17, Figures 4.6g and 4.6h, the Gryzinski model closely matches the Zatsarinny and Tayal calculations, whilst for others such as 1-20, Figure 4.6i, the Drawin model shows exceptional agreement. The Drawin and Gryzinski models show considerable variability in their relative magnitudes, being within a factor of 2 of each other for some transitions and in excess of 10^4 for some transitions to high lying states (*e.g.* Figures 4.6i and 4.6j). As for atomic nitrogen, we must again bear in mind that Panesi [58, 171] found improved agreement with experiment when using the Gryzinski model. Therefore in the present work the Zatsarinny and Tayal [170] rate coefficients are preferred where available, while the Gryzinski [163] model is applied to the remaining transitions.

Electron impact ionisation of O

Johnston [19] implemented the ionisation rate coefficients proposed by Soon and Kunc [169] for the ground and first two excited levels of atomic oxygen. The rate coefficients are calculated as described in Equations 4.104 to 4.106, where $A = 30.52$ and $\chi = 4.0$ for levels $i=1, 2$ and 3 of O. This expression is a curve-fit based on the rate coefficient derived from experimentally measured electron impact ionisation cross sections for the ground state of O.

Panesi [58] implemented the ionisation rate coefficients presented by Bultel *et al.* [55], which were obtained from the compilation of Tawara and Kato [174] and the combined binary-encounter Bethe (BEB) and scaled plane-wave Born (PWB) calculations of Kim and Desclaux [175]. The rates for the ground and first two excited states of O were presented as generalised Arrhenius curve-fits in the temperature range $2,000 \leq T_e \leq 10,000$ K.

Figure 4.7 compares the electron impact ionisation rate coefficient for various transitions of O. Again, the Bultel rates are anomalous and are not thought to be accurate for the temperature range of present interest. The two Drawin models bound the experimentally fitted model of Kunc and Soon [173], with Panesi's implementation being in closer agreement, especially for ionisation of the $2s^22p^4\ ^1S$ multiplet (see Figure 4.7c). Similarly as for atomic nitrogen, Johnston's

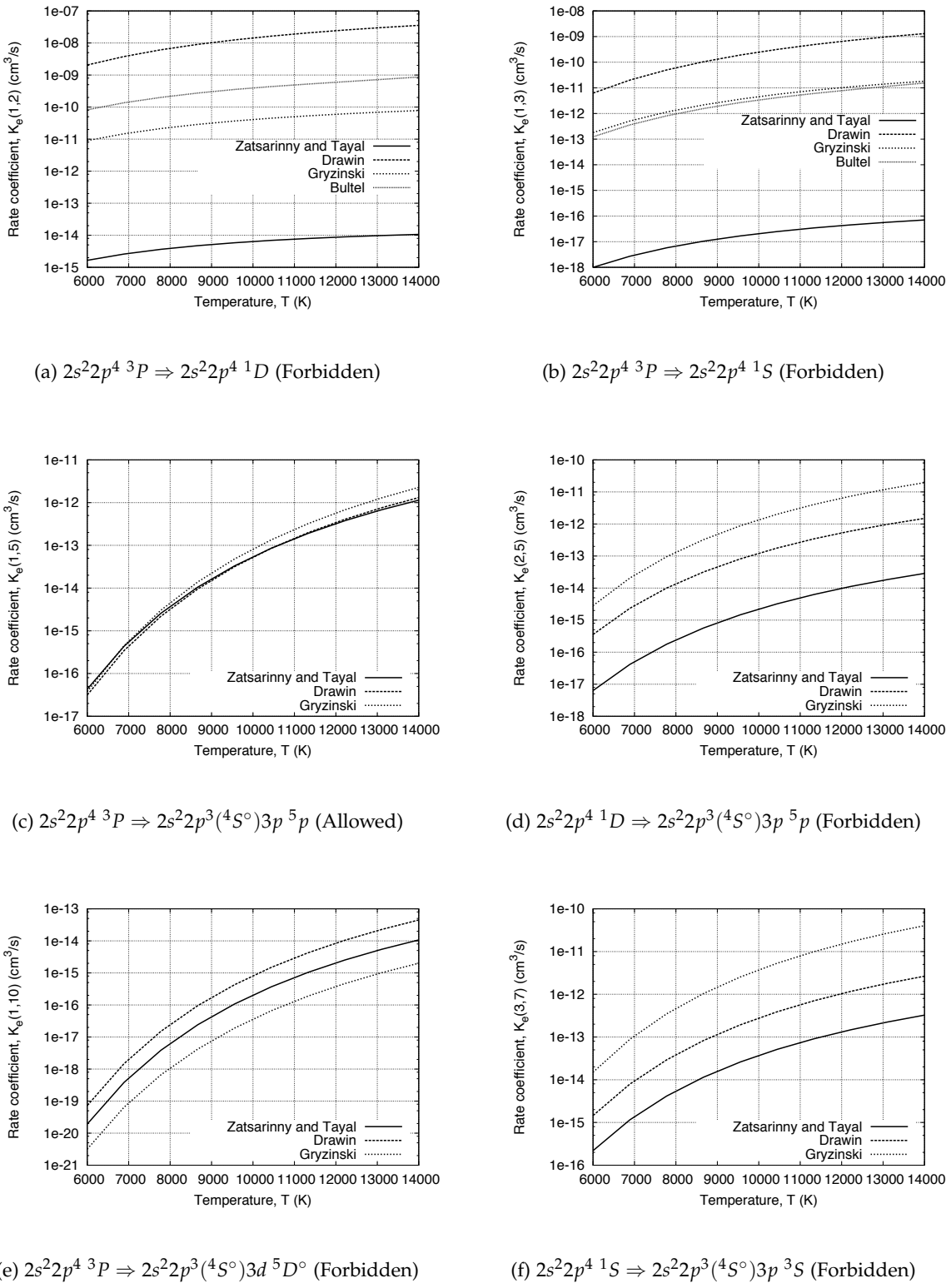


Figure 4.6: Comparison of electron impact excitation rate coefficients for atomic oxygen.

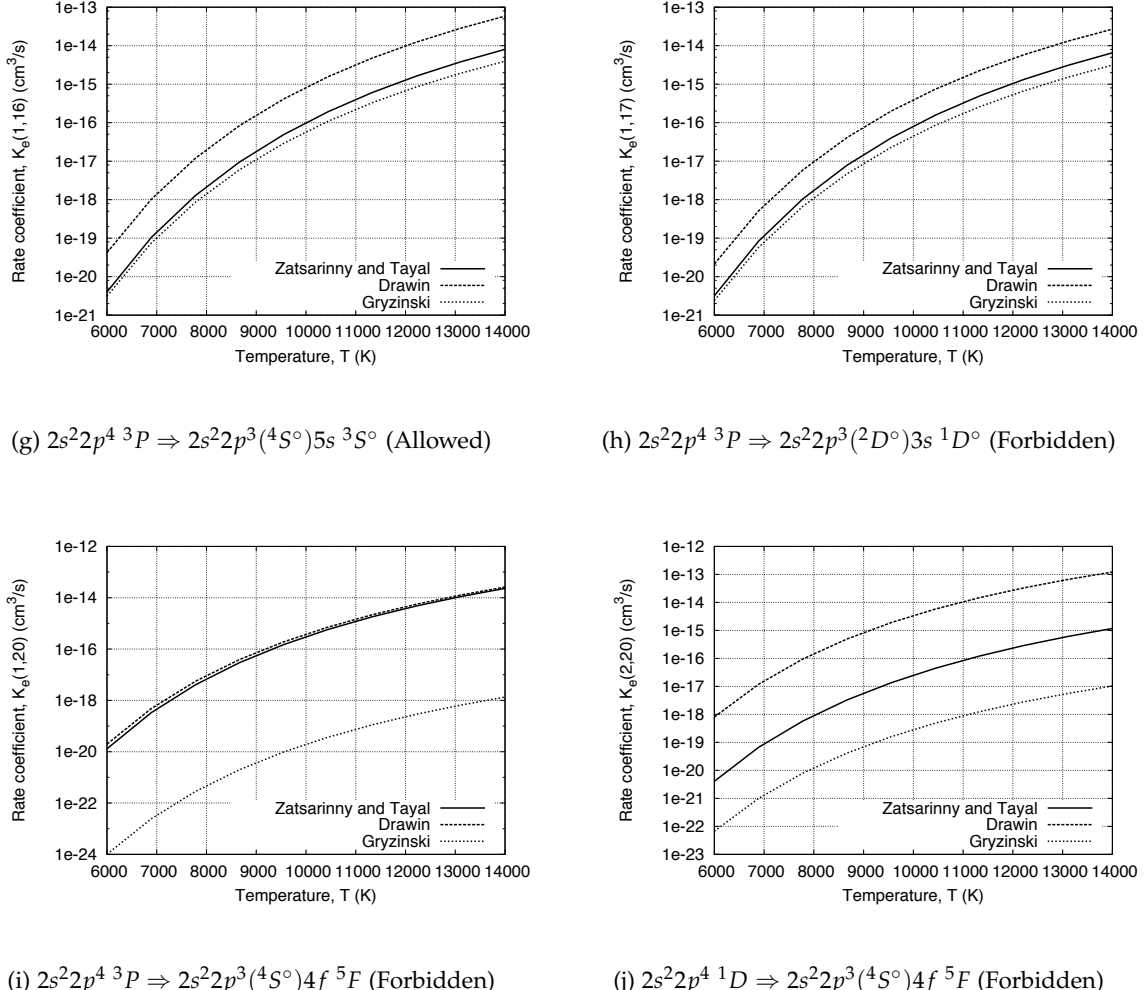


Figure 4.6: (Continued) Comparison of electron impact excitation rate coefficients for atomic oxygen.

implementation of the Drawin cross sections is between approximately 2 and 100 times smaller than Panesi's implementation for all levels. Therefore in the present work the electron impact ionisation coefficients of Kunc and Soon [173] are preferred for the first three levels, while the Drawin model implemented by Panesi [19] is used for the remaining levels.

(b) Diatomic species: N_2 and N_2^+

Johnston [19] presented collisional-radiative models for N_2 and N_2^+ compiled from both theoretically calculated and experimentally measured rate-coefficients in the literature. The majority of the collisional rate coefficients are based on the theoretical calculations of Teulet *et al.* [177], however other more accurate data was preferred where available. Since Johnston formulated

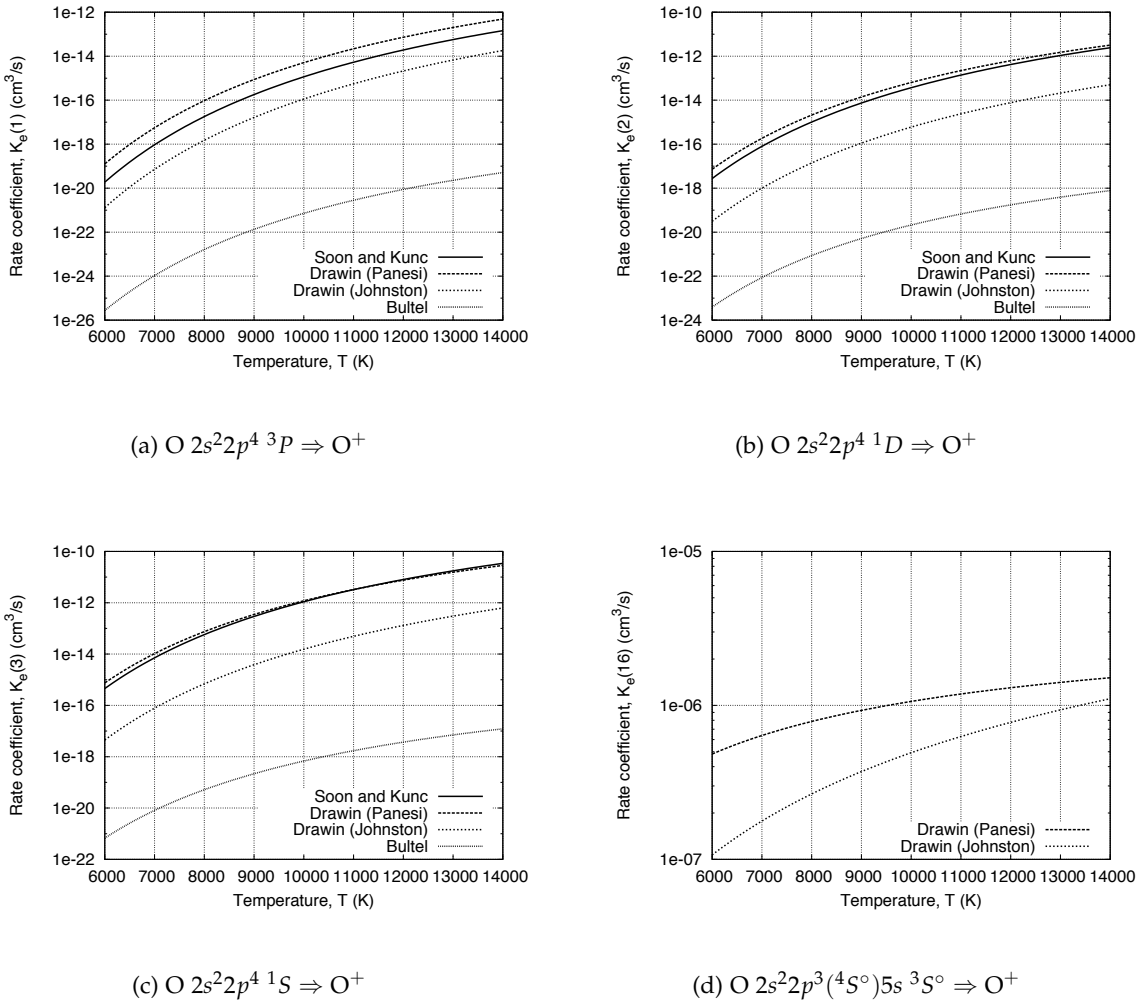


Figure 4.7: Comparison of electron impact ionisation rate coefficients for atomic oxygen.

this model, a set of collisional rate coefficients for the diatomic species CN, CO, N₂, N₂⁺, O₂ and NO have been proposed by Park [178, 179]. The rate coefficients are based on experimentally measured cross sections where available, and theoretically estimated otherwise.

The most critical reactions for N₂ and N₂⁺ at Earth re-entry conditions are those populating the upper states of radiative transitions via electron impact excitation. Figure 4.8 compares the electron impact excitation rates populating the B³Π_g state of N₂ (upper state for the First Positive band system), and Figure 4.9 compares the electron impact excitation rates populating the B²Σ_u⁺ state of N₂⁺ (upper state for the First Negative band system). While the two models agree to within a factor of 4 for the N₂ ($X^1\Sigma_g^+$) + e⁻ ⇌ N₂ (B³Π_g) + e⁻ transition, Figure 4.8a, the Park rates are substantially higher than those of Johnston for the other transitions. For the N₂ ($A^2\Pi_u$) + e⁻ ⇌ N₂ (B²Σ_u⁺) + e⁻ transition in Figure 4.9b, for example, the Park rate is

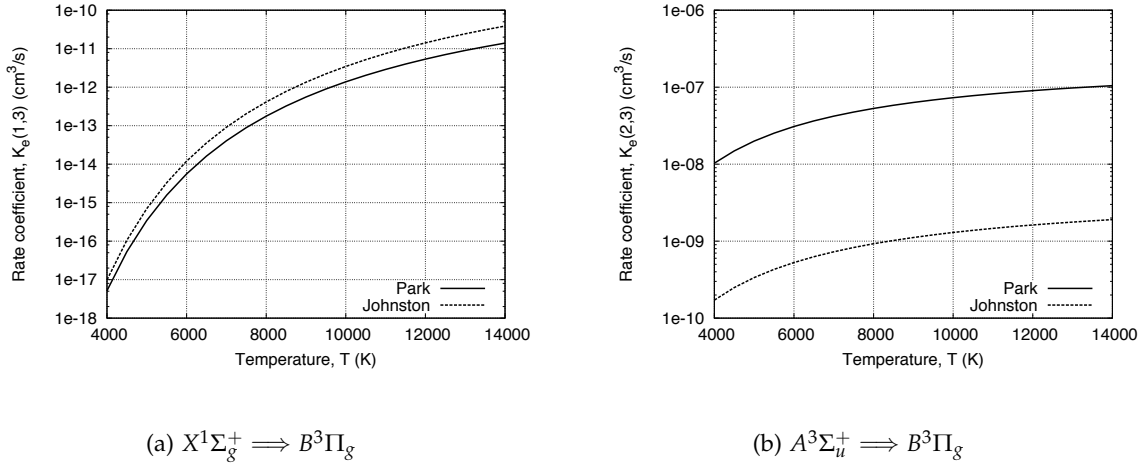


Figure 4.8: Comparison of electron impact excitation rate coefficients for transitions to the $B^3\Pi_g$ state of N_2 .

almost four orders of magnitude greater than the Johnston rate. Although not shown here, the estimated rate of Teulet *et al.* [177] for the $N_2^+ (X^2\Sigma_g^+) + e^- \rightleftharpoons N_2^+ (B^2\Sigma_u^+) + e^-$ transition is quite similar to the Park rate. In Johnston's [19] survey of the literature, this rate of Teulet was found to overestimate those from more accurate theoretical calculations. Furthermore, in Reference [63] the rates of Teulet were required to be reduced by factors of 10 and 70 for N_2 and N_2^+ respectively in order to achieve agreement with experiment. In the present work therefore we choose to adopt the Johnston [19] model. The collisional-radiative models for N_2 and N_2^+ are summarised in § D.4 and D.5 respectively. The nonequilibrium levels considered for N_2 are $X^1\Sigma_g^+$, $A^3\Sigma_u^+$, $B^3\Pi_g$ and $C^3\Pi_u$, while those for N_2^+ are $X^2\Sigma_g^+$, $A^2\Pi_u$, $B^2\Sigma_u^+$ and $C^2\Sigma_u^+$.

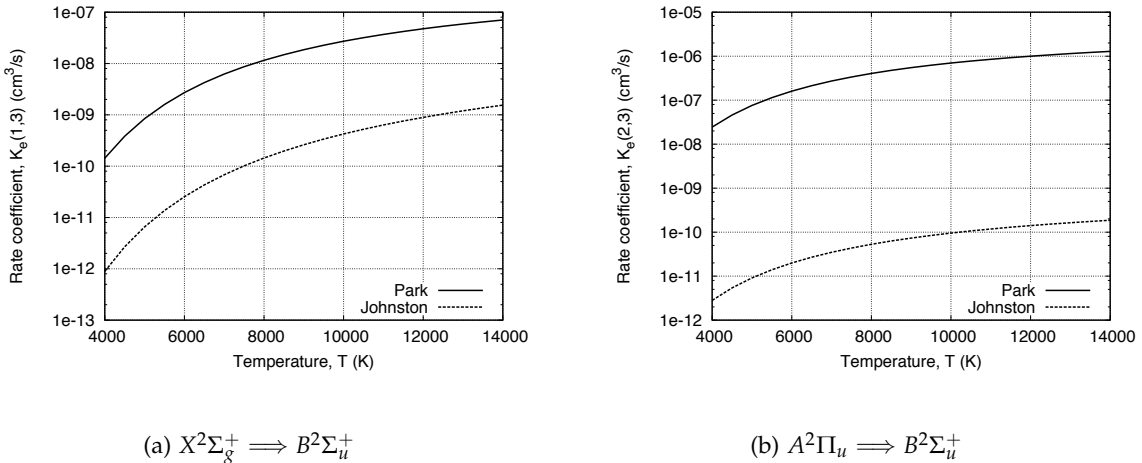


Figure 4.9: Comparison of electron impact excitation rate coefficients for transitions to the $B^2\Sigma_u^+$ state of N_2^+ .

4.3.4 Collisional-radiative model for $\text{CO}_2\text{-N}_2\text{-Ar}$ mixtures

Figures 4.10a and 4.10b present post-shock species number density and radiative emission profiles respectively for a hypothetical high-speed Mars aerocapture condition from the trajectory study of Braun *et al.* [16]. The condition corresponds to that predicted for an aerocapture vehicle with nose radius 10 m at 44.9 km altitude that entered the Martian atmosphere at 9.79 km/s. This point is just prior to peak heating and is characterised by very strong thermochemical nonequilibrium. Behind the shock CO_2 and N_2 quickly dissociate, forming an initial pool of CO and N_2 molecules and C , N and O atoms that allow exchange reactions to begin. At 1 mm behind the shock reactions have only just begun to occur and CN and C_2 systems and continuum transitions dominate the radiative emission. By 3 mm behind the shock dissociation is essentially complete and peak emission occurs, with atomic C lines, the VUV CO band systems and atomic O lines contributing 99% of the radiative emission. At peak emission the next strongest radiators are N , CN , C_2 and Ar , however their emission strength is on average two orders of magnitude less than CO and C . As equilibrium is approached the total radiation drops by an order of magnitude, C , CO and O (in that order) continue to dominate the radiative emission while the relative strength of the continuum transitions increases due to the growing free electron population. The free electron mole-fraction between peak-emission and chemical equilibrium is in the order of 10^{-2} .

Although C , CO and O are by far the strongest radiators when Boltzmann level populations is assumed, the nonequilibrium emission is likely to be significantly less due to radiative depletion of the high lying states. Therefore in the present work we chose to apply the collisional-radiative model to all the significant radiators – C , CO , O , C_2 , N , Ar and CN . Although the free electron number density is lower than for Earth re-entry, electron impact collisional processes should still

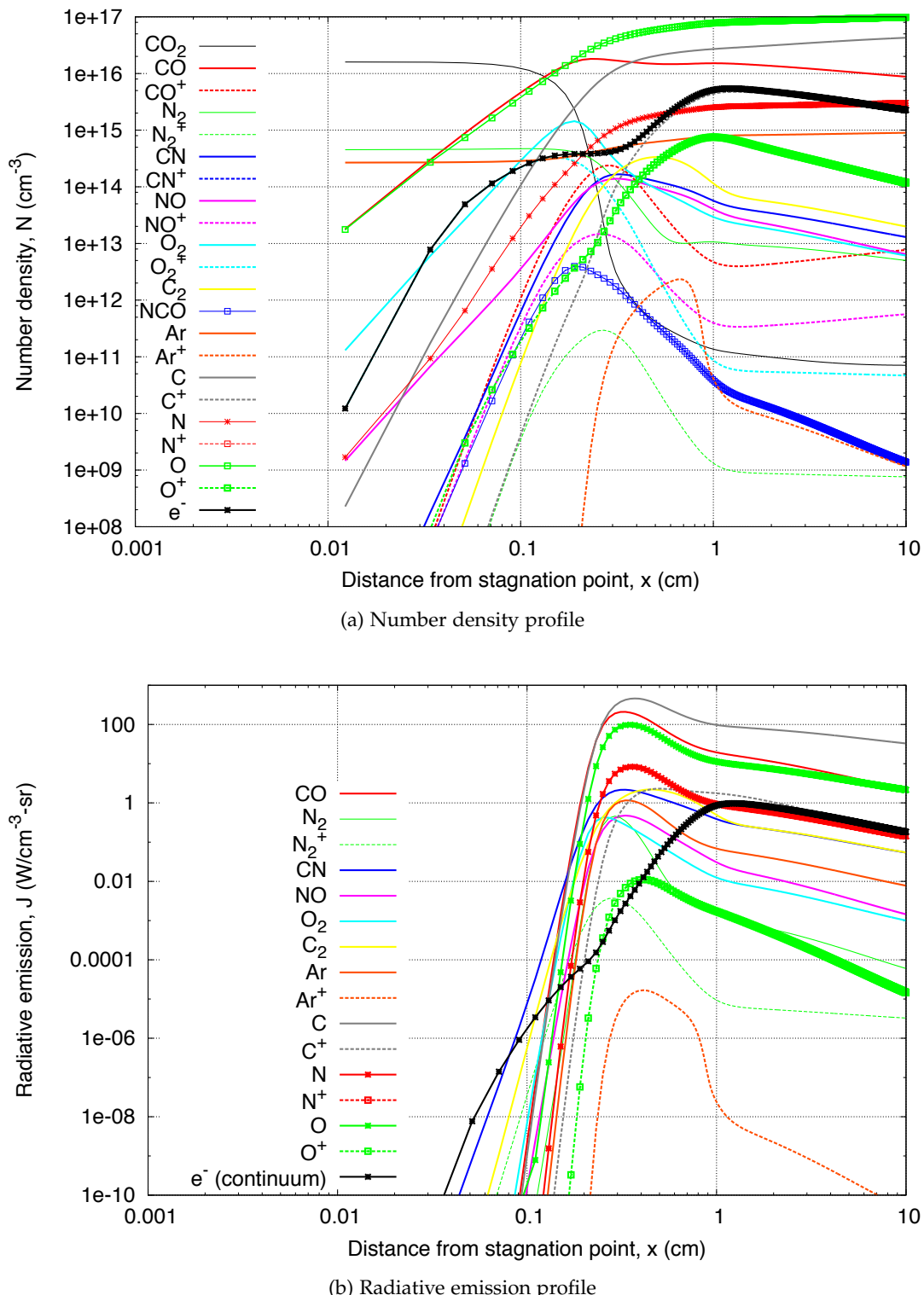


Figure 4.10: Post-shock species number density and radiative emission profiles along the stagnation streamline for a hypothetical Mars aerocapture entry condition ($p_\infty = 6.2 \text{ Pa}$, $T_\infty = 161 \text{ K}$, $u_\infty = 9,440 \text{ m/s}$).

dominate over heavy particle collisions due to their high efficiency. Thus in the present work only electron impact collisional processes will be considered.

Atomic species: Ar, C, N and O

Table 4.4 summarises the implemented rate coefficients for the collisional-radiative mechanisms considered for atomic species in CO₂–N₂–Ar mixtures. Similarly as for N₂–O₂ mixtures, the collisional mechanisms considered for atoms are electron impact excitation and ionisation, and the radiative processes considered are bound-bound optically allowed transitions. As the Drawin [162] cross sections have been shown to be appropriate for calculating non-Boltzmann emission from atomic argon [180, 181], the Drawin model proposed by Panesi [58] is applied to calculate electron impact excitation and ionisation of Ar. For atomic carbon, accurate rate-coefficients are obtained from Suno and Kato [182] for electron impact excitation and ionisation of the ground and metastable states. The remaining transitions described by the semi-empirical model of Gryzinski [163]. The collisional-radiative models selected for N and O in N₂–O₂ mixtures are retained here for application to CO₂–N₂–Ar mixtures. All radiative transition probabilities $A(i,j)$ are calculated using Equation 4.91 where the individual line transition probabilities are obtained from the NIST Atomic Species Database [80] (see Table 3.5).

(a) Electron impact excitation of C

Suno and Kato [182] compiled an extensive electron-impact ionisation, excitation and charge exchange cross section database for carbon atoms and ions. Although the database extends to electron temperatures of 1 keV as it is designed nuclear fusion applications, the presented electron impact excitation data for C is shown to agree well with the experimental data of Dunneath *et al.* [183] and others obtained in the 1 eV electron temperature range of present interest. The data are presented as curve fits for the collision strength Ω_{ij} from which the rate coefficient can be calculated as:

$$K_e(i,j) = \frac{8.010 \times 10^{-8}}{\omega_i \sqrt{T_e}} y \int_1^\infty \Omega_{ij} e^{-yX} dX \quad (4.108)$$

where T_e is in eV, $y = \Delta E_{ij}/T_e$ and $X = E_e/\Delta E_{ij}$.

Figure 4.11 compares the electron impact excitation rate coefficient for various transitions of C. For all transitions except excitation of the ground to first excited state (see Figure 4.11a), the Suno and Kato rates are between 2 and 1000 times larger than the rates predicted by the approximate models. This is in contrast to the electron impact excitation rates of N and O, where the accurate rates for low lying levels was bounded by the approximate models. It is therefore possible that the rates of Suno and Kato are not suitable for the temperature range considered. In the absence of better electron impact excitation data, however, the Suno and Kato rates are

Table 4.4: Summary of the collisional-radiative mechanisms implemented for Ar, C, N and O in CO₂-N₂-Ar mixtures.

Species	Electronic levels	CR mechanisms	Models
Ar	All	Electron impact excitation	Drawin (Reference [58])
		Electron impact ionisation	Drawin (Reference [58])
		Radiative decay	NIST Atomic Spectra Database [80]
C	All	Electron impact excitation	(a) Suno and Kato [182] (b) Gryzinski [163]
		Electron impact ionisation	(a) Suno and Kato [182] (b) Drawin (Reference [58])
		Radiative decay	NIST Atomic Spectra Database [80]
N	All	Electron impact excitation	(a) Frost <i>et al.</i> [168] (b) Gryzinski [163]
		Electron impact ionisation	(a) Soon and Kunc [169] (b) Drawin (Reference [58])
		Radiative decay	NIST Atomic Spectra Database [80]
O	All	Electron impact excitation	(a) Zatsarinny and Tayal [170] (b) Gryzinski [163]
		Electron impact ionisation	(a) Soon and Kunc [169] (b) Drawin (Reference [58])
		Radiative decay	NIST Atomic Spectra Database [80]

preferred for transitions from low lying states while the Gryzinski model is applied to the remaining transitions.

(b) Electron impact ionisation of C

Suno and Kato [182] present the electron impact ionisation cross section for the ground state of atomic carbon in the following form:

$$\sigma = \frac{1 \times 10^{-13}}{IE} \left\{ A_1 \ln(E/I) + \sum_{j=2}^{N_A} A_j \left(1 - \frac{I}{E}\right)^{j-1} \right\} \quad (4.109)$$

where I and E are the ionisation and electron energy in eV and A_j are fitting coefficients. The fitting coefficients have been selected to match the experimental measurements of Brook *et al.* [184]. Unfortunately Brook considered electron energies in the range $7 \leq E \leq 1000$ eV, which is outside the $E \approx 1$ eV range of present interest. In the absence of electron impact ionisation cross sections for the metastable state of atomic carbon, in the present work Equation 4.109 is applied where I is taken as the level-specific ionisation potential. The rate coefficient is then calculated as:

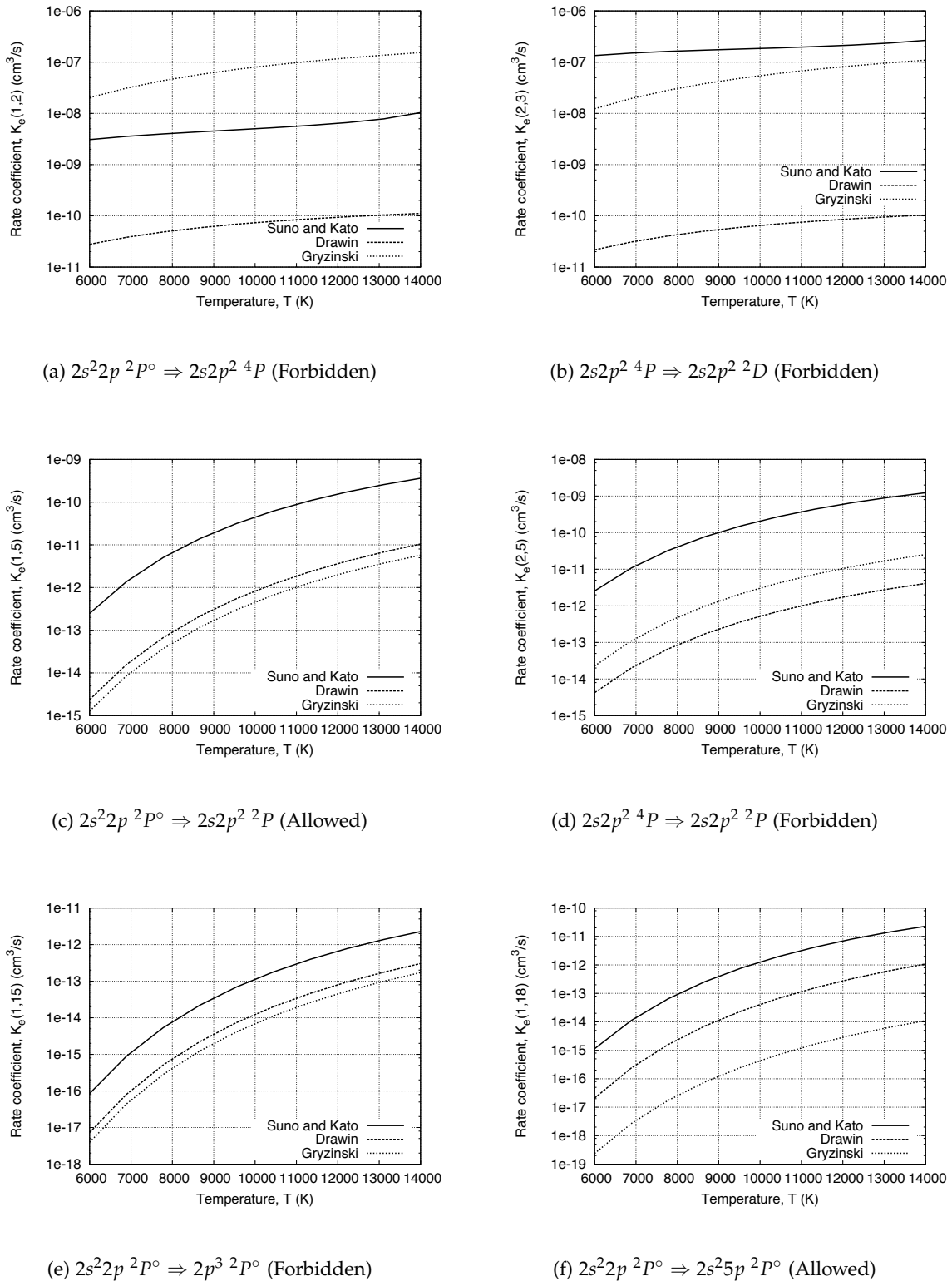


Figure 4.11: Comparison of electron impact excitation rate coefficients for atomic carbon.

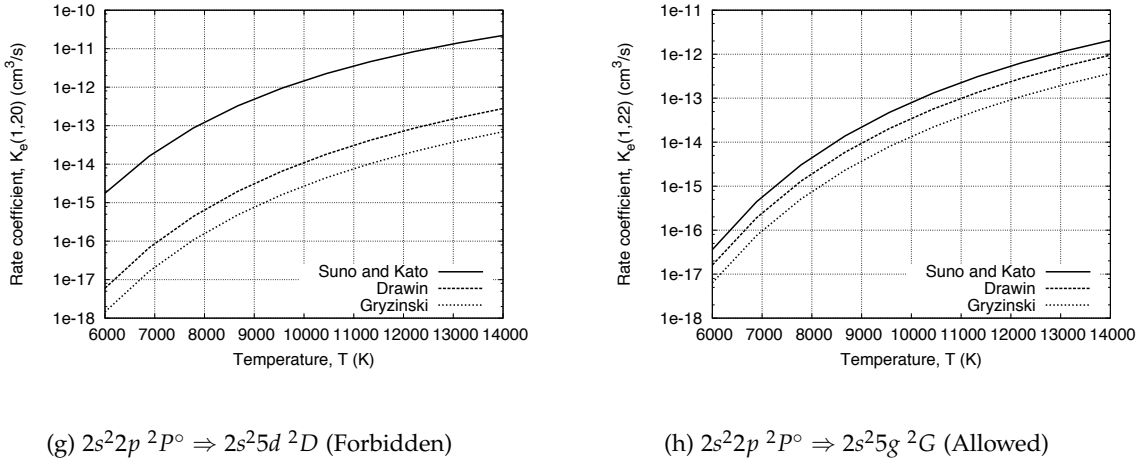


Figure 4.11: (Continued) Comparison of electron impact excitation rate coefficients for atomic carbon.

$$K_e(i, c) = \frac{8.010 \times 10^{-8}}{g_i \sqrt{T_e}} y \int_1^\infty \Omega_i e^{-yX} dX \quad (4.110)$$

where T_e is in eV, $y = I/T_e$, $X = E_e/I$ and collision strength Ω_i for level i is obtained from the cross section in Equation 4.109 via:

$$\Omega_i = \sigma_i \frac{g_i E}{1.1969 \times 10^{-15}} \quad (4.111)$$

Figure 4.12 compares the electron impact ionisation rate coefficient for various transitions of C. The bulk atomic carbon ionisation rate proposed by Park [137] is overlaid in Figure 4.12a for comparison with the ground state rates. The Suno and Kato rates are approximately three orders of magnitude greater than the semi-empirical models, and is similar to the Park rate for the ground state. Similarly as for atomic nitrogen and oxygen, Johnston's implementation of the Drawin cross sections is between approximately 2 and 100 times smaller than Panesi's implementation for all levels. Therefore in the present work the electron impact ionisation coefficients of Suno and Kato [182] are preferred for the first three levels, while the Drawin model implemented by Panesi [19] is used for the remaining levels.

Diatomlic species: C₂, CN and CO

Zalogin [185] proposed a simple collisional-radiative model for C₂, CN and CO. This model was 'tuned' to match the intensity profiles measured for a 3.45 km/s CO₂-N₂ shock tube condition, and was applied with limited success to the 8.5 km/s CO₂-N₂ EAST shock tube condition in Reference [186]. Since this model was formulated, however, a set of collisional-rate coefficients

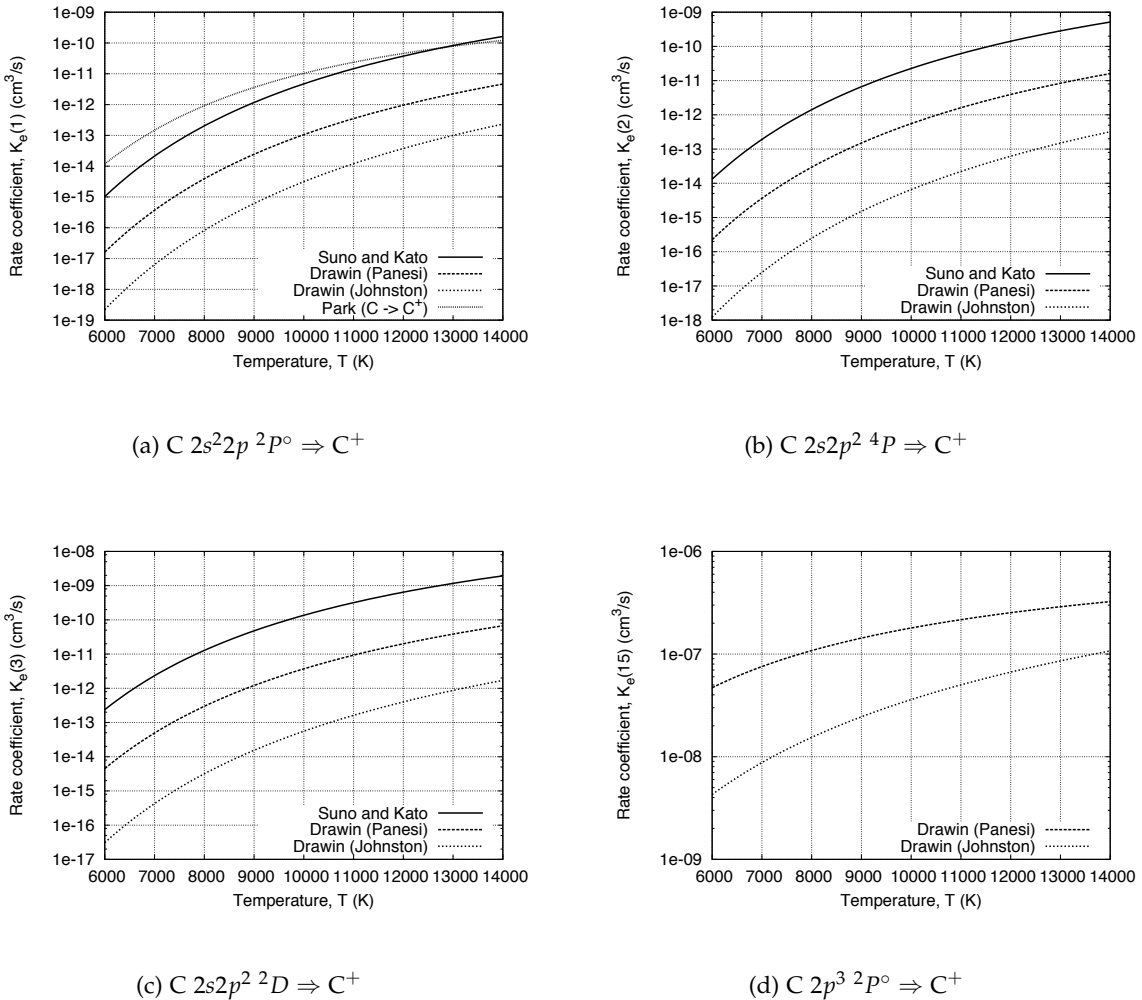


Figure 4.12: Comparison of electron impact ionisation rate coefficients for atomic carbon.

and cross sections for the diatomic species CN, CO, N₂, N₂⁺, O₂ and NO have been proposed by Park [178, 179]. Figure 4.13 compares the rates that are given by both Zalogin [185] and Park [178, 179]. The Zalogin model predicts faster collisional excitation of CN and slower collisional excitation of CO. Due to large differences between some of the rates, both models will be assessed via comparison with shock tube data in § 6.2. As the Park model is more comprehensive and based on experimental and theoretical cross sections where possible, the Park collisional excitation rates for CO and CN are tentatively accepted for inclusion in the nominal collisional-radiative models for these species. Due to numerical difficulties encountered when implementing the heavy particle impact rates given in Reference [179], however, these were omitted for CO and CN. Considering just the electron impact processes should be sufficient for the conditions of interest due to the substantial levels of ionisation. It should be emphasised that the heavy particle

impact processes would need to be considered for the collisional-radiative model to be valid for less energetic conditions where ionisation levels are low. The system radiative transition probabilities are calculated from the electronic-vibration transition moments via Equation 4.93. For C₂ we resort to the Zalogin [185] model as this species was not considered by Park in References [178, 179]. The nominal collisional-radiative models for C₂, CN and CO are summarised in § D.1 to D.3 respectively.

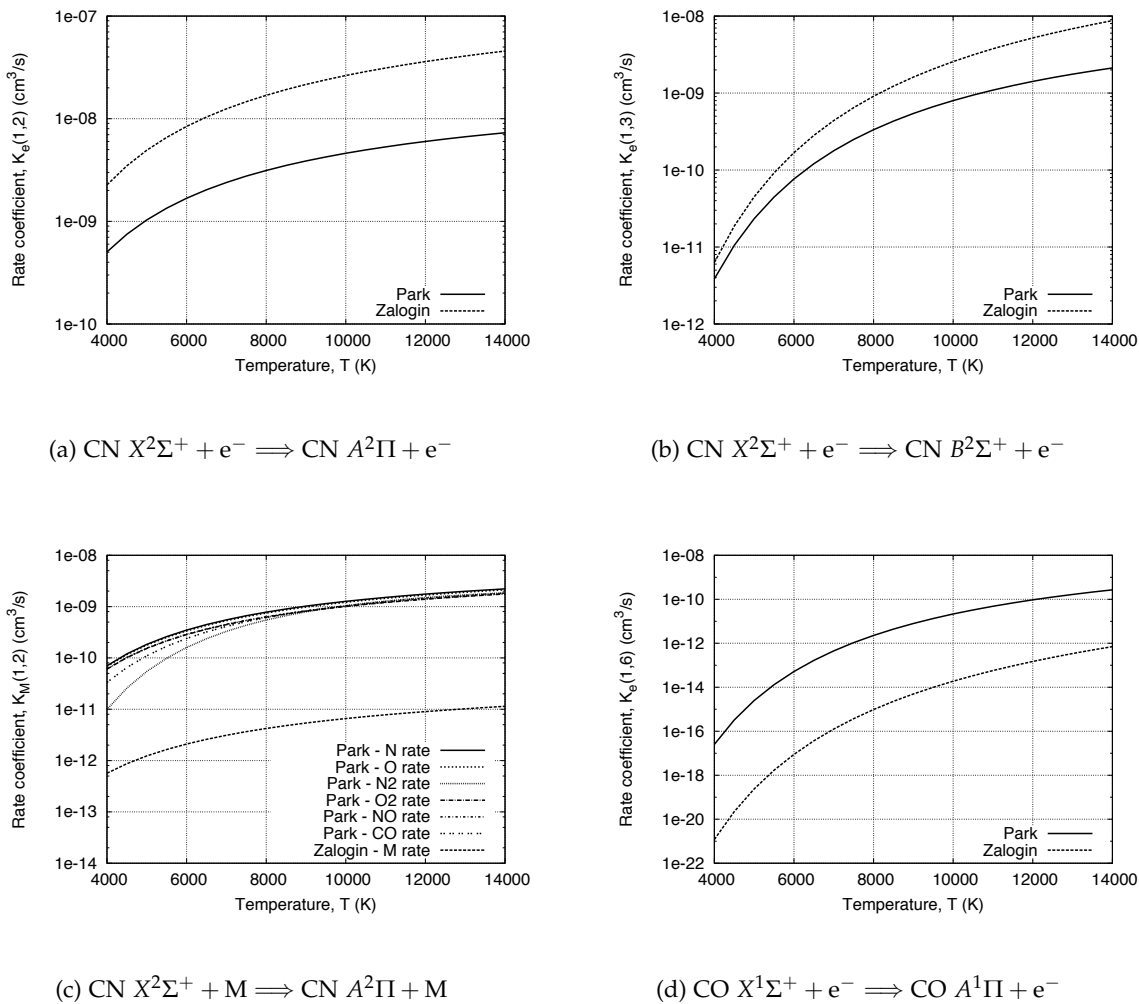


Figure 4.13: Comparison of excitation rate coefficients obtained from Park [178, 179] and Zalogin [185].

4.3.5 A note on the selection of data sources

In formulating the collisional-radiative model the sometimes contradictory issues of data source consistency and model accuracy arise. On one hand, it is desirable to formulate a model that is

both internally consistent (uses the same data source for all processes) and externally consistent (uses the same data sources as other models, such as the spectral radiation model). On the other hand, it is desirable to formulate a model that best reproduces the physical phenomena. The goal of the present work is to develop effective engineering tools, and therefore the latter approach has been preferred to give the calculations the best chance of reproducing experimental data. As an example, consider the electron impact excitation for the nitrogen atom. An internally consistent model would have to use an empirical model such as that of Drawin [162] for all transitions, however this model has been shown to give inaccurate results when applied to the excitation of low lying electronic states [58, 171]. Although it breaks the internal consistency of the model, implementing the computational chemistry rates of Frost *et al.* [168] gives much improved comparisons with experiment [58, 171]. This principle of selecting the most effective data, rather than the most consistent data, has been applied throughout the collisional-radiative model.

4.4 Summary

The models for nonequilibrium rate processes relevant to radiating shock layers have been presented. Specifically, various models for the chemical kinetic and thermal energy exchange source terms in the governing equations have been outlined, and a collisional-radiative modelling framework for the spectral radiation model described. An important observation from the discussion of the chemical kinetic models is the good agreement of the Park $s = 0.7$ model with N₂ dissociation rates predicted by computational chemistry. For thermal energy exchange, an alternative model to Park's vibration-translation exchange limiting cross section model for CO as proposed by Fujita [77] has been presented. In addition, the differences between the various chemistry-energy coupling models presented in the literature have been discussed. For the collision-radiative modelling, a QSS framework has been presented and rate coefficient models for Ar, C, N, O, C₂, CN, CO, N₂ and N₂⁺ proposed by compiling data from the literature. This chapter closes the physical modelling of high temperature gases.

Part II

Post-shock relaxation

5

Implementation of the one-dimensional post-shock relaxation equations: Poshax3

For the investigation of different chemical kinetic models and analysis of shock tube experiments, it is convenient to model a reduced set of equations describing the flowfield behind a strong shock wave. In this chapter we consider the Poshax3 code that implements the post-shock relaxation equations describing steady one-dimensional Eulerian flow presented in § 2.2. The numerical formulation of the Poshax3 code is described in § 5.1. Poshax3 is an extension of the poshax code developed by Gollan [1] to two- and three-temperature gases with fully coupled governing equations. The code is then applied to simulate shock layers characteristic of atmospheric entry at Earth and Mars in § 5.2 and 5.3 respectively. In these sections comparisons with solutions presented in the literature are made and the influence of various physical models is investigated.

5.1 Numerical formulation

The two-temperature post-shock relaxation equations derived in § 2.2 are restated below for convenience; Equations 5.1, 5.2, 5.3 and 5.4 are the conservation equations for species mass, momentum total energy and vibration-electron-electronic energy, respectively.

$$\frac{\partial}{\partial x} (\rho_s u) = \omega_s \quad (5.1)$$

$$\frac{\partial}{\partial x} (\rho u^2 + p) = 0 \quad (5.2)$$

$$\frac{\partial}{\partial x} (u (\rho E + p)) = -\frac{\partial q_{\text{rad}}}{\partial x} \quad (5.3)$$

$$\frac{\partial}{\partial x} (u (\rho e_{\text{ve}} + p_e)) = -\frac{\partial q_{\text{rad}}}{\partial x} + \dot{\Omega}_{\text{VT}} + \dot{\Omega}_{\text{ET}} + \dot{\Omega}_{\text{VC}} + \dot{\Omega}_{\text{EC}} \quad (5.4)$$

In the case of a three-temperature model, the vibration and electron-electronic energy continuity equations are treated separately, Equations 5.5 and 5.6.

$$\frac{\partial}{\partial x} (u e_{\text{v}}) = \dot{\Omega}_{\text{VT}} + \dot{\Omega}_{\text{VE}} + \dot{\Omega}_{\text{VC}} \quad (5.5)$$

$$\frac{\partial}{\partial x} (u (e_{\text{e}} + p_e)) = -\frac{\partial q_{\text{rad}}}{\partial x} + \dot{\Omega}_{\text{ET}} + \dot{\Omega}_{\text{EV}} + \dot{\Omega}_{\text{EC}} \quad (5.6)$$

The original poshax code described in Reference [1] modelled the gas dynamics by considering the conservation of total mass, momentum and energy, while integrating the chemical species and modal energy ODE's in a decoupled manner. This decoupled approach was selected in order to replicate the operator split methodology applied in the Navier–Stokes solver `mbcns` considered in that work. For the interplanetary atmospheric entry conditions of present interest, however, rapid chemical kinetic processes such as electron impact ionisation may require tighter coupling with the flowfield to be correctly modelled. Furthermore, it is useful to implement the fully coupled governing equations to evaluate the operator split methodology. To this end the Poshax3 code has been developed where the two- or three-temperature post-shock relaxation equations are integrated in a coupled manner. In the general discussion of the code that follows, for simplicity we will limit ourselves to the two-temperature governing equations.

5.1.1 Shock jump conditions

The Poshax3 computational domain is illustrated in Figure 5.1. The post-shock relaxation problem is defined by the freestream species densities $\rho_{i,0}$, temperatures $T_{\text{tr},0}$ and $T_{\text{ve},0}$ and shock speed U_s .

To calculate the immediate post-shock flow state to initialise the calculation, the species composition and vibration-electron-electronic energy mode are assumed frozen across the shock:

$$\frac{\rho_{i,1}}{\rho_1} = \frac{\rho_{i,0}}{\rho_0} \quad (5.7)$$

$$T_{\text{ve},1}(\text{or } T_{\text{vib},1} \text{ and } T_{e,1}) = T_0 \quad (5.8)$$

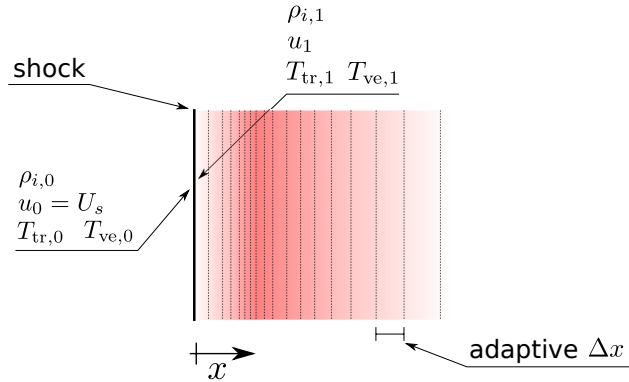


Figure 5.1: Computational domain for the one-dimensional post-shock relaxation calculations.

In contrast, the translation-rotation energy mode is assumed to instantaneously achieve its shock processed state. Shock slip is not considered, and the Rankin-Hugoniot relations give the conserved mass, momentum and energy behind the shock:

$$\rho_0 u_0 = \rho_1 u_1 \quad (5.9)$$

$$\rho_0 u_0^2 + p_0 = \rho_1 u_1^2 + p_1 \quad (5.10)$$

$$\rho_0 u_0 E_0 + u_0 p_0 = \rho_1 u_1 E_1 + u_1 p_1 \quad (5.11)$$

The remaining flow state variables, namely ρ_1 , $T_{\text{tr},1}$ and u_1 , are calculated by forming a zero-system from Equations 5.9 to 5.11 and solving via Newton iterations. This discrete treatment of the shock is in contrast to a finite-volume CFD solver where the shock is diffusively captured over a number of cells.

5.1.2 Spatial integration

The post-shock relaxation equations are then integrated in space via an explicit fourth-order Runge-Kutta integration scheme. All the conservation equations are integrated in a fully coupled manner, which is in contrast to the operator split methodology applied to the Navier-Stokes solver too be described in § 7. The spatial step Δx is adaptively selected by the ODE solver, allowing rapid convergence to equilibrium conditions. The primary thermodynamic variables ρ_i , T_{tr} , T_{ve} (or T_{vib} and T_e) and u are calculated by forming a zero-system from the conserved variables and solving via Newton iterations.

5.1.3 Radiative source term

Due to the one-dimensional space-marching nature of the Poschax3 code, a physically consistent non-local radiation transport model is difficult to define. In the present work we therefore resort to approximate models that are functions of the local gas state only.

To good approximation for inviscid post-shock flow, the optically thin and optically thick assumptions bound the possible solution space for radiation-flowfield coupling. Although net absorption can occur in the immediate post-shock region where high lying electronic states are yet to be excited [15], the affected region is small and net emission quickly takes over due to rapid collisional excitation. Under the assumption of optically thin radiation, absorption is neglected and the source term is calculated as:

$$-\nabla \cdot \vec{q}_{\text{rad}} = -\Lambda 4\pi \int_0^{\infty} j_{\nu} d\nu \quad (5.12)$$

where Λ is the escape factor and is equal to 1 for the optically thin model. Due to the omission of absorption, the optically thin solution represents the most severe case for radiation-flowfield coupling. The optically thick source term is simply zero (*i.e.* $\Lambda = 0$) as 100% local absorption is assumed, and represents a flowfield unaffected by radiation coupling. It must be noted that when a collisional-radiative electronic population model is used in Poshax3 simulations, the escape factor applied in Equation 7.45 for the radiation-flowfield coupling is also applied for the collisional-radiative model.

5.2 Application to Earth atmospheric entry

Two points of the Fire II re-entry trajectory have been simulated with the Poshax3 code. The flow conditions are summarised in Table 5.1. The point corresponding to $t = 1634$ s is a low density, high velocity condition where nonequilibrium effects are strong, while the $t = 1636$ s point is characterised by more moderate nonequilibrium effects. To verify the implementation of the governing equations, the Poshax3 results are firstly compared with the solutions presented by Panesi [58]. The effect of varying the thermodynamic, chemical kinetic, energy exchange and radiation models on the post-shock relaxation to equilibrium is then investigated. Unless otherwise stated, the implemented physical models are those listed in Table 5.2.

Table 5.1: Flow conditions for the $t = 1634$ s and $t = 1636$ s Fire II trajectory points [23]. The freestream mass fractions are assumed to be 0.767 and 0.233 for N₂ and O₂ respectively.

Trajectory point	$t = 1634$ s	$t = 1636$ s
Pressure, p_{∞} (Pa)	2.08	5.35
Temperature, T_{∞} (K)	195	210
Velocity, u_{∞} (m/s)	11,360	11,310

5.2.1 Comparison with published solutions

Simulations of the $t = 1634$ s and $t = 1636$ s Fire II trajectory points with the one-dimensional post-shock relaxation equations were performed by Panesi [58] with the shocking code. This

Table 5.2: Nominal physical models for Poshax3 simulations of the $t = 1634\text{ s}$ and $t = 1636\text{ s}$ Fire II trajectory points.

Physics component	Nominal Model
Thermodynamics	<ul style="list-style-type: none"> • Two-temperature • Reduced electronic levels • Truncated harmonic oscillators
Chemical kinetics	<ul style="list-style-type: none"> • Park (1993) reactions and rates (see Table C.1) • Modified Park dissociation model ($T_f = T_{\text{tr}}^{0.7} T_{\text{ve}}^{0.3}$)
Energy exchange	<ul style="list-style-type: none"> • Non-preferential dissociation-vibration coupling • Associative ionisation-electron coupling with $\alpha_{\text{AI}} = 0.1$ • Classical ionisation-electron coupling ($\alpha_{\text{EII}} = 1$)
Radiation	<ul style="list-style-type: none"> • Optically thick transport • Nominal atomic QSS model (see Tables 4.3) • Johnston diatomic QSS model

code has been shown to give reasonable agreement with the VSL calculations of Johnston [19] in the inviscid shock regions and also with the air radiation measurements performed in the EAST facility [171]. A two-temperature 11 species air model was implemented by Panesi [58] where thermodynamic properties were obtained by complete decoupling of the thermal modes. The electronic level summations were truncated to give the best agreement with the tabulations of Capitelli *et al.* [81], and diatomic molecules were modelled as harmonic oscillators. The chemical kinetic and vibration-translation energy exchange model proposed by Park [136] was implemented, with the translation-electron energy exchange model of Appleton and Bray [150]. Preferential dissociation-vibration coupling was not considered, and electron energy loss due to ionisation was modelled with the reduced ionisation potentials shown in Equations 4.45 and 4.46. As the purpose of the comparison is to verify the implementation of the governing equations, this physical modelling is reproduced as best as possible for the Poshax3 calculations. The implemented models differ from that presented in Table 5.2 in that harmonic oscillators are used instead of truncated harmonic oscillators, the rate controlling temperature for dissociation is $T_f = \sqrt{T_{\text{tr}} T_{\text{ve}}}$ instead of $T_f = T_{\text{tr}}^{0.7} T_{\text{ve}}^{0.3}$ and the reduced ionisation potentials are used in place of the classical potentials for ionisation-electron coupling. However, slight differences in the thermodynamic models are likely to remain due to the use of different sources for spectroscopic data (Panesi [58] uses the data of Gurvich, whereas the data of Huber and Herzberg [85] is used in the present work) and different numbers of electronic levels included for each species (Panesi [58] doesn't state which levels are considered). This can be confirmed by comparing the non-dimensional enthalpy against temperature for the N_2 molecule, Figure 5.2. The two calculations show considerable disagreement at temperatures above 2,000 K. Such differences in the thermodynamic models may result in slightly different equilibrium flow states between the

solutions. In addition, the use of T_e as the rate controlling temperature for associative ionisation-recombination was unable to be implemented in the present work.

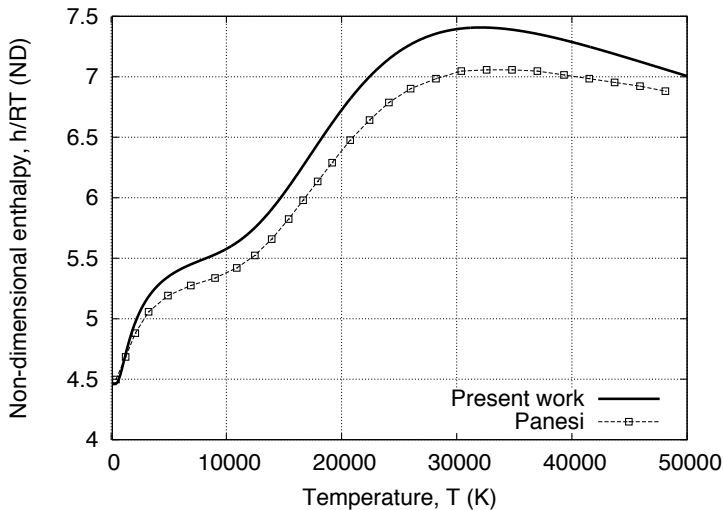


Figure 5.2: Comparison of non-dimensional enthalpy for the N_2 molecule as calculated in the present work and by Panesi [58].

Figures 5.3 and 5.4 present post-shock temperature and number density profiles for the $t = 1634\text{ s}$ and $t = 1636\text{ s}$ Fire II trajectory points respectively. For the $t = 1634\text{ s}$ case in Figure 5.3, the curves labelled Poshax3 (a) and (b) refer to calculations performed with an unlimited and a $T_{\text{trans}} < 50,000\text{ K}$ limited vibration-translation high temperature cross section σ_v (see Equation 4.27). The temperature limited Poshax3 (b) results are seen to give almost exact agreement with Panesi's calculations for the first 5 mm behind the shock and results in the same equilibration distance of approximately 18 mm. Conversely, the unlimited Poshax3 (a) results predict a slightly enlarged equilibration distance of approximately 20 mm but better match Panesi's calculations for $5 \leq x \leq 15\text{ mm}$. Panesi [58] does not state whether σ_v is limited to a particular temperature. In Figure 5.3b, the equilibrium N and O number densities agree within 1% however the equilibrium electron number density differs by 5%. This difference can be attributed to slight variations in the thermodynamic properties used in the two calculations resulting in slightly different equilibrium temperatures and concentrations.

For the $t = 1636\text{ s}$ case in Figure 5.4 the nominal model for σ_v is implemented (no limiting temperature). The agreement between the Poshax3 solution and that of Panesi is very good for both temperatures and number densities, with only slight discrepancies in the nonequilibrium concentrations in the order of 5%. It should be noted however that this condition is significantly less sensitive to the modelling of the nonequilibrium rate processes due to the lower velocity and high pressure; the equilibration distance for the $t = 1636\text{ s}$ case is approximately 8 mm compared to 20 mm for the $t = 1634\text{ s}$ case.

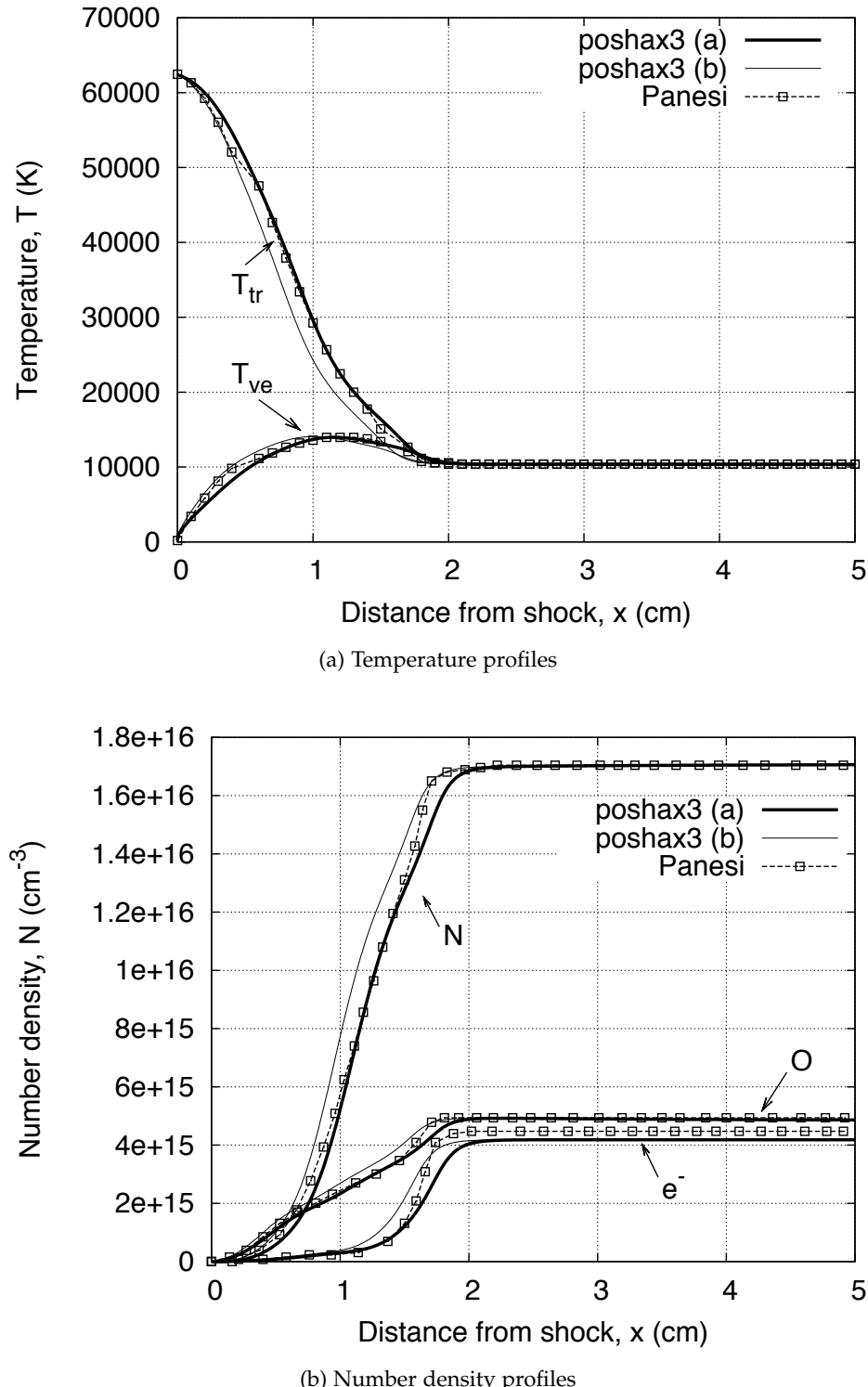


Figure 5.3: Fire II $t=1634$ s one-dimensional post-shock relaxation profiles. Comparison of two-temperature Poshax3 solution with Reference [58]. Curves (a) and (b) refer to calculations performed with an unlimited and a $T_{\text{trans}} < 50,000$ K limited σ_v parameter (see Equation 4.27).

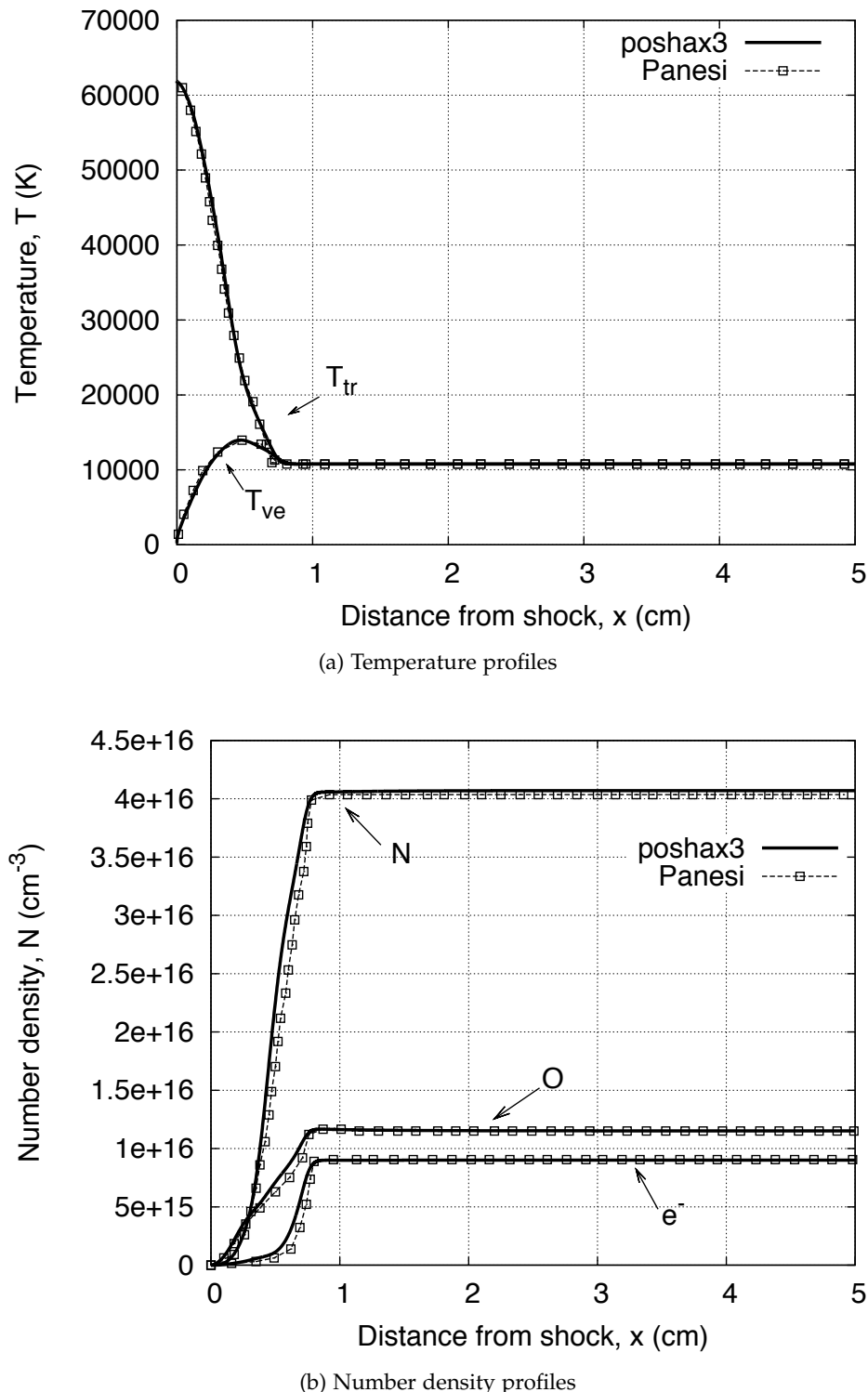


Figure 5.4: Fire II $t=1636$ s one-dimensional post-shock relaxation profiles. Comparison of two-temperature Poshax3 solution with Reference [58].

Overall, good agreement is demonstrated between calculations with the Poshax3 code and the shocking code of Panesi [58] — this verifies the basic physical modelling for N₂–O₂ mixtures.

5.2.2 Thermodynamic model variation

The results presented in § 5.2.1 modelled diatomic molecules as harmonic oscillators and considered a reduced number of electronic levels for both atomic and diatomic species as presented in Tables 3.1 and 3.2. Figures 5.5a and 5.5b compare the post-shock temperature and number density profiles for the Fire II $t = 1634\text{ s}$ case with the harmonic oscillator and truncated harmonic oscillator models using the reduced electronic level sets. A calculation including all electronic levels and truncated harmonic oscillators is also shown in order to verify the use of reduced electronic level sets. The physical modelling differs from that in Table 5.2 in that the rate controlling temperature for dissociation is $\sqrt{T_{\text{trans}} T_{\text{vib}}}$ and ionisation-electron coupling with a reduced potential is implemented.

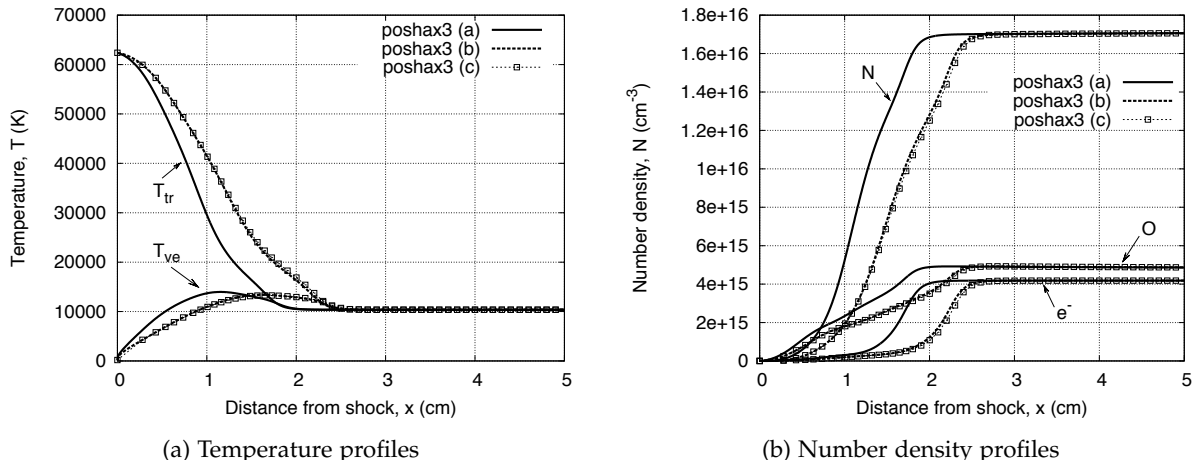


Figure 5.5: Fire II $t=1634\text{ s}$ one-dimensional post-shock relaxation profiles. Comparison of Poshax3 solutions with various thermodynamic models; (a) harmonic oscillators, reduced electronic levels, (b) truncated harmonic oscillators, reduced electronic levels and (c) truncated harmonic oscillator, all electronic levels.

The use of a truncated harmonic oscillator model for molecular vibration is observed to increase the equilibration distance from 20 mm to 25 mm. This can be attributed to the truncation reducing the energy stored in the vibrational mode, and subsequently slowing the rate of dissociation. The solution with all electronic levels included does not deviate substantially from the reduced level case, validating the use of reduced electronic level sets.

5.2.3 Dissociation rate coefficient model variation

The results presented in § 5.2.1 and § 5.2.2 implemented the Park model for nonequilibrium dissociation where the forward rate is governed by the geometric average temperature $\sqrt{T_{\text{trans}} T_{\text{vib}}}$. Figures 5.6a and 5.6b compare the post-shock temperature and number density profiles for the Fire II $t = 1634$ s case using the Park dissociation model with $\sqrt{T_{\text{trans}} T_{\text{vib}}}$ ($s = 0.5$) and $T_{\text{trans}}^{0.7} T_{\text{vib}}^{0.3}$ ($s = 0.7$) as the rate controlling temperatures. A calculation implementing the Macheret–Fridman forced harmonic oscillator dissociation model is also shown for comparison¹. The physical modelling differs from that in Table 5.2 in that ionisation-electron coupling with a reduced potential is implemented.

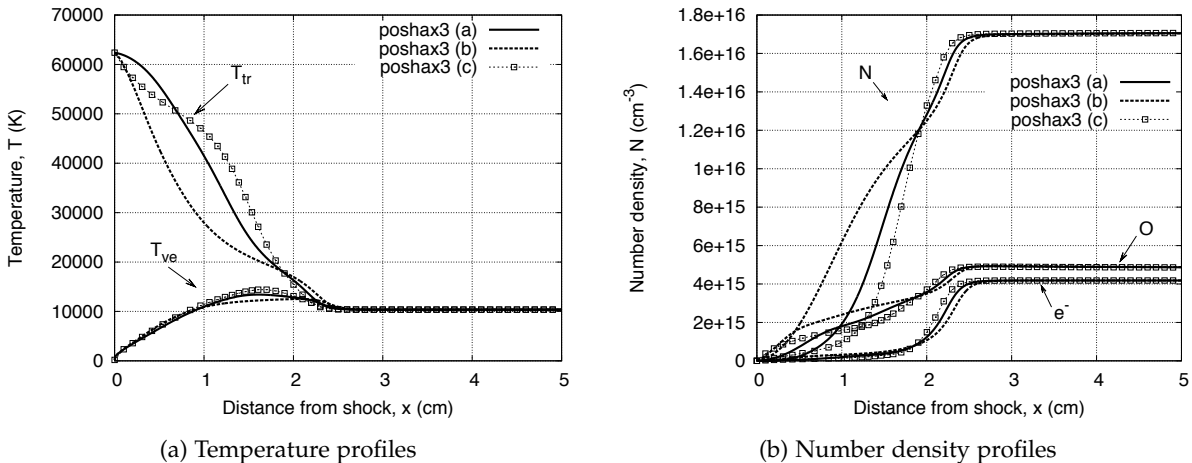


Figure 5.6: Fire II $t=1634$ s one-dimensional post-shock relaxation profiles. Comparison of Poshax3 solutions with various dissociation models; (a) Park model, $s = 0.5$, (b) Park model, $s = 0.3$ and (c) Macheret–Fridman model.

The Park $s = 0.7$ case results in increased dissociation behind the shock compared with the $s = 0.5$ case, indicated by the higher concentration of atoms in the $0 \leq x \leq 2$ cm range. This is due to the larger value of the exponent s coupling dissociation more to the translational temperature than the vibrational temperature. The Macheret–Fridman model predicts a dissociation rate in-between the two park models in the $0 \leq x \leq 0.7$ cm range, which then rapidly increases beyond the Park $s = 0.5$ case. This can be attributed to the Macheret–Fridman models consideration of two dissociation regimes; collision dominated dissociation at high gas temperatures and vibration dominated dissociation at lower gas temperatures. It should also be noted that the Macheret–Fridman model more closely follows the Park $s = 0.5$ case than the $s = 0.7$ case. Overall the three models predict similar equilibration distances and electron densities, indicating the final attainment of equilibrium is driven more by free electron processes than dissociation.

¹The Macheret–Fridman model is only valid for homonuclear diatomic species. Therefore in this calculation the Park $s = 0.7$ dissociation model is used for NO.

5.2.4 Dissociation-vibration coupling model variation

The results presented in § 5.2.1- 5.2.3 implemented a non-preferential vibration-dissociation coupling model where molecules are assumed to be created and destroyed at the average vibrational energy. Figures 5.7a and 5.7b compare the post-shock temperature and number density profiles for the Fire II $t = 1634\text{ s}$ case using the Park dissociation rate coefficient model ($s = 0.7$) with (a) the non-preferential coupling model, (b) the Park preferential coupling model proposed by Knab *et al.* [145] (see Equation 4.38) and (c) the Treanor–Marrone preferential coupling model with $U = \Theta_D/3$ (see Equation 4.40). Although use of the Treanor–Marrone preferential coupling model alongside the Park dissociation model is not physically consistent, we have included this combination here to allow for a clear comparison of the dissociation-vibration coupling with a common dissociation rate coefficient model.

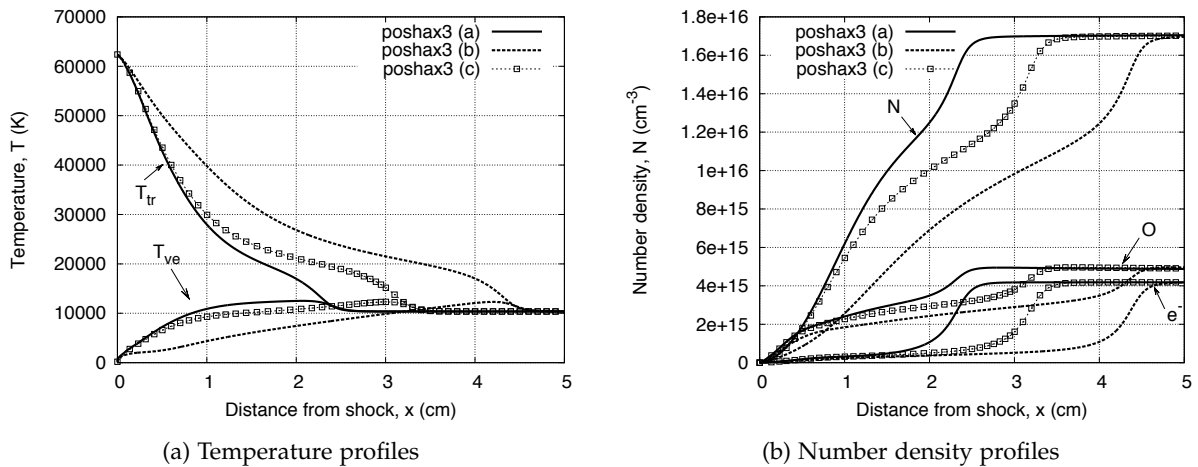


Figure 5.7: Fire II $t=1634\text{ s}$ one-dimensional post-shock relaxation profiles. Comparison of Poshax3 solutions with various dissociation-vibration coupling models; (a) non-preferential coupling (b) Park preferential coupling, $s = 0.7$ (c) Treanor–Marrone coupling, $U = \Theta_D/3$.

Compared to the non-preferential solution, the preferential dissociation-vibration coupling solutions predict significantly enlarged equilibration distances. This is due to more vibrational energy depletion upon molecular dissociation reducing the vibrational temperature, and subsequently slowing the rate of dissociation. The Park preferential model appears to produce much more aggressive coupling than the Treanor–Marrone model, with the Park model predicting equilibrium conditions almost two times further from the shock. The large difference between the three models raises concerns as to the validity of the preferential dissociation-vibration coupling at these high velocity conditions, and justifies the conservative selection of non-preferential coupling as the nominal model in the present work.

5.2.5 Chemistry-electron coupling model variation

The results presented in § 5.2.1- 5.2.4 implemented a conservative chemistry-electron coupling model where electron energy loss due to ionisation was modelled with the reduced ionisation potentials shown in Equations 4.45 and 4.46. Furthermore, electrons produced and consumed by association ionisation and recombination were assumed to have the average energy. Figures 5.8a and 5.8b compare the post-shock temperature and number density profiles for the Fire II $t = 1634\text{ s}$ case considering (a) electron impact ionisation coupling with reduced ionisation potentials (b) electron impact ionisation coupling with ground state ionisation potentials and (c) electron impact ionisation coupling with ground state ionisation potentials and associative ionisation coupling with $\alpha_{AI} = 0.1$.

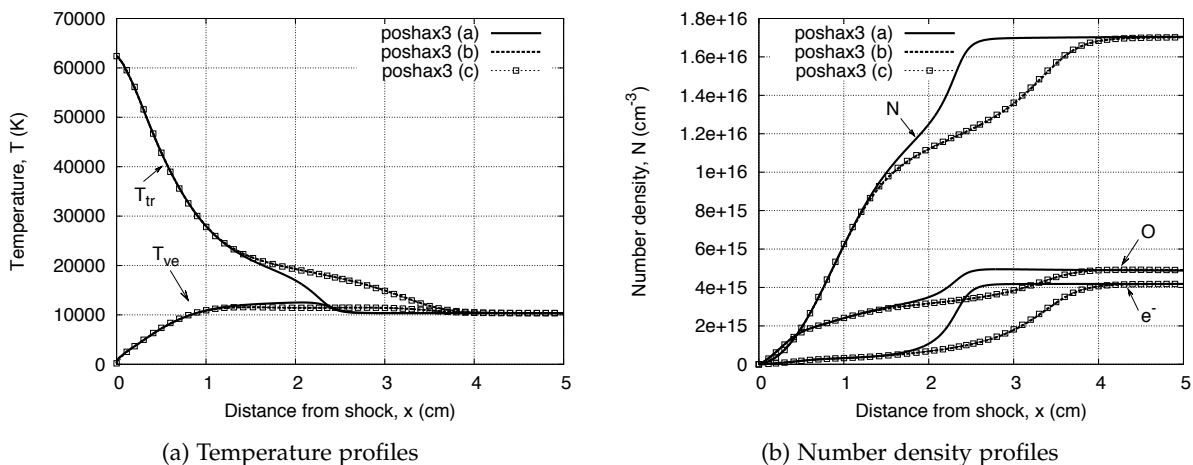


Figure 5.8: Fire II $t=1634\text{ s}$ one-dimensional post-shock relaxation profiles. Comparison of Poshax3 solutions with various chemistry-electron coupling models; (a) reduced electron impact ionisation coupling (b) classical electron impact ionisation coupling and (c) classical electron impact ionisation coupling with $\alpha_{AI} = 0.1$.

The use of the ground state ionisation potentials has a significant influence on the post-shock relaxation, increasing the equilibration distance to almost 40 mm. This can be explained by considering Equations 4.45 and 4.46 where the reduced ionisation potential for N and O are shown to be approximately one-third of the ground state potential. Again, the large difference between the two models makes it difficult to justify one over the other, however in the present work we conservatively choose to implement the ground state ionisation potentials. The effect of including association ionisation coupling with $\alpha_{AI} = 0.1$ is almost negligible, however as will be discussed in § 5.2.7 it is necessary to obtain solutions with the three-temperature model.

5.2.6 Radiation model variation

The results presented in § 5.2.1- 5.2.5 considered optically thick radiation-flowfield coupling (*i.e.* $\frac{\partial q_{\text{rad}}}{\partial x} = 0$). Figures 5.9a and 5.9b compare the post-shock electron number density and radiative emission coefficient profiles for the Fire II $t = 1634$ s case with (a) equilibrium electronic populations and optically thick radiation coupling, (b) nonequilibrium electronic populations and optically thick radiation coupling and (c) nonequilibrium electronic populations and optically thin radiation coupling. The nonequilibrium electronic populations are calculated with the QSS collisional-radiative model described in § 4.3.

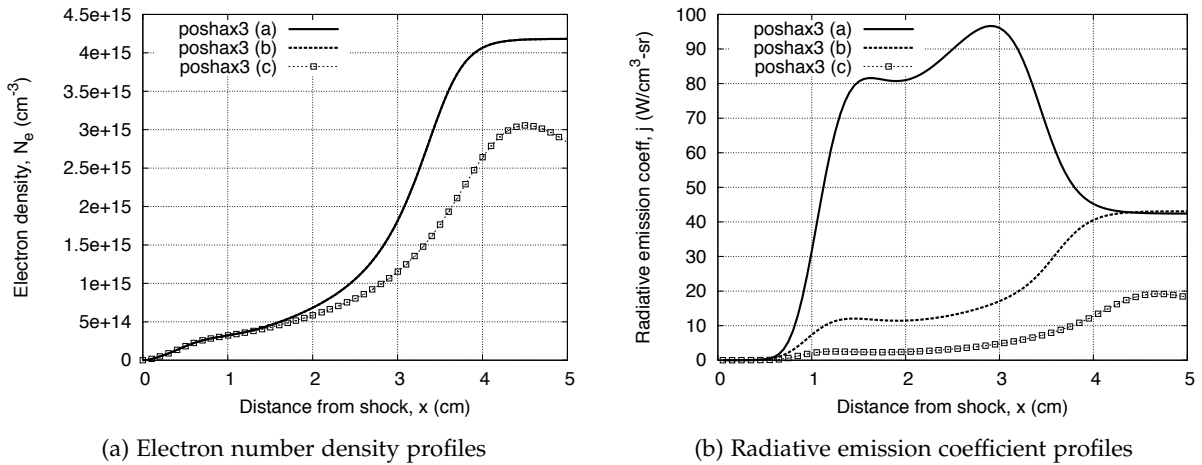
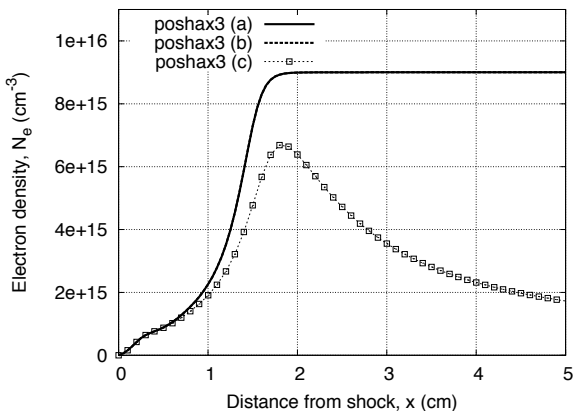


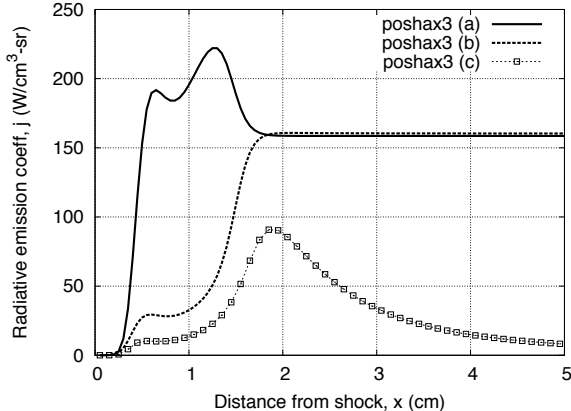
Figure 5.9: Fire II $t=1634$ s one-dimensional post-shock relaxation profiles. Comparison of Postshax3 solutions using various radiation models; (a) equilibrium, optically thick, (b) nonequilibrium, optically thick and (c) nonequilibrium, optically thin.

The radiative emission coefficient profile in 5.9b demonstrates the large difference between assuming Boltzmann and nonequilibrium electronic level populations at these conditions. The equilibrium optically thick emission quickly rises to $80 \text{ W}/\text{cm}^3\text{-sr}$ at 1.5 cm behind the shock, and peaks at almost $100 \text{ W}/\text{cm}^3\text{-sr}$ 3 cm behind the shock. In contrast, the nonequilibrium optically thick emission plateaus at approximately $10 \text{ W}/\text{cm}^3\text{-sr}$ in the nonequilibrium shock layer region, and peaks at just over $40 \text{ W}/\text{cm}^3\text{-sr}$ in the equilibrium region. The consideration of optically thin radiation-flowfield coupling reduces the radiative emission coefficient even further, plateauing at $2 \text{ W}/\text{cm}^3\text{-sr}$ in the nonequilibrium region and peaking at $20 \text{ W}/\text{cm}^3\text{-sr}$. The effect of the radiation-flowfield coupling on the chemical kinetics can be seen in 5.9a. The consideration of optically thin radiation reduces the peak electron concentration from just over $4 \times 10^{15} \text{ cm}^{-3}$ to approximately $3 \times 10^{15} \text{ cm}^{-3}$. Furthermore, equilibrium conditions are never truly attained with optically thin radiation, and after the peak the electron concentration begins to drop. It should also be noted that T_{ve} is reduced by approximately 12% at $x = 5 \text{ cm}$ as a result of applying the optically thin radiation source term.

Figures 5.10a and 5.10b compare the post-shock electron number density and radiative emission coefficient profiles for the Fire II $t = 1636$ s case. For this condition, the radiative emission is much stronger, reaching an equilibrium value of approximately $160 \text{ W/cm}^3\text{-sr}$ for the optically thick cases. Similar trends are observed between the three radiation model variations, with the equilibrium optically thick and nonequilibrium optically thin results bounding the nonequilibrium optically thick solution. Due to the much stronger emission, however, the radiative cooling effect is more clearly pronounced for the optically thin case. The electron concentration and radiative emission coefficient reach peaks at 1.8 cm behind the shock, and then fall off dramatically with the radiative emission coefficient being just $10 \text{ W/cm}^3\text{-sr}$ at $x = 5 \text{ cm}$. This phenomena of a decaying emission profile is characteristic of radiative cooling and can will be used in § 6 to determine the optically thin or thick nature of experimental measurements.



(a) Electron number density profiles



(b) Radiative emission coefficient profiles

Figure 5.10: Fire II $t=1636$ s one-dimensional post-shock relaxation profiles. Comparison of Poshax3 solutions using various radiation models; (a) Equilibrium, optically thick, (b) QSS, optically thick and (c) QSS, optically thin.

The suppression of radiative emission observed for the nonequilibrium optically thin cases is due to two inter-related phenomena: (1) radiative cooling, and (2) collision limited population of electronic levels. Insight into these phenomena can be attained by considering the electronic level population distributions at a particular point in the flow. Figures 5.11a to 5.12a present the level populations of the N atom at 1 cm increments through the $t = 1634$ s shock layer. The level populations N_i are divided by the level degeneracy g_i to aid visualisation. The Boltzmann and Saha-Boltzmann equilibrium populations are also shown to indicate the theoretical distributions due to purely bound-bound electron impact and ionisation processes respectively (see Equations 3.117 and 3.119 respectively). Between 1 and 4 cm behind the shock, the Saha-Boltzmann distribution is significantly lower than the Boltzmann distribution, indicating a state of strong nonequilibrium (*i.e.* the electron number density is much lower than the equilibrium value at

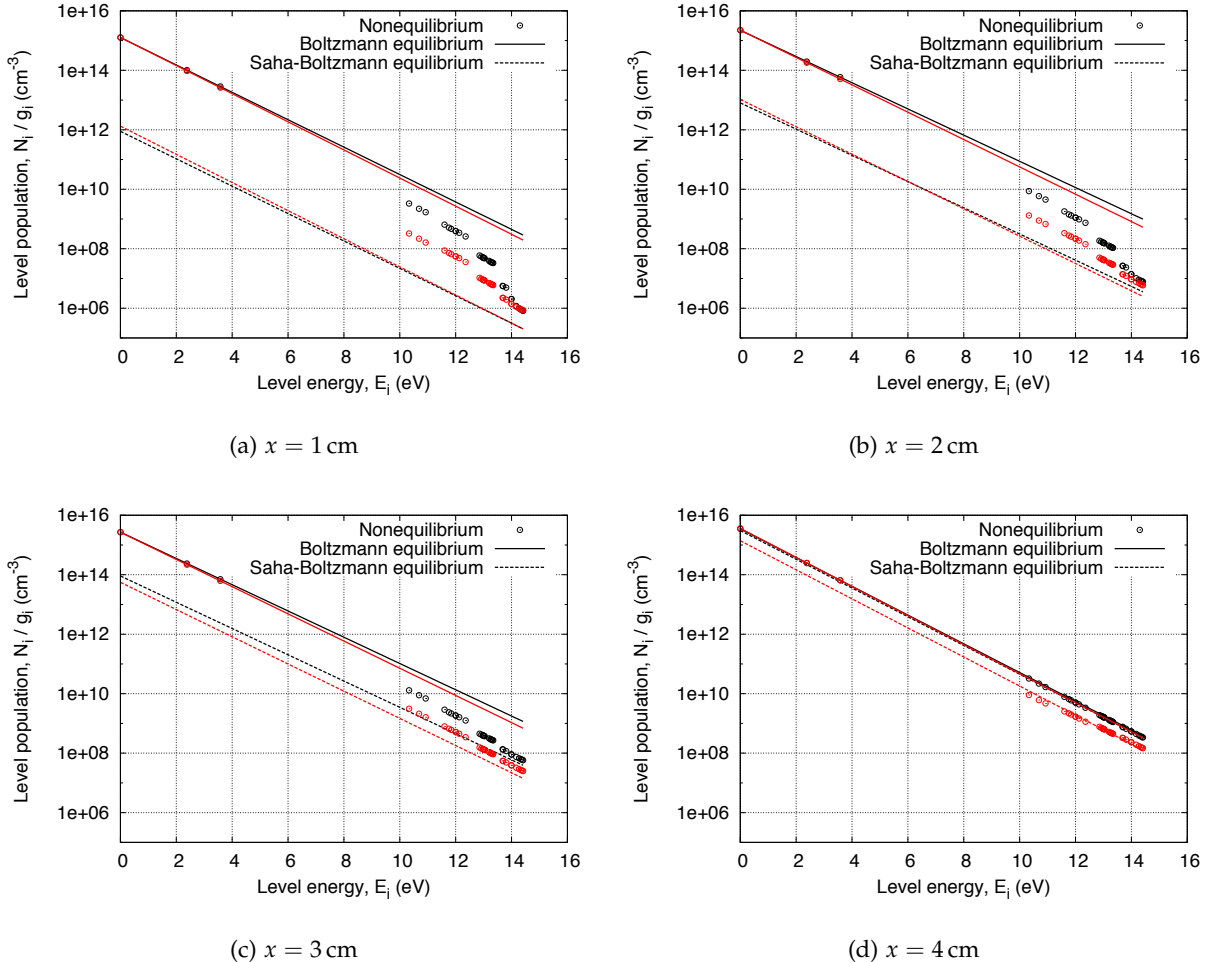


Figure 5.11: Electronic level population distributions from Poshax3 simulations of the Fire II $t=1634\text{s}$ condition. The data in black refers to results with nonequilibrium optically *thick* radiation, and the data in red refers to results with nonequilibrium optically *thin* radiation.

the current T_{ve}). At 1 and 2 cm behind the shock, the effect of radiative cooling on the electron concentration is low (see Figure 5.9a) yet the optically thick level populations are substantially lower than the optically thin level populations. This is due to depletion of high lying electronic levels due to radiative decay, which is omitted by the collisional-radiative model for the optically thick calculation. This phenomena is referred to as collision limiting, as there are not enough collisional processes to counteract the radiative depletion. At 3 cm behind the shock, the effect of radiative cooling on the gas state is apparent with the optically thin Boltzmann and Saha-Boltzmann distributions being lower than their optically thick counterparts. Therefore here both the radiative cooling and collision limiting contribute to the low electronic level populations. Finally, at 4 cm behind the shock, thermochemical equilibrium is almost achieved for the optically thick case and the Boltzmann, Saha-Boltzmann and nonequilibrium populations are essentially

equal. The optically thin solution, however, remains in thermochemical nonequilibrium due to radiative cooling as indicated by the lower Saha-Boltzmann distribution. It should be noted, however, that the optically thin solution represents the most severe case of radiative cooling and in reality much of the radiative emission will be locally reabsorbed by the gas.

5.2.7 Three temperature model

The results presented in § 5.2.1- 5.2.6 considered a two-temperature formulation of the governing equations. Figures 5.12a and 5.12b compare the post-shock temperature and number density profiles for the Fire II $t = 1634$ s case with (a) a two-temperature model, (b) a three-temperature model and (c) a three-temperature model with the vibration-electron relaxation time τ_{VE} artificially increased by a factor of 10. For the nominal three-temperature case, the vibrational temperature T_v is slightly higher than the two-temperature T_{ve} and the electron-electronic temperature T_e is slightly lower. With the increased relaxation time, T_e is less tightly coupled to T_v and is on average 25% less in the $0 \leq x \leq 2$ cm range. For both three-temperature models, however, the free electron concentration does not change appreciably from the two-temperature solution. This indicates that ionisation is driven more by the free electron concentration than their translational temperature at these conditions, and justifies the use of the two-temperature model.

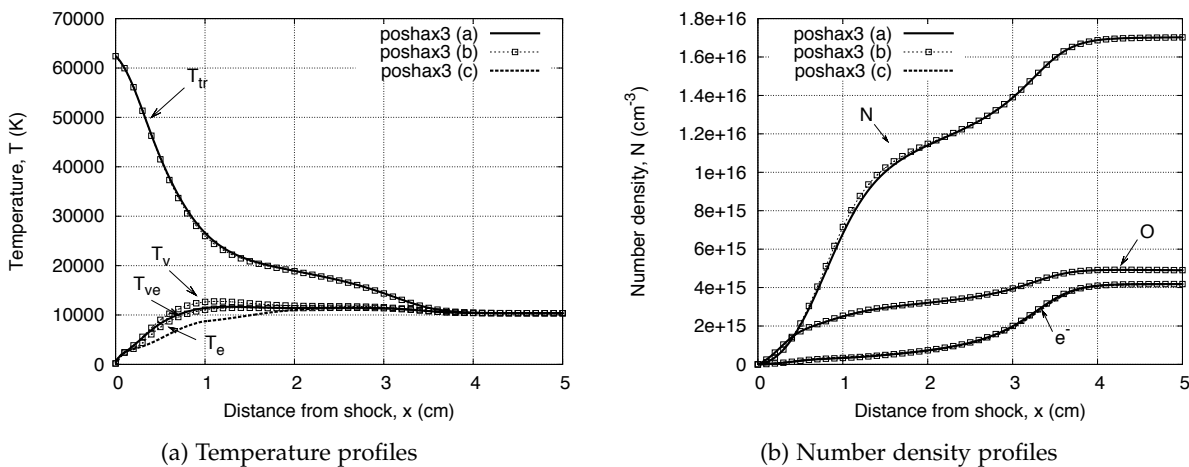


Figure 5.12: Fire II $t=1634$ s one-dimensional post-shock relaxation profiles. Comparison of Poshax3 solutions with various gas-models; (a) two-temperature model, (b) three-temperature model and (c) three temperature model, $\tau_{VE} \times 10$.

5.3 Application to Mars atmospheric entry

Two conditions representative of entry into the Martian atmosphere have also been simulated with the Poshax3 code. The flow conditions are summarised in Table 5.3. The condition labelled ‘51.4 km’ corresponds to the 51.4 km altitude point on the hypothetical 9.79 km/s Mars aerocapture trajectory proposed for a 10 m nose radius vehicle by Braun [16]. Due to the high freestream velocity and low freestream density, this condition is therefore characterised by reasonably strong nonequilibrium effects². The condition labelled ‘EAST’ is a 8.5 km/s 0.1 Torr shock tube condition performed in the NASA Ames EAST facility [3]. This condition is characterised by significantly lower velocity and high density than the 51.4 km condition, and is approximately representative of peak heating for the 9.7 km/s aerocapture trajectory. The EAST condition is therefore characterised by moderate nonequilibrium effects. To verify the implementation of the physical modelling for CO₂–N₂ mixtures, the Poshax3 results for the EAST condition are firstly compared with the solution presented by Munafo *et al.* [187]. The effect of varying the thermodynamic, chemical kinetic, energy exchange and radiation models on the post-shock radiative emission is then investigated. Unless otherwise stated, the nominal physical models are those listed in Table 5.4.

5.3.1 Comparison with published solutions

Munafo *et al.* [187] performed calculations of the 8.5 km/s 0.1 Torr CO₂–N₂ EAST shock tube condition as part of European Space Agency’s 2008 Radiation Workshop. Munafo *et al.* [187] implemented a two-temperature model and the reaction and energy exchange models proposed by Park *et al.* [29, 137]. For the comparison we also implement these models and assume all species are created and destroyed at their average energy (non-preferential dissociation and $\alpha_{AI} = 0$ and $\alpha_{EIIC} = 0$). It is unclear whether the harmonic or truncated harmonic oscillator assumptions

²Due to strong coupling between translation and vibration for the CO₂ molecule, even such low density Mars entry conditions exhibit considerably smaller equilibration distances compared to equivalent conditions in air.

Table 5.3: Representative flow conditions for entry into the Martian atmosphere. Note that the freestream mole-fractions differ for the two conditions.

Condition	51.4 km	EAST
Pressure, p_∞ (Pa)	2.79	13.3
Temperature, T_∞ (K)	154	300
Velocity, u_∞ (m/s)	9,660	8,500
X_{CO_2}	0.957	0.96
X_{N_2}	0.027	0.04
X_{Ar}	0.016	-

Table 5.4: Nominal physical models for Poshax3 simulations of the 51.4 km and EAST representative Mars entry conditions.

Physics component	Nominal Model
Thermodynamics	<ul style="list-style-type: none"> • Two-temperature • Reduced electronic levels • Truncated harmonic oscillators
Chemical kinetics	<ul style="list-style-type: none"> • Modified Park (1994) reactions and rates (see Table C.2) • Park dissociation model ($T_f = \sqrt{T_{\text{tr}} T_{\text{ve}}}$)
Energy exchange	<ul style="list-style-type: none"> • Preferential dissociation-vibration coupling (Park model) • Fujita limiting cross section for CO vibration-translation exchange • Associative ionisation-electron coupling with $\alpha_{\text{AI}} = 0.1$ • Classical ionisation-electron coupling ($\alpha_{\text{EI}} = 1$)
Radiation	<ul style="list-style-type: none"> • Optically thick transport • Nominal atomic QSS model (see Tables 4.3) • Park diatomic QSS model

were applied, and therefore both are considered. Figure 5.13 compares the post-shock temperature profiles for the Mars EAST condition with the solutions presented by Munafo *et al.* [187]. The curve labelled pohsax3 (a) models molecules as harmonic oscillators while (b) models molecules as truncated harmonic oscillators.

The Poshax3 solutions with harmonic and truncated harmonic oscillators predict peak vibrational temperatures of 13,500 K and 13,200 K respectively, while Munafo predicts a slightly lower peak of 12,750 K. The location of this peak predicted by Munafo is straddled by the Poshax3 solutions with harmonic and truncated harmonic oscillators. In addition, Munafo predicts slightly slower relaxation to equilibrium than the Poshax3 solutions with Munafo's T_{ve} being between 500 and 1,000 K greater at $x = 0.5$ cm. Considering that consistent physical modelling is not assured between the two calculations, these minor difference are acceptable. The reasonable agreement with EAST solution of Munafo *et al.* [187] verifies the basic physical modelling for CO₂-N₂ mixtures.

5.3.2 Thermodynamic model variation

The results presented in § 5.3.1 modelled diatomic molecules as harmonic oscillators and considered a reduced number of electronic levels for both atomic and diatomic species. Figures 5.14a and 5.14b compare the post-shock temperature and number density profiles for the 51.4 km Mars condition with the harmonic oscillator and truncated harmonic oscillator models using the reduced electronic level sets. A calculation including all electronic levels and modelling molecules as truncated harmonic oscillators is also shown in order to verify the use of reduced electronic level sets. The physical modelling differs from that in Table 5.4 in that the reaction model is that

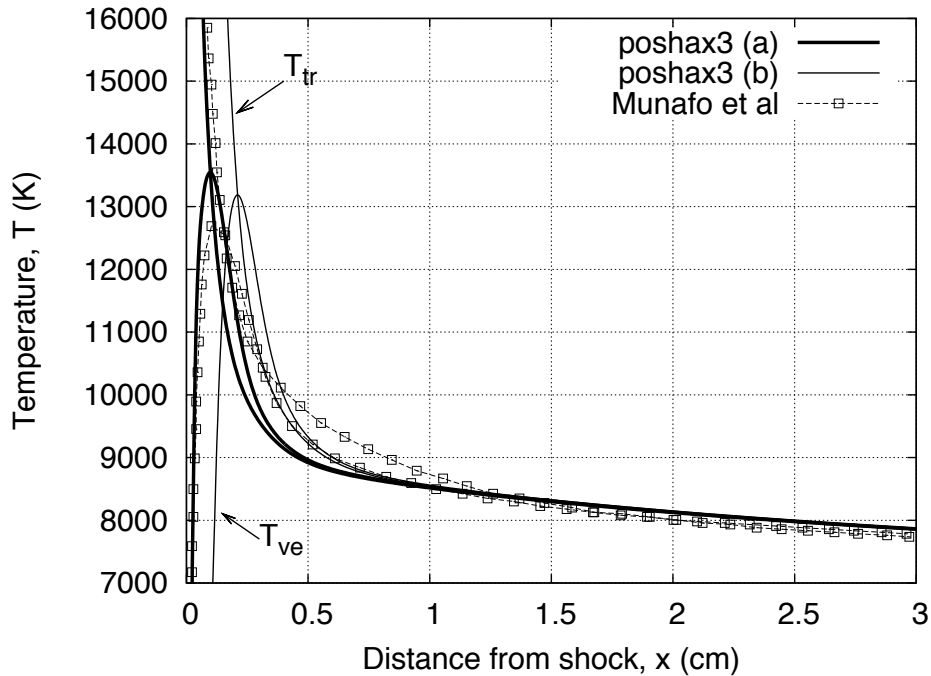


Figure 5.13: Mars EAST one-dimensional post-shock relaxation profiles. Comparison of the solution presented by Munafo *et al.* [187] with Poshax3 calculations assuming (a) harmonic oscillators and (b) truncated harmonic oscillators.

of Park *et al.* [137], all species are assumed to be created and destroyed at their average energy and Park's limiting cross section of translation-vibration exchange is used for all molecules.

Similarly as was observed for air, truncating the vibrational summation at a finite value has the effect of increasing the equilibration distance due to the reduced energy capacity of the molecules. For the Mars 51.4 km condition considered here, the effect is quite dramatic with the distance required for thermal equilibrium being increased from 0.5 cm to 1.5 cm. As the solutions with the reduced and full electronic level sets give almost identical results, the use of reduced level sets is justified. It should be noted that although thermal equilibrium is achieved rapidly in CO₂-N₂ mixtures, chemical equilibrium takes much longer. This can be observed in Figure 5.14b where the species number densities have not yet attained constant values 5 cm behind the shock.

5.3.3 Reaction model variation

The results presented in § 5.3.1 and 5.3.2 implemented the reaction model proposed by Park *et al.* [137]. In the present work a modified version of this reaction model as presented in Table C.2 is implemented. Figures 5.15a and 5.15b compare the post-shock temperature and number density profiles for the 51.4 km Mars condition with the nominal and modified Park reaction models. An additional solution considering the electron impact ionisation of N and Ar in the modified

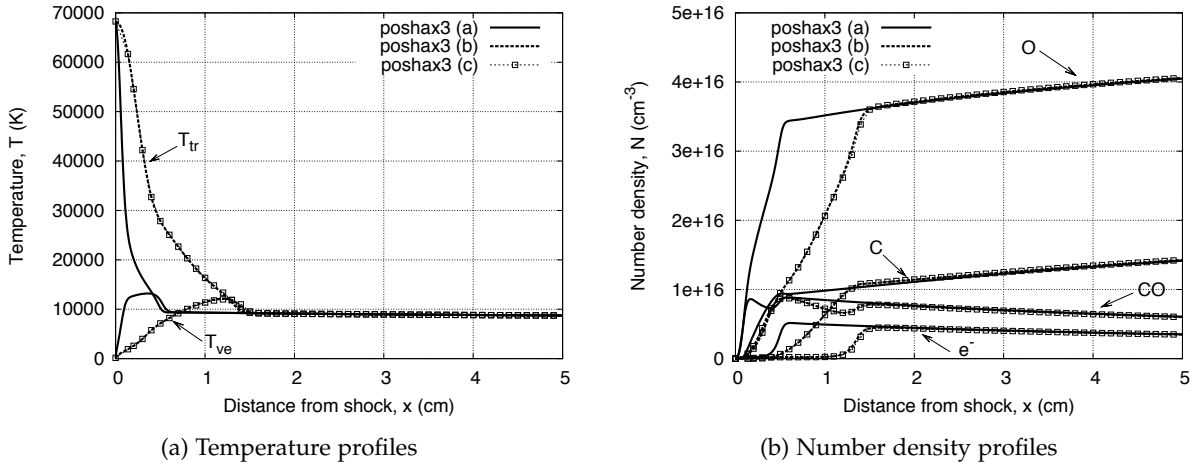


Figure 5.14: Mars 51.4 km one-dimensional post-shock relaxation profiles. Comparison of Poshax3 solutions with various thermodynamic models; (a) harmonic oscillators, reduced electronic levels, (b) truncated harmonic oscillators, reduced electronic levels and (c) truncated harmonic oscillator, all electronic levels.

model is also shown for comparison. The physical modelling differs from that in Table 5.4 in that all species are assumed to be created and destroyed at their average energy and Park's limiting cross section of translation-vibration exchange is used for all molecules.

The effect of the modified Park model is to slightly increase the rate of CO consumption and the production of C and O atoms. This is a result of the additional neutral exchange reactions and a faster C_2 dissociation rate in the modified Park model. The addition of the electron impact ionisation reactions for Ar and N does not have any appreciable influence on the electron number density and can therefore be disregarded.

5.3.4 Dissociation rate coefficient model variation

The results presented in § 5.3.1- 5.3.3 implemented the Park model for nonequilibrium dissociation where the forward rate is governed by the geometric average temperature $\sqrt{T_{\text{trans}}T_{\text{vib}}}$ ($s = 0.5$). Figures 5.16a and 5.16b compare the post-shock temperature and number density profiles for the 51.4 km Mars condition using the Park $s = 0.5$ and Macheret–Fridman dissociation models³. The physical modelling differs from that in Table 5.4 in that all species are assumed to be created and destroyed at their average energy and Park's limiting cross section for translation-vibration exchange is used for all molecules.

The effect of implementing the Macheret–Fridman model for homonuclear molecules has only a small effect on the dissociation processes. The concentration of C and O atoms is slightly

³The Macheret–Fridman model is only valid for homonuclear diatomic species. Therefore in this calculation the Park $s = 0.5$ dissociation model is used for NO, CO, CN and CO_2 .

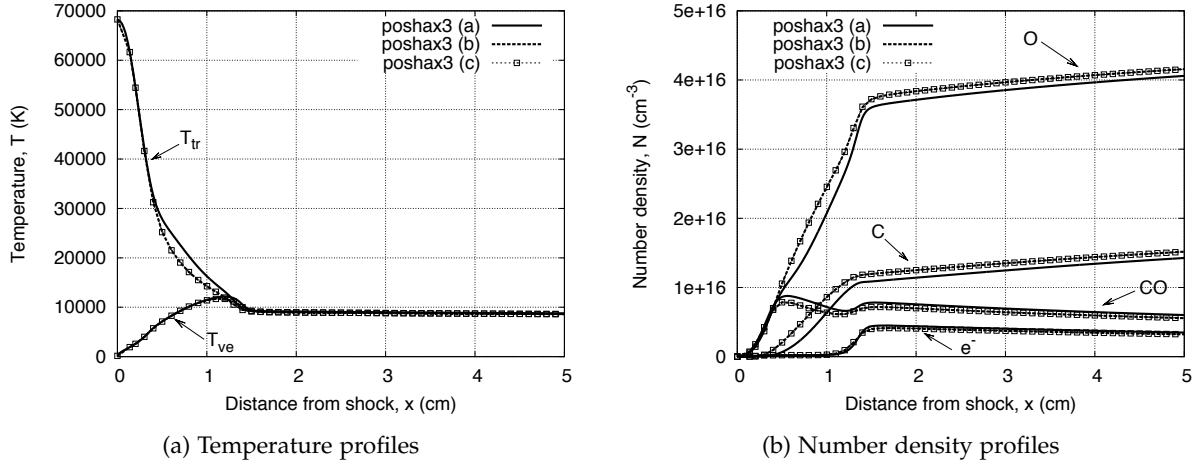


Figure 5.15: Mars 51.4 km one-dimensional post-shock relaxation profiles. Comparison of Poshax3 solutions with various reaction models; (a) nominal Park model [137], (b) modified Park model and (c) modified Park model with N and Ar electron impact ionisation.

reduced in the $0.5 \leq x \leq 1.5$ cm range, however the equilibration distance is not appreciably increased. The ability of the Park $s = 0.5$ to reproduce results using the Macheret–Fridman model is encouraging and justifies its use for $\text{CO}_2\text{--N}_2$ mixtures.

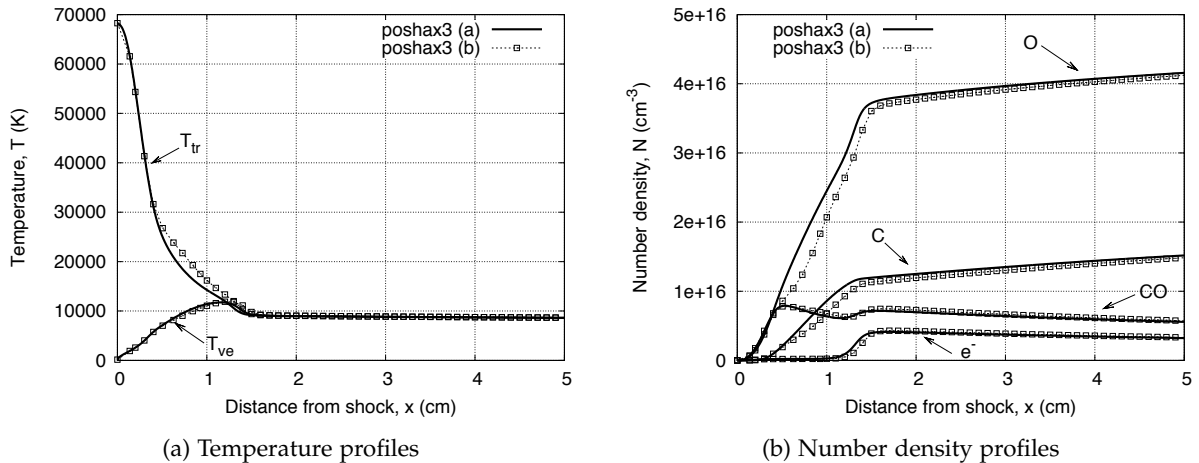


Figure 5.16: Mars 51.4 km one-dimensional post-shock relaxation profiles. Comparison of Poshax3 solutions with various dissociation models; (a) Park model, $s = 0.5$, and (b) Macheret–Fridman model.

5.3.5 Dissociation-vibration coupling model variation

The results presented in § 5.3.1- 5.3.4 implemented a non-preferential vibration-dissociation coupling model where molecules are assumed to be created and destroyed at the average vibrational energy. Figures 5.17a and 5.17b compare the post-shock temperature and number density profiles for the 51.4 km Mars condition using the Park dissociation rate coefficient model ($s = 0.7$) with (a) the non-preferential coupling model, (b) the Park preferential coupling model proposed by Knab *et al.* [145] (see Equation 4.38) and (c) the Treanor–Marrone preferential coupling model with $U = \Theta_D/3$ (see Equation 4.40). Although use of the Treanor–Marrone preferential coupling model alongside the Park dissociation model is not physically consistent, we have included this combination here to allow for a clear comparison of the dissociation-vibration coupling with a common dissociation rate coefficient model. The physical modelling differs from that in Table 5.4 in that all species except molecules are assumed to be created and destroyed at their average energy and Park’s limiting cross section of translation-vibration exchange is used for all molecules.

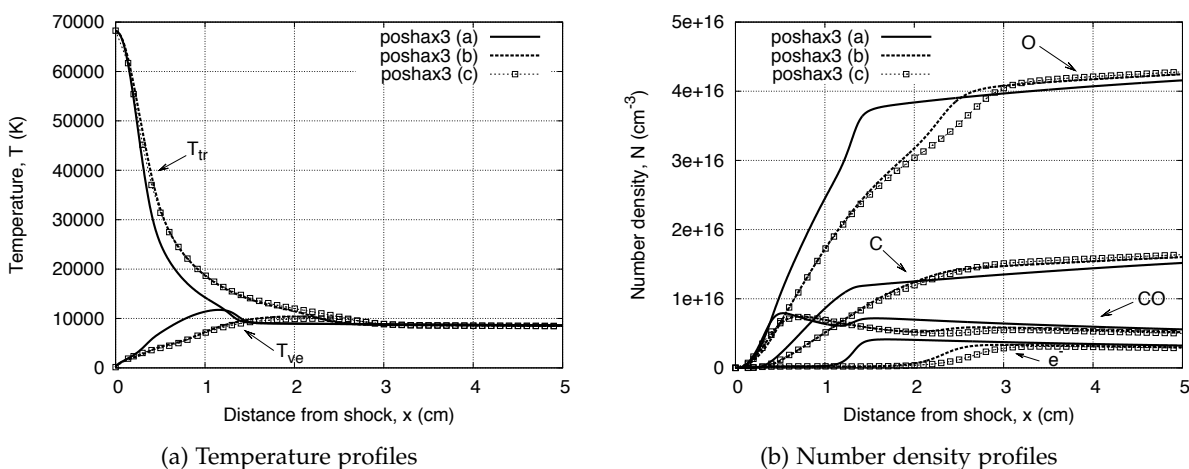


Figure 5.17: Mars 51.4 km one-dimensional post-shock relaxation profiles. Comparison of Poshax3 solutions with various dissociation-vibration coupling models; (a) non-preferential coupling (b) Park preferential coupling, $s = 0.7$ (c) Treanor–Marrone coupling, $U = \Theta_D/3$.

The addition of preferential dissociation-vibration coupling doubles the equilibration distance for this condition. This is a result of vibrational energy loss lowering T_{ve} and subsequently slowing the rate of dissociation and ionisation. In contrast to the results for air, both the Park and Treanor–Marrone coupling models give similar results. This is because a substantial population of CO molecules remain and considerably more energy is stored in the vibrational modes, preventing slight differences in the coupling models from becoming noticeable. As the two models produce similar effects on post-shock relaxation, the Park dissociation-vibration coupling model is implemented in the present work as it is consistent with the use of the geometric average temperature to control the dissociation rate coefficients.

5.3.6 Chemistry-electron coupling model variation

The results presented in § 5.3.1- 5.3.5 implemented a baseline chemistry-electron coupling model where additional energy exchange due to ionisation reactions was neglected (*i.e.* $\alpha_{AI} = 0$ and $\alpha_{EII} = 0$). Figures 5.18a and 5.18b compare the post-shock temperature and number density profiles for the 51.4 km Mars condition considering (a) baseline chemistry-electron coupling (b) classical electron impact ionisation coupling (*i.e.* $\alpha_{EII} = 1$) and (c) classical electron impact ionisation coupling and associative ionisation coupling with $\alpha_{AI} = 0.1$. The physical modelling differs from that in Table 5.4 in that Park's limiting cross section of translation-vibration exchange is used for all molecules.

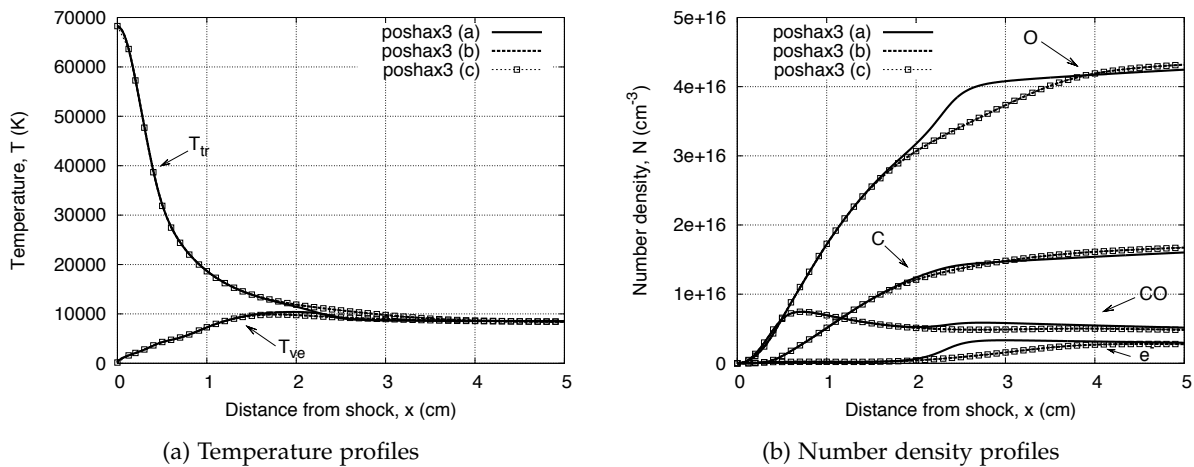


Figure 5.18: Mars 51.4 km one-dimensional post-shock relaxation profiles. Comparison of Poshax3 solutions with various chemistry-electron coupling models; (a) reduced electron impact ionisation coupling (b) classical electron impact ionisation coupling and (c) classical electron impact ionisation and associative ionisation coupling with $\alpha_{AI} = 0.1$.

The consideration of electron impact ionisation coupling slightly reduces T_{ve} as it approaches its peak of 10,000 K approximately 2 cm from the shock, and subsequently suppresses the rapid free electron production that is predicted in the $2 \leq x \leq 3$ cm range by the solution without electron impact ionisation coupling. In addition, the production of C and O atoms in this range is also reduced. This is due to slower rates of associative ionisation-recombination that occur as a consequence of the lowered electron concentration.

5.3.7 Vibration-translation exchange model variation

The results presented in § 5.3.1- 5.3.6 implemented the limiting cross sections for vibration-translation proposed by Park (see Equation 4.27). In § 4.2.1 an alternative model for this cross

section of CO proposed by Fujita [77] was described. Figures 5.18a and 5.18b compare the post-shock temperature and number density profiles for the 51.4 km Mars condition with (a) Park's limiting cross sections for all species, (b) Fujita's limiting cross section for CO and (c) Park's limiting cross sections for all species and omitting preferential dissociation-vibration coupling. For case (b) the physical modelling is as described in Table 5.4.

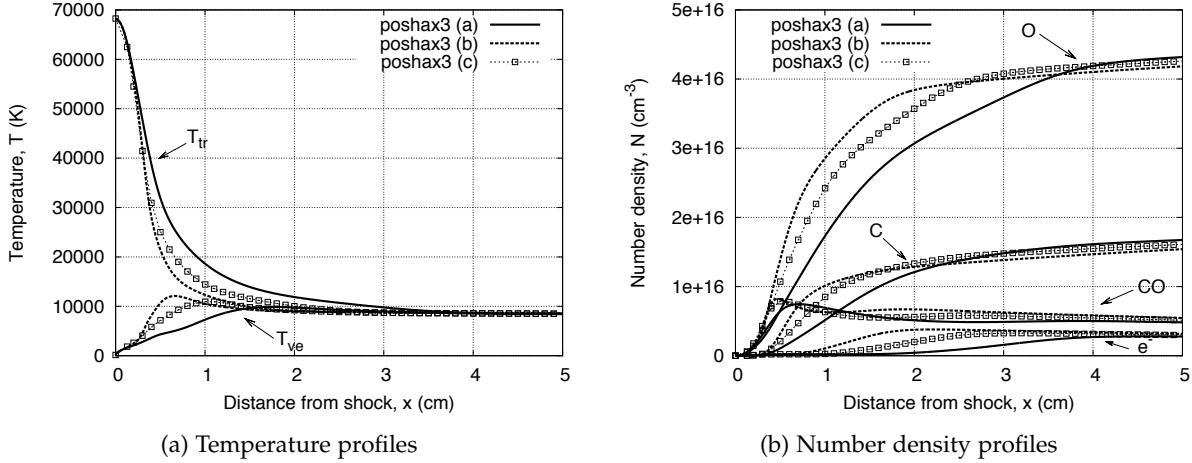


Figure 5.19: Mars 51.4 km one-dimensional post-shock relaxation profiles. Comparison of Poshax3 solutions with various vibration-translation exchange limiting cross section models; (a) Park model for all species, (b) Fujita model for CO and Park model for the remainder and (c) Park limiting cross sections for all species and omitting preferential dissociation-vibration coupling.

The use of Fujita's limiting cross section for CO drastically increases the rate of vibrational relaxation, with thermal equilibrium being attained 2 cm instead of 4 cm from the shock. The follow-on effect on chemistry is to increase the rate of C, O and e⁻ production in the $0 \leq x \leq 3$ cm range. It is interesting to note that the use of Fujita's limiting cross section for CO counteracts the effect of dissociation vibration coupling. Given that the rate coefficients and vibration-translation energy exchange model proposed by Park *et al.* [137] was developed without considering preferential dissociation-vibration coupling, it may be argued that using Park's limiting cross section without preferential dissociation-vibration coupling is more appropriate. These two models will be assessed via comparison with shock tube measurements in § 6.

5.3.8 Radiation model variation

The results presented in § 5.3.1- 5.3.7 considered optically thick radiation-flowfield coupling (*i.e.* $\frac{\partial q_{\text{rad}}}{\partial x} = 0$). Figures 5.19a and 5.19b compare the post-shock electron number density and radiative emission coefficient profiles for the 51.4 km Mars condition with (a) equilibrium electronic populations and optically thick radiation coupling, (b) nonequilibrium electronic populations and optically thick radiation coupling and (c) nonequilibrium electronic populations and optically

thin radiation coupling. The nonequilibrium electronic populations are calculated with the QSS collisional-radiative model described in § 4.3. For case (b) the physical modelling is as described in Table 5.4.

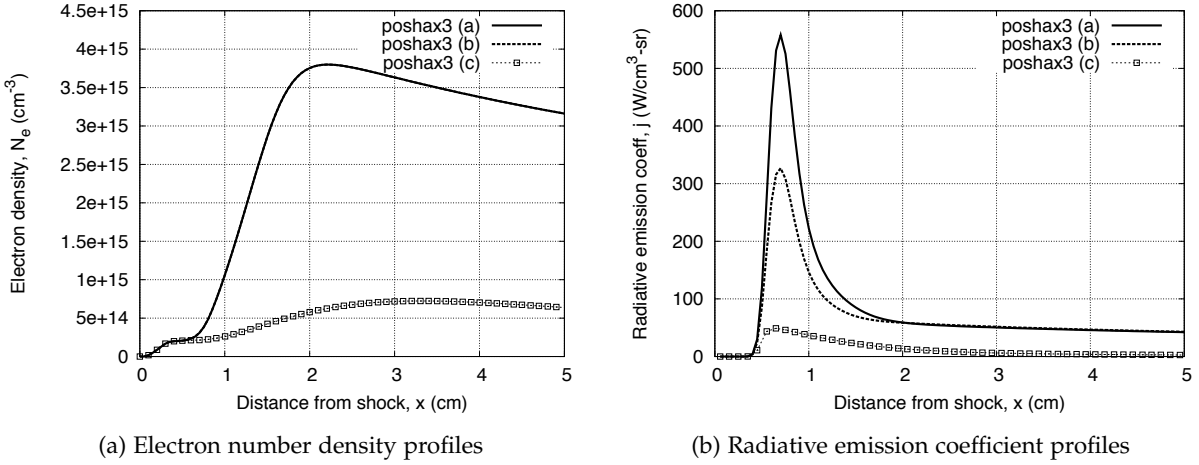


Figure 5.20: Mars 51.4 km one-dimensional post-shock relaxation profiles. Comparison of Poshax3 solutions using various radiation models; (a) equilibrium, optically thick, (b) nonequilibrium, optically thick and (c) nonequilibrium, optically thin.

The optically thick equilibrium case significantly overpredicts the radiative emission coefficient, with a peak j value of 550 W/cm²-sr compared to 310 W/cm²-sr for the nonequilibrium optically thick case. The consideration of optically thin flowfield coupling has a large radiative cooling effect for this low density condition. The peaks in electron concentration and radiative emission coefficient are reduced by a factor of approximately five compared to the optically thick case. Figures 5.20a and 5.20b compare the post-shock electron number density and radiative emission coefficient profiles for the Mars EAST condition. This condition is characterised by higher density and the radiative cooling effect is therefore not as strong as the Mars 51 km case. It should be noted that the VUV spectral region contributes the bulk of the radiation for this condition and considerable local re-absorption is expected to take place.

5.3.9 Three temperature model

The results presented in § 5.3.1- 5.3.8 considered a two-temperature formulation of the post-shock relaxation equations. Figures 5.22a and 5.22b compare the post-shock temperature and number density profiles for the Fire II $t = 1634$ s case with (a) a two-temperature model, (b) a three-temperature model and (c) a three-temperature model with the vibration-electron relaxation time τ_{VE} artificially increased by a factor of 10. Note that the x range has been reduced from $0 \leq x \leq 5$ cm to $0 \leq x \leq 2$ cm for clarity. For case (a) the physical modelling is as described in Table 5.4.

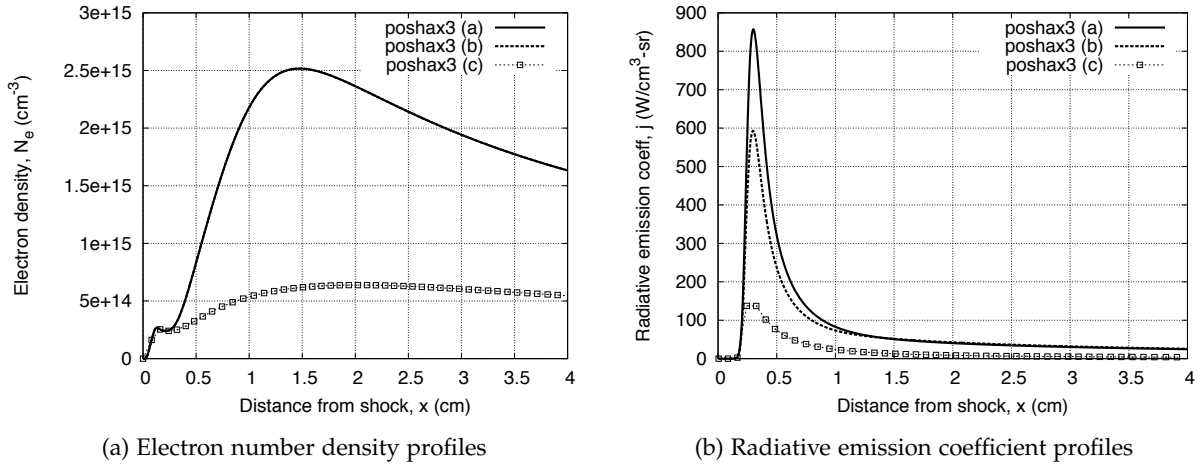


Figure 5.21: Mars EAST one-dimensional post-shock relaxation profiles. Comparison of Poshax3 solutions using various radiation models; (a) Equilibrium, optically thick, (b) QSS, optically thick and (c) QSS, optically thin.

The three-temperature model predicts a rise in T_e in the $0 \leq x \leq 0.25$ cm range that the two-temperature model does not. This is due to association ionisation coupling adding energy to the free electrons as they formed here. As the primary radiating species (CO, C and O) are only present in low concentrations at this location, the increased T_e should not have a large effect on the radiative emission coefficient profile. The effect disappears after this range and T_e is pulled up towards T_v due to vibration-electron energy exchange. This is evident by the much longer thermal equilibration observed for the three-temperature model with $\tau_{VE} \times 10$. T_e is only slightly less than the two-temperature T_{ve} in the nonequilibrium region and the effect on the free electron concentration is small. Overall the three-temperature solution is well approximated by the two-temperature model, therefore justifying its use in the present work.

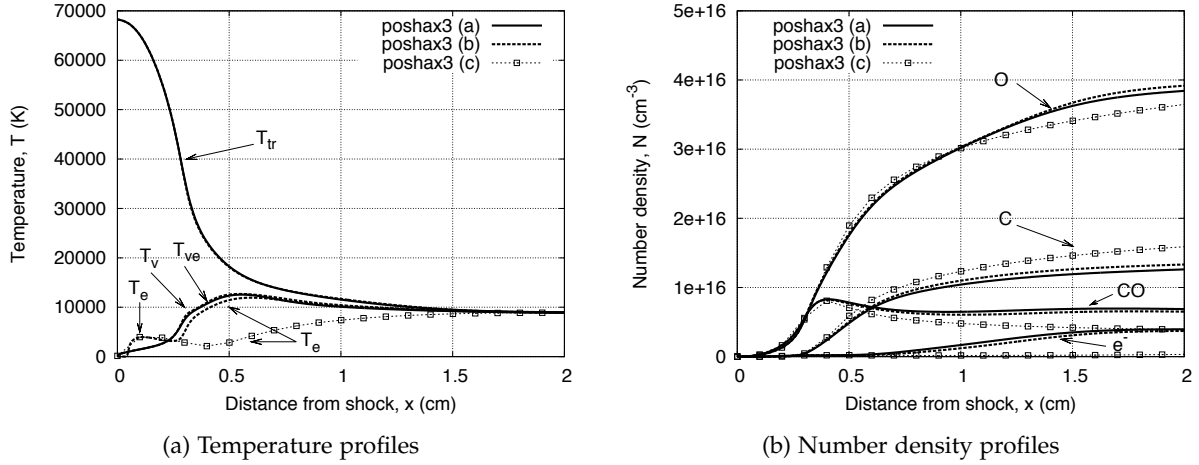


Figure 5.22: Mars 51.4 km one-dimensional post-shock relaxation profiles. Comparison of Poshax3 solutions with various gas-models; (a) two-temperature model, (b) three-temperature model and (c) three temperature model, $\tau_{VE} \times 10$.

5.4 Summary

The implementation of the post-shock relaxation equations for two- and three-temperature gases with radiation-flowfield coupling in the Poshax3 code has been presented. The ODE system is integrated in a fully coupled manner, and radiative cooling is modelled in an approximate manner via an escape factor. The implementation of the post-shock relaxation equations in the Poshax3 code has been verified via comparison with the Fire II solutions presented by Panesi [58]. Good agreement was found for both the temperature and species number density profiles. Finally, the effect of the various physical models presented in § 3 and 4 has been shown by application of the code to both Earth and Mars atmospheric entry conditions. An important finding of this analysis is the sensitivity of the post-shock relaxation to dissociation-vibration and ionisation-electron coupling.

6

Analysis of non-reflected shock tube experiments

In this chapter analyses are performed of non-reflected shock tube experiments relevant to hyperbolic atmospheric entry and Earth and Mars. Spatially and spectrally resolved spectroscopic measurements from experiments performed in two facilities are considered:

1. EAST facility at the NASA Ames Research Centre, and
2. X2 facility at the University of Queensland.

For the EAST facility, 10 km/s 0.1 and 0.3 Torr N₂–O₂ conditions and an 8.5 km/s 0.1 Torr CO₂–N₂ condition are investigated. For the X2 facility an 11 km/s 0.12 Torr N₂–O₂ condition is investigated. The primary experimental data of interest are spectroscopic measurements. The experiments in both facilities made spatially and spectrally resolved spectroscopic measurements in the ultraviolet and infrared spectral regions.¹ These measurements are obtained when the shock is in the shock tube for the EAST facility, Figure 6.1a, and when the shock is emerging out of the shock tube for the X2 facility, Figure 6.1b. In § 6.1 the one-dimensional modelling strategy for simulating the shock tube experiments is described and critically assessed by considering Navier–Stokes solutions presented in the literature, and comparing the measurements obtained in the two facilities. Comparisons with the EAST and X2 experiments using the one-dimensional post-shock relaxation equations are then presented in § 6.2 and 6.3 respectively.

¹Vacuum ultraviolet measurements have recently been made in the EAST facility, but were not available for analysis at this time.

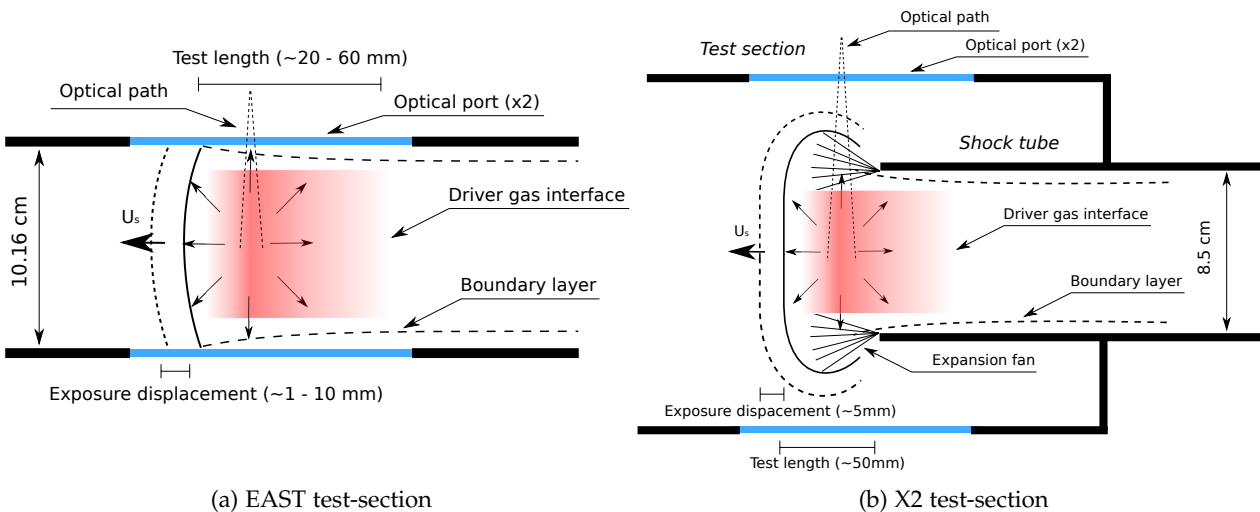


Figure 6.1: Spectroscopic measurement in the EAST and X2 non-reflected shock tube facilities.

6.1 Modelling strategy

In the present work the shock tube experiments are simulated with the one-dimensional post-shock relaxation equations. The implementation of the one-dimensional post-shock relaxation equations in the Poshax3 code was described in § 5. Such an approach proved adequate for numerous investigations of similar experiments in recent years [15, 35, 36, 56, 171]. As the one-dimensional post-shock relaxation equations neglect viscous effects and radial flow variations, however, it is useful to first consider the Navier–Stokes calculations presented in the literature and compare measurements obtained from X2 and EAST to assess the importance of these effects.

6.1.1 Assessment of the one-dimensional and inviscid assumptions

Navier–Stokes calculations have recently been presented in the literature for both the EAST [188] and X2 [1, 189] facilities. McCorkle *et al.* [188] simulated a 10 km/s 0.2 Torr condition in the EAST facility with the DPLR code using a two-temperature model. Radiation was calculated in an uncoupled manner with the NEQAIR code by integrating along lines-of-sight from the Navier–Stokes solutions. The simulations estimate the region of boundary layer influence at the wall to be less than 0.8 mm for the test gas behind the shock. Table 6.1 compares the equilibrium intensity presented in Reference [188] with those obtained using the spectral model described in § 3.3 where the equilibrium post-shock flow state is calculated using the CEA2 program [5] and assumed radially uniform (*i.e.* zero-dimensional analysis). The width of gas observed by the spectrometer is assumed to be the tube width, 10.16 cm, and the quoted uncertainties (approximately $\pm 30\%$) in the calculated radiative intensities are based on the $\pm 1.5\%$ uncertainty in shock speed. The experimentally measured values are also shown for reference. The zero-dimensional

results are greater than those from the Navier–Stokes calculations in the $165 \leq \lambda \leq 215\text{ nm}$, $180 \leq \lambda \leq 490\text{ nm}$ and $490 \leq \lambda \leq 910\text{ nm}$ spectral ranges, and equal in the $900 \leq \lambda \leq 1100\text{ nm}$ spectral range. Although it is difficult to make definitive comparisons as the radiation codes used are different, these results may indicate reabsorption is occurring in the boundary layer for certain spectral ranges. However, the differences between the two calculations are equal to or less than the uncertainty due to the shock speed measurement, and most of the experimental measurements are actually closer to the zero-dimensional calculation. For the equilibrium region of this 10 km/s 0.2 Torr condition, therefore, there is little benefit in simulating with the Navier–Stokes equations.

Table 6.1: Comparison of equilibrium intensities for a 10 km/s 0.2 Torr shock tube condition in the EAST facility.

Spectral range	Intensity, I ($\text{W}/\text{cm}^2\text{-sr}$)		
	Experiment	Navier–Stokes [188]	Zero-D analysis
$165 \leq \lambda \leq 215\text{ nm}$	1.2	1.4	1.7 ± 0.5
$180 \leq \lambda \leq 490\text{ nm}$	2.8	1.4	1.6 ± 0.5
$490 \leq \lambda \leq 910\text{ nm}$	7.4	5.6	6.8 ± 2.0
$900 \leq \lambda \leq 1100\text{ nm}$	2.9	3.8	3.8 ± 1.1

Gollan *et al.* [1, 189] simulated a 7 km/s 6 Torr $\text{N}_2\text{-CH}_4$ shock tube condition in the X2 facility with the `mbcns` Navier–Stokes solver. Thermal equilibrium was assumed and ionic species were not included in the calculations. Figure 6.2 presents CN mass-fraction profiles from the Navier–Stokes calculations presented in Reference [1] where the shock is approximately 120 mm from the shock tube exit. The CN mass-fraction profile obtained from a simulation with the one-dimensional post-shock relaxation solver `poshax` is also shown for comparison. The central 4.8 cm diameter core of the test gas is shown to be well described by the one-dimension post-shock relaxation equations, however at a radius of 3.2 cm the Navier–Stokes calculation estimates a sudden drop in CN mass-fraction that the one-dimensional calculation does not. This is likely to be caused by the expansion waves emanating from tube exit reducing the gas pressure in this region. In addition, the overshoot in CN density is considerably more diffusive in the Navier–Stokes calculation. This is due to shock capturing nature of the Navier–Stokes calculations and the omission of viscous effects in the one-dimensional calculation. Overall, however, the agreement between the two calculations is adequate considering that corrections for the width of gas observed by the spectrometer can be made when computing radiative intensity.

Further verification of the one-dimensional nature of the X2 experiments can be made by comparing with measurements from the EAST facility. Figures 6.3a and 6.3b compare optically thin radiative emission coefficient profiles from spectral measurements in the EAST and X2 facilities in the wavelength ranges $700 \leq \lambda \leq 760\text{ nm}$ and $760 \leq \lambda \leq 800\text{ nm}$ respectively. The

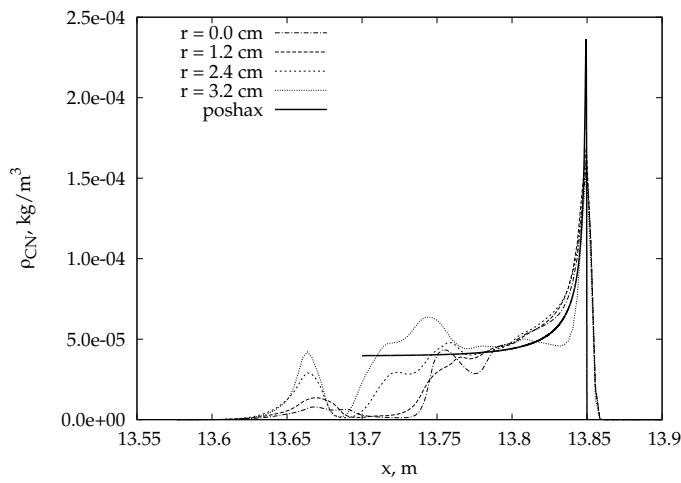


Figure 6.2: CN mass-fraction profiles from the Navier–Stokes and one-dimensional calculations performed by Gollan [1] of a 7 km/s 6 Torr N₂–CH₄ shock tube condition in the X2 facility. The Navier–Stokes solution corresponds to shock location of approximately 120 mm from the tube exit (Source: Figure 6.15b in Reference [1]).

optically thin emission coefficient is calculated by dividing the measured intensity $I_{\text{meas.}}$ by an assumed optical width ΔL_{gas} :

$$j_{\text{OT}} = \frac{I_{\text{meas.}}}{\Delta L_{\text{gas}}} \quad (6.1)$$

For the EAST measurements the comparison with the calculations of McCorkle presented in Table 6.4 indicate the gas width is approximately the tube diameter:

$$L_{\text{gas,EAST}} = D_{\text{tube}} = 10.16 \text{ cm} \quad (6.2)$$

For the X2 measurements, the optically thin emission coefficient overestimates the EAST measurements when the optical width is set to the tube diameter of 8.5 cm. Reasonable agreement can be attained, however, when the optical width is assumed to be approximately 70% of the tube diameter:

$$L_{\text{gas,X2}} = 0.7D_{\text{tube}} \approx 6 \text{ cm} \quad (6.3)$$

These results indicate that the assumption of inviscid and one-dimensional flow is adequate for an initial analysis of the non-reflected shock tube experiments in both the EAST and X2 facilities. It should be recognised, however, that the one-dimensional analysis is likely to overestimate the nonequilibrium radiation overshoot phenomena due to the omission of dissipative mechanisms such as diffusion and shock capturing. Also, the presence of the boundary layer may

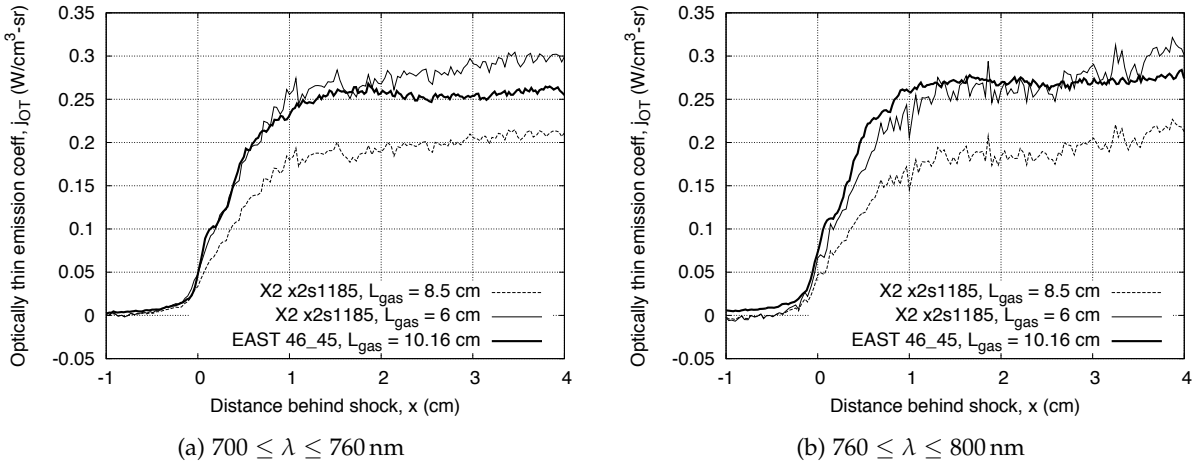


Figure 6.3: Comparison of infrared optically thin emission coefficient profiles from spectral measurements in the EAST and X2 facilities.

be significant for certain conditions. Axisymmetric simulations should therefore be pursued in future work to exactly quantify these effects on the solution.

6.1.2 Radiation-flowfield coupling

Rather than attempting to model radiation-flowfield coupling in a non-local fashion, approximate models that represent various limiting cases are applied. Firstly, optically thin and optically thick radiation-flowfield coupling as discussed in § 5.1.3 are considered, representing 100% and 0% net emission respectively. Of these two models, it is anticipated that the optically thick solution will be closer to the measured value for a number of reasons. Firstly, radiation for the conditions of present interest has significant contributions from the VUV spectral region where self-absorption is strong. Secondly, the test gas is confined within the shock tube up until just before the spectral measurement, with the reflective tube walls increasing the chance of reabsorption by the test gas. In addition to physical appropriateness of the optically thick model, it also has the benefit of being computationally efficient as the full radiation spectra does not need to be evaluated at each integration step. Therefore in the present work the nominal radiation transport model for the shock tube simulations is the optically thick model. In light of the assumption that VUV radiation will be strongly absorbed, it is also appropriate to consider a radiation-flowfield coupling model with a optically thick VUV radiation and optically thin radiation in all other spectral regions. This will be referred to as the ‘optically variable’ model and its escape factor is calculated as a function of wavelength:

$$\Lambda(\lambda) = \begin{cases} 0 & \text{for } \lambda \leq 200 \text{ nm} \\ 1 & \text{for } \lambda > 200 \text{ nm} \end{cases} \quad (6.4)$$

It should be noted that the escape factor applied to the radiative source term is also applied to the radiative decay rates in the collisional-radiative model. For example when the optically thick model is applied, radiative decay is omitted from the collisional-radiative model.

6.1.3 Calculation of spectral intensity for comparison with experiment

The spectral intensity as a function for wavelength and axial location must be computed for comparison with the experiment measurements. For a slab of radiating, homogenous gas of thickness ΔL_{gas} (see Figure 5.1) the spectral intensity I_λ at the far edge of the slab is:

$$I_\lambda = \frac{j_\lambda}{\kappa_\lambda} \left(1 - e^{-\kappa_\nu \Delta L_{\text{gas}}} \right) \quad (6.5)$$

where emission from the walls is assumed to be negligible as they are at room temperature. As discussed in § 6.1.1, the width of radiating gas observed by the spectrometer is assumed to be the tube width for the EAST experiments ($\Delta L_{\text{gas}} = 10.16 \text{ cm}$) and 70% of the tube width for the X2 experiments ($\Delta L_{\text{gas}} = 6.0 \text{ cm}$). As the experimental calibrations take into account the full optical path, the transmission of the radiation through the viewing windows, laboratory air and optical apparatus does not have to be considered.

Before the results of Equation 6.5 can be compared with experiment, the exposure time and apparatus function of the spectrometer must be considered. The effect of a finite exposure time is for the test gas to move slightly as the measurement is taking place, smearing the spectral data in the axial direction. This can be replicated in the calculations by performing a spatial convolution on the spectral intensity I_λ . The test gas is assumed to be not accelerating during the exposure, and a simple rectangular convolution function $g(x) = 1$ is therefore appropriate:

$$I_\lambda(x') = \frac{\int_{x'}^{x'+\Delta x'} I_\lambda(x) g(x) dx}{\int_{x'}^{x'+\Delta x'} g(x) dx} = \frac{\int_{x'}^{x'+\Delta x'} I_\lambda(x) g(x) dx}{\Delta x'} \quad (6.6)$$

where the exposure displacement is the product of the exposure time and shock speed, $\Delta x' = \Delta_t U_s$. It should be noted that this convolution function represents a square pulse in camera gating, perfect focus and no charge pixel charge bleed in the camera, none of which would be satisfied perfectly in the actual experiment. As the movement of the shock is most likely to represent the largest spatial smearing effect on the spectra, however, it is adequate for the analysis at hand.

Due to optical effects in the spectrograph, the intensity measured at a particular wavelength actually includes contributions from the surrounding wavelengths. This effect is quantified by the apparatus function for the spectrometer. For comparison with spectrometer data, the calculated spectra at each spatial location is spectrally convolved with the apparatus function $g(\Delta\lambda)$:

$$I'_\lambda(x') = \frac{\int_{\lambda'_{\min}}^{\lambda'_{\max}} I_\lambda(\lambda) g(\lambda - \lambda') d\lambda}{\int_{\lambda'_{\min}}^{\lambda'_{\max}} g(\lambda - \lambda') d\lambda} = \int_{\lambda'_{\min}}^{\lambda'_{\max}} I_\lambda(x') g(\lambda - \lambda') d\lambda \quad (6.7)$$

In the present work a normalised Gaussian apparatus function is assumed:

$$g(\Delta\lambda) = \frac{1}{\Delta\lambda_{\text{HWHM}}} \sqrt{\frac{\ln(2)}{\pi}} \exp\left(-\ln(2) \frac{\Delta\lambda^2}{\Delta\lambda_{\text{HWHM}}^2}\right) \quad (6.8)$$

where $\Delta\lambda_{\text{HWHM}}$ is the half-width at half-maximum of the spectrometer apparatus function. The half-width at half-maximum is dependent on the spectrometer setting for the particular shot and is provided with the experimental data.

6.1.4 Physical modelling

Unless otherwise stated, the physical modelling of thermodynamic, chemical kinetic, energy exchange and radiative processes are those described in Table 5.2 for the N₂–O₂ conditions in and Table 5.4 for the CO₂–N₂ conditions.

6.2 NASA Ames EAST Facility

A series of non-reflected shock tube spectroscopy experiments were recently performed in the EAST facility at the NASA Ames Research Center with both CO₂–N₂ [3] and N₂–O₂ [2] test gases. Here selected conditions with both test gases are considered.

6.2.1 Facility description

The EAST facility is an electric arc driven shock tube with an aluminium driven tube 10.16 cm in diameter. A schematic of the EAST facility is presented in Figure 6.4. The arc discharge is supplied to a tungsten trigger wire by a 1.2 MJ, 40 kV capacitor bank. The driver gas in the experiments was helium, and the primary diaphragm was aluminium with a burst pressure of 1.1 MPa. Shock speed is measured by pressure transducers and photomultiplier tubes located at stations G-L, N and O. For further details on the operating characteristics of the EAST facility, the interested reader is referred to References [190] and [191].

6.2.2 Spectroscopic apparatus

Spectroscopy measurements were made through the observation ports 7.4 m from the diaphragm, corresponding to station M in Figure 6.4. A schematic of the EAST test section was presented in Figure 6.1a. Spatially and spectrally resolved intensity measurements were obtained with infrared and ultraviolet imaging spectrographs. Princeton Instruments PI-MAX spectrographs

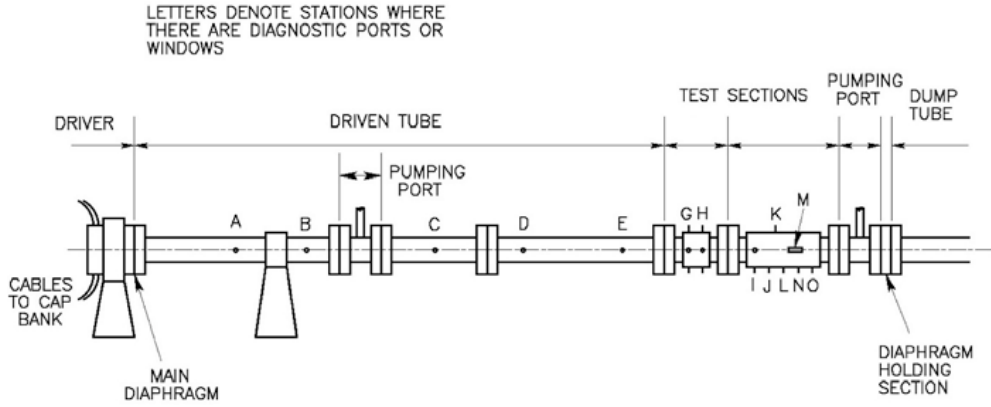


Figure 6.4: Schematic of the EAST facility at the NASA Ames Research Center (Source: Figure 3 in Reference [2]).

were used with a 1024×256 pixel CCD array for the ultraviolet measurements and a 512×512 pixel CCD array for the near-infrared measurements. Details of the spectroscopic measurements for the air and Mars conditions are to be presented in § 6.2.3 and 6.2.4.

6.2.3 Air conditions

The EAST experiments with an air test gas considered initial test gas pressures of 0.1, 0.2, 0.3 and 1.0 Torr at a nominal velocity of 10 km/s. Due to inherent variability of the arc-heated driver however, the actual shock speeds ranged from 9 to 11 km/s [2]. In the present work the 0.1 and 0.3 Torr conditions are considered as they bound the range of pressures likely to be encountered at a velocity of 10 km/s during Earth atmospheric entry.

The theoretical equilibrium intensity spectra for a 10 km/s shock through 0.3 Torr air is presented in Figure 6.5, where the spectral ranges considered by the EAST experiments are indicated. In the ultraviolet spectral region, measurements in the ranges $190 \leq \lambda \leq 365$ nm and $290 \leq \lambda \leq 485$ nm were considered. Here, the dominant spectral feature in pure air is the N_2^+ Fist Negative band system ($B^2\Sigma_u^+ \Rightarrow X^2\Sigma_g^+$) where the 0-0 band-head is located at 391 nm. Due to carbon contaminated in the facility, however, the CN molecule is formed which also radiates strongly in the UV via the Violet band system ($B^2\Sigma^+ \Rightarrow X^2\Sigma^+$). The CN Violet band system has its 0-0 band-head at 388 nm and therefore overlaps the N_2^+ Fist Negative band system. As it is difficult to quantify the level of carbon contamination, no attempt is made in the present work to simulate the formation and radiation of CN in the EAST experiments. The measured intensity in the UV is therefore anticipated to be underestimated by the calculations. Useful comparisons can still be made in the nonequilibrium region, however, as the bulk of the CN molecules are likely to be in the boundary layer and therefore exhibit a much weaker nonequilibrium overshoot behind the shock.

In the infrared spectral region, measurements in the ranges $700 \leq \lambda \leq 880$ nm and $880 \leq \lambda \leq$

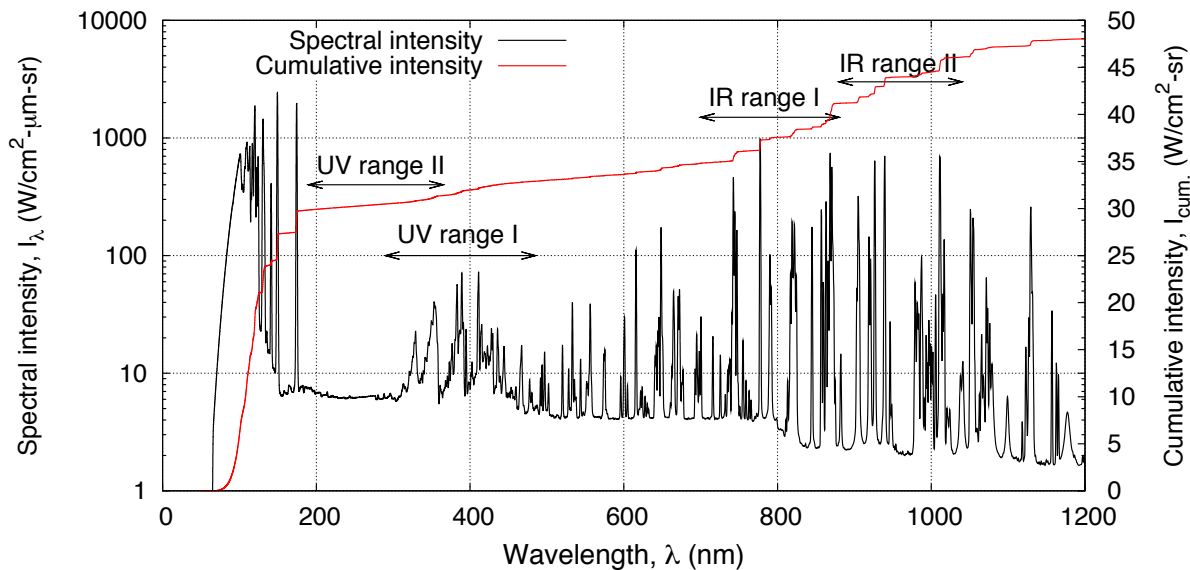


Figure 6.5: Theoretical equilibrium intensity spectra for a 10 km/s shock through 0.3 Torr air with spectral ranges considered by the EAST experiments.

Table 6.2: Summary of the dominant infrared atomic spectral features considered for the EAST air experiments.

Group	Spectral ranges	Spectral features				
		Species	λ_{CL} (nm)	i_{upper}	i_{lower}	A_{ul} (s^{-1})
N lines I	$700 \leq \lambda \leq 760$ nm	N	745.4	10	4	3.76×10^7
	$800 \leq \lambda \leq 830$ nm	N	821.4	9	4	3.1×10^7
	$850 \leq \lambda \leq 880$ nm	N	861.4	12	5	3.15×10^7
		N	869.4	8	4	2.47×10^7
N lines II	$900 \leq \lambda \leq 915$ nm	N	905.0	29	12	2.79×10^7
		N	905.2	16	7	2.97×10^7
	$931 \leq \lambda \leq 952$ nm	N	937.6	37	29	1.46×10^7
		N	939.8	11	5	2.63×10^7
O lines I	$1005 \leq \lambda \leq 1020$ nm	N	1012.0	17	8	3.75×10^7
	$760 \leq \lambda \leq 800$ nm	O	777.6	6	4	3.69×10^7
	$830 \leq \lambda \leq 850$ nm	O	844.9	7	5	3.22×10^7
O lines II	$915 \leq \lambda \leq 931$ nm	O	926.6	10	6	4.45×10^7

1040 nm were considered. Here the dominant spectral features are atomic lines, as summarised in Table 6.2. λ_{CL} is the center wavelength of the line(s), i_{lower} and i_{upper} are the corresponding lower and upper level indices of the transition (see Table B.2) and A_{ul} is the theoretical transition probability. In the results that follow, infrared intensity profiles in the four indicated groupings are presented where each group corresponds to spectral ranges dominated by either N or O atomic lines. Group 'N lines I' corresponds to atomic N transitions originating from relatively low lying levels while 'N lines II' corresponds to atomic N transitions originating from high lying levels. Both oxygen groups 'O lines I' and 'O lines II' correspond to transitions from relatively low lying levels. These transitions account for approximately 20% of the total intensity emitted in the $50 \leq \lambda \leq 1200$ nm spectral range, whereas atomic lines in the VUV account for over 50% of the total intensity. Despite that spatially resolved VUV measurements were not made, the available measurements are still relevant as the measured intensity in the optically thin near infrared region is proportional to the upper state populations of levels which also drive key VUV transitions.

0.3 Torr conditions

The two 0.3 Torr EAST conditions with an air test gas that are considered in the present analysis are summarised in Table 6.3. Shot 46/45 is slightly faster than the targeted shock speed of 10 km/s, and 46/46 is slightly slower. Due to the sensitivity of radiation to shock speed, separate simulations are performed for each shot at the appropriate shock speed when comparing with experimental data. The infrared spectrometer for shot 46/45 measured radiation in the $700 \leq \lambda \leq 880$ nm spectral range, while for shot 46/46 radiation at the higher wavelength range of $880 \leq \lambda \leq 1040$ nm was measured. For the ultraviolet spectrometer, there is some overlap between the two shots with 46/45 measuring in the $290 \leq \lambda \leq 475$ nm range and 46/46 in the $190 \leq \lambda \leq 365$ nm range. The IR exposure time for shot 46/45 is $0.075 \mu\text{s}$ which is over an order of magnitude less than for 46/46. The effect of spatial smearing will therefore be much greater for shot 46/46, and the intensity profiles will appear more diffusive.

Before analysing the experimental data, it is useful to consider the post-shock relaxation for the nominal 10 km/s shock speed condition. Figures 6.6a and 6.6b present temperature and number density profiles for the nominal 10 km/s shock through 0.3 Torr air calculated with the two-temperature model. The number density profiles are limited to those species most relevant to radiation: N_2^+ , N, O and e^- . Also indicated are the electronic-electron temperature T_e and electron concentration calculated by the three-temperature model. At this relatively high pressure, thermochemical equilibrium is achieved 1 cm behind the shock. Therefore nonequilibrium processes only play a minor role for shots 46/45 and 46/46, with the majority of the gas observed by the spectrometers being in equilibrium. Furthermore, the three-temperature electronic-electron temperature and electron concentration show close agreement with the two-temperature results,

Table 6.3: Summary of the 0.3 Torr air EAST shots [2] considered.

Shot number	46/45	46/46
Shock speed, U_s (m/s)	10340 ± 155	9880 ± 148
Pressure, p_∞ (Torr)	0.3	0.3
Effective test time (μs)	7.53	7.94
UV Spectrometer range (nm)	290 - 475	190 - 365
UV Exposure time (μs)	0.25	0.25
UV $\Delta\lambda_{\text{HWHM}}$ (Å)	4	4
IR Spectrometer range (nm)	700 - 880	880 - 1040
IR Exposure time (μs)	0.075	0.98
IR $\Delta\lambda_{\text{HWHM}}$ (Å)	8.5	10

justifying the assumption of vibration-electron-electronic equilibrium for this condition.

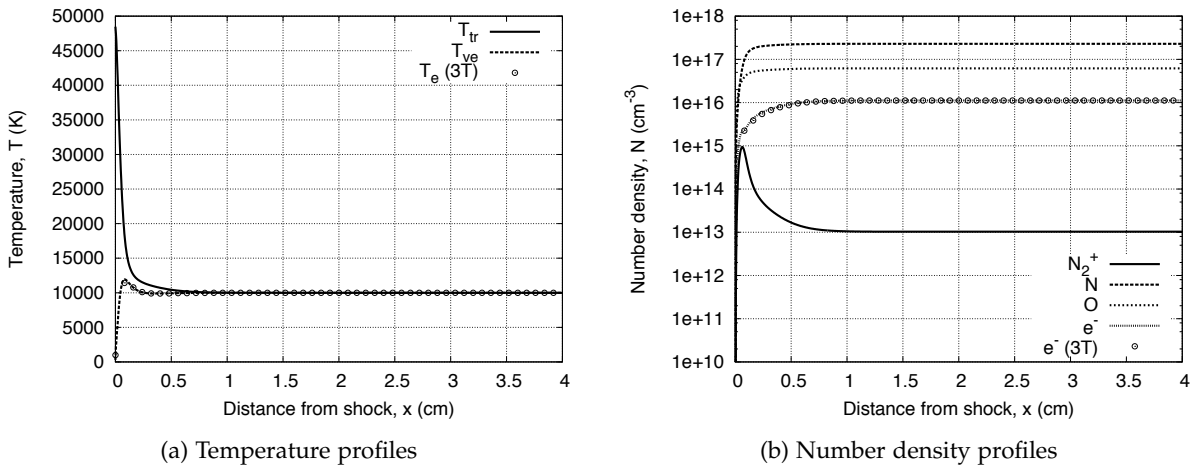


Figure 6.6: One-dimensional post-shock relaxation profiles for a 10 km/s shock through 0.3 Torr air.

Figure 6.7 present comparisons of infrared intensity profiles measurements from the 0.3 Torr conditions with various post-shock relaxation calculations performed with the Poshax3 code. The presented solutions consider variations of the radiation modelling, namely equilibrium ('Boltz.') and nonequilibrium ('QSS') electronic level populations and optically thick (' $\Lambda = 0$ '), optically thin (' $\Lambda = 1$ ') and optically variable (' $\Lambda = X$ ') emission. A calculation was also run at the upper limit of the shock speed uncertainty range (' $U_s + 1.5\%$ '). For shot 46/45, the 'N lines I' and 'O lines I' spectral groupings from Table 6.2 were considered, while for 46/46 the 'N lines II' and 'O lines II' spectral groupings were considered. The calculations performed with optically thick nonequilibrium radiation show good agreement with the experimental measurements within the

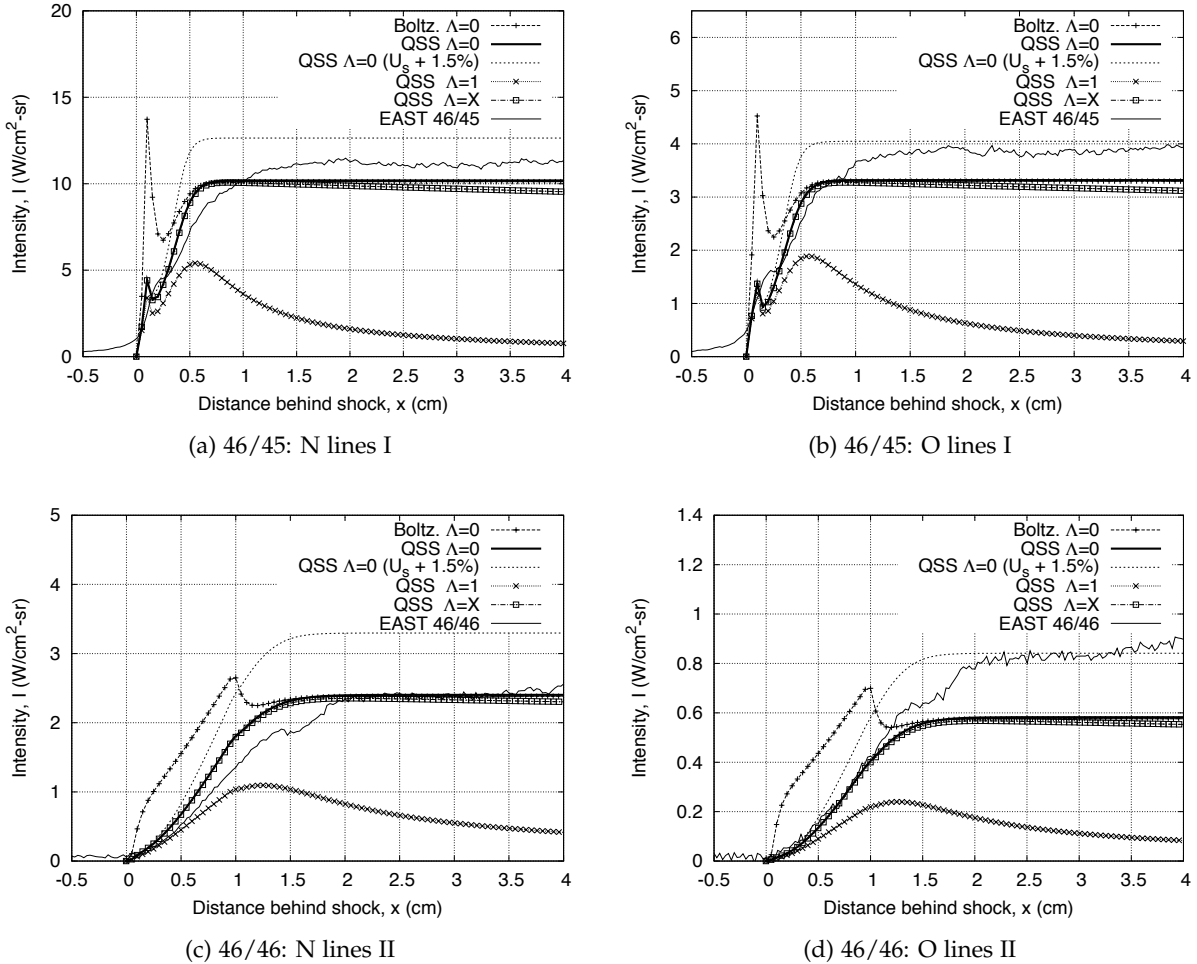


Figure 6.7: Comparison of infrared intensity profiles measured in the EAST facility for the 0.3 Torr conditions with Poshax3 calculations implementing various radiation model assumptions.

uncertainty limits imposed by the shock speed variation for all cases. The differences with measured intensity cannot be entirely attributed to shock speed variation, however, as the atomic N lines for both shots show good agreement with experiment at the nominal U_s while the atomic O lines for better agreement with $U_s + 1.5\%$. It is possible such differences are due to the transition probabilities of the atomic lines which can have uncertainties up to 100% [19]. Although the nonequilibrium region is small, the solutions with nonequilibrium electronic level populations show a clear improvement over the equilibrium solutions in the range $0 \leq x \leq 0.5$ cm, where the equilibrium radiation overestimates the experimental measurements. The plateau in intensity observed in the experimental measurements and optically thick solutions is in contrast to the slow decay estimated by the optically thin solution. This indicates that most of the radiation from N and O is reabsorbed by the gas and the optically thick assumption is accurate for these transitions. Furthermore, the assumption of strong absorption in the VUV is given weight by the

close agreement of the optically variable and optically thick solutions. For shot 46/45, an initial spike in intensity is observed 1 to 2 mm behind the shock that is reasonably well reproduced by the nonequilibrium calculations. Interestingly, this feature was not so clearly apparent in the calculations performed by Johnston *et al.* [63] and Panesi *et al.* [171]. The origin of this feature can be in part explained by considering the intensity profiles with and without N_2 and N_2^+ radiation, Figures 6.8. N_2^+ exhibits a nonequilibrium overshoot in this region as shown in Figure 6.6b, emitting radiation that extends into the near infrared, before being overcome by N and O emission as dissociation rapidly proceeds. For shot 46/46, the diffusive rise to equilibrium is mostly due to the much larger exposure displacement, and it is therefore difficult to draw any conclusions regarding the details of nonequilibrium processes for this shot.

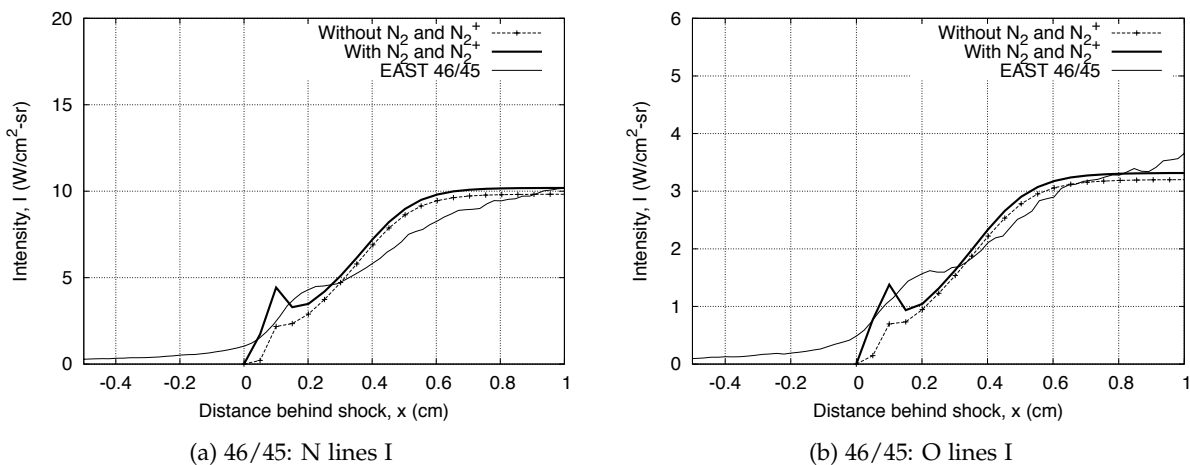


Figure 6.8: Comparison of infrared intensity profiles measured in the EAST facility for the 0.3 Torr conditions with Poschax3 calculations with and without N_2 and N_2^+ radiation.

Comparisons of the measured and calculated equilibrium infrared intensity spectra for the 0.3 Torr conditions are presented in Figure 6.9. The spectra were obtained at a distance of 4 cm from the shock. Although the upper profiles of most lines show good agreement, the measured lines exhibit rapid broadening towards the base that is not present in the calculations. A similar disagreement in the line profiles was observed in References [38, 63, 192]. This effect is most noticeable for the atomic N transitions at 745.4 and 821.4 nm in Figure 6.9a, for example, where the base of the measured lines extend for up to 10 nm past the end of the calculated lines. As will be demonstrated in § 6.3.3, this broadening of lines at their base is thought to be an artefact of the spectrometer and not a quality of shock heated air. Another difference between the calculated and measured spectra is the background emission between the lines — consider the $950 \leq \lambda \leq 975$ nm range in Figure 6.9b, for example. The calculations predict almost no radiation, whereas the measurements show a rise in cumulative intensity of approximately $0.2 \text{ W/cm}^2\text{-sr}$. A similar effect can be observed in the $795 \leq \lambda \leq 810$ nm and $830 \leq \lambda \leq 840$ nm range in

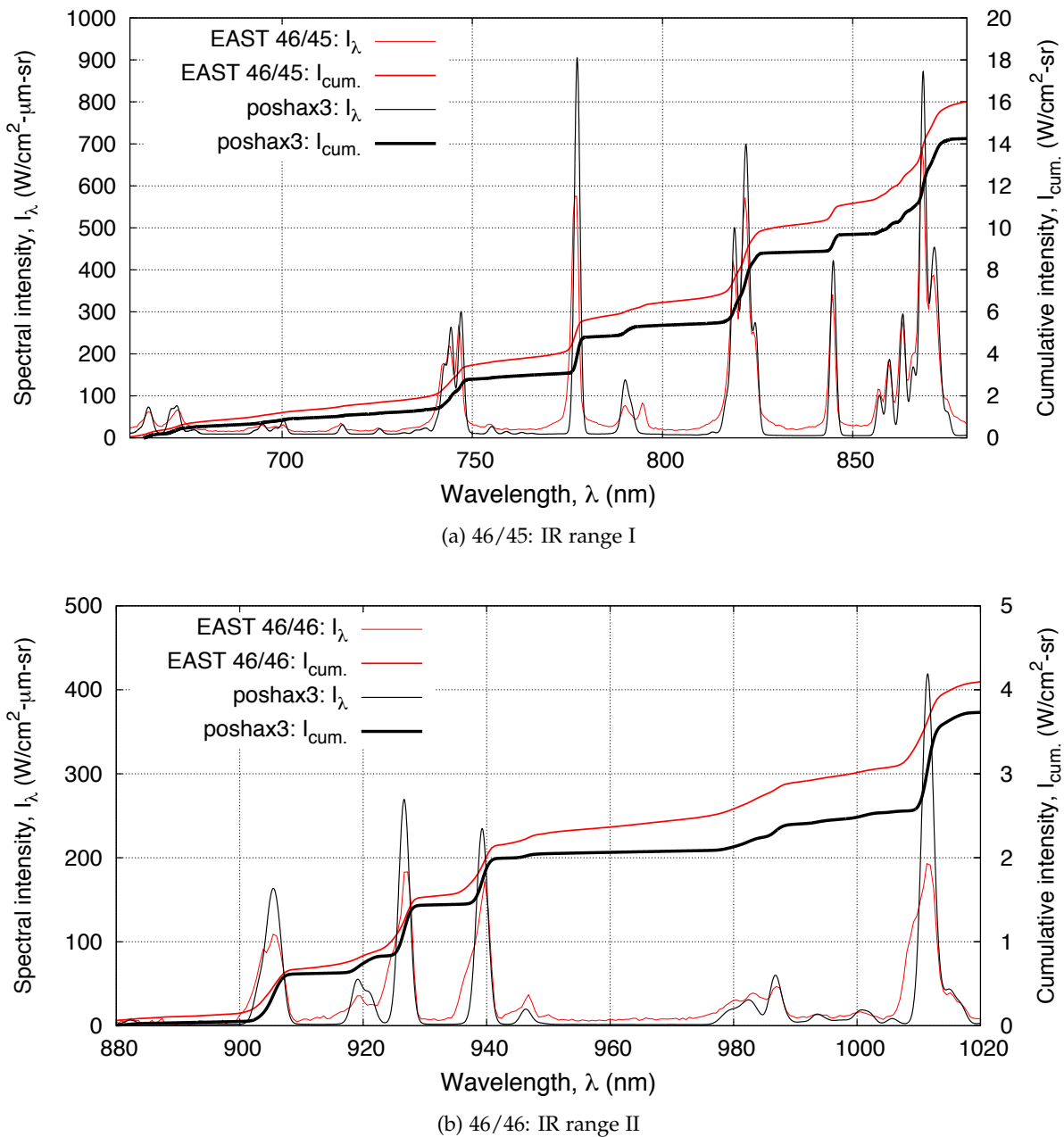


Figure 6.9: Comparison of measured and calculated equilibrium infrared intensity spectra for the EAST 0.3 Torr air conditions.

Figure 6.9a, where the void in intensity between lines in the calculation is filled in by the base of the lines and possibly additional background features in the measurements. It is unclear whether this phenomena is characteristic of shock heated air in general or an artefact of the experimental measurements. It should be noted that in Reference [63] the experimental data for this condition was shifted to force the continuum to zero between the lines, citing contamination and calibration errors as the justification for doing so.

Figure 6.10 presents comparisons of the measured and calculated ultraviolet intensity profiles from the 0.3 Torr conditions. For shot 46/45 ‘UV range I’ as indicated in Figure 6.5 is considered ($300 \leq \lambda \leq 450$ nm), while for shot 46/46 ‘UV range II’ is considered ($190 \leq \lambda \leq 360$ nm). The nonequilibrium overshoot in the N_2^+ First Negative intensity is overestimated by at least a factor of 3 by all calculations, with the nonequilibrium solution with optically thin emission giving the closest agreement. This is in contrast to the atomic lines where optically thin emission substantially underestimates the experiment measurements. It is possible that the optically thick assumption is more appropriate for the atoms than the molecules as many atomic line transitions result in high energy radiation (VUV spectra) that is readily absorbed, while N_2 and N_2^+ emit mainly in the visible and ultraviolet regions which are often optically thin. This is confirmed by the close agreement of the optically variable and optically thin solutions in the nonequilibrium region where the radiative cooling effect is not yet apparent. The substantial underestimation of the equilibrium intensity can be explained by considering the spectra presented in Figure 6.11. In the measured spectra, features of the CN Violet band system can be observed at 388 nm and atomic C lines observed at 193 and 248 nm. These are due to carbon contamination in the shock tube and therefore are not reproduced by the calculations. The background radiation level is

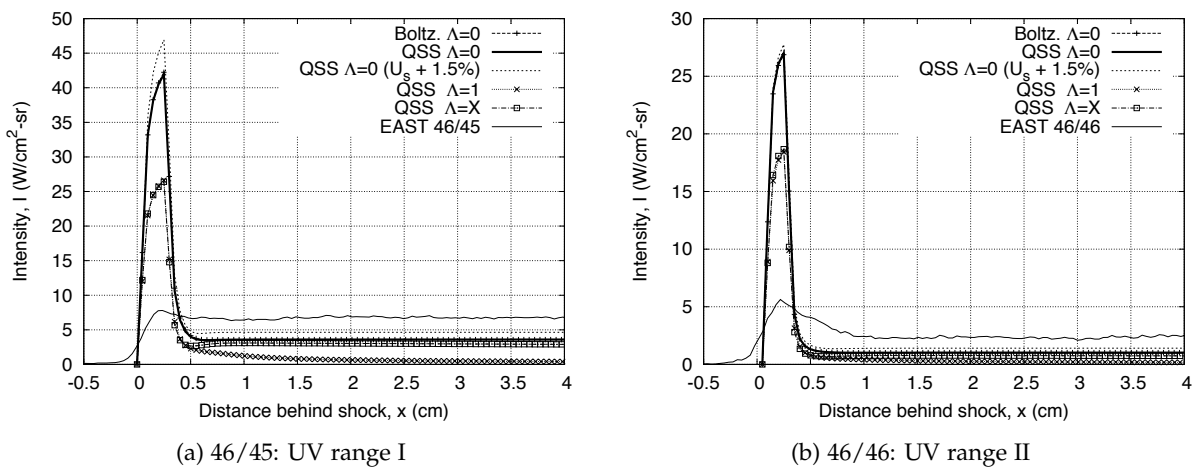


Figure 6.10: Comparison of ultraviolet intensity profiles measured in the EAST facility for the 0.3 Torr conditions with Poshax3 calculations implementing various radiation model assumptions.

also seen to be much higher in the experiment. This may be due to a number of phenomena such as (a) baseline errors in the spectrometer calibration, (b) additional radiation from carbon contaminant species such as CN and CO, (c) blackbody radiation from solid particles or (d) additional continuum or psuedo-continuum radiation mechanisms of air species not modelled in the present work [38].

Figures 6.12a and 6.12b present comparisons of the 'N lines I' and 'UV range I' intensity profiles measurements from shot 46/45 with Poshax3 calculations implementing variations on the nominal dissociation model. The x scale limit has been reduced from 4 to 1.5 cm for clarity in the nonequilibrium region. The presented solutions considered the Park $s = 0.5$ model with non-preferential coupling, the Park $s = 0.3$ model with both non-preferential and preferential coupling ('PVDC') and the Macheret-Fridman model with non-preferential coupling. The Park $s = 0.5$ and Macheret-Fridman models increase the N_2^+ contributions in the $0 \leq x \leq 0.5$ cm range due to faster dissociation rates making more N atoms available for associative ionisation reactions. The inclusion of preferential coupling leads to more diffusive equilibration, with the distance to thermochemical equilibrium being increased by a factor of two. In addition, the inclusion of preferential coupling reduces the disagreement in the ultraviolet region. Although the preferential dissociation-vibration coupling model appears to overestimate the amount of energy removal, the qualitative trend of the experimental results is somewhat similar, indicating a more moderate preferential dissociation model may be appropriate.

Figures 6.13a and 6.13b present comparisons of the 'N lines I' and 'UV range I' intensity profiles measurements from shot 46/45 with Poshax3 calculations implementing variations on the nominal electron impact ionisation coupling model. The presented solutions considered the electron impact ionisation coupling with the classical potentials ($\alpha_{\text{EII}} = 1$) and reduced potentials ($\alpha_{\text{EII}} = 0.3$). While the effect on the UV intensity profile is minimal, the atomic N line profile shows much better agreement with the classical potentials, with the $\alpha_{\text{EII}} = 0.3$ solution exhibiting much faster equilibration.

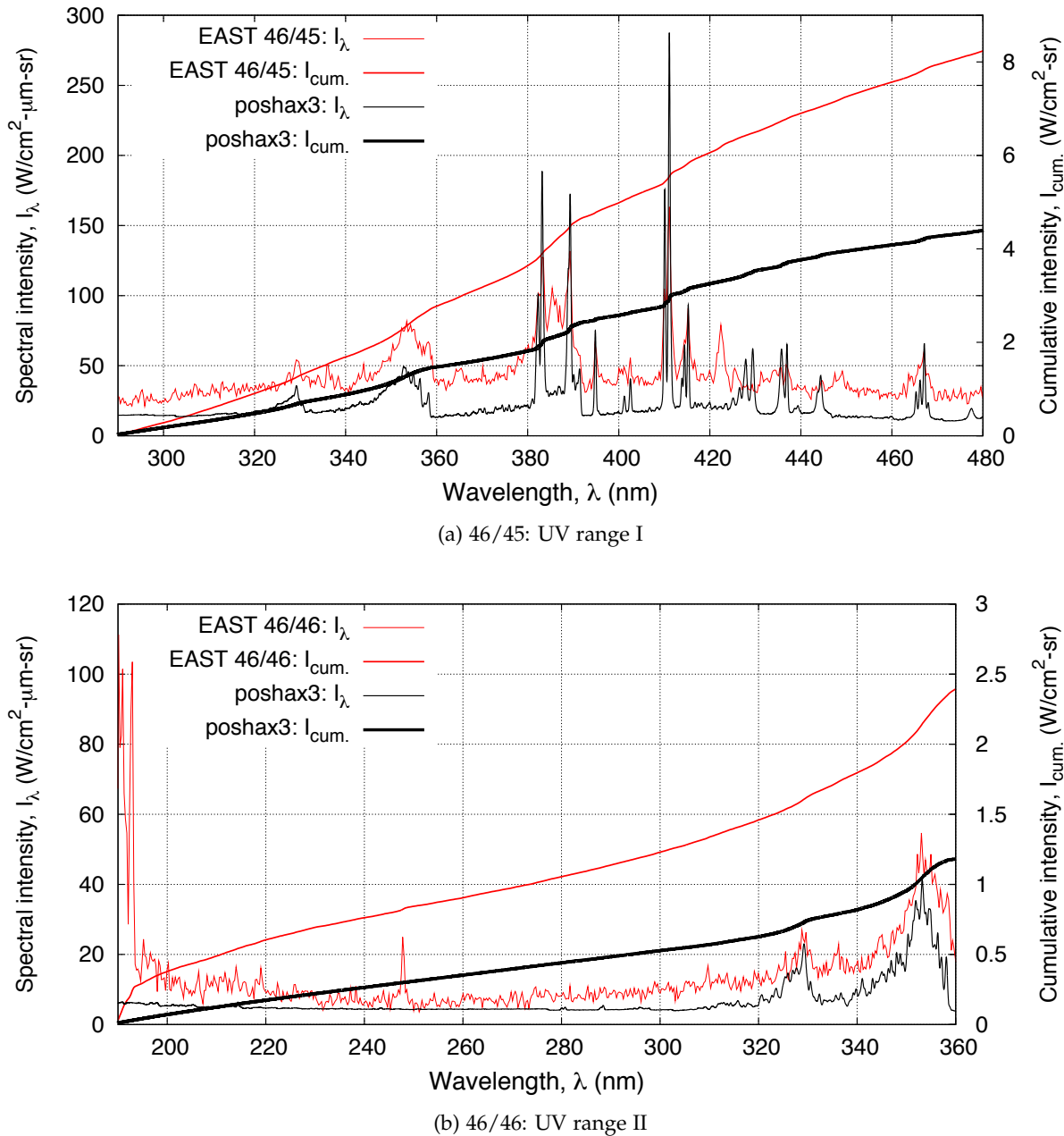


Figure 6.11: Comparison of measured and calculated equilibrium ultraviolet intensity spectra for the EAST 0.3 Torr air conditions.

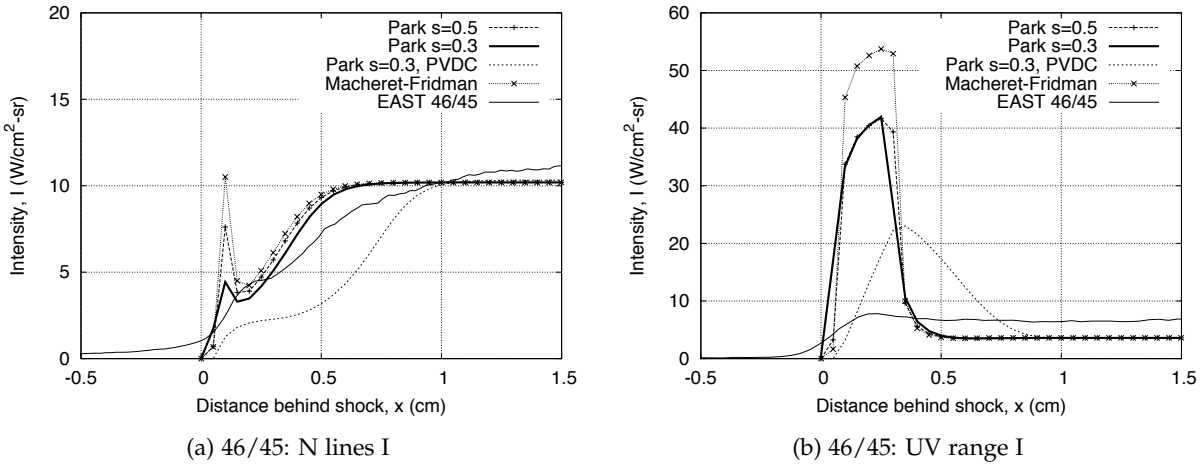


Figure 6.12: Comparison of intensity profiles measured in the EAST facility for shot 46/45 with Poshax3 calculations implementing various dissociation models.

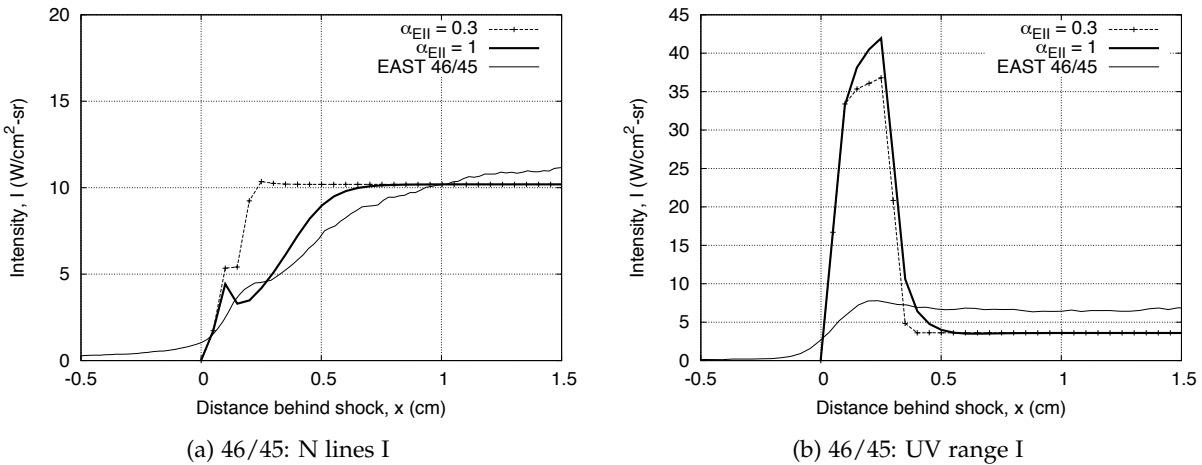


Figure 6.13: Comparison of intensity profiles measured in the EAST facility for shot 46/45 with Poshax3 calculations implementing various electron impact ionisation coupling models.

0.1 Torr conditions

The 0.1 Torr EAST conditions with an air test gas that are considered in the present analysis are summarised in Table 6.4. The shock speed for shot 46/02 is close to the nominal 10 km/s, while shot 46/07 is considerably slower at 9.2 km/s. As will be discussed, this difference in shock speed has a significant effect on the intensity profiles. The effective test time for 46/02 corresponds to a slug length of 5.7 cm while that for 46/07 corresponds to a slug length of 2.6 cm. Therefore the comparisons performed for shot 46/07 will not be valid in the $2.6 \leq x \leq 4.0$ cm range. The spectral ranges for these shots are the same as those considered for the 0.3 shots: for shot 46/02

spectral regions ‘UV range II’ and ‘IR range II’ were measured, whilst ‘UV range I’ and ‘IR range I’ were measured for shot 46/07 (see Figure 6.5).

Table 6.4: Summary of the 0.1 Torr air EAST shots [2] considered.

Shot number	46/02	46/07
Shock speed, U_s (m/s)	9890 ± 148	9165 ± 137
Pressure, p_∞ (Torr)	0.1	0.1
Effective test time (μs)	5.761	2.821
UV Spectrometer range (nm)	190 - 365	290 - 475
UV Exposure time (μs)	1.0	0.25
UV $\Delta\lambda_{\text{HWHM}}$ (Å)	4	4
IR Spectrometer range (nm)	880 - 1040	700 - 880
IR Exposure time (μs)	0.98	0.5
IR $\Delta\lambda_{\text{HWHM}}$ (Å)	10	8.5

Figures 6.14a and 6.14b present temperature and number density profiles for the nominal 10 km/s shock through 0.1 Torr air. Also indicated are the electronic-electron temperature T_e and electron concentration calculated by the three-temperature model. The nonequilibrium region for this condition is considerably larger than for the 0.3 Torr condition, with thermochemical equilibrium being attained approximately 3 cm from the shock front. Although the exposure times for these shots are quite high (up to 1 μs), the maximum exposure displacement is approximately 1 cm and the nonequilibrium region should still be reasonably well resolved. In addition, the three-temperature electronic-electron temperature and electron concentration show close agreement with the two-temperature results, justifying the assumption of vibration-electron equilibrium for this condition.

Before proceeding with the experiment comparisons, it is necessary to note the effect of the slower shock speed for shot 46/07. Figure 6.15a presents the electron number density profiles for the nominal 10 km/s shock through 0.1 Torr air and that for shots 46/02 and 46/07. While shot 46/02 exhibits a similar monotonic rise to equilibrium that is similar to the 10 km/s shock, shot 46/07 exhibits a peak followed by decay to equilibrium. This effect can be attributed to a higher rate of associative ionisation-recombination compared to electron impact ionisation at the slower shock speed [58]. As the shock speed is increased to 10 km/s, the rate of electron impact ionisation grows rapidly while the rate of associative ionisation-recombination remains approximately constant. Due to the strong coupling of atomic emission with the electron number density, the intensity profile for shot 46/07 exhibits a noticeable peak while that for shot 46/02 is monotonic, as illustrated in Figure 6.15b.

Figure 6.16 presents comparisons of the measured and calculation infrared intensity profiles

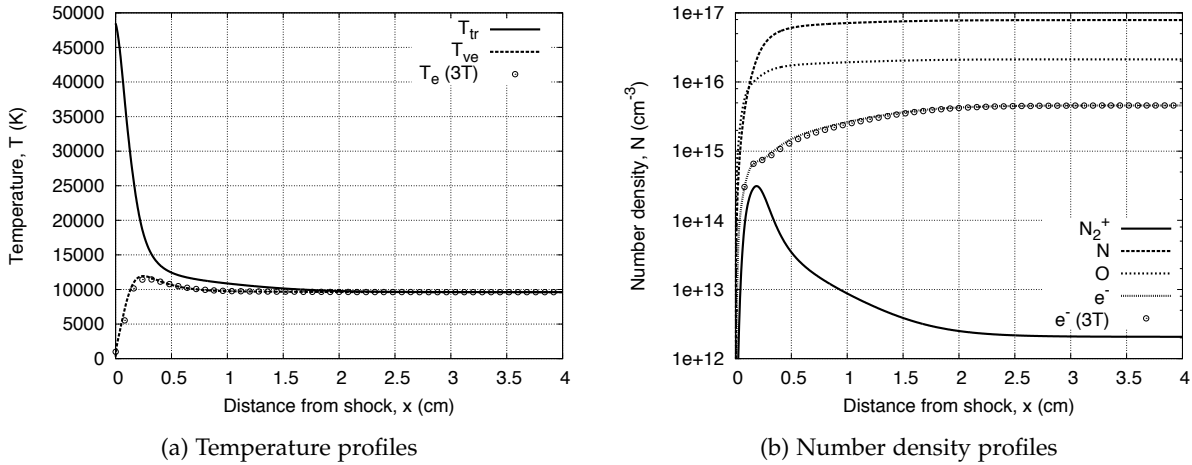


Figure 6.14: One-dimensional post-shock relaxation profiles for a 10 km/s shock through 0.1 Torr air.

for the 0.1 Torr conditions. For shot 46/07, a nonequilibrium overshoot in atomic N and O intensity is observed 0.5 cm from the shock, while for shot 46/02 this feature is suppressed due to the faster shock speed. As was observed for the 0.3 Torr conditions, the solution with optically thick nonequilibrium radiation shows reasonable agreement with experiment within the uncertainty due to shock speed variation for most cases. An exception is the oxygen lines measured in the $915 \leq \lambda \leq 931$ nm range by shot 46/02, where the calculated equilibrium intensity for the $U_s + 1.5\%$ case underestimates the measured level by approximately 25%. Again, the optically thin solution underestimates the experimental data and the optically variable and optically thick solutions are in close agreement with the experiment, indicating strong reabsorption of atomic line radiation even at this lower pressure. Figure 6.17 present comparisons with the measured equilibrium infrared intensity spectra for the 0.1 Torr conditions. For shot 46/07 the equilibrium spectra was taken at 2.2 cm from the shock instead of 4 cm due to the reduced effective test time. For 'IR range I' measured in shot 46/07, the integrated intensities over the more prominent lines are underestimated, while for 'IR range II' measured in shot 46/02 the integrated intensities over the lines show good agreement, however the experimental measurements show a background intensity that is not predicted. This background only plays a minor role in the intensity profiles presented in Figure 6.16 due to the selective spectral regions considered. Similarly as for the 0.3 Torr conditions, the calculated line-widths are more narrow than in the measured spectra.

Figure 6.18 compares the measured and calculated ultraviolet intensity profiles for the 0.1 Torr conditions. The equilibrium and nonequilibrium optically thick solutions are almost identical, while the optically thin and optically variable solutions shows improved agreement with experiment in the vicinity of the overshoot. A similar trend was observed for the 0.3 Torr conditions, and can be explained by the lack of radiative emission in the highly absorbing VUV region for N_2 .

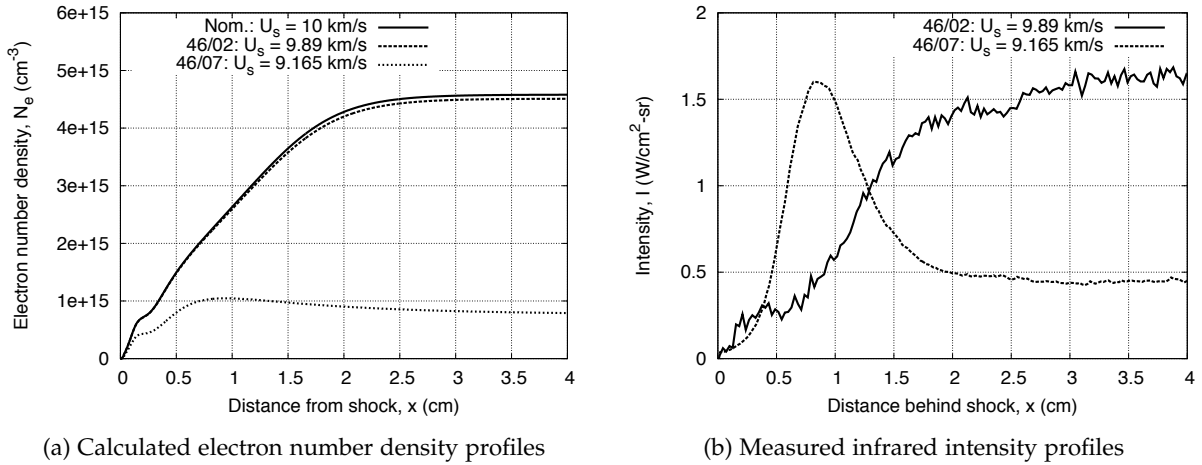


Figure 6.15: Effect of shock speed on post-shock relaxation profiles for the 0.1 Torr EAST conditions. The intensity profiles represent $880 \leq \lambda \leq 1040$ nm for shot 46/02 and $700 \leq \lambda \leq 880$ nm for shot 46/07.

and N_2^+ . Figure 6.19 presents comparisons with the measured equilibrium ultraviolet intensity spectra. Again contaminant C and CN spectral features can be observed at 190, 245 and 388 nm and the overall integrated intensity is subsequently underestimated by the calculations.

Figures 6.20a and 6.20b present comparisons of the ‘N lines I’ and ‘UV range I’ intensity profiles measurements from shot 46/02 with Poshax3 calculations implementing various dissociation models. The presented solutions considered the Park $s = 0.5$ model with non-preferential coupling, the Park $s = 0.3$ model with both non-preferential and preferential coupling (‘PVDC’) and the Macheret-Fridman model with non-preferential coupling. Based on the improved agreement with the equilibrium intensity in Figure 6.16d, these calculations have been performed at the upper shock speed bound ($U_s + 1.5\%$). For the atomic N lines, varying the dissociation rate coefficient model has minimal effect on the intensity profile. The inclusion of preferential dissociation-vibration coupling gives a much more diffusive rise to the equilibrium plateau that does not at all match the trend observed in the measurements. In contrast, for the ultraviolet intensity profiles where N_2^+ is the dominant radiator, the calculation with preferential dissociation-vibration coupling gives a greatly improved agreement with experiment.

Figures 6.21a and 6.21b present comparisons of the ‘N lines I’ and ‘UV range I’ intensity profiles measurements from shot 46/02 with Poshax3 calculations implementing various electron impact ionisation coupling models. The presented solutions considered the electron impact ionisation coupling with the classical potentials ($\alpha_{EII} = 1$) and reduced potentials ($\alpha_{EII} = 0.3$). While the effect on the UV intensity profile is minimal, the atomic N line profile shows much better agreement with the classical potentials, with the $\alpha_{EII} = 0.3$ solution exhibiting much faster equilibration.

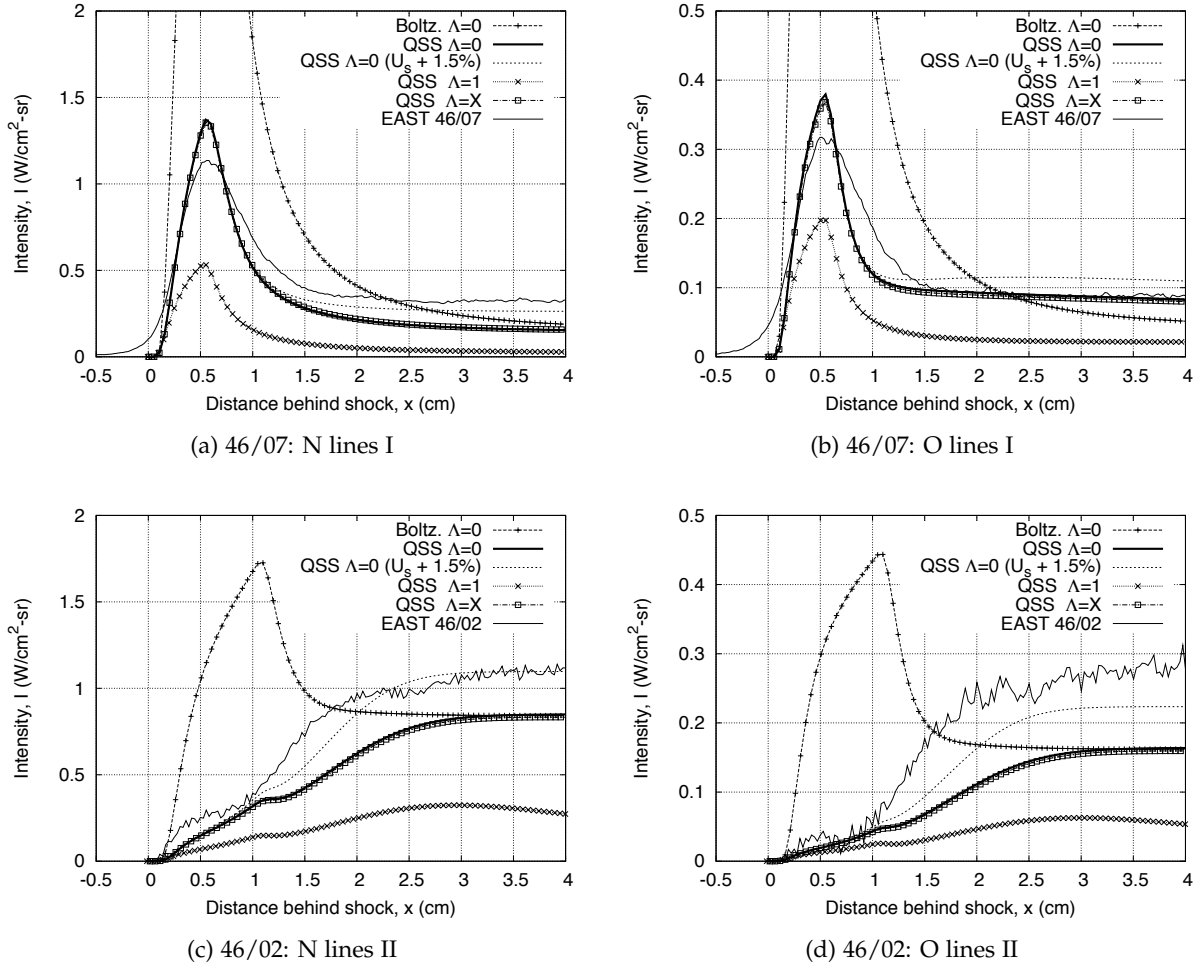


Figure 6.16: Comparison of infrared intensity profiles measured in the EAST facility for the 0.1 Torr conditions with Poshax3 calculations implementing various radiation model assumptions.

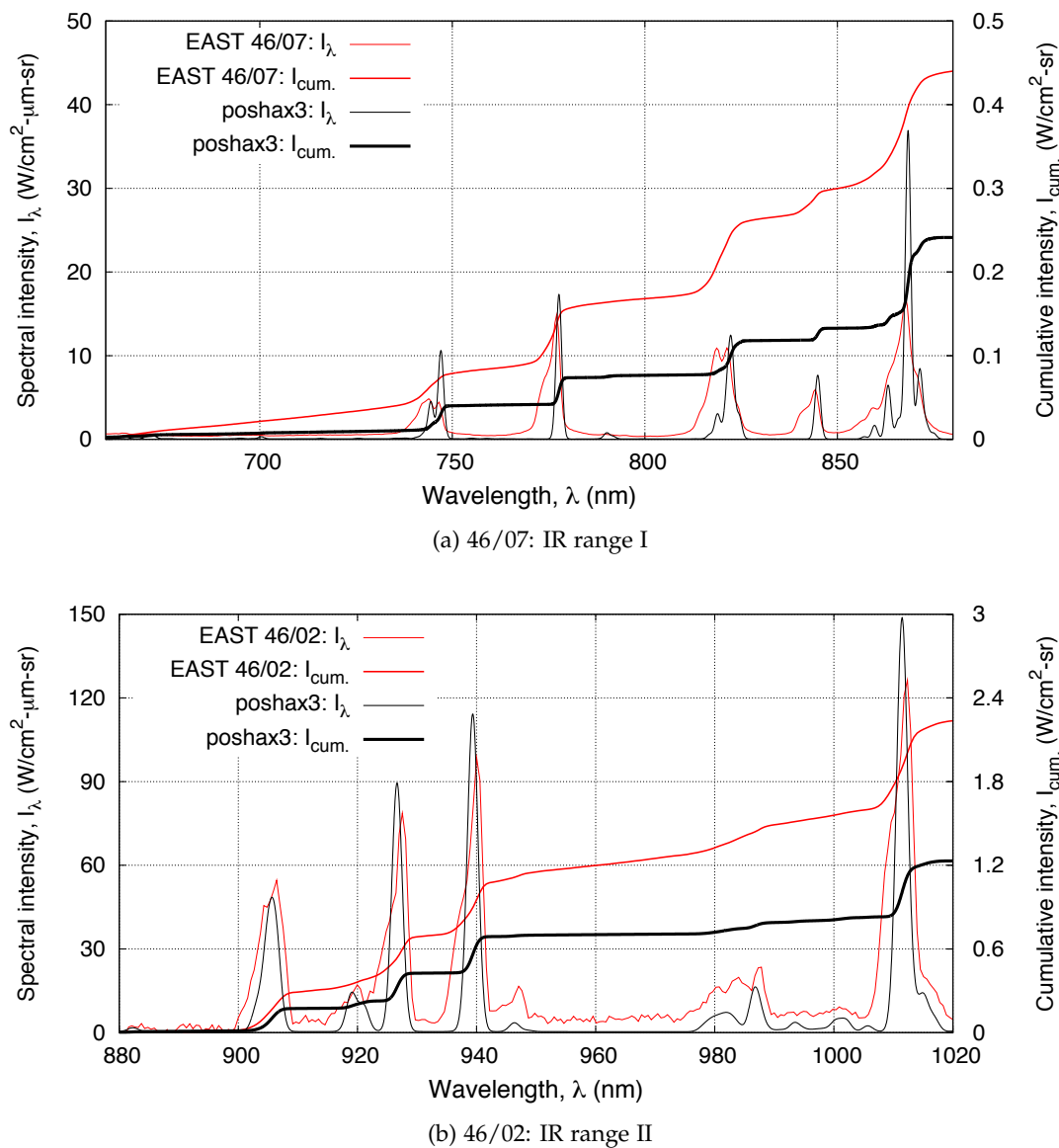


Figure 6.17: Comparison of measured and calculated equilibrium infrared intensity spectra measured for the 0.1 Torr EAST air conditions.

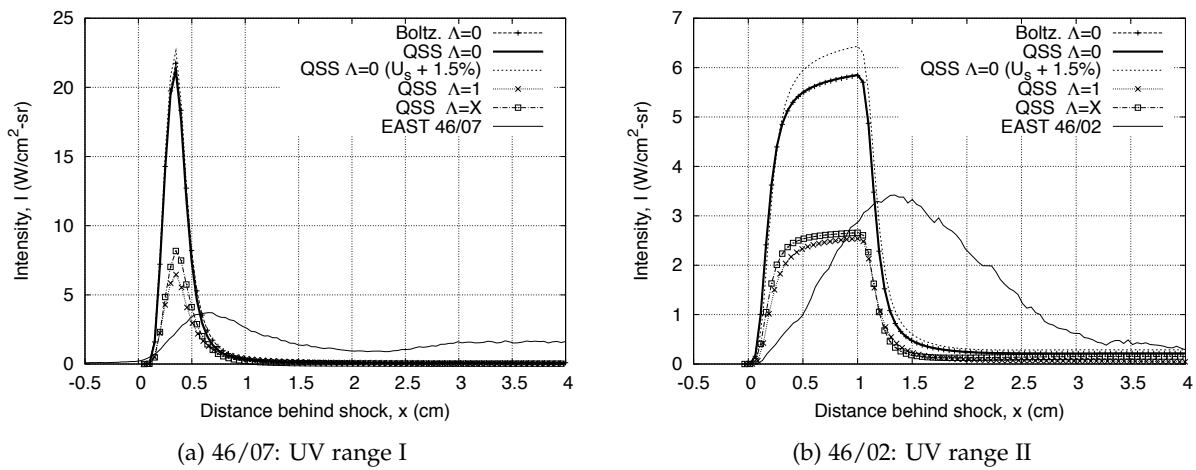


Figure 6.18: Comparison of ultraviolet intensity profiles measured in the EAST facility for the 0.1 Torr conditions with Poshax3 calculations implementing various radiation model assumptions.

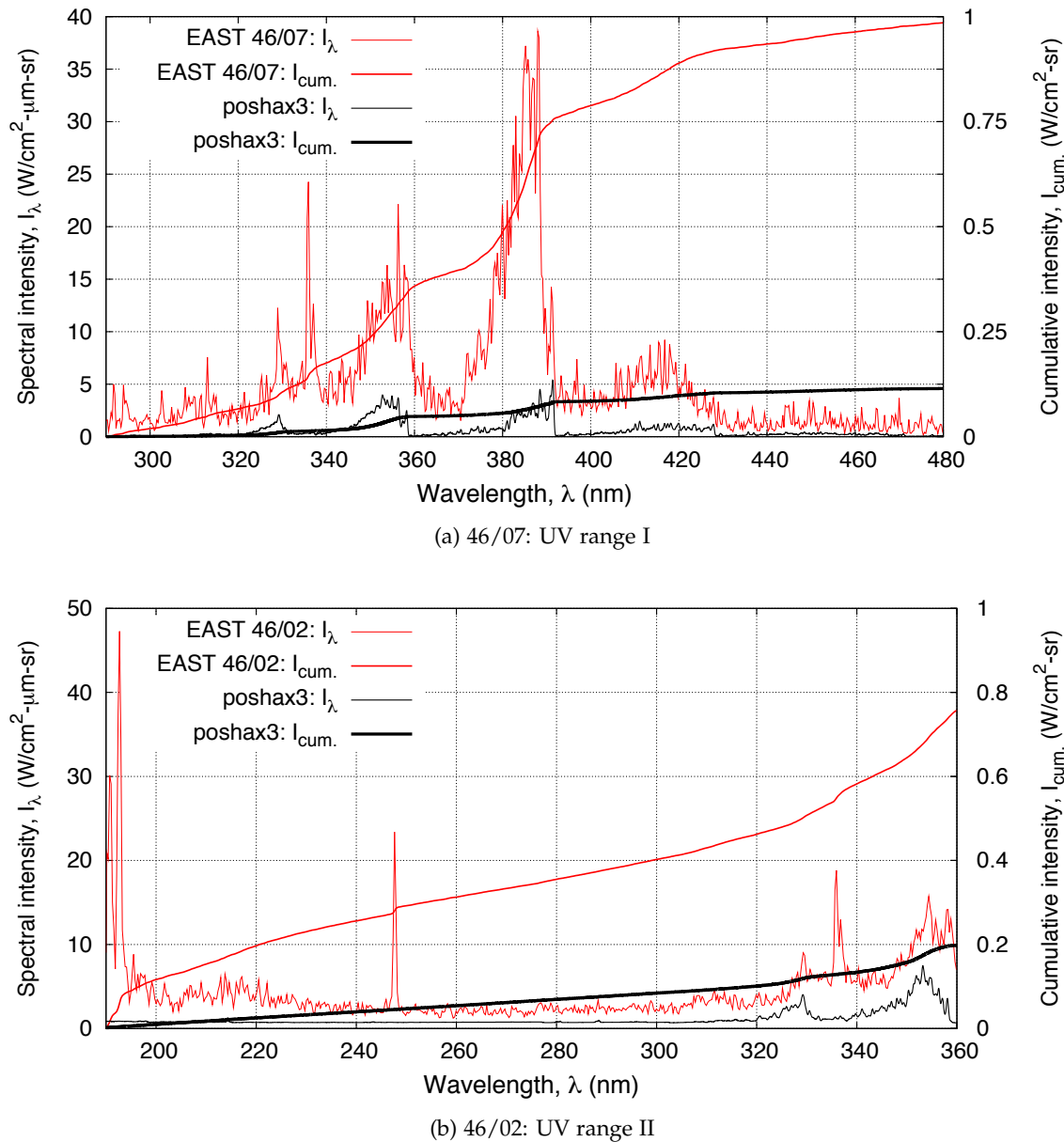


Figure 6.19: Comparison of measured and calculated equilibrium ultraviolet intensity spectra for the 0.1 Torr EAST conditions.

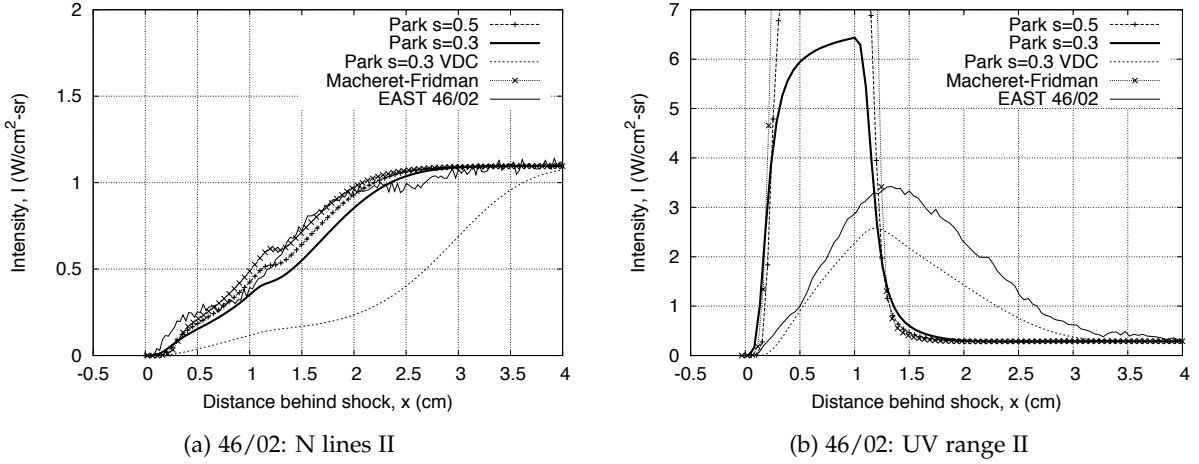


Figure 6.20: Comparison of intensity profiles measured in the EAST facility for shot 46/02 with Poshax3 calculations implementing various dissociation models. Note that these calculations have been performed at the upper shock speed bound ($U_s + 1.5\%$).

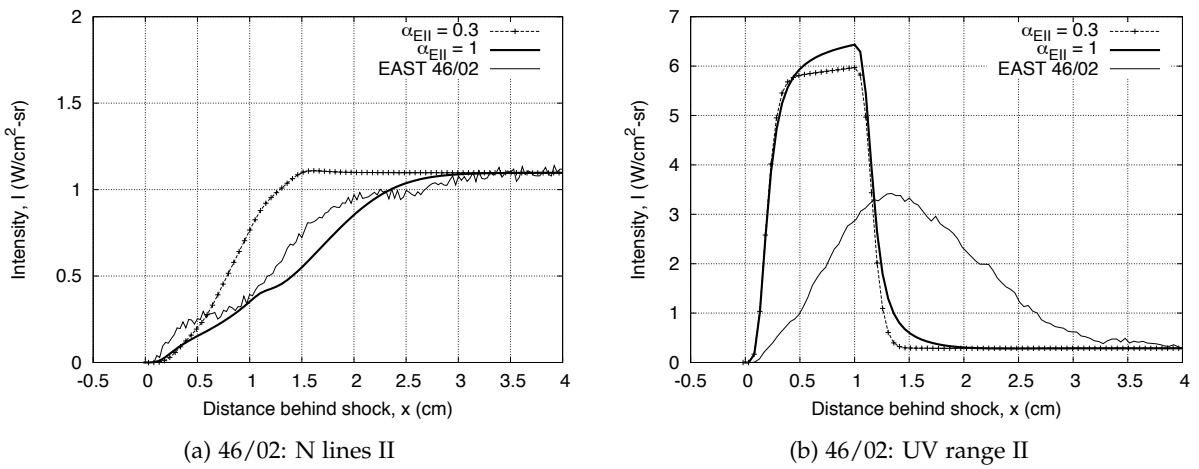


Figure 6.21: Comparison of intensity profiles measured in the EAST facility for shot 46/02 with Poshax3 calculations implementing various electron impact ionisation coupling models. Note that these calculations have been performed at the upper shock speed bound ($U_s + 1.5\%$).

Summary and concluding remarks

Comparisons with air shock tube experiments performed in the EAST facility with freestream pressures of 0.3 and 0.1 Torr and a nominal shock speed of 10 km/s have been presented. Good agreement is demonstrated between the calculated and measured atomic line profiles for the 0.3 Torr shots when the uncertainty in shock speed is taken into consideration. Slight discrepancies emerge for the lower density 0.1 Torr conditions, however, with the variation in shock speed unable to account for all the differences observed for the atomic transitions. It is interesting to note that when using the nominal shock speeds the plateau in all the atomic line profiles are slightly underestimated. From comparison of the spectra, it is evident that much of the difference between experiment and calculation occurs away from the line centres. The line profiles for both conditions exhibit rapid broadening towards the base, and a background continuum is observed between the lines; these features are not present in the calculated spectra, and the latter is one of the main causes of the underestimation. Using ground state potentials for electron impact ionisation-electron coupling is found to give a much better agreement with experiment than the reduced potentials. The nonequilibrium overshoot observed in N_2^+ emission is overestimated for both the 0.1 and 0.3 Torr conditions, and the equilibrium intensity level is underestimated due to carbon contamination. The consideration of preferential dissociation-vibration coupling improves the agreement with the diatomic emission, but subsequently makes the atomic line profiles too diffusive. The optically thick assumption is found to give the best results for atomic transitions, while the optically thin assumption is found to give the best results for diatomic transitions. In summary, the *total* measured radiation (in both nonequilibrium and equilibrium regions) intensity was able to be estimated within 25% for the 0.3 Torr conditions and within 50% for the 0.1 Torr conditions when spectral features due to carbon contamination are disregarded and the results from the best performing physical models are considered. Thus the present comparison is slightly less accurate than that presented by Johnston [63], where agreement within 15% and 40% for the 0.3 and 0.1 Torr conditions was found.

6.2.4 Mars conditions

Experiments were performed in the EAST facility with a 96% CO_2 and 4% N_2 test gas to simulate a trajectory point characteristic of an aerocapture manoeuvre at Mars, as reported in Reference [3]. The freestream pressure was 0.1 Torr and the targeted shock speed was 8.5 km/s. This corresponds approximately to the peak heating point of the hypothetical 9.79 km/s aerocapture trajectory discussed in Reference [16].

The calculated peak intensity spectra for the nominal 8.5 km/s shock through 0.1 Torr CO_2-N_2 is presented in Figure 6.22, where the measured EAST peak intensity spectra segments have been combined and overlaid for reference. Also, the spectral features to be considered in the intensity profile comparisons are indicated. The spectral distribution of the radiative emission differs from

Table 6.5: Summary of the 0.1 Torr Mars EAST shots [3] considered.

Shot number	46/18	46/19
Shock speed, U_s (m/s)	8548 ± 128	8386 ± 126
Pressure, p_∞ (Torr)	0.1	0.1
Effective test time (μs)	6.9	4.3
UV Spectrometer range (nm)	190 - 360	290 - 480
UV Exposure time (μs)	0.25	0.25
UV FWHM (Å)	4.0	4.0
IR Spectrometer range (nm)	650 - 880	480 - 700
IR Exposure time (μs)	0.25	0.25
IR FWHM (Å)	4.0	4.0

the air conditions just considered in that the VUV region is even more dominant and molecular band radiation plays a more significant role. The ultraviolet spectral ranges considered are the same as those for the air conditions, $190 \leq \lambda \leq 365$ nm ('UV range I') and $290 \leq \lambda \leq 485$ nm ('UV range II'). Here the transitions² of interests are the contributions of the CO Fourth Positive system at 215 nm, the atomic C line at 248 nm, the CN Violet $\Delta v = -1, 0$ bands at 366 nm and the C₂ Swan $\Delta v = -2, -1$ bands at 453 nm. The spectral ranges measured by the infrared spectrometer were $480 \leq \lambda \leq 700$ nm ('IR range I') and $650 \leq \lambda \leq 880$ nm ('IR range II'). In contrast to air, the near infrared spectra for CO₂-N₂ mixtures only has a handful of strong transitions. Those present, however, are the C₂ Swan $\Delta v = 0, 1$ bands at 528 nm, the atomic O lines at 777 and 845 nm and the atomic C line at 833 nm. Perhaps the most important features measured in the experiments are the CO Fourth Positive bands and atomic C line in the middle ultraviolet spectral region³. CO and C strongly radiate in the vacuum ultraviolet and contribute the bulk of the radiative flux experienced during atmospheric entry at Mars. Although the VUV region was not directly measured, the features observed in the middle ultraviolet region should exhibit similar spatial profiles as they have the same or similar upper electronic states (e.g. the CO Fourth Positive bands measured at 215 nm are actually part of a system that extends deep into the VUV region).

Figures 6.23a and 6.23b present temperature and number density profiles for the nominal 8.5 km/s shock through 0.1 Torr CO₂-N₂, where the number densities of CN and C₂ have been multiplied by a factor of 200 for clarity on this scale. The calculations were performed with the nominal physical modelling for CO₂-N₂ mixtures as described in Table 5.4, which considers a two-temperature gas model and optically thick radiation. The T_{ve} profile for a calculation with optically thin ($\Lambda = 1$) radiation is also shown for reference. Although calculations with

²Note that in the present work we define the change in vibrational quantum number as: $\Delta v = v_u - v_l$. This differs from other radiation literature where it is sometimes defined as $\Delta v = v_l - v_u$.

³The middle ultraviolet region is defined as having wavelengths in the range $200 \leq \lambda \leq 300$ nm.

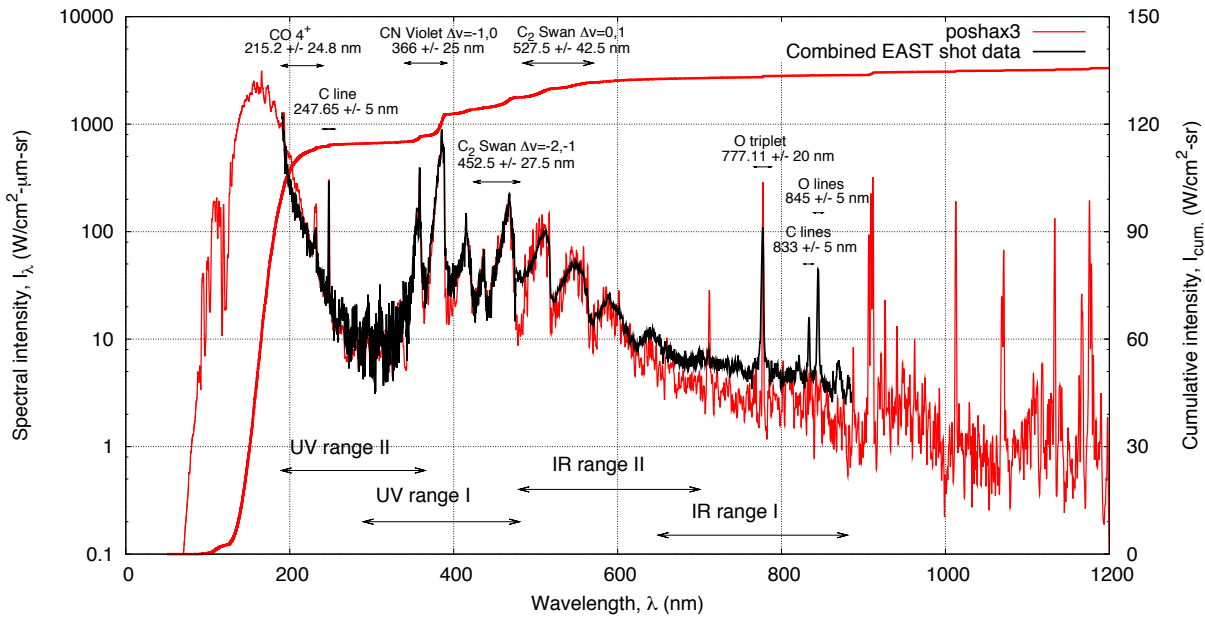


Figure 6.22: Calculated and measured peak intensity spectra for the 8.5 km/s 0.1 Torr $\text{CO}_2\text{-N}_2$ condition in the EAST facility.

the three-temperature model at this condition were not successful, the calculations performed in § 5.3 for the 9.66 km/s 2.79 Pa Mars condition gave reasonably similar results for the two- and three-temperature models. As the EAST condition has a higher pressure and slower shock, the two-temperature model should also be sufficient here. While Figure 6.23a shows thermal equilibration just 0.5 cm behind, chemical equilibrium is yet to be achieved at the end of the 3 cm range presented in Figure 6.23b. The atoms and electrons exhibit monotonic relaxations to equilibrium, while the molecules all exhibit nonequilibrium peaks close to the maximum in T_{ve} at 0.2 cm from the shock, followed by a slow decay. The intensity profiles should therefore differ from the air conditions in that a clear equilibrium plateau will not be present. Also, the consideration of optically thin radiation drops the maximum T_{ve} from 13,000 K to 10,000 K and delays its occurrence by 0.1 cm.

Results

Figure 6.24 presents comparisons of the diatomic band intensity profiles measurements from the 8.5 km/s Mars conditions with Poshax3 calculations considering various radiation model assumptions. The effect of the shock speed uncertainty is not as great as was the case for the 10 km/s air conditions and is therefore not shown. As predicted, the intensity profiles exhibit a nonequilibrium peak followed by slow decay to an equilibrium level that is not attained in the slug of measured gas. In all cases the nonequilibrium optically thin case demonstrates the closest agreement with experiment, although only the CN Violet profile is quite accurately reproduced.

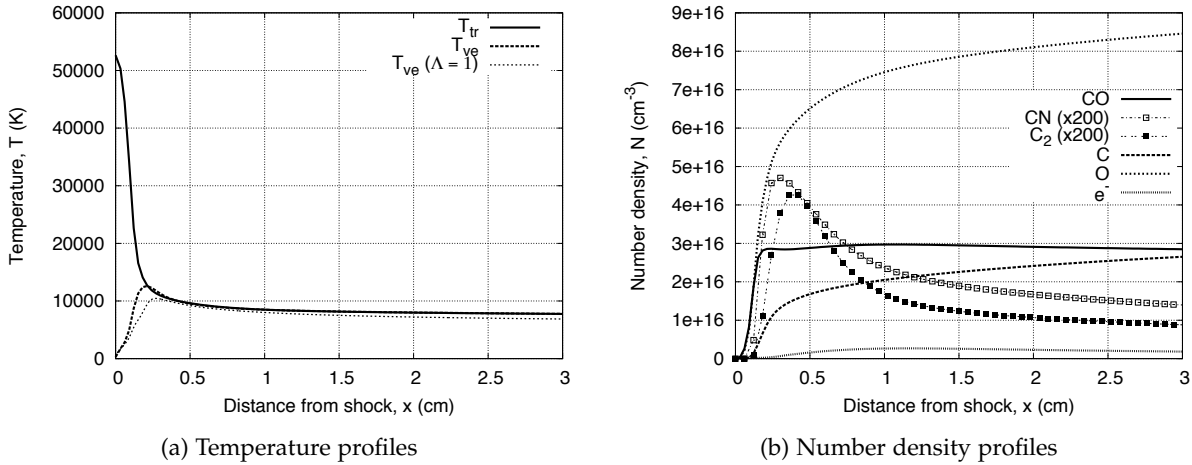


Figure 6.23: One-dimensional post-shock relaxation profiles for a 8.5 km/s shock through 0.1 Torr CO₂-N₂.

For the CO Fourth Positive and C₂ bands the nonequilibrium peak is overestimated by a factor of at least two, and the optically thick nonequilibrium solution is close to the equilibrium solution. By 1.5 cm from the shock, however, the optically thin solution accurately reproduces the decaying intensity profiles. This is in contrast to the air conditions where the optically thick model was required to correctly calculate the plateau in intensity. A comparison of the measured and calculated CN Violet spectra at peak intensity ($x = 0.3$ cm) is presented in Figure 6.25. The calculated spectra is from the solution with nonequilibrium optically thin radiation. The integrated intensity over the $340 \leq \lambda \leq 425$ nm range is overestimated by 20%, where the largest contribution comes from the $\Delta v = 0$ bands. It should be noted that the agreement between the measured and calculated spectra gradually improves with increasing wavelength, and may indicate an error in the spectrometer calibration.

Figure 6.26 presents comparisons of the atomic line intensity profiles measurements from the 8.5 km/s Mars conditions with Poshax3 calculations implementing various radiation model assumptions. For all transitions the solutions with optically thin radiation give the closest agreement for $x \geq 1.5$ cm, again indicating minimal reabsorption of radiation for this condition. However the nonequilibrium peak is only accurately reproduced for the atomic C line at 833 nm, with the 248 nm C line peak being overestimated by a factor of 3 and the oxygen lines at 777 and 845 nm being underestimated by factors of 2 and 8 respectively. In addition, for carbon the nonequilibrium and equilibrium optically thick solutions are very similar, while for oxygen the equilibrium solution is much higher. This may indicate that the collisional excitation rates for carbon are too fast while those for oxygen are too slow. A comparison of the measured and calculated atomic O 777 nm triplet spectra at peak intensity ($x = 0.3$ cm) is presented in Figure 6.27. The calculated spectra is from the calculation with optically thin radiation and is scaled

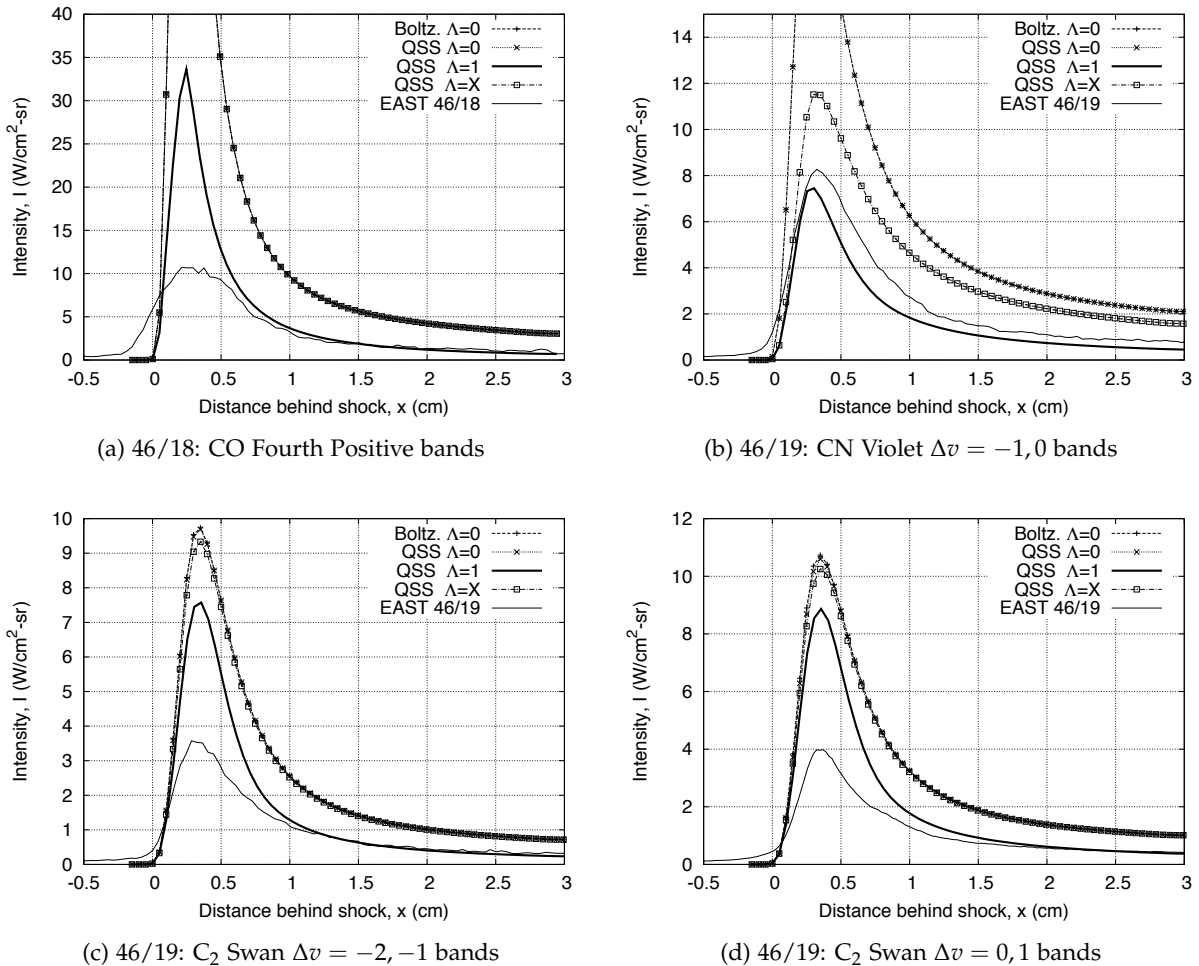


Figure 6.24: Comparison of measured diatomic band intensity profiles for the 8.5 km/s EAST Mars condition with Poshax3 calculations implementing various radiation model assumptions.

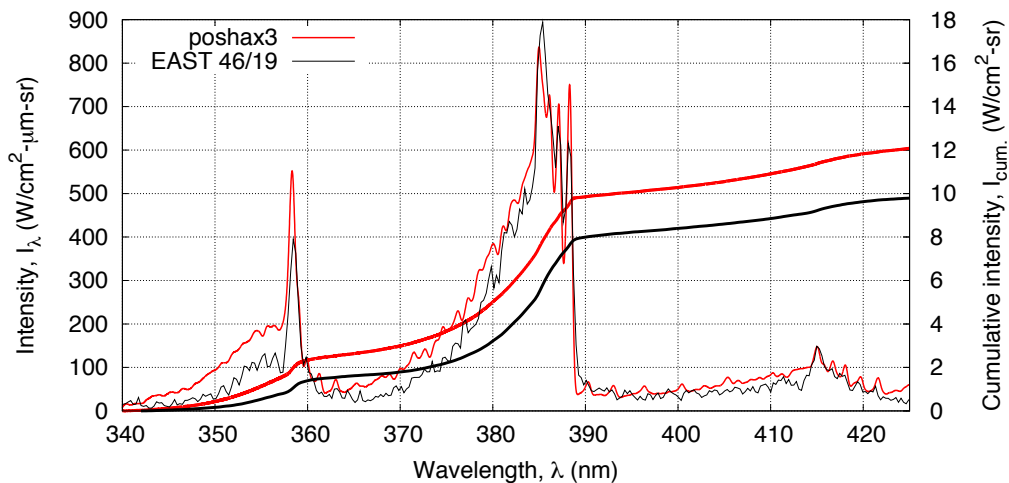


Figure 6.25: Comparison of measured and calculated CN Violet spectra at $x=0.3$ cm.

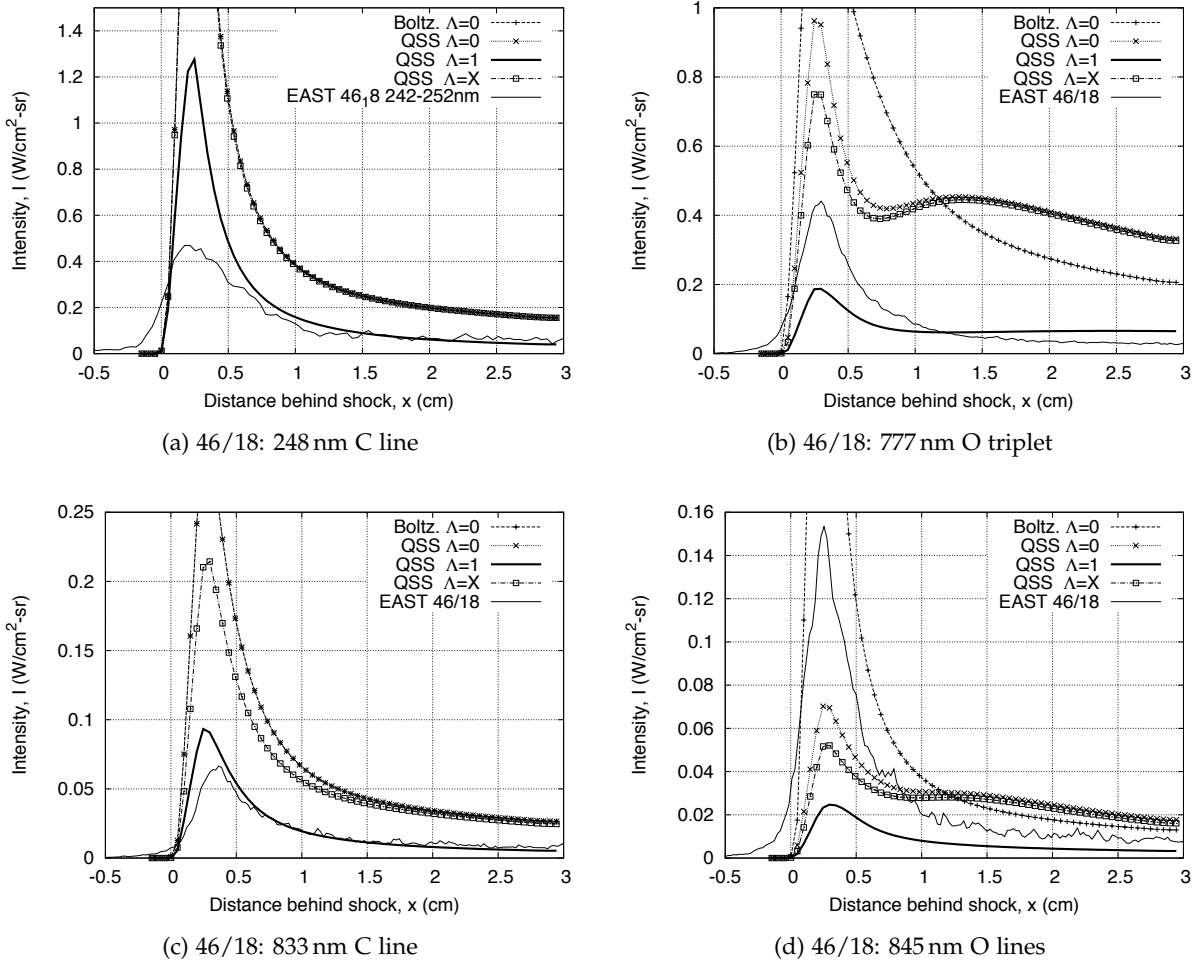


Figure 6.26: Comparison of atomic line intensity profiles measured in the EAST facility for the 8.5 km/s Mars condition with Poshax3 calculations implementing various radiation model assumptions.

by a factor of 3 to compare the line profiles. While the measured line profile is skewed more towards the lower wavelengths than the calculation, the right side profile is in reasonable agreement. This is in contrast to the line profiles observed for air where the bases were much wider in the experiments.

As previously mentioned, CO and C transitions in the VUV region dominate the radiative heating environment for Mars atmospheric entry. It is therefore appropriate to now consider the influence of physical modelling variations on the middle ultraviolet intensity profiles of these species. Figures 6.28a and 6.28b present comparisons of the CO Fourth positive and 248 nm C line intensity profiles implementing various chemical reaction models. The solution labelled ‘Park’ considers the chemical reaction model proposed by Park *et al.* [137] while the solution labelled ‘modified Park’ considers the modified model proposed in the present work (see Table C.2). As

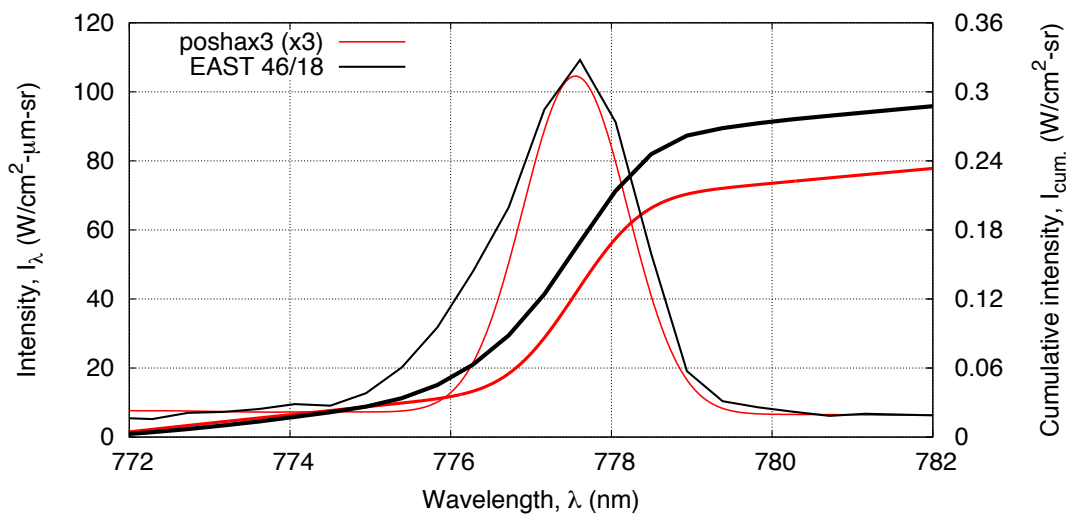


Figure 6.27: Comparison of measured and calculated atomic O 777 nm triplet spectra at $x=0.3$ cm.

noted in § 5.3.3, the modified reaction model considers the faster C_2 dissociation rate proposed by Lee *et al.* [35] and additional CO exchange reactions proposed by Losev *et al.* [140], which lead to a decreased level of CO and an increased level of C and O. This effect can be seen in the intensity profiles where the CO peak is slightly lower in the modified case and the C peak is slightly higher.

Figure 6.29 presents comparisons of the middle ultraviolet CO and C intensity profiles with calculations implementing various models for the limiting translation-vibration exchange cross section, σ_v . The solution labelled ‘Fujita’ considers the model proposed by Fujita [77] for CO, the solution labelled ‘Park’ considers the model of Park *et al.* [137] and the solution labelled ‘Park NP’ considers the Park model with non-preferential dissociation-vibration coupling. The ‘Park NP’ solution is included as it is not clear that preferential dissociation-vibration coupling was considered in Reference [137]. As discussed in § 4.2.1, the model of Park *et al.* [137] is semi-empirical and is fitted to experimental data while the model of Fujita [77] is a fit to computational chemistry calculations. The ‘Fujita’ solution overestimates the peak intensities by a factor of 3 while the ‘Park’ solution shows a much improved agreement. Also the slope of the intensity profile before the peak is in much closer agreement with the ‘Park’ solution than with the ‘Park NP’ solution, validating the use of a preferential dissociation-vibration coupling model for this condition.

For other transitions, however, the use of the Park model for σ_v does not give an improved agreement with experiment. Figures 6.30a and 6.30b present comparisons of the CN Violet $\Delta v = -1, 0$ and C_2 Swan $\Delta v = 0, 1$ intensity profiles with calculations considering the various models for the vibration-translation limiting cross section. In both cases the Fujita model gives the best agreement with the measured profiles.

Figure 6.31 presents comparisons of the CO Fourth Positive and CN Violet intensity profiles with calculations implementing the diatomic collisional-radiative models of Zalogin [185] and Park [178, 179]. Note that the C line at 248 nm is not considered in this comparison as the diatomic collisional-radiative model only has a very small effect on this transition. The use of the Park collisional-radiative model gives improved agreement with experiment for both transitions, however the CO Fourth Positive profile remains overestimated by a factor of 3. In Figure 6.29a, however, it was demonstrated that by using the Park model for σ_v alongside the Park collisional-radiative model good agreement with experiment can be achieved. Therefore these results validate the use of the Park collisional-radiative model for this condition.

Summary and concluding remarks

Comparisons with Mars shock tube experiments performed in the EAST facility with a freestream pressure of 0.1 Torr and a nominal shock speed of 8.5 km/s have been presented. For most transitions the relaxation from the peak intensity shows excellent agreement with experiment when the optically thin assumption is applied, however the nonequilibrium overshoot is consistently overestimated. Much improved agreement with the nonequilibrium overshoot of the critical CO and C transitions is found when the vibration-translation exchange limiting cross section model of Park [137] is employed for CO instead of the more recent computational chemistry based model of Fujita [77]. In contrast, the overshoot in the CN Violet $\Delta v = -1,0$ and C₂ Swan $\Delta v = 0,1$ bands is more accurately described by the Fujita model. Implementing a preferential dissociation-vibration coupling model instead of a non-preferential model is also found to give much improved agreement for the CO and C transitions. Also, implementing the rates of Park [178, 179] instead of Zalogin [185] for the diatomic collisional-radiative modelling improves the agreement with experiment, especially for the CN Violet bands. It is interesting to note that although some differences in the atomic line profiles exist, the rapid broadening at the base observed for the air conditions is not present. Higher resolution spectra are required to investigate this phenomena further. In summary, the *total* measured nonequilibrium radiation intensity for this condition is able to be estimated within 50% when the results from best performing physical models are considered. It should be noted, however, that while some features such as CN Violet $\Delta v = -1,0$, the C line at 833 nm and the CO Fourth Positive system are able to be very accurately reproduced, others such as the infrared O lines and C line at 248 nm show up to a factor of 3 difference. Although Munafo *et al.* [187] and Boubert and Rond [193], amongst others, have also been able to find good agreement for the UV diatomic transitions, the present analysis is the first to rigorously analyse all the critical transitions measured in the experiments.

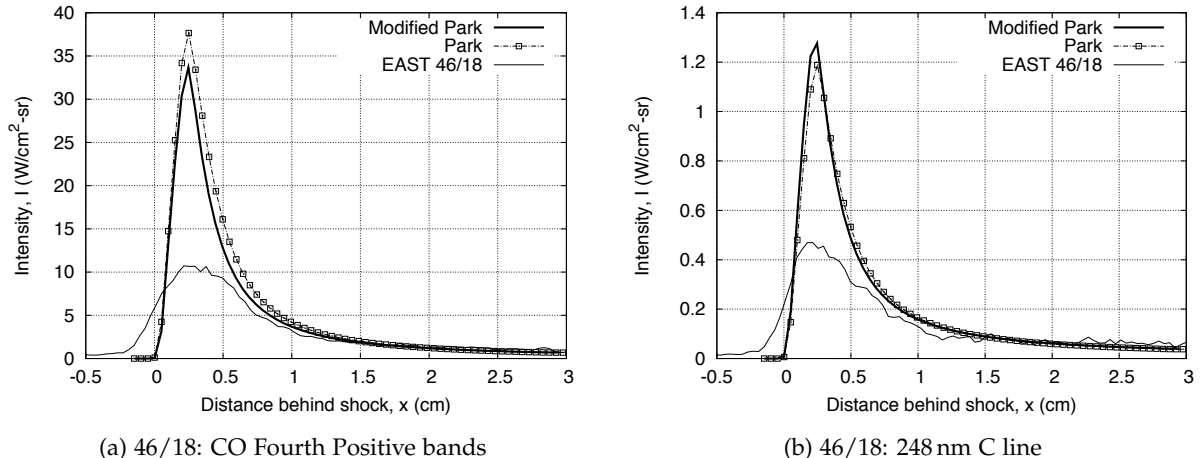


Figure 6.28: Comparison of middle ultraviolet intensity profiles measured in the EAST facility for the 8.5 km/s Mars condition with post-shock relaxation calculations implementing various chemical reaction models.

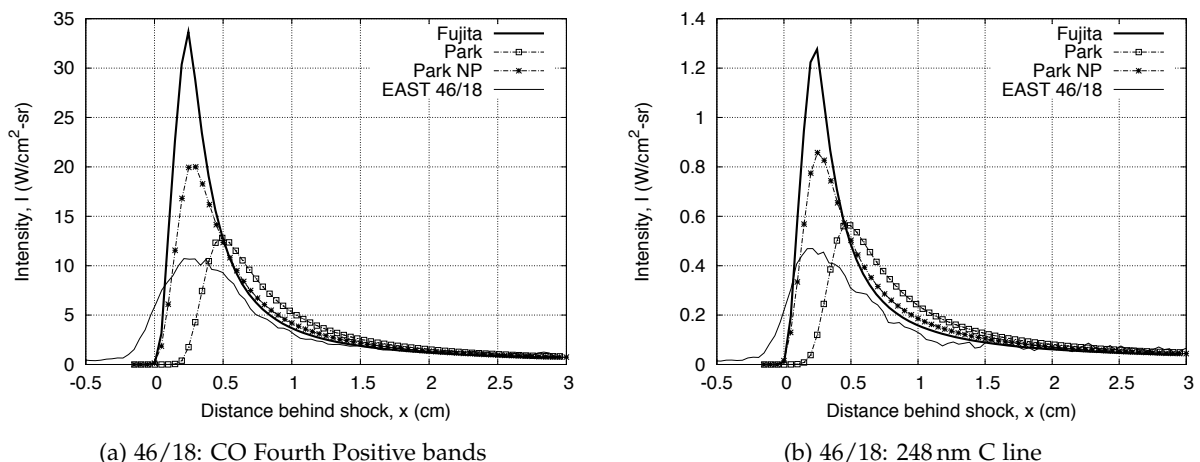


Figure 6.29: Comparison of middle ultraviolet intensity profiles measured in the EAST facility for the 8.5 km/s Mars condition with post-shock relaxation calculations implementing various limiting translation-vibration exchange cross section models.

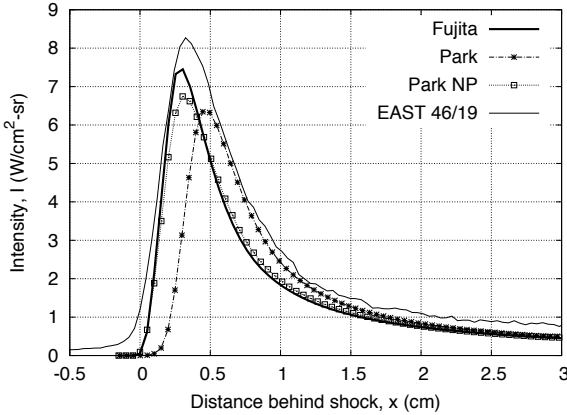
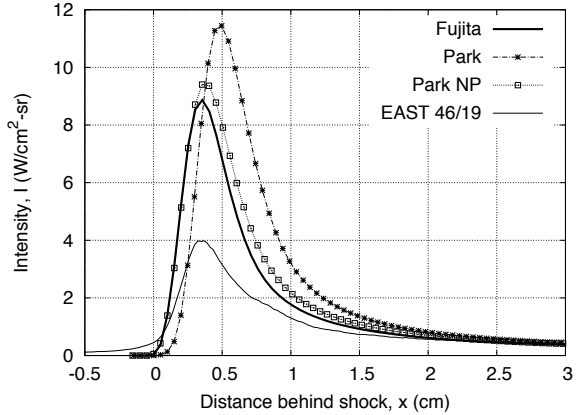
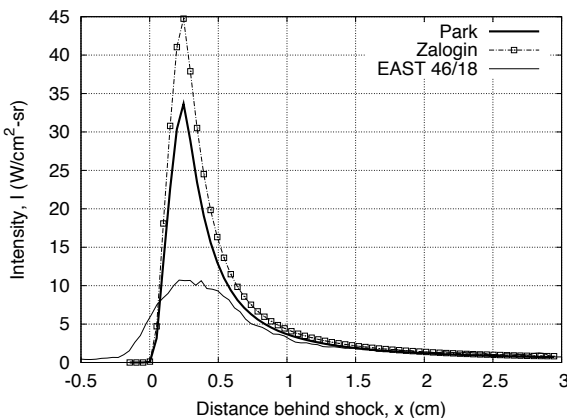
(a) 46/19: CN Violet $\Delta v = -1,0$ bands(b) 46/19: C₂ Swan $\Delta v = 0,1$ bands

Figure 6.30: Comparison of selected intensity profiles measured in the EAST facility for the 8.5 km/s Mars condition with post-shock relaxation calculations implementing various limiting translation-vibration exchange cross section models.



(a) 46/18: CO Fourth Positive bands

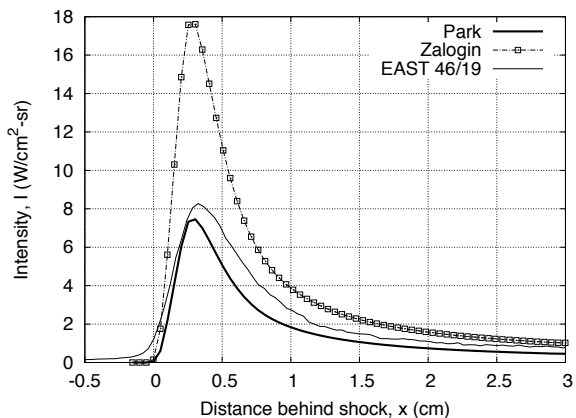
(b) 46/18: CN Violet $\Delta v = -1,0$ bands

Figure 6.31: Comparison of selected intensity profiles measured in the EAST facility for the 8.5 km/s Mars condition with post-shock relaxation calculations implementing various collisional-radiative models.

6.3 University of Queensland X2 Facility

A series of non-reflected shock tube spectroscopy experiments were recently performed in the X2 facility with a N₂–O₂ test gas. Shots were first performed with a shock speed of 10 km/s and freestream pressures of 0.1 to 0.4 Torr to provide a secondary set of data replicating the EAST campaign. Good agreement was found between the two sets of data as demonstrated in Figures 6.3a and 6.3b. A series of shots with a shock speed of 11 km/s and a freestream pressure of 16 Pa were then performed. To the best of the authors knowledge, this represents the only shock tube spectroscopy data set available at this velocity with spectrally and spatially resolved measurements in both the ultraviolet and infrared. As the 10 km/s EAST data has just been analysed, the present analysis of the X2 data is limited to the unique 11 km/s condition.

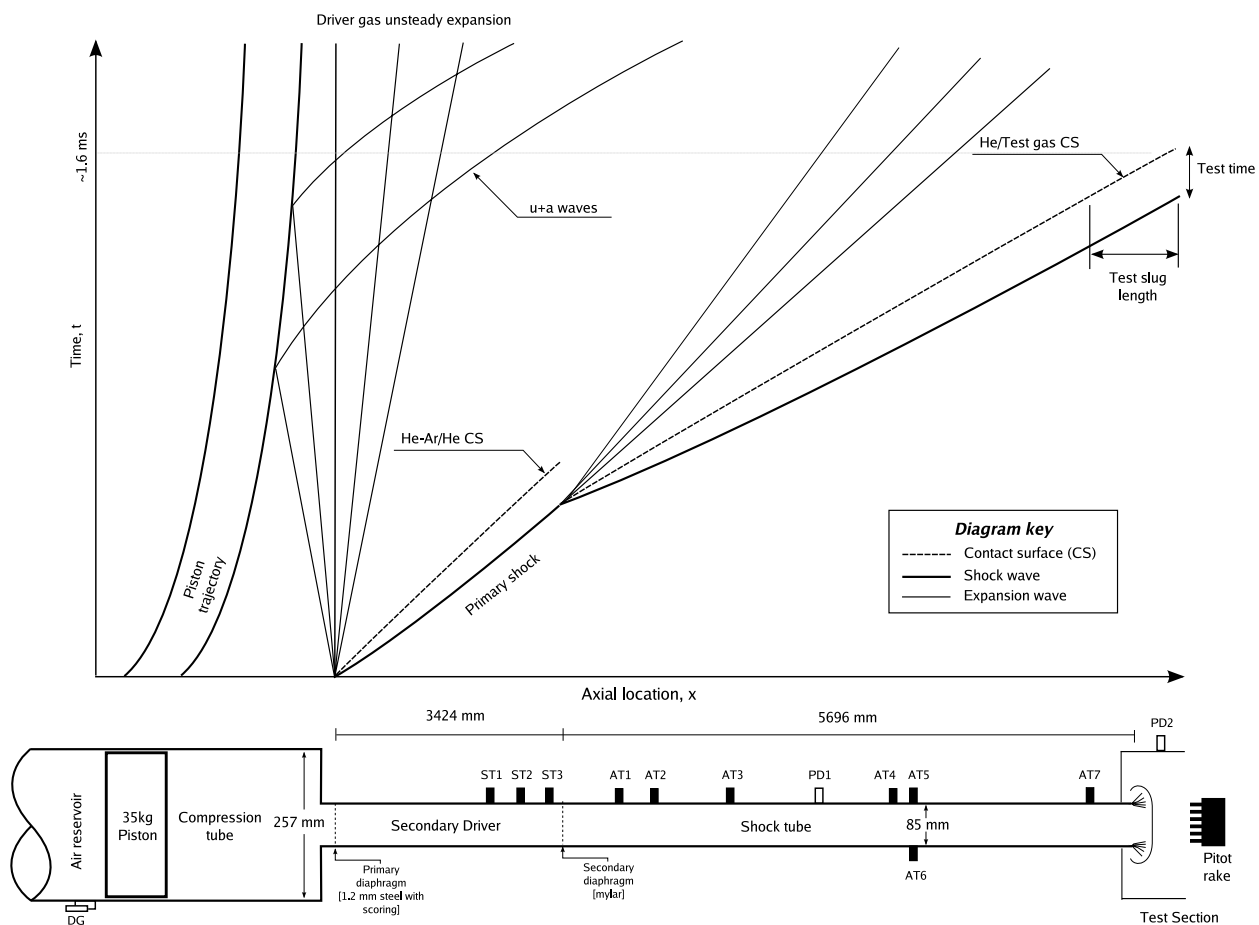


Figure 6.32: Space-time diagram and schematic of the X2 facility in dual-driver non-reflected shock tube mode.

6.3.1 Facility description

The X2 facility is a free-piston driven impulse facility located at the University of Queensland. The experiments considered here utilised the dual driver, non-reflected shock tube mode of operation as illustrated in Figure 6.32. The high pressure air reservoir propels a 35 kg single-stage piston, compressing the driver gas in the compression tube until the rupture pressure of the primary diaphragm is reached. The rupturing primary diaphragm drives a shock through the secondary driver, which in turn ruptures the mylar secondary diaphragm and drives the secondary shock through the test gas in the shock tube. The secondary driver allows high secondary shock speeds to be achieved via the total pressure and enthalpy gain of an additional shock and unsteady expansion [39]. Measurements of the flow condition and shock speed are made with flush wall mounted pressure sensors (PCB transducers) labelled ST 1 to 3 and AT 1 to 7 in Figure 6.32. The PCB transducers are axially located to an accuracy of ± 0.5 mm, and the shock timing is accurate within $0.5 \mu\text{s}$. For the conditions of present interest this implies an uncertainty in the measured shock speed of approximately 2.5%.

6.3.2 Spectroscopic apparatus

Spectroscopic measurements were made of the shock as it emerges into the test section, Figure 6.33. Spatially and spectrally resolved intensity measurements were obtained with infrared and ultraviolet imaging spectrographs. Acton Research Spectra Pro SP2300 series spectrographs were coupled with a 1024×256 pixel Princeton Instruments PI-MAX CCD array for the ultra-violet measurements, and a 512×512 pixel Princeton Instruments PI-MAX CCD array for the near-infrared measurements. Spectra recorded with 150, 600 and 1800 lines/mm gratings are considered in the this analysis. For all shots both spectrometers had slit widths of 100 nm, gate widths of 500 ns and an intensifier gain of 255. The spectrometers were calibrated by placing a tungsten-halogen spectral lamp 500 mm from the spectrometer slit entrance, as the limitations of the spectral lamp prevented an *in-situ* calibration. The optical losses for each mirror, lens and window were then individually determined and a final calibration factor was obtained. As demonstrated in Figures 6.3a and 6.3b, good agreement is obtained between the X2 and EAST data when a test gas width of 6 cm is assumed. The calibration procedure is estimated to be accurate within $\pm 20\%$.

6.3.3 Air conditions

The five 16 Pa 11 km/s air shots considered in the present analysis are summarised in Table 6.6. Numerous other shots were performed, however many did not exhibit a constant equilibrium plateaus as expected; all the shots considered here exhibit a clear plateau that is essential for the comparison with calculations. As the shots exhibit up to a 5% deviation from the nominal shock speed, separate simulations are performed for each. The theoretical equilibrium intensity spectra

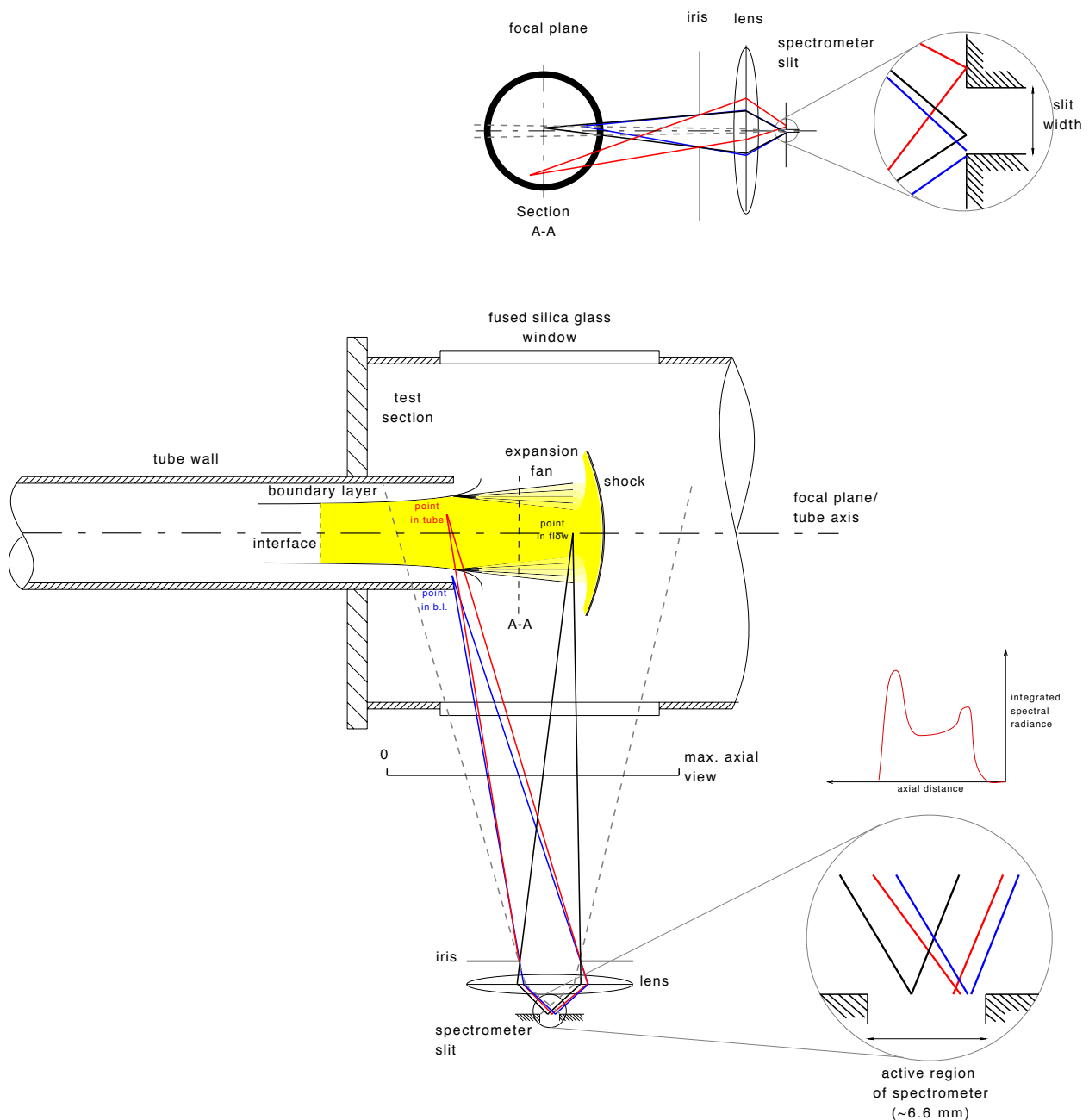


Figure 6.33: Schematic of spectrometer optical measurements for the X2 shock tube experiments. Note that the optical path behind the iris has been simplified for presentation; the actual experiment used a series of flat and curved mirrors instead of a lens.

for an 11 km/s shock through 16 Pa air is presented in Figure 6.34, where the spectral ranges considered are indicated. While all shots recorded data from the infrared spectrometer, only shot x2s1149 recorded ultraviolet spectra. This was with the coarse 150 lines/mm grating in the range $300 \leq \lambda \leq 600$. Here the dominant radiation mechanism in Figure 6.34 is the N_2^+ First Negative

band system, however significant levels of CN Violet radiation were recorded in the equilibrium region as was the case for the EAST data. For shots x2s1145, x2s1149 and x2s1151 the 600 lines/mm grating was used on the infrared spectrometer, and for shots x2s1153 and x2s1154 the fine 1800 lines/mm grating was used to target the oxygen triplet at 777 nm and the N line at 745 nm respectively. The dominant transitions in each of the infrared spectrometer ranges are summarised in Table 6.7. All the transitions originate from relatively low lying electronic levels, except for the N line at 648.7 nm which originates from level $2s^22p^2(^3P)3p$ with energy 13.7 eV. In the following analysis intensity profiles are compared for each of the listed spectral ranges. The $652 \leq \lambda \leq 660$ nm range is not included in the intensity profile analysis as the measured spectra show the strong H α line here which is typically not considered for the Earth re-entry problem as the H₂O concentration in the upper atmosphere is low.

Table 6.6: Summary of the 16 Pa 11 km/s air X2 shots considered in the present analysis.

Shot number	x2s1145	x2s1149	x2s1151	x2s1153	x2s1154
Shock speed, [†] U_s (m/s)	10450	11300	11140	10670	10670
Pressure, p_∞ (Pa)	16	16	16	16	16
Effective test time (μ s)	2.87	2.65	2.69	2.81	2.34
UV Spectrometer range (nm)	300-600	-	-	-	-
UV Exposure time (μ s)	0.5	-	-	-	-
UV $\Delta\lambda_{HWHM}$ (Å)	5	-	-	-	-
IR Spectrometer range (nm)	686-763	752 - 828	631 - 709	771 - 783	738 - 750
IR Exposure time (μ s)	0.5	0.5	0.5	0.5	0.5
IR $\Delta\lambda_{HWHM}$ (Å)	3.5	3.5	3.5	1	1

[†] The uncertainty in the quoted shock speeds is $\pm 2.5\%$.

Figures 6.35a and 6.35b present temperature and number density profiles for the nominal 11 km/s shock through 16 Pa air. Also indicated are the electronic-electron temperature T_e and electron concentration calculated by the three-temperature model. Thermochemical equilibrium is estimated to occur 1 cm behind the shock. Given that the 0.5 μ s exposure time results in a smearing distance of approximately 0.55 cm, however, the equilibrium plateau in intensity should be achieved between 1.5 and 2 cm behind the shock. The three temperature solution does not differ significantly from the two-temperature model for this condition, and the calculations performed in this analysis therefore use the two-temperature model.

Results

Figure 6.36a presents a comparison of the measured and calculated ultraviolet intensity profiles for shot x2s1145. The equilibrium spectra averaged between 2 and 3 cm behind the shock are

Table 6.7: Summary of the dominant infrared atomic spectral features considered for the X2 air experiments.

Spectral ranges		Spectral features			
Species	λ_{CL} (nm)	i_{upper}	i_{lower}	A_{ul} (s^{-1})	
600 lines/mm grating					
631 $\leq \lambda \leq$ 652 nm	N	648.7	28	8	4.9×10^6
652 $\leq \lambda \leq$ 660 nm [†]	H	656.5	-	-	-
660 $\leq \lambda \leq$ 701 nm	N	675.4	28	8	1.16×10^6
700 $\leq \lambda \leq$ 760 nm	N	745.4	10	4	3.76×10^7
760 $\leq \lambda \leq$ 800 nm	O	777.6	6	4	3.69×10^7
800 $\leq \lambda \leq$ 828 nm	N	821.4	9	4	3.1×10^7
1800 lines/mm grating					
738 $\leq \lambda \leq$ 750 nm	N	745.4	10	4	3.76×10^7
771 $\leq \lambda \leq$ 783 nm	O	777.6	6	4	3.69×10^7

[†] Range not considered in the intensity profile comparison.

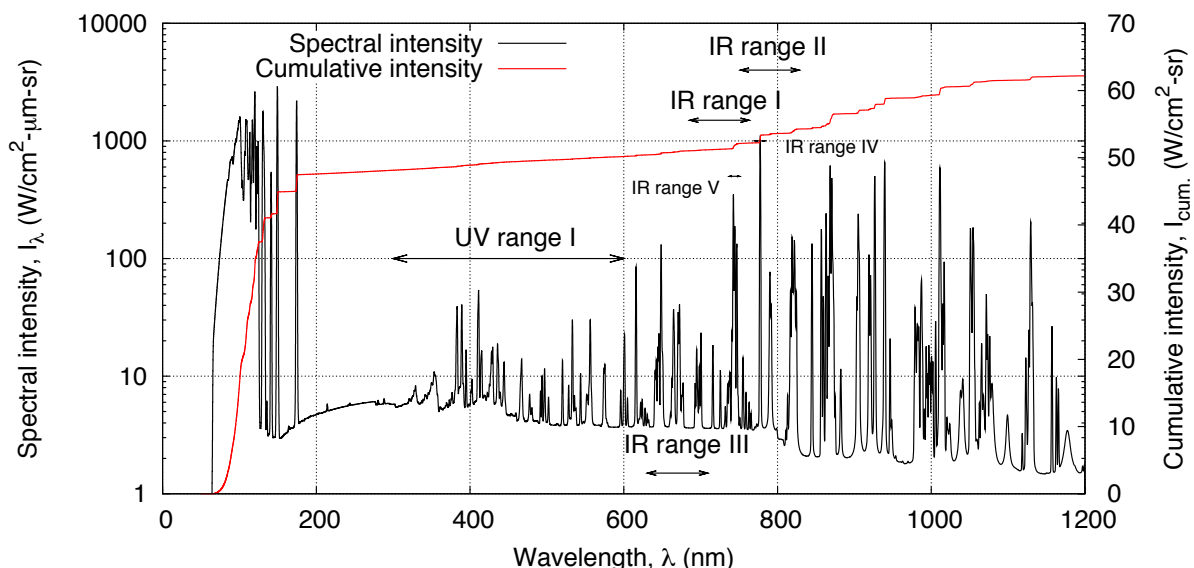


Figure 6.34: Theoretical equilibrium intensity spectra for a 11 km/s shock through 16 Pa air with spectral ranges considered by the X2 experiments.

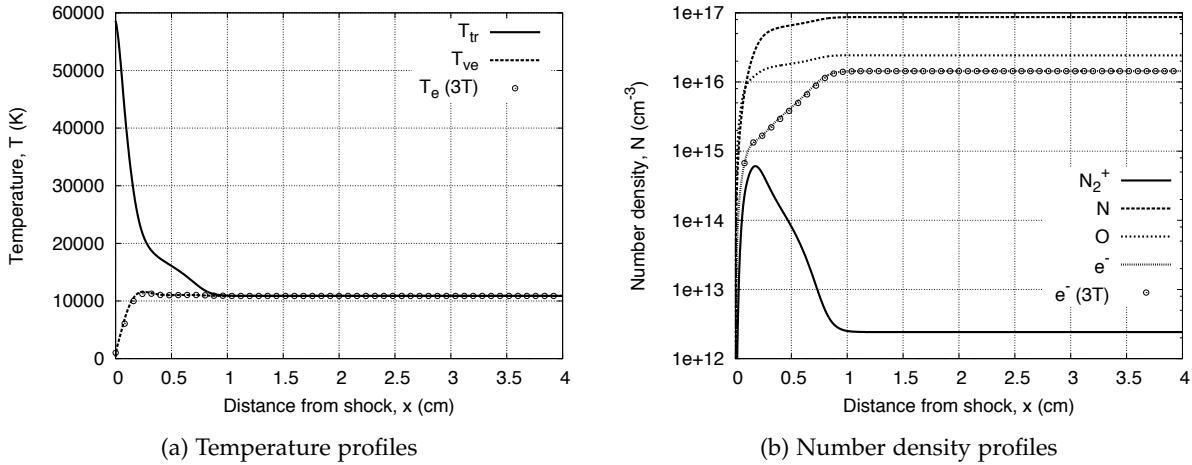


Figure 6.35: One-dimensional post-shock relaxation profiles for a 11 km/s shock through 16 Pa air.

compared in Figure 6.36b. The nonequilibrium calculations show good agreement with the measured nonequilibrium overshoot due in the N_2^+ First Negative system. The experiment, however, then shows a much higher plateau level than the calculations. A similar elevated plateau level was observed in the EAST campaign, and can be again be attributed to one or more of the phenomena proposed in Reference [38]. The CN Violet 0-0 band head can be seen at 390 nm in Figure 6.36b, and the additional radiation between 400 and 600 nm is possibly due to a combination of contaminant band systems such as CN Red and C₂ Swan and atomic lines from contaminant species such as C and H. Also, it is possible lines from atomic nitrogen and oxygen that are not

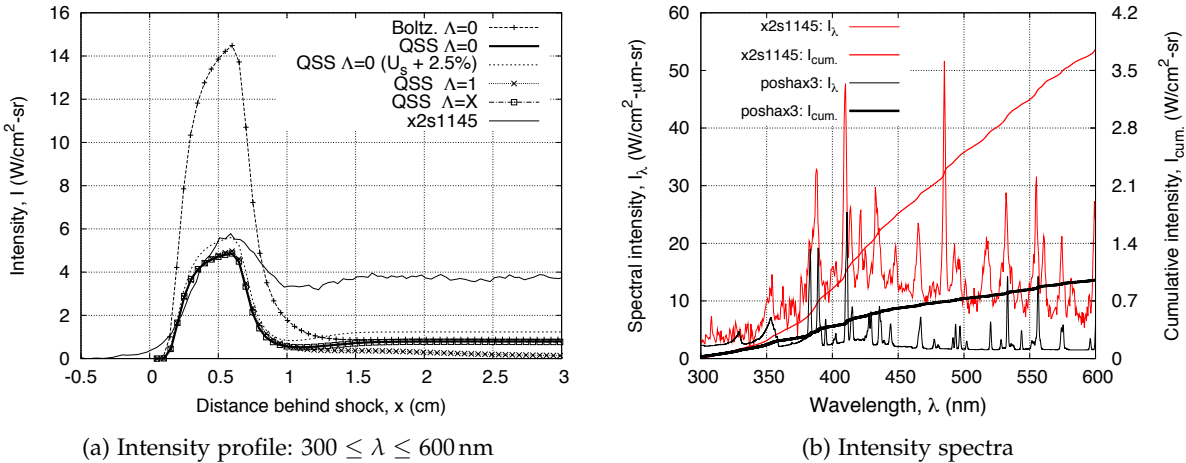


Figure 6.36: Comparison of measured and calculated ultraviolet intensity measurements for shot x2s1145.

included in the NIST database are present in this spectral region [129]. The strong line at 487 nm is the H β transition, which occurs due to the water vapour present in the laboratory air.

Figure 6.37a presents a comparison of the measured and calculated infrared intensity profiles for shot x2s1145. The profiles represent the integrated intensity in the $700 \leq \lambda \leq 760$ nm range where the atomic N lines at 746 nm are the dominant transitions. The equilibrium spectra are compared in Figure 6.37b. The measured intensity profile exhibits an initial plateau twice as large as estimated by the nonequilibrium calculations. Given that the equilibrium calculation shows a larger intensity in this region, it is possible the level of nonequilibrium is being overestimated. However the equilibrium plateau intensity is also significantly underestimated, with the $U_s + 2.5\%$ case still not reaching the same level. The measured equilibrium spectra show a significant level of background radiation between 690 and 740 nm that is not predicted by the calculations. The cumulative intensity gain over the N lines between 740 and 750 nm is also underestimated by the calculations, with the bases of the three lines merging into a continuum in the measured spectra.

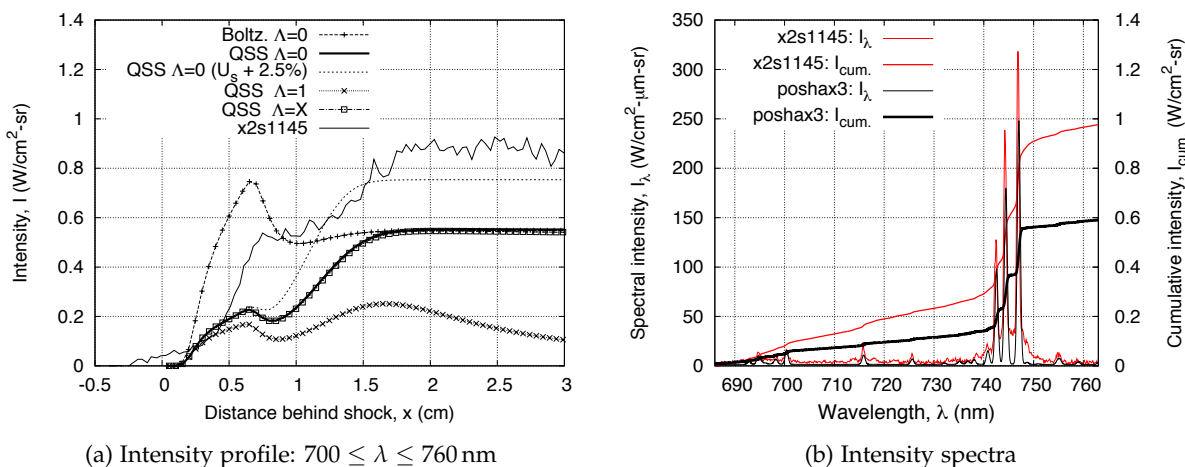


Figure 6.37: Comparison of measured and calculated infrared intensity measurements for shot x2s1145.

Shot x2s1154 also measured the atomic N lines at 746 nm, but with the finer 1800 lines/mm grating. Figure 6.38a presents a comparison of the measured and calculated infrared intensity profiles for shot x2s1154, and the equilibrium spectra are compared in Figure 6.38b. For this shot, the intensity profile shows good agreement with the nonequilibrium optically thick calculation within the level of uncertainty imposed by the shock speed measurement. As was observed in the EAST campaign, the lines are much wider at the bases in the measurements than the calculations. Comparing Figures 6.37b and 6.38b, it is clear that the degree of broadening at the line bases is dependent on the grating resolution. This seems to indicate that it is an artefact of the spectrometer, and not a quality of shock heated air. It is necessary to note that these lines

were underestimated for shot x2s1145 and overestimated for shot x2s1154. This discrepancy is possibly due to differences in the calibration of the two gratings and variations in the width of core flow between the two shots.

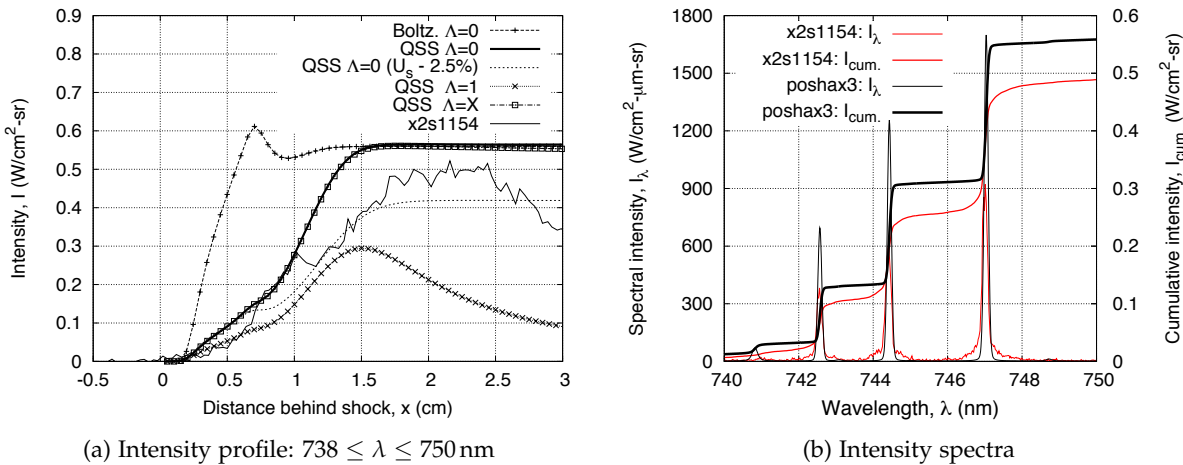


Figure 6.38: Comparison of measured and calculated infrared intensity measurements for shot x2s1154.

Figure 6.39 presents comparisons of the measured and calculated infrared intensity profiles for shot x2s1149. Figure 6.39a considers the $760 \leq \lambda \leq 800$ nm range where the 777 nm oxygen triplet is the dominant radiator, and Figure 6.39b considers the $800 \leq \lambda \leq 828$ nm range where nitrogen lines dominate. Similarly as for the atomic N lines measured with the 600 lines/mm grating in shot x2s1145, both the spectral ranges are underestimated by the calculations even after the velocity variation is taken into consideration. Despite the disagreement in the equilibrium level, the slope of the nonequilibrium region is well reproduced in both spectral ranges.

Figure 6.40a compares the measured and calculated infrared intensity profile in the $771 \leq \lambda \leq 783$ nm range for shot x2s1153 using the 1800 lines/mm grating. The equilibrium spectra are compared in Figure 6.40b where the calculated intensity has been reduced by a factor of two for clarity. As was observed for the atomic N lines at 746 nm, these measurements with the 1800 lines/mm grating are of a lower intensity than for the 600 lines/mm grating (shot x2s1149). With the uncertainty shock speed taken into consideration, the nonequilibrium optically thick calculation shows reasonable agreement with the measured intensity profile, however the initial plateau at $x = 1$ cm is not reproduced.

Figure 6.41 present comparisons of the measured and calculated infrared intensity profiles for shot x2s1151. As indicated in the equilibrium spectra in Figure 6.42, the H α line radiates strongly at 656 nm and is therefore omitted from the spectral ranges considered in the intensity profiles. Adding 1.46×10^{15} particles/cm $^{-3}$ of atomic H was found to give reasonable agreement with the measured H α line. This corresponds to a mole fraction of 1% and is likely due to water

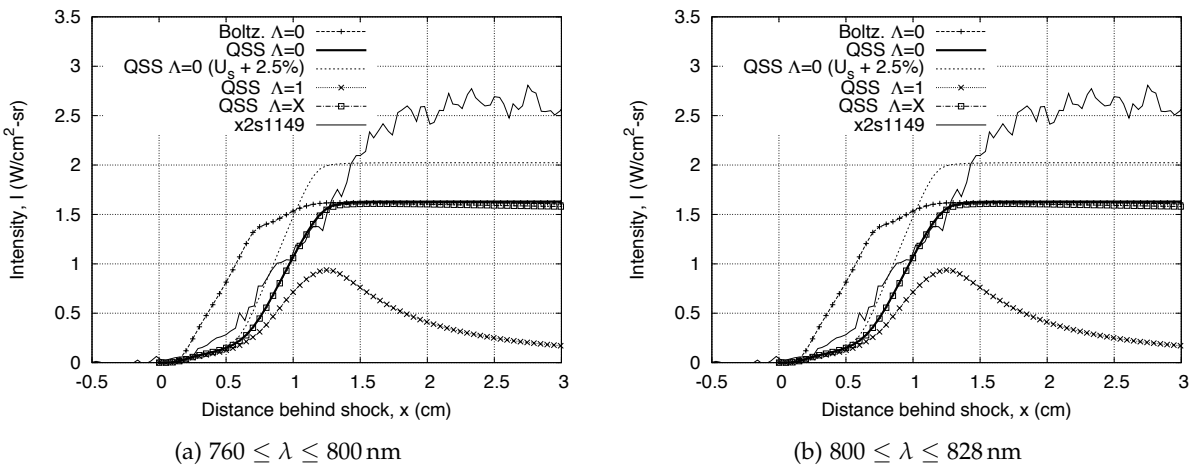


Figure 6.39: Comparison of measured and calculated infrared intensity profiles for shot x2s1149.

vapour in the laboratory air. For this shot both calculated intensity profiles show good agreement with experiment when shock speed variation is taken into consideration.

Summary and concluding remarks

Comparisons with air shock tube experiments performed in the X2 facility with a freestream pressure of 16 Pa and a nominal shock speed of 11 km/s have been presented. While the nonequilibrium overshoot in N_2^+ was significantly overestimated for the EAST air conditions, here good agreement is found. This may be due to the implemented physical models performing better at this higher velocity condition. The equilibrium plateau is once again underestimated due to the presence of carbon contamination, however. For the atomic lines, the measured equilibrium intensities were underestimated for shots using the 600 lines/mm grating, and overestimated for shots using the finer 1800 lines/mm grating. This discrepancy can partly be explained by the background continuum that was measured in the experiments but not present in the calculations; the larger range of the 600 lines/mm grating allows more background continuum signal to be measured. Also, the rapid broadening of the atomic line profiles at the bases observed in the EAST air campaign is also present in the X2 data. By comparing the line profiles from shots with the 600 and 1800 lines/mm gratings it has been concluded that this broadening is an artefact of the spectrometer. Finally it should be noted that this analysis was performed based on the assumption of a 6 cm width of test gas. Although this assumption was based on comparisons with the EAST data, it is possible that differences between shots and flow non-uniformities lead to different widths of test gas. Using the 8.5 cm diameter of the shock tube as the test gas width would increase the presented calculated results by approximately 40%. In summary, the *total* measured radiation intensity (in both nonequilibrium and equilibrium regions) was able to be estimated within 30% when spectral features due to carbon contamination are disregarded and

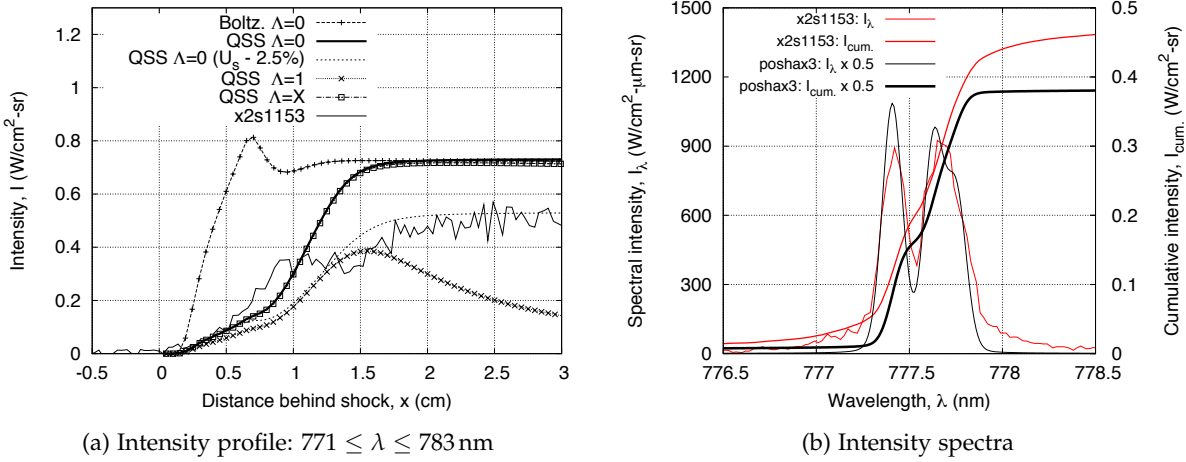


Figure 6.40: Comparison of measured and calculated infrared intensity measurements for shot x2s1153.

the results from the best performing physical models are considered. The underestimation of the atomic lines in the range $760 \leq \lambda \leq 828 \text{ nm}$ is the biggest contributor to this error.

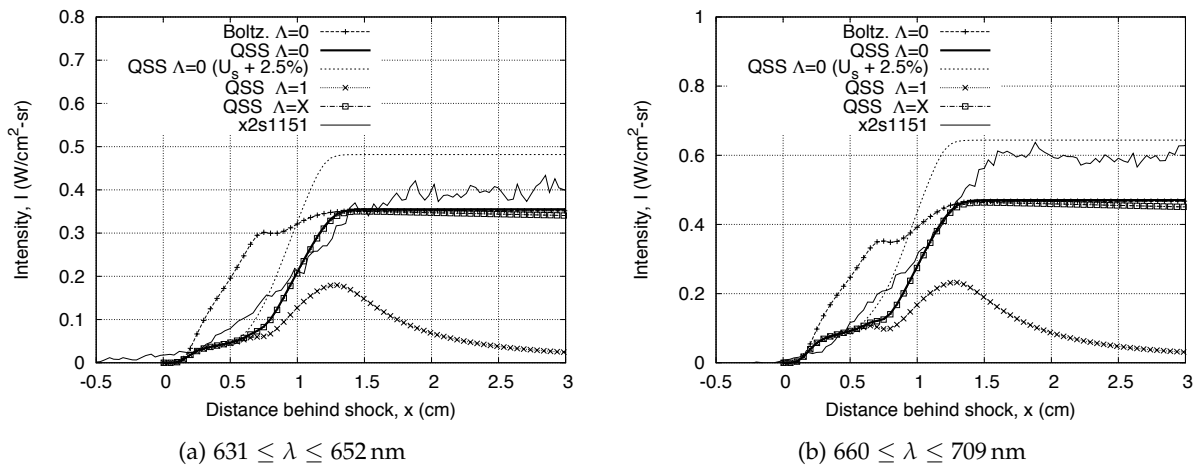


Figure 6.41: Comparison of measured and calculated infrared intensity profiles for shot x2s1151.

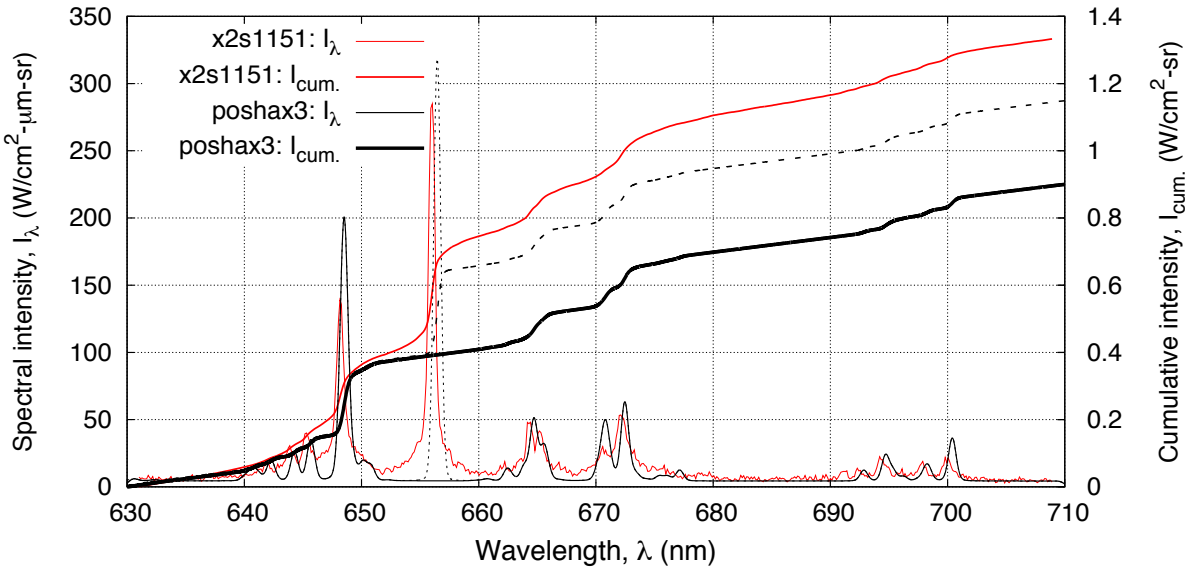


Figure 6.42: Comparison of measured and calculated x2s1151 equilibrium infrared intensity spectra.

6.4 Summary

One-dimensional post-shock relaxation analyses have been performed of non-reflected shock tube experiments relevant to hyperbolic entry at Earth and Mars. In § 6.2.3 experiments performed in the EAST facility with a N₂–O₂ test gas were analysed. Data from experiments with freestream pressures of 0.1 and 0.3 Torr were considered, and the nominal shock speed for both was 10 km/s. In § 6.2.4 experiments performed in the EAST facility with a CO₂–N₂ test gas were analysed. A condition with a freestream pressure of 0.1 Torr and a nominal shock speed of 8.5 km/s was considered. In § 6.2.3 experiments performed in the X2 facility with a N₂–O₂ test gas were analysed. Data from experiments with freestream pressure of 16 Pa and a nominal shock speed of 11 km/s were considered. Detailed summaries for each experiment set have been provided at the end of each respective section.

Overall, the comparison with the EAST and X2 data has shown that the *total* measured radiation is able to be estimated within 30% for N₂–O₂ mixtures and within 50% for CO₂–N₂ mixtures. Given that the spectrometer calibrations have an uncertainty of approximately ±20 %, and that the uncertainty of the radiation calculation is at least ±30 % (see § 3.3.4), the comparison is encouraging. However, three areas of concern emerge from these analyses; (1) the underestimation of infrared spectra due to differences in line shapes and background continuum levels, (2) the inability of a single physical model set to accurately reproduce all spectral features, and (3) the presence of carbon contamination. Firstly, to address the underestimation of infrared spectra due to differences in line shapes and background continuum levels, a higher fidelity spectral model

is required. Specifically, a more detailed treatment of the line-profiles and the inclusion of additional mechanisms such as photodissociation, negative ion and molecule continua is called for. Also, comparisons of atomic line spectra measured in X2 campaign revealed that the line profiles are highly sensitive to the resolution of the spectrograph grating. Further spectral measurements therefore need to be made with various grating resolutions to quantify this effect. Secondly, different physical modelling was required to achieve good agreement with the various spectral features measured in the EAST air and Mars campaigns. Specifically, for the air conditions preferential vibration-dissociation coupling was required to reproduce the N_2^+ First Negative emission, however a non-preferential model was required to reproduce atomic line emission. For the Mars conditions, CO and C transitions are accurately reproduced when the vibration-translation exchange limiting cross section model of Park [137] is employed, while CN and C_2 transitions are more accurately reproduced when the model of Fujita [77] is employed. Such a discrepancies may indicate the physical modelling of dissociation is inadequate; a vibrationally specific chemistry model should be implemented to test this hypothesis. Finally, the presence of carbon contamination in the experiments with an air test gas is a concern. Although the CN Violet band system is the only contaminant mechanism definitively identified, it is possible other features such as atomic C lines and continuum transitions are present but not identified. Computationally, efforts should be made to model the presence of carbon in the experiments; experimentally, efforts should be made to reduce carbon contamination as it may unduly influence the pure test gas chemical kinetics.

Despite these shortcomings, the comparisons with the non-reflected shock tube data have allowed the most appropriate physical models to be identified for each gas mixture, and have demonstrated the ability of the computational tools developed in this work to predict accurate radiation intensity levels. This closes the post-shock relaxation part of this thesis, and we can proceed with confidence in implementing the physical models inside a Navier-Stokes solver.

Part III

Two-dimensional flowfields

7

Implementation of the Navier–Stokes equations: Eilmer3

In this chapter the implementation of the Navier–Stokes equations presented in § 2.1 is described. As part of this thesis, modifications have been made to an existing Navier–Stokes solver to allow for the physical models described in the previous chapters to be implemented. In addition, a ray-tracing based radiation transport model has been developed for the flow-field solver. In § 7.1 an overview of the code structure and supporting programs is given. In § 7.2 the specific form of the governing equations implemented in the flow solver for the gas dynamics are described. The chemical kinetic and thermal energy exchange source terms are applied in an operator split fashion and are described separately in § 7.3 and 7.4. The models developed for radiation–flowfield coupling are described in § 7.5, and the method for calculating the diffusion fluxes is outlined in § 7.6. The Fire II $t = 1634\text{ s}$ trajectory point is then simulated with the Euler equations in § 7.7, and comparisons are made with a solution obtained using the post-shock relaxation equations to assess the loose coupling methodology for chemical and thermal nonequilibrium. The chapter is summarised in § 7.8.

7.1 Overview of the code

The Eilmer3 code [194] is an extension of the single-block Navier–Stokes integrator CNS4U [195] to structured multiple-block domains. The code solves the compressible Navier–Stokes equations via a cell-centred time-dependent finite-volume formulation. The governing equations are expressed in integral form over arbitrary quadrilateral cells, with the time rate-of-change of conserved quantities in each cell specified as a summation of the mass, momentum and energy flux through the cell interfaces. The code is capable of considering planar, axisymmetric and fully three-dimensional geometries. When simulating gases with finite-rate chemistry and thermal energy exchange, as is considered in the present work, these physical processes are treated with an operator-split approach. The computational core of Eilmer3 is written in a combination of C and C++, with the option for user-defined functions such as boundary conditions provided as Lua scripts. Preprocessing (*i.e.* grid generation) and postprocessing is handled by a collection of Python programs. All of the flow-field calculations performed in the present work implemented the OpenMPI version of the code where the computational domain is divided into multiple blocks that are each handled by individual processors on a multiple-instruction, multiple-data cluster computer. Boundary conditions are handled by two arrays of ghost cells buffering each block edge. For the calculation of the radiative source terms by the ray-tracing method, a separate code that makes use of the OpenMP API for implementation on a shared-memory multiple-processor computer has been written.

7.2 Governing Equations for the Gas Dynamics

The code is formulated around the integral form of the Navier–Stokes equations, which can be expressed as:

$$\frac{\partial}{\partial t} \int_V U dV = - \int_S (\bar{F}_i - \bar{F}_v) \cdot \hat{n} dA + \int_V Q dV \quad (7.1)$$

where S is the bounding surface and \hat{n} is the outward-facing unit normal of the control surface. For axisymmetric flow as considered in the present study, V is the volume and A the area of the cell boundary per unit radian in the radial direction.

The array of conserved quantities is dependent on the thermal model and geometry under consideration. In the present work two-dimensional geometry and a two-temperature thermal model are considered, and the array of conserved quantities is:

$$U = \begin{bmatrix} \rho \\ \rho u_x \\ \rho u_y \\ \rho E \\ \rho e_{ve} \\ \rho f_s \end{bmatrix} \quad (7.2)$$

Here, the conserved quantities are respectively density, x -momentum per volume, y -momentum per volume, total energy per volume, vibrational-electronic-electron energy per volume and mass density of species s . The volumetric translation-rotation energy ρe_{tr} does not appear in the array of conserved quantities as it can be calculated from the definition of total energy:

$$\rho e_{\text{tr}} = \rho E - \frac{1}{2} \rho (u_x^2 + u_y^2) - \rho e_{\text{ve}} \quad (7.3)$$

In contrast, both total and all individual species continuity equations are considered in Equation 7.2, as the redundant information allows the mass-conserved formulation of the chemical kinetic ODE system proposed by Gollan [1] to be implemented. Thus for N_{species} chemical species and $N_{\text{modes}} = 2$ thermal modes, there are $4 + N_{\text{species}} + (N_{\text{modes}} - 1) = 5 + N_{\text{species}}$ conserved quantities in Equation 7.2.

The flux vectors are divided into inviscid and viscous contributions. For the two temperature model, the inviscid component is:

$$\bar{F}_i = \begin{bmatrix} \rho u_x \\ \rho u_x^2 + p \\ \rho u_y u_x \\ \rho E u_x + p u_x \\ \rho e_{\text{ve}} u_x + p_e u_x \\ \rho f_s u_x \end{bmatrix}_{\hat{i}} + \begin{bmatrix} \rho u_y \\ \rho u_x u_y \\ \rho u_y^2 + p \\ \rho E u_y + p u_y \\ \rho e_{\text{ve}} u_y + p_e u_y \\ \rho f_s u_y \end{bmatrix}_{\hat{j}}, \quad (7.4)$$

and the viscous component is:

$$\bar{F}_v = \begin{bmatrix} 0 \\ \tau_{xx} \\ \tau_{yx} \\ \tau_{xx} u_x + \tau_{yx} u_y + q_x \\ q_{x,\text{ve}} \\ J_{x,s} \end{bmatrix}_{\hat{i}} + \begin{bmatrix} 0 \\ \tau_{xy} \\ \tau_{yy} \\ \tau_{xy} u_x + \tau_{yy} u_y + q_y \\ q_{y,\text{ve}} \\ J_{y,s} \end{bmatrix}_{\hat{j}}, \quad (7.5)$$

where the axisymmetric viscous stresses are:

$$\begin{aligned} \tau_{xx} &= 2\mu \frac{\partial u_x}{\partial x} + \lambda \left(\frac{\partial u_x}{\partial x} + \frac{\partial u_y}{\partial y} + \frac{u_y}{y} \right), \\ \tau_{yy} &= 2\mu \frac{\partial u_y}{\partial y} + \lambda \left(\frac{\partial u_x}{\partial x} + \frac{\partial u_y}{\partial y} + \frac{u_y}{y} \right), \\ \tau_{xy} = \tau_{yx} &= \mu \left(\frac{\partial u_x}{\partial y} + \frac{\partial u_y}{\partial x} \right), \end{aligned} \quad (7.6)$$

and the secondary viscosity coefficient λ is expressed in terms of the primary coefficient μ via

Stokes hypothesis, $\lambda = -\frac{2}{3}\mu$. The viscous heat fluxes are:

$$\begin{aligned} q_x &= k_{tr} \frac{\partial T_{tr}}{\partial x} + k_{ve} \frac{\partial T_{ve}}{\partial x} + \sum_s^{\text{species}} J_{x,s} h_s \\ q_y &= k_{tr} \frac{\partial T_{tr}}{\partial y} + k_{ve} \frac{\partial T_{ve}}{\partial y} + \sum_s^{\text{species}} J_{y,s} h_s \\ q_{x,ve} &= k_{ve} \frac{\partial T_{ve}}{\partial x} + \sum_s^{\text{species}} J_{x,s} h_{ve,s} \\ q_{y,ve} &= k_{ve} \frac{\partial T_{ve}}{\partial y} + \sum_s^{\text{species}} J_{y,s} h_{ve,s} \end{aligned} \quad (7.7)$$

The vector of source terms is separated into geometric, chemical kinetic, thermal energy exchange and radiation contributions in order to apply the operator-splitting integration approach:

$$Q = Q_{\text{geom.}} + Q_{\text{chem.}} + Q_{\text{therm.}} + Q_{\text{rad.}} \quad (7.8)$$

The geometric source term vector for axisymmetric geometries is:

$$Q_{\text{geom.}} = \begin{bmatrix} 0 \\ 0 \\ (p - \tau_{\theta\theta}) A_{xy} / V \\ 0 \\ 0 \\ 0 \end{bmatrix} \quad (7.9)$$

where A_{xy} is the projected area of the cell in the (x,y)-plane and:

$$\tau_{\theta\theta} = 2\mu \frac{u_y}{y} + \lambda \left(\frac{\partial u_x}{\partial x} + \frac{\partial u_y}{\partial y} + \frac{u_y}{y} \right). \quad (7.10)$$

For planar geometries $Q_{\text{geom.}}$ is a zero vector. See the original ICASE report [195] for a derivation of these terms.

The chemistry source term vector is:

$$Q_{\text{chem.}} = \begin{bmatrix} 0 \\ 0 \\ 0 \\ 0 \\ \sum_m^{N_{\text{mol}}} \Omega_m^{VC} + \sum_i^{N_{\text{ion}}} \Omega_i^{EC} \\ M_s \dot{\omega}_s \end{bmatrix} \quad (7.11)$$

and the thermal energy exchange source term vector is:

$$Q_{\text{therm.}} = \begin{bmatrix} 0 \\ 0 \\ 0 \\ 0 \\ \sum_m^{N_{\text{mol.}}} \Omega_m^{\text{VT}} + \sum_s^{N_{\text{species}}} \Omega_s^{\text{ET}} \\ 0 \end{bmatrix} \quad (7.12)$$

Note that the energy source terms due to chemical reactions (Ω_m^{VC} and Ω_m^{EC}) are applied alongside the chemical kinetic source terms rather than the other thermal energy exchange source terms. Finally, the radiation source term vector applies the radiative divergence to the total and vibration-electron-electronic energy equations:

$$Q_{\text{rad.}} = \begin{bmatrix} 0 \\ 0 \\ 0 \\ -\nabla \cdot \vec{q}_{\text{rad}} \\ -\nabla \cdot \vec{q}_{\text{rad}} \\ 0 \end{bmatrix} \quad (7.13)$$

where any purely rotational component of the radiative source term has been neglected.

7.2.1 Discretised Equations and Time-Stepping Procedure

The conservation equations are applied to straight-edged quadrilateral cells for which the boundary, projected onto the (x,y)-plane, consists of four straight lines. These lines (or cell interfaces) are labelled North, East, South and West and the integral equation is approximated by the algebraic expression:

$$\frac{dU}{dt} = -\frac{1}{V} \sum_{\text{NESW}} (\bar{F}_i - \bar{F}_v) \cdot \hat{n} dA + Q \quad (7.14)$$

where U and Q now represent cell-average values. An operator-splitting approach as advocated by Oran and Boris [196] (see Chapter 11 of their text) is applied whereby the physical mechanisms are applied in a decoupled fashion. The time integration of the ODE system shown in Eq. 7.14 is then approximated by:

$$\begin{aligned} \int_{\Delta t} \frac{dU}{dt} dt &= \int_{\Delta t} \left(\frac{dU}{dt} \right)_{\text{inv.}} dt + \int_{\Delta t} \left(\frac{dU}{dt} \right)_{\text{visc.}} dt \\ &+ \int_{\Delta t} \left(\frac{dU}{dt} \right)_{\text{chem.}} dt + \int_{\Delta t} \left(\frac{dU}{dt} \right)_{\text{therm.}} dt \end{aligned} \quad (7.15)$$

where:

$$\left(\frac{dU}{dt} \right)_{\text{inv.}} = -\frac{1}{V} \sum_{\text{NESW}} (\bar{F}_i) \cdot \hat{n} dA + Q_{\text{geom.}} + Q_{\text{rad.}} \quad (7.16)$$

$$\left(\frac{dU}{dt} \right)_{\text{visc.}} = -\frac{1}{V} \sum_{\text{NESW}} (-\bar{F}_v) \cdot \hat{n} dA \quad (7.17)$$

$$\left(\frac{dU}{dt} \right)_{\text{chem.}} = Q_{\text{chem.}} \quad (7.18)$$

$$\left(\frac{dU}{dt} \right)_{\text{therm.}} = Q_{\text{therm.}} \quad (7.19)$$

Temporal integration of the discretised equations proceeds in a *loosely coupled* fashion. The order of operations for a single time-step for a radiating gas in thermochemical nonequilibrium is shown in Figure 7.1. The radiative source term vector, Q_{rad} , is applied closely coupled with the inviscid fluxes. Due to the computational expense of the radiative transport calculation, however, Q_{rad} is not re-evaluated for the corrector step.

The advantage of the operator-splitting approach is that the optimal integration scheme for each component of the physics can be implemented. This is especially useful for solving large chemical kinetic systems. The resultant set of ODE systems are integrated in a time via a simple predictor-corrector method for the inviscid increment, an explicit Euler method for the viscous increment, an α -QSS method for the species production terms of the chemistry increment and a 4th order Runge-Kutta-Fehlberg method for the thermal energy exchange increment. The form of the predictor-corrector method applied to the inviscid increment is:

$$\begin{aligned} \Delta U^{(1)} &= \Delta t \left(\frac{dU^{(n)}}{dt} \right)_{\text{inv.}} \\ U^{(1)} &= U^{(n)} + \Delta U^{(1)} \\ \Delta U^{(2)} &= \Delta t \left(\frac{dU^{(1)}}{dt} \right)_{\text{inv.}} \\ U^{(n+1)} &= U^{(1)} + \frac{1}{2} (\Delta U^{(2)} - \Delta U^{(1)}) \end{aligned} \quad (7.20)$$

where the subscripts (1) and (2) indicate intermediate results and the inviscid temporal derivatives are given in Equations 7.16. The integration of the chemical kinetic and thermal energy exchange source terms are described in § 7.3 and 7.4. To maintain stability when applying the inviscid and viscous updates, a CFL number of 0.5 is enforced when selecting size of the time step.

1. compute gas transport due to inviscid flux:
 - (a) apply inviscid boundary conditions or exchange data at boundaries for each block as appropriate
 - (b) reconstruct the flow field state on both sides of each interface
 - (c) compute the inviscid fluxes $\bar{F}_i \cdot \hat{n}$
 - (d) compute the radiative source term $-\nabla \cdot q_{rad}$ for each cell
 - (e) integrate Eq. 7.16 over the timestep
 - (f) decode the conserved quantities and update the gas-state
 - (g) repeat for corrector update
2. compute gas transport due to viscous flux:
 - (a) apply viscous boundary conditions at solid walls
 - (b) compute the viscous fluxes as $\bar{F}_v \cdot \hat{n}$
 - (c) integrate Eq. 7.17 over the timestep
 - (d) decode the conserved quantities and update the gas-state
3. compute change of gas state due to chemical reactions:
 - (a) compute all chemical source terms
 - (b) integrate Eq. 7.18 over the timestep
 - (c) decode the conserved quantities and update the gas-state
 - (d) redo via smaller subcycles if failed and apply call to equation-of-state more frequently
4. compute change of gas state due to thermal energy exchange:
 - (a) compute all chemical source terms
 - (b) integrate Eq. 7.19 over the timestep
 - (c) decode the conserved quantities and update the gas-state
 - (d) redo via smaller subcycles if failed and apply call to equation-of-state more frequently

Figure 7.1: Sequence of operations for a time-step update in Eilmer3.

7.2.2 Inviscid flux

The flow-state at the cell interfaces are reconstructed using a piecewise-parabolic scheme and then the interface fluxes can then be calculated via an appropriate flux-calculator. The reconstruction scheme has third-order truncation errors and with the van Albada limiter [197] applied, a sine function is reconstructed with an effective truncation error order of 2.7. Typically, reconstruction is done for density, internal energy, velocity components, and species mass fractions. Other flow quantities that are needed at the interfaces for the inviscid flux calculation are then obtained from the thermochemical model.

An appropriate flux-calculator for a given cell is selected in an adaptive fashion via a simple shock detection algorithm. Specifically, we indicate a strong compression at cell-interface $i + \frac{1}{2}$ when:

$$\frac{u_{n,i+1} - u_{n,i}}{\min(a_{i+1}, a_i)} < \text{Tol} \quad (7.21)$$

where Tol is the compression tolerance and is typically set at -0.05. If a cell-interface is identified as having a strong compression (*i.e.* in the vicinity of a shock), the equilibrium flux method (EFM) [198] is used to calculate the inviscid flux for all interfaces attached to the cell. The EFM calculator is a dissipative scheme and assumes that the gas is in equilibrium and the molecular velocities of the gas either side of the interface can be described with the Boltzmann distribution. If a strong compression is not indicated (*i.e.* the majority of the flowfield away from shocks), the inviscid fluxes are computed with the AUSMDV [199] scheme because of its reasonably low dissipation.

7.2.3 Viscous flux

Following the inviscid increment, the viscous flux calculation is then performed based on the updated cell-centre flow state. The spatial derivates required in the viscous stress and heat flux terms, Eq. 7.6 and 7.7, are obtained by applying the divergence theorem to each of the secondary cells surrounding a primary-cell vertex and then averaging the vertex derivatives to obtain a cell centre value. Secondary cells of half size are used along the boundaries and viscous boundary conditions for velocity (*e.g.* no slip) and temperature are applied at those boundary interfaces. The viscous effects are able to be added to the solution in an incremental fashion to aid stability; for example, the applied viscosity μ_i^* at time step i is:

$$\mu_i^* = \mu_i \frac{i}{N_{\text{incr}}} \quad (7.22)$$

where N_{incr} is a factor controlling the rate of addition of viscous effects. This factor is also applied to the modal thermal conductivities and the binary diffusion coefficients. In the present work N_{incr} is typically set to 1×10^4 and a CFL number of 0.25 is used when $i/N_{\text{incr}} < 1$.

7.2.4 Boundary conditions

As the inviscid and viscous increments are separated, so must the respective boundary conditions for each. Inviscid boundary conditions are applied by setting the flow-state in the ghost cells such that a particular flux condition will be generated at the interface. For example, a slip wall boundary condition is applied by copying the gas state from the CFD cell to the ghost cell and reflecting the normal velocity, Figure 7.2. It should be noted that the separation of inviscid and viscous increments requires that all solid surfaces in Eilmer3 apply the slip wall boundary condition for the inviscid increment.

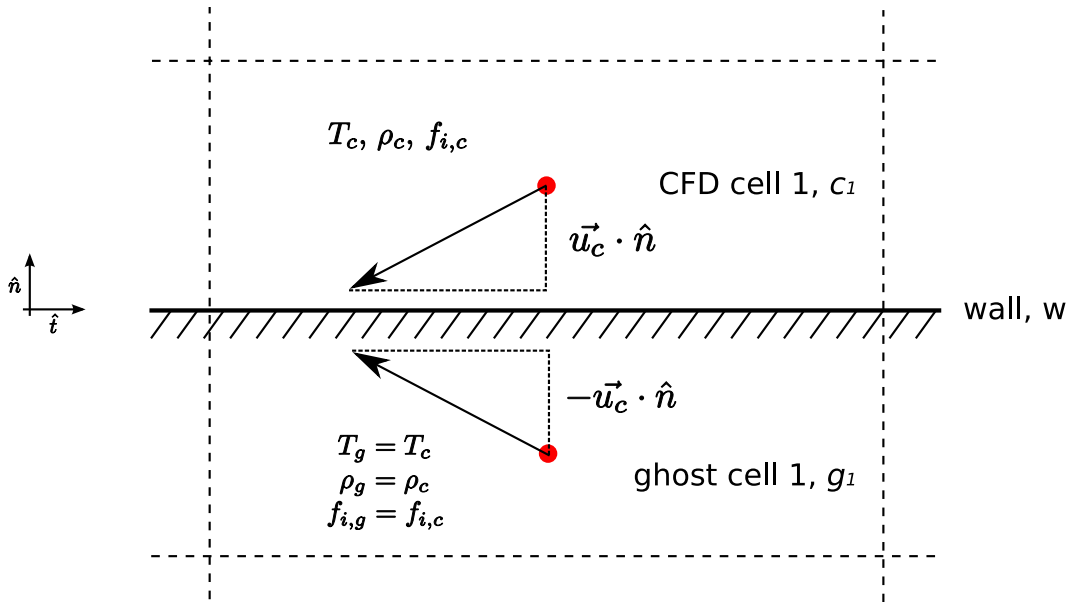


Figure 7.2: Application of the slip wall boundary condition where the reflected normal component of velocity is applied to the ghost cells.

In contrast, viscous boundary conditions are applied by directly setting the interface conditions. For example, a no-slip boundary condition is applied by setting the tangential velocity at the wall interface to zero. The boundary conditions applied to temperatures and chemical species at solid surfaces are of particular importance for calculating the surface heat-flux of aeroshell or subscale model forebodies. Surface catalyticity is able to be modelled as either (1) non-catalytic, or (2) super-catalytic. A non-catalytic boundary simply applies the chemical composition in the adjacent cell to the wall interface, while a super-catalytic boundary applies the freestream chemical composition to the wall interface. While ideally the catalytic surface would be modelled by considering the reaction kinetics due to the presence of the solid surface, these two simplified cases are easy to apply and bound the possible solution space for surface catalyticity.

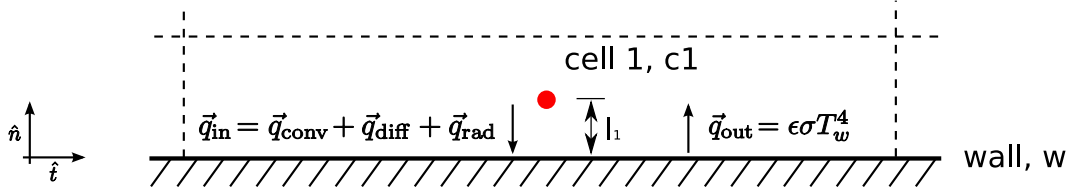


Figure 7.3: Schematic of CFD geometry at wall surface for surface energy balance boundary condition.

Both fixed and variable temperature boundary conditions are able to be applied to solid surfaces. The fixed temperature boundary condition is simply applied by fixing the temperature of the wall interface to certain value. The variable temperature boundary condition allows the wall

temperature to dynamically vary in response to the transient heating environment by considering a surface energy balance at the wall interface, Figure 7.3. The surface energy balance imposes the condition that the normal components of the various heating and cooling mechanisms at the surface must sum to zero:

$$\vec{q}_{\text{in}} \cdot \hat{n} + \vec{q}_{\text{out}} \cdot \hat{n} = 0 \quad (7.23)$$

where \vec{q} are the energy flux vectors and \hat{n} is the outward-facing wall normal unit vector. The incident heat energy flux is comprised of contributions from convection, diffusion and radiation:

$$\vec{q}_{\text{in}} \cdot \hat{n} = \vec{q}_{\text{conv.}} \cdot \hat{n} + \vec{q}_{\text{diff.}} \cdot \hat{n} + \vec{q}_{\text{rad.}} \cdot \hat{n}, \quad (7.24)$$

where:

$$\vec{q}_{\text{conv.}} \cdot \hat{n} = -K_{\text{tr},w} \left(\frac{T_{\text{tr},c_1} - T_w}{l_1} \right) - K_{\text{ve},w} \left(\frac{T_{\text{ve},c_1} - T_w}{l_1} \right) \quad (7.25)$$

$$\vec{q}_{\text{diff.}} \cdot \hat{n} = - \sum_s^{N_{\text{species}}} J_{s,w} h_{s,w} \quad (7.26)$$

and $\vec{q}_{\text{rad.}} \cdot \hat{n}$ is calculated by the radiative transport algorithm (see Section 7.5). A simple form of the surface energy balance is to consider radiative equilibrium at the surface; that is, all or some fraction of the incident heat is re-radiated out by the hot surface. The heat re-radiated by the hot wall at temperature T_w with emissivity ϵ , assuming a ‘black body’, is given by the Stefan–Boltzmann law:

$$\vec{q}_{\text{out}} \cdot \hat{n} = \epsilon \sigma T_w^4 \quad (7.27)$$

Rearranging to solve for T_w and substituting Equations 7.23 and 7.24 into Equation 7.27 gives:

$$T_w = \left(\frac{\vec{q}_{\text{out}} \cdot \hat{n}}{\epsilon \sigma} \right)^{1/4} = \left(\frac{-\vec{q}_{\text{in}} \cdot \hat{n}}{\epsilon \sigma} \right)^{1/4} = \left(\frac{-\vec{q}_{\text{conv.}} \cdot \hat{n} - \vec{q}_{\text{diff.}} \cdot \hat{n} - \vec{q}_{\text{rad.}} \cdot \hat{n}}{\epsilon \sigma} \right)^{1/4} \quad (7.28)$$

As the incident heat flux is dependent on the wall temperature, the radiative equilibrium wall temperature is calculated via an iterative procedure:

$$T_w^{(n)} = \left(\frac{-\vec{q}_{\text{conv.}}(T_w^{(n-1)}) \cdot \hat{n} - \vec{q}_{\text{diff.}}(T_w^{(n-1)}) \cdot \hat{n} - \vec{q}_{\text{rad.}}(T_w^{(0)}) \cdot \hat{n}}{\epsilon \sigma} \right)^{1/4} \quad (7.29)$$

$$T_w^{(n+1)} = f_{\text{relax}} T_w^{(n)} + (1 - f_{\text{relax}}) T_w^{(n-1)} \quad (7.30)$$

where f_{relax} is conservatively set to 0.05 and the test for convergence is:

$$\frac{\left| \vec{q}_{\text{in}}(T_w^{(n)}).\hat{n} - \vec{q}_{\text{in}}(T_w^{(n-1)}).\hat{n} \right|}{\vec{q}_{\text{in}}(T_w^{(n)}).\hat{n}} \leq 10^{-4} \quad (7.31)$$

The radiative heat flux, however, is not re-evaluated at the new wall temperature in Equation 7.29 due to the computational expense and the weak dependence of $\vec{q}_{\text{rad}.}\hat{n}$ on T_w for the flat to convex surfaces of present interest.

7.3 Chemical kinetics

As discussed in Section 7.2.1, the source terms relating to non-equilibrium chemical kinetics in Eilmer3 are decoupled from all other physical processes (*i.e.* inviscid and viscous gas-dynamics and thermal energy exchange). Thus when the chemical kinetic increment is applied to an individual cell, the conserved variables of total mass, momentum and energy are held constant. From Equation 7.15, the integral equation to solved when applying the chemical kinetic increment is:

$$\int_{\Delta t} \left(\frac{dU}{dt} \right)_{\text{chem.}} dt = \int_{\Delta t} Q_{\text{chem.}} dt \quad (7.32)$$

Substituting in the definitions for the vector of conserved quantities U and the chemical kinetic source term vector $Q_{\text{chem.}}$ defined in Equations 7.2 and 7.11 respectively gives:

$$\int_{\Delta t} \begin{bmatrix} \dot{\rho} \\ \rho \dot{u}_x \\ \rho \dot{u}_y \\ \rho \dot{E} \\ \rho \dot{e}_{\text{ve}} \\ \rho \dot{f}_s \end{bmatrix}_{\text{chem.}} dt = \int_{\Delta t} \begin{bmatrix} 0 \\ 0 \\ 0 \\ 0 \\ \sum_m^{N_{\text{mol}}} \Omega_m^{\text{VC}} + \sum_i^{N_{\text{ion}}} \Omega_i^{\text{EC}} \\ M_s \dot{\omega}_s \end{bmatrix} dt \quad (7.33)$$

where Ω_m^{VC} is the rate-of-change in vibrational energy of molecule m due to chemical reactions, Ω_i^{EC} is the rate-of-change in free electron energy due to chemical reactions involving ion i and $\dot{\omega}_s$ is the molar production rate of species s due to chemical reactions.

The strategy for solving Equation 7.33 in the present work is that proposed by Gollan [1] in § 4.2.3. The species production rate source terms $M_s \dot{\omega}_s$ are applied via an α -QSS integration scheme under a mass-conserved formulation of the ODE system, whilst the vibroelectronic source terms due to chemical reactions $\sum_m^{N_{\text{mol}}} \Omega_m^{\text{VC}} + \sum_i^{N_{\text{ion}}} \Omega_i^{\text{EC}}$ are applied via an explicit Euler integration step. Therefore in the present implementation the chemical kinetic increment is decoupled into two distinct stages:

$$\int_{\Delta t} \begin{bmatrix} \dot{\rho} \\ \rho \dot{u}_x \\ \rho \dot{u}_y \\ \dot{\rho} E \\ \rho \dot{e}_{ve} \\ \rho \dot{f}_s \end{bmatrix}_{\text{chem.}} dt = \int_{\Delta t} \begin{bmatrix} 0 \\ 0 \\ 0 \\ 0 \\ 0 \\ M_s \omega_s \end{bmatrix} dt + \int_{\Delta t} \begin{bmatrix} 0 \\ 0 \\ 0 \\ 0 \\ \sum_m^{N_{\text{mol}}} \Omega_m^{VC} + \sum_i^{N_{\text{ion}}} \Omega_i^{EC} \\ 0 \end{bmatrix} dt \quad (7.34)$$

The ODE system for applying the species production source term is then reformulated to be in terms of the species concentrations $[X_s]$:

$$\int_{\Delta t} \frac{d [X_s]}{dt} = \int_{\Delta t} \omega_s \quad (7.35)$$

where the species density is related to the species concentration by:

$$\rho f_s = M_s [X_s] \quad (7.36)$$

As the bulk gas density is assumed constant during the chemical kinetic increment, the ODE for applying the chemistry-energy coupling terms is reformulated to be in terms of the vibroelectronic energy per mixture mass:

$$\int_{\Delta t} \frac{de_{ve}}{dt} = \int_{\Delta t} \left(\sum_m^{N_{\text{mol}}} \frac{\Omega_m^{VC}}{\rho} + \sum_i^{N_{\text{ion}}} \frac{\Omega_i^{EC}}{\rho} \right) \quad (7.37)$$

Finally, the pressures and temperatures for each cell are then updated by an equation-of-state evaluation.

7.4 Thermal energy exchange

Similarly as for the chemical kinetic increment, the source terms relating to thermal energy exchange are decoupled from all other physical processes and the conserved variables of total mass, momentum and energy are held constant. From Equation 7.15, the integral equation to solved when applying the thermal energy exchange increment is:

$$\int_{\Delta t} \left(\frac{dU}{dt} \right)_{\text{therm.}} dt = \int_{\Delta t} Q_{\text{therm.}} dt \quad (7.38)$$

Substituting in the definitions for the vector of conserved quantities U and the thermal energy exchange source term vector $Q_{\text{therm.}}$ defined in Equations 7.2 and 7.12 respectively gives:

$$\int_{\Delta t} \begin{bmatrix} \dot{\rho} \\ \rho \dot{u}_x \\ \rho \dot{u}_y \\ \rho \dot{E} \\ \rho \dot{e}_{ve} \\ \rho \dot{f}_s \end{bmatrix}_{\text{therm.}} dt = \int_{\Delta t} \begin{bmatrix} 0 \\ 0 \\ 0 \\ 0 \\ \sum_m^{N_{\text{mol}}} \Omega_m^{VT} + \sum_s^{N_{\text{species}}} \Omega_s^{ET} \\ 0 \end{bmatrix} dt \quad (7.39)$$

where Ω_m^{VT} is the vibration-translation energy exchange source term for molecule m and Ω_s^{ET} is the electron-translation energy exchange source term for species s .

As the conserved mass is assumed to be constant over the increment, the ODE system is reformulated to be in terms of the vibroelectronic energy per unit of mixture mass:

$$\int_{\Delta t} \frac{de_{ve}}{dt} = \int_{\Delta t} \left(\sum_m^{N_{\text{mol}}} \frac{\Omega_m^{VT}}{\rho} + \sum_s^{N_{\text{species}}} \frac{\Omega_s^{ET}}{\rho} \right) \quad (7.40)$$

This equation is then integrated in time over the time-step Δt via a fourth order Runge-Kutta-Fehlberg algorithm, and the pressures and temperatures for each cell are updated by an equation-of-state evaluation.

7.5 Radiation transport

The radiation source term in the Navier-Stokes equations (see Equations 2.13 and 7.13) is the negative divergence of the local radiative heat flux vector:

$$-\nabla \cdot \vec{q}_{\text{rad}} = -\nabla \cdot \int_0^\infty \vec{I}_\nu d\nu \quad (7.41)$$

For application to computational grids it is convenient to express Equation 7.41 as the difference between the local emission and absorption:

$$-\nabla \cdot \vec{q}_{\text{rad}} = \int_0^\infty \int_{4\pi} \kappa_\nu I_\nu d\omega d\nu - 4\pi \int_0^\infty j_\nu d\nu \quad (7.42)$$

A variety of models are implemented in Eilmer3 to solve for the radiative source term:

1. Optically-thin model
2. Tangent-slab model
3. Ray-tracing model

Descriptions of these of models are provided in § 7.5.2 to 7.5.4 respectively. Firstly, however, the flowfield coupling methodology is outlined in the following section.

7.5.1 Flowfield coupling

A useful parameter for estimating the degree of radiation-flowfield coupling is the Goulard number [200]:

$$\Gamma = \frac{2q_{\text{rad}}}{\frac{1}{2}\rho_{\infty}u_{\infty}^3} \quad (7.43)$$

where q_{rad} is the radiative heat flux incident at the stagnation point, ρ_{∞} the freestream density and u_{∞} the freestream velocity. The Goulard number is a measure of the conversion of energy flux in the freestream to radiative energy flux incident on the vehicle. When the Goulard number becomes large ($\Gamma > 0.01$) radiation-flowfield coupling should be taken into consideration due to significant levels of radiative flux through the shock layer.

As the radiation transport procedure is computationally expensive, it is desirable to update the radiation source terms at a reasonably low frequency (*i.e.* a *loosely* coupled approach). When a radiation transport calculation at time-step n is performed, ρ , T_e and $\nabla \cdot \vec{q}_{\text{rad}}$ for each cell are stored. For each of the subsequent flowfield time-steps m where a complete radiation transport calculation is not performed the radiative divergence is rescaled to account for variations in the gas-state:

$$(-\nabla \cdot \vec{q}_{\text{rad}})_m = \begin{cases} \frac{(\rho T_e^4)_m}{(\rho T_e^4)_n} (-\nabla \cdot \vec{q}_{\text{rad}})_n & \text{for } (-\nabla \cdot \vec{q}_{\text{rad}})_n > 0 \\ \frac{(\rho T_e^{-4})_m}{(\rho T_e^{-4})_n} (-\nabla \cdot \vec{q}_{\text{rad}})_n & \text{for } (-\nabla \cdot \vec{q}_{\text{rad}})_n < 0 \end{cases} \quad (7.44)$$

The frequency of the radiation update is dependent on the transient behavior of the flowfield; for example, during the initial period of flow development the update frequency needs to be high to account for shifting shock positions, while as the solution approaches steady state the update frequency can be substantially reduced.

7.5.2 Optically-thin model

The optically-thin model neglects reabsorption, reducing Eq. 7.42 to:

$$-\nabla \cdot \vec{q}_{\text{rad}} = -4\pi \int_0^{\infty} j_{\nu} d\nu \quad (7.45)$$

For the radiating shock layers of present interest, the majority of the radiative emission is in the vacuum-ultraviolet spectral region where reabsorption is significant. The optically-thin model will therefore substantially overestimate the radiative divergence, and is not an appropriate model for the work at hand.

7.5.3 Tangent-slab model

The tangent-slab model allows the effect of reabsorption to be modelled while avoiding a complete directional integration of the local intensity field. A one-dimensional variation of properties is considered along each line-of-sight normal to the vehicle surface. Computationally, a line of cells is used to represent the normal line-of-sight as demonstrated in Figure 7.4. This is a good approximation to the body normal direction for the shock-aligned grids implemented in the present work. If a single column of blocks is used to define the computational domain-between the inflow and vehicle surface boundaries, the tangent-slab model is inherently parallelisable as all the information required for the calculation is contained in the local block.

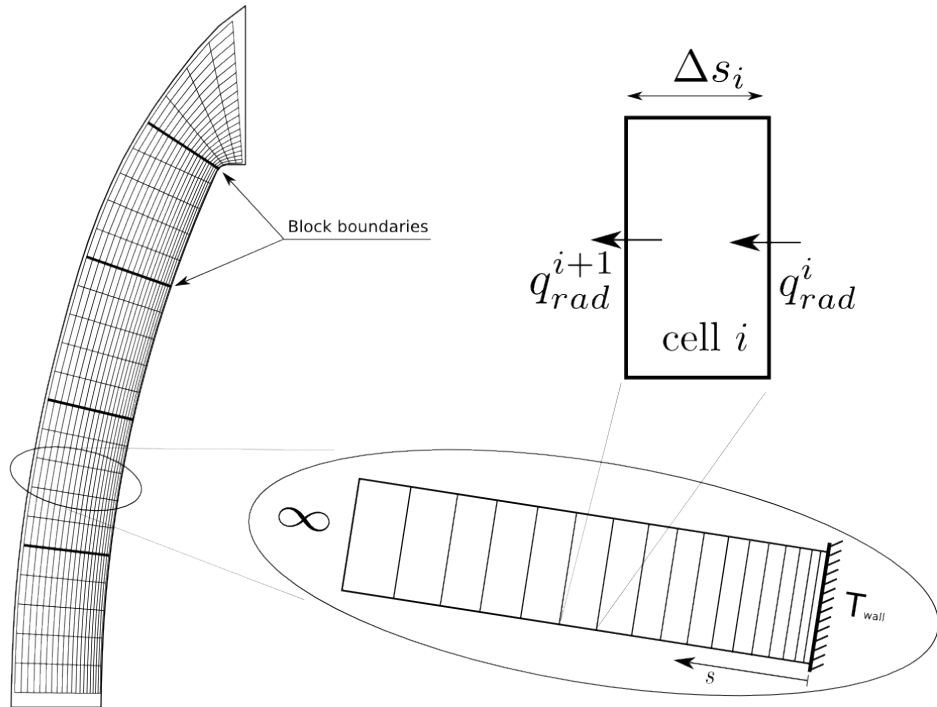


Figure 7.4: Schematic of tangent-slab calculation domain along lines of cells on a multi-block grid.

Given that the infinite-slab arrangement will result in zero net radiative flux in the transverse directions, the definition of the radiative divergence for slab i reduces to:

$$-(\nabla \cdot \vec{q}_{\text{rad}})_i = -\left(\frac{\partial q_{\text{rad}}}{\partial s}\right)_i \approx \frac{-\left(q_{\text{rad}}^{(i+1)} - q_{\text{rad}}^{(i)}\right)}{\Delta s_i} \quad (7.46)$$

where $q_{\text{rad}}^{(i)}$ is the radiative flux at the i^{th} cell interface (*i.e.* preceding the cell from right-to-left) and Δs_i is the width of the cell in the (approximately) body normal direction. The solution for the radiative flux in a gaseous medium between two parallel, infinite-slabs as a function of the

spectral optical thickness τ_ν is derived in the text by Modest [201]. If we consider the computational domain to be a collection of N_{slabs} isothermal slabs with the spectral range discretised into N_ν frequency intervals the radiative flux at interface i can be expressed as:

$$q_{\text{rad}}^{(i)} = \sum_{k=1}^{N_\nu} 2\pi I_{\nu_k, \text{wall}} E_3 \left(\tau_{\nu_k}^{(i)} \right) + 2\pi \sum_{j=1}^{N_{\text{slabs}}} S_{\nu_k}^{(j)} \left[E_3 \left(\left| \tau_{\nu_k}^{(i)} - \tau_{\nu_k}^{(j)} \right| \right) - E_3 \left(\left| \tau_{\nu_k}^{(i)} - \tau_{\nu_k}^{(j-1)} \right| \right) \right] \Delta\nu_k \quad (7.47)$$

where $S_{\nu_k}^{(i)}$ is the source function for the i^{th} isothermal cell at frequency ν_k , $I_{\nu_k, \text{wall}}$ is the intensity emitted by the wall and the optical thickness $\tau_{\nu_k}^{(i)}$ is calculated as:

$$\tau_{\nu_k}^{(i)} = \sum_{l=1}^i \kappa_{\nu_k}^{(l)} \Delta s_l \quad (7.48)$$

The E_n term is the n^{th} order exponential integral with form:

$$E_n(x) = \int_1^\infty \omega^{-n} \exp(-\omega x) d\omega \quad (7.49)$$

The E_3 curve fit derived by Johnston [19] is implemented for the Eilmer3 tangent-slab model:

$$E_3(x) = 0.0929e^{-4.08x} + 0.4071e^{-1.33x} \quad (7.50)$$

The intensity emitted by the wall with emissivity ϵ_{wall} is calculated as [78]:

$$I_{\nu, \text{wall}} = 2\pi \epsilon_{\text{wall}} \sigma T_{\text{wall}}^4 \quad (7.51)$$

where T_{wall} is the blackbody wall temperature.

7.5.4 Ray-Tracing Model

A ray-tracing model combining elements of both Discrete Transfer [72–74] and Monte Carlo [75, 202] radiation transport models has been implemented in the Eilmer3 framework. The basic principle of ray-tracing based models is the direct numerical integration of the radiant energy field over direction and space via the generation of a ‘radiation sub-grid’ mapped over the CFD grid. The radiation sub-grid consists of rays distributed isodirectionally from each point of interest in the flowfield, with the flow state and radiation spectra defined at distributed points along each ray. An example of a radiation sub-grid on a simple axisymmetric CFD grid is illustrated in Figure 7.5. Although the ray-tracing model has been implemented in Eilmer3 for planar, axisymmetric and 3D geometries, only the planar and axisymmetric formulations are described herein.

The Discrete Transfer model proposed by Elbert and Cinella [73] uses the radiation sub-grid to solve directly for the radiative divergence via Eq. 7.42. The modified Discrete Transfer model method proposed by Karl [74] uses the radiation sub-grid to solve for the heat flux vectors

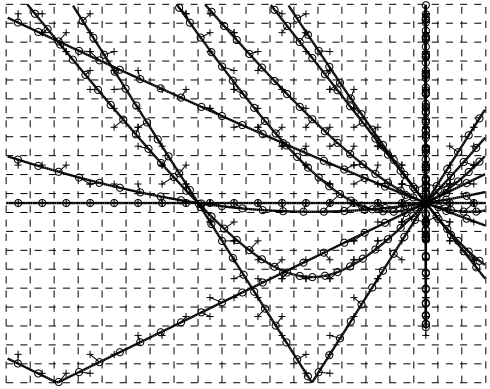


Figure 7.5: Example radiation sub-grid on a simple axisymmetric grid (Reference [74]).

throughout the flowfield, from which the divergence at the cell centres can be calculated. In contrast, the ray-tracing model developed in the present work uses the radiative sub-grid to transport packets of radiant energy through the computational domain. This is similar to a photon Monte-Carlo method in that radiation is treated as a discrete quantity rather than a continuous field, however the ray-distribution is kept uniform and energy attenuation is not modelled in a statistical fashion.

Mathematical formulation

The total radiative divergence for a finite-volume cell is calculated as the difference between the total emissive power $E_{\text{ems.}}$ and absorptive power $E_{\text{abs.}}$ divided by the cell volume V :

$$-\nabla \cdot \vec{q}_{\text{rad}} = \frac{-(E_{\text{ems.}} - E_{\text{abs.}})}{V} \quad (7.52)$$

where:

$$E_{\text{ems.}} = \int_V \int_0^{4\pi} \int_{\nu_{\min}}^{\nu_{\max}} j_\nu d\nu d\omega dV = \sum_r^{N_{\text{ems. rays}}} \sum_n^{N_\nu} E_{r,n} \quad (7.53)$$

$$E_{\text{abs.}} = \sum_r^{N_{\text{abs. rays}}} \sum_n^{N_\nu} (-\Delta E_{r,n}) \quad (7.54)$$

Here $N_{\text{abs. rays}}$ is the total number of ray segments traversing the current cell, $N_{\text{ems. rays}}$ is the total number of rays emitted by this cell and the frequency domain has been divided into N_ν intervals between ν_{\min} and ν_{\max} . $E_{r,n}$ is the power carried by photon packet n with frequency interval $\Delta\nu_n$ from ray r with solid angle $\Delta\omega_r$:

$$E_{r,n} = j_\nu \Delta\nu_n \Delta\omega_r V \quad (7.55)$$

The radiative power lost by photon packet n while traversing from points s_i to s_f along a ray is calculated from Beers law:

$$-\Delta E_{r,n} = -(1 - e^{-\kappa_{vn}(s)} \Delta s) E_{r,n}(s_i) \quad (7.56)$$

where $\Delta s = s_f - s_i$. Similarly, the radiative heat flux incident on wall elements q_{rad} is calculated as the sum of the remaining energy from all incident rays $N_{\text{inc. rays}}$ divided by the wall element area A :

$$q_{\text{rad}} = \frac{E_{\text{abs.}}}{A} = \frac{\sum_r \sum_n^{N_{\text{inc. rays}}} E_{r,n}}{A} \quad (7.57)$$

Ray-tracing and radiation sub-grid

The ray-tracing method for planar and axisymmetric grids of quadrilateral cells described by Elbert and Cinella [73] and Karl [74] is implemented in the present work with slight modifications. The radiation sub-grid coordinates of a point at distance L along a ray with elevation and azimuth angles ϕ and θ originating from position x_0, y_0 are:

$$x' = x_0 + L \cos(\phi) \cos(\theta) \quad (7.58)$$

$$y' = y_0 + L \sin(\phi) \quad (7.59)$$

$$z' = L \cos(\phi) \sin(\theta) \quad (7.60)$$

The corresponding CFD grid coordinates are then calculated from the following transformation:

$$x = x' \quad (7.61)$$

$$y = \sqrt{y'^2 + z'^2} \quad (7.62)$$

This transformation has the effect of reflecting rays intersecting the symmetry axis at $y = 0$, as required (see Figure 7.5). For planar geometries the radiation sub-grid is formed in the x - y plane as the CFD domain is symmetrical along the z axis. For ray i of N_{rays} the elevation and azimuth angles are calculated as:

$$\theta = \begin{cases} 0 & \text{for } 0 \leq \alpha < \pi/2 \\ \pi & \text{for } \pi/2 \leq \alpha < 3\pi/2 \\ 0 & \text{for } 3\pi/2 \leq \alpha < 2\pi \end{cases} \quad (7.63)$$

$$\phi = \begin{cases} \alpha & \text{for } 0 \leq \alpha < \pi/2 \\ \pi - \alpha & \text{for } \pi/2 \leq \alpha < 3\pi/2 \\ \alpha - \pi/2 & \text{for } 3\pi/2 \leq \alpha < 2\pi \end{cases} \quad (7.64)$$

where $\alpha = i \frac{2\pi}{N_{\text{rays}}}$. For axisymmetric geometries the radiation sub-grid must be formed in three-dimensions as the CFD domain is radially symmetrical about $y = 0$. Elbert and Cinella [73] and Karl [74] use the symmetric vertices of the icosahedron platonic solid to generate the axisymmetric elevation and azimuth angles. This approach, however, limits the total number of rays to a set of fixed values as the 20 icosahedron faces must be subdivided equally to achieve approximate uniformity. To allow for an arbitrary number of axisymmetric rays, the so-called ‘Golden Section Spiral’ method [203] of generating uniform points on a sphere has been implemented. As illustrated in Figure 7.6, this method arranges nodes on the surface of a unit sphere by considering spirals with successive longitudes chosen according to the golden ratio $\frac{\sqrt{5}-1}{2}$.

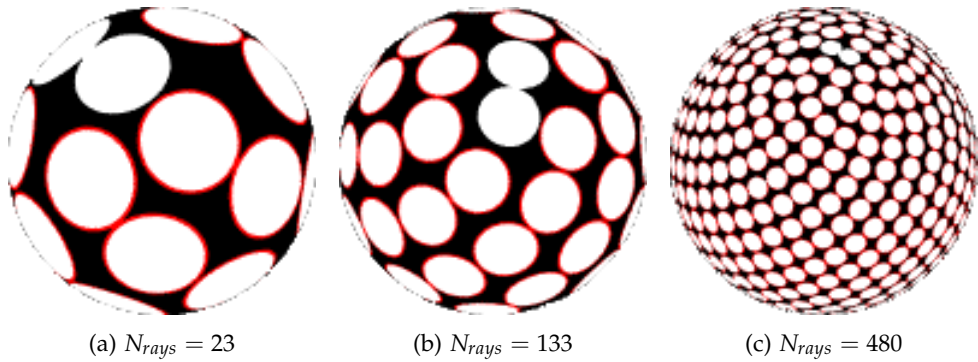


Figure 7.6: Approximately uniform points on a sphere generated via the ‘Golden Section Spiral’ method [203].

The unit sphere coordinates of ray i of N_{rays} are calculated as:

$$x^* = r \cos(\alpha) \quad (7.65)$$

$$y^* = w \quad (7.66)$$

$$z^* = r \sin(\alpha) \quad (7.67)$$

where:

$$w = i \frac{2}{N_{\text{rays}}} - 1 + N_{\text{rays}} \quad (7.68)$$

$$r = \sqrt{1 - w^2} \quad (7.69)$$

$$\alpha = i\pi(3 - \sqrt{5}) \quad (7.70)$$

The elevation and azimuth angles are then calculated as:

$$\phi = \arcsin(y^*) \quad (7.71)$$

$$\theta = \begin{cases} \arctan\left(\frac{z^*}{x^*}\right) & \text{for } x^* > 0 \text{ and } z^* > 0 \\ \pi/2 & \text{for } x^* = 0 \text{ and } z^* > 0 \\ \pi - \arctan\left(\frac{z^*}{-x^*}\right) & \text{for } x^* < 0 \text{ and } z^* > 0 \\ \pi & \text{for } x^* < 0 \text{ and } z^* = 0 \\ \pi + \arctan\left(\frac{-z^*}{x^*}\right) & \text{for } x^* < 0 \text{ and } z^* < 0 \\ 3\pi/2 & \text{for } x^* = 0 \text{ and } z^* < 0 \\ 2\pi - \arctan\left(\frac{-z^*}{x^*}\right) & \text{for } x^* > 0 \text{ and } z^* < 0 \\ 0 & \text{for } x^* > 0 \text{ and } z^* = 0 \end{cases} \quad (7.72)$$

The angular distribution of the rays for this method is not as uniform as that for the subdivided icosahedron approach, however the ray number flexibility is a distinct advantage.

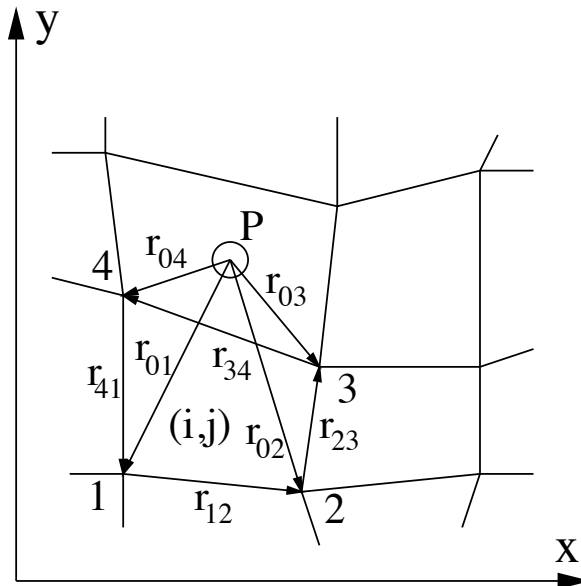


Figure 7.7: Mapping of the radiation sub-grid onto the CFD grid, Reference [74].

The core of the ray-tracing method is a cell searching algorithm that allows the radiation sub-grid to be mapped onto the CFD grid, Figure 7.7. For a given trial cell with indices i and j the following cross-products are evaluated:

$$a_{12} \cdot \vec{n} = \vec{r}_{01} \times \vec{r}_{12} \quad (7.73)$$

$$a_{23} \cdot \vec{n} = \vec{r}_{02} \times \vec{r}_{23} \quad (7.74)$$

$$a_{34} \cdot \vec{n} = \vec{r}_{03} \times \vec{r}_{34} \quad (7.75)$$

$$a_{41} \cdot \vec{n} = \vec{r}_{04} \times \vec{r}_{41} \quad (7.76)$$

where \vec{n} is the unit vector normal to the x-y plane. If all four cross-products are positive the point p is inside the trial cell. Otherwise, the indices of the next trial cell are obtained according to:

$$\text{if } (a_{23} < 0 \text{ and } a_{41} > 0) \text{ then } i = i + 1 \quad (7.77)$$

$$\text{if } (a_{23} > 0 \text{ and } a_{41} < 0) \text{ then } i = i - 1 \quad (7.78)$$

$$\text{if } (a_{12} < 0 \text{ and } a_{34} > 0) \text{ then } j = j + 1 \quad (7.79)$$

$$\text{if } (a_{12} > 0 \text{ and } a_{34} < 0) \text{ then } j = j - 1 \quad (7.80)$$

As the mapping of the radiation sub-grid is performed successively for each point along a ray, a good initial guess is always available and the above method is highly efficient.

Solution procedure

The procedure for calculating the radiative divergence at the centers of all cells in Eilmer3 is as described in Figure 7.8. Note that the frequency range is able to be divided up into multiple blocks, allowing the total memory requirement for the calculation to be reduced. This is necessary when the CFD and spectral grids are very fine.

1. Perform geometric ray-tracing to define the radiation sub-grid
2. Calculate emission and absorption spectra for each cell and wall element
3. Trace each energy packet through the grid
 - (a) Subtract emitted energy from origin cell
 - (b) Add absorbed energy to each traversed cell
 - (c) Record exiting energy on wall elements
4. Evaluate $-\nabla \cdot \vec{q}_{\text{rad}}$ for each cell and q_{rad} for each wall element from the results
5. Repeat steps 2 - 4 for each frequency block

Figure 7.8: Sequence of operations for calculating the radiative divergence at the centers of all cells in Eilmer3.

Initially the ray-tracing radiation transport calculation was parallelised via geometric domain decomposition in order to allow the radiation calculation to be performed inside the OpenMPI Eilmer3 executable [204]. This approach, however, requires excessive block-to-block communication and memory in order to transfer the spectral information of rays traversing block boundaries. In the present implementation, the ray-tracing radiation transport calculation is instead parallelised via OpenMP where each processor has access to all data describing the computational

domain. The OpenMP implementation is considerably more efficient than the OpenMPI implementation and requires significantly less memory. For the OpenMP implementation, the radiation transport problem is divided amongst the available processors on a cell-by-cell basis when computing spectra, and a ray-by-ray basis when tracing and integrating along lines-of-sight. The advantage of this parallelisation strategy over the standard block-by-block approach is that an arbitrary number of cells per block and rays per cell can be efficiently parallelised.

Verification and validation

It is necessary at this point to verify the implementation and validate the theory of the ray-tracing radiation transport model. For this purpose, the infinite-cylinder test case proposed by Karl [74] is considered. This test case is performed at four different grid and ray resolutions and with 1, 2 and 4 CPU cores to test the convergence and parallelisability of the method.

The computational domain for the planar and axisymmetric test cases is shown in Figure 7.9. The present implementation of the ray-tracing algorithm only permits reflective boundary conditions along the $y = 0$ line; the east and west boundaries are therefore considered to be walls, rather than symmetry boundaries. As will be demonstrated, however, the aspect ratio of 10:1 is sufficient to permit the infinite-slab and infinite-cylinder approximations at the slab mid-section ($x = 5$ m). Grid resolutions of 8×8 , 16×16 , 32×32 and 64×64 uniformly spaced cells are considered, with the number of rays set to 8, 16, 32 and 64 for the planar case and 32, 64, 128 and 256 rays for the axisymmetric case¹. For the planar test case a temperature gradient is applied from $T_i = 0$ K at $y = 0$ m to $T_f = 10,000$ K at $y = 1$ m, while for the axisymmetric test case the temperature is constant at 10,000 K. A ‘grey-gas’ is assumed with a constant absorption coefficient of $\kappa = 1.0 \text{ m}^{-1}$, making the total emissive power density:

$$J = \frac{\kappa\sigma T^4}{\pi} \quad (7.81)$$

¹More rays are required for axisymmetric geometries compared with planar geometries to achieve similar accuracy as the radiation sub-grid must be formed in three dimensions rather than just two.

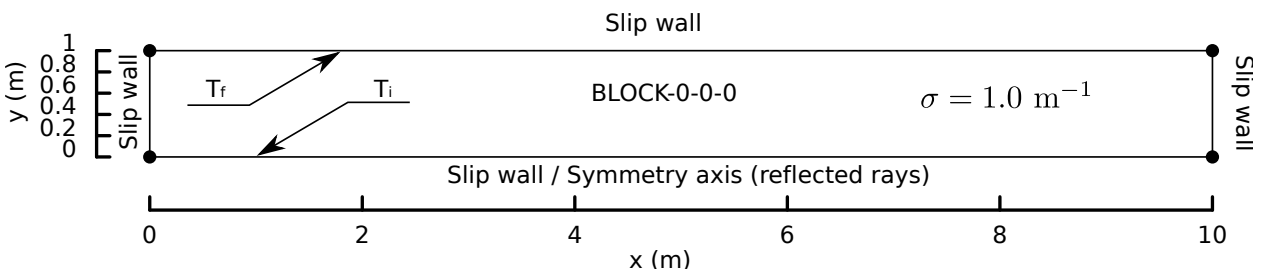


Figure 7.9: Single-block computational domains for the infinite-slab and infinite-cylinder test cases (not-to-scale).

Although the radiation from a grey-gas can be described without considering spectral distributions, for this test case this is desirable so as to maintain similarity with the non-Planck spectra the model is designed to be applied to. The spectral emission and absorption coefficients are then calculated as:

$$j_\nu = \kappa B_\nu(T) \quad (7.82)$$

$$\kappa_\nu = \kappa \quad (7.83)$$

where $B_\nu(T)$ is the Planck function:

$$B_\nu(T) = \frac{2h}{c^3} \frac{\nu^3}{e^{\frac{h\nu}{kT}} - 1} \quad (7.84)$$

The spectral range considered is 10 to 3000 nm, and is discretised with 500 intervals. Integrating the Planck function with this discretisation matches the Stephan-Maxwell equation to within 0.1%. The exact solution for the planar test case is obtained from the tangent-slab approximation presented in Equations 7.46 to 7.51, and the exact solution for the axisymmetric test case is obtained from the analytical expressions presented by Sakai *et al.* [205].

Planar infinite-slab test case Before analysing the radiative diverge fields, it is useful to consider the heat flux profiles to verify the tangent-slab approximation. Figure 7.10 presents the heat-flux profiles along the top edge of the planar infinite-slab from the 8×8 grid with 8 rays, the 16×16 grid with 16 rays and the 32×32 grid with 32 rays. The heat flux profiles for the ray-tracing calculations are approximately uniform for $3 \leq x \leq 7$, and the heat flux at $x=5$ m converges to the tangent-slab approximation with increasing resolution. The test case is therefore well described by the tangent-slab approximation for the mid-point cross section at $x = 5$ m.

Figure 7.11 presents the radiative divergence results for the planar infinite-slab test case; comparisons of radiative divergence are shown in the left column, and the resulting errors compared with the tangent-slab solution are shown in the right column. The profiles are taken from the mid-point cross section where $x = 5$ m. In all plots the optical thickness τ_y is used as the spatial coordinate, defined as:

$$\tau_y = \int_0^y \kappa_y dy \quad (7.85)$$

A complete summary of the planar infinite-slab results is presented in Table 7.1. The quoted error in $\nabla \cdot \vec{q}_{\text{rad}}$ is the average of the absolute percentage difference along the $x = 5$ m profile referenced to the tangent-slab solution, and the quoted error in q_{rad} is the percentage difference from the tangent-slab solution at $x = 5$ m and $y = 1$ m. All simulations were run using the serial version of the code on a single core of a Linux workstation with two Intel Dual Core Xeon Pro 5130 CPU's (4MB cache, 2.00GHz, 1333MHz FSB).

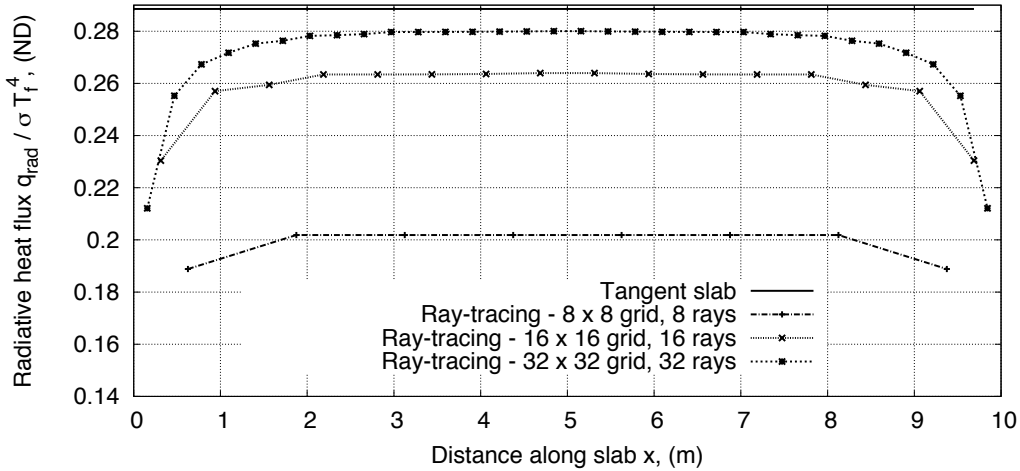


Figure 7.10: Comparison of heat-flux profiles along the top edge of the planar infinite-slab.

Table 7.1: Tabulated results for the planar infinite-slab radiation transport test case.

Grid Resolution (N _{cells,x} × N _{cells,y})	Ray resolution N _{rays}	Memory (MB)	Wall time (s)	Av. ∇ · q̃ _{rad} Error (%)	q _{rad} Error (%)
8 × 8	8	-	0.46	25.63	-28.07
	16	-	0.48	5.17	-4.51
	32	-	0.79	5.24	1.19
16 × 16	8	70	1.46	27.90	-28.75
	16	76	2.37	5.35	-5.95
	32	89	4.36	1.86	0.67
32 × 32	8	129	9.95	29.34	-29.58
	16	168	16.66	6.70	-7.18
	32	254	31.69	0.87	-0.23

In general, the results demonstrate the ray-tracing radiation transport model converges towards the exact solution with increasing grid and ray resolution for planar geometries. An exception is the 8 × 8 cell grid with 32 rays, where the average error in $\nabla \cdot \tilde{q}_{\text{rad}}$ increases from 5.17% for the 16 ray case to 5.24%. This anomaly can be attributed to the coarse grid resolution providing an inadequate description of the temperature gradient, resulting in convergence towards a solution with significant error. For the 16 × 16 and 32 × 32 grid cases, the error in both $\nabla \cdot \tilde{q}_{\text{rad}}$ and q_{rad} reduces in magnitude approximately in proportion to the number of rays squared. From Figure 7.11, the ray-traced solutions are observed to be most accurate close to the symmetry boundary at $\tau_y = 0$ and least accurate at the outer boundary where $\tau_y = 1$. This is due to the linear temperature gradient that has a maximum at $\tau_y = 1$; as τ_y increases, the total emission increases due to the higher temperature, and thus the absolute error is able to increase. Overall the ray-tracing model performs very well for the planar test case.

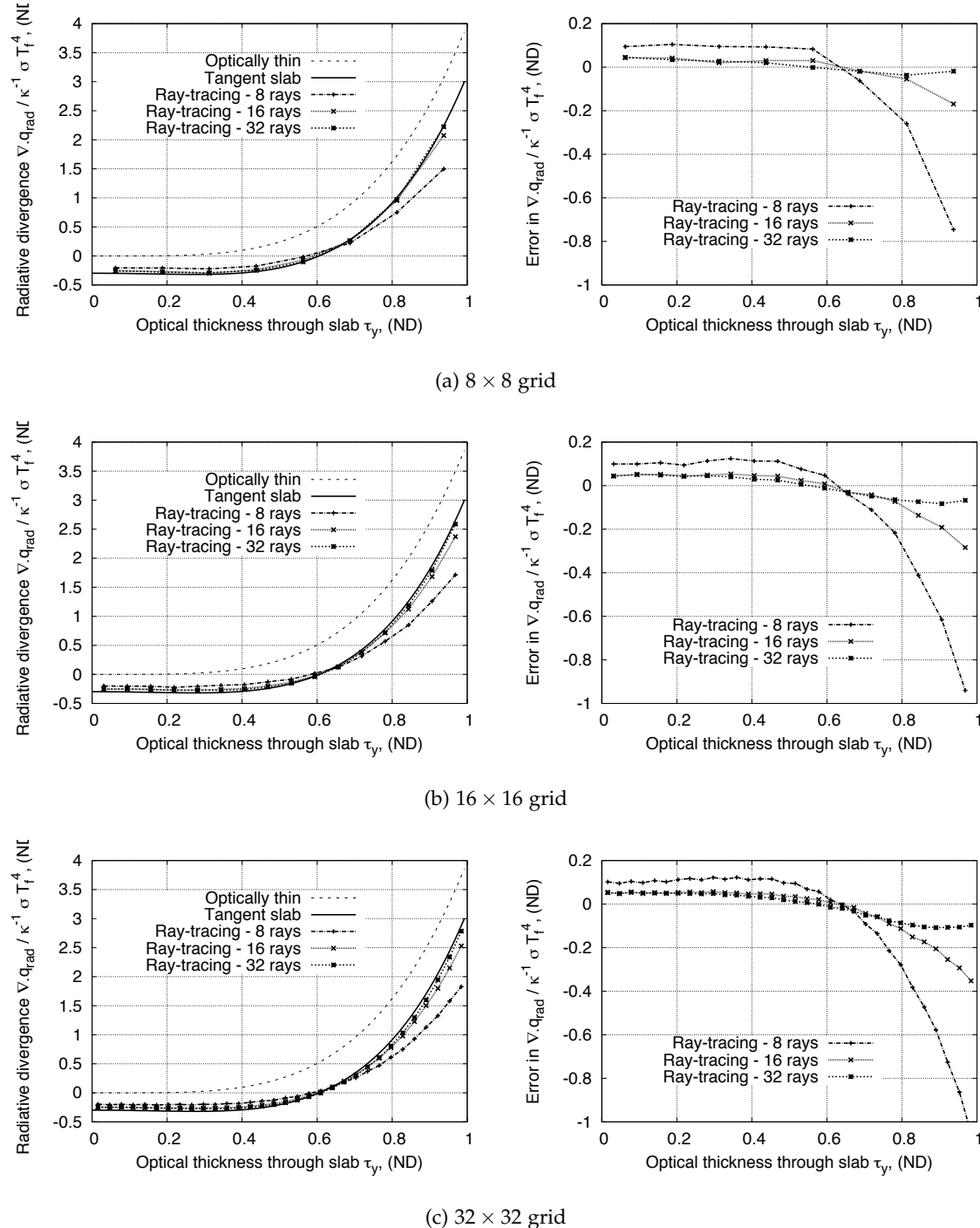


Figure 7.11: Comparison of radiative divergence solution and error profiles at $x = 5$ m for the planar infinite-slab radiation transport test case. The spatial coordinate is the optical thickness as defined in Equation 7.85.

Axisymmetric infinite-cylinder test case Figure 7.12 presents the heat-flux profiles along the outer surface ($y = 1$ m) of the cylinder from the 8×8 grid with 32 rays, the 16×16 grid with 64 rays, the 32×32 grid with 128 rays and the 64×64 grid with 256 rays. The heat flux profiles are approximately uniform for $3 \leq x \leq 7$ m, and the heat flux at $x=5$ m is seen to converge towards the infinite-cylinder approximation with increasing resolution. The test case is therefore well described by the infinite-cylinder approximation for the mid-point cross section at $x = 5$ m.

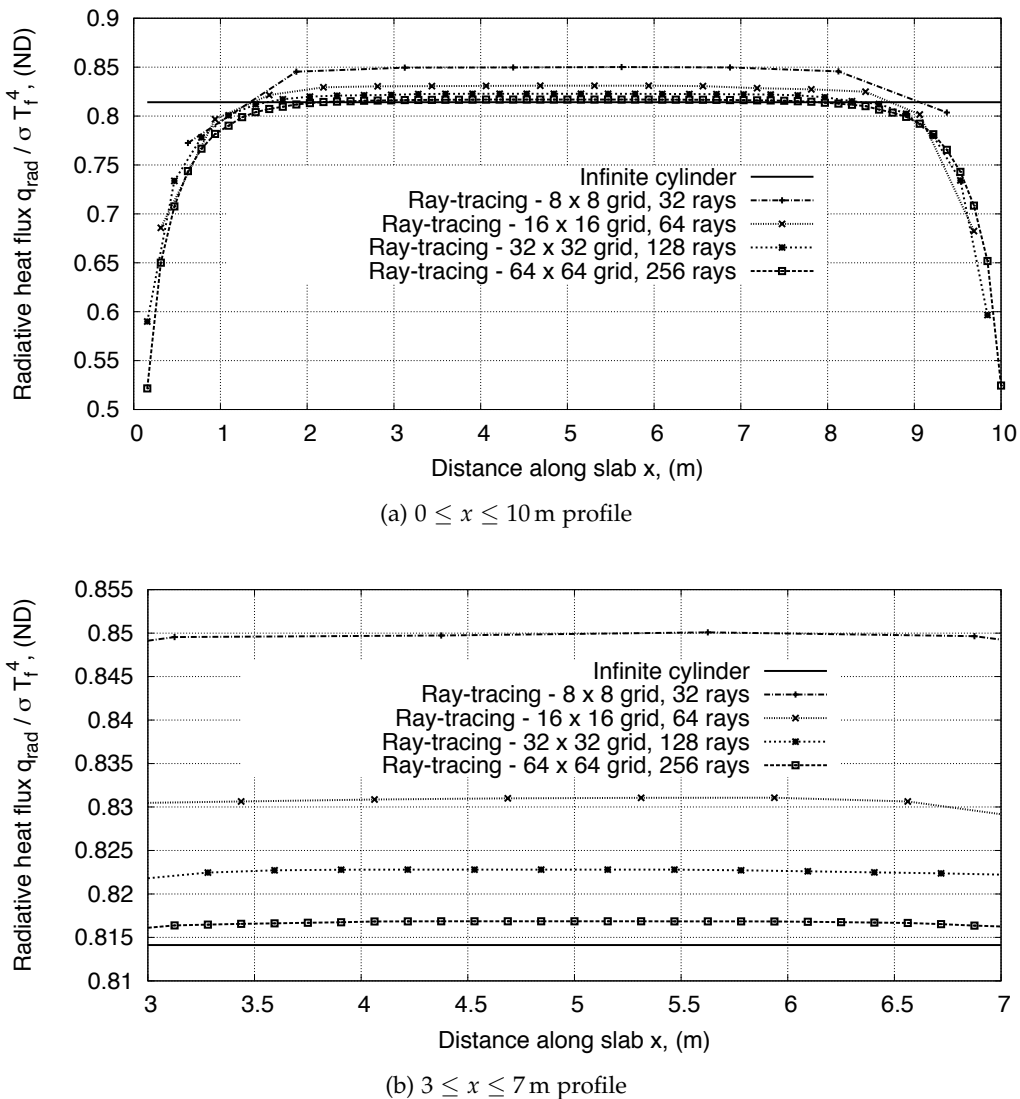


Figure 7.12: Comparison of heat-flux profiles for the axisymmetric infinite-cylinder test case along the outer surface ($y = 1$ m).

Figure 7.13 presents radiative divergence and error profiles for the infinite-cylinder test case; comparisons of radiative divergence are shown in the left column, and the resulting absolute errors compared with the infinite-cylinder solution are shown in the right column. The profiles

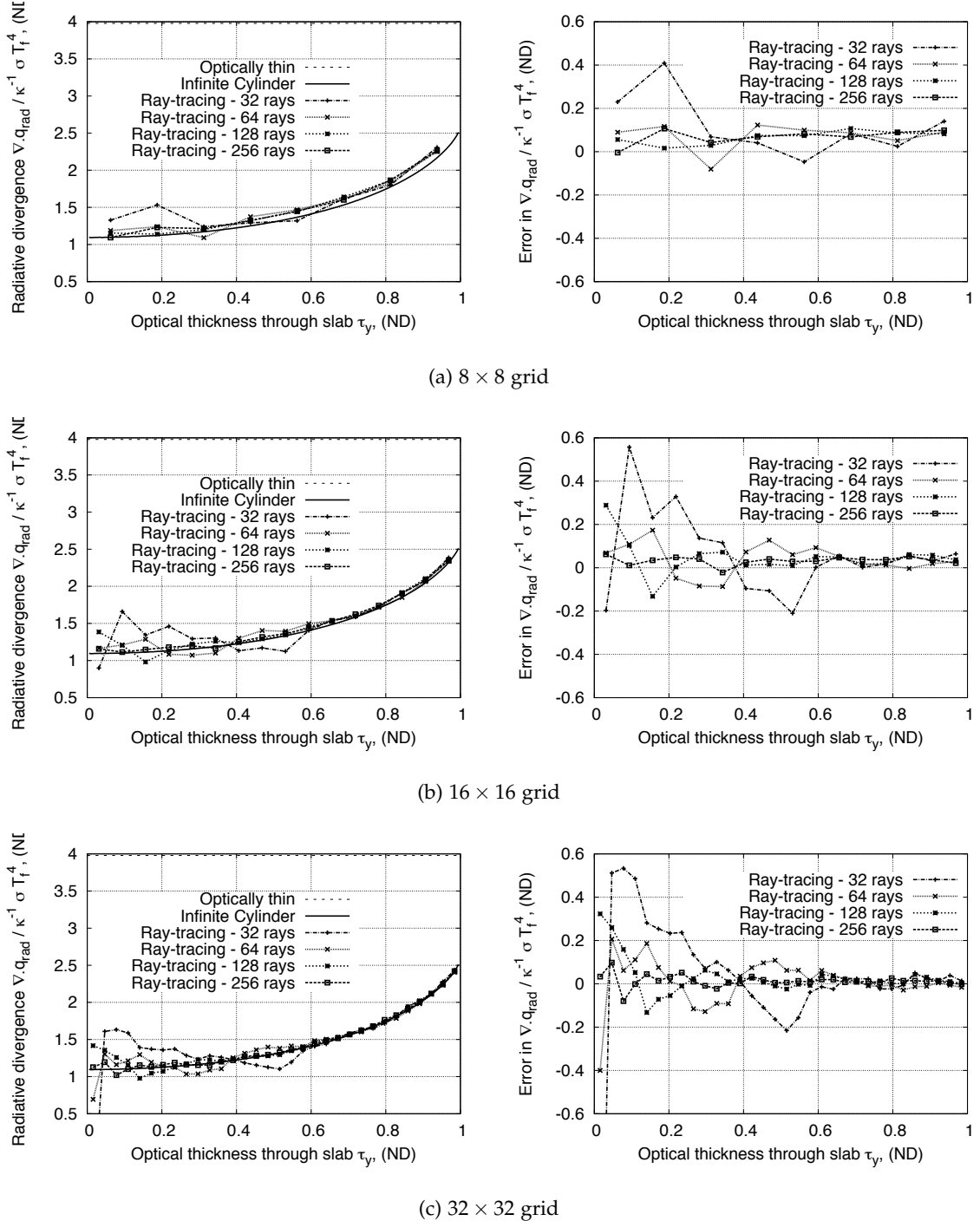


Figure 7.13: Comparison of radiative divergence solution and error profiles at $x = 5\text{ m}$ for the axisymmetric infinite-cylinder radiation transport test case. The spatial coordinate is the optical thickness as defined in Equation 7.85.

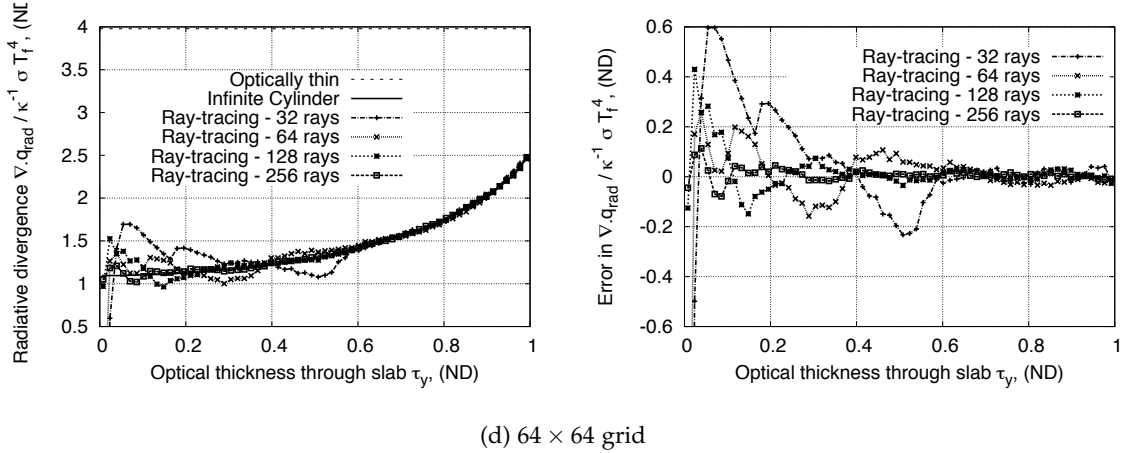


Figure 7.13: (Continued) Comparison of radiative divergence solution and error profiles at $x = 5$ m for the axisymmetric infinite-cylinder radiation transport test case. The spatial coordinate is the optical thickness as defined in Equation 7.85.

are taken from the mid-point cross section where $x = 5$ m. A quantitative summary of the infinite-cylinder results are presented in Table 7.2. The quoted error in $\nabla \cdot \vec{q}_{\text{rad}}$ is the average of the absolute percentage difference along the $x = 5$ m profile referenced to the infinite-cylinder solution, and the quoted error in q_{rad} is the percentage difference from the infinite-cylinder solution at $x = 5$ m and $\tau_y = 1$ m. All simulations were run using the serial version of the code on a single core of a Linux workstation with two Intel Dual Core Xeon Pro 5130 CPU's.

In general, the results demonstrate the ray-tracing model converges towards the exact solution with increasing grid and ray resolution for axisymmetric geometries. For all grid resolutions the average error in $\nabla \cdot \vec{q}_{\text{rad}}$ decreases with increasing ray resolution, and the smallest average error in $\nabla \cdot \vec{q}_{\text{rad}}$ is obtained from the simulation with the largest number of total rays (32×32 cell grid with 128 rays per cell). While the error in q_{rad} improves with increasing grid resolution, it is approximately constant for each grid resolution and only weakly dependent on ray resolution. The total memory usage and wall time is approximately linearly proportional to the total number of rays ($N_{\text{cells},x} \times N_{\text{cells},y} \times N_{\text{rays}}$) as is to be expected. From the results in Figure 7.13, however, it is evident the ray-tracing model performs poorly close to the symmetry axis at $y = 0$. For the 32×32 cell grid with 128 rays, for example, the error in $\nabla \cdot \vec{q}_{\text{rad}}$ at $\tau_y = 0.016$ is approximately 27.3% whilst the error in $\nabla \cdot \vec{q}_{\text{rad}}$ at $\tau_y = 0.984$ is approximately 0.1%. This behaviour is due to the vanishingly small volume per radian for cells close to the symmetry axis; rays emitted from elsewhere in the grid are unlikely to intersect such a small target volume. In an attempt to provide more rays in this region, the ray density was clustered towards the symmetry axis. With the same number of total rays, however, this strategy did not provide a consistent improvement in accuracy. Therefore in the present work it is proposed the ray density N_{rays} be increased uniformly for all cells until the solution at the symmetry axis is acceptable.

Table 7.2: Tabulated results for the axisymmetric infinite-cylinder radiation transport test case.

Grid Resolution $(N_{\text{cells},x} \times N_{\text{cells},y})$	Ray resolution N_{rays}	Memory (MB)	Wall time (s)	Av. $\nabla \cdot \tilde{\mathbf{q}}_{\text{rad}}$	\mathbf{q}_{rad}
				Error (%)	Error (%)
8×8	32	27	0.53	9.08	4.37
	64	29	1.02	6.42	4.22
	128	32	1.97	4.58	4.40
	256	43	3.86	4.88	4.55
16×16	32	43	3.79	9.57	1.84
	64	60	7.30	4.59	2.07
	128	95	14.63	4.32	2.36
	256	161	29.09	2.49	2.20
32×32	32	162	29.39	12.65	0.79
	64	278	56.89	4.74	0.86
	128	526	113.64	3.34	1.07
	256	1003	225.77	1.40	9.58
64×64	32	1006	231.69	15.39	0.17
	64	1876	449.81	6.38	0.21
	128	3676	902.20	3.17	0.42
	256	7281	1812.17	1.24	0.34

Table 7.3 compares the computational resource usage for the 32×32 cell grid and 128 ray case run with the OpenMP version of the code using 1, 2 and 4 CPU cores of the same Linux workstation used for the resolution studies. The results indicate the ray-tracing model performs reasonably well under parallelisation for simple grids. The speed-ups for the 2 and 4 block cases are 1.70 and 3.19 respectively, giving parallelised code fractions of 70 and 73% according to Gustafson's law [206]. Furthermore, the increase in the memory usage for the 2 and 4 core cases is minimal, being only 7.6 and 12.5% respectively. Unfortunately there is significant efficiency penalty paid by using the OpenMP version of the code on a single core compared to using the serial version of the code. The serial version of the code completes the calculation in 113.64 s, whilst the OpenMP version of the code completes the calculation in 160.75 s – a 42% efficiency drop. This is due to the overhead associated with the OpenMP threading and is unavoidable.

Table 7.3: Comparison of resource usage for the 32×32 cell grid and 128 ray infinite-cylinder radiation transport test case with 1, 2 and 4 blocks.

Number of CPU cores, N_{core}	Memory (MB)	Wall time (s)	Speed up
1	526	160.75	-
2	566	94.39	1.70
4	592	50.47	3.19

7.6 Mass diffusion

In the planetary entry flow regime of interest, pressure and thermal diffusion effects are generally negligible compared to mass diffusion due to concentration gradients. Ideally, an appropriate mass diffusion model for ionised plasmas should consider multicomponent and ambipolar diffusion [207]. In previous work with `mbcns` [1, 204], the precursor CFD code to `Eilmer3`, the approximate form of Fick's first law, the Stefan-Maxwell equations as described by Sutton and Gnoffo [207] and the Self-Consistent Effective Binary Diffusion (SCEBD) model proposed by Ramshaw and Chang [208] have been implemented. Although all these models are available within the framework of `Eilmer3` (see Appendix E for a description of the Fick's, Stefan-Maxwell and SCEBD diffusion models), numerical difficulties have prevented their use in the present work. Instead, the constant Lewis number model implemented by Moss [209], Candler [210] and Suzuki *et al.* [211], amongst others, is implemented. The effective diffusion coefficients \tilde{D}_i for all neutral species are calculated in a simple manner by assuming a constant Lewis number:

$$\tilde{D}_i = \frac{\mathcal{L}_e \mu}{\mathcal{P}_r} \quad (7.86)$$

where \mathcal{L}_e is the Lewis number and \mathcal{P}_r is the Prandtl number. The Prandtl number is defined as:

$$\mathcal{P}_r = \frac{\mu c_p}{K} \quad (7.87)$$

where c_p is the total specific heat at constant pressure and K is the total conductivity. In the present work the Lewis number is set to 1.4 based on the recommendations of Moss [209] for reacting air.

In the presence of an electric field induced by an electron pressure gradient, the diffusion of ions and electrons must proceed at the same rate to maintain charge neutrality. In an ionised gas with zero electric current, this effect can be modelled via applying the ambipolar corrections proposed by Gnoffo [151]. The effective diffusion coefficient for ions is set to twice the value given by Equation 7.86:

$$\tilde{D}_{\text{ion}} = 2 \frac{\mathcal{L}_e \mu}{\mathcal{P}_r} \quad (7.88)$$

The effective diffusion coefficient for free electrons is then calculated as follows so as to maintain charge neutrality:

$$\tilde{D}_e = M_e \frac{\sum_i^{N_{\text{ions}}} \tilde{D}_i x_i}{\sum_i^{N_{\text{ions}}} M_i x_i} . \quad (7.89)$$

Finally, the diffusive mass flux of species i is calculated according to the approximate form of Fick's first law:

$$\vec{J}_i = -\rho \tilde{D}_i \nabla f_i \quad (7.90)$$

7.7 Comparison with the post-shock relaxation equations

In this section the Eilmer3 code is compared with the post-shock relaxation solutions presented in § 5.2. For this comparison the low density $t = 1634\text{ s}$ trajectory point of the Fire II flight experiment is selected due to its largely nonequilibrium shock layer. Also, viscous effects are omitted (*i.e.* the Euler equations are implemented) for consistency with the post-shock relaxation equations.

7.7.1 Simulation description

The freestream conditions for the Fire II $t = 1634\text{ s}$ trajectory point are summarised in Table 7.4. Note that the freestream mass fractions for air are assumed to be 0.767 and 0.233 for N_2 and O_2 respectively. The axisymmetric computational domain and grid for the Euler simulations are presented in Figures 7.14a and 7.14b respectively. The grid consists of 60 cells in the body normal direction and 80 cells in the body surface direction (60 cells between the stagnation point and the shoulder and 20 cells between the shoulder and outflow boundary). Because the vehicle surface is modelled as a slip wall for these inviscid simulations, no clustering of cells is applied. The computational domain is divided into 8 equally sized blocks in order to run the calculation on a cluster computer. The implemented physical models are those listed in Table 5.2.

Table 7.4: Freestream conditions and heat-shield parameters for the Fire II 1634 s trajectory point [23].

Flight time, t (s)	1634
Altitude (km)	76.42
Density, ρ_∞ (kg/m^3)	3.72×10^{-5}
Temperature, T_∞ (K)	195
Velocity, u_∞ (m/s)	11,360
Nose radius, R_n (m)	0.9347

7.7.2 Results

Figures 7.15a and 7.15b present the total energy and mass residuals, respectively, from the Euler simulations of the Fire II $t = 1634\text{ s}$ trajectory point. Chemical reactions are modelled as frozen for the first body length of flow to prevent numerical difficulties during the flow establishment period. After the chemical reactions have been turned on, the residuals steadily drop by four orders of magnitude over the 10 body lengths of flow simulated. The solution is therefore deemed to be converged at this time. The simulation took 1.5 hours to run on $8 \times 2.26\text{ GHz L5520 Intel CPU's}$.

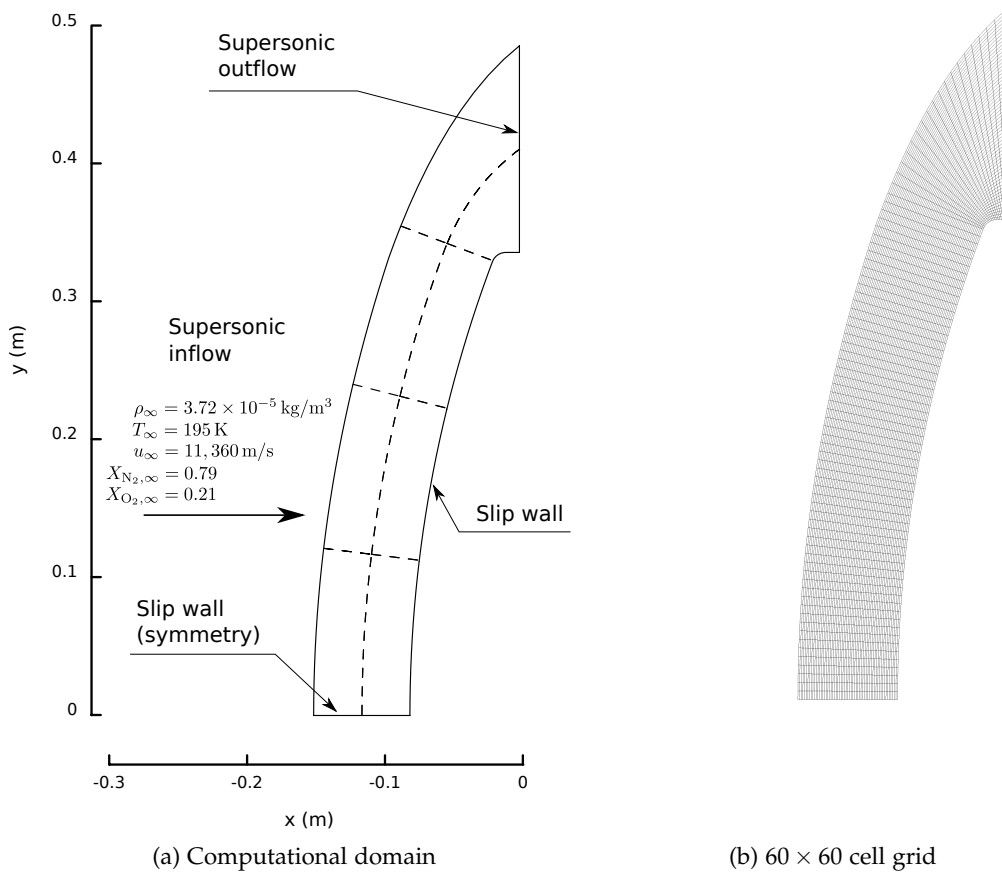


Figure 7.14: Computational domain and grid for Euler simulations of the Fire II $t = 1634 \text{ s}$ trajectory point.

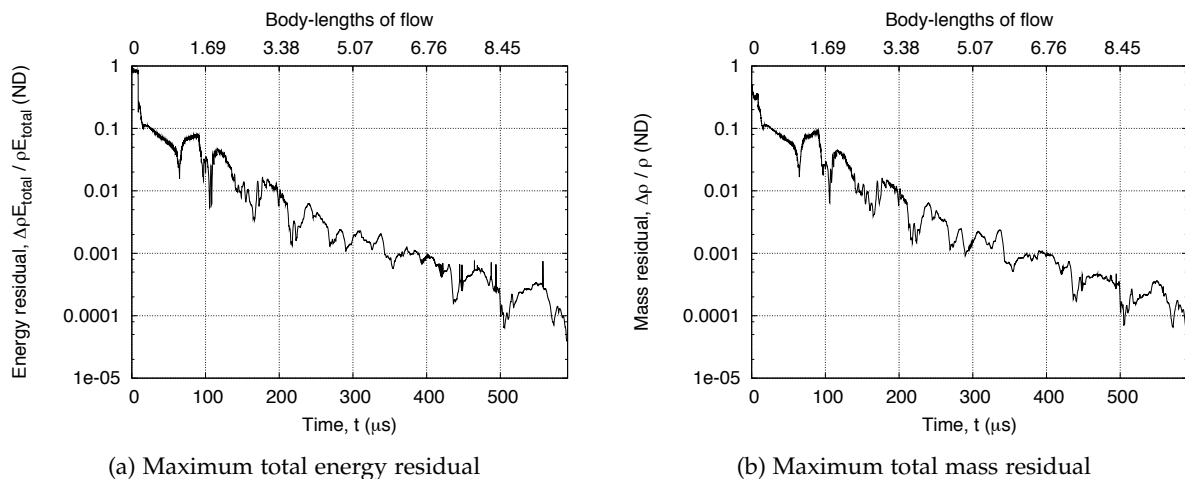


Figure 7.15: Maximum total energy and mass residuals as a function of time from Euler simulations of the Fire II $t = 1634 \text{ s}$ trajectory point on a 60×80 cell grid.

Figure 7.16a and 7.16b compare the temperature and number density profiles along the stagnation streamline with the solution obtained with the one-dimensional post-shock relaxation equations using the Poshax3 code. As the Poshax3 solution does not consider the presence of the vehicle surface downstream of the shock, the solution has been positioned such that the locations of the peaks in T_{tr} approximately coincide. The peak translation-rotation temperature behind the shock in the Eilmer3 simulation is 60,000 K while the Rankine-Hugoniot relaxations in the Poshax3 simulation predict post-shock translation-rotation temperature of 62,400 K. This difference can be attributed to the shock capturing nature of the Eilmer3 code.

Despite this slight discrepancy at the shock-front, the two solutions show reasonable agreement through the shock layer. The Eilmer3 solution exhibits faster thermal relaxation over the first 1.4 cm behind the shock, however, increasing the rate of N, O and e^- production (*i.e.* the rate of dissociation and ionisation) in this region. Consequently the peak in T_{ve} is reached 2 mm earlier, and then drops to a slightly lower level prior to equilibration on account of the lowered molecular population. This is a difficult test case for the operator-split chemical kinetic and energy exchange ODE solvers due to the strong coupling between the nonequilibrium processes and the gas dynamics, and therefore this small disagreement is considered acceptable.

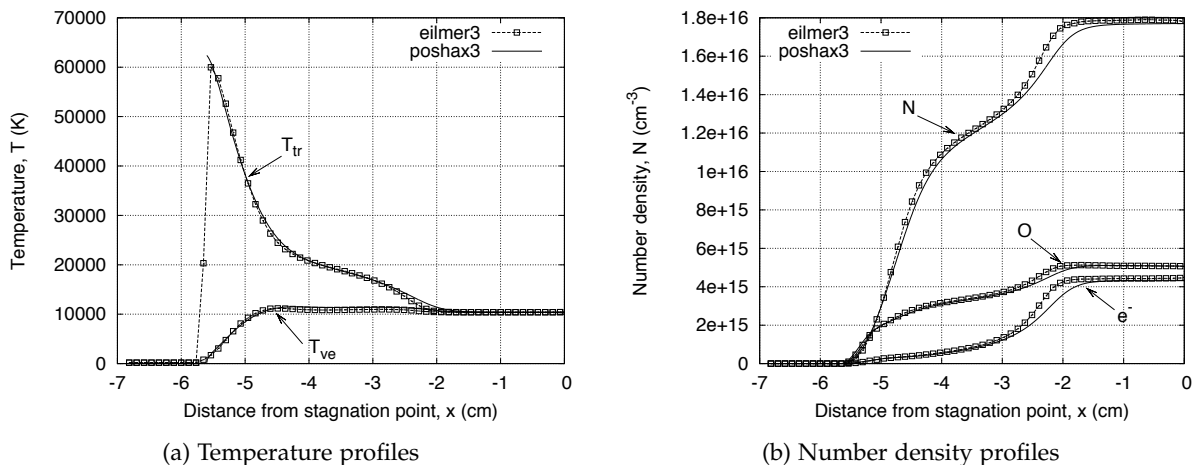


Figure 7.16: Comparison of stagnation line profiles for the Fire II $t = 1634$ s trajectory point calculated with the Euler equations (Eilmer3) and the one-dimensional post-shock relaxation equations (Poshax3).

7.8 Summary

In this chapter the implementation of the Navier–Stokes equations in the Eilmer3 code has been described. An overview of the code structure and supporting programs was given, and the mathematical form of the discretised governing equations was presented. The code integrates

the equations in a time-accurate manner, and the planar and axisymmetric formulations were considered. The operator-split method for calculating the chemical and thermal increments was described, as were the models for diffusion and radiation-flowfield coupling. Particular attention was given to describing a novel ray-tracing based radiation transport model implemented in this work. The model was assessed by application to planar and axisymmetric test cases; while good accuracy was demonstrated for planar geometries, some discrepancies emerged near the symmetry axis for axisymmetric geometries. Finally the operator-split approach for modelling the thermochemical nonequilibrium source terms was assessed via comparisons with the full coupled one-dimensional post-shock relaxation equations. The test case considered was the Fire II $t = 1634\text{ s}$ trajectory point and good agreement was found between the two solutions.

8

Simulation of expansion tunnel experiments

In this chapter we apply the Navier–Stokes code *Eilmer3* to simulate two expansion tunnel experiments performed in the X2 facility. Both the facility operation and the recompression shock formed over the test models is considered. Specifically, two conditions are investigated:

1. 47 MJ/kg N₂–O₂ condition with a 1:10 scale Hayabusa model, and
2. 37 MJ/kg CO₂–N₂ condition with a 25 mm diameter cylinder.

In § 8.1 the operation of the X2 facility in the expansion tunnel mode of operation is described, and in § 8.2 the modelling strategy for calculating the freestream conditions is elaborated. The results for the N₂–O₂ and CO₂–N₂ conditions are then presented in § 8.3 and 8.4 respectively. Conclusions drawn from the analyses are summarised in § 8.5.

8.1 Facility description

The X2 facility is a free-piston driven impulse facility located at the University of Queensland. The experiments considered here utilised the single-driver, expansion tunnel mode of operation as illustrated in Figure 8.1. The expansion tunnel configuration differs from the dual driver shock tube configuration discussed in § 6.3 in that the test gas is initially located between the primary and secondary diaphragms (region 1) instead of downstream of the secondary diaphragm (region 2). In addition, a Mach 10 full capture hypersonic nozzle designed by Scott [212] is attached to

the end of the acceleration tube, which expands the flow diameter from 85 to 208 mm (area ratio of 1:6) over a length of 1.4 m.

The high pressure air reservoir propels a 35 kg single-stage piston, compressing the driver gas in the compression tube until the rupture pressure of the primary diaphragm is reached. The rupturing primary diaphragm drives a shock through the test gas in the shock tube (region 1 to 1*), which in turn ruptures the Mylar secondary diaphragm and drives the secondary shock through the low pressure air in the acceleration tube (region 2 to 2*). The shock heated test gas is then processed by the reflected shock and accelerated by the unsteady expansion initiated by the rupturing of the secondary diaphragm (region 1 * to 3). Finally, the test gas undergoes steady expansion through the hypersonic nozzle and into the test section for re-compression over a sting-mounted test model (region 3 to 4). The usable core flow for atmospheric entry type conditions is typically between 90 and 130 mm, and the period of steady test flow is typically

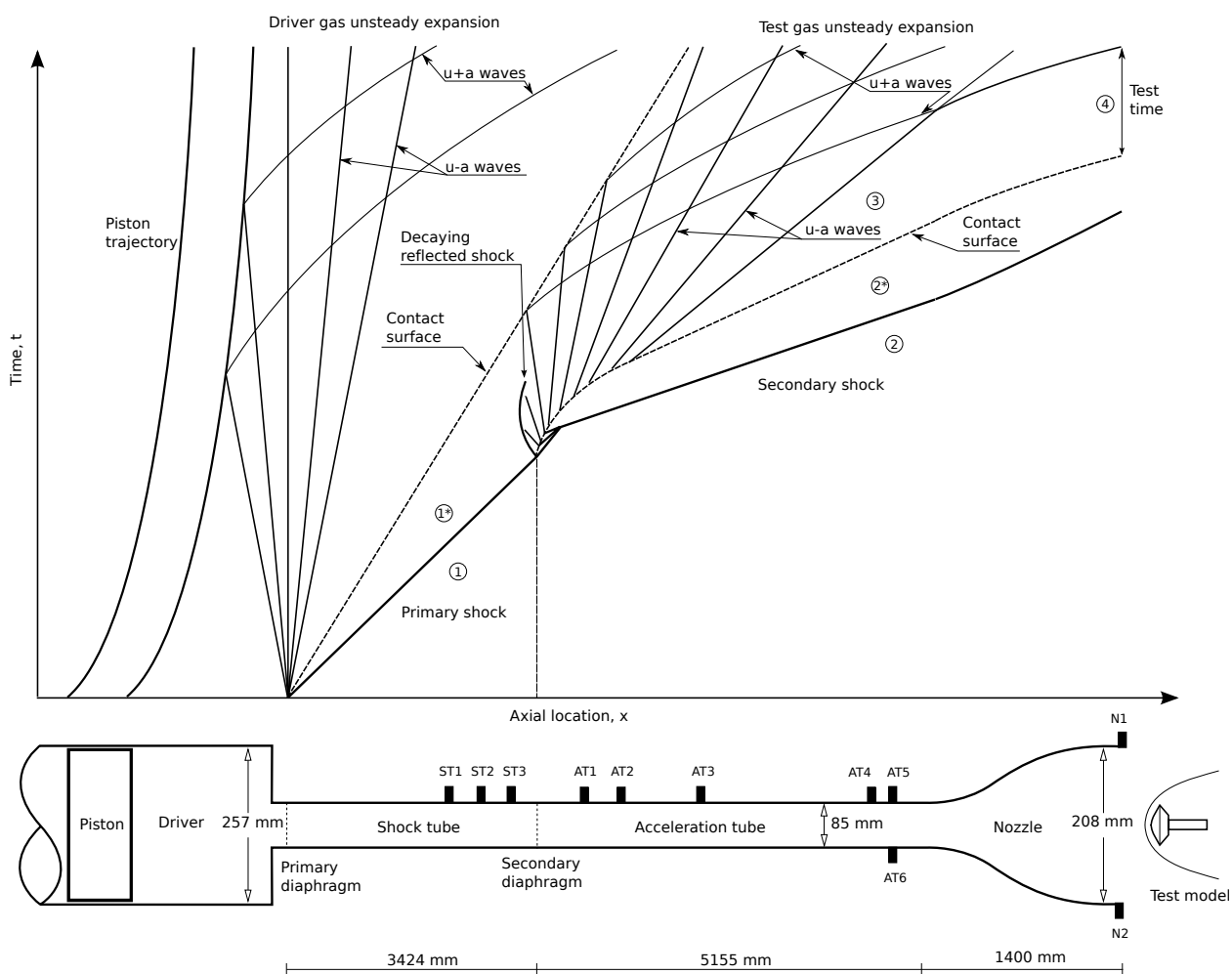


Figure 8.1: Space-time diagram and schematic of the X2 facility in single-driver expansion tunnel mode.

between 50 and 200 μs [212, 213]. Measurements of the flow condition and shock speed are made with flush wall mounted pressure sensors (PCB) labelled ST 1 to 3, AT 1 to 5 and N 1 and 2 in Figure 8.1. The PCB transducers have a response time of 2 μs and are axially located to an accuracy of $\pm 0.5 \text{ mm}$ and have a diameter of 6 mm. During condition development a rake of pitot probes is installed in the test section in place of the test model, Figure 8.2, allowing the flow quality to be assessed both radially and temporally.

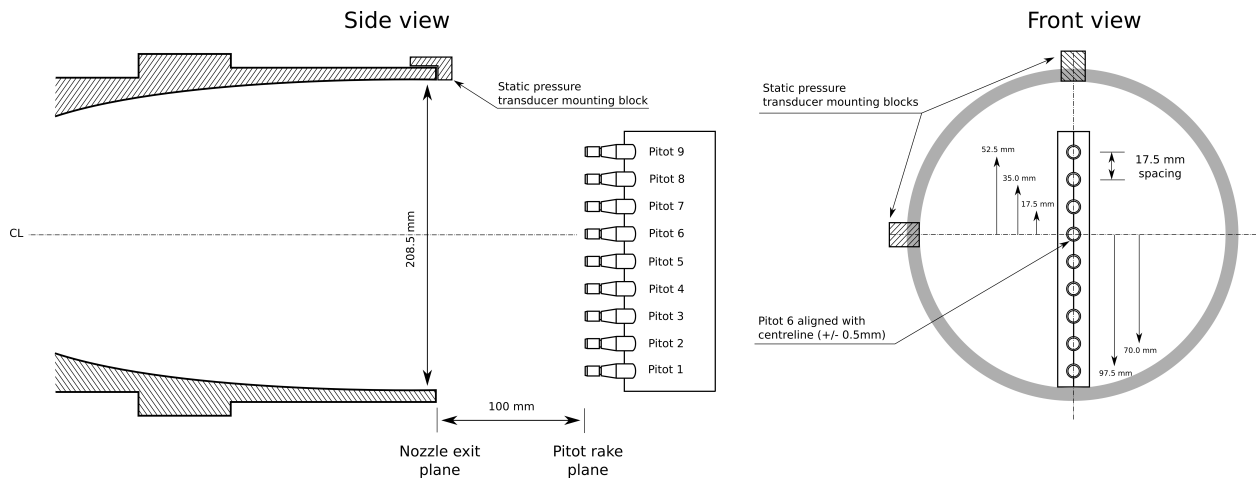


Figure 8.2: Positioning of Pitot rake in the test section during condition development.

8.2 Modelling strategies

The approach developed for simulating expansion tunnel flow at the University of Queensland in recent years has been to perform a hybrid simulation of the whole facility. This approach is described in § 8.2.1. Applying the physical models developed in this thesis to this strategy proved to be computationally prohibitive, however, due to the excessive time required to run the simulations. In the present work a simplified modelling strategy is therefore proposed, and is described in § 8.2.2.

8.2.1 Hybrid simulation of the whole facility

The expansion tunnel operation just described can be divided into four distinct stages:

1. Free-piston compression of the driver gas and primary diaphragm rupture,
2. Primary shock propagation through the shock tube flow,
3. Secondary diaphragm rupture and unsteady test gas expansion, and
4. Secondary shock propagation through the acceleration tube.

Stages (1) and (2) involve all the important flow processes occurring at high pressures and relatively moderate velocities. For the 47 MJ/kg air condition, for example, the primary shock speed is ~ 5 km/s and the post shock pressure is ~ 800 kPa. In contrast, stages (3) and (4) involve the test gas being expanded to low pressure and high velocities; for the 47 MJ/kg air condition, the secondary shock speed is ~ 9 km/s and the post shock pressure is ~ 5 kPa. Accordingly, Jacobs *et al.* [214] proposed a hybrid simulation strategy for the X3 facility where the shock tube is simulated by the quasi-one-dimensional Lagrangian code L1d and the acceleration tube is simulated with the Navier–Stokes equations. The Navier–Stokes simulation is initialised from the L1d solution at the moment of secondary diaphragm rupture, where L1d applies a simple holding-time rupture model. This strategy has also been applied successfully to the X2 facility by Scott *et al.* [212], Brandis *et al.* [215] and Potter *et al.* [213] with finite-rate chemical kinetics and single temperature gas models.

There are three drawbacks to this hybrid simulation strategy: (1) the driver gas conditions must be estimated, (2) a simplified model of secondary diaphragm rupture must be used, and (3) the computational expense of simulating the whole facility with detailed physical models. Firstly, the temperature and pressure of the driver gas at rupture conditions must be estimated as the L1d code does not correctly model the heat loss in the compression tube when the piston stroke is included in the simulation [212]. As a consequence a trial-and-error approach must be used to determine these parameters by matching the measured primary shock speed. Secondly, one would like to implement an inertial diaphragm rupture model in the one-dimensional simulation, however this makes the Navier–Stokes simulation difficult to initialise. The inertial diaphragm rupture model such as that considered by Bakos and Morgan [216] allows the diaphragm to provide inertial resistance to the unsteady expansion, and thus model the rupture process in a more physically realistic manner than a holding time model where the diaphragm acts as a wall for a small period of time. This was shown in Reference [217] where the measured shock propagation in the acceleration tube was more accurately reproduced by the inertial diaphragm model than the holding time model. Finally, the accurate determination of the freestream conditions requires a detailed chemical kinetic model which requires a large amount of computational resources when the whole facility is simulated. Furthermore, thermal nonequilibrium has been shown to occur in the hypersonic nozzle [217] and therefore a two- or multitemperature model should be used. With moderate grid resolution, a reduced chemical kinetic model, a simplified transport model and a single temperature gas model, Navier–Stokes simulations of the acceleration tube and nozzle take a number of weeks to run on a cluster computer. Given the need for multiple runs to achieve a match with experimentally measured shock speeds and pressures, this modelling strategy is impractical for the present thesis work.

8.2.2 Simplified modelling strategy

The simplified strategy applied in the present work involves two stages: (1) estimation of the test gas flow state at the nozzle entrance, and (2) simulation of the hypersonic nozzle with the Navier–Stokes equations and detailed physical models. Verification of the calculated freestream conditions is obtained by comparison with the measured Pitot pressure level in the test section. Note that in the following discussion the integer subscripts refer to the flow regions indicated in Figures 8.1 and 8.3.

Due to the low pressure and high shock speed in the acceleration tube, the secondary shock is likely to be fully developed (*i.e.* the contact surface and the shock front are moving at the same speed due to mass loss to the boundary layer [218]). Although Navier–Stokes simulations performed by Jacobs *et al.* [214] demonstrated that the test gas velocity is 2.1% higher than the shock speed for a 36.9 MJ/kg air expansion tunnel condition, as a first approximation in the present work the the test gas velocity at the nozzle entrance, u_3 , is approximated as the shock speed:

$$u_3 \approx U_{s,2} \quad (8.1)$$

Given that the secondary shock speed can only be accurately measured to within approximately $\pm 2.5\%$, this is a reasonable approximation. An estimate of the pressure at the nozzle entrance p_3 can be obtained by selecting an appropriate averaging period on the AT5 pressure trace:

$$p_3 \approx p_{\text{AT5}}(\Delta t_{\text{test gas}}) \quad (8.2)$$

This transducer is approximately 0.5 m from the nozzle entrance. The temperature and chemical composition, however, are not so easily estimated due to the complexity of the secondary diaphragm rupture process. A wave diagram of the secondary diaphragm rupture process is presented in Figure 8.3. A packet of test gas in region '1' is first processed by the primary shock, and then by the reflected shock that forms due to the presence of the secondary diaphragm. As the pressure builds behind the reflected shock, the diaphragm is sheared from the tube walls and pushed downstream, with the mass of the diaphragm providing inertial resistance to this motion. The diaphragm motion generates compression waves that coalesce into the secondary shock, and an unsteady expansion of the test gas resulting in flow state '4'.

As demonstrated in References [216, 217], the inertia of the diaphragm must be taken into consideration to correctly calculate the test gas composition. Simulations are therefore performed of the secondary diaphragm rupture with the decaying inertial diaphragm model as described in Reference [217] using the L1d code [219]. The L1d code is a quasi-one-dimensional Lagrangian flow code developed at the University of Queensland for simulating free-piston driven impulse facilities. The code is capable of modelling entire free-piston driven facilities via a Lagrangian description of pistons, gases and diaphragms. Good agreement with experimental pressure traces

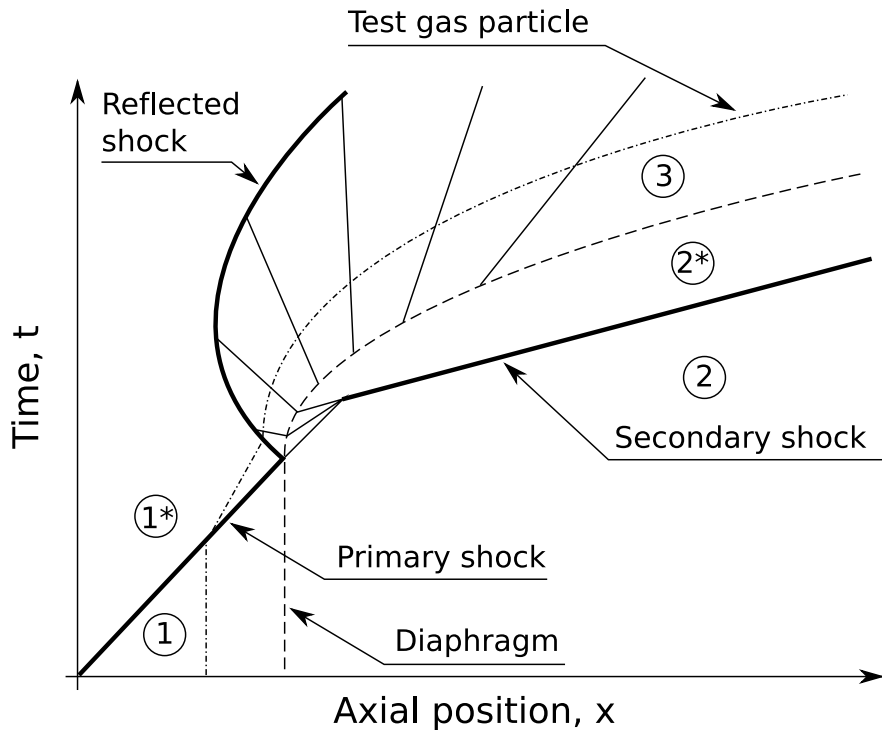


Figure 8.3: Wave diagram of the secondary diaphragm rupture process. The flow region numbering is consistent with Figure 8.1.

in the high pressure ($p > 100 \text{ kPa}$) regions of both shock tube and expansion tunnel experiments have been demonstrated in numerous studies (e.g. References [189, 213]). For further description of the L1d code the interested reader is referred to References [219, 220]. The computational domain for these simulations is illustrated in Figure 8.4. The problem is initialised at the moment of primary shock impact on the diaphragm, and therefore the left flow state is approximated as the shock processed test gas in region '1*' and the right flow state is the low pressure air in region '2'. This allows the reflected shock and subsequent unsteady expansion to be modelled without directly simulating the primary shock. The diaphragm is modelled as a piston with no axial width, and the initial mass m_i is set to $68 \mu\text{g}$ corresponding to an 85 mm diameter mylar diaphragm approximately $13 \mu\text{m}$ thick. As the mylar diaphragm is likely to break up and become vaporised by the shock heated test gas, its mass is modelled as decaying in time. The rate of decay is calculated as:

$$\frac{dm}{dt} = \begin{cases} f_{\text{decay}} \times m & \text{for } m > m_{\text{limit}} \\ 0 & \text{for } m \leq m_{\text{limit}} \end{cases} \quad (8.3)$$

where f_{decay} is a time constant and m_{limit} an imposed lower mass limit to prevent numerical instabilities. In Reference [217] a decay time constant of $5 \times 10^4 \text{ s}^{-1}$ was found to give excellent

agreement with the shock arrival time at the AT1 transducer, and this value is therefore implemented in the present work. As the L1d code models viscous effects via empirical correlations that are only accurate at high pressures, viscous effects are omitted from the simulations. As a consequence, however, the secondary shock speed and fully expanded test gas temperature and pressure (flow region '3') are overestimated. Nevertheless the estimated chemical composition of the test gas remains valid as the bulk of the recombination occurs early in the unsteady expansion when the pressure and temperature is high. Therefore only the chemical composition is extracted from the L1d simulations. Although thermal equilibrium is likely due to the high pressure of the test gas behind the primary shock, the two-temperature model is implemented for the L1d calculations to ensure this is the case.

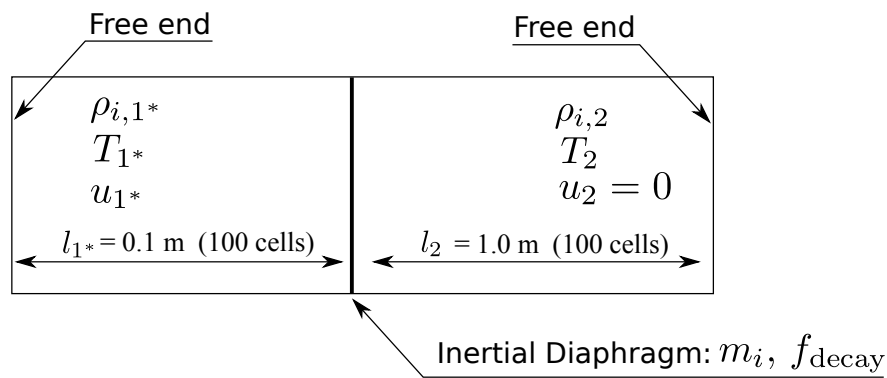


Figure 8.4: Computational domain for L1d simulations of the secondary diaphragm rupture.

Navier–Stokes simulations are then performed of the hypersonic nozzle with various entrance temperatures until the measured Pitot pressure level during the test time is matched. The computational domain and grid for the hypersonic nozzle simulations are presented in Figures 8.5a and 8.5b. Note that the grid is presented at one-quarter of the nominal 1900×43 resolution for clarity. The computational domain is extended 500 mm upstream of the nozzle entrance to allow time for the boundary layer to develop. The inflow boundary conditions is the estimated nozzle entrance conditions presented in a radially and temporally uniform manner. The tube wall is considered to be a no-slip wall fixed at room temperature, and the symmetry boundary is a slip wall. The outflow boundary is the supersonic outlet condition, where the CFD cell flow state is extrapolated into the ghost cells. The initial condition is the low pressure air initially in the acceleration tube (flow region '2'). A two-temperature model is implemented for these simulations as thermal nonequilibrium is likely to occur due to the rapid drop in pressure through the nozzle.

The freestream conditions so determined can then be used as inflow conditions for the detailed simulation of the re-compression over the test-model. Overall, this strategy has the advantage of being relatively simple and quick to perform and makes direct use of the experimentally measured shock speed and pressure levels.

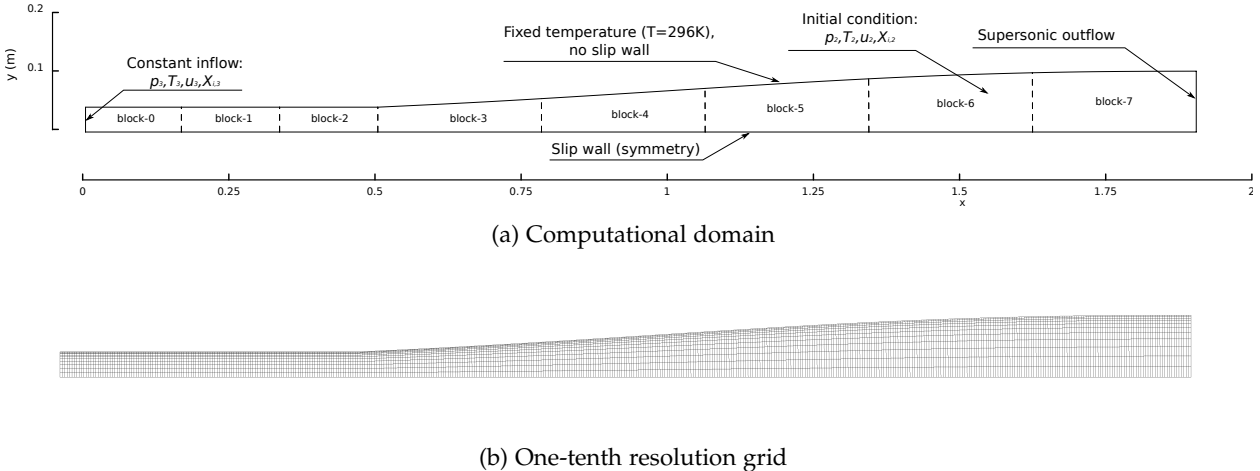


Figure 8.5: Computational domain and grid for simulations of the X2 hypersonic nozzle flow.

8.3 47 MJ/kg N₂-O₂ condition: subscale Hayabusa model

The Hayabusa spacecraft was developed by the Japan Aerospace Exploration Agency to return a sample of a near-Earth asteroid to Earth for scientific analysis. The re-entry of the spacecraft into the Earth's atmosphere in June 2010 occurred at an estimated velocity of 12.2 km/s and was observed by a number of teams via ground and airborne instruments [221]. In support of the observation campaign, Buttsworth *et al.* [221] performed emission spectroscopy measurements of the shock layer formed over a one-tenth scale model of the Hayabusa forebody in the X2 expansion tunnel facility. The condition total enthalpy was 47 MJ/kg and the binary scaling parameter ρL was approximately $6.7 \times 10^{-5} \text{ kg/m}^2$, corresponding to an effective flight velocity of 9.7 km/s at an altitude of 65 km for the full scale Hayabusa vehicle¹. A description of the experiment is provided in § 8.3.1. In § 8.3.2 the freestream conditions for this experiment are estimated via the strategy outline in § 8.2. Simulations are then performed of the recompression shock formed over the subscale model in § 8.3.3. From these solutions to the subscale shock layer, intensity profiles are extracted and compared with the measured data. In § 8.3.4 the binary-scaling rationale is assessed for this experiment by comparisons with simulations of an effective flight condition.

8.3.1 Experiment description

Spectroscopic measurement of a subscale aeroshell

Experiments were performed with both steel and epoxy coated steel forebody models to simulate the re-entry aerothermal environment without and with surface ablation. Schematics

¹The effective flight condition is calculated by applying the binary scaling hypothesis: $H_{\text{total, flight}} = H_{\text{total, exp.}}$ and $(\rho L)_{\text{flight}} = (\rho L)_{\text{exp.}}$

of both subscale models are presented in Figure 8.6. The models are mounted in the test-section during the experiments by a sting attached to the aft-section. In the present work only the uncoated steel model experiments are considered, as the Eilmer3 code does not yet have ablative boundary capabilities for multispecies and multitemperature gas-models. Both ultraviolet and infrared spectra were measured along the stagnation streamline, and high-speed camera footage of the shock establishment was also recorded. An illustration of the optical arrangement in the test section for spectroscopic and high speed camera measurement of the shock layer is presented in Figure 8.7. Acton Research Spectra Pro SP2300 series spectrographs were coupled with a 1024×256 pixel Princeton Instruments PI-MAX CCD array for the ultraviolet measurements, and a 512×512 pixel Princeton Instruments PI-MAX CCD array for the near-infrared measurements. The ultraviolet spectra were obtained with the coarse 150 lines/mm grating in the range $233 \leq \lambda \leq 638$ nm, while the infrared spectra considered were obtained with the 600 lines/mm grating in the range $696 \leq \lambda \leq 880$ nm. For all shots both spectrometers had slit widths of 100 nm, gate widths of $10 \mu\text{s}$ and an intensifier gain of 255.

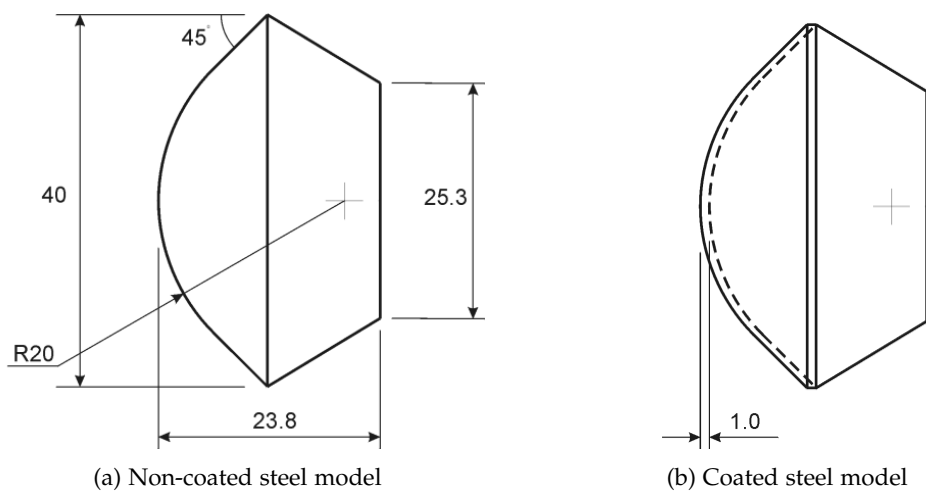


Figure 8.6: One-tenth scale Hayabusa models tested in the X2 expansion tunnel.

Flow condition

A 47 MJ/kg N₂-O₂ expansion tunnel condition was developed for the subscale Hayabusa spectroscopy experiments. The fill conditions, measured shock speeds and measured pressure levels for shot x2s1217 are summarised in Table 8.1. A static pressure trace at the AT5 transducer is presented in Figure 8.8a, and a centreline Pitot pressure trace in the test-section is presented in Figure 8.8b. The averaging periods used to estimate the test gas pressure at the nozzle entrance, p_3 , and the Pitot pressure in the test-section, p_{pitot} in Table 8.1 are indicated with the ‘test gas’ label. The blue bars in Figure 8.8b represent the $10 \mu\text{s}$ spectrometer exposure time, that is triggered

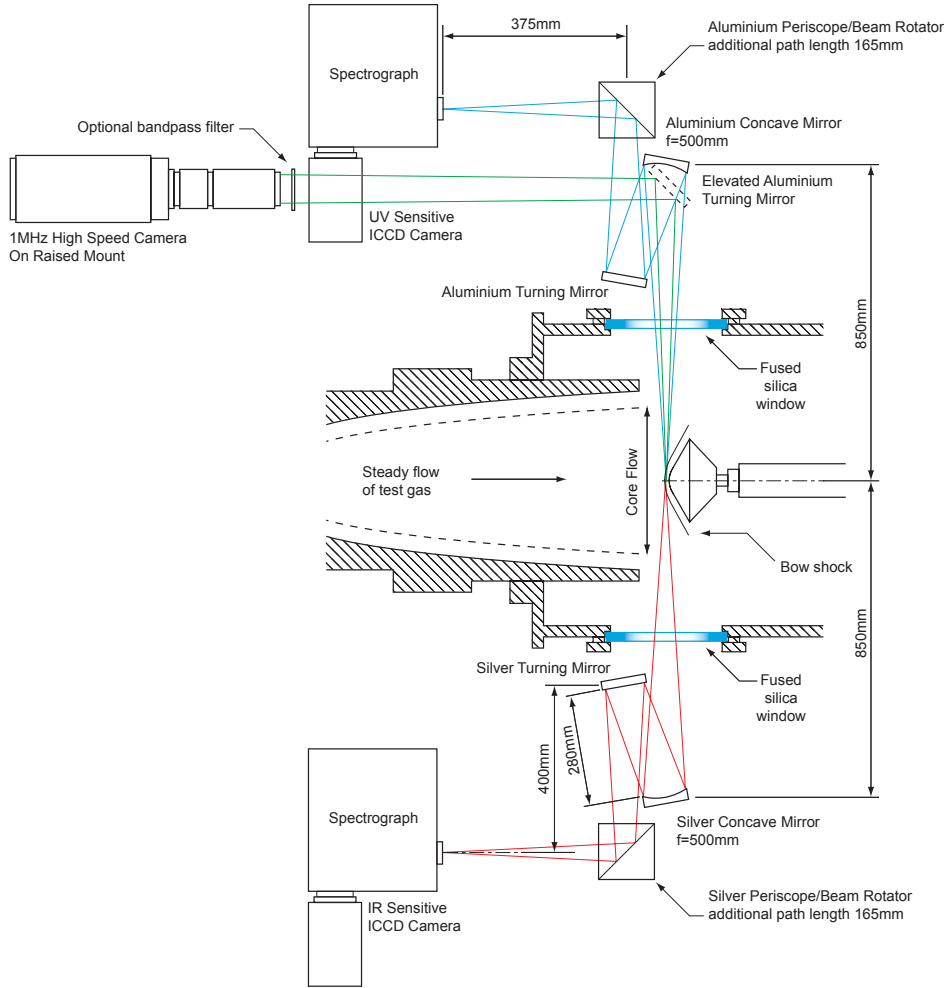


Figure 8.7: Optical arrangement in the test section for spectroscopic measurement of the subscale Hayabusa shock layer.

approximately $65\ \mu\text{s}$ after shock arrival by a photomultiplier tube². Although the flow quality of this condition is excellent with a steady flow period in-excess of $200\ \mu\text{s}$, only the first $70\ \mu\text{s}$ of test gas is relevant in the present analysis due to the temporal location of the spectroscopic measurements.

8.3.2 Estimation of freestream conditions

From the initial fill conditions and measured shock speeds and pressure levels presented in Table 8.1, the nozzle entrance conditions are estimated using the strategy outlined in § 8.2. A two-temperature 11 species gas-model was used for both the secondary diaphragm and nozzle simulations. Dissociation reactions are assumed to be governed by the geometric average temperature $\sqrt{T_{\text{tr}} T_{\text{ve}}}$ as recommended for expansion flows by Lino da Silva [143]. Non-preferential

²The location of the peak Pitot pressure has been taken to indicate shock arrival in Figure 8.8b.

Table 8.1: Fill conditions and experimentally measured pressures and shock speeds for the 47 MJ/kg N₂-O₂ expansion tunnel condition.

Shock tube	
Test gas composition	$X_{N_2} = 0.79$
	$X_{O_2} = 0.21$
Initial test gas pressure, p_1 (Pa)	3100 ± 50
Primary shock speed, $U_{s,1}$ (m/s)	4980 ± 53
Post shock pressure, p_1^* (kPa)	820 ± 70
Acceleration tube	
Initial air pressure, p_2 (Pa)	10 ± 0.1
Secondary shock speed [†] , $U_{s,2}$ (m/s)	9010 ± 230
Post shock pressure, p_2^* (Pa)	4100 ± 600
Test gas pressure [‡] , p_3 (kPa)	5700 ± 950
Test section	
Pitot pressure [§] , p_{pitot} (kPa)	131 ± 8

[†] Measured between transducers AT5 and AT6 as indicated in Figure 8.1

[‡] Average between 38 and 81 μ s after shock arrival at AT5 as indicated in Figure 8.8a

[§] Average between 43 and 113 μ s after shock arrival at the Pitot probe as indicated in Figure 8.8b

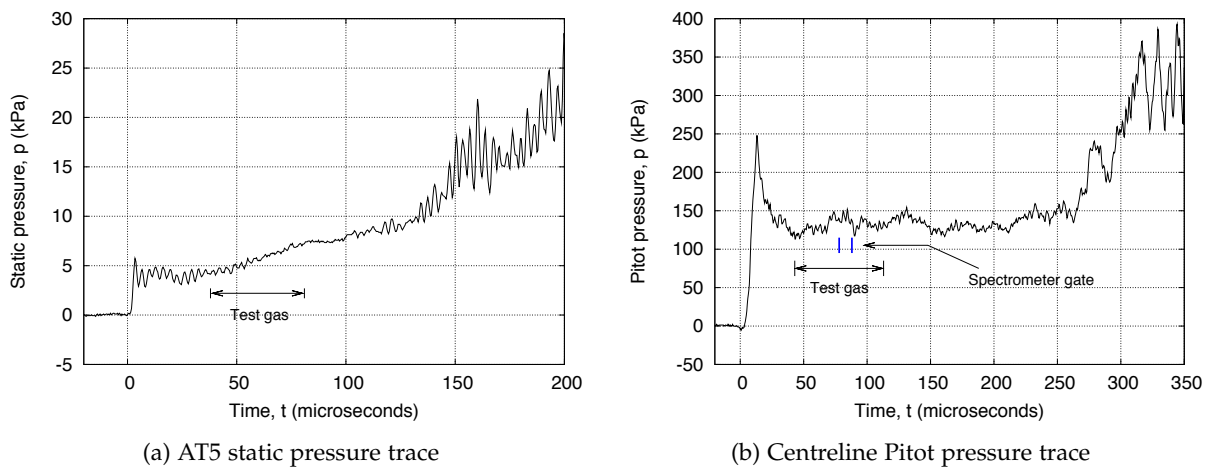


Figure 8.8: Measured pressure traces for shot x2s1217.

energy-chemistry coupling is applied due to the tendency of the preferential models to overestimate the amount of energy added to the flow upon recombination in expansion flows. For the nozzle calculations, the transport coefficients are calculated with the Gupta and Yos [92] and the collision cross sections proposed by Wright *et al.* [88, 94, 98, 99] as described in § 3.2.

The estimated test gas flow state behind the primary shock (region '1*'), at the nozzle entrance (region '3') and at the nozzle exit (region '4') are summarised in Table 8.2. The quoted uncertainty levels have been estimated via a perturbation analysis considering the variation in the measured shock speed and pressure levels. The L1d simulations of the secondary diaphragm rupture estimate the N₂ concentration at the nozzle entrance to be very similar to the composition behind the primary shock. Figure 8.9 presents pressure and N₂ mass-fraction histories of a test gas packet originating just upstream of the secondary diaphragm. The initial sudden increase in pressure and drop in N₂ mass-fraction is due to the reflected shock forming off the diaphragm. Despite that significant dissociation occurs due to the reflected shock, the N₂ mass-fraction recovers almost to the level behind the primary shock due to recombination during the unsteady expansion process. The bulk of this recombination can be seen to occur at pressures greater than one atmosphere, as was anticipated when formulating the modelling strategy in § 8.2.2.

For the Navier–Stokes simulations of the nozzle, an entrance temperature of 1,200 K was found to give good agreement with the measured Pitot pressure trace, Figure 8.10. It should be noted, however, that the test gas is disturbed in the simulations by a steady shock system that

Table 8.2: Estimated test gas flow states for the 47 MJ/kg N₂–O₂ expansion tunnel condition.

Flow state	Behind primary shock (region '1*')	Nozzle entrance (region '3')	Nozzle exit (region '4')
Density, ρ (kg/m ³)	$3.81 \pm 0.04 \times 10^{-1}$	$1.32 \pm 0.22 \times 10^{-2}$	$1.73 \pm 0.32 \times 10^{-3}$
Pressure, p (Pa)	$819 \pm 37 \times 10^3$	5700 ± 950	654 ± 113
T_{fr} (K)	6031 ± 155	1200 ± 50	1069 ± 54
T_{ve} (K)	6031 ± 155	1200 ± 50	1202 ± 70
Velocity, u (m/s)	4506 ± 104	9010 ± 230	9121 ± 232
Mach number, M	2.8 ± 0.1	11.5 ± 0.3	12.5 ± 0.3
Total enthalpy, H_{total} (MJ/kg)	22.7 ± 1.1	46.9 ± 2.3	47.1 ± 2.3
Mole-fractions: [‡]			
X_{N_2}	$5.94 \pm 0.11 \times 10^{-1}$	$6.01 \pm 0.11 \times 10^{-1}$	$6.27 \pm 0.11 \times 10^{-1}$
X_{O_2}	$1.95 \pm 0.49 \times 10^{-3}$	$6.27 \pm 1.58 \times 10^{-5}$	$5.75 \pm 1.44 \times 10^{-3}$
X_{NO}	$2.41 \pm 0.19 \times 10^{-2}$	$6.63 \pm 0.52 \times 10^{-4}$	$2.18 \pm 0.17 \times 10^{-4}$
X_{NO^+}	$1.34 \pm 0.26 \times 10^{-4}$	$7.52 \pm 1.46 \times 10^{-5}$	$7.24 \pm 1.40 \times 10^{-5}$
X_{N}	$6.74 \pm 1.48 \times 10^{-2}$	$6.30 \pm 1.38 \times 10^{-2}$	$3.63 \pm 0.80 \times 10^{-2}$
X_{O}	$3.12 \pm 0.00 \times 10^{-1}$	$3.35 \pm 0.00 \times 10^{-1}$	$3.30 \pm 0.00 \times 10^{-1}$
X_{e^-}	$1.34 \pm 0.26 \times 10^{-4}$	$7.52 \pm 1.46 \times 10^{-5}$	$7.24 \pm 1.40 \times 10^{-5}$

[‡] Species with mole-fractions less than 1×10^{-6} at the nozzle entrance not shown.

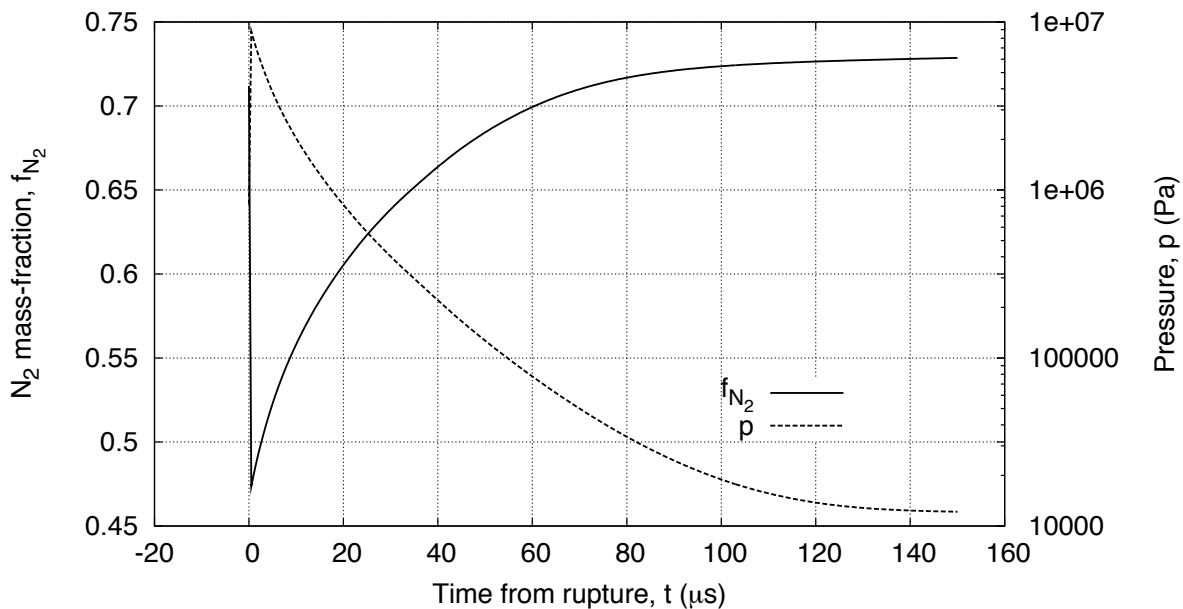


Figure 8.9: N₂ mass-fraction and pressure histories of a test gas packet originating just upstream of the secondary diaphragm for the 47 MJ/kg N₂-O₂ expansion tunnel condition.

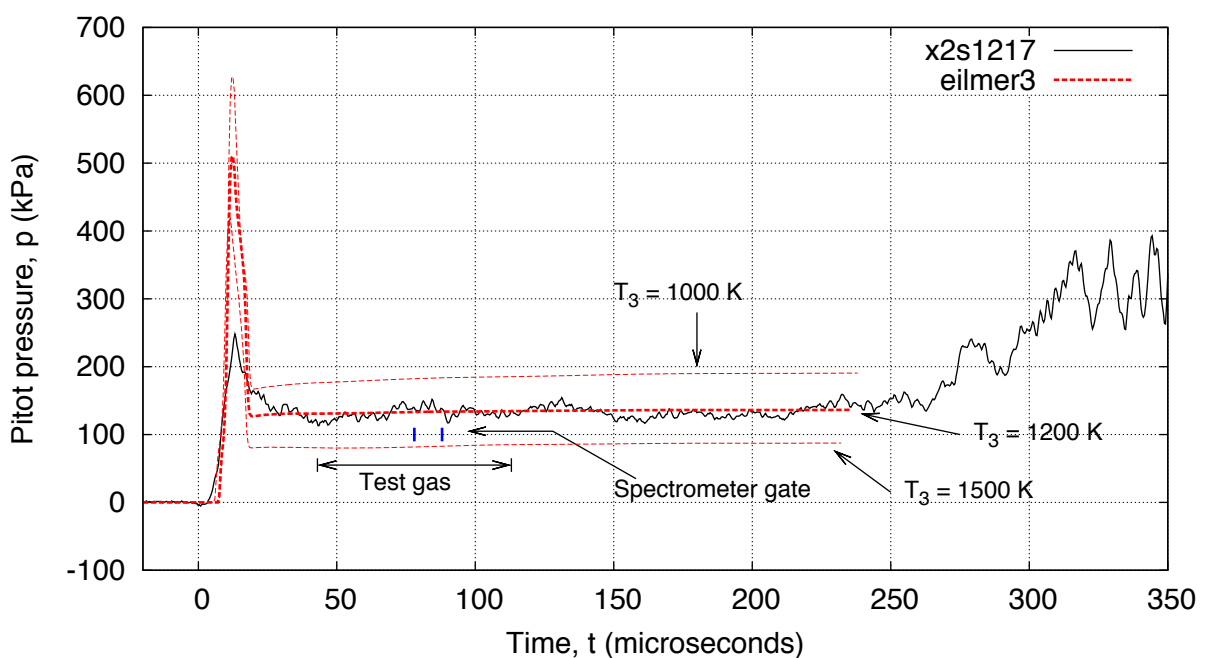


Figure 8.10: Comparison of measured and calculated centreline Pitot pressure level for the 47 MJ/kg N₂-O₂ condition.

forms off the boundary layer against the tube wall. This can be seen by comparing the viscous and inviscid density contour plots in Figure 8.11. In the viscous simulations, the conical shock that forms off the boundary layer converges to a point and dissipates approximately 200 mm upstream of the nozzle entrance, producing a new nozzle entrance condition. Centreline profiles of T_{tr} , T_{ve} , N_2 mass-fraction and density from the inviscid and viscous simulations at steady state conditions are presented in Figure 8.12. While the shock system momentarily increases both the translation-rotation temperature and density, both recover to the undisturbed inviscid levels 40 cm from the nozzle exit. Furthermore, T_{ve} and the N_2 mass-fraction are only perturbed by 1.2% and 0.2% in the vicinity of the shock system. The differences between the inviscid and viscous solutions towards the nozzle exit ($0.6 \leq x \leq 1.4$ m) are due to the large boundary layer growth in the viscous simulations, resulting in a lower expansion of the test gas than the inviscid solution. The inability of the inviscid simulations to capture this effect is the reason viscous simulations of the nozzle are required. Given that the nozzle entrance temperature T_3 in this modelling strategy is tuned to match the Pitot pressure for the condition, the slight disturbance caused by the shock system to the chemical and thermal state is tolerable. Furthermore, the variation in the measured shock speed and pressure levels leads to uncertainty in the freestream temperatures and total enthalpy of approximately 5%.

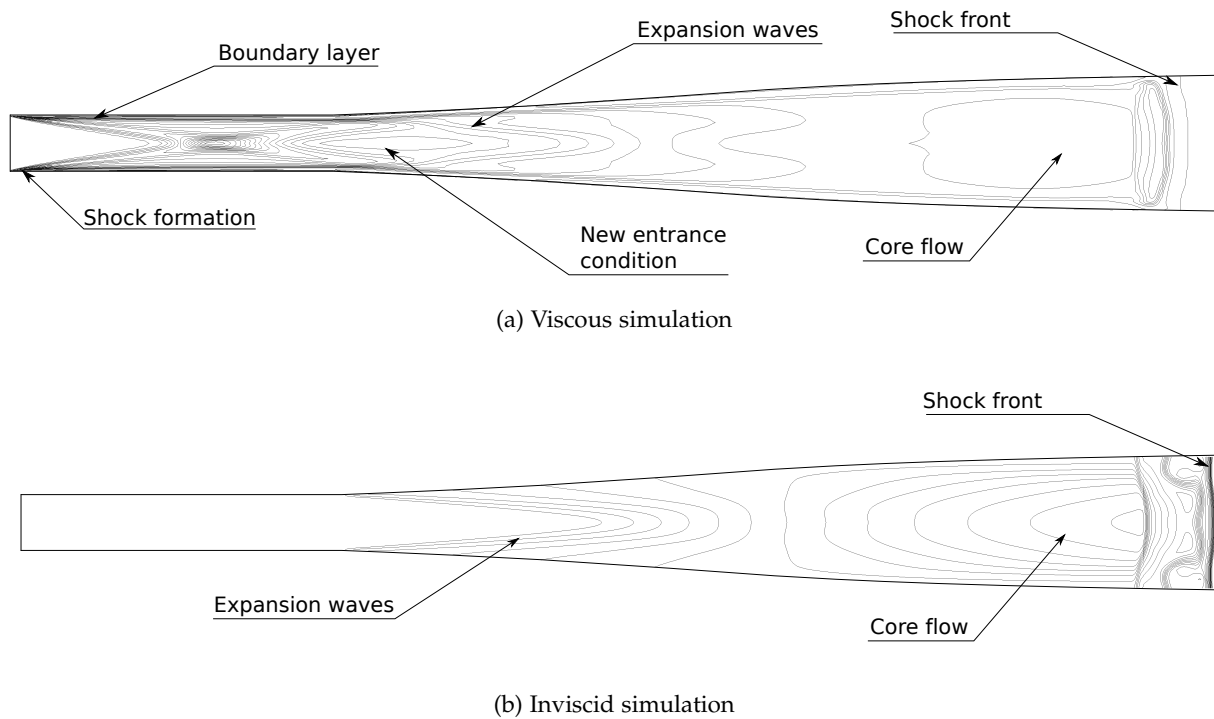


Figure 8.11: Density contours at $t = 220 \mu\text{s}$ from viscous and inviscid simulations of the X2 nozzle for the $47 \text{ MJ/kg N}_2\text{--O}_2$ condition.

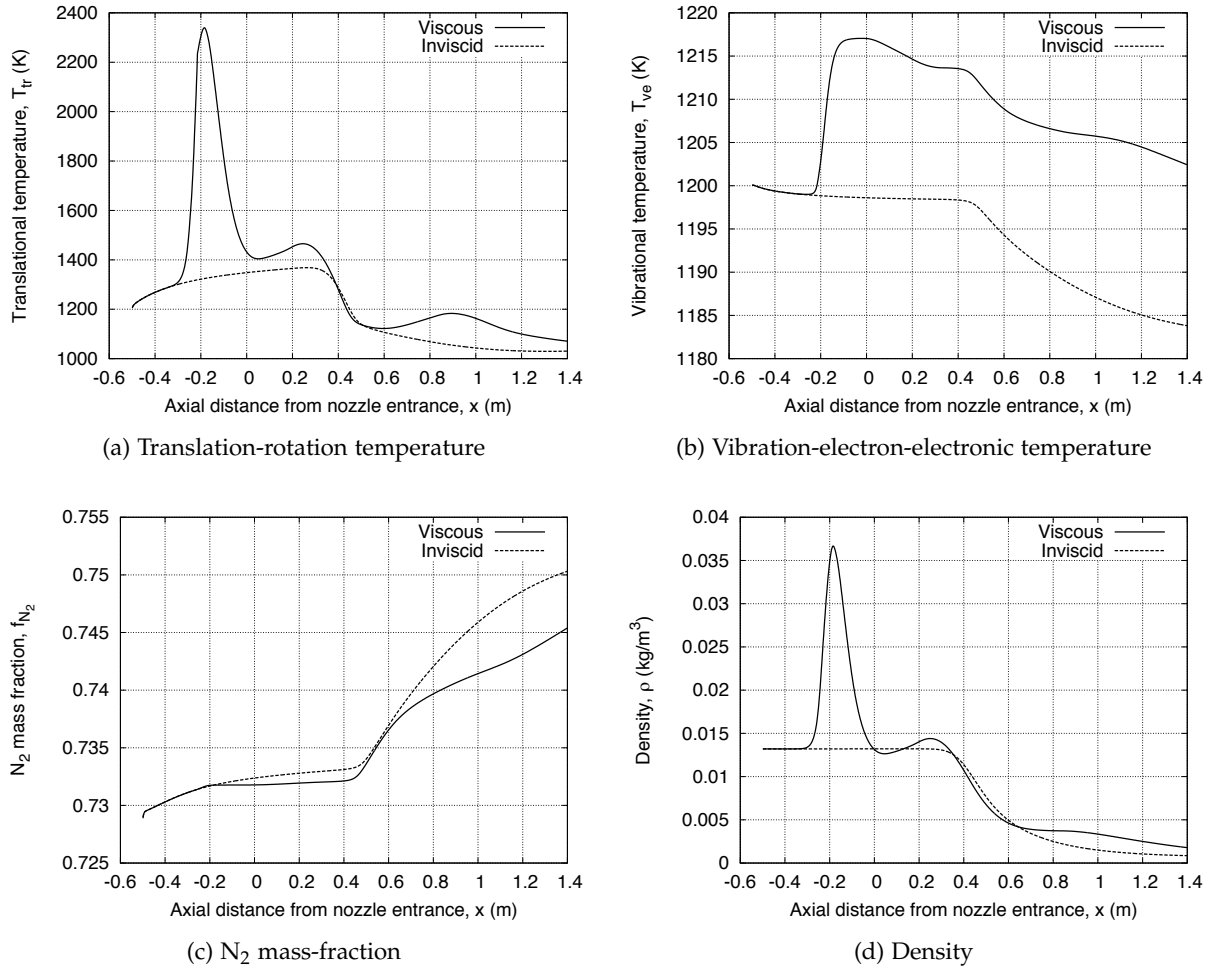


Figure 8.12: Comparison of centreline profiles from viscous and inviscid simulations of the X2 nozzle for the 47 MJ/kg N₂-O₂ condition.

8.3.3 Radiating shock layer simulations: subscale model

The freestream conditions averaged over the test-time presented in Table 8.2 are now applied to simulate the recompression of the test gas over the subscale Hayabusa model. Time accurate inviscid simulations are first presented with and without the wake region included to assess its influence on the solution and determine the time required for flow establishment. A grid resolution study for simulations restricted to the forebody region with the full Navier-Stokes equations is then performed. After determining an appropriate grid, radiatively coupled solutions are performed and comparisons with the spectral measurements from the experiments are presented. Finally, an investigation of the binary scaling hypothesis is undertaken via comparison with the flowfield predicted for an effective flight condition. Unless otherwise stated, the physical modelling is as presented in Table 5.2.

Inviscid simulations

The computational domain and grid for the inviscid simulations with and without the wake region are presented in Figures 8.13 and 8.14 respectively, where the grids are presented at one-half resolution for clarity. The forebody region for both simulations use the same 120×120 cell

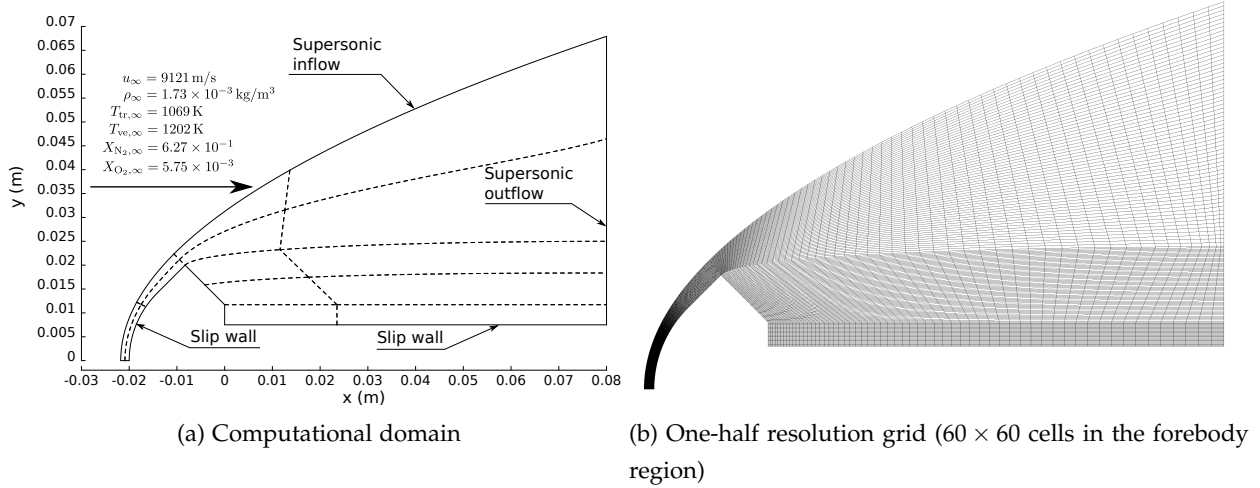


Figure 8.13: Computational domain and grid for inviscid simulations of the subscale Hayabusa model *with* the wake region include.

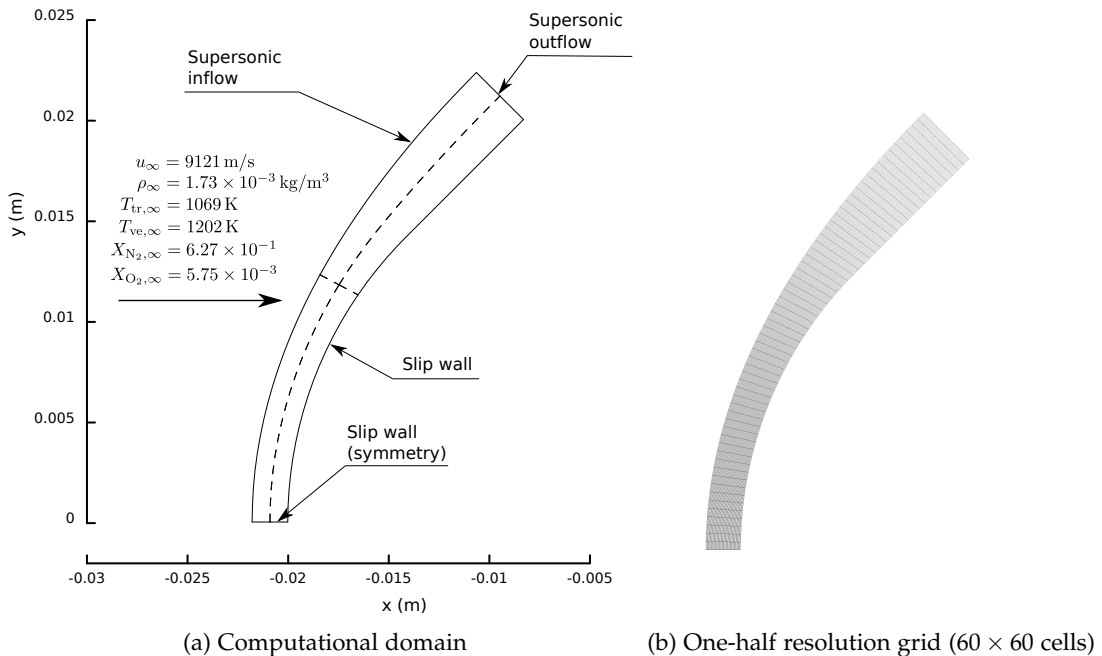


Figure 8.14: Computational domain and grid for inviscid simulations of the subscale Hayabusa model *without* the wake region include.

uniformly spaced grid. For the simulation with the wake region included, the grid is extended approximately 4 body lengths in the aft direction with a relatively crude mesh (120×120 cells) that is clustered towards the body in the axial direction. The computational domain for the simulation without the wake region included is terminated by an outflow boundary extended perpendicular to the forebody at the shoulder. Figures 8.15a and 8.15b present the maximum energy residuals as a function of time for the inviscid simulations with and without the wake region included. For the simulation with the wake region included, the recirculation region shown in Figure 8.16 prevents the residual from dropping below 1×10^{-3} , and an approximately constant level is achieved after $35 \mu\text{s}$ of flow. In contrast, the residual for the forebody simulation shows excellent convergence, dropping to 1×10^{-9} after over the 30 body lengths of flow simulated.

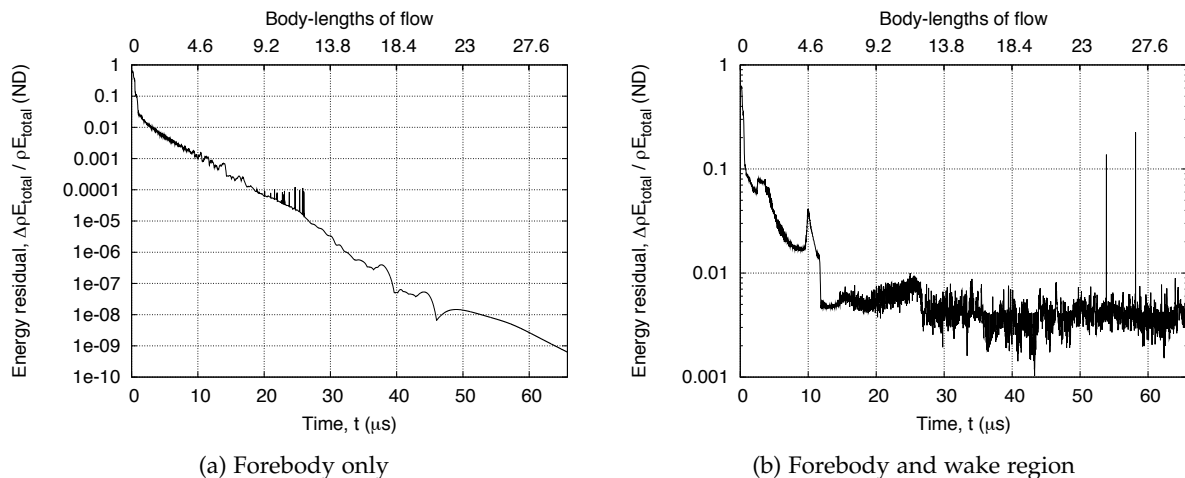


Figure 8.15: Maximum energy residuals as a function of time from inviscid simulations of the subscale Hayabusa model.

Figure 8.17 compares the shock detachment against time from the inviscid simulations with that measured in shot x2s1262. This shot had a secondary shock speed between AT4 and AT5 of $9021 \pm 230 \text{ m/s}$, which is very similar to shot x2s1217 ($9010 \pm 230 \text{ m/s}$) that was used to determine the freestream conditions. The transient experimental data is obtained by post-processing the location of the shock in luminosity images obtained by the high-speed camera. The measured data has an uncertainty of $\pm 0.16 \text{ mm}$ due to the relatively low number of pixels capturing the shock (e.g. approximately 8 during steady flow). The simulated shock standoff data has been shifted in time to approximately correspond to the arrival of the test gas at the model surface. The measured data exhibits a rapid increase in shock detachment over the first $25 \mu\text{s}$ of flow due to the shock heated air in-front of the test gas that is not modelled by the CFD. The simulations with and without the wake region included exhibit very similar trends, with a constant shock detachment of 1.33 mm being attained after $20 \mu\text{s}$ of flow. A similar establishment time is observed in the measured data, however the shock detachment distance at steady state is slightly higher at

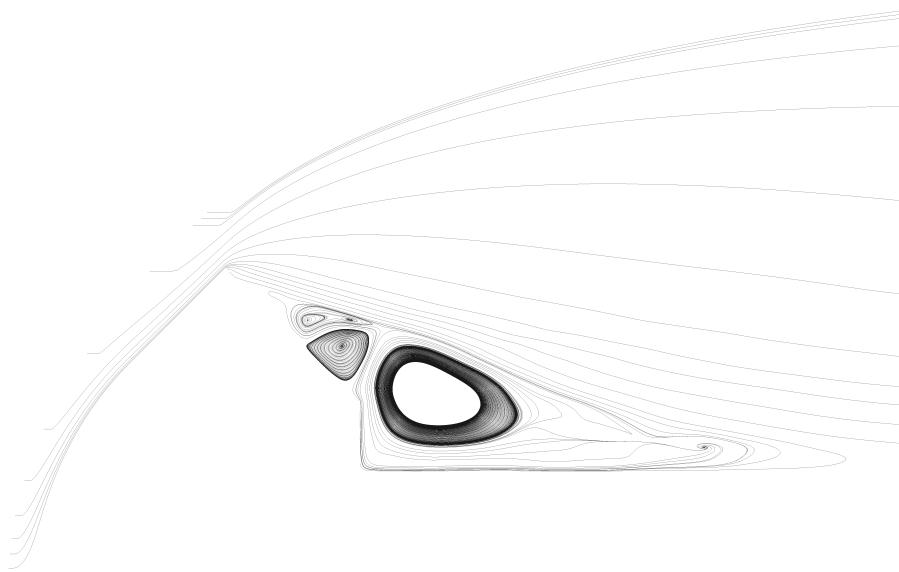


Figure 8.16: Velocity streamlines from inviscid simulation of the subscale Hayabusa model with aft region included after 30 body-lengths of flow.

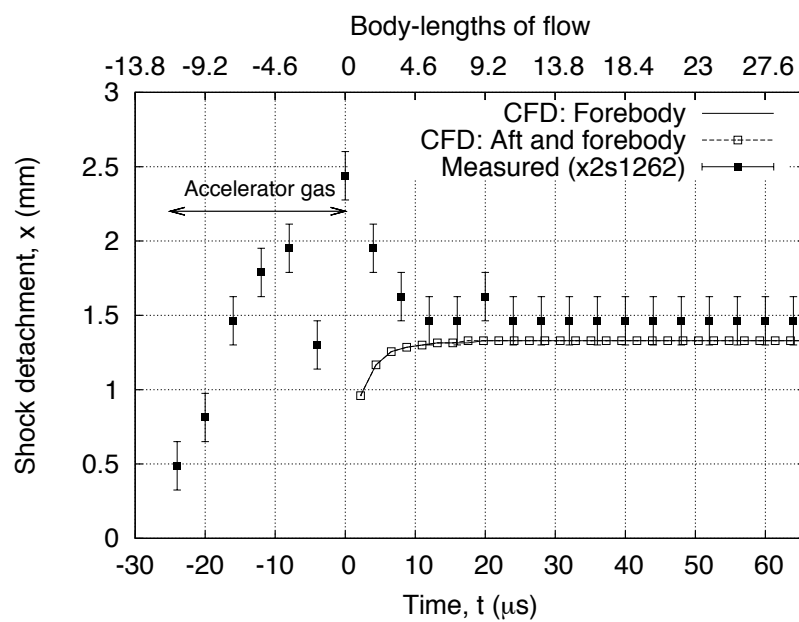


Figure 8.17: Comparison of shock detachment against time from inviscid simulations of the subscale Hayabusa model with measured data.

1.46 ± 0.16 mm. These results indicate that the $40 \mu\text{s}$ of test gas that passes over the model prior to the spectroscopic measurements being taken (see Figure 8.8b) is sufficient for steady state conditions to be achieved.

Of additional concern is the effect of the supersonic outflow boundary on the shock layer for the simulations considering just the forebody. Figure 8.18 presents superimposed density contour plots after 30 body lengths of flow from the inviscid simulations in the forebody region. The contours in red denote the simulation without the aft region, and the contours in black denote the simulation with the aft region included. Terminating the computational domain at the forebody shoulder has only a very slight affect on the solution, and we can proceed with confidence to detailed simulations of the forebody region with the full Navier-Stokes equations.

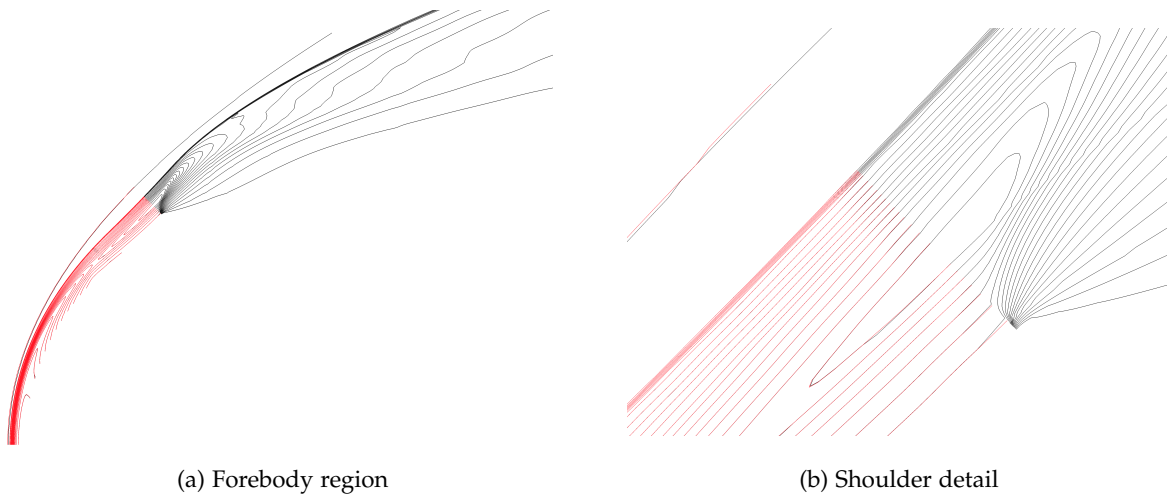


Figure 8.18: Density contour plots after 30 body lengths of flow from the inviscid simulations of the subscale Hayabusa model. The contours in red denote the simulation without the aft region, and the contours in black denote the simulation with the aft region included.

Viscous simulations

For the calculation of the radiative emission from the shock layer with the full Navier-Stokes equations, the computational domain is restricted to the forebody only to reduce the computational expense of the simulations. The computational domain and moderate resolution 60×60 cell grid are presented in Figures 8.19a and 8.19b respectively. Due to the short duration the surface is exposed to the shock heated air and test gas flow prior to the spectroscopic measurements ($\approx 75 \mu\text{s}$), the model surface is essentially adiabatic and a fixed temperature of 296 K is applied. As metallic surfaces are known to be strong catalysts for reactions, a super catalytic boundary condition is also applied that forces the species concentrations to that of room temperature air. The grid is only clustered weakly towards the wall as here we are interested in capturing the whole shock layer, rather than capturing the boundary layer to a high degree of accuracy.

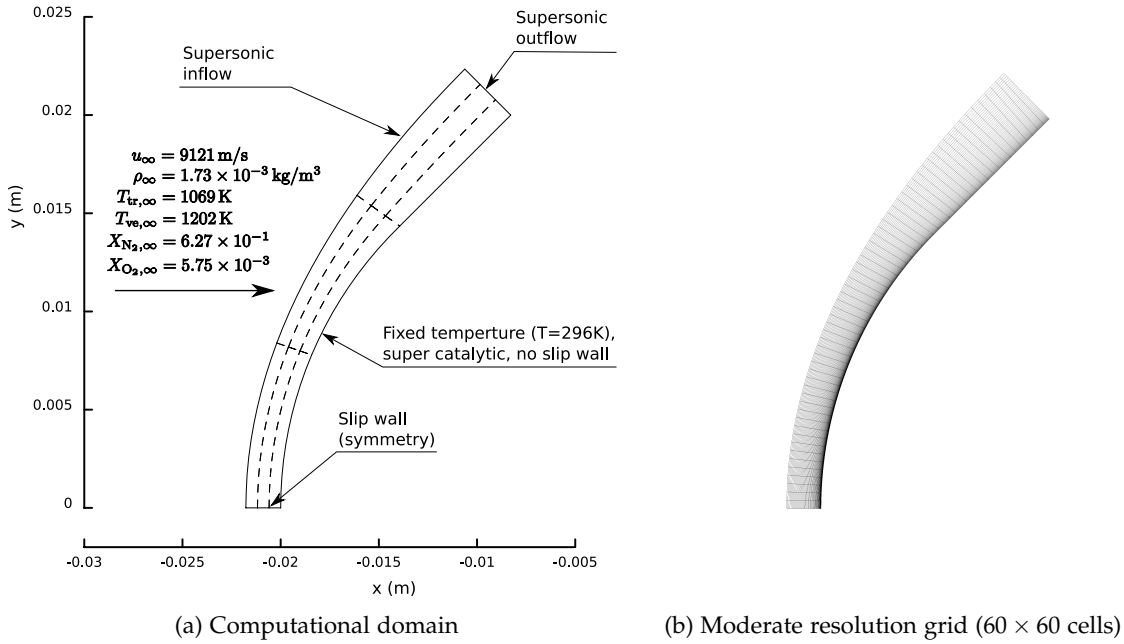


Figure 8.19: Computational domain and grid for viscous simulations of the subscale Hayabusa model forebody.

The viscous simulations are initialised by a converged (30 body lengths of flow) inviscid solution obtained on a coarse 30×30 cell grid to avoid numerical difficulties encountered when attempting to model viscous effects during the flow establishment period. Although this is not ideal (as the viscous simulation cannot be correlated temporally with the experiment), the inviscid simulations presented in the previous section demonstrated that the flow over the model is well established by the time the spectroscopic measurements are obtained. The viscous effects are added to the solution in an incremental fashion with $N_{\text{incr.}} = 1 \times 10^4$ to aid stability as described in § 7.2.3. The initial viscous simulations without radiation-flowfield coupling are run for 10 body lengths of flow; the maximum total energy and mass residuals for a viscous simulation performed on the moderate resolution 60×60 grid are presented in Figures 8.20a and 8.20b. Good convergence is achieved in this period with the residuals dropping by over three orders of magnitude.

Grid resolution study To assess the influence of the grid on the solution, viscous simulations without radiation-flowfield coupling were first performed on 30×30 , 60×60 , 90×90 and 120×120 cell grids. Figures 8.21a and 8.21b compare the translation-rotation temperature profiles and electron number density profiles along the stagnation streamline for these four grids. The most sensitive features to grid resolution are the location of the shock front, the peak in T_{tr} and the peak in the electron number density. The 60×60 cell grid shows reasonable agreement with the higher resolution grids and represents a good comprise between computational efficiency

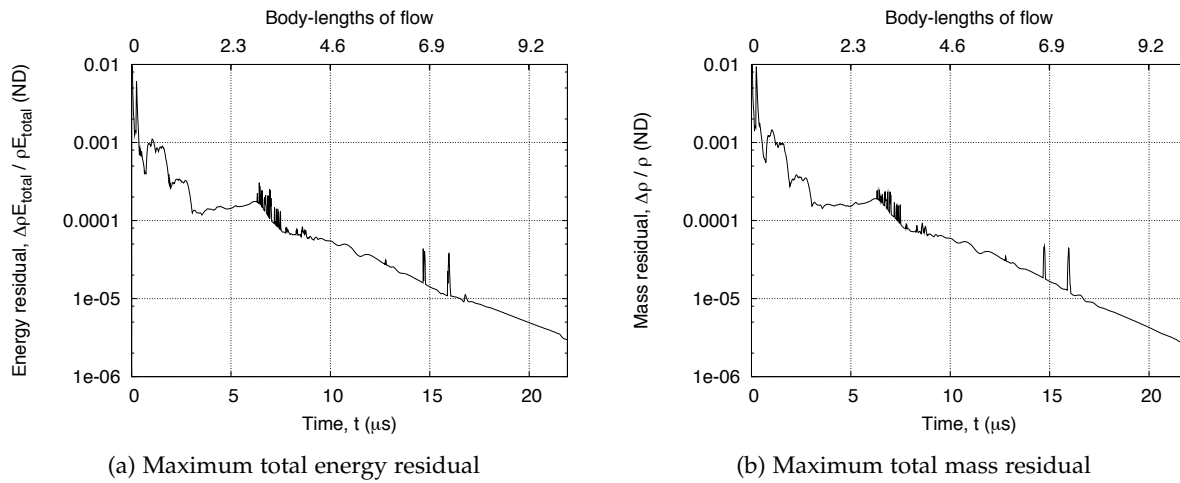


Figure 8.20: Maximum total energy and mass residuals as a function of time from viscous simulations of the subscale Hayabusa model on a 60×60 cell grid.

and accuracy, and therefore will be used in the subsequent analyses.

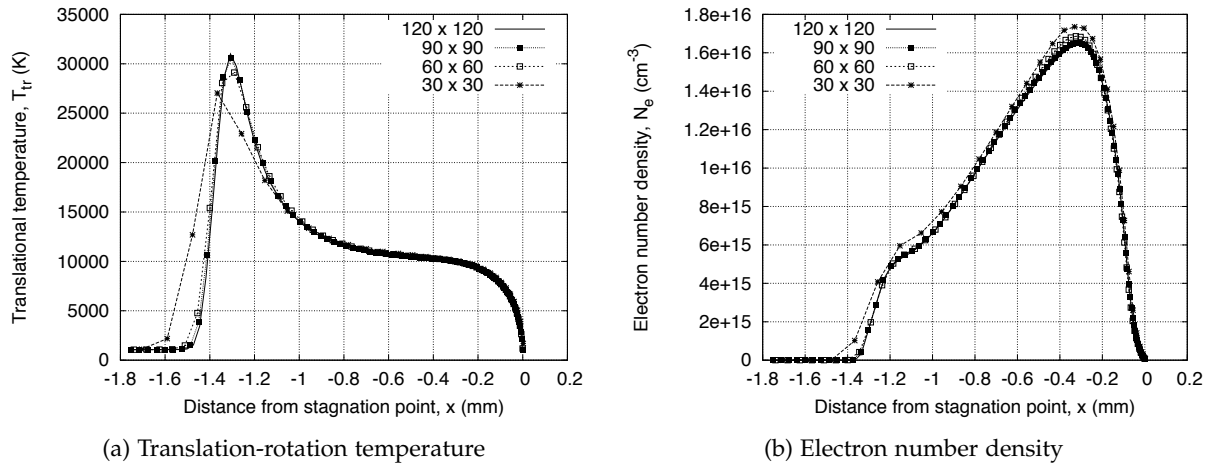


Figure 8.21: Stagnation streamline profiles from viscous simulations of the subscale Hayabusa model with various grid resolutions.

Radiation-flowfield coupling Prior to comparing with the experimental measurements it is necessary to assess the influence of radiation-flowfield coupling on the solution. Figure 8.22 compares the *uncoupled* radiative divergence profiles from various tangent-slab calculations ('TS') and an optically thin solution ('OT'). Tangent-slab calculations were performed with equilibrium ('Boltz.') and nonequilibrium ('QSS') electronic level populations, where nonequilibrium calculations were performed for both optically thick ($\Lambda = 0$) and optically thin ($\Lambda = 1$) radiative

transitions. The radiators considered are N_2^+ , N_2 , N , N^+ , O , O^+ and e^- , and the spectral range considered is $50 \leq \lambda \leq 1200\text{ nm}$. The nonequilibrium solutions with optically thin and thick radiative transitions are essentially the same, and the peak magnitude of the equilibrium solution is only greater by 30%. This indicates the populating of electronic levels is collision dominated and that the degree of nonequilibrium is low for this condition. Flowfield reabsorption is strong in the middle region of the shock layer as indicated by the overestimation of the divergence magnitude by the optically thin solution. The radiative flux incident at the stagnation point is 41.4 W/cm^2 for the nonequilibrium tangent-slab solution with optically thin transitions, corresponding to a Gouliard number of 1.26×10^{-3} , less than the 0.01 threshold that indicates significant radiation-flowfield coupling. Nevertheless the tangent-slab calculations show slight reabsorption at the very front of the shock layer ($x \approx -1.3\text{ mm}$), near optically thin radiative cooling in the first 0.1 mm behind the shock ($x \approx -1.2\text{ mm}$) and reabsorption in the boundary layer ($x \approx -0.02\text{ mm}$) that may affect the solution.

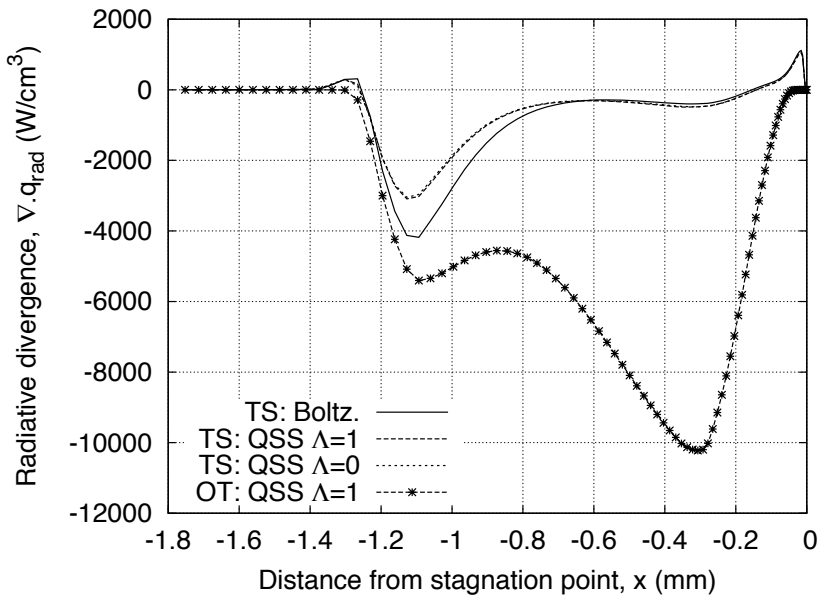


Figure 8.22: Comparison of uncoupled radiative divergence profiles along the stagnation streamline for the subscale Hayabusa model.

Due to the shape of the Hayabusa forebody, the tangent-slab equations should provide a reasonable approximation to the radiative divergence field. This is confirmed by the comparison of uncoupled tangent-slab and ray-traced radiative divergence profiles in Figure 8.23. The ray-traced solution was obtained using 128 rays per cell. The two models show excellent agreement for the profiles corresponding to cells in row 0 (stagnation streamline) and 30 (half-way up the grid). The tangent-slab calculation is much more efficient, however, taking just 5 minutes to run on 16 CPU's compared to 3 hours for the ray-traced solution on the same hardware.

Radiatively coupled simulations using the tangent-slab equations are therefore performed.

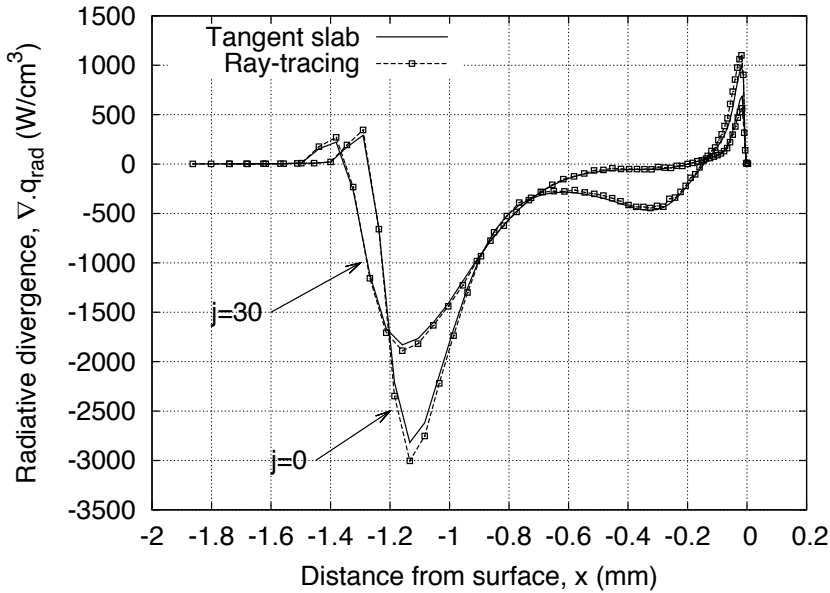


Figure 8.23: Comparison of radiative divergence profiles from *uncoupled* tangent-slab and ray-tracing calculations of the subscale Hayabusa model.

The loosely coupled strategy shown in Equation 7.44 was implemented, where the radiative divergence was updated every 10 time-steps for the first body-length of flow, and every 100 time-steps for the remainder. The uncoupled solution was used as the initial flowfield and a converged solution was obtained after 2 body-lengths of flow, Figure 8.24a. Figure 8.24b presents a comparison of the stagnation streamline T_{tr} and T_{ve} profiles with and without radiation-flowfield

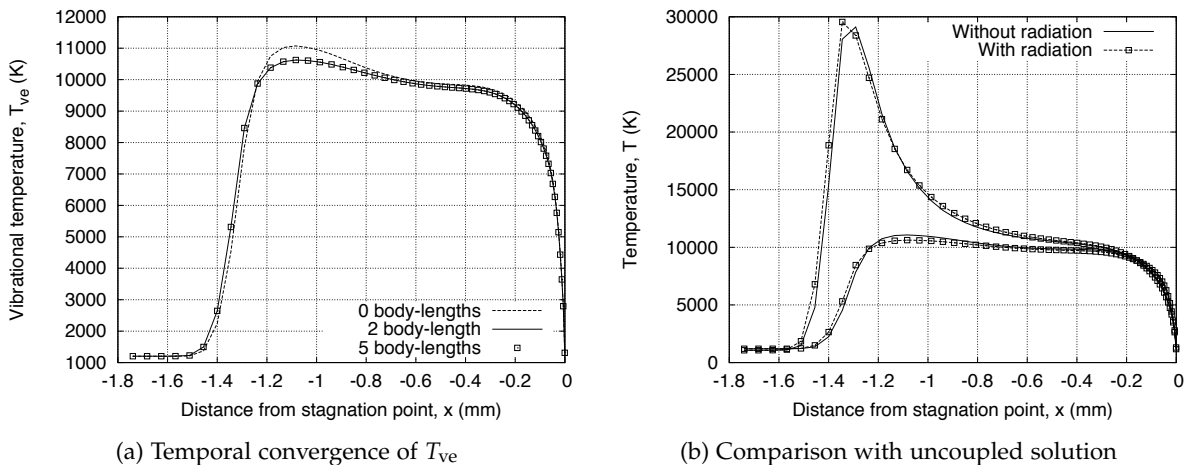
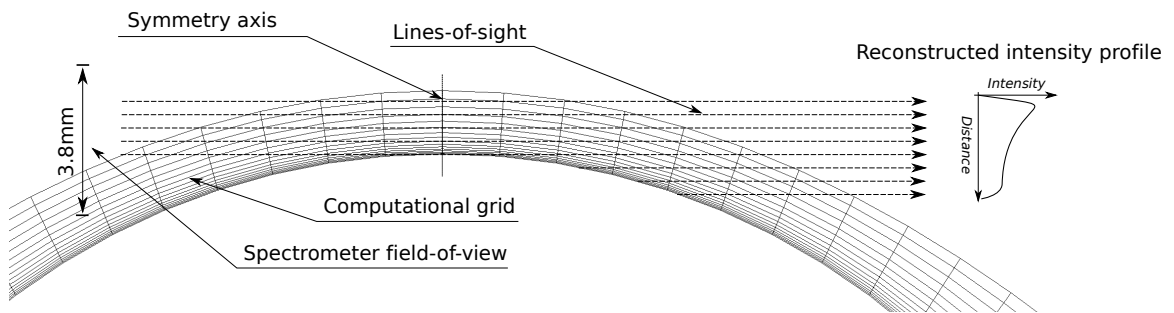


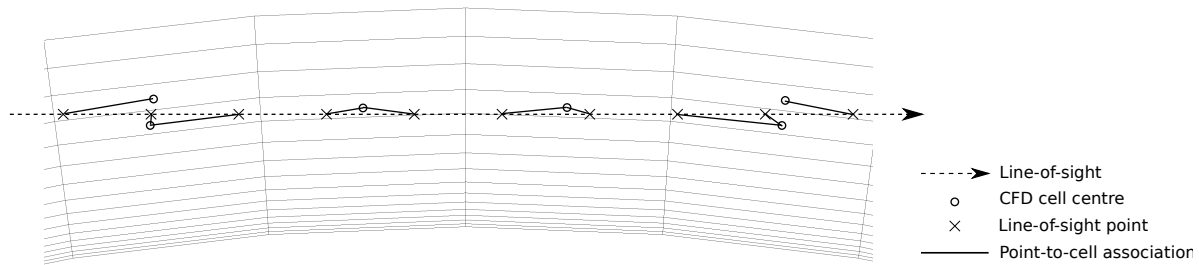
Figure 8.24: Temperature profiles along the stagnation streamline from simulations of the subscale Hayabusa model with radiation-flowfield coupling.

coupling. The effect of radiation-flowfield coupling is to slightly increase the shock detachment and lower the peak in T_{ve} . While the increase in shock detachment may seem counterintuitive for a radiatively coupled simulation, it can be explained by the heating of the shock front due to the reabsorption noted in Figure 8.22 and the generally low level of net emission preventing significant radiative cooling. The reabsorption in the boundary layer has minimal effect on the solution due to the higher density in this region.

Comparison with measured spectra Due to the reduction in T_{ve} when radiation-flowfield coupling is considered and the strong dependence of radiation on this temperature, the radiatively coupled solution is to be used for the comparison with the spectral measurements. We recall that the spectral measurements were made along the stagnation streamline as illustrated in Figure 8.7. Figures 8.25a and 8.25b illustrate the extraction of lines-of-sight from the axisymmetric computational grid for comparison with the measurements. The computational domain is firstly reflected in the symmetry axis, and then lines-of-sight are traced through the grid with uniform spacing in the axial direction. Evenly spaced points along each line-of-sight are then created and associated with the cell centre properties of the cell they are located in. An improvement of this technique would be to interpolate the flow state at each line-of-sight point, however the



(a) Generation of optical lines-of-sight



(b) Associating CFD cell centre to line-of-sight points

Figure 8.25: Reconstruction of an intensity profile from the axisymmetric computational domain for comparison with the subscale Hayabusa spectral measurements.

association method implemented here proved adequate. The intensity profiles are then able to be reconstructed by solving for the radiative intensity along each line-of-sight:

$$I_\nu(s + \Delta s) = I_\nu(s) e^{-\kappa_\nu \Delta s} + S_\nu \left(1 - e^{-\kappa_\nu \Delta s}\right) \quad (8.4)$$

where the radiative source function S_ν is j_ν / κ_ν and the gas-state is assumed constant over the spatial increment Δs .

Spectroscopic data from two different shots is used for the comparison, as summarised in Table 8.3. While the secondary shock speed for shot x2s1258 is very similar to that for Pitot shot x2s1217 used in determining the freestream conditions, the secondary shock speed for shot x2s1259 is 5.6% lower. Unfortunately, the IR spectrometer data from shot x2s1258 is unusable as an optical filter was not used, and the resultant spectra was contaminated by second order effects. Therefore the IR comparisons must use the x2s1259 data, where the anomalous shock speed brings the validity of the freestream conditions into question.

Table 8.3: Summary of shots with spectroscopic measurements used for comparison with the subscale Hayabusa simulations.

Shot	Secondary shock speed, $U_{s,2}$ (m/s)	Test section	Spectrometers	
			UV	IR
x2s1217	9010 ± 230	Pitot rake	-	-
x2s1258	8948 ± 223	Steel model	$210 \leq \lambda \leq 638 \text{ nm}$	$570 \leq \lambda \leq 874 \text{ nm}^\dagger$
x2s1259	8498 ± 202	Steel model	$210 \leq \lambda \leq 638 \text{ nm}$	$570 \leq \lambda \leq 874 \text{ nm}$

[†] Data unusable due to absence of optical filter

Figure 8.26 compares the measured and calculated ultraviolet intensity profiles, integrated over the $233 \leq \lambda \leq 638 \text{ nm}$ wavelength range. The profiles are positioned such that the location of the stagnation point corresponds to $x = 0 \text{ mm}$. This is clearly marked in the calculated profiles by a sudden drop in the intensity, which is also apparent in the measured data but the drop occurs over a distance of 0.3 mm. This gradual change is due to the finite depth-of-field limiting the focusing ability of the spectrometer. Given that the sharp rise in intensity behind shock is likely to be smeared over a similar distance, the shock detachment at the stagnation point is in reasonable agreement. The calculated intensity in the middle of the shock layer, however, is approximately 4 times larger in magnitude than the measured data. Also the peak intensity for shot x2s1258 is approximately 20% higher than for shot x2s1259 which has the 5.6% lower shock speed. Comparisons of the measured and calculated peak ultraviolet intensity spectra are presented in Figures 8.27a and 8.27b. The peak in the calculated intensity occurs at $x = -1.05 \text{ mm}$, and the peak in the measured intensity occurs at $x = -0.80 \text{ mm}$ for shot x2s1258 and $x = -0.86 \text{ mm}$ for shot x2s1259. The dominant feature in the calculated spectra is the N₂⁺ First Negative system, whereas the CN Violet system dominates both the measured spectra. The

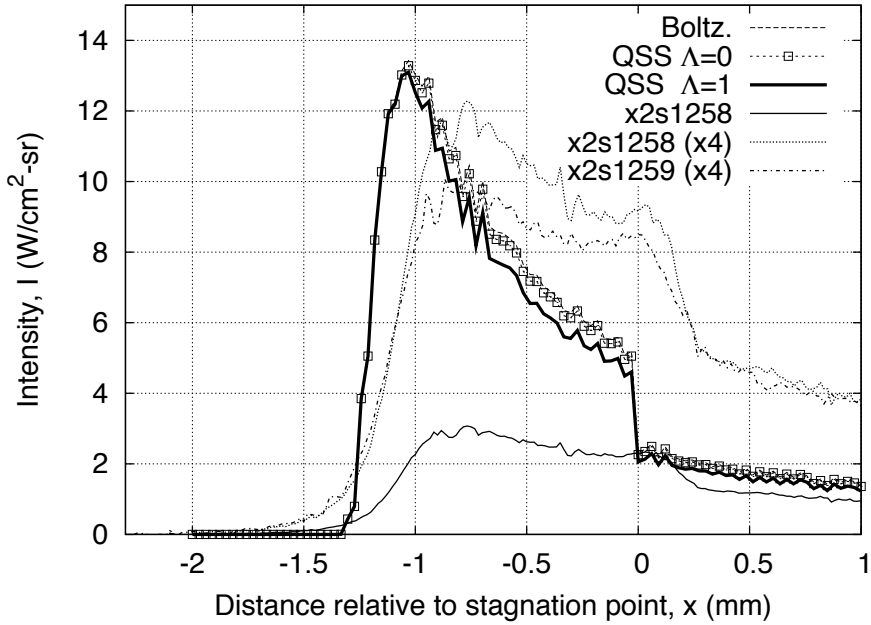


Figure 8.26: Comparison of measured and calculated ultraviolet ($233 \leq \lambda \leq 638$ nm) intensity profiles along the symmetry plane of the subscale Hayabusa model.

closer comparison of the $300 \leq \lambda \leq 450$ nm spectral range in Figure 8.27b clearly demonstrates that the N_2^+ First Negative system is absent from both sets of measured spectra. While the presence of the CN Violet system can be attributed to carbon contamination in the experiment, the absence of the N_2^+ First Negative in the measured data is more difficult to explain. Possible reasons for this discrepancy are:

1. the measured spectra are incorrectly calibrated, and the CN Violet emission is much stronger than shown, therefore saturating out the N_2^+ First Negative system,
2. the implemented physical models are not appropriate for these binary scaled conditions, resulting in an erroneously high N_2^+ First Negative system signal in the calculated results, or
3. the freestream conditions are incorrect, resulting in an erroneously high N_2^+ First Negative system signal in the calculated results.

Following the parametric study of the shock layer radiation resulting from variations in the freestream conditions presented in Appendix F, however, the first of these appears the most likely explanation.

Figures 8.28a and 8.28b compare the measured and calculated infrared intensity profiles for N and O lines respectively. The spectral ranges considered by Figure 8.28a are $700 \leq \lambda \leq 760$ nm, $800 \leq \lambda \leq 830$ nm and $850 \leq \lambda \leq 880$ nm, and those considered by Figure 8.28b are $760 \leq \lambda \leq$

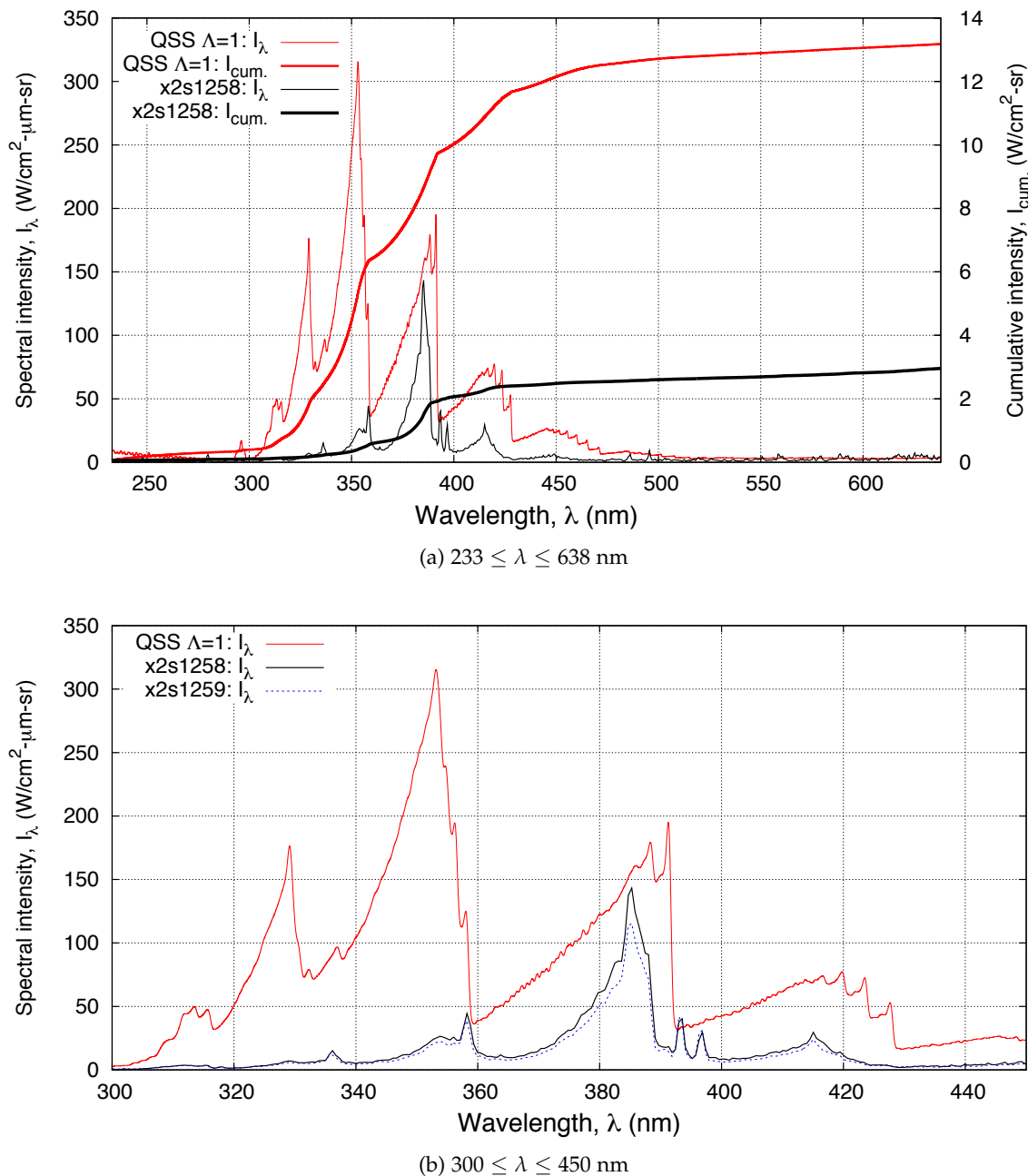
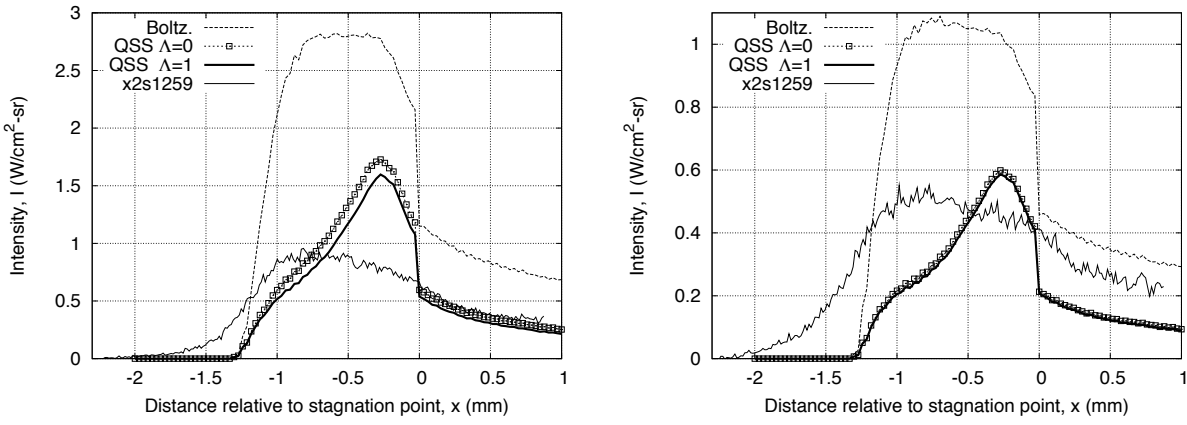


Figure 8.27: Comparison of measured and calculated peak ultraviolet intensity spectra along the symmetry plane of the subscale Hayabusa model (Calculated: $x = -1.05$ mm, x2s1258: $x = -0.80$ mm, x2s1259: $x = -0.86$ mm).



(a) N lines ($700 \leq \lambda \leq 760$ nm, $800 \leq \lambda \leq 830$ nm and $850 \leq \lambda \leq 880$ nm)
(b) O lines ($760 \leq \lambda \leq 800$ nm and $830 \leq \lambda \leq 850$ nm)

Figure 8.28: Comparison of measured (x2s1259) and calculated infrared intensity profiles along the symmetry plane of the subscale Hayabusa model.

800 nm and $830 \leq \lambda \leq 850$ nm. Again the profiles are positioned such that the location of the stagnation point corresponds to $x = 0$ mm, however the drop in intensity is difficult to discern in the measured data. This is in contrast to the ultraviolet spectra where the drop is clearly visible, and indicates the infrared spectrometer is not as well focused on the model as the ultraviolet spectrometer. As a consequence the rise in intensity behind the shock is likely to be steeper than it appears in the measurements. The calculation with Boltzmann radiation overestimates the nonequilibrium calculations by a factor of approximately two, indicating significant electronic nonequilibrium throughout the shock layer. Furthermore, the similarity of the optically thin and thick solutions indicates radiative depopulation of excited electronic states is weak. Figures 8.29a and 8.29b compare the measured and calculated infrared intensity profiles for N and O lines respectively, where a Gaussian convolution with half-width at half-maximum of 0.25 mm has been applied to the calculated profiles in an attempt to account for the finite depth-of-field. The convolution slightly improves the agreement with experiment. While the measured and calculated intensity levels are of a similar magnitude, the profiles exhibit considerably different spatial trends. The measured data exhibits a peak 0.9 mm from the stagnation point, whereas the calculated data peaks at just 0.3 mm from the body which corresponds to the peak electron number density as shown in Figure 8.21b. This discrepancy may indicate the chemical kinetics are not well described in the simulations; possible causes are incorrect freestream conditions, incorrect physical modelling, or both. Given the 33% reduction in calculated IR radiation 0.75 mm behind the shock due to a freestream velocity of 8.5 km/s instead of 9.1 km/s found in Appendix F, it is likely the anomalous secondary shock speed for shot x2s1259 is contributing somewhat to the

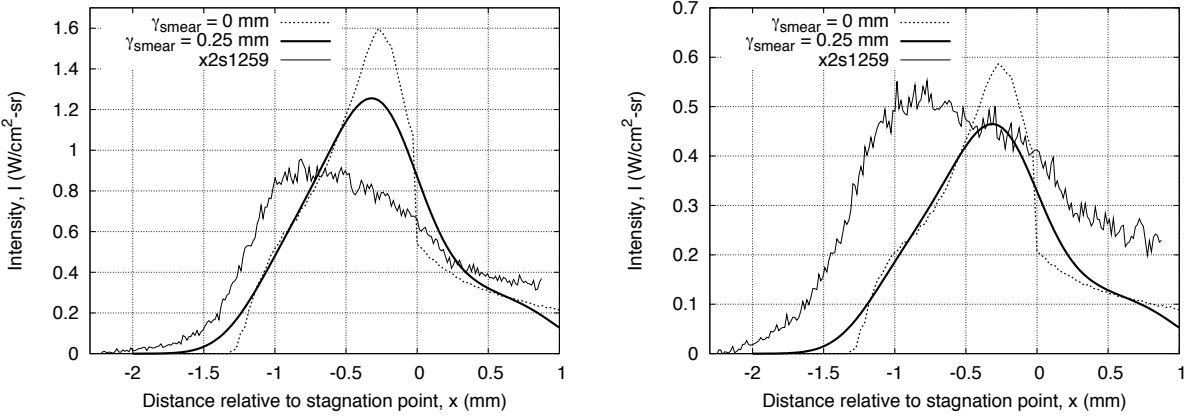


Figure 8.29: Comparison of measured and calculated infrared intensity profiles along the symmetry plane of the subscale Hayabusa model, where a Gaussian spatial convolution has been applied to the calculated profile. The calculated profiles correspond to ‘QSS $\Lambda = 1$ ’ from Figure 8.28.

discrepancies observed here. Also, the presence of carbon in the freestream may significantly alter the shock layer chemical kinetics. The poor spatial resolution of the experimental data makes the comparison difficult, however, and improved spectral measurements are required to draw definite conclusions.

A comparison of the measured and calculated peak infrared intensity spectra is presented in Figure 8.30. The calculated cumulative intensity overestimates the measured data by 80%. As was observed for the air shock tube conditions in § 6, the measured line profiles exhibit rapid broadening towards the base that is not captured in the calculations. Also a background continuum is observed in the measured data that contributes significantly to the total intensity.

8.3.4 Radiating shock layer simulations: effective flight condition

Using the binary scaling hypothesis, effective flight conditions for the subscale Hayabusa experiment can be derived from the following relations:

$$(\rho_\infty L)_{\text{exp.}} = (\rho_\infty L)_{\text{flight}} \quad (8.5)$$

$$H_{\text{total,exp.}} = H_{\text{total,flight.}} \quad (8.6)$$

Table 8.4 summarises the effective flight conditions for the experiments with the subscale Hayabusa model. Due to the thermochemical excitation of the freestream in the expansion tunnel experiments, the effective flight velocity is 5% faster than the 9.1 km/s estimated for the

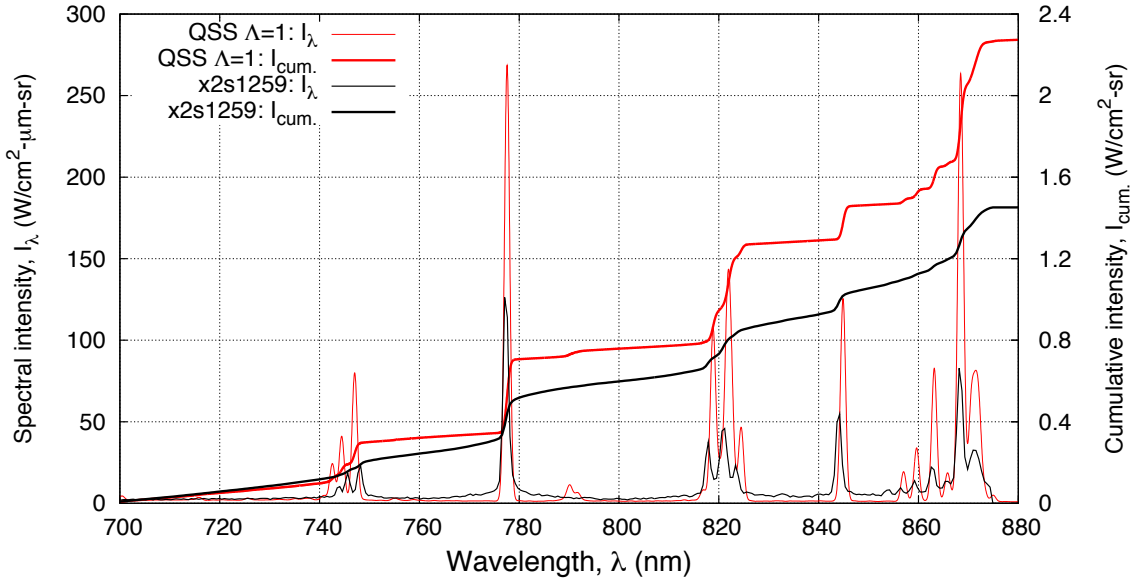


Figure 8.30: Comparison of measured and calculated peak infrared intensity spectra along the symmetry plane of the subscale Hayabusa model (CFD: $x = -0.3$ mm, x2s1259: $x = -0.9$ mm).

experiment. The actual peak heating condition for the Hayabusa probe was predicted to occur at an altitude of 60 km and velocity of 10.5 km/s [211], 5 km lower in altitude and 0.8 km/s higher in velocity than for the experiment effective flight condition. Nevertheless the condition at hand is still relevant as it is representative of a trajectory point just after peak-heating for a less energetic entry such as lunar return. Also, it is very similar in pressure and velocity to EAST shot 46/02 (13.3 Pa and 9.89 km/s) that was analysed in the shock tube mode in § 6.2.3. Using a radiative equilibrium wall boundary condition, simulations with radiation-flowfield coupling predicted a wall temperature of approximately 2,300 K at the stagnation point. This is substantially higher than the 296 K wall temperature in the subscale experiments, and therefore some differences are expected in the boundary layer region.

Table 8.4: Effective flight conditions for the Hayabusa expansion tunnel experiments.

Altitude (km)	65
Density, ρ_∞ (kg/m ³)	1.73×10^{-4}
Pressure, p_∞ (Pa)	11.5
Temperature, T_∞ (K)	230
Velocity, u_∞ (m/s)	9679
Wall temperature, T_w (K)	~ 2300
Nose radii, R_n (cm)	20

Simulation strategy

The simulation strategy for the effective flight condition is similar to that for the viscous simulations of the subscale model. Inviscid simulations on a coarse 30×30 cell grid are first performed and used as an initial condition for the viscous simulation without radiation, which is in turn used as an initial condition for a radiatively coupled simulation. The computational domain and 60×60 cell grid for the viscous simulations are presented in Figures 8.31a and 8.31b respectively. The grid is a 1:10 scaled copy of that used for the subscale model simulations. Radiative equilibrium and super catalytic boundary conditions are applied to the vehicle surface, where ϵ is set to 0.9 for the radiative equilibrium boundary condition. In an actual flight, however, the wall temperature will be lower than that predicted by the radiative equilibrium assumption due to ablation and in-depth heat penetration of the TPS, and the chemical reactions at the surface will occur at a finite rate. The implemented boundary condition therefore represents an upper bound on the heat-flux to the vehicle surface, although as diffusion is modelled via a constant Lewis number the diffusive heat transfer is likely to be underpredicted.

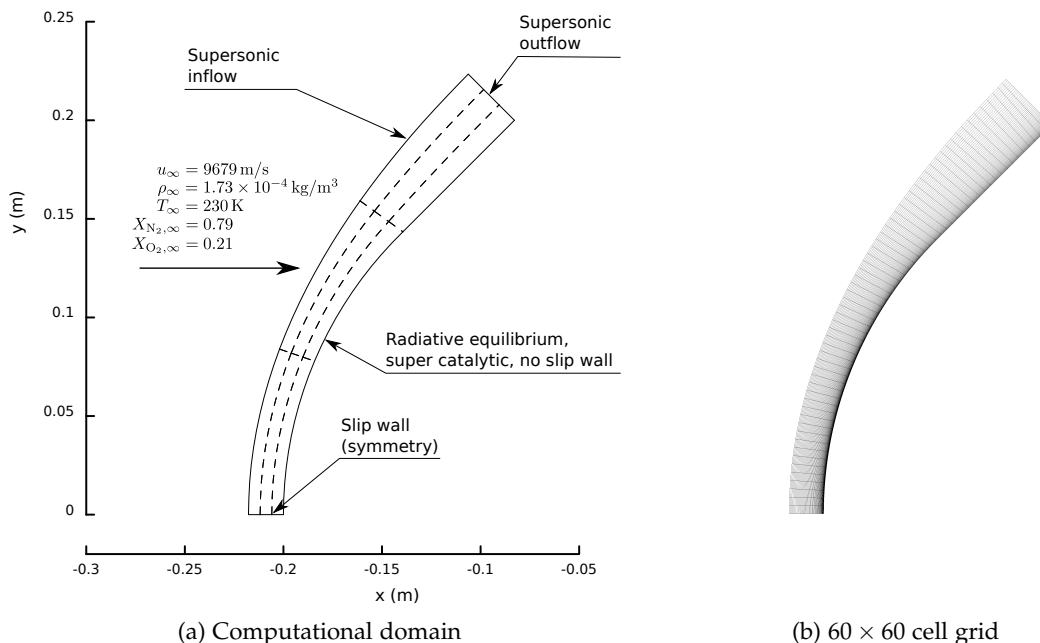


Figure 8.31: Computational domain and grid for viscous simulations of the Hayabusa forebody at effective flight conditions.

Results

Radiation-flowfield coupling Prior to comparing with the subscale solutions, it is useful to note the effect of radiation-flowfield coupling for the flight condition. Figure 8.32a illustrates the

temporal convergence of T_{ve} , and Figure 8.32b compares temperature profiles along the stagnation streamline from both radiatively uncoupled and coupled simulations. A converged solution is attained in 3 body-lengths, compared with 2 body-lengths for the subscale model. The effect of the radiation-flowfield coupling for the flight condition is qualitatively similar to what was observed for the subscale model, with the shock detachment increased and the peak in T_{ve} reduced. In this case the effect is more pronounced, however, with T_{ve} being reduced by 2,000 K at the peak compared with 500 K for the subscale model. As will be discussed, this disparity is due to the breakdown of binary scaling for flowfields with strong radiative coupling.

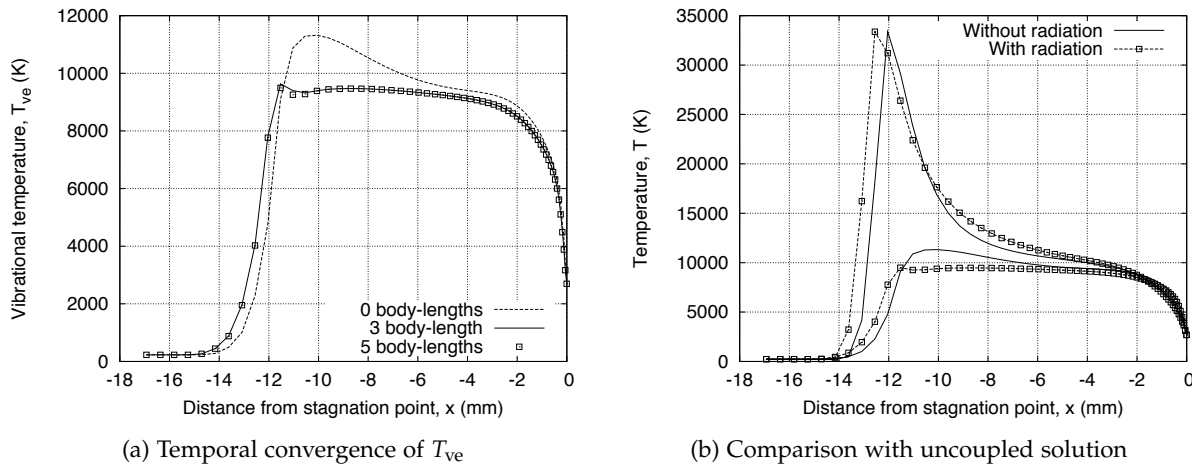


Figure 8.32: Temperature profiles along the stagnation streamline from radiatively coupled simulations of the Hayabusa probe at effective flight conditions.

Comparison with subscale solutions In the results that follow the flight and subscale flowfields are compared via appropriately scaled parameters to assess the degree to which the experiment is representative of flight conditions. In addition, a hypothetical ‘ideal subscale’ flowfield is also considered, where the thermochemical state of the freestream is the same as the flight condition (i.e. the flow produced by a perfect expansion tunnel that only adds kinetic energy and no thermal or chemical energy to the test gas). This hypothetical case allows the effect of a thermochemically excited freestream to be quantified.

Figures 8.33a to 8.33f compare stagnation streamline profiles from radiatively *uncoupled* flight, subscale and ideal subscale solutions. The axial distance x has been presented in the non-dimensional form x/R_n where R_n is the appropriate nose radii, while number density and radiative divergence are scaled by R_n to reflect that the scaling is based on the ρL parameter³. Also, the scaled electron number densities in Figure 8.33c and 8.33d have been multiplied by a factor

³ $N_i R_n \equiv \frac{1}{m_i} f_i(\rho R_n)$ and $\nabla \cdot \vec{q}_{\text{rad}} R_n \equiv -\bar{Q}_{\text{rad}}(\rho R_n)$ where $-\bar{Q}_{\text{rad}}$ is the radiative source term expressed in units of W/kg.

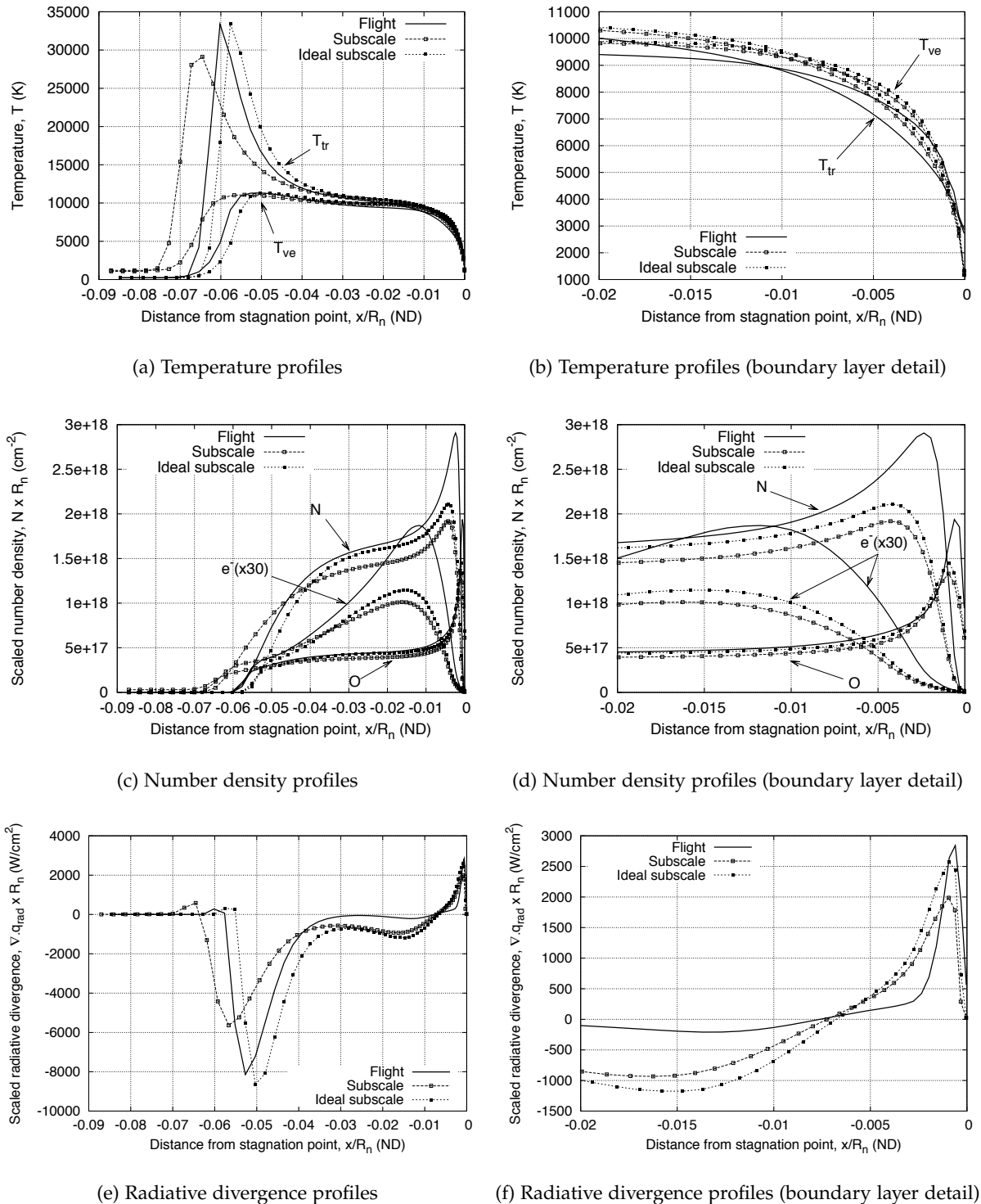


Figure 8.33: Flowfield property profiles along the stagnation streamline from effective flight, subscale and ideal subscale Hayabusa flowfields *without* radiation-flowfield coupling.

30 for clarity. While the temperature profiles in Figures 8.33a show reasonable agreement in the middle of the shock layer ($-0.05 \leq x/R_n \leq -0.02$), discrepancies exist at the shock front and in the boundary layer. The most noticeable difference is the $\sim 12.5\%$ larger shock standoff estimated for the the subscale case compared to the effective flight case. The cause of this disparity can be attributed to the thermochemically excited freestream generated by the expansion tunnel, as the ideal subscale case shows a shock standoff slightly less than the flight case. Although a larger shock standoff implies a lower average density through the shock layer, it is difficult to explain how the excited freestream gives rise to this due to the complexity of the chemical kinetic processes taking place. In the boundary layer, the N, O and e^- number density profiles begin to fall earlier in the subscale cases. This is due to the break-down of the binary scaling rationale in flows with strong three body reactions such dissociative and ionisational recombination. By scaling according to ρL binary reactions such as dissociation and electron impact ionisation are correctly scaled, while three body reactions are not. In addition, the temperatures in the subscale simulations exhibit much stronger gradients close to the wall due to the lower wall temperature of the model surface compared to the flight condition. This generates higher convective heat-flux to the surface for the subscale model. The scaled radiative divergence shown in Figures 8.33e and 8.33f is proportional to the radiative energy lost and gained on a per particle (or per mass) basis. While the peak radiative cooling level in the immediate post-shock region is closely matched by the ideal subscale case, it is underestimated in the subscale case. Also the flight condition shows close to zero net emission in the $-0.03 \leq x/R_n \leq -0.01$ range, while the subscale cases show substantial net emission. This may be due to the slight underestimation of the N, O and e^- scaled number density levels estimated in this region for the subscale case. Despite these differences, the scaled radiative divergence profiles are reasonably similar for the three cases. As will be shown in the comparison of the radiatively coupled solutions, however, matching the $\nabla \cdot \vec{q}_{\text{rad}} \times R_n$ product is not sufficient for achieving similarity in radiation-flowfield coupling.

Figures 8.34a to 8.34f compare stagnation streamline profiles from radiatively *coupled* flight, subscale and ideal subscale solutions using the tangent-slab equations. Where the T_{ve} profile after the nonequilibrium peak was in good agreement for all three cases without radiation coupling, the introduction of radiation coupling leads to substantial overprediction of the plateau in T_{ve} by the subscale cases. This is due to a greater radiative cooling effect for the flight case. Consider ‘non-dimensional’ cubes of length R_n for both the subscale and flight cases, filled with gas at the freestream density ρ_∞ . The flight cube is heavier than the subscale cube:

$$(R_n^3 \rho_\infty)_{\text{flight}} \gg (R_n^3 \rho_\infty)_{\text{exp.}} \quad (8.7)$$

Therefore although the uncoupled $\nabla \cdot \vec{q}_{\text{rad}} \times R_n$ products where shown to be reasonably similar in Figure 8.33e, the flight case will loose more energy per non-dimensional volume. The disparity in radiative-cooling is also reflected in the *coupled* scaled radiative divergence profiles

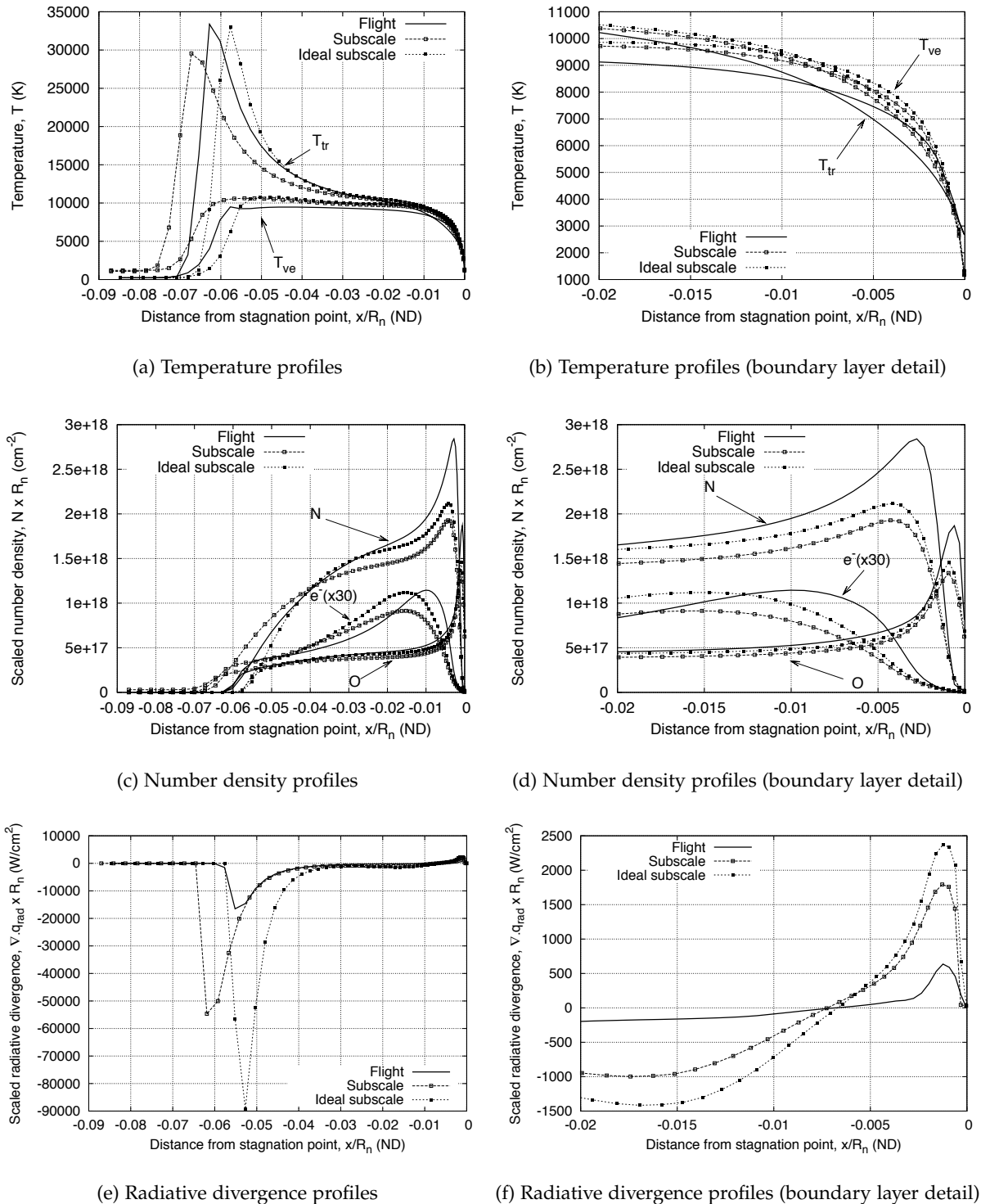


Figure 8.34: Flowfield property profiles along the stagnation streamline from effective flight, subscale and ideal subscale Hayabusa flowfields *with* radiation-flowfield coupling.

shown in Figures 8.34e and 8.34f, where $\nabla \cdot \vec{q}_{\text{rad}} \times R_n$ for the flight condition is now much lower than both subscale cases. Comparing Figures 8.33c and 8.34c, it is interesting to note that the disparity in radiative-cooling levels actually improves the agreement between the subscale and flight number density profiles; the larger radiative cooling effect for the flight case brings the N, O and e^- number densities down towards the subscale levels. Due to the overprediction of T_{ve} by the experiment, however, similitude between the subscale and flight radiative flux levels is not achieved. Figure 8.35a compares the radiative heat flux spectra incident at the stagnation point from radiatively *uncoupled* simulations of the subscale and effective flight Hayabusa flow-fields, while Figure 8.35b compares the flux spectra from radatively *coupled* simulations. For the uncoupled simulations, the flight and subscale spectral flux are in close agreement with the total radiative flux only differing by 8.6%. When radiative coupling is introduced, the flight total radiative flux is reduced by 80% due to the cooling effect while the subscale result is only reduced by 25%. Nevertheless, the subscale flux spectra is qualitatively similar to flight, with the largest contributions being due to the N_2 Birge-Hopfield I in the VUV region and the N_2^+ First Negative in the UV region. These molecular band systems dominate due to the strongly nonequilibrium shock layer (see Figure 8.34c) resulting in much higher N_2 and N_2^+ concentrations than would occur for a larger equilibrium shock layer. Merrifield and Fertig [222] and Lamet *et al.* [223, 224] also found large contributions from the N_2 VUV systems for the similar Fire II peak heating condition. The relevance of N_2 and N_2^+ radiation for Earth re-entry has also been confirmed experimentally by Yamada *et al.* [37], where significant emission from the N_2 Second Positive and N_2^+ First Negative systems were measured in shock tube experiments representative of the Hayabusa entry. Although no strong evidence of N_2 VUV emission was found in these experiments, the measurements only went down to 120 nm whereas the peak of the Birge-Hopfield I system in Figure 8.35b is at 105 nm. Finally, it should be noted that while the tangent-slab equations accurately reproduce the ray-traced radiative divergence field for this geometry (see Figure 8.23), the radiative heat flux is overestimated. This can be seen in the comparison of radiative heat-flux profiles along the forebody surface in Figure 8.36. Reducing the tangent-slab solution by a factor of 0.85 gives reasonable agreement with the ray-traced solution. Therefore the tangent-slab based flux spectra presented in Figures 8.35a and 8.35b are likely to overestimate the actual levels by approximately 18%.

Effect of surface catalyticity model A super catalytic boundary condition was implemented at the vehicle surface in the previous effective flight condition simulations for consistency with the subscale experiments, where the metallic surface is assumed to be strongly catalytic. As previously mentioned, in actual flight the chemical recombination at the vehicle surface proceeds at a finite rate. It is therefore useful at this point to compare simulations of the effective flight condition with a super catalytic and a non-catalytic vehicle surface, as these two models bound the full possible range of solutions obtainable with a finite-rate catalyticity model.

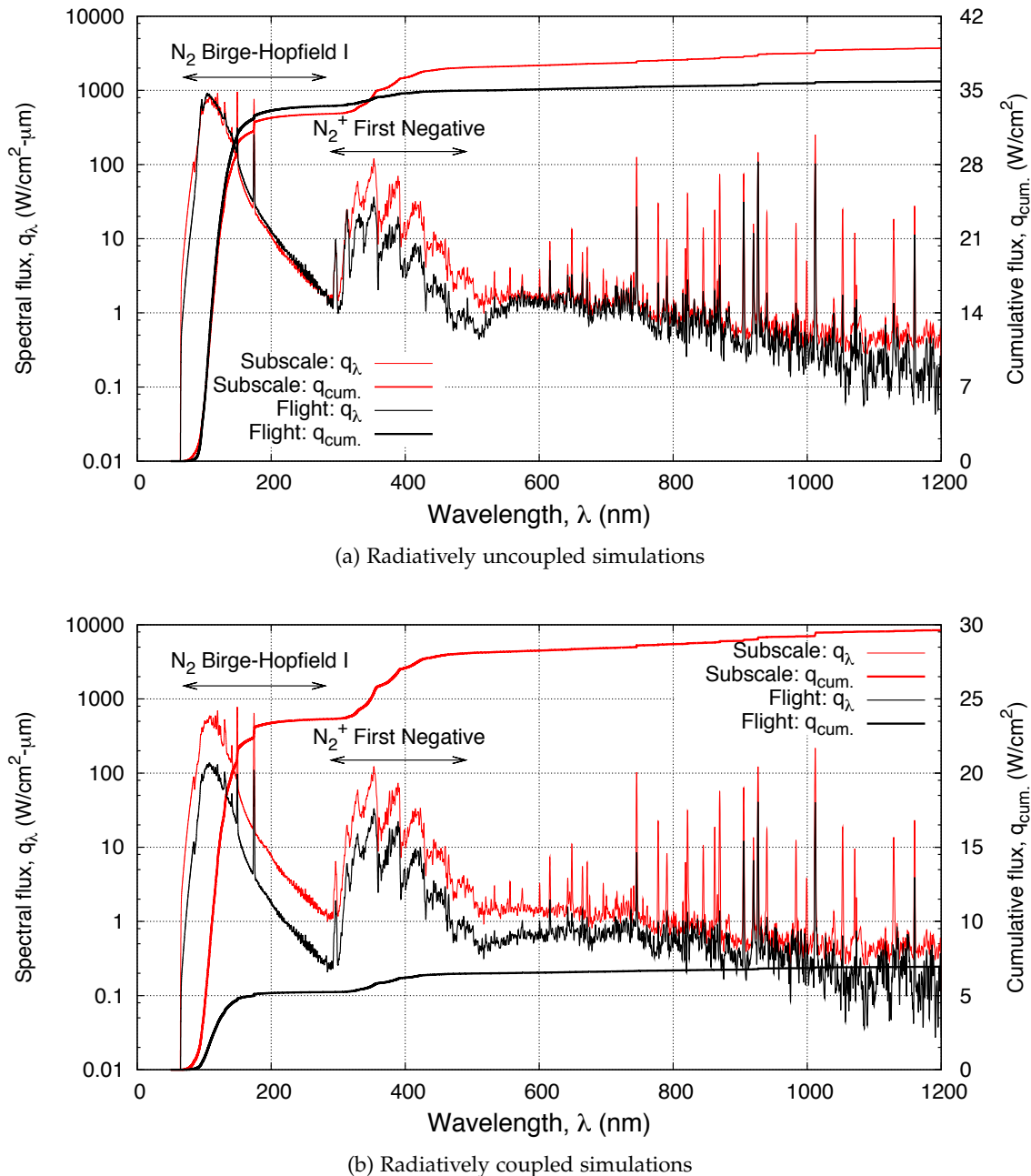


Figure 8.35: Comparison of radiative flux spectra incident at the stagnation point from simulations of the subscale and effective flight Hayabusa flowfields. Note that the spectra have been averaged over $\Delta\lambda = 1 \text{ nm}$ for presentation.

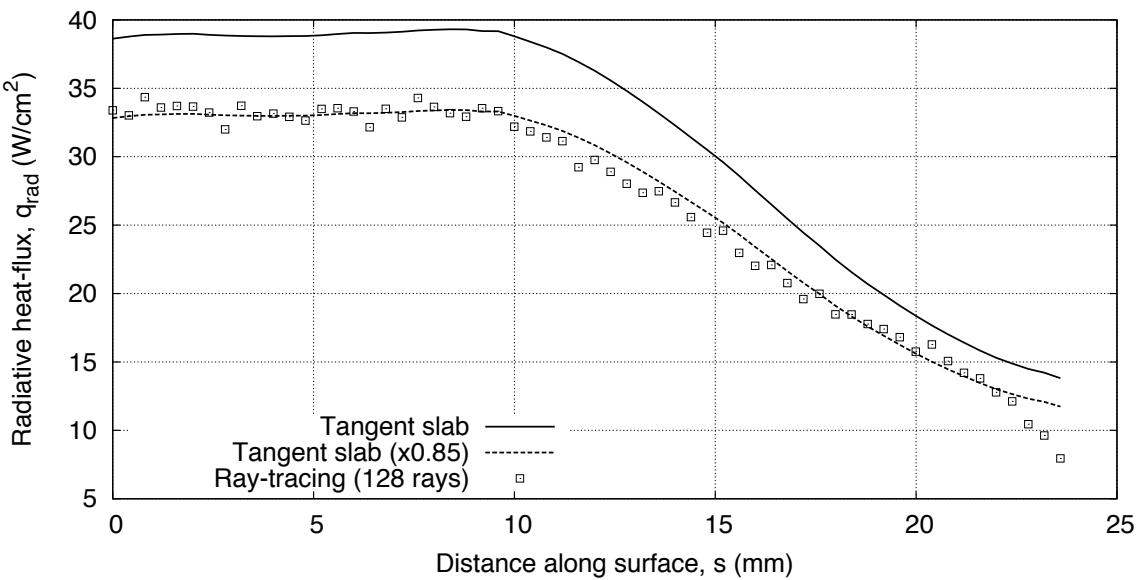


Figure 8.36: Comparison of radiative heat-flux profiles along the forebody surface of the subscale Hayabusa model from radiatively *uncoupled* tangent-slab and ray-tracing calculations.

Figure 8.37 compares stagnation streamline profiles from radiatively coupled simulations of the effective flight condition, one with a fully catalytic vehicle surface and the other with a non-catalytic vehicle surface. The presented profiles are restricted to the boundary layer region only as the two solutions are essentially identical for $x < -0.15$ cm. It should be noted that the presented spatial range of $-0.15 \leq x \leq 0$ cm is equivalent to a non-dimensional spatial range of $-0.0075 \leq x/R_n \leq 0$ cm, which is more constrained than the boundary layer detail profiles presented in Figures 8.33 and 8.34. As can be observed in Figures 8.37a and 8.37b, implementing a non-catalytic model results in considerably less chemical recombination at the vehicle surface. Most importantly for radiation, in the non-catalytic case the diatomic nitrogen number density is substantially reduced and the atomic nitrogen number density substantially increased in the range $x > -0.07$ cm. This has the effect of slightly increasing the local peak in radiative divergence (net absorption) and shifting its location towards the vehicle surface, Figure 8.37d. Due to both this change in radiative divergence and the increased number of electrons in the boundary layer, the vibration-electron-electronic temperature is reduced as the wall is approached in the non-catalytic case, Figure 8.37c.

Figure 8.38a compares the radiative heat flux spectra incident at the stagnation point from simulations of the effective flight Hayabusa flowfields with super catalytic and non-catalytic vehicle surfaces. The total radiative flux for the non-catalytic case is 7.2 W/cm^2 , slightly greater than the 6.9 W/cm^2 for the super catalytic case. The difference in the two spectra occurs almost entirely in the VUV region of the spectra, Figure 8.38b, where the N₂ Birge-Hopfield I is the dominant spectral feature. This can be explained by the previous observation that nitrogen

recombination is substantially reduced in the non-catalytic case (see Figure 8.37b), resulting in less N₂ present to absorb Birge-Hopfield I radiation in the boundary-layer.

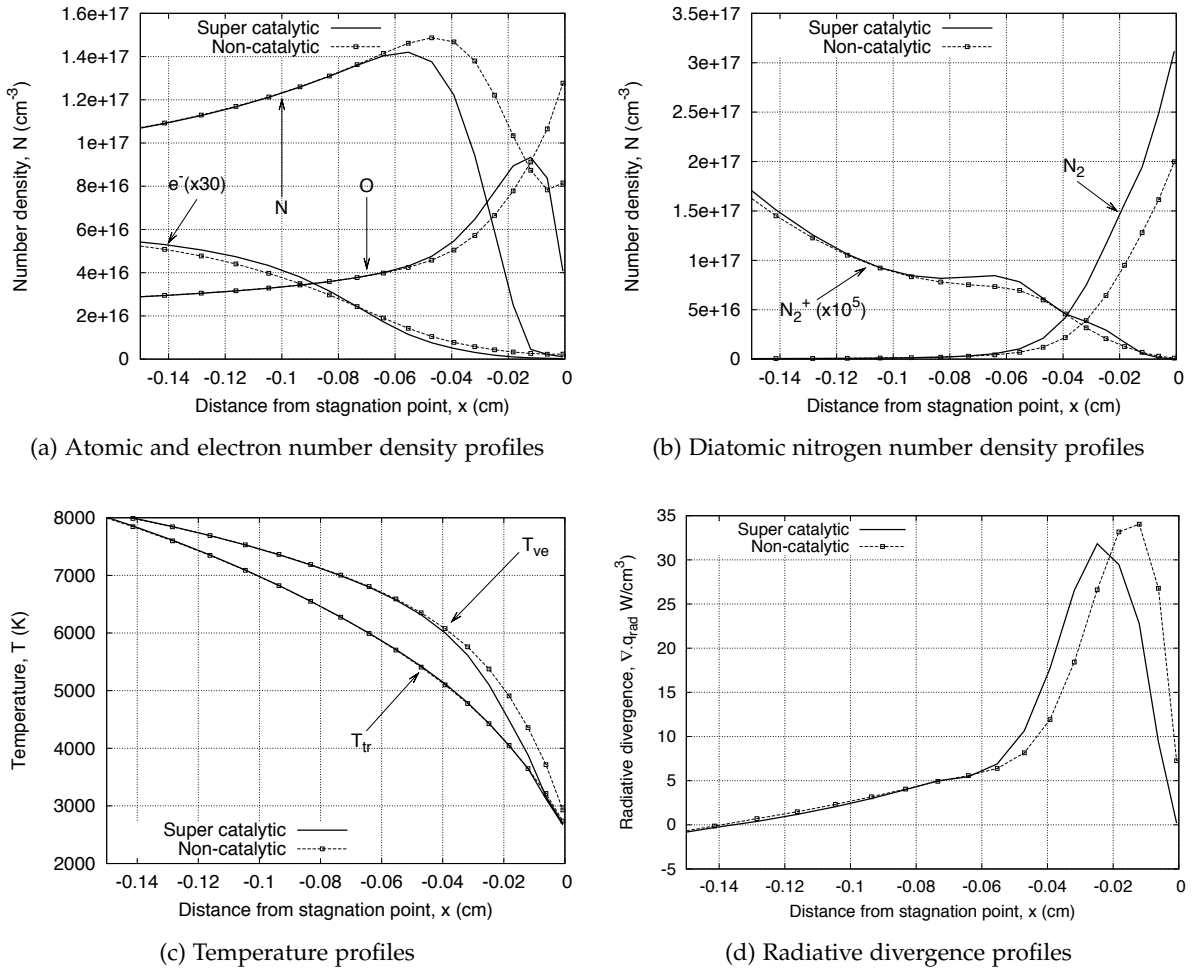


Figure 8.37: Flowfield property profiles along the stagnation streamline from effective flight Hayabusa flowfields with super catalytic and non-catalytic vehicle surfaces. Note that the profiles are restricted to the boundary layer region only.

Effect of N₂ electronic transition moment source As discussed in § 3.3.2, there is considerable variation in the electronic transition moments for the VUV transitions of the N₂ molecule proposed in the literature. Given the very large contribution of these transitions to the Hayabusa radiative heat flux found in the previous calculations, it is useful to investigate the effect of using a different set of N₂ electronic transition moments on the solution. For this purpose, radiatively-coupled simulations of the effective flight condition have been performed using the N₂ electronic transition moments collated by Hyun [66]. The reader is reminded that the previous calculations implemented the electronic transition moments from Chauveau *et al.* [123] for N₂ and N₂⁺.

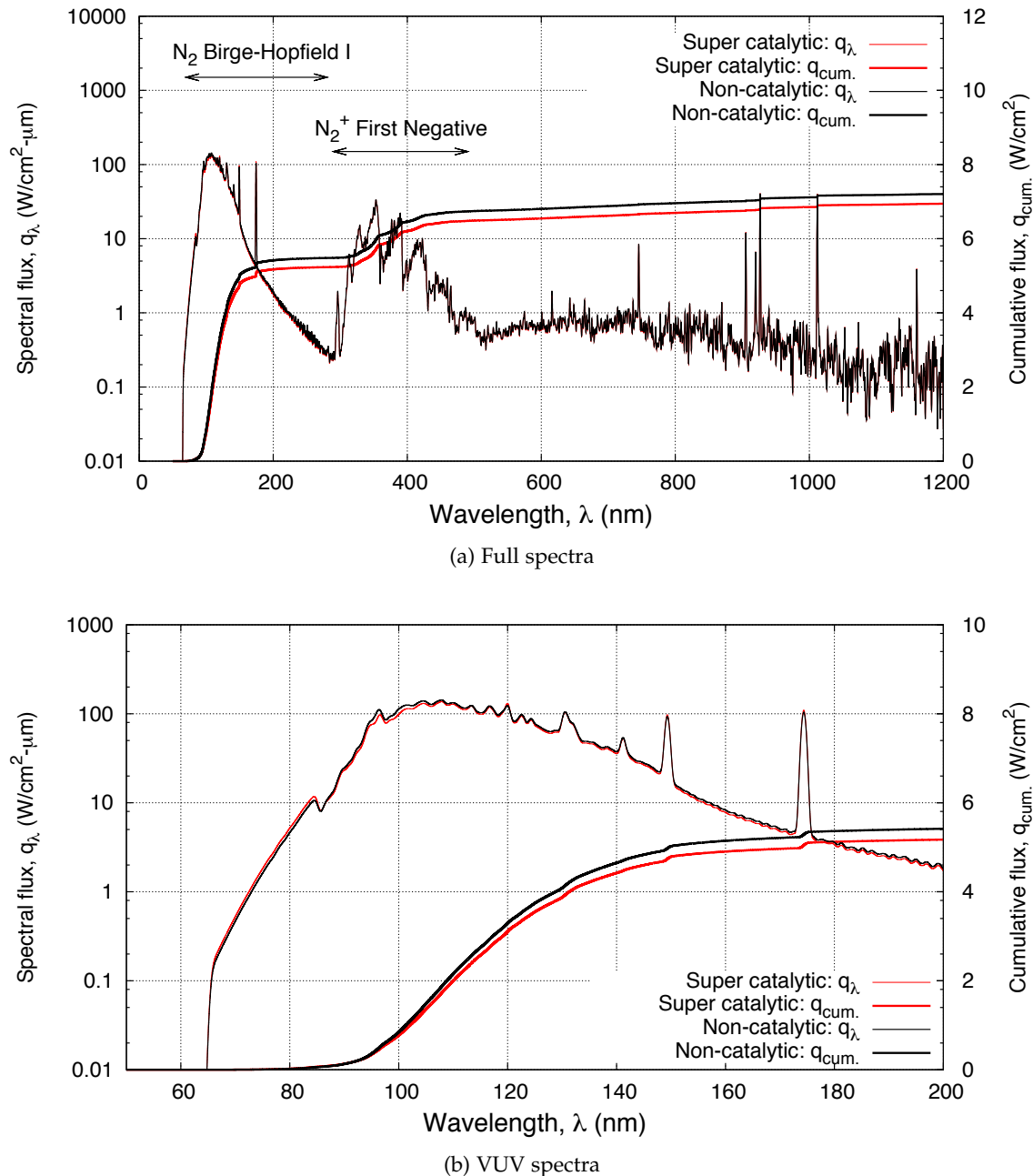


Figure 8.38: Comparison of radiative flux spectra incident at the stagnation point from simulations of the effective flight Hayabusa condition with super catalytic and non-catalytic vehicle surfaces. Note that the spectra have been averaged over $\Delta\lambda = 1 \text{ nm}$ for presentation.

Figure 8.39a compares the radiative heat flux spectra incident at the stagnation point from radiatively *uncoupled* simulations of the effective flight Hayabusa condition, while Figure 8.39b compares the flux spectra from radatively *coupled* simulations. For the uncoupled simulations, the heat flux using the N₂ transition moments from Hyun [66] is over 4 times lower as that using the transition moments from Chauveau *et al.* [123]. In contrast, for the coupled simulations the Hyun heat flux is only 29% lower due to the stronger radiative cooling effect for the simulation implementing the Chauveau transition moments. The sensitivity of the radiative heat flux to the N₂ transition moments for this condition warrants further investigation into their accuracy.

Summary and concluding remarks

A 47 MJ/kg N₂-O₂ expansion tunnel experiment performed in the X2 facility with a subscale Hayabusa model has been analysed. Freestream conditions were first estimated by a simplified strategy considering one-dimensional simulations of the secondary diaphragm rupture and Navier-Stokes simulations of the nozzle expansion. The test gas was calculated to be in a thermochemically excited state, with the thermochemical enthalpy contributing approximately 11.7% of the total when referenced to that of the initial test gas. While most of the O₂ remains in a dissociated state following the processing of the test gas by the primary shock, considerable N₂ recombination was estimated to occur during the unsteady expansion.

The radiating shock layer formed over the subscale Hayabusa model were then simulated with the axisymmetric Navier-Stokes equations. Initial inviscid simulations confirmed the establishment of steady flow in the period of flow available prior to the spectral measurements being made. Intensity profiles were extracted from a viscous simulation with radiation-flowfield coupling modelled using the tangent-slab equations. In the UV spectral region, the calculations predicted a high level of N₂⁺ First Negative emission that was not present in the measured spectra where only the CN Violet system was apparent. In the IR spectral region where atomic lines are the dominant spectral features, the calculated and measured peak intensity levels were the same order of magnitude but the spatial profiles were qualitatively different. Comparisons of the peak intensity IR spectra revealed similar broadened line profiles and background continuum as observed for the air shock tube experiments in § 6.

Finally, comparisons with an effective flight condition based on the binary scaling hypothesis were made. The effect of radiation coupling on the flowfield was found to be much greater for the flight condition, resulting in a factor of 5 difference in the radiative flux incident at the stagnation point. Also the thermochemically excited freestream was found to increase the shock detachment compared to an ideal freestream without any excitation. For both the subscale and effective flight conditions, the N₂ Birge-Hopfield I and N₂⁺ First-Negative system made the most significant contributions to the radiative heat flux. Simulations of the effective flight condition with a non-catalytic vehicle surface boundary condition demonstrated a slight increase (4.3%) in

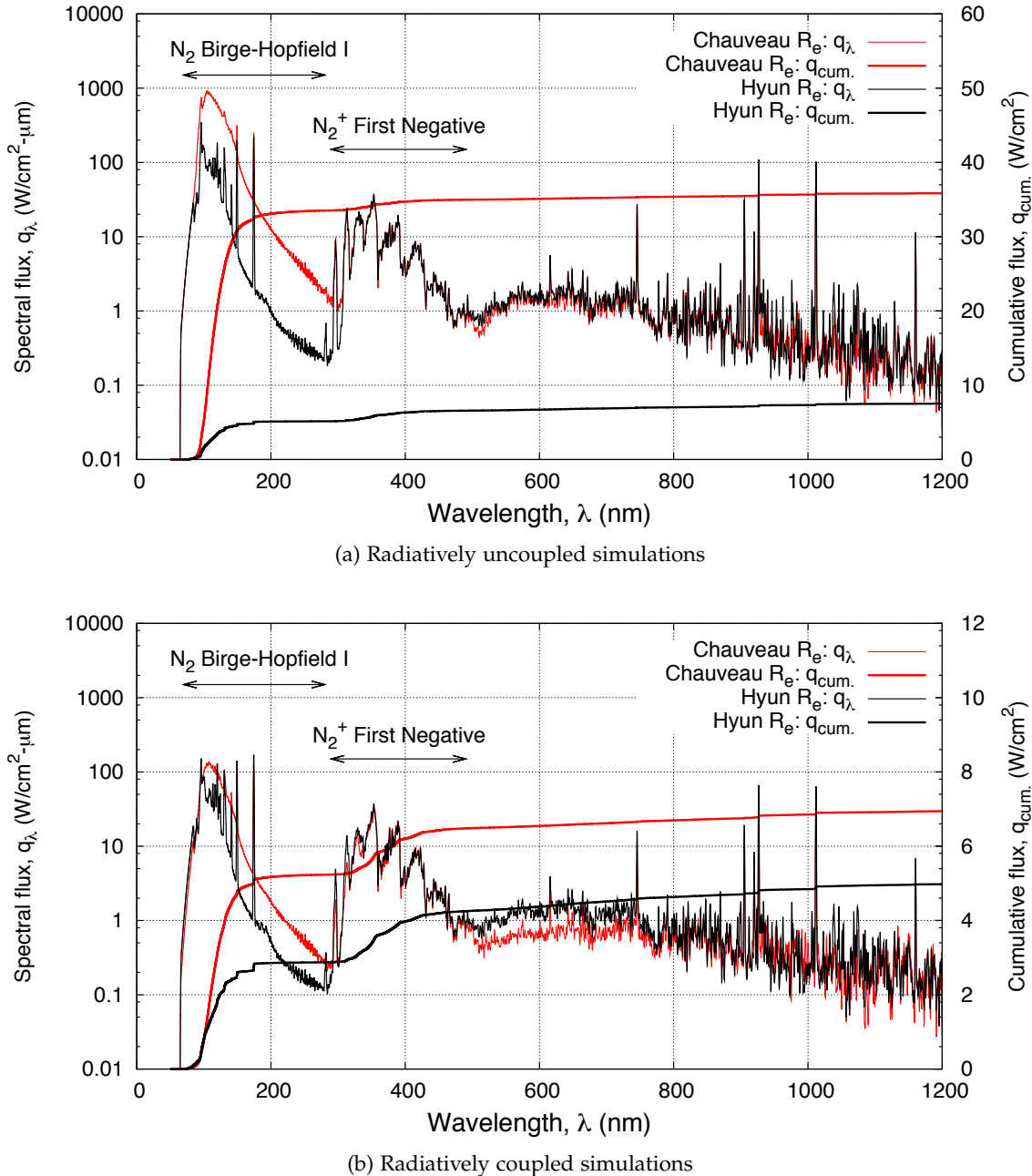


Figure 8.39: Comparison of radiative flux spectra incident at the stagnation point from simulations of the effective flight Hayabusa condition with various electronic transition moment (R_e) datasets for the N_2 molecule. Note that the spectra have been averaged over $\Delta\lambda = 1 \text{ nm}$ for presentation.

radiative heat flux at the stagnation point compared to simulations using a super catalytic vehicle surface boundary condition. This was attributed to slightly higher nitrogen recombination in the outer boundary layer resulting in increased N₂ emission in the VUV spectral region. Simulations of the effective flight condition with the N₂ electronic transition moments of Hyun [66] instead of the usual Chauveau *et al.* [123] data resulted in a 29% lower radiative heat flux.

The poor agreement between the calculated and measured intensity profiles for this condition is a concern. There are a number of factors that may have contributed to the observed discrepancies, both on the experimental and computational sides:

1. Incorrect freestream conditions (including carbon contamination),
2. Inappropriate physical models,
3. Incorrect calibration of the spectrometers, and
4. Shot-to-shot variation.

The parametric study in Appendix F demonstrated that variations in the freestream conditions, most notably velocity, N₂ concentration and carbon contamination, can significantly alter the level of shock layer radiation for this condition. While this alone cannot account for the observed discrepancies, it highlights the need for a more accurate means of determining freestream conditions. In particular, the level of carbon (and other species) contamination in the freestream needs to be quantified and included in the simulations as this may significantly alter the shock layer chemical kinetics. Also, the physical models that were found to give reasonable agreement for the air shock tube conditions in § 6 may not be accurate for these binary scaled conditions. Firstly, however, efforts need to be made to improve the quality of the experiments such that the comparisons can be made with more confidence. Specifically, the spectrometer calibrations need to be confirmed, the depth-of-field of the IR spectral measurements needs to be improved, and shot-to-shot repeatability must be addressed. Although the experiment was found to overpredict the radiative heat flux experienced by the full-scale Hayabusa probe at effective flight conditions, it remains a valuable data set for the validation of chemical kinetic and radiation models. Furthermore, analysis of the experiments performed with an epoxy coating on the model forebody as described in Reference [221] would provide a unique opportunity to study an ablation layer via detailed spectral measurements.

8.4 37 MJ/kg CO₂-N₂ condition

Ultraviolet spectroscopy measurements of the radiating shock layer formed over a 25 mm cylinder with a CO₂-N₂ test gas have been performed in the X2 facility by Eichmann *et al.* [225]. The total enthalpy of the flow condition was 37 MJ/kg and the binary scaling parameter ρL was

approximately $4.85 \times 10^{-5} \text{ kg/m}^2$, corresponding to an effective flight velocity of 9.5 km/s at an altitude of 65 km in the Martian atmosphere for a vehicle with a characteristic length of 2.5 m. Such a condition may be encountered by a toroidal ballute performing a high altitude aero-assist manoeuvre, as discussed in § 1.2, where the finite-length cylinder is representative of a section of the toroid. A description of the experiment is provided in § 8.4.1. In § 8.4.2 the freestream conditions for this experiment are estimated via the strategy outline in § 8.2. Simulations are then performed of the recompression shock formed over the cylinder in § 8.4.3. From these solutions to the subscale shock layer, intensity profiles are extracted and compared with the measured data. Note that the binary scaling hypothesis is not investigated for this condition as Navier–Stokes simulations of the effective flight condition were unable to be performed.

8.4.1 Experiment description

Spectroscopic measurement of a blunt-body shock layer

The nominal test model for the 37 MJ/kg CO₂–N₂ condition is a 25 mm diameter steel cylinder 75 mm in length. In this analysis data from a 25 mm diameter steel cylinder 100 mm in length is also considered. The cylinder is mounted in the test-section during the experiments by a sting attached to the rear of the cylinder. Ultraviolet spectra were measured along the stagnation streamline, and high-speed camera footage of the shock establishment was also recorded. An illustration of the optical arrangement in the test section for spectroscopic and high speed camera measurement of the shock layer is presented in Figure 8.40. An Acton Research Spectra Pro SP2300 series spectrograph was coupled with a 1024 × 256 pixel Princeton Instruments PI-MAX CCD array for the ultraviolet measurements. The ultraviolet spectra considered in this analysis were obtained with the 600 lines/mm grating in the ranges $315 \leq \lambda \leq 443 \text{ nm}$, $389 \leq \lambda \leq 513 \text{ nm}$ and $457 \leq \lambda \leq 581 \text{ nm}$. For all shots both spectrometers had slit widths of 50 μm, gate widths of 20 μs and an intensifier gain of 240.

Flow condition

A 37 MJ/kg CO₂–N₂ expansion tunnel condition was developed for the 25 mm cylinder spectroscopy experiments. The fill conditions, measured shock speeds and measured pressure levels from shot x2s1319 are summarised in Table 8.5. A static pressure trace at the AT5 transducer is presented in Figure 8.41a, and Pitot pressure traces in the test-section is presented in Figure 8.41b. Note that the centreline Pitot pressure transducer was not functioning during this campaign, and therefore the two transducers either side of the centreline are presented in Figure 8.41b. The averaging periods used to estimate the test gas pressure at the nozzle entrance, p_3 , and the Pitot pressure in the test-section, p_{pitot} in Table 8.1 are indicated with the ‘test gas’ label. The blue bars in Figure 8.41b represent the 10 μs spectrometer exposure time, that is triggered approximately

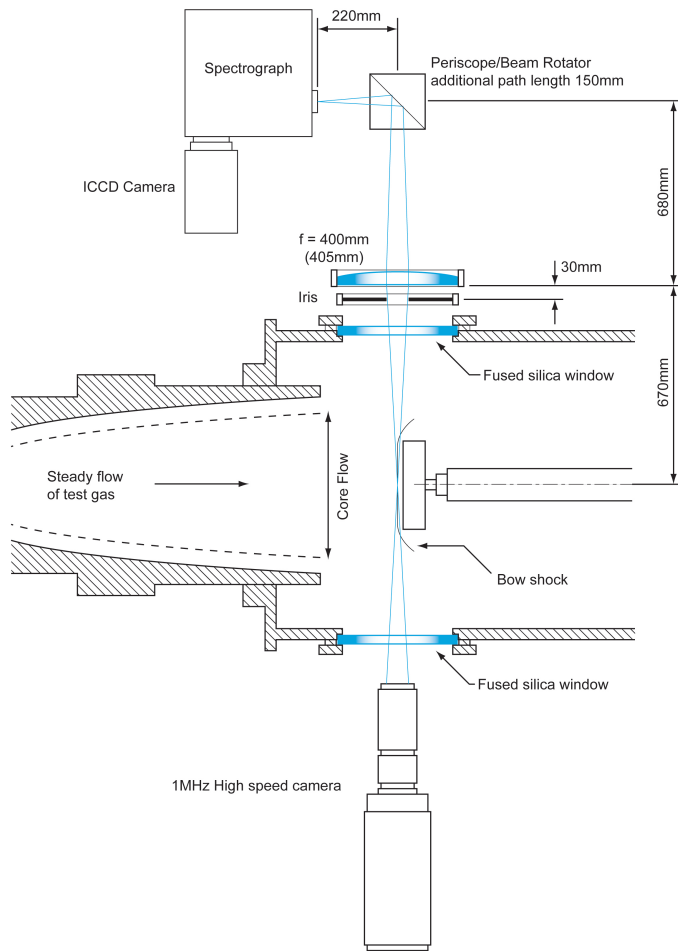


Figure 8.40: Illustration of optical arrangement in the test section for spectroscopic measurement of the 25mm cylinder.

$65 \mu\text{s}$ after shock arrival by a photomultiplier tube⁴. For this condition the period of steady flow is limited to the $50 \mu\text{s}$ indicated, significantly less than the $200 \mu\text{s}$ of steady flow observed for the $48 \text{ MJ/kg N}_2\text{-O}_2$ condition discussed in § 8.3. It is possible the higher nozzle entrance Mach number for this condition prevents a clean expansion of the test gas. Nevertheless the flow quality up to the time the spectroscopic measurements are made is reasonable, exhibiting a standard deviation of less than 10%.

8.4.2 Estimation of freestream conditions

From the initial fill conditions and measured shock speeds and pressure levels presented in Table 8.5, the nozzle entrance conditions are estimated using the strategy outlined in § 8.2. A two-temperature 20 species gas-model was used for both the secondary diaphragm and nozzle

⁴The location of the peak Pitot pressure has been taken to indicate shock arrival in Figure 8.41b.

Table 8.5: Fill conditions and experimentally measured pressures and shock speeds for the 37 MJ/kg CO₂–N₂ expansion tunnel condition.

Shock tube	
Test gas composition	X _{CO₂} = 0.96
	X _{N₂} = 0.04
Initial test gas pressure, p_1 (Pa)	2100 ± 50
Primary shock speed, $U_{s,1}$ (m/s)	4700 ± 50
Post shock pressure, p_1^* (kPa)	750 ± 60
Acceleration tube	
Initial air pressure, p_2 (Pa)	10 ± 0.1
Secondary shock speed [†] , $U_{s,2}$ (m/s)	8420 ± 200
Post shock pressure, p_2^* (Pa)	4000 ± 600
Test gas pressure [‡] , p_3 (kPa)	3800 ± 400
Test section	
Pitot pressure [§] , p_{pitot} (kPa)	136 ± 10

[†] Measured between transducers AT5 and AT6 as indicated in Figure 8.1

[‡] Average between 34 and 76 μ s after shock arrival at AT5 as indicated in Figure 8.41a

[§] Average between 39 and 89 μ s after shock arrival at the Pitot probe as indicated in Figure 8.41b

simulations. Dissociation reactions are assumed to be governed by the geometric average temperature $\sqrt{T_{\text{tr}} T_{\text{ve}}}$. Non-preferential energy-chemistry coupling is applied due to the tendency of the preferential models to overestimate the amount of energy added to the flow upon recombination in expansion flows. For the nozzle calculations, the transport coefficients are calculated with the Gupta and Yos [92] and the collision cross sections proposed by Wright *et al.* [88, 94, 98, 99] and Bruno *et al.* [6] as described in § 3.2.

The estimated test gas flow state behind the primary shock (region '1*'), at the nozzle entrance (region '3') and at the nozzle exit are summarised in Table 8.6. The quoted uncertainty levels have been estimated via a perturbation analysis considering the variation in the measured shock speed and pressure levels. The uncertainty in the nozzle entrance temperature is much higher than for the 47 MJ/kg N₂–O₂ condition as the Pitot pressure was found to be much less sensitive to T_3 . The L1d simulations of the secondary diaphragm rupture estimate a lower CO₂ mass-fraction at the nozzle entrance than behind the primary shock. Figure 8.42 presents pressure and CO₂ mass-fraction histories of a test gas packet originating just upstream of the secondary diaphragm. The reflected shock almost completely dissociates what CO₂ remains behind the primary shock, and slight recombination is estimated to occur during the unsteady expansion. As was the case for

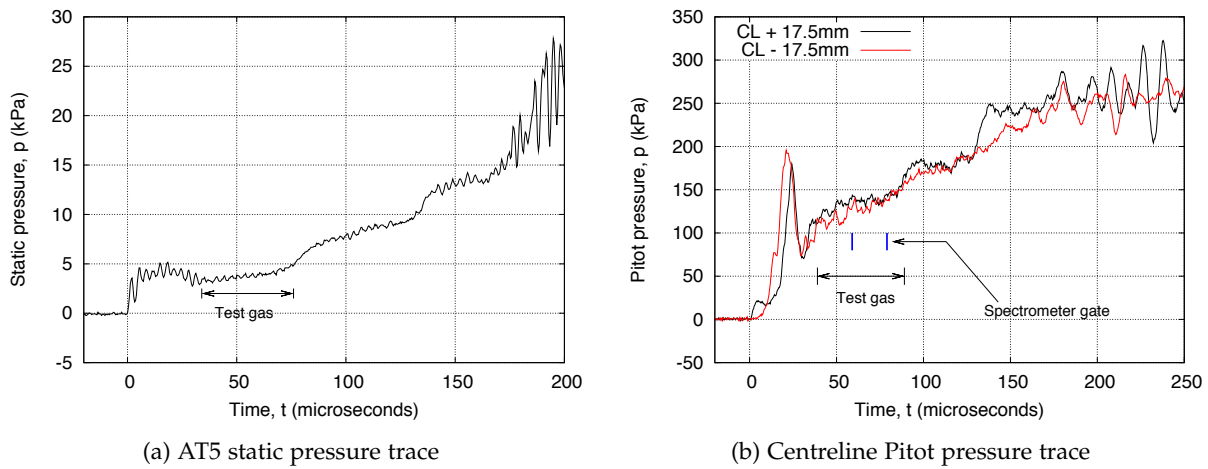


Figure 8.41: Measured pressure traces for shot x2s1319.

the 48 MJ/kg N₂-O₂ condition, the bulk of this recombination can be seen to occur at pressures greater than one atmosphere.

Figure 8.43 compares the measured Pitot pressure level with that estimated by Navier-Stokes simulations of the nozzle with various entrance temperatures. An entrance temperature of 1,250 K was found to give the best agreement with the average Pitot pressure level measured during the test time (~ 136 kPa). As was observed for the 47 MJ/kg N₂-O₂ condition, the test gas is disturbed by a shock system emanating from the growing boundary layer just upstream of the inflow plane. Comparisons of centreline profiles from viscous and inviscid simulations of the nozzle are presented in Figure 8.44. Due to the higher Mach number, the effect of the shock disturbance is more severe than for the air condition. While density recovers to the inviscid level 40 cm downstream of the nozzle entrance, the translation-rotation temperature remains 7.7% higher at this location. The CO₂ mass-fraction is increased by approximately 3.5% due to the shock system and does not recover to the inviscid level due to chemical freezing. The viscous vibration-electron-electronic temperature is 7.4% higher than the inviscid solution 40 cm downstream of the nozzle entrance, and this difference remains through the remainder of the expansion. Due to this perturbation, additional uncertainty limits of $\pm 3.5\%$ and $\pm 7.4\%$ are placed on the freestream temperatures and composition respectively.

8.4.3 Radiating shock layer simulations: subscale model

The freestream conditions averaged over the test-time presented in Table 8.6 are now applied to simulate the recompression of the test gas over the 25 mm cylinder. Time accurate inviscid simulations are first presented with and without the wake flow included to determine the time required for flow establishment, and assess the accuracy of a reduced computational domain.

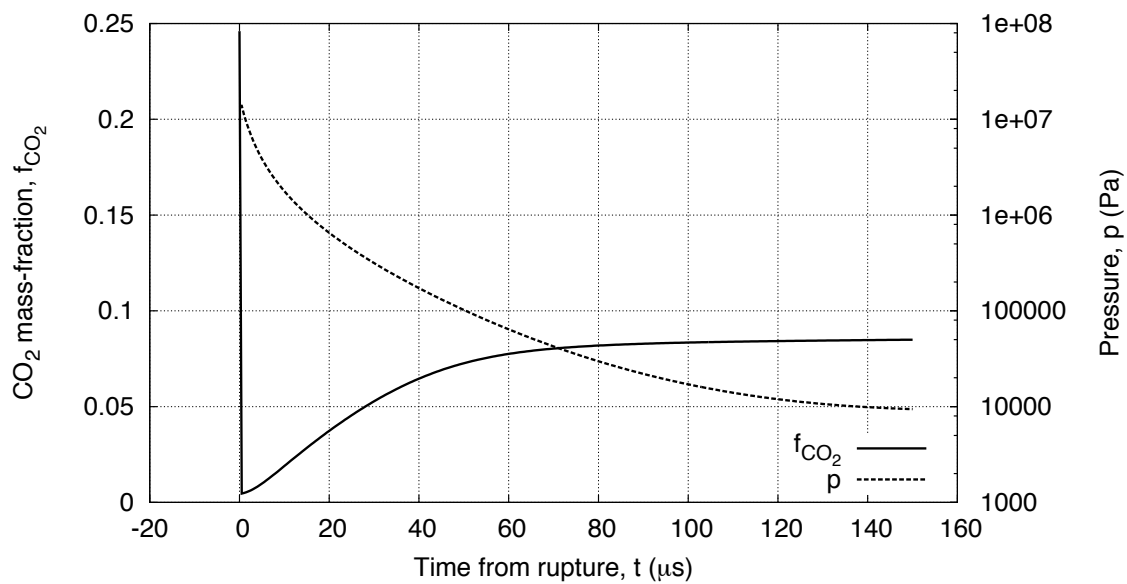


Figure 8.42: CO_2 mass-fraction and pressure histories of a test gas packet originating just upstream of the secondary diaphragm for the 37 MJ/kg $\text{CO}_2\text{-N}_2$ expansion tunnel condition.

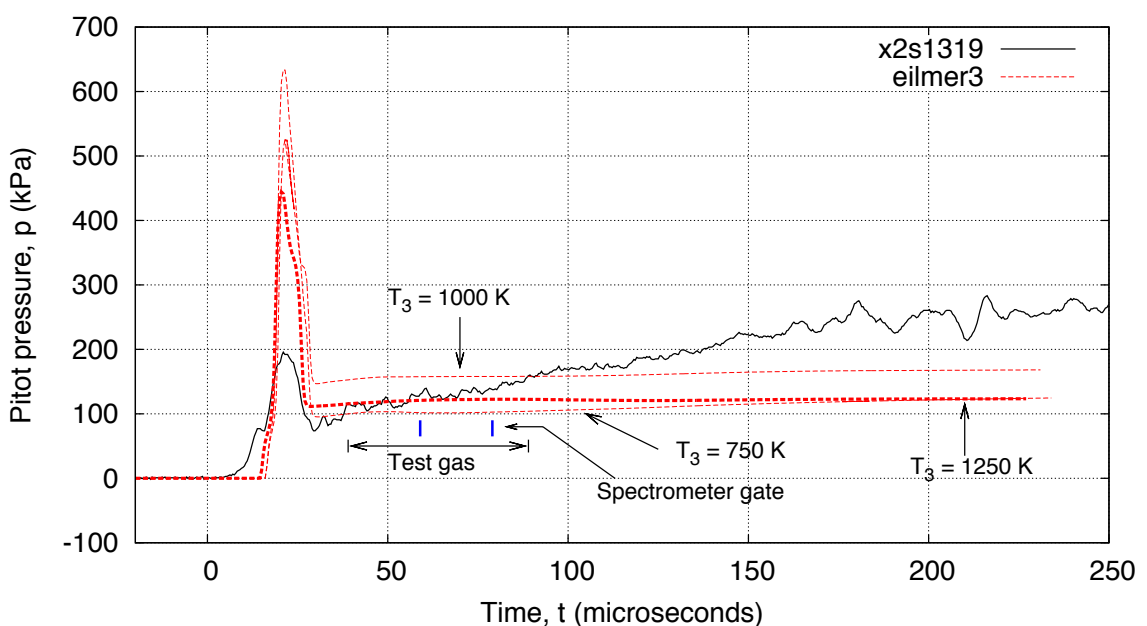


Figure 8.43: Comparison of measured and calculated centreline Pitot pressure level for the 37 MJ/kg $\text{CO}_2\text{-N}_2$ condition.

Table 8.6: Estimated test gas flow states for the 37 MJ/kg CO₂-N₂ expansion tunnel condition.

Flow state	Behind primary shock (region '1*')	Nozzle entrance (region '3')	Nozzle exit (region '4')
Density, ρ (kg/m ³)	$7.19 \pm 0.39 \times 10^{-1}$	$1.24 \pm 0.53 \times 10^{-2}$	$1.79 \pm 0.05 \times 10^{-3}$
Pressure, p (Pa)	$776 \pm 16 \times 10^3$	4000 ± 600	592 ± 12
T_{tr} (K)	3899 ± 38	1250 ± 500	1062 ± 25
T_{ve} (K)	3899 ± 38	1250 ± 500	1209 ± 140
Velocity, u (m/s)	4447 ± 47	8420 ± 200	8525 ± 202
Mach number, M	3.8 ± 0.1	11.4 ± 3.3	12.8 ± 3.7
Total enthalpy, H_{total} (MJ/kg)	11.6 ± 0.3	36.7 ± 1.8	36.7 ± 1.8
Mole-fractions: [‡]			
X_{CO_2}	$1.36 \pm 0.10 \times 10^{-1}$	$4.98 \pm 0.37 \times 10^{-2}$	$6.03 \pm 0.50 \times 10^{-2}$
X_{CO}	$5.00 \pm 0.01 \times 10^{-1}$	$5.22 \pm 0.01 \times 10^{-1}$	$5.30 \pm 0.02 \times 10^{-1}$
X_{N_2}	$1.92 \pm 0.04 \times 10^{-2}$	$1.90 \pm 0.04 \times 10^{-2}$	$1.96 \pm 0.06 \times 10^{-2}$
X_{NO}	$1.48 \pm 0.01 \times 10^{-2}$	$9.65 \pm 0.07 \times 10^{-3}$	$9.95 \pm 0.09 \times 10^{-3}$
X_{O_2}	$1.56 \pm 0.03 \times 10^{-1}$	$1.12 \pm 0.02 \times 10^{-1}$	$1.39 \pm 0.03 \times 10^{-1}$
X_N	$6.06 \pm 0.78 \times 10^{-5}$	$3.26 \pm 0.42 \times 10^{-6}$	$1.66 \pm 0.24 \times 10^{-9}$
X_O	$1.73 \pm 0.10 \times 10^{-1}$	$2.87 \pm 0.17 \times 10^{-1}$	$2.41 \pm 0.16 \times 10^{-1}$

[‡] Species with mole-fractions less than 1×10^{-6} at the nozzle entrance not shown.

A grid resolution study for simulations restricted to the forebody region with the full Navier-Stokes equations is then performed. Finally radiatively coupled solutions are presented and comparisons with the spectral measurements from the experiments are made. Unless otherwise stated the physical modelling is as presented in Table 5.2.

Inviscid simulations

The computational domain and grid for the inviscid simulations with and without the wake region are presented in Figures 8.45 and 8.46 respectively, where the grids are presented at one-half resolution for clarity. The forebody region for both simulations use the same 120×120 cell uniformly spaced grid. For the simulation with the wake region included, the grid is extended approximately 4 body lengths (25 mm cylinder diameter) in the aft direction with a relatively crude mesh (120×120 cells) that is clustered towards the body in the axial direction. The computational domain for the simulation without the wake region included is terminated by an outflow boundary extended perpendicular from the top of the cylinder. Figures 8.47a and 8.47b present the maximum energy residuals as a function of time for the inviscid simulations with and without the wake region included. For the simulation with the wake region included, the unsteady wake-flow prevents the residual from dropping below 1×10^{-2} , and an approximately constant level is achieved after $25 \mu s$ of flow. In contrast, the residual for the forebody simulation

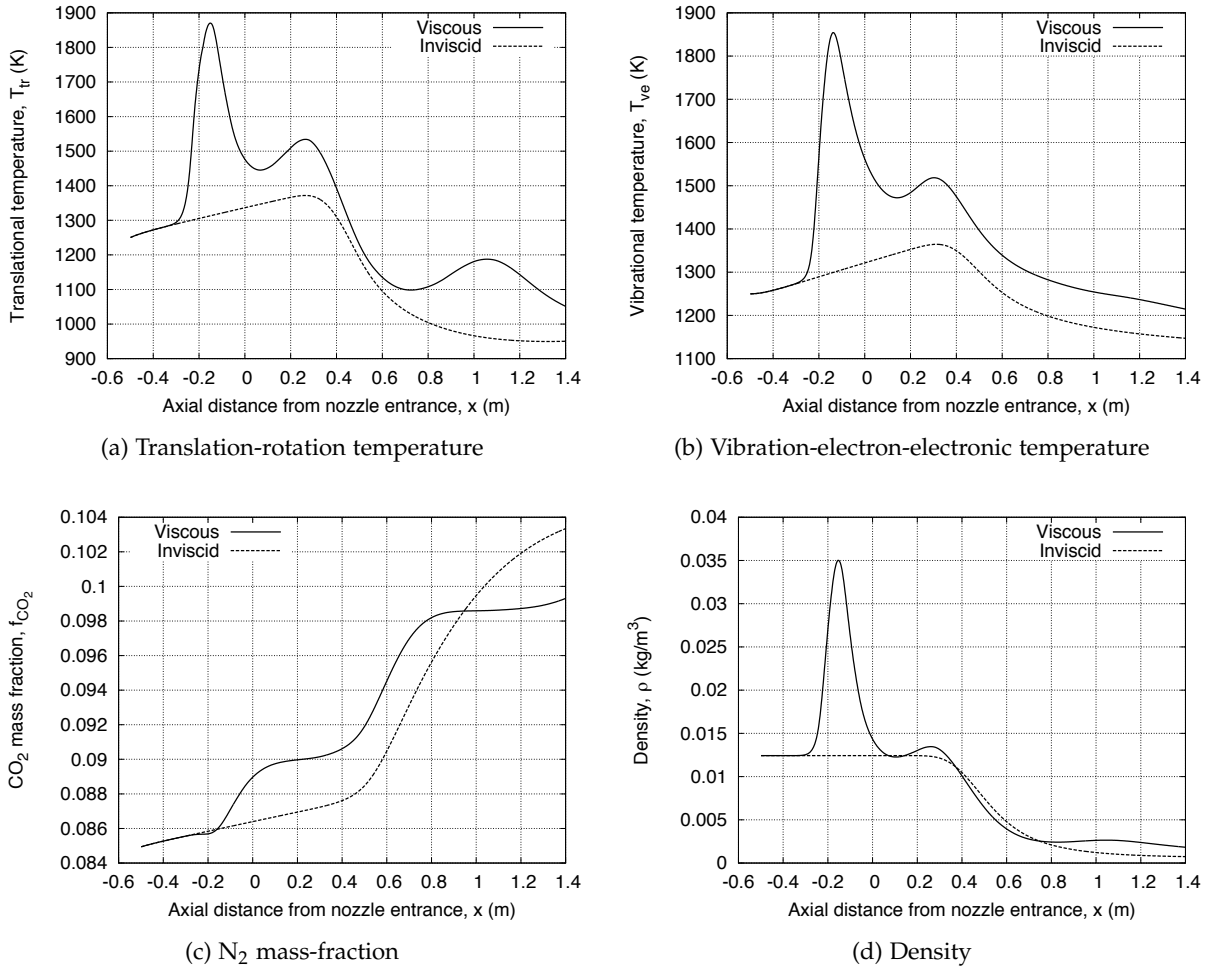


Figure 8.44: Comparison of centreline profiles from viscous and inviscid simulations of the X2 nozzle for the 37 MJ/kg $\text{CO}_2\text{-N}_2$ condition.

shows good convergence, dropping to 1×10^{-4} after over the 15 body lengths of flow simulated.

Figure 8.48 compares the shock detachment against time from the inviscid simulations with that measured in shot x2s1413. This shot had a secondary shock speed between AT4 and AT5 of 8480 ± 201 m/s, which is very similar to shot x2s1319 (8420 ± 200 m/s) that was used to determine the freestream conditions. The transient experimental data is obtained by post-processing the location of the shock in luminosity images obtained by the high-speed camera. The measured data has an uncertainty of ± 0.3 mm due to the relatively low number of pixels capturing the shock (e.g. approximately 9 during steady flow). The simulated shock standoff data has been shifted in time to approximately correspond to the arrival of the test gas at the model surface. The measured data exhibits a rapid increase in shock detachment over the first $20 \mu\text{s}$ of flow due to the shock heated air in-front of the test gas that is not modelled. The simulations with

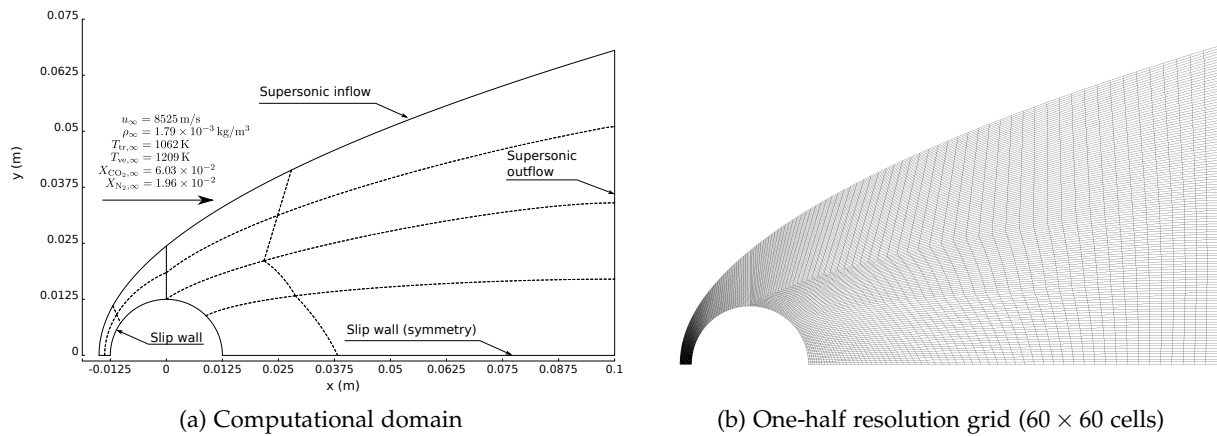


Figure 8.45: Computational domain and grid for inviscid simulations of the 25 mm cylinder *with* the wake region include.

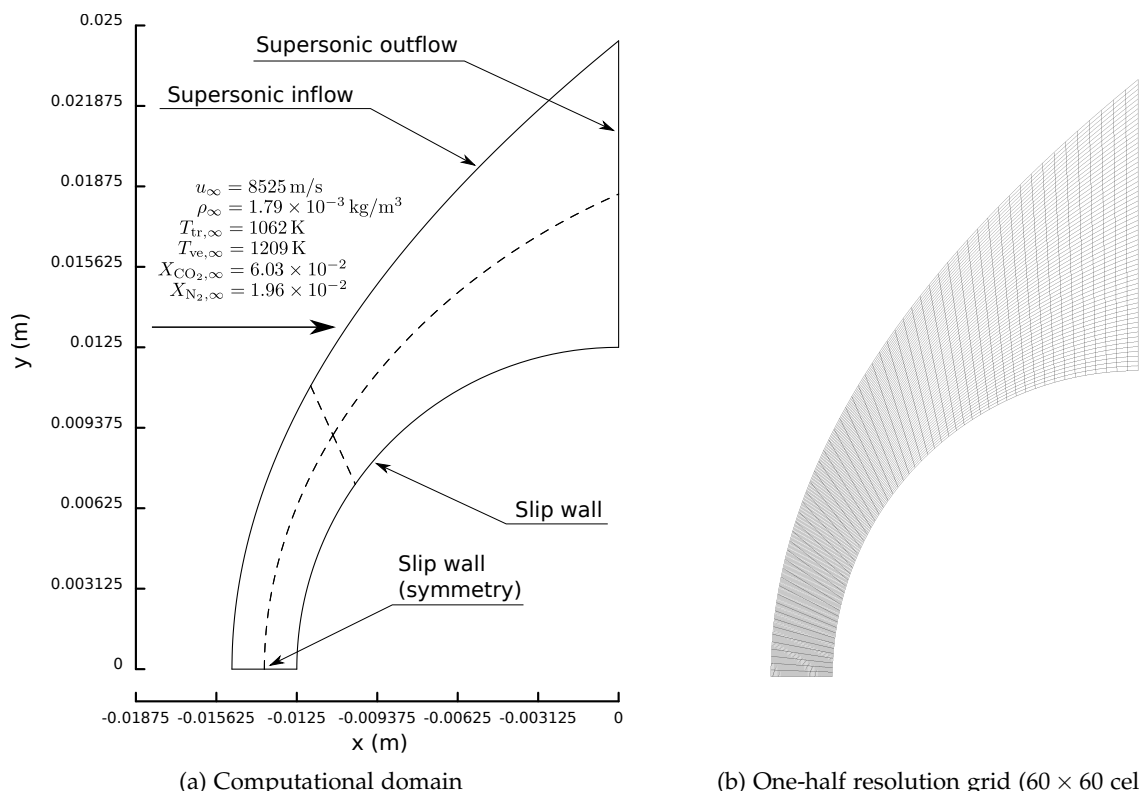


Figure 8.46: Computational domain and grid for inviscid simulations of the 25 mm cylinder *without* the wake region include.

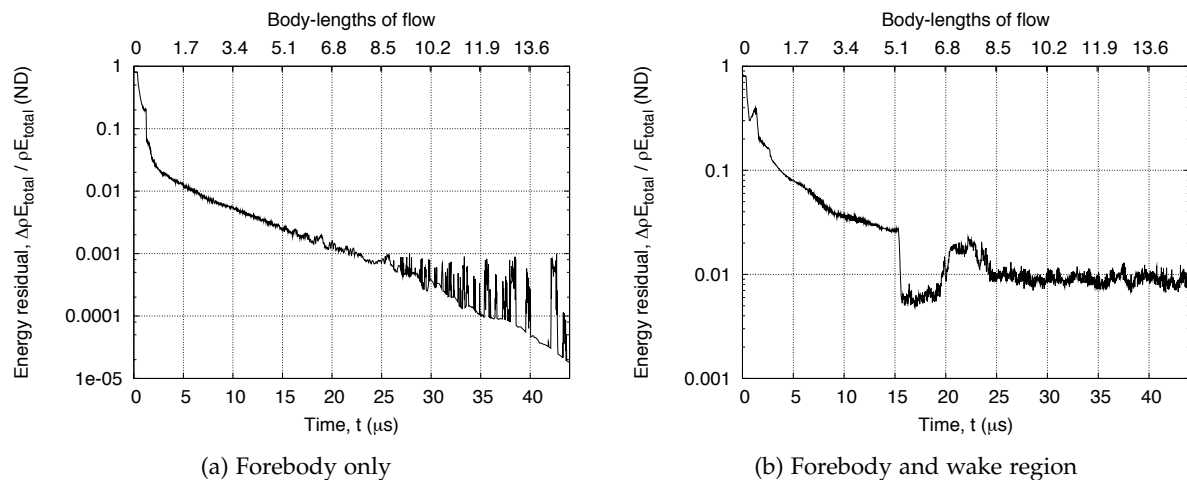


Figure 8.47: Maximum energy residuals as a function of time from inviscid simulations of the 25 mm cylinder.

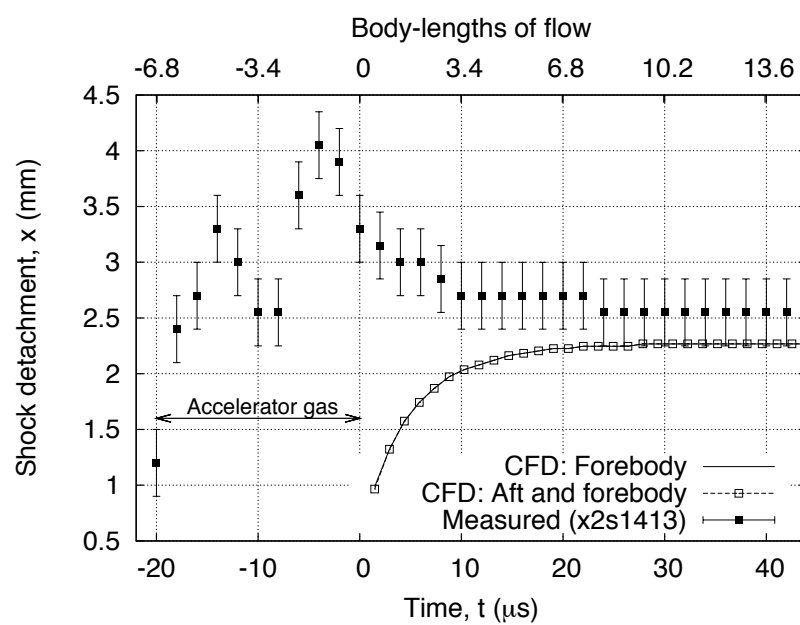


Figure 8.48: Comparison of shock detachment against time from inviscid simulations of the 25 mm cylinder with measured data.

and without the wake region included exhibit very similar trends, with a constant shock detachment of 2.27 mm being attained after 30 μ s of flow. A similar establishment time is observed in the measured data, however the shock detachment distance at steady state is slightly higher at 2.55 ± 0.2 mm. These results indicate that the 40 μ s of test gas that passes over the model prior to the spectroscopic measurements being taken (see Figure 8.41b) is sufficient for steady state conditions to be achieved.

Figure 8.49 presents superimposed density contour plots after 15 body lengths of flow from the inviscid simulations in the forebody region. The contours in red denote the simulation without the aft region, and the contours in black denote the simulation with the aft region included. Terminating the computational domain 90 degrees around the cylinder has only a very slight affect on the solution, and we can proceed with confidence to detailed simulations of the forebody region with the full Navier–Stokes equations.

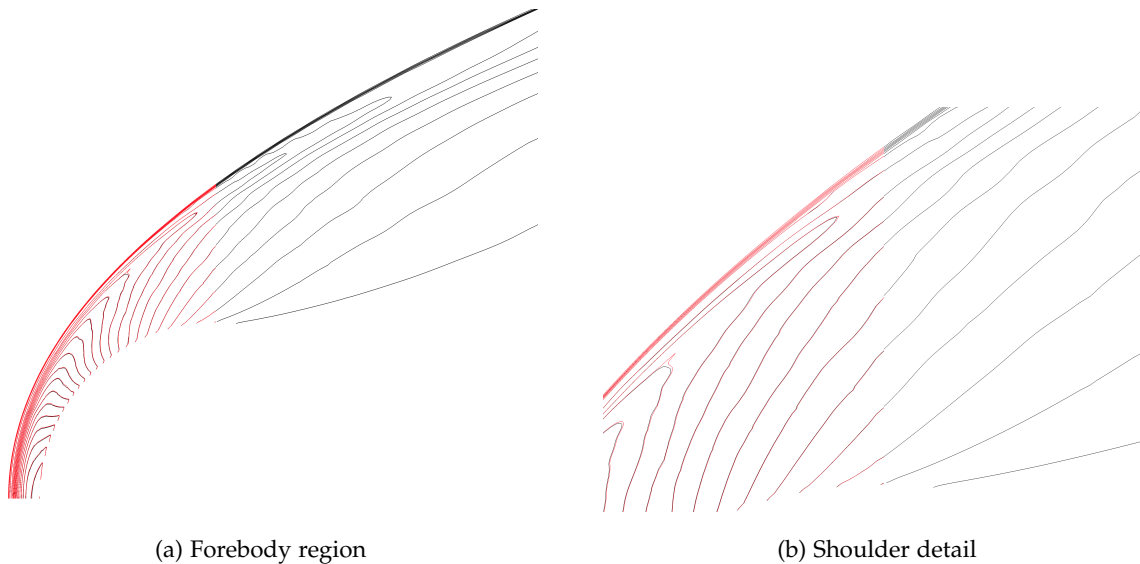


Figure 8.49: Density contour plots after 15 body lengths of flow from the inviscid simulations of the 25 mm cylinder. The contours in red denote the simulation without the wake region, and the contours in black denote the simulation with the wake region included.

Viscous simulations

The computational domain and moderate resolution 60×60 cell grid for viscous simulation of the 25 mm cylinder are presented in Figures 8.50a and 8.50b respectively. Similarly as for the Hayabusa model, a fixed temperature (296 K) wall boundary condition is applied to the model surface. Diffusion induced surface heat flux for CO₂ based gases is known to be large when surface catalyticity is modelled [226]. Simulations with a catalytic wall were not successful, however, and the results presented here consider a non-catalytic wall at the model surface. As a

result, the diffusion induced heat-flux at the surface is zero. The grid is clustered weakly towards the surface, with approximately 10 cells describing the boundary layer at the stagnation point.

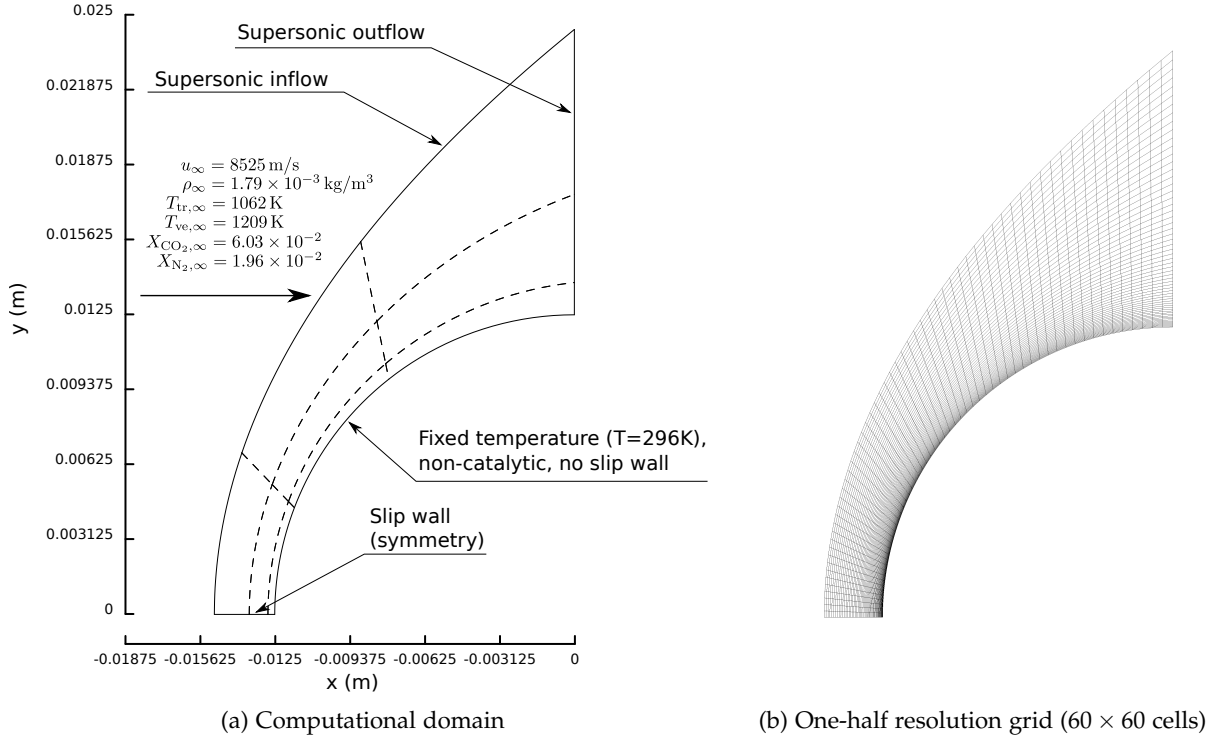


Figure 8.50: Computational domain and grid for viscous simulations of the 25 mm cylinder.

The viscous simulations are initialised by a converged (15 body lengths of flow) inviscid solution obtained on a coarse 30×30 cell grid. The viscous effects are added to the solution in an incremental fashion with $N_{\text{incr.}} = 1 \times 10^4$ as described in § 7.2.3. The initial viscous simulations without radiation-flowfield coupling are run for 5 body lengths of flow. The maximum total energy and mass residuals for a viscous simulation performed on the moderate resolution 60×60 grid are presented in Figures 8.51a and 8.51b. While the reasonable convergence occurs during the first $2.5 \mu\text{s}$ when the viscous effects are being added, the residuals subsequently fail to drop below 1×10^{-3} . This is thought to be due to inadequate resolution near the model surface where the thermal gradients are large. Simulations with finer resolution in this region were attempted, but proved computationally prohibitive for the time accurate integration. Despite the poor convergence in the boundary layer, the rest of the shock layer is reasonably steady.

Grid solution study Figures 8.52a and 8.52b compare the translation-rotation temperature profiles and electron number density profiles along the stagnation streamline from viscous simulations on 30×30 , 60×60 , 90×90 and 120×120 cell grids. Radiation-flowfield coupling is not considered for these simulations. The 90×90 cell grid solution shows good agreement with the

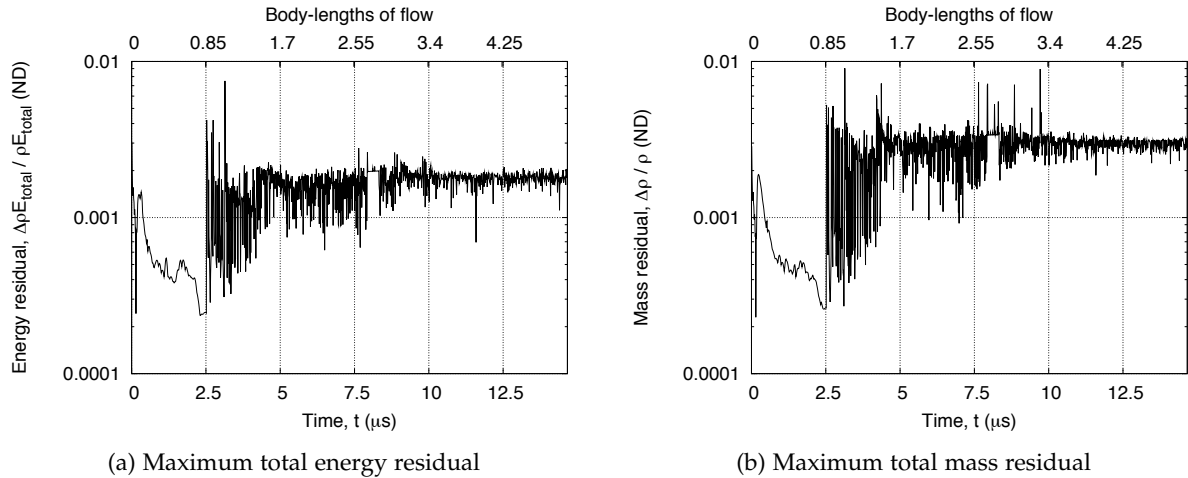


Figure 8.51: Maximum total energy and mass residuals as a function of time from viscous simulations of the 25 mm cylinder on a 60×60 cell grid.

120×120 cell grid solution throughout, while the 60×60 cell grid exhibits slightly higher translational temperatures and lower electron number densities in the $-1.75 \leq x \leq -1$ mm range where electron impact ionisation is the dominant process. Radiatively coupled simulations simulations with the 90×90 cell grid proved computationally prohibitive, however, and the 60×60 cell grid is therefore used for the radiatively coupled simulations and experiment comparison.

Radiation-flowfield coupling Figure 8.53 compares the *uncoupled* radiative divergence profiles from various tangent-slab calculations ('TS') and an optically thin solution ('OT'). Tangent-slab calculations were performed with equilibrium ('Boltz.') and nonequilibrium ('QSS') electronic level populations, where nonequilibrium calculations were performed for both optically thick ($\Lambda = 0$) and optically thin ($\Lambda = 1$) radiative transitions. The radiators considered are C₂, CO, CN, C, C⁺, N, N⁺, O, O⁺ and e^- , and the spectral range considered is $50 \leq \lambda \leq 1200$ nm. As was observed for the Hayabusa model, the nonequilibrium solutions with optically thin and thick radiative transitions are essentially the same, and the peak magnitude of the equilibrium solution is only greater by 10%. This indicates the populating of electronic levels is collision dominated and that the degree of nonequilibrium is low for this condition. Reabsorption is strong through-out the whole shock layer, as indicated by the overestimation of the net emission by the optically thin solution. The radiative flux incident at the stagnation point is 236 W/cm^2 for the nonequilibrium calculation with optically thin radiative transitions, corresponding to a Goulard number of 8.53×10^{-3} , slightly less than the 0.01 threshold that indicates significant

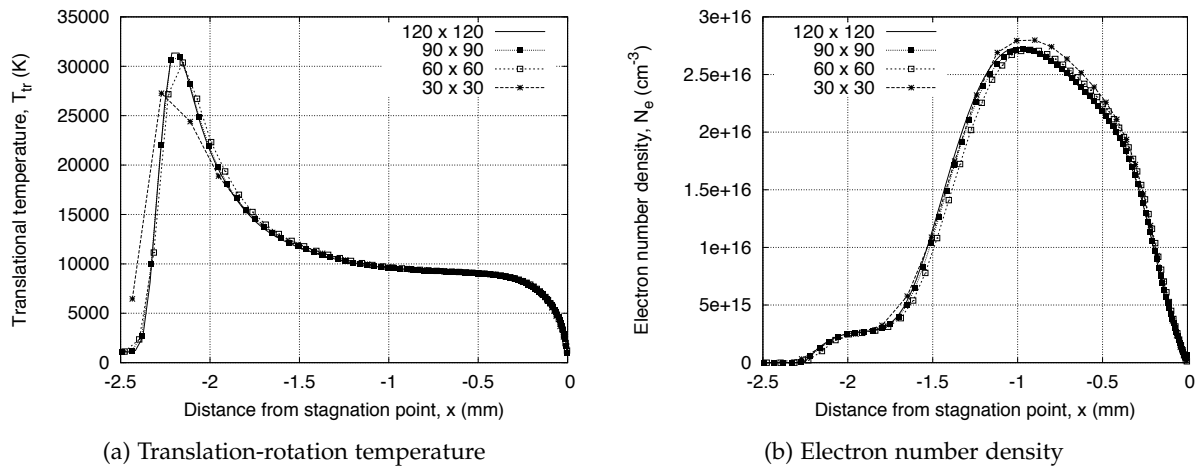


Figure 8.52: Stagnation streamline profiles from viscous simulations of the 25 mm cylinder with various grid resolutions.

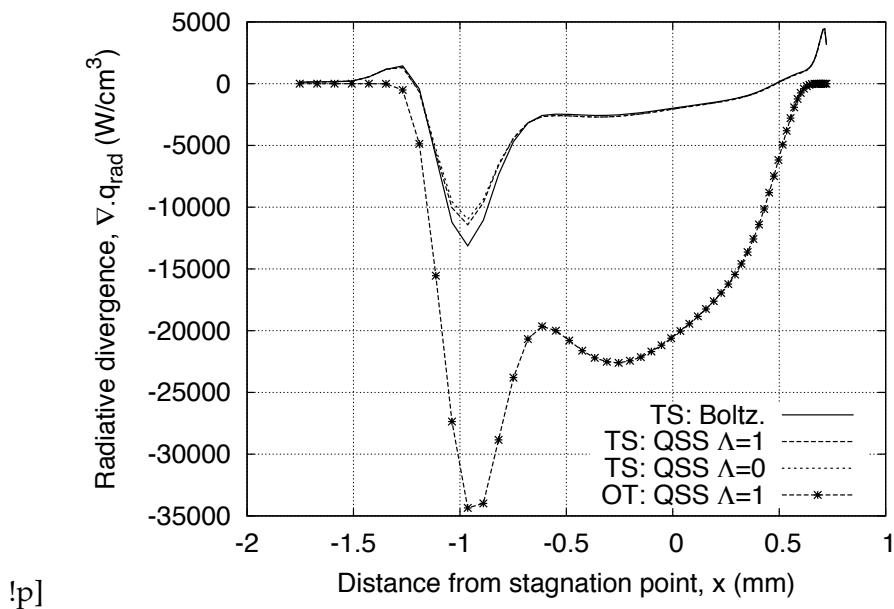


Figure 8.53: Comparison of uncoupled radiative divergence profiles along the stagnation streamline for the 25 mm cylinder.

radiation-flowfield coupling. However the simulations of the Hayabusa model demonstrated that radiation-flowfield coupling can be significant at low Goulard numbers, especially in the vicinity of the shock front, and radiatively coupled solutions are required.

Figure 8.54 compares the *uncoupled* radiative divergence profiles along the stagnation streamline ($j=0$) and half-way up the grid ($j=30$) from *uncoupled* tangent-slab and ray-tracing calculations, and Figure 8.55 compares the radiative heat flux profiles along the cylinder surface for the two calculations. The ray-traced solution was obtained using 128 rays per cell nominally with both energetic and geometric clustering. The agreement between the radiative divergence solutions is not as close as was observed for the Hayabusa simulations, with the tangent-slab model underestimating the peak radiative net emission by 20%. Also where the tangent-slab flux for the Hayabusa simulations could be scaled by a constant factor to match the ray-traced solution, here the tangent-slab solution underestimates \bar{q}_{rad} at the stagnation point and overestimates elsewhere. This is due to the strong curvature of the shock layer invalidating the tangent-slab approximation. Given the prediction for relatively weak radiation-flowfield coupling by low the Goulard number, the 20% underestimation of radiative divergence by the tangent-slab model is acceptable.

Radiatively coupled simulations using the tangent-slab equations are therefore performed. The loosely coupled strategy shown in Equation 7.44 was implemented, where the radiative divergence was updated every 10 time-steps for the first body-length of flow, and every 100 time-steps for the remainder. The uncoupled solution was used as the initial flowfield and a converged solution was obtained after 2 body-lengths of flow, Figure 8.56a. Figure 8.56b presents a comparison of the stagnation streamline T_{tr} and T_{ve} profiles with and without radiation-flowfield coupling. As was observed for the Hayabusa model, the effect of radiation-flowfield coupling is to slightly increase the shock detachment due to reabsorption in the shock front region and lower the peak in T_{ve} due to net emission. The reabsorption in the boundary layer has minimal effect on the solution due to the higher density in this region.

Comparison with measured spectra Due to the reduction in T_{ve} when radiation-flowfield coupling is considered and the strong dependence of radiation on this temperature, the radiatively coupled solution is to be used for the comparison with the spectral measurements. Figures 8.57a and 8.57b illustrate the extraction of lines-of-sight from the 2D planar computational grid for comparison with the measurements. Due to the planar nature of the simulations the shock curvature at the ends of the cylinder cannot be captured, and the shock layer is assumed to be axially uniform along the 75 mm length of the cylinder. The line of cells adjacent to the symmetry axis are therefore used to describe the flow properties encountered by the lines-of-sight.

Figures 8.58a to 8.58d compare the measured and calculated ultraviolet intensity profiles. The features considered are the CN Violet $\Delta v = -1, 0$ bands in the range $341 \leq \lambda \leq 390$ nm, the CN Violet $\Delta v = 1$ band in the range $400 \leq \lambda \leq 425$ nm, the C₂ Swan $\Delta v = -2, -1$ bands in the range

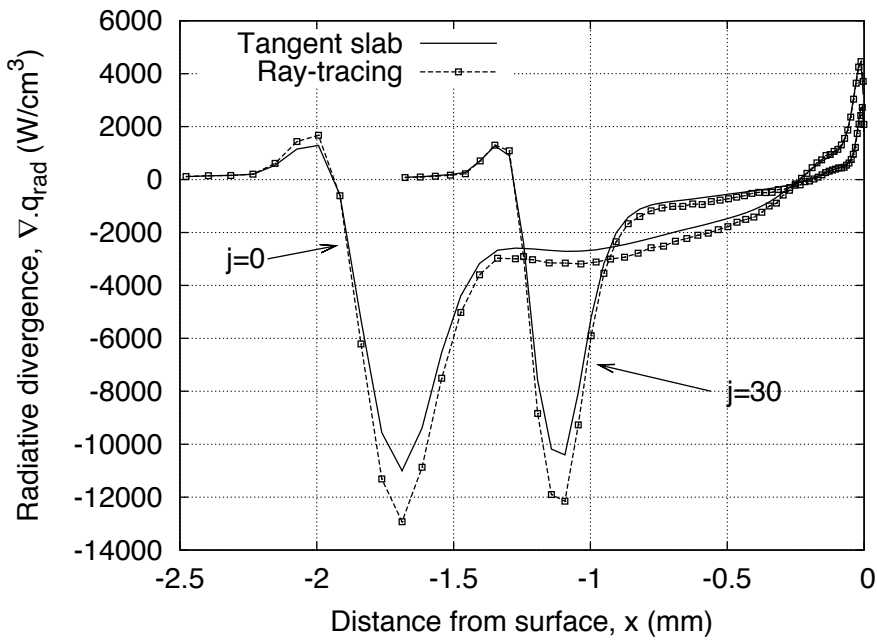


Figure 8.54: Comparison of radiative divergence profiles from *uncoupled* tangent-slab and ray-tracing calculations of the 25 mm cylinder

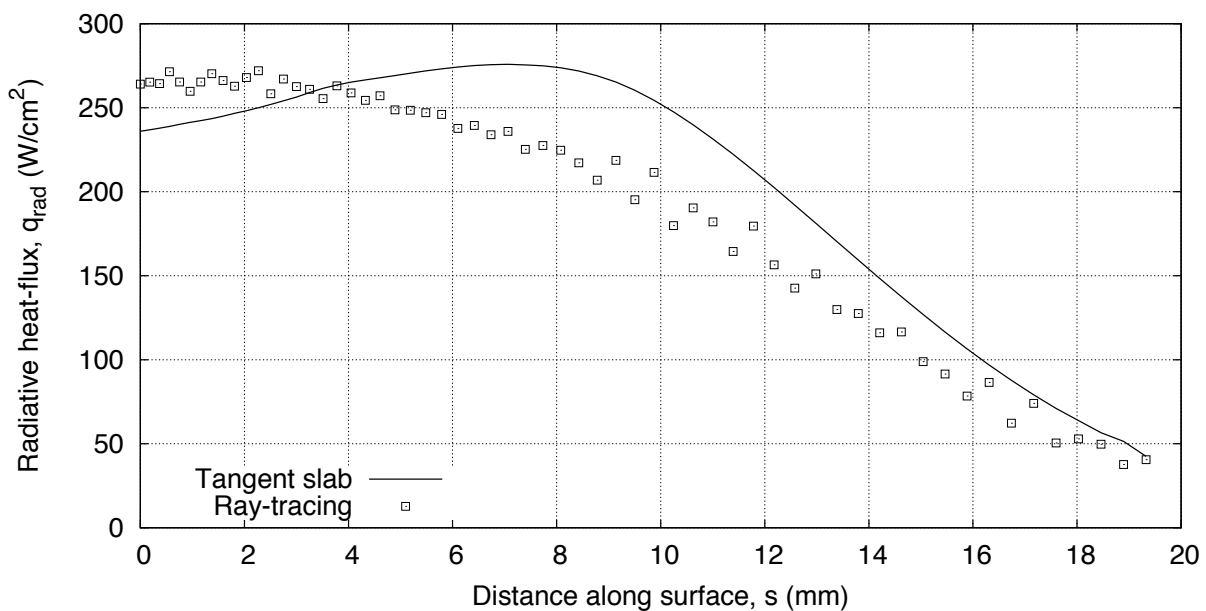


Figure 8.55: Comparison of radiative flux incident at the model surface from *uncoupled* tangent-slab and ray-tracing calculations of the 25 mm cylinder

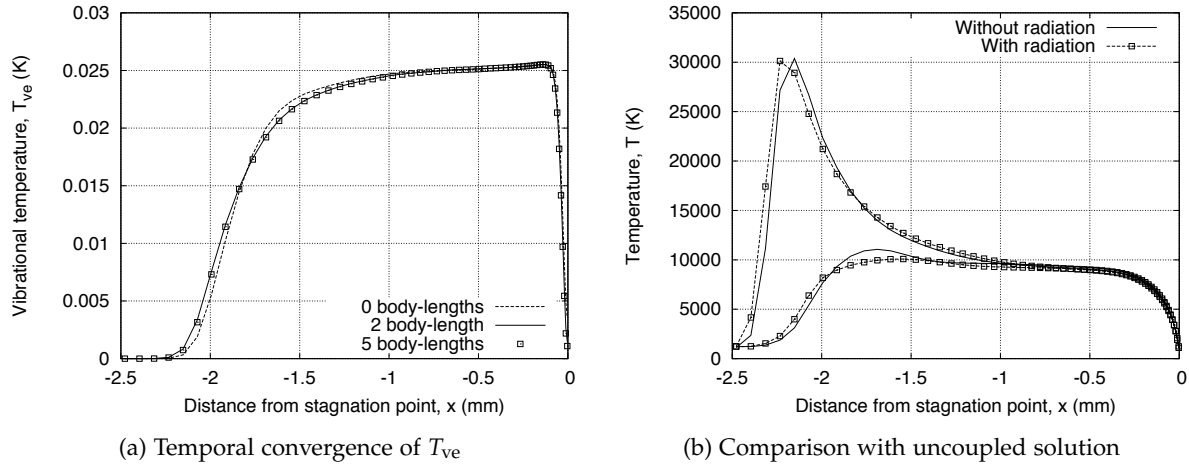


Figure 8.56: Temperature profiles along the stagnation streamline from simulations of the 25 mm cylinder with radiation-flowfield coupling.

$425 \leq \lambda \leq 480$ nm and the C₂ Swan $\Delta v = 0, 1$ bands in the range $485 \leq \lambda \leq 570$ nm. These ranges were selected for consistency with those considered in the EAST condition analysis presented in § 6.2.4. The calculations substantially overestimate the measured intensity levels for all shots. The measured data has therefore been scaled by factors of 10 and 100 as indicated to allow a qualitative comparison. The measured data presented in Figure 8.58d was from an experiment considering a 100 mm long cylinder, while the remainder used the nominal 75 mm long cylinder. The line-of-sight calculations for each were modified accordingly. The presented data considers measurements from different shots. Table 8.7 compares the secondary shock speeds from these spectral measurement shots with that for the Pitot shot x2s1319, which was used for determining the freestream conditions in § 8.4.2. While shots x2s1409 and x2s1290 agree with shot x2s1319 to within the uncertainty the shock speed is measured, x2s1324 is 7.2% higher. The higher shock speed is expected to result in a higher intensity level for this shot owing to the $\sim 11\%$ increase in enthalpy.

Table 8.7: Comparison of secondary shock speeds measured between AT4 and AT5 for various shots targeting the 37 MJ/kg CO₂-N₂ expansion tunnel condition.

Shot	Relevance	Secondary shock speed, U _{s,2} (m/s)
x2s1319	Freestream conditions	8420 ± 200
x2s1409	Data in Figures 8.58a and 8.58b	8173 ± 187
x2s1324	Data in Figure 8.58c	9023 ± 228
x2s1290	Data in Figure 8.58d	8224 ± 189

The profiles are positioned such that the location of the stagnation point corresponds to

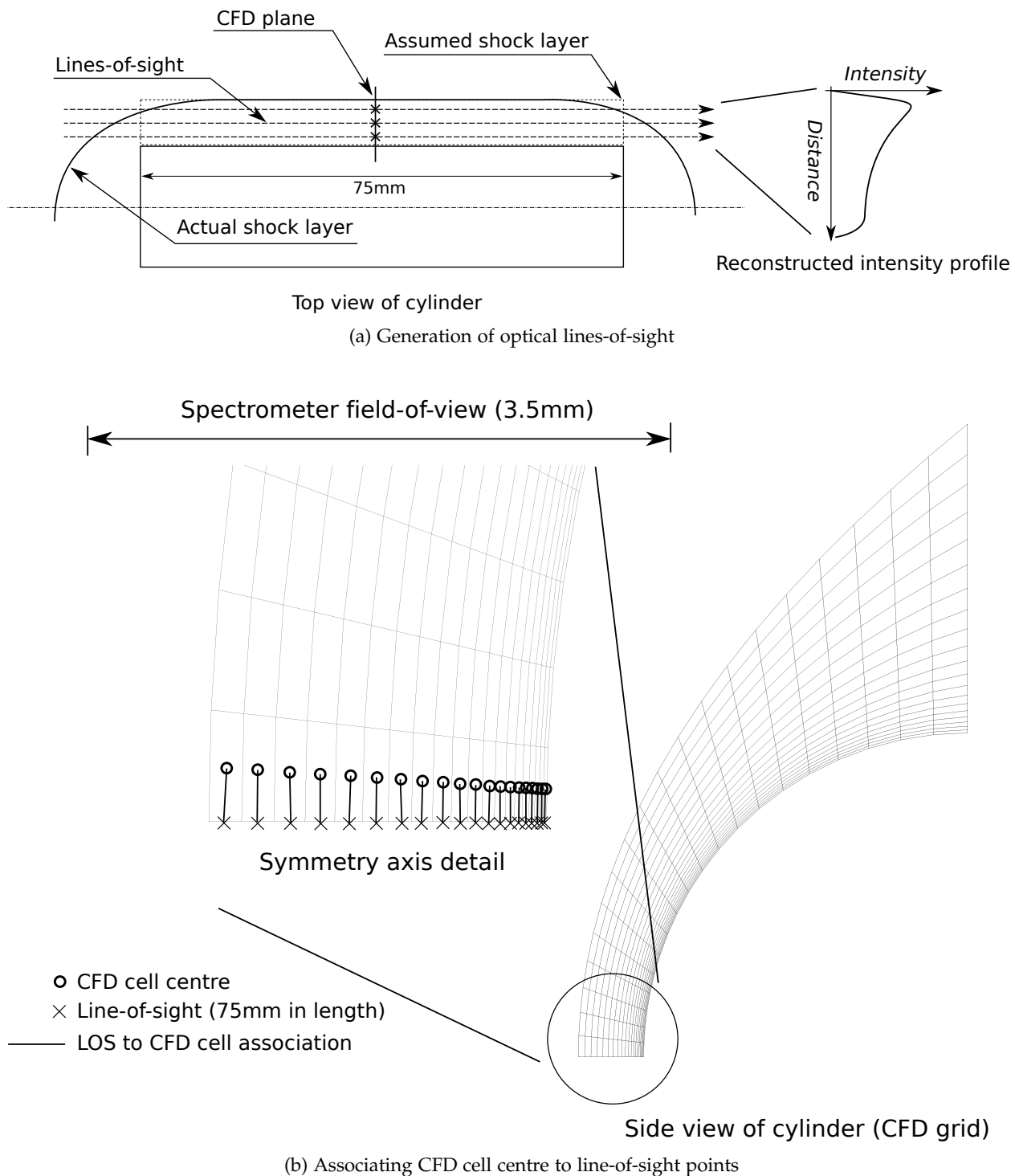


Figure 8.57: Reconstruction of an intensity profile from the planar computational domain for comparison with the 25 mm cylinder spectral measurements.

$x = 0$ mm. For the measured data this positioning was determined by matching with the intensity decay in the calculated profile due to the presence of the boundary layer. Due to the shock spilling around the edges of the cylinder, however, it is possible that the location of the stagnation point in the measured data is actually closer to the shock front than indicated. For the positioning shown, the shock detachment appears to be underestimated in the calculations by between 0.2 and 0.5 mm.

Leaving the discrepancies in magnitude and shock detachment aside, the measured and calculated data show reasonable qualitative agreement. The ratio of the peak-to-plateau intensity is in good agreement for all profiles except the C₂ Swan $\Delta v = -2, -1$ bands, which was obtained from shot x2s1324 with the higher shock speed. The rate of initial rise to the peak intensity is also in good agreement. The rate of decay from the peak intensity to the equilibrium plateau is overestimated, however.

Figures 8.59a, 8.59b and 8.59c compare the calculated and measured peak emission spectra from three different shots with the spectrometer centred at 380, 420 and 520 nm respectively. The same scaling factors have been applied to the measured data. Also shown in the figures are the spectral ranges considered for the intensity profile comparisons. Good qualitative agreement is demonstrated for the CN Violet $\Delta v = -1, 0, 1$ bands in Figure 8.59a and for the C₂ Swan $\Delta v = 0, 1$ bands in Figure 8.59c. The C₂ Swan $\Delta v = -2, -1$ bands in Figure 8.59b, however, are hardly noticeable in the measured spectra yet are stronger than the CN Violet $\Delta v = 1$ band in the calculated spectra. Given that the C₂ Swan $\Delta v = -1$ band is clearly present in the measured spectra from shot x2s1290 (Figure 8.59c), it is difficult to explain why it is not present in shot x2s1324 (Figure 8.59b). A possible explanation is the faster shock speed for shot x2s1324 (9023 m/s) compared to shot x2s1290 (8224 m/s). Significant contamination can also be observed in the measured spectra, most notably in the $315 \leq \lambda \leq 443$ nm range presented in Figure 8.59a where contaminant lines are scattered over the CN Violet band system. Many of these lines have been identified as originating from Fe, and the two lines at 396 nm and 399 nm are from the Ca⁺ ion. These contaminant features are believed to occur due to secondary diaphragm debris impacting on the model surface and vaporising a small amount of the steel model surface.

Summary and concluding remarks

A 37 MJ/kg CO₂-N₂ expansion tunnel experiment performed in the X2 facility with a 25 mm diameter cylinder model has been analysed. Freestream conditions were first estimated by a simplified strategy considering one-dimensional simulations of the secondary diaphragm rupture and Navier-Stokes simulations of the nozzle expansion. The test gas was calculated to be in a thermochemically excited state, with the thermochemical enthalpy contributing approximately 19.8% of the total when referenced to that of the initial test gas. This is almost double the thermochemical enthalpy estimated for the 47 MJ/kg N₂-O₂ condition. Whereas substantial

N_2 recombination was found during the unsteady expansion for the 47 MJ/kg $\text{N}_2\text{-O}_2$ condition, for this condition only weak recombination of CO_2 occurs and the final mole-fraction is just 6 %. Thus the freestream conditions generated by the expansion tunnel are quite different to that encountered in flight.

The radiating shock layer formed over the 25 mm diameter cylinder model were then simulated with the two-dimensional (planar) Navier–Stokes equations. Initial inviscid simulations confirmed the establishment of steady flow in the period of flow available prior to the spectral measurements being made. Intensity profiles were extracted from a viscous simulation with radiation-flowfield coupling modelled using the tangent-slab equations. The calculated intensity levels were between one and two orders of magnitude greater than the measured values, and the shock detachment was between 9 and 22% less than inferred from the measured spectra. Despite these differences, good qualitative agreement was found in the post-shock relaxation.

As the CN and C_2 intensity profiles were reproduced within a factor of 2 for the EAST shock tube analysis performed in § 6.2.4, it is more likely that the large overestimation of the measured spectra found here represents a problem with the spectrometer calibration than the physical modelling. Also the substantial shot-to-shot variation brings the accuracy of the calculated freestream conditions into question. Before any definite conclusions can be drawn from this analysis, these experimental short-comings need to be addressed.

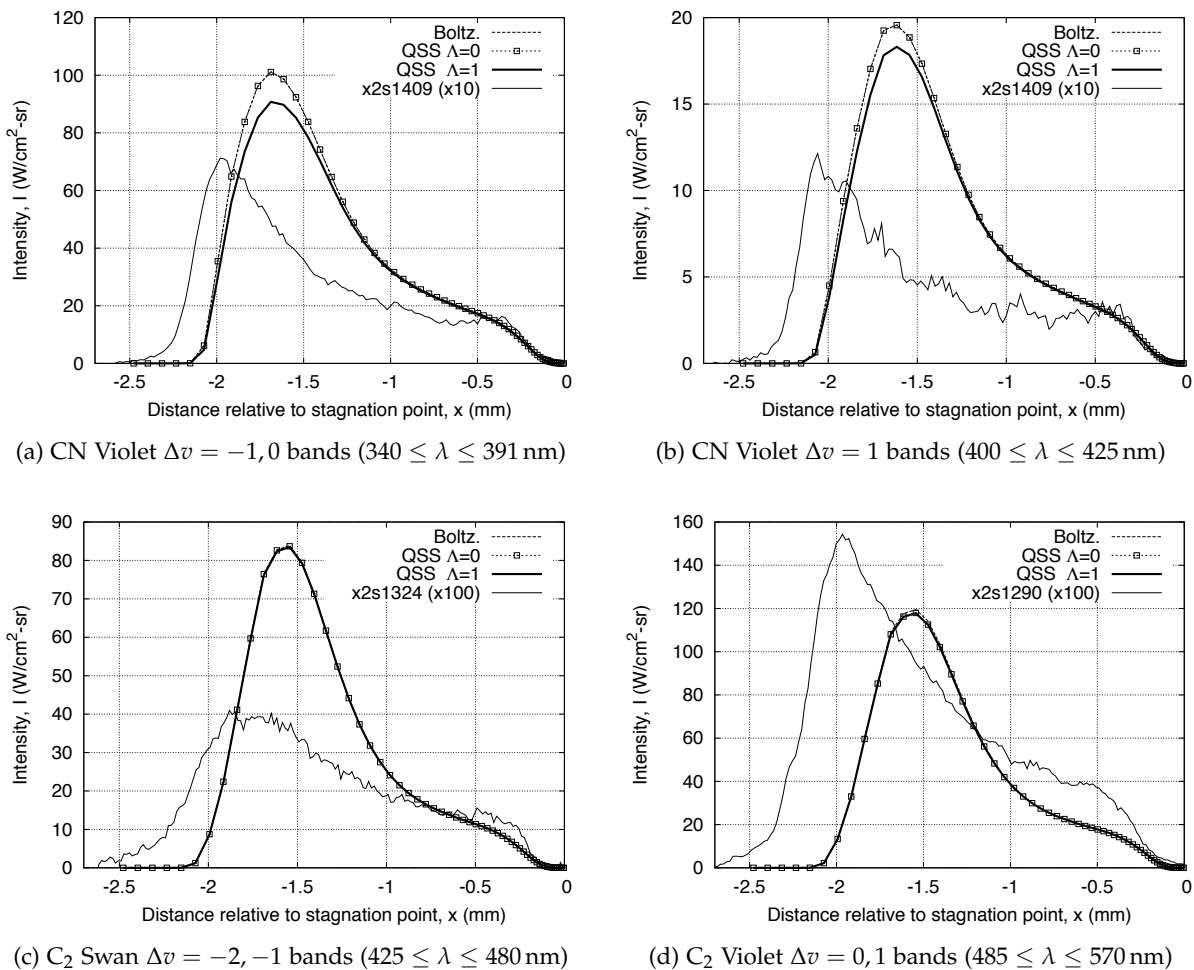


Figure 8.58: Comparison of measured and calculated ultraviolet intensity profiles along the symmetry plane of the 25 mm cylinder model.

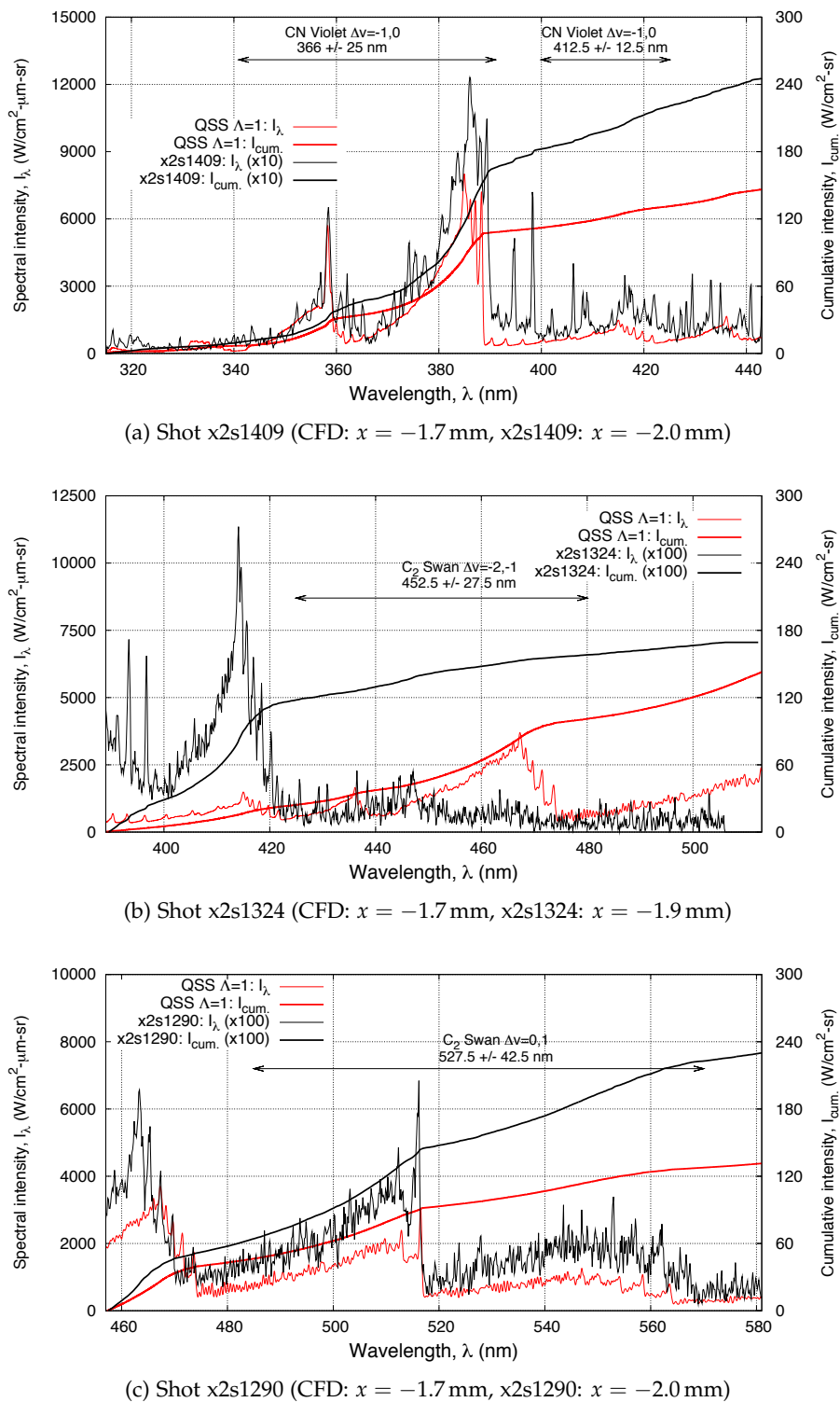


Figure 8.59: Comparison of calculated and measured peak intensity spectra from the 25 mm cylinder experiment.

8.5 Summary

A novel, simplified modelling strategy for calculating the freestream conditions of expansion tunnel experiments has been described. This strategy has been applied to a 47 MJ/kg N₂-O₂ condition and a 37 MJ/kg CO₂-N₂ performed in the X2 facility in § 8.3 and 8.4 respectively. The freestream conditions have then been applied to simulate the radiating shock layers formed over the test models, and comparisons with spectral measurements have been made. For the N₂-O₂ condition, an assessment of the binary scaling hypothesis was performed via comparisons with an effective flight condition. Detailed summaries for each experiment have been provided at the end of the each respective section.

Although some notable discrepancies were found when comparing the measured and calculated radiation intensities, a number of important observations regarding the experiments can be made. Firstly, the significant shot-to-shot variation observed in both experiments needs to be addressed. As the Pitot pressure measurement is critical to the freestream calculation, and given that the Pitot rake cannot be installed in the test section for the shots making spectral measurements of the model, significant shot-to-shot variation makes the determination of accurate freestream conditions very difficult. A solution to this problem would be to place a single Pitot probe in the test section such that it doesn't disturb the spectral measurements, or even build a Pitot probe into the model itself. Secondly, efforts need to be made to minimise spatial smearing of the spectral measurements. The poor depth-of-field for the Hayabusa IR measurements made it difficult to conclusive observations from the comparison with calculations. Installing an iris in the optical path of the spectrometer may address this problem. Thirdly, significant levels of contamination from C, Fe and Ca⁺ where identified in the measured spectra. The model surface itself is likely to be a source of all three contaminants, however most of the carbon contamination is likely to originate from the secondary diaphragm. Efforts should be made to use new models without damage from tunnel debris where possible, and the model surface should be carefully cleaned prior to the experiment. As contamination from the secondary diaphragm is difficult to avoid, attempts should be made to incorporate it into the simulations.

Improvements to the simulation strategies should also be pursued. Specifically, Navier-Stokes simulations of the entire facility with a two-temperature model and an inertial model of the secondary diaphragm should be performed. Such calculations are outside the scope of this thesis and are recommended for future work. Navier-Stokes simulations of the radiating shock layer with parametric variation of the freestream conditions should also be pursued.

Overall, however, this analysis has demonstrated the potential value of expansion tunnel testing. Although similarity between subscale and flight radiative heating was not found when the binary scaling hypothesis was applied, expansion tunnel testing remains a valuable platform for the validation of physical models and radiation transport models.

9

Conclusion

The role of radiation in heating atmospheric entry vehicles is not presently well understood. In particular, the contribution of *nonequilibrium* radiation to the surface heating rate is highly uncertain. A combination of experimental measurement and computational modelling of radiating shock layers allows new physical models to be formulated, implemented and assessed. In this thesis a set of computational tools for the computational modelling of radiating shock layers have been developed. Specific attention was given to developing models suitable for describing radiation in the nonequilibrium thermochemical regime characteristic of hyperbolic entry at Earth and Mars. Although the implemented models are not state-of-the-art, they provide a framework for more advanced models to build on.

Part I of this thesis presented the mathematical formulation of the proposed physical models for describing radiating shock layers.

In § 2 the governing equations for two types of flowfield solvers were presented: the compressible Navier–Stokes equations, and the one-dimensional post-shock relaxation equations. The consideration of these equations allowed the required areas of physical modelling to be identified.

In § 3 the first of these areas was considered, namely the properties of high temperature gases. Specifically, models for thermodynamic, transport and spectral radiation coefficients of a multicomponent, multitemperature and partially ionised gas were described. The thermodynamic properties were derived by assuming the complete decoupling of the thermal modes. Comparisons with the fully coupled thermodynamic properties tabulated by Capitelli *et al.* [81]

demonstrated good agreement for most atomic species at temperatures less than 10,000 K, while diatomic species show discrepancies at temperatures as low as 4,000 K. These discrepancies were deemed tolerable due to the strongly dissociated shock layers of interest. A transport coefficient model was developed based on the Gupta-Yos [92] equations. A near complete set of binary collision cross sections for the Ar-C-N-O elemental system were compiled by searching the literature for the best available data. Comparisons with the viscosity of air as calculated with the CEA2 code [5] demonstrated good agreement for temperatures up to 20,000 K. Comparisons with the Mars viscosity tabulations of Bruno *et al.* [6] calculated with a high-order Chapman-Enskog method demonstrated good agreement for moderate levels of ionisation. For the calculation of spectral radiation coefficients, a line-by-line model for atomic and diatomic species was presented. Electronic level and atomic line data was obtained from NIST [80, 85], and the diatomic electronic transition moments presented by Chauveau *et al.* [123] and Babou *et al.* [124] were implemented. Continuum transitions were modelled by the step model of Johnston [19] for N and O photoionisation and with hydrogenic approximations otherwise. The model implementation was verified by comparisons with the SPRADIAN07 code [66]. Large differences were found between the Hyun [66] and Chauveau *et al.* [123] electronic transition moments for the N₂ VUV transitions.

The second area of required physical modelling, namely nonequilibrium rate processes, was considered in § 4. The chemical kinetic and thermal energy exchange models implemented by the flowfield solvers were presented, as was the collisional-radiative framework for the spectral radiation module. For the chemical kinetic modelling, both engineering and advanced level models were considered for describing chemical reactions in the presence of thermal nonequilibrium. An important observation was the good agreement of the Park $s = 0.7$ model with N₂ dissociation rates estimated by computational chemistry [147]. For the thermal nonequilibrium modelling, the energy exchange models required for two- and three-temperature descriptions of a partially ionised gas were described. An alternative model to the Park [29] vibration-translation exchange limiting cross section model for CO as proposed by Fujita [77] was presented. Particular attention was given to describing chemistry-energy coupling models that were consistent with the chemical kinetic models. For the collision-radiative modelling, a QSS framework was presented and rate coefficient models for Ar, C, N, O, C₂, CN, CO, N₂ and N₂⁺ were proposed by compiling and comparing data from the literature. For the critical electron impact excitation rates of atoms from low-lying states, efforts were made to implement rate coefficients derived from experiments and computational chemistry.

Part II was then focused on the implementation and application of these physical models in the one-dimensional post-shock relaxation equations.

The implementation of the one-dimensional post-shock relaxation equations in the Poshax3 code was described in § 5. The governing equations were integrated in a fully coupled manner and the radiative source term was modelled in a simplified fashion via an escape factor. The

implementation was verified via comparison with the Fire II solutions presented by Panesi [58]. Excellent agreement was found for both the temperature and species number density profiles at the high altitude $t = 1634\text{ s}$ and $t = 1636\text{ s}$ trajectory points.

The effect of the various physical models presented in § 3 and 4 was then investigated by application the code to both Earth and Mars atmospheric entry conditions. An important finding of this analysis was the sensitivity of the post-shock relaxation to dissociation-vibration and ionisation-electron coupling. Also, implementing the Fujita [77] vibration-translation exchange limiting cross section model for CO was found to greatly increase the rate of vibrational relaxation for $\text{CO}_2\text{-N}_2$ mixtures. The Poshax3 code was then applied to analyse shock tube experiments performed in the NASA Ames EAST and University of Queensland X2 facilities. For the EAST facility, 10 km/s $\text{N}_2\text{-O}_2$ and 8.5 km/s $\text{CO}_2\text{-N}_2$ conditions were considered. For the X2 facility, an 11 km/s $\text{N}_2\text{-O}_2$ condition was considered. The comparison with the EAST and X2 data demonstrated that the *total* measured radiation is able to be estimated within 30% for $\text{N}_2\text{-O}_2$ mixtures and within 50% for $\text{CO}_2\text{-N}_2$ mixtures when the best performing physical models are implemented. Three of areas of concern emerged for these analyses, however. Firstly, the infrared spectra of air was found to be underestimated mainly due to differences in line shapes and background continuum levels. To address this discrepancy, it was proposed additional continuum mechanisms be considered in the spectral model and high resolution spectroscopy measurements be pursued. Secondly, it was found that no single physical model set was able to accurately reproduce all spectral features for both the air and Mars conditions. Specifically, for the air conditions preferential vibration-dissociation coupling was required to reproduce the N_2^+ First Negative emission, however a non-preferential model was required to reproduce atomic line emission. For the Mars conditions, CO and C transitions are accurately reproduced when the vibration-translation exchange limiting cross section model of Park [137] is employed, while CN and C_2 transitions are more accurately reproduced when the model of Fujita [77] is employed. As these discrepancies were all related to dissociation phenomena, it was suggested that a vibrationally specific model may be able to resolve them. Thirdly, the significant levels of carbon contamination were found in both the EAST and X2 facilities when an air test gas was used. This was identified via the presence of CN Violet and atomic C line radiation. As the chemical kinetics of air may be unduly effected by the presence of carbon, it was suggested future analyses should attempt to model its presence.

Part III, the third and final part of this thesis, then considered the modelling of radiating shock layers in two-dimensions.

In § 7 the implementation of the axisymmetric and planar Navier-Stokes equations in the time-accurate Eilmer3 code was described. An overview of the code structure and supporting programs was given, and the mathematical form of the discretised governing equations was presented. The operator-split method for calculating the chemical and thermal increments was described, as were the models for diffusion and radiation-flowfield coupling. Particular attention

was given to describing a novel ray-tracing based radiation transport model developed in this work. The model was assessed by application to planar and axisymmetric test cases; while good accuracy was demonstrated for planar geometries, some discrepancies emerged near the symmetry axis for axisymmetric geometries. Finally the operator-split approach for modelling the thermochemical nonequilibrium source terms was assessed via comparisons with the fully coupled one-dimensional post-shock relaxation equations. The test case considered was the strongly nonequilibrium Fire II $t = 1634\text{ s}$ trajectory point, and good agreement was found between the two solutions.

The *Eilmer3* code was then applied to simulate two radiating shock layer experiments performed in the University of Queensland X2 facility configured as an expansion tunnel. Firstly, a 47 MJ/kg N₂-O₂ condition with a subscale Hayabusa model was considered. Secondly, a 37 MJ/kg CO₂-N₂ condition with a 25 mm diameter cylinder model was considered. For both experiments, a new (simplified) technique for estimating the freestream conditions was applied, and the radiating shock layers formed over the models were then simulated. Comparisons with spectral measurements were made with radiatively coupled flowfield solutions. For the 47 MJ/kg N₂-O₂ condition, the peak intensity level was found to be in good agreement however the calculations estimated the peak to be much closer to the body than measured in the experiments. Also the level of N₂⁺ emission in the ultraviolet violet region was overestimated by at least an order of magnitude. It was suggested that these discrepancies could be attributed to a lower level of N₂ in the freestream than was calculated. An assessment of the binary scaling hypothesis was also performed via comparisons with an effective flight condition. The effect of radiation coupling on the flowfield was found to be much greater for the flight condition, resulting in a factor of 5 difference in the radiative flux incident at the stagnation point. Also the thermochemically excited freestream was found to increase the shock detachment compared to an ideal freestream without any excitation. A 29% reduction in radiative heat flux for the effective flight condition was found when implementing the N₂ electronic transition moments of Hyun [66] instead of Chauveau *et al.* [123]. For the 36 MJ/kg CO₂-N₂ condition, the calculated intensity levels of CN Violet and C₂ Swan were between one and two orders of magnitude greater than the measured values, and the shock detachment was between 9 and 22% less than that inferred from the measured spectra. Despite these differences, good qualitative agreement was found in the post-shock relaxation region. A number of important conclusions were drawn from these analyses. On the experimental side, the shot-to-shot variation, spatial smearing of spectra and contamination were identified as areas in need of improvement. Computationally, it was suggested that complete simulations of the facility with a two-temperature model and an inertial diaphragm model were required to assess the validity of the simplified modelling strategy. Despite a number of short-comings to both the experiments and calculations being identified, the analyses demonstrated the potential value of the expansion tunnel testing for the investigation of radiating shock layers.

9.1 Accomplishments and unique contributions

As was mentioned in the introduction, this thesis was built on the chemical and thermal nonequilibrium framework developed by Gollan [1]. In the conclusion of that thesis, the recommendations for future work were:

- the modelling of surface catalycity effects by the inclusion of appropriate wall boundary conditions;
- the extension of the vibrational nonequilibrium modelling to include polyatomic molecules;
- the modelling of transport properties for the multitemperature gas; and
- the coupling of the flow solver to a radiation transport solver.

In this thesis, all these recommendations have been addressed, although the modelling of surface catalyticity effects was treated in a relatively crude manner. Furthermore, a number of additional accomplishments have been made:

- the development of appropriate physical models for partially ionised gases;
- the implementation of the fully-coupled post-shock relaxation equations;
- the implementation of the two-temperature Navier–Stokes equations; and
- the development of a line-by-line spectral radiation model with a collisional-radiative capability for electronic levels.

The computational tools developed in this thesis are now in use by a variety of research groups around the world. In addition to code development, accomplishments have been made with respect to the simulation of radiating shock layer experiments. Most notably, a novel simplified simulation strategy for expansion tunnel flows has been devised and implemented.

A number of unique contributions to the field of radiating shock layer modelling have also been made in this thesis. In § 6.3 an analysis was performed of spatially and spectrally resolved radiation measurements for a series of shock tube experiments in the X2 facility with an air test gas targetting a shock speed of 11 km/s. Both ultraviolet and infrared spectra were considered. Although air shock tube experiments with speeds of up to 18 km/s were performed in the 1960’s [227], these experiments only measured intensity profiles at a single wavelength. Of the spatially and spectrally resolved air shock tube experiments recently performed in the EAST facility, the fastest condition analysed in the literature is 10.34 km/s [63]. Fujita *et al.* [34] measured spectrally and spatially resolved radiation for an 11.9 km/s air shock tube condition, however only the $270 \leq \lambda \leq 520$ nm spectral range was considered and comparisons with intensity profiles were not performed. The comparison of both ultraviolet and infrared intensity profiles and

spectra for a 11 km/s air shock tube experiment in the present work therefore represents a unique contribution to the radiation literature.

In § 7.5.4 a ray-tracing based radiation transport model combining elements of both Discrete Transfer [72–74] and Monte-Carlo [75, 202] methods was presented. The method is novel in that the radiative energy is treated as a discrete quantity (Monte-Carlo approach), yet spectral reabsorption is not treated in a statistical manner (Discrete Transfer approach). Furthermore, the ray-tracing model is able to be run in a parallel manner on a shared-memory, multiple-processor computer. To the best of the authors knowledge, this is the first time such a ray-tracing based radiation transport model has been presented in the literature.

In § 8.3 and 8.4 simulations of radiating shock layers generated by expansion tunnel flow with the Navier–Stokes equations and coupled non-Boltzmann radiation were presented. Comparisons with spatially and spectrally resolved radiation intensity measurements are also performed. Again, to the best of the authors knowledge, this is the first time such simulations been performed and compared with experimental spectra. Furthermore, comparisons were made with simulations of an effective flight condition also considering coupled non-Boltzmann radiation; such a comparison has not previously been presented in the literature.

9.2 Recommendations for future work

Following the work presented in this thesis, recommendations for future work can be made in two areas; (1) computational modelling, and (2) experimental measurements.

9.2.1 Computational modelling

One of the main observations from the comparisons with shock tube experiments presented in this work was the inability of a single physical model set to describe all the observed spectral features. Specifically, it was found that different dissociation-vibration coupling and vibration-translation exchange models were required to explain the various features. It is therefore proposed that future work should seek to consider state-specific chemical kinetics in the flowfield solvers. A logical progression in this direction would be to first implement an electronically specific model, and then implement a vibrationally specific model. Given the success of vibrationally specific models for improving the agreement with CN radiation in Titan mixtures [61], it is possible such a model would also improve agreement with air and Mars test gases.

The spectral radiation model implemented in this work modelled bound-bound atomic and diatomic transitions via a line-by-line model, and atomic continuum transitions by step and hydrogenic models. Notable omissions were therefore bound-bound polyatomic transitions and diatomic continuum transitions. Future work should therefore seek to develop models for these processes. The photoionisation and photodetachment of diatomic molecules can be significant

at low temperatures ($T \lesssim 6,000\text{ K}$), for example, as encountered in the boundary layer of an aeroshell. Furthermore, non-hydrogenic models for atomic continuum transitions should be implemented. The cross sections contained in the TOPBase database [131] would be a good starting point for this. Models for the negative ion continuum, which can contributes significantly for Earth re-entry [133], should also be implemented. In the present work atomic lines were treated as multiplets for energies less than 6 eV to maximise the computational efficiency of the Navier–Stokes calculations — the validity of applying this simplification should be investigated, especially for flowfields close to the optically thick limit. Given the sensitivity of radiative intensity for EAST air conditions to variation in Stark widths demonstrated in Reference [63], individual line Stark broadening parameters (*e.g.* from References [129, 228, 229]) should be considered in place of the curve fit model implemented in the present work. Given the large differences found between the Hyun [66] and Chauveau *et al.* [123] N₂ VUV electronic transition moment datasets, and the importance of these transitions for predicting re-entry heat flux, further investigation into the accuracy of these datasets is called for.

In the introduction it was stated that a long term application for this work is the simulation of aeroshells at flight conditions. Such simulations were not possible in the present work with the Navier–Stokes equations¹ due to the time-accurate nature of the Eilmer3 code (*i.e.* the stiffness of the chemical and thermal increments mandates the use of very small time steps). Future work should therefore pursue the development of a fully-implicit steady-state integration technique.

The analyses of the expansion tunnel conditions in § 8.3 found substantial disagreement with the measured data for both the air and Mars gas conditions. It was suggested that this may be due to the simplified facility simulation strategy outlined in § 8.2.2 producing erroneous freestream conditions. To test this hypothesis, complete facility simulations with the two-temperature Navier–Stokes equations and an inertial diaphragm rupture model should be pursued.

9.2.2 Experimental measurements

Another important observation made from the comparisons with shock tube experiments was the presence of a continuum background and broad atomic line profile bases that where not predicted by the calculations. While it is possible the continuum background will be explained by the consideration of diatomic and negative ion continua, the broad atomic line profile bases are not able to explained by the present line profile theory (*i.e.* the Voigt profile). The X2 measurements with various grating densities, however, revealed that this broadening appeared to be an artefact of the spectrometer. Future experimental work should therefore seek to clarify this discrepancy by performing a comprehensive investigation of the atomic line profiles with

¹Although a simulation of the effective flight condition for the subscale Hayabusa experiments was presented in § 8.3.4, the velocity was less than that encountered at peak-heating and the boundary layer was not properly resolved.

various grating densities. Spectra at relevant temperatures and pressures from other 'clean' facilities, such as plasma torches, should also be considered to determine whether the background continuum is the result of carbon contamination.

Finally, the analyses of the expansion tunnel experiments in § 8 were made difficult by the shot-to-shot variation and lack of test gas measurements for the shots with spectral measurements. As the author has had some experience with operating impulse facilities, the inherent difficulties in reducing shot-to-shot variation are understood. Future expansion tunnel work should therefore seek to measure as many parameters of the test flow as possible during shots with spectral measurements. Static pressure measurements could be made by flush mounting pressure transducers at the nozzle exit. Pitot pressure measurements could be made by strategically positioning a single transducer in the test-section such that it does not disturb the experiment, or building it into the model itself. Calorimeters embedded in the model surface would also be useful in attempting to determine the total enthalpy of the flow.

References

- [1] R. GOLLAN. *Computational Modelling of High-Temperature Gas Effects with Application to Hypersonic Flows*. Ph.D. thesis, The University of Queensland, St Lucia, Australia (2008).
- [2] J. H. GRINSTEAD, M. C. WILDER, J. OLEJNICZAK, D. W. BOGDANOFF, AND G. A. ALLEN. *Shock-heated air radiation measurements at lunar return conditions*. Tech. Rep. AIAA Paper 2008-1244, Reno, Nevada (2008).
- [3] J. H. GRINSTEAD, M. C. WILDER, M. J. WRIGHT, D. W. BOGDANOFF, AND G. A. ALLEN. *Shock radiation measurements for Mars aerocapture radiative heating analysis*. Aiaa paper 2008-1272, Reno, Nevada (2008).
- [4] M. D'SOUZA, T. EICHMANN, D. POTTER, R. MORGAN, T. MCINTYRE, P. JACOBS, AND N. MUFFORD. *Observation of an ablating surface expansion tunnel flow*. AIAA Journal **48**(7), 1557-1560 (2010).
- [5] B. J. McBRIDE AND S. GORDON. *Computer program for calculation of complex chemical equilibrium compositions and applications. Part 2: Users manual and program description*. Reference Publication 1311, NASA (1996).
- [6] C. BRUNO, M. CAPITELLI, C. CATALFAMO, R. CELIBERTO, G. COLONNA, P. DIOMEDE, D. GIORDANO, C. GORSE, A. LARICCHIUTA, S. LONGO, D. PAGANO, AND F. PIRANI. *Transport properties of high-temperature Mars atmosphere components*. ESA STR-256, European Space Agency (2008).
- [7] J. KISSEL, F. KRUEGER, J. SILÉN, AND B. CLARK. *The Cometary and Interstellar Dust Analyzer at comet 81P/Wild 2*. Science **304**(5678), 1774-1776 (2004).
- [8] G. WEBSTER. *NASA's next Mars rover nears completion*. Viewed 26 April 2011, <http://www.nasa.gov/mission_pages/msl/news/msl20110406.html> (2011).
- [9] M. VIOTTI. *Mars Science Laboratory: Entry, descent and landing configuration*. Viewed 17 August 2010, <<http://marsprogram.jpl.nasa.gov/msl/mission/spacecraft/edlconfig/>> (n.d.).
- [10] D. BROWN. *Mars Reconnaissance Orbiter Arrival: NASA Press Kit*. Viewed 16 September 2010, <<http://mars.jpl.nasa.gov/mro/files/mro/mro-arrival.pdf>> (2006).

- [11] P. BOUCHER. *Aurora's roadmap to Mars.* Viewed 17 August 2010, <http://www.esa.int/export/esaCP/SEMXYZY274OD_index_0.html> (2003).
- [12] M. LOCKWOOD. *Titan aerocapture systems analysis.* AIAA Paper 2003-4799, Huntsville, Alabama (2003).
- [13] N. TAKASHIMA, B. HOLLIS, E. ZOBY, K. SUTTON, J. OLEJNICZAK, M. WRIGHT, AND D. PRABHU. *Preliminary aerothermodynamics of Titan aerocapture aeroshell.* AIAA Paper 2003-4952, Huntsville, Alabama (2003).
- [14] J. OLEJNICZAK, M. WRIGHT, D. PRABHU, N. TAKASHIMA, B. HOLLIS, E. ZOBY, AND K. SUTTON. *An analysis of the radiative heating environment for aerocapture at Titan.* AIAA Paper 2003-4953, Huntsville, Alabama (2003).
- [15] D. BOSE, M. WRIGHT, D. BOGDANOFF, G. RAICHE, AND G. ALLEN JR. *Modeling and experimental assessment of CN radiation behind a strong shockwave.* Journal of Thermophysics and Heat Transfer **20**(2) (2006).
- [16] R. BRAUN, R. POWELL, AND L. HARTUNG. *Effect of interplanetary trajectory options on a manned Mars aerobrake configuration.* Technical Paper 3019, NASA Langley Research Center (1990).
- [17] A. MIELE, T. WANG, W. LEE, AND Z. ZHAO. *Optimal trajectories for the aeroassisted flight experiment.* Acta Astronautica **21**(11-12), 735-747 (1990).
- [18] P. A. GNOFFO, K. J. WEILMUENSTER, D. R. OLYNICK, AND H. HAMILTON. *Computational aerothermodynamic design issues for hypersonic vehicles.* Journal of Spacecraft and Rockets **36**(1), 21-43 (1999).
- [19] C. JOHNSTON. *Nonequilibrium shock-layer radiative heating for Earth and Titan entry.* Ph.D. thesis, Virginia Polytechnic Institute and State University, Blacksburg, Virginia (2006).
- [20] M. WRIGHT, C. TANG, K. EDQUIST, B. HOLLIS, AND P. KRASA. *A review of aerothermal modeling for Mars entry missions.* AIAA Paper 2010-0443 (2010).
- [21] C. JOHNSTON, B. HOLLIS, AND K. SUTTON. *Radiative heating methodology for the Huygens Probe.* AIAA paper 2006-3426 (2006).
- [22] E. S. CORNETTE. *Forebody temperatures and calorimeter heating rates measured during Project Fire 2 reentry at 11.35 kilometers per second.* NASA TM X-1305 (1966).
- [23] D. CAUCHON. *Radiative heating results from the FIRE II flight experiment at a reentry velocity of 11.4 km/s.* Tech. rep., NASA Technical Memorandum, TM X-1402 (1967).
- [24] D. LEE AND W. GOODRICH. *The aerothermodynamic environment of the Apollo Command Module during superorbital entry.* NASA Technical Note D-6792 (1972).

- [25] C. PARK. *Stagnation-point radiation for Apollo 4*. Journal of Thermophysics and Heat Transfer **18**(3), 348-357 (2004).
- [26] B. BOTTIN. *Aerothermodynamic Model of An Inductively-Coupled Plasma Wind Tunnel*. Phd thesis, Université de Liège and von Karman Institute for Fluid Dynamics (1999).
- [27] G. PALUMBO, R. CRAIG, E. WHITING, AND C. PARK. *Measured specific intensity from 120 to 900 nm at the stagnation point of a model in an arcjet flow of 7.8 km/s*. Journal of Quantitative Spectroscopy and Radiation Transfer **57**(2), 207-236 (1997).
- [28] C. PARK, M. E. NEWFIELD, D. G. FLETCHER, T. GOCKEN, AND S. SHARMA. *Spectroscopic emission measurements within the blunt-body shock layer in an arcjet flow*. Journal of Thermophysics and Heat Transfer **13**(1), 60-67 (1999).
- [29] C. S. PARK. *Nonequilibrium Hypersonic Aerothermodynamics* (John Wiley and Sons, 1990).
- [30] R. ALLEN, P. ROSE, AND J. CAMM. *Nonequilibrium and equilibrium radiation at super-satellite entry velocities*. Research Report 156, Avco-Everett Research Laboratories, Everett, MA (1962).
- [31] J. ARNOLD, V. REIS, AND H. WOODWARD. *Theoretical and experimental studies of equilibrium and nonequilibrium radiation to bodies entering postulated Martian and Venusian atmospheres at high speeds*. AIAA Paper 65-0166 (1965).
- [32] G. THOMAS AND W. MENARD. *Experimental measurements of nonequilibrium and equilibrium radiation from planetary atmospheres*. AIAA Journal **4**(2), 227-237 (1966).
- [33] S. SHARMA AND W. GILLESPIE. *Nonequilibrium and equilibrium shock front radiation measurements*. Journal of Thermophysics and Heat Transfer **5**(3), 257 - 265 (1991).
- [34] K. FUJITA, S. SATO, T. ABE, AND Y. EBINUMA. *Experimental investigation of air radiation from behind a strong shock wave*. Journal of thermophysics and heat transfer **16**(1), 77-82 (2002).
- [35] E.-S. LEE, C. PARK, AND K.-S. CHANG. *Shock-tube determination of CN formation rate in a CO₂-N₂ mixture*. Journal of Thermophysics and Heat Transfer **21**(1), 50 - 56 (2007).
- [36] C. ROND, P. BOUBERT, J.-M. FELIO, AND A. CHIKHAOUI. *Nonequilibrium radiation behind a strong shock wave in CO₂-N₂*. Chemical Physics (Netherlands) **340**(1-3), 93 - 104 (2007).
- [37] G. YAMADA, H. TAKAYANAGI, T. SUZUKI, AND K. FUJITA. *Analysis of shock layer radiation in vacuum-ultraviolet region for HAYABUSA return conditions*. AIAA Paper 2010-237, Orlando, Florida (2010).
- [38] D. BOSE, E. McCORKLE, D. BOGDANOFF, AND G. ALLEN JR. *Comparisons of air radiation model with shock tube measurements*. AIAA Paper 2009-1030 (2009).

- [39] R. MORGAN. *Handbook of shock waves*, vol. 1, chap. Shock Tubes and Tunnels: Facilities, Instrumentation, and Techniques (2001).
- [40] T. MCINTYRE, A. BISHOP, AND H. RUBINSZTEIN-DUNLOP. *Experimental and numerical studies of ionizing flow in a super-orbital expansion tube*. AIAA Paper 2001-752, Reno, Nevada (2001).
- [41] B. CAPRA. *Aerothermodynamic simulation of subscale models of the FIRE II and Titan Explorer vehicles in expansion tubes*. Ph.D. thesis, The University of Queensland, St Lucia, Australia (2006).
- [42] J. GRINSTEAD, M. WILDER, D. REDA, AND C. CORNELISON. *Shock tube and ballistic range facilities at NASA Ames Research Center*. Paper presented at the AVT-186 RTO AVT/VKI Lecture Series held at the von Karman Institute, Rhode-Saint-Genése, Belgium (2010).
- [43] E. WALTERS. *Free-flight measurements of radiative heating to the front face of the apollo reentry capsule as a function of angle of attack*. NASA Technical Memorandum X-851 (1964).
- [44] D. COMPTON AND D. COOPER. *Measurements of radiative heating on sharp cones*. AIAA Journal 3(1), 107-114 (1965).
- [45] D. COOPER. *High-resolution experimental spectra and theoretical studies of equilibrium radiation from a blunt body traveling at 37,000 ft/sec*. AIAA Paper 66-104 (1966).
- [46] D. COMPTON. *Measure of ultraviolet (575 Å - 1800 Å) radiation from nitrogen at temperatures from 13,000 K to 16,000 K*. AIAA Paper 66-422 (1966).
- [47] D. COMPTON AND D. COOPER. *Free-flight measurements of stagnation-point convective heat transfer at velocities to 41000 ft/sec*. NASA Technical Note D-2871 (1965).
- [48] G. BIRD. *Molecular Gas Dynamics and the Direct Simulation of Gas Flows* (Oxford University Press, New York, 1994).
- [49] R. ALLEN. *Nonequilibrium shock front rotational vibrational and electronic temperature measurements*. Journal of Quantitative Spectroscopy and Radiative Transfer 5(3), 511 - 523 (1965).
- [50] C. PARK. *Assessment of two-temperature kinetic model for ionizing air*. Journal of Thermophysics and Heat Transfer 3(3), 233-244 (1989).
- [51] R. GRESSMAN, C. LAUX, AND C. KRUGER. *Experimental study of kinetic mechanisms of recombining atmospheric pressure air plasmas*. AIAA Paper 97-2364, Atlanta, GA (1997).
- [52] A. BRANDIS, R. MORGAN, T. MCINTYRE, AND P. JACOBS. *Nonequilibrium radiation intensity measurements in simulated Titan atmospheres*. AIAA Paper 2008-4136, Seattle, Washington (2008).

- [53] G. CHABAN, R. JAFFE, D. SCHWENKE, , AND W. HUO. *Dissociation cross sections and rate coefficients for nitrogen from accurate theoretical calculations*. Meeting Paper AIAA-2008-1209-247 (2008).
- [54] R. JAFFE, D. SCHWENKE, G. CHABAN, AND W. HUO. *Vibrational and rotational excitation and relaxation of nitrogen from accurate theoretical calculations*. Aiaa paper 2008-1208-273 (2008).
- [55] A. BULTEL, B. CHÉRON, A. BOURDON, O. MOTAPON, AND I. SCHNEIDER. *Collisional-radiative model in air for Earth re-entry problem*. Physics of Plasmas **13**(4), 11 (2006).
- [56] T. MAGIN, L. CAILLAULT, A. BOURDON, AND C. O. LAUX. *Nonequilibrium radiative heat flux modeling for the Huygens entry probe*. Journal of Geophysical Research - Planets **111**(E07S12) (2006).
- [57] J. SARRETTE, A. GOMES, J. BACRI, C. LAUX, AND C. KRUGER. *Collisional-radiative modeling of quasi-thermal air plasmas with electronic temperatures between 2000 and 13000 K*. Journal of Quantitative Spectroscopy and Radiative Heat Transfer **53**(2), 142-152 (2001).
- [58] M. PANESI. *Physical models for nonequilibrium plasma flow simulations at high speed re-entry conditions*. Ph.D. thesis, von Karman Institute for Fluid Dynamics, Rhode-St-Genése, Belgium (2009).
- [59] L. PIERROT, R. GESSMAN, C. LAUX, AND C. KRUGER. *Collisional-radiative modeling of nonequilibrium effects in nitrogen plasmas*. AIAA Paper 99-3478, Norfolk, VA (1999).
- [60] S. CHAUVEAU, C. LAUX, J. KELLEY, AND C. KRUGER. *Vibrationally specific collisional-radiative model for nonequilibrium air plasmas*. AIAA Paper 2002-2229, Maui, Hawaii (2002).
- [61] A. BRANDIS, C. LAUX, AND T. MAGIN. *Simulation of nonequilibrium radiation using vibrationally specific nitrogen models*. AIAA Paper 2008-3814, Seattle, Washington (2008).
- [62] M. FURUDATE, K. FUJITA, AND T. ABE. *Coupled rotational-vibrational relaxation of molecular hydrogen at high temperatures*. Journal of Thermophysics and Heat Transfer **20**(3), 457-464 (2006).
- [63] C. JOHNSTON. *A comparison of east shock-tube radiation measurements with a new air radiation model*. AIAA Paper 2008-1245, Reno, Nevada (2008).
- [64] R. PATCH, W. SHACKLEFORD, AND S. PENNER. *Approximate spectral absorption coefficient calculations for electronic band systems belonging to diatomic molecules*. Journal of Quantitative Spectroscopy and Radiative Transfer **2**, 263-271 (1962).
- [65] L. HARTUNG. *Predicting radiative heat transfer in nonequilibrium flow fields: Theory and User's manual for the LORAN code*. NASA Technical Memorandum 4564 (1994).

- [66] S.-Y. HYUN. *Radiation code SPRADIAN07 and its applications*. Ph.D. thesis, KAIST, Daejeon, Korea (2009).
- [67] C. LAUX. *Radiation and nonequilibrium collisional-radiative models*. VKI special course on physico-chemical models for high enthalpy and plasma flows modeling, Rhode-St-Genése, Belgium (2002).
- [68] M. WINTER, B. PFEIFFER, M. FERTIG, M. AUWETER-KURTZ, AND A. SMITH. *Recent status of the Plasma Radiation Database PARADE*. 37th AIAA Thermophysics Conference, Portland, Oregon (AIAA 2004-2585) (2004).
- [69] M. F. MODEST. *Modified differential approximation for radiative transfer in general three-dimensional media*. Journal of Thermophysics and Heat Transfer **3**(3) (1989).
- [70] D. BOSE AND M. WRIGHT. *View-factor-based radiation transport in a hypersonic shock layer*. Journal of Thermophysics and Heat Transfer **14**(1), 553-555 (2000).
- [71] L. HARTUNG. *Nonequilibrium radiative heating prediction method for aeroassist flowfields with coupling to flowfield solvers*. Ph.D. thesis, Department of Mechanical and Aerospace Engineering, North Carolina State University (1991).
- [72] N. SHAH. *The computation of radiation heat transfer*. Ph.D. thesis, Faculty of Engineering, University of London (1979).
- [73] G. ELBERT AND P. CINNELLA. *Truly two-dimensional algorithms for radiative heat transfer calculations in reactive flows*. Computational Fluids **24**(5), 523-552 (1995).
- [74] S. KARL. *Simulation of Radiative Effects in Plasma Flows*. DC report, von Karman Institute for Fluid Dynamics, Rhode-St-Genése, Belgium (2001).
- [75] W.-J. YANG, H. TANIGUCHI, AND K. KUDO. *Advances in Heat Transfer*. In J. Hartnett and T. Irvine, eds., *Radiative heat transfer by the Monte Carlo method*, vol. 27 (Academic Press, 1995).
- [76] P. A. JACOBS. *MB_CNS: a computer program for the simulation of transient, compressible flows*. Department of Mechanical Engineering Report 7/98, The University of Queensland, St Lucia, Australia (1998).
- [77] K. FUJITA. *Vibrational relaxation and dissociation kinetics of CO by CO-O collisions*. AIAA Paper 2008-3919 (2008).
- [78] W. VINCENTI AND C. KRUGER. *Introduction to Physical Gas Dynamics* (John Wiley and Sons, New York, USA, 1965).

- [79] K. HUBER AND G. HERZBERG. *Molecular Spectra and Molecule Structure IV. Constants of Diatomic Molecules* (Van Nostrand Reinhold, New York, 1950).
- [80] Y. RALCHENKO, A. KRAMIDA, J. READER, AND THE NIST ASD TEAM. *NIST Atomic Spectra Database (version 3.1.5)*. [Online]. Available: <http://physics.nist.gov/asd3> [2010, March 22]. National Institute of Standards and Technology, Gaithersburg, MD. (2008).
- [81] M. CAPITELLI, G. COLONNA, D. GIORDANO, L. MARAFFA, A. CASAVOLA, P. MINELLI, D. PAGANO, L. PIETANZA, AND F. TACCOGNA. *Tables of internal partition functions and thermodynamic properties of high-temperature Mars-atmosphere species from 50 K to 50000 K*. ESA STR-246, European Space Agency, Noordwijk, The Netherlands (2005).
- [82] M. BORN AND J. OPPENHEIMER. *Zur quantentheorie der molekeln*. Ann Physik **84**(20), 457-484 (1927).
- [83] D. GIORDANO. *Impact of the Born-Oppenheimer approximation on aerothermodynamics*. Journal of Thermophysics and Heat Transfer **21**(3), 647-657 (2007).
- [84] R. JAFFE. *The calculation of high-temperature equilibrium and nonequilibrium specific heat data for N₂, O₂ and NO*. AIAA Paper 87-1633, Honolulu, Hawaii (1987).
- [85] K. HUBER AND G. HERZBERG. *Constants of diatomic molecules*. In P. Linstrom and W. Mallard, eds., *NIST Chemistry WebBook, NIST Standard Reference Database Number 69* (National Institute of Standards and Technology, Gaithersburg MD, 20899, <http://webbook.nist.gov>, (retrieved May 8, 2010)).
- [86] P. CINNELLA AND B. GROSSMAN. *Upwind technique for flow with multiple translational temperatures*. AIAA Paper 90-1660 (1990).
- [87] J. O. HIRSCHFELDER, C. F. CURTISS, AND R. B. BIRD. *Molecular Theory of Gases and Liquids* (Wiley, New York, 1967), 4th ed.
- [88] M. WRIGHT, D. BOSE, G. PALMER, AND E. LEVIN. *Recommended collision integrals for transport property computations, Part 1: Air species*. AIAA Journal **43**(12), 2558-2564 (2005).
- [89] G. PALMER AND M. WRIGHT. *Comparison of methods to compute high-temperature gas viscosity*. Journal of Thermophysics and Heat Transfer **17**(2), 232-239 (2003).
- [90] C. WILKE. *A viscosity equation for gas mixtures*. Journal of Chemical Physics **18**, 517-519 (1950).
- [91] B. ARMALY AND L. SUTTON. *Viscosity of multicomponent partially ionized gas mixtures*. AIAA Paper 80-1495 (1980).

- [92] R. GUPTA, J. YOS, R. THOMPSON, AND K.-P. LEE. *A Review of Reaction Rates and Thermodynamic and Transport Properties for an 11-Species Air Model for Chemical and Thermal Nonequilibrium Calculations to 30,000 K.* Reference Publication 1232, NASA (1990).
- [93] A. MURPHY AND C. ARUNDELL. *Transport coefficient of argon, nitrogen, oxygen, argon-nitrogen, and argon-oxygen plasmas.* Plasma Chemistry and Plasma Processing **14**(4), 451-490 (1994).
- [94] M. WRIGHT, H. HWANG, G. PALMER, AND D. SCHWENKE. *Recommended collision integrals for transport property computations, Part 2: Mars and Venus entries.* AIAA Journal **45**(1), 281-288 (2007).
- [95] J. YOS. *Transport properties of nitrogen, hydrogen, oxygen and air to 30000K.* TR AD-TM-63-7, Avco Corporation (1963).
- [96] F. PIRANI, M. ALBERTÍ, A. CASTRO, M. TEIXIDOR, AND D. CAPPELLETTI. *Atom-bond pairwise additive representation for intermolecular potential energy surfaces.* Chemical Physics Letters **394**(1-3), 37-44 (2004).
- [97] F. PIRANI, G. MACIEL, D. CAPPELLETTI, AND V. AQUILANTI. *Experimental benchmarks and phenomenology of interatomic forces: open-shell and electronic anisotropy effects.* International Reviews in Physical Chemistry **25**(1-2), 165-199 (2006).
- [98] E. LEVIN AND M. WRIGHT. *Collision integrals for ion-neutral interactions of air and argon.* Journal of Thermophysics and Heat Transfer **18**(1), 143-147 (2004).
- [99] M. WRIGHT AND E. LEVIN. *Collision integrals for ion-neutral interactions of nitrogen and oxygen.* Journal of Thermophysics and Heat Transfer **19**(1), 148-156 (2005).
- [100] J. STALLCOP, H. PARTRIDGE, A. PRADHAN, AND E. LEVIN. *Potential energies and collision integrals for interactions of carbon and nitrogen atoms.* Journal of Thermophysics and Heat Transfer **14**(4), 480-488 (2000).
- [101] J. STALLCOP, H. PARTRIDGE, AND E. LEVIN. *Effective potential energies and transport cross sections for atom molecule interactions of nitrogen and oxygen.* Physical Review A **64**(4), 042722 (2001).
- [102] J. STALLCOP, H. PARTRIDGE, AND E. LEVIN. *Effective potential energies and transport cross sections for interactions of hydrogen and nitrogen.* Physical Review A **62**(6), 062709 (2000).
- [103] E. LEVIN, H. PARTRIDGE, AND J. STALLCOP. *Collision integrals for high temperature transport properties for N–N, O–O and N–O.* Journal of Thermophysics and Heat Transfer **4**(4), 469-477 (1990).

- [104] T. TANG AND J. TOENNIES. *An improved simple model for the van der Waals potential based on universal damping functions for the dispersion coefficients.* Journal of Chemical Physics **80**(8), 3726-3741 (1984).
- [105] M. CAPITELLI, C. GORSE, S. LONGO, AND D. GIORDANO. *Collision integrals for high temperature air species.* Journal of Thermophysics and Heat Transfer **14**(2), 259-268 (2000).
- [106] J. STALLCOP, H. PARTRIDGE, AND E. LEVIN. *Collision integrals for the interaction of the ions of nitrogen and oxygen in a plasma at high temperatures and pressures.* Physics of Fluids B **4**(2), 386-391 (1992).
- [107] P. NEUFELD, A. JANZEN, AND R. AZIZ. *Empirical equations to calculate 16 of the transport collision integrals $\omega^{(l,s)*}$ for the Lennard-Jones (12-6) potential.* The Journal of Chemical Physics **57**(3), 1100-1102 (1972).
- [108] M. CAPITELLI, D. CAPPELLETTI, G. COLONNA, C. GORSE, A. LARICCHIUTA, G. LIUTI, S. LONGO, AND F. PIRANI. *On the possibility of using model potentials for collision integral calculations of interest for planetary atmospheres.* Chemical Physics **338**(1), 62-68 (2007).
- [109] R. SVEHLA. *Transport coefficients for the NASA Lewis Chemical Equilibrium Program.* Technical Memorandum 4647, NASA Lewis Research Center, Cleveland, Ohio (1995).
- [110] Y. ZEL'DOVICH AND Y. RAIZER. *Physics of shock waves and high-temperature hydrodynamic phenomena* (New York: Academic Press, 1967).
- [111] I. KovÁCS. *Rotational structure in the Spectra of Diatomic molecules* (Adam Hilger Ltd., London, 1969).
- [112] E. WHITING. *An empirical approximation to the Voigt profile.* Journal of Quantitative Spectroscopy and Radiative Transfer **8**(6), 1374 - 1384 (1968).
- [113] J. OLIVERO AND R. LONGBOTHUM. *Empirical fits to the Voigt line width: a brief review.* Journal of Quantitative Spectroscopy and Radiative Transfer **17**(2), 233-236 (1977).
- [114] W. E. NICOLET. *Advanced methods for calculating radiation transport in ablation-product contaminated boundary layers.* Contractor Report CR-1656, NASA, Washington, D.C. (1970).
- [115] G. TRAVING. *Plasma diagnostics*, chap. Interpretation of Line Broadening and Line Shift (AIP Press, 1995).
- [116] H. GRIEM. *Plasma Spectroscopy* (McGraw Hill, 1964).
- [117] W. PAGE, D. COMPTON, W. BORUCKI, AND D. CIFFONE. *Radiative transfer in inviscid non-adiabatic stagnation region shock layers.* AIAA Paper 68-784 (1968).

- [118] A. THORNE. *Spectrophysics* (Chapman and Hall, 1974).
- [119] S. GOLDEN. *Approximate spectral absorption coefficients of electronic transitions in diatomic molecules*. Journal of Quantitative Radiation Transfer **7**, 225-250 (1967).
- [120] C. LAUX, T. SPENCE, C. KRUGER, AND R. ZARE. *Optical diagnostics of atmospheric pressure air plasmas*. Plasma Sources Science and Technology **12**, 125-138 (2003).
- [121] Y. BABOU, P. RIVIÈRE, M.-Y. PERRIN, AND A. SOUFIANI. *High-temperature and nonequilibrium partition function and thermodynamic data of diatomic molecules*. International Journal of Thermophysics **30**, 416-438 (2009).
- [122] C. PRASAD AND P. BERNATH. *Fourier transform jet-emission spectroscopy of the $A^2\pi_i-X^2\sigma^+$ transition of cn*. Journal of Molecular Spectroscopy **156**(2), 327-340 (1992).
- [123] S. CHAUVEAU, M.-Y. PERRIN, P. RIVIÈRE, AND A. SOUFIANI. *Contributions of diatomic molecular electronic systems to heated air radiation*. Journal of quantitative spectroscopy and radiative transfer **72**(4), 503-530 (2002).
- [124] Y. BABOU, P. RIVIÈRE, M.-Y. PERRIN, AND A. SOUFIANI. *Spectroscopic data for the prediction of radiative transfer in CO₂-N₂*. Journal of Quantitative Spectroscopy and Radiative Transfer **110**, 89-108 (2009).
- [125] R. MULLIKEN. *The interpretation of band spectra. Part IIc. Empirical band types*. Review of Modern Physics **3**(89), 89-115 (1931).
- [126] J. O. ARNOLD, E. E. WHITING, AND G. C. LYLE. *Line by line calculation of spectra from diatomic molecules and atoms assuming a Voigt line profile*. Journal of Quantitative Spectroscopy and Radiation Transfer **9**, 775-798 (1969).
- [127] C. LAUX. *Optical diagnostics and radiative emission of air plasmas*. Ph.D. thesis, Stanford University (1993).
- [128] C. LAUX AND C. KNUCINNUT. *Arrays of radiative transition probabilities for the N₂ First and Second Positive, NO Beta and Gamma, N₂⁺ First Negative and O₂ Schumann-Runge band systems*. Journal of Quantitative Spectroscopy and Radiative Transfer **48**(1), 9-24 (1992).
- [129] C. JOHNSTON, B. HOLLIS, AND K. SUTTON. *Spectrum modeling for air shock-layer radiation at lunar-return conditions*. Journal of Spacecraft and Rockets **45**(5), 856-878 (2008).
- [130] S. CHAUVEAU, C. DERON, M.-Y. PERRIN, P. RIVIÈRE, AND A. SOUFIANI. *Radiative transfer in LTE air plasmas for temperatures up to 15,000 K*. Journal of Quantitative Spectroscopy and Radiative Transfer **77**(2), 113-130 (2003).

- [131] W. CUNTO, C. MENDOZA, F. OCHSENBEIN, AND C. ZEIPPEN. *TOPbase at the CDS*. *Astronomy and Astrophysics* **275**(1), 5-8 (1993).
- [132] W. WIESE. *New reference data table for carbon, nitrogen and oxygen spectra*. *Spectrochimica Acta, Part B: Atomic Spectroscopy* **51**(8), 775 - 777 (1996). URL [http://dx.doi.org/10.1016/0584-8547\(96\)01490-5](http://dx.doi.org/10.1016/0584-8547(96)01490-5).
- [133] B. KLEB AND C. JOHNSTON. *Uncertainty analysis of air radiation for lunar return shock layers*. AIAA Paper 2008-6388, Honolulu, Hawaii (2008).
- [134] C. GULDBERG. *Concerning the laws of chemical affinity*. C. M. Forhandlinger: Videnskabs-Selskabet i Christiana (11) (1864).
- [135] C. GULDBERG AND P. WAAGE. *Studies concerning affinity*. C. M. Forhandlinger: Videnskabs-Selskabet i Christiana (35) (1864).
- [136] C. PARK. *Review of chemical-kinetic problems of future NASA missions, II: Earth entries*. *Journal of Thermophysics and Heat Transfer* **7**(3), 385-398 (1993).
- [137] C. PARK, J. HOWE, R. JAFFE, AND G. CANDLER. *Review of chemical-kinetic problems of future NASA missions, II: Mars entries*. *Journal of Thermophysics and Heat Transfer* **8**(1), 9 - 22 (1994).
- [138] V. GORELOV, M. GLADYSHEV, A. KIREEV, AND S. SHILENKOV. *Nonequilibrium ionization behind a strong shock wave in the Mars atmosphere*. *Journal of Applied Mechanics and Technical Physics* **41**(6), 970-976 (2000).
- [139] T. GÖKÇEN. *N₂ - CH₄ - Ar chemical kinetic model for simulations of Titan atmospheric entry*. *Journal of Thermophysics and Heat Transfer* **21**(1), 9 - 18 (2007).
- [140] G. CHERNYI AND S. LOSEV. *Development of thermal protection system for interplanetary flight*. ISTC Report 036-96, International Science and Technology Center, Moscow State University (1999).
- [141] S. GORDON AND B. MCBRIDE. *Computer program for calculation of complex chemical equilibrium compositions and applications. Part 1: Analysis*. NASA Reference Publication 1311, United States (1994).
- [142] O. KNAB, H.-H. FRÜHAUF, AND E. MESSERSCHMID. *Theory and validation of the physically consistent coupled vibration-chemistry-vibration model*. *Journal of Thermophysics and Heat Transfer* **9**(2), 219-226 (1995).
- [143] M. LINO DA SILVA, V. GUERRA, AND J. LOUREIRO. *Two-temperature models for nitrogen dissociation*. *Chemical Physics* **342**, 275-287 (2007).

- [144] P. MARRONE AND C. TREANOR. *Chemical relaxation with preferential dissociation from excited vibrational levels.* Physics of Fluids **6**(9), 1215 - 1221 (1963).
- [145] O. KNAB, H.-H. FRÜHAUF, AND S. JONES. *Multiple temperature description of reaction rate constants with regard to consistent chemical-vibration coupling.* AIAA Paper 1992-2947 (1992).
- [146] S. MACHERET AND W. RICH. *Nonequilibrium dissociation rates behind strong shock waves: classical model.* Chemical Physics (Netherlands) **174**, 25-43 (1993).
- [147] A. BOURDON, M. PANESI, A. BRANDIS, T. MAGIN, G. CHABAN, AND W. HUO. *Simulation of flows in shock-tube facilities by means of a detailed chemical mechanism for nitrogen excitation and dissociation.* In *Proceedings of the Summer Program 2008*, pp. 5–16 (Center for Turbulence Research, 2008).
- [148] F. THIVET, M.-Y. PERRIN, AND S. CANDEL. *A unified nonequilibrium model for hypersonic flows.* Physics of Fluids A (Fluid Dynamics) **3**(11), 2799 - 2812 (1991).
- [149] R. MILLIKAN AND D. WHITE. *Systematics of vibrational relaxation.* Journal of Chem Phys **39**(12), 3209 - 3213 (1963).
- [150] J. APPLETON AND K. BRAY. *The conservation equations for a nonequilibrium plasma.* Journal of Fluid Mechanics **20**(4), 659-672 (1964).
- [151] P. A. GNOFFO, R. N. GUPTA, AND J. L. SHINN. *Conservation equations and physical models for hypersonic air flows in thermal and chemical nonequilibrium.* Technical Paper 2867, NASA, United States (1989).
- [152] J. LEE. *Electron-impact vibrational excitation rates in the flowfield of Aeroassisted Orbital Transfer Vehicle.* AIAA Paper 85-1035 (1985).
- [153] G. CANDLER AND C. PARK. *The computation of radiation from nonequilibrium hypersonic flows.* AIAA Paper 88-2678 (1988).
- [154] J. LEE. *Electron-impact vibrational relaxation in high-temperature nitrogen.* Journal of Thermophysics and Heat Transfer **7**(3), 399 - 405 (1993).
- [155] A. BOURDON AND P. VERVISCH. *Electron-vibration exchange models in nitrogen flows.* Physical Review E **55**(4), 4634-4641 (1997).
- [156] G. SCHULTZ. *Vibrational excitation of N₂, CO and H₂ by electron impact.* Physical Review **135**(4A), 988-994 (1964).
- [157] C. PARK. *The limits of two-temperature model.* AIAA Paper 2010-911, Orlando, Florida (2010).

- [158] C. TREANOR AND P. MARRONE. *Effect of dissociation on rate of vibrational relaxation.* Physics of Fluids **5**(9), 1022 - 1026 (1962).
- [159] J. LEE. *Basic governing equations for the flight regimes of aeroassisted orbital transfer vehicles.* AIAA Paper 84-1729 (1984).
- [160] L. HARTUNG. *Development of a nonequilibrium radiative heating prediction method for coupled flowfield solutions.* Journal of Thermophysics and Heat Transfer **6**, 618-625 (1992).
- [161] N. KUDRYAVSTEV, L. KUZNETSOVA, AND S. SURZHIKOV. *Kinetics and nonequilibrium radiation of CO₂-N₂ shock waves.* AIAA Paper 2001-2728 (2001).
- [162] H. DRAWIN. *Plasma diagnostics*, chap. Collision and transport cross sections, pp. 842–876 (1968).
- [163] M. GRYZINSKI. *Classical theory of electronic and ionic inelastic collisions.* Physical review **115**, 374-383 (1959).
- [164] C. ALLEN. *Astrophysical Quantities* (London, 1962).
- [165] H. VAN REGEMORTER. *Rate of collisional excitation in stellar atmospheres.* Astrophysical Journal **136**, 906-915 (1962).
- [166] C. PARK. *Comparison of electron and electronic temperature in a recombining nozzle flow of ionized nitrogen - hydrogen mixture: Part 1. Theory.* Journal of Plasma Physics **9**, 187-215 (1973).
- [167] M. PANESI, T. MAGIN, A. BOURDON, A. BULTEL, AND O. CHAZOT. *Analysis of the FIRE II flight experiment by means of a collisional radiative model.* AIAA Paper 2008-1205 (2008).
- [168] R. FROST, P. AWAKOWICZ, H. SUMMERS, AND N. BADNELL. *Calculated cross sections and measured rate coefficients for electron-impact excitation of neutral and singly ionized nitrogen.* Journal of Applied Physics **84**(6), 2989 - 3003 (1998).
- [169] W. SOON AND J. KUNC. *Thermal nonequilibrium in partially ionized atomic oxygen.* Physical Review A **41**(2), 825-843 (1990).
- [170] O. ZATSARINNY AND S. TAYAL. *Electron collisional excitation rates for O I using the B-spline R-matrix approach.* The Astrophysical Journal Supplement Series **148**, 575-582 (2003).
- [171] M. PANESI, Y. BABOU, AND O. CHAZOT. *Predictions of nonequilibrium radiation: analysis and comparison with EAST experiments.* Aiaa 2008-3812, Seattle, Washington (2008).
- [172] K. BERRINGTON, P. BURKE, AND W. ROBB. *The scattering of electrons by atomic nitrogen.* Journal of Physics B: Atomic and molecular physics **8**(15), 2500-2511 (1975).

- [173] J. KUNC AND W. SOON. *Collisional-radiative nonequilibrium in partially ionized atomic nitrogen.* Physical Review A **40**(10), 5822-5842 (1989).
- [174] H. TAWARA AND M. KATO. *Electron impact ionization data for atoms and ions - updated in 1998.* NIFS Data Series S **51**, 596p (1999).
- [175] Y.-K. KIM AND J.-P. DESCLAUX. *Ionization of carbon, nitrogen and oxygen by electron impact.* Physical Review A **66**(1), 012708 1-12 (2002).
- [176] Y. ITIKAWA AND A. ICHIMURA. *Cross sections for collisions of electrons and photons with atomic oxygen.* Journal of Physical and Chemical Reference Data **19**(3), 637-652 (1990).
- [177] P. TEULET, J. SARRETTE, AND A. GOMES. *Calculation of electron-impact inelastic cross-section and rate coefficients for diatomic molecules. Application to air molecules.* Journal of Quantitative Spectroscopy and Radiative Transfer **62**(5), 549-569 (1999).
- [178] C. PARK. *Rate parameters for electronic excitation of diatomic molecules II. Electron-impact processes.* AIAA Paper 2008-1446, Reno, Nevada (2008).
- [179] C. PARK. *Rate parameters for electronic excitation of diatomic molecules II. Heavy particle-impact processes.* AIAA Paper 2008-1446, Reno, Nevada (2008).
- [180] J. VLČEK. *A collisional-radiative model applicable to argon discharges over a wide range of conditions. I: Formulation and basic data.* Journal of Physics D: Applied Physics **22**(5), 623-631 (1989).
- [181] A. BOGAERTS, R. GIJBELS, AND J. VLCEK. *Collisional-radiative model for an argon glow discharge.* Journal of Applied Physics **84**(1), 121-136 (1998).
- [182] H. SUNO AND T. KATO. *Cross section database for carbon atoms and ions: Electron-impact ionization, excitation, and charge exchange in collisions with hydrogen atoms.* Atomic Data and Nuclear Tables **92**(4), 407-455 (2006).
- [183] K. DUNSEATH, W. FON, V. BURKE, R. REID, AND C. NOBLE. *Electron-impact excitation of the $n \leq 4$ levels of carbon.* Journal of Physics B: Atomic, Molecular and Optical Physics **30**(2), 277-287 (1997).
- [184] E. BROOK, M. HARRISON, AND A. SMITH. *Measurements of electron impact ionisation cross sections of He, C, O and N atoms.* Journal of Physics B (Atomic and Molecular Physics) **11**(17), 3115-3132 (1978).
- [185] G. ZALOGIN, P. KOZLOV, L. KUZNETSOVA, S. LOSEV, V. MAKAROV, Y. ROMANENKO, AND S. SURZHIKOV. *Radiation excited by shock waves in a CO₂-N₂-Ar mixture: Experiment and theory.* Technical Physics (Russia) **46**(6), 654 - 61 (2001).

- [186] D. POTTER, R. GOLLAN, P. JACOBS, AND P. LEYLAND. *Numerical simulations and analysis of the 8.5 km/s CO₂-N₂ EAST shock tube condition*. In H. Lacoste and L. Ouwehand, eds., *Proceedings of the 3rd International Workshop on Radiation of High Temperature Gases in Atmospheric Entry*, ESA SP-667 (European Space Agency, Heraklion, Greece, 2008).
- [187] A. MUNAFO, M. PANESI, Y. BABOU, AND O. CHAZOT. *Calculations of non equilibrium radiative signature for CO₂-N₂ shock tube experiments: contribution to TC2 test case*. In H. Lacoste and L. Ouwehand, eds., *Proceedings of the 3rd International Workshop on Radiation of High Temperature Gases in Atmospheric Entry*, ESA SP-667 (European Space Agency, Heraklion, Greece, 2008).
- [188] E. McCORKLE AND H. HASSAN. *Role of viscous effects on NEQAIR prediction of EAST measurements*. AIAA Paper 2010-236 (2010).
- [189] R. GOLLAN, C. JACOBS, P. JACOBS, R. MORGAN, T. MCINTYRE, M. MACROSSAN, D. BUTTSWORTH, T. EICHMANN, AND D. POTTER. *A simulation technique for radiating shock tube flows*. 26th International Symposium on Shock Waves (ISSW26) pp. 465–470 (2007).
- [190] S. SHARMA AND C. PARK. *Operating characteristics of a 60- and 10-cm Electric Arc-Driven Shock Tube - Part I: The Driver*. Journal of Thermophysics and Heat Transfer 4(3), 259-265 (1990).
- [191] S. SHARMA AND C. PARK. *Operating characteristics of a 60- and 10-cm Electric Arc-Driven Shock Tybe - Part II: The Driven Section*. Journal of Thermophysics and Heat Transfer 4(3), 266-272 (1990).
- [192] E. McCORKLE, D. BOSE, D. HASH, AND H. HASSAN. *Improved modeling of shock layer radiation in air*. AIAA Paper 2009-1028, Orlando, Florida (2009).
- [193] P. BOUBERT AND C. ROND. *Radiation behind a strong shock wave in Martian-like mixtures. description of test case TC2-M2 : CN and C₂ radiation behind a shock wave in CO/N₂, CO₂/N₂ mixtures and in pure CO₂. rebuilding of test cases TC2-M1 and TC2-M2*. In H. Lacoste and L. Ouwehand, eds., *Proceedings of the 3rd International Workshop on Radiation of High Temperature Gases in Atmospheric Entry*, ESA SP-667 (European Space Agency, Heraklion, Greece, 2008).
- [194] P. JACOBS, R. GOLLAN, A. DENMAN, B. O'FLAHERTY, D. POTTER, P. J. PETRIE-REPAR, AND I. JOHNSTON. *Eilmer's theory book: Basic models for gas dynamics and thermochemistry*. Mechanical Engineering Report 2010/09, School of Mechanical and Mining Engineering, The University of Queensland, Brisbane, Australia. (2010).
- [195] P. A. JACOBS. *Single-block Navier-Stokes integrator*. ICASE Interim Report 18 (1991).

- [196] E. ORAN AND J. BORIS. *Numerical Simulation of Reactive Flow* (Cambridge University Press, New York, USA, 2001), 2nd ed.
- [197] G. D. VAN ALBADA, B. VAN LEER, AND W. W. ROBERTS. *A comparative study of computational methods in cosmic gas dynamics*. ICASE Report 81-24 (1981).
- [198] M. N. MACROSSAN. *The equilibrium flux method for the calculation of flows with non-equilibrium chemical reactions*. Journal of Computational Physics **80**(1), 204–231 (1989).
- [199] Y. WADA AND M. S. LIOU. *A flux splitting scheme with high-resolution and robustness for discontinuities*. AIAA Paper 94-0083 (1994).
- [200] R. GOULARD. *The coupling of radiation and convection in detached shock layers*. Journal of Quantitative Spectroscopy and Radiative Heat Transfer **1**, 249-257 (1961).
- [201] M. F. MODEST. *Radiative Heat Transfer* (Academic Press, London, 2003), 2nd ed.
- [202] A. WANG AND M. MODEST. *Spectral Monte Carlo models for nongray radiation analyses in inhomogeneous participating media*. International Journal of Heat and Mass Transfer **50**(19-20), 3877-3889 (2007).
- [203] P. BOUCHER. *Points on a sphere*. Viewed 26th of February 2009, <<http://www.xsi-blog.com/archives/115>> (2006).
- [204] D. POTTER AND S. KARL. *Validation of aerothermo-chemistry models for re-entry application. TN 3.2: Engineering models for radiation*. AMOD Technical Note 3.2, European Space Agency, Noordwijk, The Netherlands (2009).
- [205] K. SAWADA, T. SAKAI, AND M. MATSUDA. *Application of Planck-Rosseland-Gray model for high enthalpy arc heaters*. AIAA Paper 98-0861 (1998).
- [206] J. GUSTAFSON. *Reevaluating Amdahl's law*. Communications of the ACM **31**(5), 532-533 (1988).
- [207] K. SUTTON AND P. GNOFFO. *Multi-component diffusion with application to computational aerothermodynamics*. AIAA Paper 98-2575 (1998).
- [208] J. RAMSHAW AND C. CHANG. *Computational fluid dynamics modeling of multicomponent thermal plasmas*. Plasma Chemistry and Plasma Processing **12**(3), 299-325 (1992).
- [209] J. MOSS. *Reacting viscous-shock-layer solutions with multicomponent diffusion and mass injection*. Technical Report R-411, NASA (1974).
- [210] G. CANDLER AND R. MACCORMACK. *Computation of weakly ionized hypersonic flows in thermochemical nonequilibrium*. Journal of Thermophysics and Heat Transfer **5**(11), 266 (1991).

- [211] K. SUZUKI, K. FUJITA, AND T. ABE. *Chemical nonequilibrium viscous shock-layer analysis over ablating surface of superorbital re-entry capsule*. Report SP 17, The Institute of Space and Astronautical Science (2003).
- [212] M. SCOTT. *Development and modelling of expansion tubes*. Ph.D. thesis, University of Queensland, St Lucia, Australia (2006).
- [213] D. POTTER, R. GOLLAN, T. EICHMANN, P. JACOBS, R. MORGAN, AND T. MCINTYRE. *Simulation of CO₂-N₂ expansion tunnel flows for the study of radiating shock layers*. In P. Jacobs, T. McIntyre, M. Cleary, D. Buttsworth, D. Mee, R. Clements, R. Morgan, and C. Lemckert, eds., *16th Australasian Fluid Mechanics Conference*, pp. 373–380 (School of Engineering, The University of Queensland, 2007).
- [214] P. A. JACOBS, T. B. SILVESTER, R. G. MORGAN, M. P. SCOTT, R. J. GOLLAN, AND T. J. MCINTYRE. *Superorbital expansion tube operation: estimates of flow conditions via numerical simulation*. Tech. rep., AIAA Paper 2005-264 (2005).
- [215] A. BRANDIS, R. GOLLAN, M. SCOTT, R. MORGAN, P. JACOBS, AND P. GNOFFO. *Expansion tube operating conditions for studying nonequilibrium radiation relevant to Titan Aerocapture*. 42nd Joint Propulsion Conference and Exhibit, 9 - 12 July 2006, Sacramento, California (2006).
- [216] R. BAKOS AND R. MORGAN. *Chemical recombination in an expansion tube*. AIAA Journal **32**(6), 1316 - 1319 (1994).
- [217] D. POTTER, R. GOLLAN, T. EICHMANN, T. MCINTYRE, R. MORGAN, AND P. JACOBS. *Simulation of CO₂-N₂ expansion tunnel flows for the study of radiating shock layers*. AIAA Paper 2008-1280, Reno, Nevada (2008).
- [218] H. MIRELS. *Test time in low-pressure shock tubes*. Physics of Fluids **6**(9), 1201 - 1214 (1963).
- [219] P. JACOBS. *Shock tube modelling with L1d*. Department of Mechanical Engineering Report 13/98, University of Queensland, St Lucia, Australia (1998).
- [220] P. JACOBS, R. GOLLAN, D. POTTER, D. GILDFIND, T. EICHMANN, B. O'FLAHERTY, AND D. BUTTSWORTH. *CFD tools for design and simulation of transient flows in hypersonic facilities*. Paper presented at the AVT-186 RTO AVT/VKI Lecture Series held at the von Karman Institute, Rhode-Saint-Genése, Belgium (2010).
- [221] D. BUTTSWORTH, M. D'SOUZA, D. POTTER, T. EICHMANN, N. MUDFORD, M. McGILVRAY, T. MCINTYRE, P. JACOBS, AND R. MORGAN. *Expansion tunnel radiation experiments to support Hayabusa re-entry observations*. AIAA Paper 2010-634, Orlando, Florida (2010).

- [222] J. MERRIFIELD AND M. FERTIG. *Pogress on the simulation of radiation-flowfield coupled simulations*. In H. Lacoste and L. Ouwehand, eds., *Sixth European Symposium on Aerothermodynamics for Space Vehicles*, ESA SP-659 (European Space Agency, Versailles, France, 2009).
- [223] J.-M. LAMET, Y. BABOU, P. RIVIÈRE, A. SOUFIANI, AND M.-Y. PERRIN. *Radiative transfer in Earth re-entry: application to the project Fire ii experiment*. In H. Lacoste and L. Ouwehand, eds., *Proceedings of the 2nd International Workshop on Radiation of High Temperature Gases in Atmospheric Entry*, ESA SP-629 (European Space Agency, Rome, Italy, 2006).
- [224] J.-M. LAMET, P. RIVIÈRE, L. TESSÉ, A. SOUFIANI, AND M.-Y. PERRIN. *Radiation modelling for air plasma in nonequilibrium conditions: application to Earth atmospheric re-entry*. In H. Lacoste and L. Ouwehand, eds., *Proceedings of the 3rd International Workshop on Radiation of High Temperature Gases in Atmospheric Entry*, ESA SP-667 (European Space Agency, Heraklion, Greece, 2008).
- [225] T. EICHMANN, A. BRANDIS, D. POTTER, T. MCINTYRE, AND H. RUBINSZTEIN-DUNLOP. *Radiating hypersonic flow studies using a super-orbital exapnsion tube*. AIAA Paper 2008-4135, Seattle, Washington (2008).
- [226] D. BOSE AND M. WRIGHT. *Uncertainty analysis of laminar aeroheating predictions for Mars entries*. AIAA Paper 2005-4682 (2005).
- [227] C. PARK. *Overview of radiation problems in planetary entry*. In *Proceedings of the International Workshop on Radiation of High Temperature Gases in Atmospheric Entry, Park II*, ESA SP-583 (European Space Agency, Porquerolles, France, 2005).
- [228] K. WILSON AND W. E. NICOLET. *Spectral absorption coefficients of Carbon, Nitrogen and Oxygen atoms*. Journal of Quantitative Spectroscopy and Radiative Transfer 7(6), 891-941 (1967).
- [229] H. GRIEM. *Spectral line broadening by plasmas* (Academic Press, New York, 1974).
- [230] T. GÖKÇEN. *N₂ - CH₄ -Ar chemical kinetic model for simulations of atmospheric entry to Titan*. AIAA Paper 2004-2469 (2004).
- [231] W. TSANG AND J. HERRON. *Chemical kinetic data base for propellant combustion I. Reactions involving NO, NO₂, HNO, HNO₂, HCN and N₂O*. Journal of Physical and Chemical Reference Data 20(4), 609-663 (1991).
- [232] W. HUO AND H. THUEMMEL. *Molecular physics and hypersonic flows*, chap. Electron-air molecule collisions in hypersonic flows, pp. 115–138 (Kluwer Academic Publishers, 1995).
- [233] J. ZOBEL, U. MAYER, K. JUNG, AND H. EHRHARDT. *Absolute differential cross sections for electron-impact excitation of CO near threshold: I. The valence states of CO*. Journal of Physics B: Atomic, Molecular and Optical physics 29(4), 813-838 (1996).

- [234] L. MORGAN AND J. TENNYSON. *Electron impact excitation cross sections for CO*. Journal of Physics B: Atomic, Molecular and Optical Physics **26**(15), 2429-2441 (1993).
- [235] R. OLSZEWSKI, P. WOLINSKI, AND M. ZUBEK. *Excitation of carbon monoxide by electron impact in the 8-17 ev energy range*. Chemical Physics Letters **297**(5-6), 537-542 (1998).
- [236] M. CAPITELLI, C. FERREIRA, B. GORDIETS, AND A. OSIPOV. *Plasma Kinetics in Atmospheric Gases* (Springer-Verlag, Berlin, 2000).
- [237] I. KUROCHKIN, L. POLAK, A. PUSTOGAROV, D. SLOVETSKII, AND V. UKOLOV. *Thermochemical nonequilibrium in an arc plasma stabilized by nitrogen injected through the porous wall of a channel - Particle excitation mechanisms and vibrational nonequilibrium*. High temperature (English translation) **16**(6), 995-1004 (1979).
- [238] F. FRESNET, G. BARAVIAN, L. MAGNE, S. PASQUIERS, C. POSTEL, V. PUECH, AND A. ROUSSEAU. *Influence of water on NO removal by pulsed discharge in N₂/H₂O/NO mixtures*. Plasma Sources Science and Technology **11**(2), 152+160 (2002).
- [239] S. PANCHESHNYI, S. STARIKOVSKAIA, AND A. STARIKOVSKII. *Collisional deactivation of N₂(C³π_u, v = 0, 1, 2, 3) states by N₂, O₂, H₂ and H₂O molecules*. Chemical Physics **262**, 349-357 (2000).
- [240] V. GORELOV, M. GLADYSHEV, A. KIREEV, I. YEGOROV, Y. PLASTININ, AND G. KARABADZHAK. *Experimental and numerical study of nonequilibrium ultraviolet NO and N emission in shock layer*. Journal of Thermophysics and Heat Transfer **12**(2), 172-179 (1998).
- [241] O. NAGY. *Excitation cross-sections of N₂⁺ molecular ion by electron impact and the vibrational energy levels of the three target states*. Chemical Physics **286**(1), 109-114 (2003).
- [242] R. FLAGAN AND J. APPLETON. *Excitation mechanisms of the nitrogen First-Positive and First-Negative radiation at high temperature*. Journal of Chemical Physics **56**(3), 1163-1173 (1972).
- [243] C. WILKE. *Diffusional properties of multicomponent gases*. Chemical engineering progress **46**(5), 95-104 (1950).
- [244] R. GROSSE AND G. CANDLER. *Diffusion flux modeling: application to direct entry problems*. AIAA Paper 2005-389 (2005).
- [245] M. D'SOUZA, T. EICHMANN, D. POTTER, N. MUDFORD, R. MORGAN, AND T. MCINTYRE. *An experimental investigation of radiation over an ablating Stardust model at 9.8km/s*. 61st International Astronautical Congress, Prague, CZ (2010).

A

Transport collision integrals

Table A.1 summarises the collision integrals implemented in the present work for calculating the transport properties of gas mixtures in the Ar-C-N-O elemental system. The valid temperature ranges for the collision-integrals proposed by Stallcop *et al.* [106] are presented in terms of the following reduced temperature:

$$T^* = 4132.5 \left(T^{\frac{3}{2}} / \sqrt{n_e} \right) \quad (\text{A.1})$$

where T_{trans} is the temperature governing heavy particle translation and n_e is the electron number density in cm^{-3} . The accuracy of the collision integrals proposed by Bruno *et al.* [] are left blank as this information was not provided with the data. As a guide, however, Wright *et al.* [94] conservatively estimated the uncertainty of collision integrals obtained with similar phenomenological potential surfaces to be 25% for the neutral-neutral interactions and 40% for the ion-neutral interactions.

Table A.1: Implemented collision integrals for the C-N-O-Ar elemental system.

Colliders	Temp. range	Acc.	Reference	Colliders	Temp. range	Acc.	Reference
$\text{CO}_2 - \text{CO}_2$	300 – 20,000 K	20%	Wright et al [94]	$\text{CO}_2 - \text{CO}^+$	50 – 50,000 K	-	Bruno et al. [6]
$\text{CO}_2 - \text{CO}$	300 – 20,000 K	20%	Wright et al [94]	$\text{CO}_2 - \text{N}_2^+$	50 – 50,000 K	-	Bruno et al. [6]
$\text{CO}_2 - \text{N}_2$	300 – 20,000 K	20%	Wright et al [94]	$\text{CO}_2 - \text{CN}^+$	50 – 50,000 K	-	Bruno et al. [6]
$\text{CO}_2 - \text{CN}$	500 – 20,000 K	30%	Wright et al [94]	$\text{CO}_2 - \text{NO}^+$	50 – 50,000 K	-	Bruno et al. [6]
$\text{CO}_2 - \text{NO}$	300 – 20,000 K	20%	Wright et al [94]	$\text{CO}_2 - \text{O}_2^+$	50 – 50,000 K	-	Bruno et al. [6]
$\text{CO}_2 - \text{O}_2$	300 – 20,000 K	20%	Wright et al [94]	$\text{CO}_2 - \text{C}_2$	50 – 50,000 K	-	Bruno et al. [6]
$\text{CO}_2 - \text{Ar}$	50 – 50,000 K	-	Bruno et al. [6]	$\text{CO}_2 - \text{NCO}$	50 – 50,000 K	-	Bruno et al. [6]
$\text{CO}_2 - \text{C}$	500 – 20,000 K	30%	Wright et al [94]	$\text{CO}_2 - \text{Ar}^+$	50 – 50,000 K	-	Bruno et al. [6]
$\text{CO}_2 - \text{N}$	300 – 20,000 K	25%	Wright et al [94]	$\text{CO}_2 - \text{C}^+$	50 – 50,000 K	-	Bruno et al. [6]
$\text{CO}_2 - \text{O}$	500 – 20,000 K	30%	Wright et al [94]	$\text{CO}_2 - \text{N}^+$	50 – 50,000 K	-	Bruno et al. [6]
$\text{CO}_2 - \text{e}^-$	1000 – 20,000 K	30%	Wright et al [94]	$\text{CO}_2 - \text{O}^+$	50 – 50,000 K	-	Bruno et al. [6]
$\text{CO} - \text{CO}^+$	300 – 15,000 K	40%	Wright et al [94]	$\text{CO} - \text{CO}$	300 – 20,000 K	20%	Wright et al [94]
$\text{CO} - \text{N}_2^+$	50 – 50,000 K	-	Bruno et al. [6]	$\text{CO} - \text{N}_2$	300 – 20,000 K	20%	Wright et al [94]
$\text{CO} - \text{CN}^+$	50 – 50,000 K	-	Bruno et al. [6]	$\text{CO} - \text{CN}$	500 – 15,000 K	30%	Wright et al [94]
$\text{CO} - \text{NO}^+$	50 – 50,000 K	-	Bruno et al. [6]	$\text{CO} - \text{NO}$	300 – 20,000 K	20%	Wright et al [94]
$\text{CO} - \text{O}_2^+$	50 – 50,000 K	-	Bruno et al. [6]	$\text{CO} - \text{O}_2$	300 – 20,000 K	20%	Wright et al [94]
$\text{CO} - \text{C}_2$	50 – 50,000 K	-	Bruno et al. [6]	$\text{CO} - \text{C}_2$	50 – 50,000 K	-	Bruno et al. [6]
$\text{CO} - \text{Ar}$	50 – 50,000 K	-	Bruno et al. [6]	$\text{CO} - \text{Ar}^+$	50 – 50,000 K	-	Bruno et al. [6]
$\text{CO} - \text{C}$	500 – 15,000 K	30%	Wright et al [94]	$\text{CO} - \text{C}$	500 – 15,000 K	30%	Wright et al [94]
$\text{CO} - \text{N}$	300 – 20,000 K	20%	Wright et al [94]	$\text{CO} - \text{N}$	300 – 20,000 K	20%	Wright et al [94]
$\text{CO} - \text{O}$	500 – 20,000 K	30%	Wright et al [94]	$\text{CO} - \text{O}$	500 – 20,000 K	30%	Wright et al [94]
$\text{CO} - \text{e}^-$	1000 – 20,000 K	30%	Wright et al [94]	$\text{CO} - \text{e}^-$	T* > 4	10%	Wright et al [94]
$\text{CO}^+ - \text{CO}^+$	T* > 4	10%	Stallcop et al. [106]	$\text{CO}^+ - \text{N}_2$	50 – 50,000 K	20%	Bruno et al. [6]
$\text{CO}^+ - \text{N}_2^+$	T* > 4	10%	Stallcop et al. [106]	$\text{CO}^+ - \text{CN}$	50 – 50,000 K	-	Bruno et al. [6]
$\text{CO}^+ - \text{CN}^+$	T* > 4	10%	Stallcop et al. [106]	$\text{CO}^+ - \text{NO}$	50 – 50,000 K	-	Bruno et al. [6]
$\text{CO}^+ - \text{NO}^+$	T* > 4	10%	Stallcop et al. [106]	$\text{CO}^+ - \text{O}_2$	50 – 50,000 K	-	Bruno et al. [6]
$\text{CO}^+ - \text{O}_2^+$	T* > 4	10%	Stallcop et al. [106]	$\text{CO}^+ - \text{C}_2$	50 – 50,000 K	-	Bruno et al. [6]
$\text{CO}^+ - \text{NCO}$	50 – 50,000 K	-	Bruno et al. [6]	$\text{CO}^+ - \text{Ar}$	50 – 50,000 K	-	Bruno et al. [6]
$\text{CO}^+ - \text{Ar}^+$	T* > 4	10%	Stallcop et al. [106]	$\text{CO}^+ - \text{C}$	50 – 50,000 K	-	Bruno et al. [6]
$\text{CO}^+ - \text{C}^+$	T* > 4	10%	Stallcop et al. [106]	$\text{CO}^+ - \text{N}$	50 – 50,000 K	-	Bruno et al. [6]
$\text{CO}^+ - \text{N}^+$	T* > 4	10%	Stallcop et al. [106]	$\text{CO}^+ - \text{O}$	50 – 50,000 K	-	Bruno et al. [6]
$\text{CO}^+ - \text{O}^+$	T* > 4	10%	Stallcop et al. [106]	$\text{CO}^+ - \text{e}^-$	T* > 4	10%	Stallcop et al. [106]
$\text{N}_2 - \text{N}_2$	300 – 10,000 K	10%	Wright et al. [88]	$\text{N}_2 - \text{N}_2^+$	50 – 50,000 K	-	Bruno et al. [6]
$\text{N}_2 - \text{CN}$	500 – 20,000 K	-	Wright et al [94]	$\text{N}_2 - \text{CN}^+$	50 – 50,000 K	-	Bruno et al. [6]
$\text{N}_2 - \text{NO}$	300 – 15,000 K	25%	Wright et al. [88]	$\text{N}_2 - \text{NO}^+$	50 – 50,000 K	-	Bruno et al. [6]
$\text{N}_2 - \text{O}_2$	300 – 15,000 K	20%	Wright et al. [88]	$\text{N}_2 - \text{O}_2^+$	50 – 50,000 K	-	Bruno et al. [6]
$\text{N}_2 - \text{C}_2$	50 – 50,000 K	-	Bruno et al. [6]	$\text{N}_2 - \text{NCO}$	50 – 50,000 K	-	Bruno et al. [6]
$\text{N}_2 - \text{Ar}$	300 – 15,000 K	20%	Wright et al. [88]	$\text{N}_2 - \text{Ar}^+$	300 – 15,000 K	20%	Levin et al [98]
$\text{N}_2 - \text{C}$	300 – 10,000 K	-	Wright et al [94]	$\text{N}_2 - \text{C}^+$	50 – 50,000 K	-	Bruno et al. [6]
$\text{N}_2 - \text{N}$	300 – 10,000 K	10%	Wright et al. [88]	$\text{N}_2 - \text{N}^+$	300 – 12000 K	20%	Wright et al [99]
$\text{N}_2 - \text{O}$	300 – 15,000 K	20%	Wright et al. [88]	$\text{N}_2 - \text{O}^+$	300 – 12000 K	20%	Wright et al [99]
$\text{N}_2 - \text{e}^-$	500 – 20,000 K	28%	Wright et al. [88]	$\text{N}_2^+ - \text{N}_2^+$	T* > 4	10%	Stallcop et al. [106]
$\text{N}_2^+ - \text{CN}$	50 – 50,000 K	-	Bruno et al. [6]	$\text{N}_2^+ - \text{CN}^+$	T* > 4	10%	Stallcop et al. [106]

table continued on next page...

table continued from previous page...

Colliders	Temp. range	Acc.	Reference	Colliders	Temp. range	Acc.	Reference
$\text{N}_2^+ - \text{NO}$	300 – 12000 K	20%	Wright et al [99]	$\text{N}_2^+ - \text{NO}^+$	$T^* > 4$	10%	Stallcop et al. [106]
$\text{N}_2^+ - \text{O}_2$	300 – 12000 K	20%	Wright et al [99]	$\text{N}_2^+ - \text{O}_2^+$	$T^* > 4$	10%	Stallcop et al. [106]
$\text{N}_2^+ - \text{C}_2$	50 – 50,000 K	-	Bruno et al. [6]	$\text{N}_2^+ - \text{NCO}$	50 – 50,000 K	-	Bruno et al. [6]
$\text{N}_2^+ - \text{Ar}$	300 – 15,000 K	20%	Levin et al [98]	$\text{N}_2^+ - \text{Ar}^+$	$T^* > 4$	10%	Stallcop et al. [106]
$\text{N}_2^+ - \text{C}$	50 – 50,000 K	-	Bruno et al. [6]	$\text{N}_2^+ - \text{C}^+$	$T^* > 4$	10%	Stallcop et al. [106]
$\text{N}_2^+ - \text{N}$	300 – 12000 K	20%	Wright et al [99]	$\text{N}_2^+ - \text{N}^+$	$T^* > 4$	10%	Stallcop et al. [106]
$\text{N}_2^+ - \text{O}$	300 – 12000 K	20%	Wright et al [99]	$\text{N}_2^+ - \text{O}^+$	$T^* > 4$	10%	Stallcop et al. [106]
$\text{N}_2^+ - \text{e}^-$	$T^* > 4$	10%	Stallcop et al. [106]	$\text{CN} - \text{CN}$	500 – 20,000 K	30%	Wright et al [94]
$\text{CN} - \text{CN}^+$	300 – 15,000 K	50%	Wright et al [94]	$\text{CN} - \text{NO}$	50 – 50,000 K	-	Bruno et al. [6]
$\text{CN} - \text{NO}^+$	50 – 50,000 K	-	Bruno et al. [6]	$\text{CN} - \text{O}_2$	500 – 20,000 K	30%	Wright et al [94]
$\text{CN} - \text{O}_2^+$	50 – 50,000 K	-	Bruno et al. [6]	$\text{CN} - \text{C}_2$	50 – 50,000 K	-	Bruno et al. [6]
$\text{CN} - \text{NCO}$	50 – 50,000 K	-	Bruno et al. [6]	$\text{CN} - \text{Ar}$	50 – 50,000 K	-	Bruno et al. [6]
$\text{CN} - \text{Ar}^+$	50 – 50,000 K	-	Bruno et al. [6]	$\text{CN} - \text{C}$	500 – 20,000 K	30%	Wright et al [94]
$\text{CN} - \text{C}^+$	50 – 50,000 K	-	Bruno et al. [6]	$\text{CN} - \text{N}$	500 – 20,000 K	30%	Wright et al [94]
$\text{CN} - \text{N}^+$	50 – 50,000 K	-	Bruno et al. [6]	$\text{CN} - \text{O}$	500 – 20,000 K	30%	Wright et al [94]
$\text{CN} - \text{O}^+$	50 – 50,000 K	-	Bruno et al. [6]	$\text{CN} - \text{e}^-$	1000 – 20,000 K	50%	Wright et al [94]
$\text{CN}^+ - \text{CN}^+$	$T^* > 4$	10%	Stallcop et al. [106]	$\text{CN}^+ - \text{NO}$	50 – 50,000 K	-	Bruno et al. [6]
$\text{CN}^+ - \text{NO}^+$	$T^* > 4$	10%	Stallcop et al. [106]	$\text{CN}^+ - \text{O}_2$	50 – 50,000 K	-	Bruno et al. [6]
$\text{CN}^+ - \text{O}_2^+$	$T^* > 4$	10%	Stallcop et al. [106]	$\text{CN}^+ - \text{C}_2$	50 – 50,000 K	-	Bruno et al. [6]
$\text{CN}^+ - \text{NCO}$	50 – 50,000 K	-	Bruno et al. [6]	$\text{CN}^+ - \text{Ar}$	50 – 50,000 K	-	Bruno et al. [6]
$\text{CN}^+ - \text{Ar}^+$	$T^* > 4$	10%	Stallcop et al. [106]	$\text{CN}^+ - \text{C}$	50 – 50,000 K	-	Bruno et al. [6]
$\text{CN}^+ - \text{C}^+$	$T^* > 4$	10%	Stallcop et al. [106]	$\text{CN}^+ - \text{N}$	50 – 50,000 K	-	Bruno et al. [6]
$\text{CN}^+ - \text{N}^+$	$T^* > 4$	10%	Stallcop et al. [106]	$\text{CN}^+ - \text{O}$	50 – 50,000 K	-	Bruno et al. [6]
$\text{CN}^+ - \text{O}^+$	$T^* > 4$	10%	Stallcop et al. [106]	$\text{CN}^+ - \text{e}^-$	$T^* > 4$	10%	Stallcop et al. [106]
$\text{NO} - \text{NO}$	300 – 15,000 K	20%	Wright et al. [88]	$\text{NO} - \text{NO}^+$	50 – 50,000 K	-	Bruno et al. [6]
$\text{NO} - \text{O}_2$	300 – 15,000 K	25%	Wright et al. [88]	$\text{NO} - \text{O}_2^+$	300 – 12000 K	20%	Wright et al [99]
$\text{NO} - \text{C}_2$	50 – 50,000 K	-	Bruno et al. [6]	$\text{NO} - \text{NCO}$	50 – 50,000 K	-	Bruno et al. [6]
$\text{NO} - \text{Ar}$	300 – 15,000 K	25%	Wright et al. [88]	$\text{NO} - \text{Ar}^+$	300 – 15,000 K	20%	Levin et al [98]
$\text{NO} - \text{C}$	500 – 20,000 K	25%	Wright et al [94]	$\text{NO} - \text{C}^+$	50 – 50,000 K	-	Bruno et al. [6]
$\text{NO} - \text{N}$	500 – 15,000 K	25%	Wright et al. [88]	$\text{NO} - \text{N}^+$	300 – 12000 K	20%	Wright et al [99]
$\text{NO} - \text{O}$	500 – 15,000 K	25%	Wright et al. [88]	$\text{NO} - \text{O}^+$	300 – 12000 K	20%	Wright et al [99]
$\text{NO} - \text{e}^-$	2000 – 20,000 K	35%	Wright et al. [88]	$\text{NO}^+ - \text{NO}^+$	$T^* > 4$	10%	Stallcop et al. [106]
$\text{NO}^+ - \text{O}_2$	300 – 12000 K	20%	Wright et al [99]	$\text{NO}^+ - \text{O}_2^+$	$T^* > 4$	10%	Stallcop et al. [106]
$\text{NO}^+ - \text{C}_2$	50 – 50,000 K	-	Bruno et al. [6]	$\text{NO}^+ - \text{NCO}$	50 – 50,000 K	-	Bruno et al. [6]
$\text{NO}^+ - \text{Ar}$	300 – 15,000 K	20%	Levin et al [98]	$\text{NO}^+ - \text{Ar}^+$	$T^* > 4$	10%	Stallcop et al. [106]
$\text{NO}^+ - \text{C}$	50 – 50,000 K	-	Bruno et al. [6]	$\text{NO}^+ - \text{C}^+$	$T^* > 4$	10%	Stallcop et al. [106]
$\text{NO}^+ - \text{N}$	300 – 12000 K	20%	Wright et al [99]	$\text{NO}^+ - \text{N}^+$	$T^* > 4$	10%	Stallcop et al. [106]
$\text{NO}^+ - \text{O}$	300 – 12000 K	20%	Wright et al [99]	$\text{NO}^+ - \text{O}^+$	$T^* > 4$	10%	Stallcop et al. [106]
$\text{NO}^+ - \text{e}^-$	$T^* > 4$	10%	Stallcop et al. [106]	$\text{O}_2 - \text{O}_2$	300 – 15,000 K	20%	Wright et al. [88]
$\text{O}_2 - \text{O}_2^+$	50 – 50,000 K	-	Bruno et al. [6]	$\text{O}_2 - \text{C}_2$	50 – 50,000 K	-	Bruno et al. [6]
$\text{O}_2 - \text{NCO}$	50 – 50,000 K	-	Bruno et al. [6]	$\text{O}_2 - \text{Ar}$	300 – 15,000 K	20%	Wright et al. [88]
$\text{O}_2 - \text{Ar}^+$	300 – 15,000 K	20%	Levin et al [98]	$\text{O}_2 - \text{C}$	500 – 20,000 K	30%	Wright et al [94]
$\text{O}_2 - \text{C}^+$	300 – 20,000 K	20%	Wright et al [94]	$\text{O}_2 - \text{N}$	500 – 15,000 K	25%	Wright et al. [88]
$\text{O}_2 - \text{N}^+$	300 – 12000 K	20%	Wright et al [99]	$\text{O}_2 - \text{O}$	300 – 10,000 K	10%	Wright et al. [88]
$\text{O}_2 - \text{O}^+$	300 – 12000 K	20%	Wright et al [99]	$\text{O}_2 - \text{e}^-$	1000 – 20,000 K	20%	Wright et al. [88]
$\text{O}_2^+ - \text{O}_2^+$	$T^* > 4$	10%	Stallcop et al. [106]	$\text{O}_2^+ - \text{C}_2$	50 – 50,000 K	-	Bruno et al. [6]

table continued on next page...

table continued from previous page...

Colliders	Temp. range	Acc.	Reference	Colliders	Temp. range	Acc.	Reference
O ₂ ⁺ – NCO	50 – 50,000 K	-	Bruno <i>et al.</i> [6]	O ₂ ⁺ – Ar	300 – 15,000 K	20%	Levin <i>et al</i> [98]
O ₂ ⁺ – Ar ⁺	T* > 4	10%	Stallcop <i>et al.</i> [106]	O ₂ ⁺ – C	50 – 50,000 K	-	Bruno <i>et al.</i> [6]
O ₂ ⁺ – C ⁺	T* > 4	10%	Stallcop <i>et al.</i> [106]	O ₂ ⁺ – N	300 – 12000 K	20%	Wright <i>et al</i> [99]
O ₂ ⁺ – N ⁺	T* > 4	10%	Stallcop <i>et al.</i> [106]	O ₂ ⁺ – O	300 – 12000 K	20%	Wright <i>et al</i> [99]
O ₂ ⁺ – O ⁺	T* > 4	10%	Stallcop <i>et al.</i> [106]	O ₂ ⁺ – e ⁻	T* > 4	10%	Stallcop <i>et al.</i> [106]
C ₂ – C ₂	50 – 50,000 K	-	Bruno <i>et al.</i> [6]	C ₂ – NCO	50 – 50,000 K	-	Bruno <i>et al.</i> [6]
C ₂ – Ar	50 – 50,000 K	-	Bruno <i>et al.</i> [6]	C ₂ – Ar ⁺	50 – 50,000 K	-	Bruno <i>et al.</i> [6]
C ₂ – C	50 – 50,000 K	-	Bruno <i>et al.</i> [6]	C ₂ – C ⁺	50 – 50,000 K	-	Bruno <i>et al.</i> [6]
C ₂ – N	50 – 50,000 K	-	Bruno <i>et al.</i> [6]	C ₂ – N ⁺	50 – 50,000 K	-	Bruno <i>et al.</i> [6]
C ₂ – O	50 – 50,000 K	-	Bruno <i>et al.</i> [6]	C ₂ – O ⁺	50 – 50,000 K	-	Bruno <i>et al.</i> [6]
C ₂ – e ⁻	-	-	None	NCO – NCO	50 – 50,000 K	-	Bruno <i>et al.</i> [6]
NCO – Ar	50 – 50,000 K	-	Bruno <i>et al.</i> [6]	NCO – Ar ⁺	50 – 50,000 K	-	Bruno <i>et al.</i> [6]
NCO – C	50 – 50,000 K	-	Bruno <i>et al.</i> [6]	NCO – C ⁺	50 – 50,000 K	-	Bruno <i>et al.</i> [6]
NCO – N	50 – 50,000 K	-	Bruno <i>et al.</i> [6]	NCO – N ⁺	50 – 50,000 K	-	Bruno <i>et al.</i> [6]
NCO – O	50 – 50,000 K	-	Bruno <i>et al.</i> [6]	NCO – O ⁺	50 – 50,000 K	-	Bruno <i>et al.</i> [6]
NCO – e ⁻	-	-	None	Ar – Ar	300 – 20,000 K	5%	Wright <i>et al.</i> [88]
Ar – Ar ⁺	300 – 15,000 K	20%	Levin <i>et al</i> [98]	Ar – C	50 – 50,000 K	-	Bruno <i>et al.</i> [6]
Ar – C ⁺	50 – 50,000 K	-	Bruno <i>et al.</i> [6]	Ar – N	50 – 50,000 K	-	Bruno <i>et al.</i> [6]
Ar – N ⁺	300 – 15,000 K	20%	Levin <i>et al</i> [98]	Ar – O	50 – 50,000 K	-	Bruno <i>et al.</i> [6]
Ar – O ⁺	300 – 15,000 K	20%	Levin <i>et al</i> [98]	Ar – e ⁻	1000 – 20,000 K	15%	Wright <i>et al.</i> [88]
Ar ⁺ – Ar ⁺	T* > 4	10%	Stallcop <i>et al.</i> [106]	Ar ⁺ – C	50 – 50,000 K	-	Bruno <i>et al.</i> [6]
Ar ⁺ – C ⁺	T* > 4	10%	Stallcop <i>et al.</i> [106]	Ar ⁺ – N	50 – 50,000 K	-	Bruno <i>et al.</i> [6]
Ar ⁺ – N ⁺	T* > 4	10%	Stallcop <i>et al.</i> [106]	Ar ⁺ – O	50 – 50,000 K	-	Bruno <i>et al.</i> [6]
Ar ⁺ – O ⁺	T* > 4	10%	Stallcop <i>et al.</i> [106]	Ar ⁺ – e ⁻	T* > 4	10%	Stallcop <i>et al.</i> [106]
C – C	300 – 20,000 K	5%	Wright <i>et al</i> [94]	C – C ⁺	300 – 20,000 K	25%	Wright <i>et al</i> [94]
C – N	300 – 20,000 K	5%	Wright <i>et al</i> [94]	C – N ⁺	300 – 15,000 K	25%	Wright <i>et al</i> [94]
C – O	300 – 20,000 K	25%	Wright <i>et al</i> [94]	C – O ⁺	300 – 15,000 K	20%	Wright <i>et al</i> [94]
C – e ⁻	2000 – 15,000 K	30%	Wright <i>et al</i> [94]	C ⁺ – C ⁺	T* > 4	10%	Stallcop <i>et al.</i> [106]
C ⁺ – N	50 – 50,000 K	-	Bruno <i>et al.</i> [6]	C ⁺ – N ⁺	T* > 4	10%	Stallcop <i>et al.</i> [106]
C ⁺ – O	50 – 50,000 K	-	Bruno <i>et al.</i> [6]	C ⁺ – O ⁺	T* > 4	10%	Stallcop <i>et al.</i> [106]
C ⁺ – e ⁻	T* > 4	10%	Stallcop <i>et al.</i> [106]	N – N	300 – 20,000 K	5%	Wright <i>et al.</i> [88]
N – N ⁺	50 – 50,000 K	-	Bruno <i>et al.</i> [6]	N – O	300 – 20,000 K	5%	Wright <i>et al.</i> [88]
N – O ⁺	50 – 50,000 K	-	Bruno <i>et al.</i> [6]	N – e ⁻	2000 – 20,000 K	35%	Wright <i>et al.</i> [88]
N ⁺ – N ⁺	T* > 4	10%	Stallcop <i>et al.</i> [106]	N ⁺ – O	300 – 12000 K	20%	Wright <i>et al</i> [99]
N ⁺ – O ⁺	T* > 4	10%	Stallcop <i>et al.</i> [106]	N ⁺ – e ⁻	T* > 4	10%	Stallcop <i>et al.</i> [106]
O – O	300 – 20,000 K	5%	Wright <i>et al.</i> [88]	O – O ⁺	50 – 50,000 K	-	Bruno <i>et al.</i> [6]
O – e ⁻	1000 – 20,000 K	30%	Wright <i>et al.</i> [88]	O ⁺ – O ⁺	T* > 4	10%	Stallcop <i>et al.</i> [106]
O ⁺ – e ⁻	T* > 4	10%	Stallcop <i>et al.</i> [106]	e ⁻ – e ⁻	T* > 4	10%	Stallcop <i>et al.</i> [106]

B

Atomic electronic levels

In this appendix the electronic level sets implemented for the neutral atomic species in the *spectral radiation* model are presented. The level data is combination of the data presented in the NIST database [80] and that from the text of Park [29]. Note that these sets are different from those used for the thermodynamic model which are described in § 3.1.3. The level data for C, N and O are presented in § B.1, B.2 and B.3 respectively.

B.1 Atomic Carbon, C

Table B.1: Electronic level model for atomic carbon, C.

Level index, i	Configuration	Term	Degeneracy, g_i	Energy, E_i (eV)
1	$2s^22p^2$	3P	9	0.00
2	$2s^22p^2$	1D	5	1.26
3	$2s^22p^2$	1S	1	2.68
4	$2s2p^3$	$^5S^\circ$	5	4.18
5	$2s^22p(^2P^\circ)3s$	$^3P^\circ$	9	7.49
6	$2s^22p(^2P^\circ)3s$	$^1P^\circ$	3	7.68
7	$2s2p^3$	$^3D^\circ$	15	7.95
8	$2s^22p(^2P^\circ)3p$	1P	3	8.54
9	$2s^22p(^2P^\circ)3p$	3D	15	8.64
10	$2s^22p(^2P^\circ)3p$	3S	3	8.77
11	$2s^22p(^2P^\circ)3p$	3P	9	8.85
12	$2s^22p(^2P^\circ)3p$	1D	5	9.00
13	$2s^22p(^2P^\circ)3p$	1S	1	9.17
14	$2s2p^3$	$^3P^\circ$	9	9.33
15	$2s^22p(^2P^\circ)3d$	$^1D^\circ$	5	9.63
16	$2s^22p(^2P^\circ)4s$	$^3P^\circ$	9	9.69
17	$2s^22p(^2P^\circ)3d$	$^3F^\circ$	21	9.70
18	$2s^22p(^2P^\circ)3d$	$^3D^\circ$	15	9.71
19	$2s^22p(^2P^\circ)4s$	$^1P^\circ$	3	9.71
20	$2s^22p(^2P^\circ)3d$	$^1F^\circ$	7	9.74
21	$2s^22p(^2P^\circ)3d$	$^1P^\circ$	3	9.76
22	$2s^22p(^2P^\circ)3d$	$^3P^\circ$	9	9.83
23	$2s^22p(^2P^\circ)4p$	1P	3	9.99
24	$2s^22p(^2P^\circ)4p$	3D	15	10.02
25	$2s^22p(^2P^\circ)4p$	3S	3	10.06
26	$2s^22p(^2P^\circ)4p$	3P	9	10.08
27	$2s^22p(^2P^\circ)4p$	1D	5	10.14
28	$2s^22p(^2P^\circ)4p$	1S	1	10.20
29	$2s^22p(^2P^\circ)4d$	$^1D^\circ$	5	10.35
30	$2s^22p(^2P^\circ)5s$	$^3P^\circ$	9	10.39
31	$2s^22p(^2P^\circ)4d$	$^4F^\circ$	21	10.39
32	$2s^22p(^2P^\circ)4d$	$^3D^\circ$	15	10.39

table continued on next page...

table continued from previous page...

Level index, i	Configuration	Term	Degeneracy, g_i	Energy, E_i (eV)
33	$2s^2 2p(^2P^\circ) 5s$	${}^1P^\circ$	3	10.40
34 [†]	-	-	12	10.40
35 [†]	-	-	84	10.43
36 [†]	-	-	36	10.54
37 [†]	-	-	60	10.71
38 [†]	-	-	192	10.73
39 [†]	-	-	432	10.88
40 [†]	-	-	588	10.99
41 [†]	-	-	768	11.05
42 [†]	-	-	972	11.10
43 [†]	-	-	1200	11.13

[†]High lying level data obtained from Park [29].

B.2 Atomic nitrogen, N

Table B.2: Electronic level model for atomic nitrogen, N.

Level index, i	Configuration	Term	Degeneracy, g_i	Energy, E_i (eV)
1	$2s^2 2p^3$	${}^4S^\circ$	4	0.00
2	$2s^2 2p^3$	${}^2D^\circ$	10	2.38
3	$2s^2 2p^3$	${}^2P^\circ$	6	3.58
4	$2s^2 2p^2(^3P) 3s$	4P	12	10.33
5	$2s^2 2p^2(^3P) 3s$	2P	6	10.69
6	$2s^2 2p^4$	4P	12	10.93
7	$2s^2 2p^2(^3P) 3p$	${}^2S^\circ$	2	11.60
8	$2s^2 2p^2(^3P) 3p$	${}^4D^\circ$	20	11.76
9	$2s^2 2p^2(^3P) 3p$	${}^4P^\circ$	12	11.84
10	$2s^2 2p^2(^3P) 3p$	${}^4S^\circ$	4	12.00
11	$2s^2 2p^2(^3P) 3p$	${}^2D^\circ$	10	12.01
12	$2s^2 2p^2(^3P) 3p$	${}^2P^\circ$	6	12.12
13	$2s^2 2p^2(^1D) 3s$	2D	10	12.36
14	$2s^2 2p^2(^3P) 4s$	4P	12	12.86
15	$2s^2 2p^2(^3P) 4s$	2P	6	12.92
16	$2s^2 2p^2(^3P) 3d$	2P	6	12.97

table continued on next page...

table continued from previous page...

Level index, i	Configuration	Term	Degeneracy, g_i	Energy, E_i (eV)
17	$2s^22p^2(^3P)3d$	4F	28	12.98
18	$2s^22p^2(^3P)3d$	2F	12	13.00
19	$2s^22p^2(^3P)3d$	4P	14	13.00
20	$2s^22p^2(^3P)3d$	4D	20	13.02
21	$2s^22p^2(^3P)3d$	2D	10	13.03
22	$2s^22p^2(^3P)4p$	$^2S^\circ$	2	13.20
23	$2s^22p^2(^3P)4p$	$^4D^\circ$	20	13.24
24	$2s^22p^2(^3P)4p$	$^4P^\circ$	12	13.27
25	$2s^22p^2(^3P)4p$	$^2D^\circ$	10	13.29
26	$2s^22p^2(^3P)4p$	$^4S^\circ$	4	13.32
27	$2s^22p^2(^3P)4p$	$^2P^\circ$	6	13.34
28*	-	-	90	13.68
29*	-	-	126	13.70
30*	-	-	54	13.81
31*	-	-	90	13.99
32*	-	-	288	14.00
33†	-	-	648	14.17
34†	-	-	882	14.27
35†	-	-	1152	14.34
36†	-	-	1458	14.38
37†	-	-	1800	14.41

*A grouping of NIST [80] multiplets.

†High lying level data obtained from Park [29].

B.3 Atomic nitrogen, O

Table B.3: Electronic level model for atomic oxygen, O.

Level index, i	Configuration	Term	Degeneracy, g_i	Energy, E_i (eV)
1	$2s^22p^4$	3P	9	0.01
2	$2s^22p^4$	1D	5	1.97
3	$2s^22p^4$	1S	1	4.19
4	$2s^22p^3(^4S^\circ)3s$	$^5S^\circ$	5	9.15
5	$2s^22p^3(^4S^\circ)3s$	$^3S^\circ$	3	9.52
6	$2s^22p^3(^4S^\circ)3p$	5P	15	10.74

table continued on next page...

table continued from previous page...

Level index, i	Configuration	Term	Degeneracy, g_i	Energy, E_i (eV)
7	$2s^22p^3(^4S^\circ)3p$	3P	9	10.99
8	$2s^22p^3(^4S^\circ)4s$	${}^5S^\circ$	5	11.84
9	$2s^22p^3(^4S^\circ)4s$	${}^3S^\circ$	3	11.93
10	$2s^22p^3(^4S^\circ)3d$	${}^5D^\circ$	25	12.08
11	$2s^22p^3(^4S^\circ)3d$	${}^3D^\circ$	15	12.09
12	$2s^22p^3(^4S^\circ)4p$	5P	15	12.29
13	$2s^22p^3(^4S^\circ)4p$	3P	9	12.36
14	$2s^22p^3(^2D^\circ)3s$	${}^3D^\circ$	15	12.54
15	$2s^22p^3(^4S^\circ)5s$	${}^5S^\circ$	5	12.66
16	$2s^22p^3(^4S^\circ)5s$	${}^3S^\circ$	3	12.70
17	$2s^22p^3(^4S^\circ)3s$	${}^1D^\circ$	5	12.73
18	$2s^22p^3(^4S^\circ)4d$	${}^5D^\circ$	25	12.75
19	$2s^22p^3(^4S^\circ)4d$	${}^3D^\circ$	15	12.76
20	$2s^22p^3(^4S^\circ)4f$	5F	35	12.77
21	$2s^22p^3(^4S^\circ)4f$	3F	21	12.77
22	$2s^22p^3(^4S^\circ)5p$	5P	15	12.85
23	$2s^22p^3(^4S^\circ)5p$	3P	9	12.88
24	$2s^22p^3(^4S^\circ)5d$	${}^5D^\circ$	25	13.07
25	$2s^22p^3(^4S^\circ)5d$	${}^3D^\circ$	15	13.07
26	$2s^22p^3(^4S^\circ)5f$	5F	35	13.07
27	$2s^22p^3(^4S^\circ)5f$	3F	21	13.07
28 [†]	$n = 6$	-	288	13.22
29 [†]	$n = 7$	-	392	13.34
30 [†]	$n = 8$	-	512	13.40
31 [†]	$n = 9$	-	648	13.45
32 [†]	$n = 10$	-	800	13.48

[†]High lying level data obtained from Park [29].

C

Chemical kinetic models

C.1 N₂–O₂ mixtures

The implemented reaction scheme for shock heated N₂–O₂ mixtures is detailed in Table C.1.

Table C.1: Reaction scheme for shock heated N₂–O₂–Ar mixtures.

	Reaction	M	T_x	C (cm ³ mole ⁻¹ s ⁻¹)	n	E_a (K)	Source
<i>Dissociation</i>							
1.	$N_2 + M \rightleftharpoons N + N + M$	N	T_a	3.0×10^{22}	-1.60	113,200	Park (1990)
		O		3.0×10^{22}			
		N ₂		7.0×10^{21}			
		O ₂		7.0×10^{21}			
		NO		7.0×10^{21}			
		N ⁺		3.0×10^{22}			
		O ⁺		3.0×10^{22}			
		N ₂ ⁺		7.0×10^{21}			
		O ₂ ⁺		7.0×10^{21}			
		NO ⁺		7.0×10^{21}			
		e ⁻		1.2×10^{25}			

table continued on next page...

table continued from previous page...

	Reaction	M	T_x	C ($\text{cm}^3 \text{ mole}^{-1} \text{ s}^{-1}$)	n	E_a (K)	Source
2.	$\text{O}_2 + \text{M} \rightleftharpoons \text{O} + \text{O} + \text{M}$	N	T_a	1.0×10^{22}	-1.50	59,500	Sharma et al (1991)
	O			1.0×10^{22}			
	N_2			2.0×10^{21}			
	O_2			2.0×10^{21}			
	NO			2.0×10^{21}			
	N^+			1.0×10^{22}			
	O^+			1.0×10^{22}			
	N_2^+			2.0×10^{21}			
	O_2^+			2.0×10^{21}			
	NO^+			2.0×10^{21}			
3.	$\text{NO} + \text{M} \rightleftharpoons \text{N} + \text{O} + \text{M}$	N	T_a	1.1×10^{17}	0.00	75,500	Park (1990)
	O			1.1×10^{17}			
	N_2			5.0×10^{15}			
	O_2			5.0×10^{15}			
	NO			1.1×10^{17}			
	N^+			1.1×10^{17}			
	O^+			1.1×10^{17}			
	N_2^+			5.0×10^{15}			
	O_2^+			5.0×10^{15}			
	NO^+			5.0×10^{15}			
	NO exchange reactions						
4.	$\text{NO} + \text{O} \rightleftharpoons \text{N} + \text{O}_2$		T	8.4×10^{12}	0.00	19,450	Park (1990)
5.	$\text{N}_2 + \text{O} \rightleftharpoons \text{NO} + \text{N}$		T	6.4×10^{17}	-1.00	38,400	Park (1990)
	Associative ionisation reactions						
6.	$\text{N} + \text{O} \rightleftharpoons \text{NO}^+ + \text{e}^-$		T	8.8×10^8	1.00	31,900	Park (1993)
7.	$\text{O} + \text{O} \rightleftharpoons \text{O}_2^+ + \text{e}^-$		T	7.1×10^2	2.70	80,600	Park (1993)
8.	$\text{N} + \text{N} \rightleftharpoons \text{N}_2^+ + \text{e}^-$		T	4.4×10^7	1.50	67,500	Park (1993)
	Charge exchange reactions						
9.	$\text{NO}^+ + \text{O} \rightleftharpoons \text{N}^+ + \text{O}_2$		T	1.0×10^{12}	0.50	77,200	Park (1990)
10.	$\text{N}^+ + \text{N}_2 \rightleftharpoons \text{N}_2^+ + \text{N}$		T	1.0×10^{12}	0.50	11,200	Park (1990)
11.	$\text{O}_2^+ + \text{N} \rightleftharpoons \text{N}^+ + \text{O}_2$		T	8.7×10^{13}	0.14	28,600	Park (1990)
12.	$\text{O}^+ + \text{NO} \rightleftharpoons \text{N}^+ + \text{O}_2$		T	1.4×10^5	1.90	26,600	Park (1990)
13.	$\text{O}_2^+ + \text{N}_2 \rightleftharpoons \text{N}_2^+ + \text{O}_2$		T	9.9×10^{12}	0.00	40,700	Park (1990)
14.	$\text{O}_2^+ + \text{O} \rightleftharpoons \text{O}^+ + \text{O}_2$		T	4.0×10^{12}	-0.09	18,000	Park (1990)
15.	$\text{NO}^+ + \text{N} \rightleftharpoons \text{O}^+ + \text{N}_2$		T	3.4×10^{13}	-1.08	12,800	Park (1990)
16.	$\text{NO}^+ + \text{O}_2 \rightleftharpoons \text{O}_2^+ + \text{NO}$		T	2.4×10^{13}	0.41	32,600	Park (1990)
17.	$\text{NO}^+ + \text{O} \rightleftharpoons \text{O}_2^+ + \text{N}$		T	7.2×10^{12}	0.29	48,600	Park (1990)
18.	$\text{O}^+ + \text{N}_2 \rightleftharpoons \text{N}_2^+ + \text{O}$		T	9.1×10^{11}	0.36	22,800	Park (1990)
19.	$\text{NO}^+ + \text{N} \rightleftharpoons \text{N}_2^+ + \text{O}$		T	7.2×10^{13}	0.00	35,500	Park (1990)

table continued on next page...

table continued from previous page...

	Reaction	M	T _x	C (cm ³ mole ⁻¹ s ⁻¹)	n	E _a (K)	Source
Electron-impact ionisation reactions							
20.	O + e ⁻ ⇌ O ⁺ + e ⁻ + e ⁻		T _e	3.9 × 10 ³³	-3.78	158,500	Park (1990)
21.	N + e ⁻ ⇌ N ⁺ + e ⁻ + e ⁻		T _e	2.5 × 10 ³⁴	-3.82	168,600	Park (1990)
Radiative recombination reactions							
22.	O ⁺ + e ⁻ ⇌ O + hν		T _e	1.07 × 10 ¹¹	-0.52		Park (1993)
23.	N ⁺ + e ⁻ ⇌ N + hν		T _e	1.52 × 10 ¹¹	-0.48		Park (1993)

C.2 CO₂-N₂-Ar mixtures

The implemented reaction scheme for shock heated CO₂-N₂-Ar mixtures is detailed in Table C.2.

Table C.2: Reaction scheme for shock heated CO₂-N₂-Ar mixtures.

	Reaction	M	T _x	C (cm ³ mole ⁻¹ s ⁻¹)	n	E _a (K)	Source
<i>Dissociation</i>							
1.	C ₂ + M ⇌ C + C + M	All	T _{av}	3.7 × 10 ¹⁴	0.0	69900	Park <i>et al.</i> [137]
		All		7.5 × 10¹⁶			Lee <i>et al.</i> [35]
2.	N ₂ + M ⇌ N + N + M		T _{av}	7.0 × 10 ²¹	-1.6	113200	Park <i>et al.</i> [137]
		C, N, O		3.0 × 10 ²²			Park <i>et al.</i> [137]
		e ⁻		1.2 × 10 ²⁵			Park <i>et al.</i> [137]
		e ⁻		3.0 × 10²⁴			Gökçen [230]
3.	O ₂ + M ⇌ O + O + M		T _{av}	2.0 × 10 ²¹	-1.5	59750	Park <i>et al.</i> [137]
		C, N, O		1.0 × 10 ²²			Park <i>et al.</i> [137]
4.	CN + M ⇌ C + N + M	All	T _{av}	2.50 × 10 ¹⁴	0.0	71000	Park <i>et al.</i> [137]
		All		2.53 × 10¹⁴			Gökçen [230]
5.	CO + M ⇌ C + O + M		T _{av}	2.3 × 10 ²⁰	-1.0	129000	Park <i>et al.</i> [137]
		C, N, O		3.4 × 10 ²⁰			Park <i>et al.</i> [137]
		Ar		2.3 × 10 ¹⁹			Park <i>et al.</i> [137]
6.	NO + M ⇌ N + O + M		T _{av}	5.0 × 10 ¹⁵	0.0	75500	Park <i>et al.</i> [137]
		C, N, O,		1.1 × 10 ¹⁷			Park <i>et al.</i> [137]
		NO, CO ₂		9.64 × 10¹⁴	0.0	74700	Tsang <i>et al.</i> [231]
		N ₂		1.45 × 10¹⁵			Tsang <i>et al.</i> [231]
		CO ₂		2.41 × 10¹⁵			Tsang <i>et al.</i> [231]
7.	CO ₂ + M ⇌ CO + O + M		T _{av}	6.9 × 10 ²¹	-1.5	63275	Park <i>et al.</i> [137]
		C, N, O		1.4 × 10 ²²			Park <i>et al.</i> [137]
		Ar		6.9 × 10 ²⁰			Park <i>et al.</i> [137]
8.	NCO + M ⇌ CO + N + M	All	T _{av}	6.3 × 10 ¹⁶	-0.5	24000	Park <i>et al.</i> [137]

table continued on next page...

table continued from previous page...

	Reaction	M	T_x	C ($\text{cm}^3 \text{ mole}^{-1} \text{ s}^{-1}$)	n	E_a (K)	Source
<i>Neutral exchange</i>							
9.	$\text{N}_2 + \text{O} \rightleftharpoons \text{NO} + \text{N}$		T	6.4×10^{17}	-1.0	38370	Park <i>et al.</i> [137]
10.	$\text{NO} + \text{O} \rightleftharpoons \text{N} + \text{O}_2$		T	8.4×10^{12}	0.0	19450	Park <i>et al.</i> [137]
11.	$\text{CO} + \text{C} \rightleftharpoons \text{C}_2 + \text{O}$		T	2.0×10^{17}	-1.0	58000	Park <i>et al.</i> [137]
12.	$\text{CO} + \text{O} \rightleftharpoons \text{C} + \text{O}_2$		T	3.9×10^{13}	-0.18	69200	Park <i>et al.</i> [137]
13.	$\text{CO} + \text{N} \rightleftharpoons \text{CN} + \text{O}$		T	1.0×10^{14}	0.0	38600	Park <i>et al.</i> [137]
14.	$\text{N}_2 + \text{C} \rightleftharpoons \text{CN} + \text{N}$		T	1.10×10^{14}	-0.11	23200	Park <i>et al.</i> [137]
				5.24×10^{13}	0.0	22600	Gökçen [230]
15.	$\text{CN} + \text{O} \rightleftharpoons \text{NO} + \text{C}$		T	1.6×10^{13}	0.1	14600	Park <i>et al.</i> [137]
16.	$\text{CN} + \text{C} \rightleftharpoons \text{C}_2 + \text{N}$		T	5.0×10^{13}	0.0	13000	Park <i>et al.</i> [137]
17.*	$\text{CO} + \text{CO} \rightleftharpoons \text{C} + \text{CO}_2$		T	2.3×10^9	0.5	65170	Losev <i>et al.</i> [140]
18.	$\text{CO}_2 + \text{O} \rightleftharpoons \text{O}_2 + \text{CO}$		T	2.1×10^{13}	0.0	27800	Park <i>et al.</i> [137]
19.*	$\text{C}_2 + \text{N}_2 \rightleftharpoons \text{CN} + \text{CN}$		T	1.5×10^{13}	0.0	21000	Gökçen [230]
20.	$\text{CO} + \text{NO} \rightleftharpoons \text{NCO} + \text{O}$		T	3.8×10^{17}	-0.873	51600	Park <i>et al.</i> [137]
21.	$\text{CN} + \text{O}_2 \rightleftharpoons \text{NCO} + \text{O}$		T	6.6×10^{12}	0.0	-200	Park <i>et al.</i> [137]
22.	$\text{CN} + \text{CO}_2 \rightleftharpoons \text{NCO} + \text{CO}$		T	4.0×10^{14}	0.0	19200	Park <i>et al.</i> [137]
23.	$\text{CN} + \text{NO} \rightleftharpoons \text{NCO} + \text{N}$		T	1.0×10^{14}	0.0	21200	Park <i>et al.</i> [137]
24.	$\text{CN} + \text{CO} \rightleftharpoons \text{NCO} + \text{C}$		T	1.5×10^{16}	-4.87	65800	Park <i>et al.</i> [137]
25.*	$\text{CO} + \text{N} \rightleftharpoons \text{NO} + \text{C}$		T	2.9×10^{11}	0.50	53630	Losev <i>et al.</i> [140]
26.*	$\text{NO} + \text{CO} \rightleftharpoons \text{CO}_2 + \text{N}$		T	4.6×10^8	0.50	12070	Losev <i>et al.</i> [140]
<i>Associative ionisation</i>							
27.	$\text{N} + \text{O} \rightleftharpoons \text{NO}^+ + \text{e}^-$		T	8.8×10^8	1.0	31900	Park <i>et al.</i> [137]
28.	$\text{O} + \text{O} \rightleftharpoons \text{O}_2^+ + \text{e}^-$		T	7.1×10^2	2.7	80600	Park <i>et al.</i> [137]
29.	$\text{C} + \text{O} \rightleftharpoons \text{CO}^+ + \text{e}^-$		T	8.8×10^8	1.0	33100	Park <i>et al.</i> [137]
30. [†]	$\text{N} + \text{N} \rightleftharpoons \text{N}_2^+ + \text{e}^-$		T	4.4×10^7	1.5	67500	Gökçen [139]
31. [†]	$\text{C} + \text{N} \rightleftharpoons \text{CN}^+ + \text{e}^-$		T	1.0×10^{15}	1.5	164400	Gökçen [139]
<i>Charge exchange</i>							
32.	$\text{NO}^+ + \text{C} \rightleftharpoons \text{NO} + \text{C}^+$		T	1.0×10^{13}	0.0	23200	Park <i>et al.</i> [137]
33.	$\text{O}_2^+ + \text{O} \rightleftharpoons \text{O}^+ + \text{O}_2$		T	4.0×10^{12}	-0.09	18000	Park <i>et al.</i> [137]
34.	$\text{NO}^+ + \text{N} \rightleftharpoons \text{O}^+ + \text{N}$		T	3.4×10^{13}	-1.08	12800	Park <i>et al.</i> [137]
35.	$\text{NO}^+ + \text{O} \rightleftharpoons \text{O}_2^+ + \text{N}$		T	7.2×10^{12}	0.29	48600	Park <i>et al.</i> [137]
36.	$\text{CO} + \text{C}^+ \rightleftharpoons \text{CO}^+ + \text{C}$		T	1.0×10^{13}	0.0	31400	Park <i>et al.</i> [137]
37.	$\text{O}_2 + \text{C}^+ \rightleftharpoons \text{O}_2^+ + \text{C}$		T	1.0×10^{13}	0.0	9400	Park <i>et al.</i> [137]
38. [†]	$\text{C}^+ + \text{N}_2 \rightleftharpoons \text{N}_2^+ + \text{C}$		T	1.11×10^{14}	-0.11	50000	Gökçen [139]
39. [†]	$\text{CN}^+ + \text{N} \rightleftharpoons \text{CN} + \text{N}^+$		T	9.8×10^{12}	0.0	40700	Gökçen [139]
<i>Electron impact ionisation</i>							
40.	$\text{C} + \text{e}^- \rightleftharpoons \text{C}^+ + \text{e}^- + \text{e}^-$		T_v	3.9×10^{33}	-3.78	130700	Park <i>et al.</i> [137]
41. [†]	$\text{N} + \text{e}^- \rightleftharpoons \text{N}^+ + \text{e}^- + \text{e}^-$		T_v	2.5×10^{34}	-3.82	168600	Gökçen [139]
42.	$\text{O} + \text{e}^- \rightleftharpoons \text{O}^+ + \text{e}^- + \text{e}^-$		T_v	3.9×10^{33}	-3.78	158500	Park <i>et al.</i> [137]

table continued on next page...

table continued from previous page...

Reaction	M	T _x	C (cm ³ mole ⁻¹ s ⁻¹)	n	E _a (K)	Source
<i>Radiative recombination</i>						
43.	O ⁺ + e ⁻ ⇌ O + hν	T _v	1.07 × 10 ¹¹	-0.52	0	Park <i>et al.</i> [137]
44.	C ⁺ + e ⁻ ⇌ C + hν	T _v	2.02 × 10 ¹¹	-0.46	0	Park <i>et al.</i> [137]

* New reactions from the scheme of Lee *et al.* [35] not included by Park *et al.* [137].

† Additional reactions from Gökçen [139] N₂-CN₄ scheme not considered by Lee *et al.* [35].

D

Diatomical collisional-radiative models

In this Appendix the collisional-radiative models for diatomic molecules implemented in this work are presented. The collisional rates are expressed in generalised Arrhenius form (see Equation 4.55), and the radiative transitions are expressed via the average radiative transition probability for the system. If the radiative transition rates are not provided in the literature, they are calculated from the electronic-vibration transition moments via Equation 4.93. The collisional-radiative models for C₂, CN, CO, N₂ and N₂⁺ are presented in § D.1 to D.5 respectively.

D.1 Collisional-radiative model for C₂

The implemented collisional-radiative model for C₂ is from Zalogin [185], and is presented in Table D.1.

Reaction	A (cm ³ /s)	n	E_a (K)	Source
<i>Electron impact excitation</i>				
C ₂ (X ^{1Σ_g⁺) + e⁻ ⇌ C₂ (d^{3Π_g) + e⁻}}	1.3 × 10 ⁻⁸	0.00	28,807	Zalogin [185]
<i>Heavy particle impact excitation</i>				
C ₂ (X ^{1Σ_g⁺) + M ⇌ C₂ (d^{3Π_g) + M}}	8.6 × 10 ⁻¹¹	0.00	28,807	Zalogin [185]
<i>Radiative transitions</i>				
Reaction	A (s ⁻¹)	Source		
C ₂ (X ^{1Σ_g⁺) ⇌ C₂ (d^{3Π_g) + hν}}	9.3 × 10 ⁶	Zalogin [185]		

Table D.1: Implemented collisional-radiative model for C₂.

D.2 Collisional-radiative model for CN

The implemented collisional-radiative model for CN uses the electron impact excitation cross sections and electron impact dissociation coefficients compiled by Park [178], and is presented in Table D.2. The electron impact excitation rate coefficients have been calculated from the cross sections given in Reference [178] via Equations 4.61 to 4.67, and then curve-fitted to the generalised Arrhenius expression. Heavy particle impact processes are omitted and the radiative transition probabilities have been calculated via Equation 4.93.

Reaction	A (cm ³ /s)	n	E_a (K)	Source
<i>Electron impact excitation</i>				
CN ($X^2\Sigma^+$) + e ⁻ ⇌ CN ($A^2\Pi$) + e ⁻	1.9×10^{-9}	0.24	13,302	Same as N ₂
CN ($X^2\Sigma^+$) + e ⁻ ⇌ CN ($B^2\Sigma^+$) + e ⁻	3.1×10^{-7}	-0.25	37,052	Same as N ₂
CN ($X^2\Sigma^+$) + e ⁻ ⇌ CN ($a^4\Sigma^+$) + e ⁻	1.6×10^{-14}	1.09	46,616	Same as N ₂
CN ($X^2\Sigma^+$) + e ⁻ ⇌ CN ($D^2\Pi$) + e ⁻	3.0×10^{-9}	0.16	78,393	Same as N ₂
CN ($A^2\Pi$) + e ⁻ ⇌ CN ($B^2\Sigma^+$) + e ⁻	1.0×10^{-5}	-0.22	23,750	Huo <i>et al.</i> [232]
CN ($A^2\Pi$) + e ⁻ ⇌ CN ($a^4\Sigma^+$) + e ⁻	5.9×10^{-8}	0.18	33,314	Huo <i>et al.</i> [232]
CN ($A^2\Pi$) + e ⁻ ⇌ CN ($D^2\Pi$) + e ⁻	2.0×10^{-5}	-0.29	65,091	Huo <i>et al.</i> [232]
CN ($B^2\Sigma^+$) + e ⁻ ⇌ CN ($a^4\Sigma^+$) + e ⁻	5.2×10^{-12}	0.70	9,564	Huo <i>et al.</i> [232]
CN ($B^2\Sigma^+$) + e ⁻ ⇌ CN ($D^2\Pi$) + e ⁻	4.6×10^{-8}	0.22	41,341	Huo <i>et al.</i> [232]
CN ($a^4\Sigma^+$) + e ⁻ ⇌ CN ($D^2\Pi$) + e ⁻	6.9×10^{-5}	-0.40	31,777	Huo <i>et al.</i> [232]
<i>Electron impact dissociation</i>				
CN ($X^2\Sigma^+$) + e ⁻ ⇌ C + N + e ⁻	1.3×10^{15}	0.43	88,966	Park [178]
CN ($A^2\Pi$) + e ⁻ ⇌ C + N + e ⁻	5.9×10^{15}	0.46	75,564	Park [178]
CN ($B^2\Sigma^+$) + e ⁻ ⇌ C + N + e ⁻	2.4×10^{15}	0.55	51,576	Park [178]
CN ($a^4\Sigma^+$) + e ⁻ ⇌ C + N + e ⁻	1.6×10^{15}	0.60	41,890	Park [178]
CN ($D^2\Pi$) + e ⁻ ⇌ C + N + e ⁻	6.3×10^{15}	0.92	9,964	Park [178]
<i>Radiative transitions</i>				
Reaction	A (s ⁻¹)			Source
CN ($A^2\Pi$) ⇌ CN ($B^2\Sigma^+$) + hν	9.3×10^5			This work (Eq. 4.93)
CN ($X^2\Sigma^+$) ⇌ CN ($A^2\Pi$) + hν	1.7×10^6			This work (Eq. 4.93)
CN ($X^2\Sigma^+$) ⇌ CN ($B^2\Sigma^+$) + hν	2.0×10^8			This work (Eq. 4.93)

Table D.2: Implemented collisional-radiative model for CN.

D.3 Collisional-radiative model for CO

The implemented collisional-radiative model for CO uses the electron impact excitation cross sections and electron impact dissociation coefficients compiled by Park [178], and is presented in Table D.3. The electron impact excitation rate coefficients have been calculated from the cross sections given in Reference [178] via Equations 4.61 to 4.67, and then curve-fitted to the generalised Arrhenius expression. Heavy particle impact processes are omitted and the radiative transition probabilities have been calculated via Equation 4.93.

Reaction	A (cm ³ /s)	n	E_a (K)	Source
<i>Electron impact excitation</i>				
$\text{CO}(\text{X}^1\Sigma^+) + \text{e}^- \rightleftharpoons \text{CO}(\text{a}^2\Pi) + \text{e}^-$	3.9×10^{-6}	-0.34	70,049	Zobel <i>et al.</i> [233]
$\text{CO}(\text{X}^1\Sigma^+) + \text{e}^- \rightleftharpoons \text{CO}(\text{a}'^3\Sigma^+) + \text{e}^-$	1.2×10^{-6}	-0.28	80,320	Zobel <i>et al.</i> [233]
$\text{CO}(\text{X}^1\Sigma^+) + \text{e}^- \rightleftharpoons \text{CO}(\text{d}^3\Delta) + \text{e}^-$	3.5×10^{-7}	-0.27	87,938	Zobel <i>et al.</i> [233]
$\text{CO}(\text{X}^1\Sigma^+) + \text{e}^- \rightleftharpoons \text{CO}(\text{e}^3\Sigma^-) + \text{e}^-$	5.3×10^{-7}	-0.22	92,412	Morgan <i>et al.</i> [234]
$\text{CO}(\text{X}^1\Sigma^+) + \text{e}^- \rightleftharpoons \text{CO}(\text{A}^1\Pi) + \text{e}^-$	1.3×10^{-5}	-0.43	93,629	Olszewski <i>et al.</i> [235]
$\text{CO}(\text{a}^2\Pi) + \text{e}^- \rightleftharpoons \text{CO}(\text{a}'^3\Sigma^+) + \text{e}^-$	5.6×10^{-7}	-0.07	10,271	Huo <i>et al.</i> [232]
$\text{CO}(\text{a}^2\Pi) + \text{e}^- \rightleftharpoons \text{CO}(\text{d}^3\Delta) + \text{e}^-$	5.4×10^{-6}	-0.31	17,889	Huo <i>et al.</i> [232]
$\text{CO}(\text{a}^2\Pi) + \text{e}^- \rightleftharpoons \text{CO}(\text{e}^3\Sigma^-) + \text{e}^-$	9.4×10^{-6}	-0.36	22,364	Huo <i>et al.</i> [232]
$\text{CO}(\text{a}^2\Pi) + \text{e}^- \rightleftharpoons \text{CO}(\text{A}^1\Pi) + \text{e}^-$	2.1×10^{-6}	-0.25	23,580	Huo <i>et al.</i> [232]
$\text{CO}(\text{a}'^3\Sigma^+) + \text{e}^- \rightleftharpoons \text{CO}(\text{d}^3\Delta) + \text{e}^-$	8.8×10^{-7}	-0.14	7,618	Huo <i>et al.</i> [232]
$\text{CO}(\text{a}'^3\Sigma^+) + \text{e}^- \rightleftharpoons \text{CO}(\text{e}^3\Sigma^-) + \text{e}^-$	8.2×10^{-6}	-0.38	12,092	Huo <i>et al.</i> [232]
$\text{CO}(\text{a}'^3\Sigma^+) + \text{e}^- \rightleftharpoons \text{CO}(\text{A}^1\Pi) + \text{e}^-$	1.3×10^{-6}	-0.27	13,309	Huo <i>et al.</i> [232]
$\text{CO}(\text{d}^3\Delta) + \text{e}^- \rightleftharpoons \text{CO}(\text{e}^3\Sigma^-) + \text{e}^-$	1.0×10^{-7}	0.07	4,475	Huo <i>et al.</i> [232]
$\text{CO}(\text{d}^3\Delta) + \text{e}^- \rightleftharpoons \text{CO}(\text{A}^1\Pi) + \text{e}^-$	4.6×10^{-8}	0.09	5,691	Huo <i>et al.</i> [232]
$\text{CO}(\text{e}^3\Sigma^-) + \text{e}^- \rightleftharpoons \text{CO}(\text{A}^1\Pi) + \text{e}^-$	1.8×10^{-9}	0.36	1,216	Huo <i>et al.</i> [232]
<i>Electron impact dissociation</i>				
$\text{CO}(\text{X}^1\Sigma^+) + \text{e}^- \rightleftharpoons \text{C} + \text{O} + \text{e}^-$	2.1×10^{14}	0.37	129,271	Park [178]
$\text{CO}(\text{a}^2\Pi) + \text{e}^- \rightleftharpoons \text{C} + \text{O} + \text{e}^-$	3.1×10^{15}	0.52	58,742	Park [178]
$\text{CO}(\text{a}'^3\Sigma^+) + \text{e}^- \rightleftharpoons \text{C} + \text{O} + \text{e}^-$	3.3×10^{15}	0.56	48,352	Park [178]
$\text{CO}(\text{d}^3\Delta) + \text{e}^- \rightleftharpoons \text{C} + \text{O} + \text{e}^-$	4.2×10^{15}	0.61	40,635	Park [178]
$\text{CO}(\text{e}^3\Sigma^-) + \text{e}^- \rightleftharpoons \text{C} + \text{O} + \text{e}^-$	3.9×10^{15}	0.64	36,098	Park [178]
$\text{CO}(\text{A}^1\Pi) + \text{e}^- \rightleftharpoons \text{C} + \text{O} + \text{e}^-$	4.8×10^{15}	0.64	34,864	Park [178]
<i>Radiative transitions</i>				
Reaction	A (s ⁻¹)			Source
$\text{CO}(\text{X}^1\Sigma^+) \rightarrow \text{CO}(\text{A}^1\Pi) + h\nu$	1.4×10^9			This work (Eq. 4.93)

Table D.3: Implemented collisional-radiative model for CO.

D.4 Collisional-radiative model for N₂

The implemented collisional-radiative model for N₂ is that compiled by Johnston [19], and is presented in Table D.4.

Reaction	A (cm ³ /s)	n	E_a (K)	Source
<i>Electron impact excitation</i>				
N ₂ ($X^1\Sigma_g^+$) + e ⁻ ⇌ N ₂ ($A^3\Sigma_u^+$) + e ⁻	4.0×10^{-9}	0.1	71,610	Chernyi [140]
N ₂ ($X^1\Sigma_g^+$) + e ⁻ ⇌ N ₂ ($B^3\Pi_g$) + e ⁻	4.6×10^{-8}	- 0.1	85,740	Chernyi [140]
N ₂ ($X^1\Sigma_g^+$) + e ⁻ ⇌ N ₂ ($C^3\Pi_u$) + e ⁻	3.8×10^{-9}	0.1	127,900	Capitelli [236]
N ₂ ($A^3\Sigma_u^+$) + e ⁻ ⇌ N ₂ ($B^3\Pi_g$) + e ⁻	5.0×10^{-9}	0.0	13,495	Chernyi [140]
N ₂ ($B^3\Pi_g$) + e ⁻ ⇌ N ₂ ($C^3\Pi_u$) + e ⁻	2.9×10^{-9}	0.28	46,655	Teulet [177]
<i>Electron impact dissociation</i>				
N ₂ ($X^1\Sigma_g^+$) + e ⁻ ⇌ N + N + e ⁻	4.11×10^{-33}	6.16	113,263	Teulet [177]
N ₂ ($A^3\Sigma_u^+$) + e ⁻ ⇌ N + N + e ⁻	6.61×10^{-20}	2.98	41,669	Teulet [177]
N ₂ ($B^3\Pi_g$) + e ⁻ ⇌ N + N + e ⁻	4.50×10^{-23}	3.73	55,586	Teulet [177]
N ₂ ($C^3\Pi_u$) + e ⁻ ⇌ N + N + e ⁻	5.14×10^{-21}	3.27	12,892	Teulet [177]
<i>Heavy particle impact excitation</i>				
N ₂ ($X^1\Sigma_g^+$) + N ₂ ⇌ N ₂ ($A^3\Sigma_u^+$) + N ₂	1.83×10^{-12}	-0.5	71,600	Kurochkin [237]
N ₂ ($A^3\Sigma_u^+$) + N ₂ ⇌ N ₂ ($B^3\Pi_g$) + N ₂	1.99×10^{-11}	0.0	13,495	Chernyi [140]
N ₂ ($B^3\Pi_g$) + N ₂ ⇌ N ₂ ($C^3\Pi_u$) + N ₂	8.47×10^{-11}	0.0	42,476	Fresnet [238]
Reaction	A (s ⁻¹)			Source
N ₂ ($B^3\Pi_g$) ⇌ N ₂ ($A^3\Sigma_u^+$) + h ν	1.4×10^5			Chernyi [140]
N ₂ ($C^3\Pi_u$) ⇌ N ₂ ($B^3\Pi_g$) + h ν	2.6×10^7			Panchesnyi [239]

Table D.4: Implemented collisional-radiative model for N₂.

D.5 Collisional-radiative model for N_2^+

The implemented collisional-radiative model for N_2^+ is that compiled by Johnston [19], and is presented in Table D.5.

Reaction	A (cm ³ /s)	n	E_a (K)	Source
<i>Electron impact excitation</i>				
$\text{N}_2^+ \left(X^2\Sigma_g^+ \right) + e^- \rightleftharpoons \text{N}_2^+ \left(A^2\Pi_u \right) + e^-$	7.1×10^{-11}	0.0	13,300	Gorelov [240]
$\text{N}_2^+ \left(X^2\Sigma_g^+ \right) + e^- \rightleftharpoons \text{N}_2^+ \left(B^2\Sigma_u^+ \right) + e^-$	2.0×10^{-11}	0.73	36,649	Nagy [241]
$\text{N}_2^+ \left(X^2\Sigma_g^+ \right) + e^- \rightleftharpoons \text{N}_2^+ \left(C^2\Sigma_u^+ \right) + e^-$	6.6×10^{-9}	0.41	85,038	Teulet [177]
$\text{N}_2^+ \left(A^2\Pi_u \right) + e^- \rightleftharpoons \text{N}_2^+ \left(B^2\Sigma_u^+ \right) + e^-$	1.0×10^{-9}	0.0	23,500	Gorelov [240]
$\text{N}_2^+ \left(A^2\Pi_u \right) + e^- \rightleftharpoons \text{N}_2^+ \left(C^2\Sigma_u^+ \right) + e^-$	1.3×10^{-7}	0.11	78,403	Teulet [177]
$\text{N}_2^+ \left(B^2\Sigma_u^+ \right) + e^- \rightleftharpoons \text{N}_2^+ \left(C^2\Sigma_u^+ \right) + e^-$	3.9×10^{-9}	0.34	49,622	Teulet [177]
<i>Electron impact dissociation</i>				
$\text{N}_2^+ \left(X^2\Sigma_g^+ \right) + e^- \rightleftharpoons \text{N}^+ + \text{N} + e^-$	8.02×10^{-31}	5.54	101,117	Teulet [177]
$\text{N}_2^+ \left(A^2\Pi_u \right) + e^- \rightleftharpoons \text{N}^+ + \text{N} + e^-$	8.27×10^{-26}	4.38	88,142	Teulet [177]
$\text{N}_2^+ \left(B^2\Sigma_u^+ \right) + e^- \rightleftharpoons \text{N}^+ + \text{N} + e^-$	2.58×10^{-32}	5.81	64,328	Teulet [177]
$\text{N}_2^+ \left(C^2\Sigma_u^+ \right) + e^- \rightleftharpoons \text{N}^+ + \text{N} + e^-$	1.31×10^{-28}	4.93	35,906	Teulet [177]
<i>Heavy particle impact excitation</i>				
$\text{N}_2^+ \left(X^2\Sigma_g^+ \right) + \text{N}_2 \rightleftharpoons \text{N}_2^+ \left(A^2\Pi_u \right) + \text{N}_2$	3.8×10^{-2}	-2.33	12,978	Nagy [241]
$\text{N}_2^+ \left(X^2\Sigma_g^+ \right) + \text{N}_2 \rightleftharpoons \text{N}_2^+ \left(B^2\Sigma_u^+ \right) + \text{N}_2$	1.9×10^{-2}	-2.33	36,600	Flagan [242]
Reaction	A (s ⁻¹)			Source
$\text{N}_2^+ \left(A^2\Pi_u \right) \rightleftharpoons \text{N}_2^+ \left(X^2\Sigma_g^+ \right) + h\nu$	6.7×10^4			Chernyi [140]
$\text{N}_2^+ \left(B^2\Sigma_u^+ \right) \rightleftharpoons \text{N}_2^+ \left(X^2\Sigma_g^+ \right) + h\nu$	1.5×10^7			Gorelov [240]
$\text{N}_2^+ \left(C^2\Sigma_u^+ \right) \rightleftharpoons \text{N}_2^+ \left(X^2\Sigma_g^+ \right) + h\nu$	1.4×10^7			Chernyi [140]

Table D.5: Implemented collisional-radiative model for N_2^+ .

E

Multicomponent Diffusion models

Three multicomponent diffusion models are implemented within the `eilmer3` framework:

- Fick's first law,
- Stefan-Maxwell equations as described by Sutton and Gnoffo [207], and
- Self-Consistent Effective Binary Diffusion (SCEBD) model proposed by Ramshaw and Chang [208]

E.1 Fick's first law

The approximate form of Fick's first law gives the diffusive mass flux of species i as:

$$\vec{J}_i = -\rho \tilde{D}_i \nabla f_i \quad (\text{E.1})$$

where \tilde{D}_i is the effective mixture diffusion coefficient for species i and ∇f_i is the mass-fraction divergence. The effective mixture diffusion coefficient is obtained from the multicomponent diffusion coefficients D_{ij} by applying the mixture rule of Wilke [243] with the ambipolar correction proposed by Gnoffo [151]. The Wilke mixture rule gives the effective mixture diffusion coefficient as:

$$\tilde{D}_i = \frac{1 - x_i}{\sum_{j \neq i}^{N_{\text{species}}} \frac{x_j}{D_{ij}}} . \quad (\text{E.2})$$

To impose the ambipolar assumption, the effective mixture diffusion coefficients for ions is set to twice the value given by the Wilke mixture rule:

$$\tilde{D}_{\text{ion}} = 2 (\tilde{D}_{\text{ion}})_{\text{Wilke}} \quad (\text{E.3})$$

and the effective mixture diffusion coefficient for electrons is calculated so as to enforce charge neutrality:

$$\tilde{D}_e = M_e \frac{\sum_i^{N_{\text{ions}}} \tilde{D}_i x_i}{\sum_i^{N_{\text{ions}}} M_i x_i} . \quad (\text{E.4})$$

E.2 Stefan-Maxwell equations

The Stefan-Maxwell equations as described by Sutton and Gnoffo [207] gives the diffusive mass flux of species i as:

$$\vec{J}_i = -\rho \tilde{D}_i \nabla f_i + \frac{f_i}{(1 - x_i)} \tilde{D}_i \sum_{j \neq i} \left(\rho \frac{M_i}{M} \nabla f_i + \frac{M}{M_j} \frac{\mathbf{J}_j}{\mathcal{D}_{ij}} \right) \quad (\text{E.5})$$

The resulting system of equations is iterated to the suggested tolerance of 1×10^{-6} by applying:

$$\vec{J}_i^{N+1} = \vec{J}_i^N - f_i \sum_j \vec{J}_j^N \quad (\text{E.6})$$

The initial guess for each species is calculated using the Fick's-Wilke method outlined above.

E.3 Self-Consistent Effective Binary Diffusion (SCEBD) model

The Self-Consistent Effective Binary Diffusion (SCEBD) model is an approximation of the full Stefan-Maxwell equations, and includes an ambipolar correction to ensure charge neutrality as assumed for the multi-component plasmas under consideration. The SCEBD model is able to produce similar results to the complete full Stefan-Maxwell equations whilst remaining computationally efficient [244].

The SCEBD expression for the diffusive flux of species i is:

$$\vec{J}_i = \begin{cases} -M_i \tilde{D}_i \nabla c_i + f_i \sum_{j \neq e} M_j \tilde{D}_j \nabla c_j + A_i & \text{for } i \neq e \\ -\left(\frac{1}{q_e}\right) \sum_{j \neq e} q_j \vec{J}_j & \text{for } i = e \end{cases} ' \quad (\text{E.7})$$

where A_i is the ambipolar forced diffusion flux:

$$A_i = \left(\frac{1}{q_e \rho_e} \right) \left[M_i q_i \rho_i \tilde{D}_i - f_i \sum_{j \neq e} M_j q_j \rho_j \tilde{D}_j \right] \nabla c_e, \quad (\text{E.8})$$

c is mole-fraction, f is mass-fraction and q is charge. The effective mixture diffusion coefficients \tilde{D}_i for heavy-particle are calculated via the Wilke [243] mixing rule:

$$\tilde{D}_i = \frac{1 - x_i}{\sum_{j=1}^{N_{\text{species}}} \frac{x_i}{D_{ij}}} . \quad (\text{E.9})$$

where D_{ij} are the binary diffusion coefficients.

F

Parametric study of freestream conditions for the subscale Hayabusa model

The freestream conditions for the simulation of the subscale Hayabusa model in § 8.3.3 were calculated using the simplified modelling strategy described in § 8.2.2. Due to the approximations made in this calculation, the possibility exists that the actual freestream conditions deviate somewhat from the calculated freestream conditions. Furthermore, significant shot-to-shot variation (up to $\pm 5.6\%$ variation in secondary shock speed) was observed in the campaign. It is therefore useful to observe how the radiating shock layer formed over the subscale model changes in response to variations in the freestream conditions. As such a parametric study involves collating many solutions, axisymmetric simulations are impractical, and the one-dimensional post-shock relaxation solver Poshax3 (see § 5) has been used to quickly obtain solutions representative of the stagnation streamline. Exactly the same physical models are implemented as for the Eilmer3 simulations (see Table 5.2).

A comparison of temperature and species number density profiles from Poshax3 and Eilmer3 simulations are presented in Figures F.1a and F.1b, where the Eilmer3 profile has been extracted from the stagnation streamline. Both solutions are from radiatively *uncoupled* solutions. While there are some slight discrepancies due to the inherent differences between the two sets of governing equations (see § 7.7.2), the Poshax3 solution is seen to be a good representation of the Eilmer3 solution. In the analysis that follow, the radiation intensity in the middle of the shock

layer at $x = 0.75$ mm will be calculated from the Poshax3 solutions. From the Eilmer3 solutions, the width of the shock layer observed by the spectrometer at 0.75 mm from the shock front is approximately 10 mm – the radiation intensity will therefore be calculated by assuming the $x = 0.75$ mm flow state extends for 10 mm in the line-of-sight direction. Although this is not ideal as it does account for the curvature of the shock, it is sufficient for observing the *relative* change in the radiation due to variations in the freestream conditions.

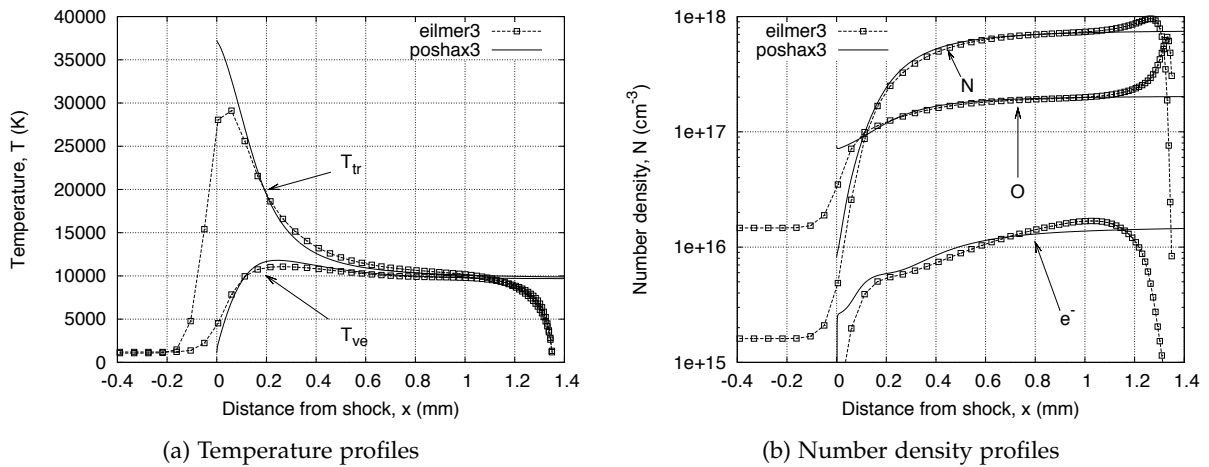


Figure F.1: Comparison of stagnation line profiles for the subscale Hayabusa shock layer calculated with Eilmer3 and Poshax3.

Figure F.2 presents the results of the parametric study. The critical parameters selected for variation are freestream velocity, Figure F.2a, density, Figure F.2b, temperature (where it is assumed $T_{tr} = T_{ve}$), Figure F.2c, and N_2 mass-fraction, Figure F.2d. The nominal levels for each parameter (taken from Table 8.2) are indicated by the label 'Nom.'. Velocity has been studied in the range 8.2 to 10 km/s based on the $\pm 5.6\%$ maximum observed shot-to-shot variation in secondary shock speed, and the ± 0.2 km/s uncertainty in the experimental measurement. The response of both UV and IR radiation to velocity is highly non-linear, with both increasing with velocity over most of the studied range (UV shows a minimum at 8.75 km/s). UV radiation varies between 28% below and 218% above the nominal level calculated at 9.12 km/s, while IR radiation varies between 38% below and 125% above the nominal level. Density has been studied in the range 1.40 to 2.05 g/m³ based on the ± 0.3 g/m³ uncertainty in the freestream calculation. While IR radiation varies linearly with density, the trend in the UV is nonlinear with a minimum at 1.8 g/m³. UV radiation varies between 1% below and 18% above the nominal level calculated at 1.73 g/m³, while IR radiation varies between 27% below and 33% above the nominal level. Temperature has been studied in the range 500 to 2000 K based on the range of freestream temperatures obtained using other facility modelling techniques for similar conditions (see References [221, 245]). The response in radiation to temperature is almost linear, with UV radiation varying by 8% below

and 33% above the nominal level at 1069 K, and IR varying by 4% below and 8% above the nominal level. Finally, the N₂ mass-fraction has been studied over the entire possible range (complete dissociation to complete recombination). UV radiation varies significantly over this range, with an increase of 1200% at complete dissociation from the nominal level calculated at 74.6% N₂, and a decrease of 13% at complete recombination. Conversely, IR radiation only increases by 33% at complete dissociation, and decreases by 2% at complete recombination.

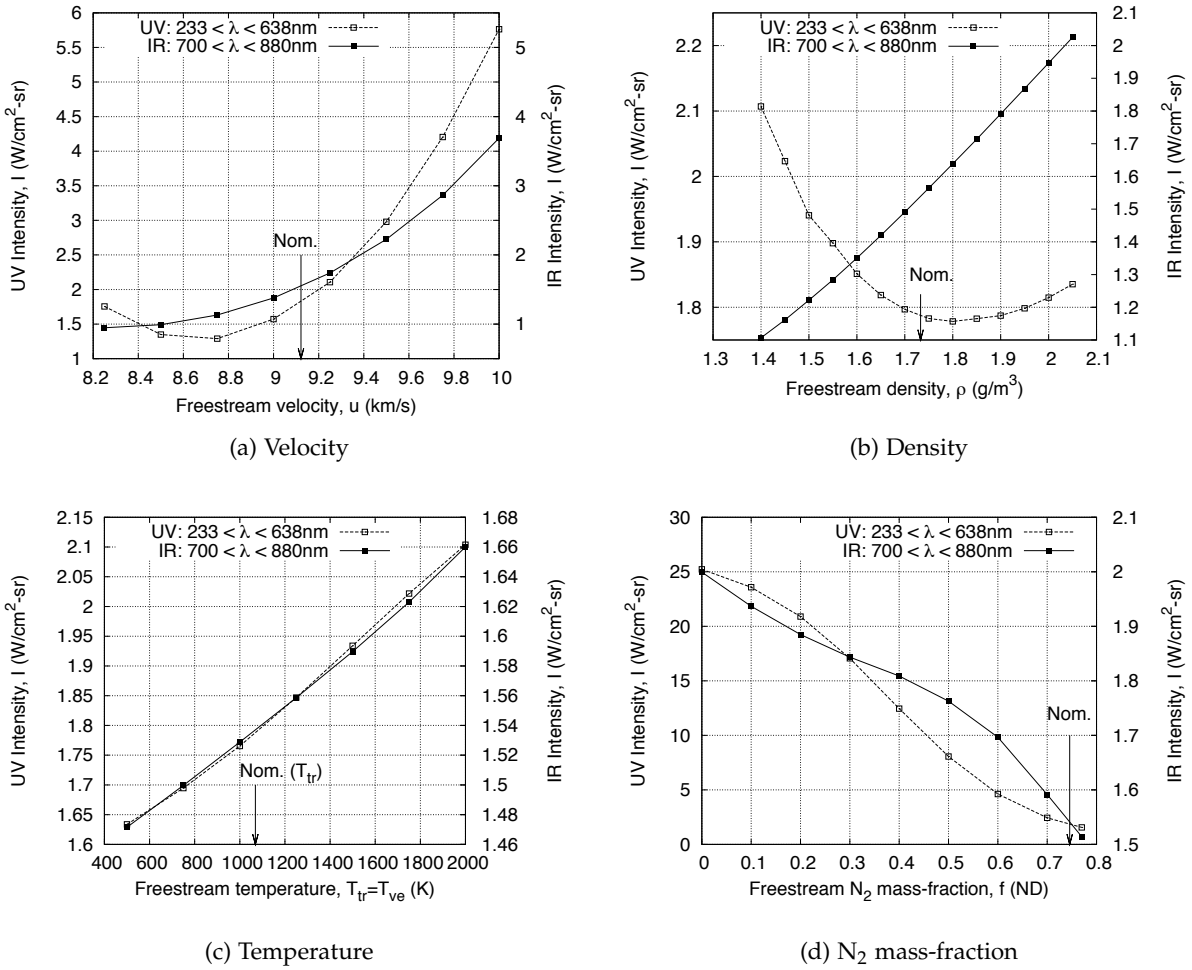


Figure F.2: Effect of freestream property variation on UV and IR radiation intensity at $x = 0.75$ mm from Poshax3 simulations of the subscale Hayabusa stagnation streamline shock relaxation.

Another freestream parameter worth investigating is carbon contamination, as the measured UV spectra in Figure 8.27b show strong CN Violet emission. For this analysis the physical models for CO₂-N₂ mixtures described in Table 5.4 are implemented, however the rate controlling temperature for dissociation is changed to $T_f = T_{tr}^{0.7} T_{ve}^{0.3}$ for consistency with the previous calculations. Also, reactions present in the N₂-O₂ scheme (see Table C.1) but absent from the CO₂-N₂

scheme (see Table C.2) have been included, and N_2 and N_2^+ radiation is calculated by applying the QSS models described in Appendix D. In the study, the freestream atomic carbon mass-fraction is varied between 0 and 10%. If it is assumed the presence of carbon is due to the vaporisation products of the secondary diaphragm entering the test gas, a carbon contamination level of 10% is entirely possible based on the relative masses of the test gas and secondary diaphragms:

$$\frac{m_{\text{diaphragm}}}{m_{\text{test gas}}} = \frac{\rho_{\text{Mylar}} \Delta x_{\text{diaphragm}} \pi r_{\text{tube}}^2}{\rho_{\text{test gas}} L_{\text{tube}} \pi r_{\text{tube}}^2} = \frac{\rho_{\text{Mylar}} \Delta x_{\text{diaphragm}}}{\rho_{\text{test gas}} L_{\text{tube}}} \approx 0.14 \quad (\text{F.1})$$

where ‘tube’ refers to the shock tube where the test gas initially resides, and $\rho_{\text{test gas}}$ is the initial test gas density. Figure F.3 presents the results of the carbon contamination study. While IR radiation is reduced by 9% due to 10% carbon contamination, UV radiation is increased by 1000%. The reduction in IR radiation is likely to be due to nitrogen and oxygen atoms being taken up in reactions with carbon atoms, and the increase in UV radiation is due to the formation of CN. Figure F.4 compares the UV spectra at $x = 0.75$ mm from the Poshax3 calculations considering 0%, 2% and 4% carbon contamination with the measured spectra from shot x2s1258. It is observed that with as low as 2% carbon contamination the N_2^+ First Negative system is almost completely covered over by the CN Violet system, and the calculated UV spectra begins to look similar to that measured in the experiment.

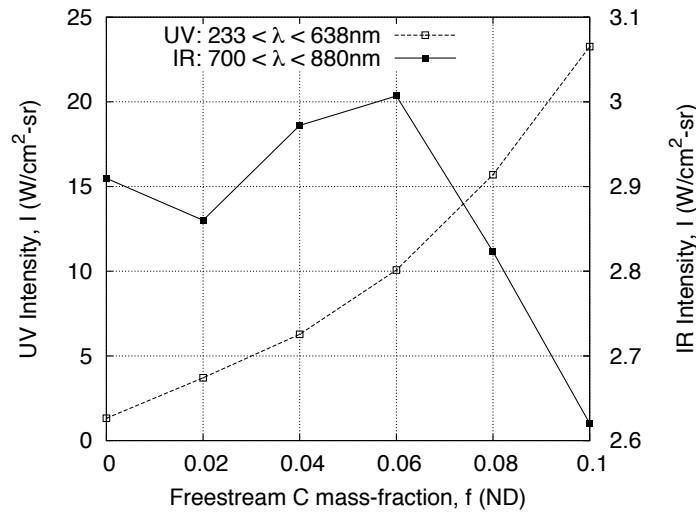


Figure F.3: Effect of freestream carbon contamination on UV and IR radiation intensity at $x = 0.75$ mm from Poshax3 simulations of the subscale Hayabusa stagnation streamline shock relaxation.

The results of this study have a number of implications for the overestimation of N_2^+ First Negative radiation in § 8.3.3 (see Figures 8.26 and 8.27). Firstly, the maximum decrease in UV radiation found in this study was 28% due to velocity variation – however, for the calculated level of N_2^+ First Negative radiation in Figure 8.27 to be in agreement with the measured spectra, it

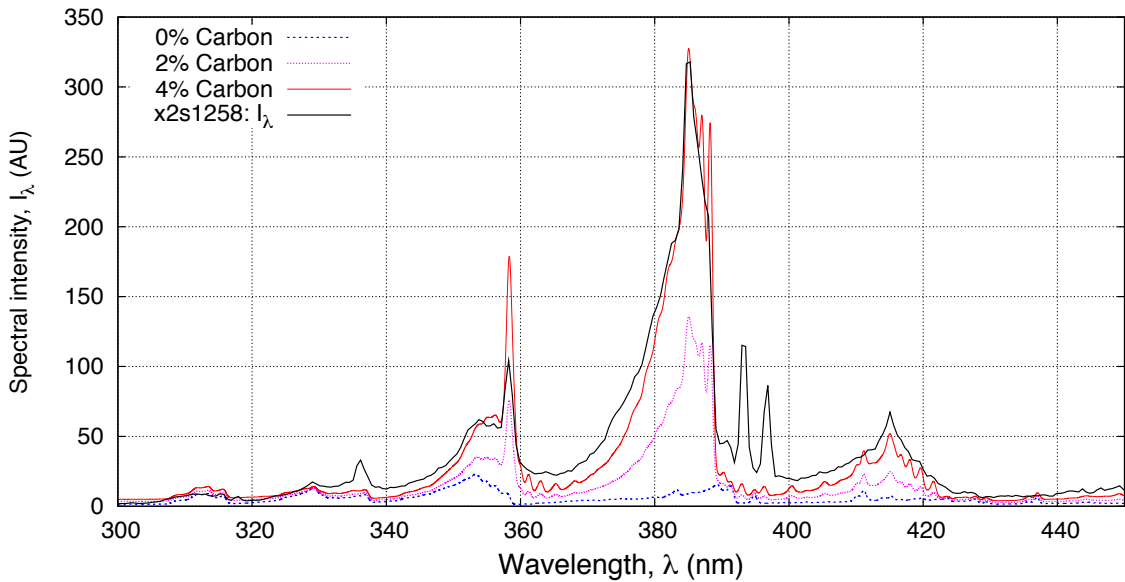


Figure F.4: Comparison of calculated (Poshax3) and measured (x2s1258) UV spectra at 0.75 mm from the shock front for the subscale Hayabusa experiment.

would have to decrease by at least an order-of-magnitude or 90%. This suggests that errors in the freestream conditions are not likely to be responsible for the overestimation of N_2^+ First Negative radiation. Secondly, it was found that with as low as 2% carbon contamination the N_2^+ First Negative system is almost completely covered over by the CN Violet system. A plausible explanation for the overestimation of N_2^+ First Negative radiation is therefore that the measured UV spectra are incorrectly calibrated, and the CN Violet intensity is at least an order-of-magnitude stronger than shown in Figure 8.27. This does not preclude the possibility that errors in the freestream conditions are contributing to the observed difference between calculation and measurements, however.